FACULTY OF MATHEMATICAL, PHYSICAL AND NATURAL SCIENCES

Department of Earth Sciences

PhD in Earth Sciences - XXXV Cycle

Hydrogeological and hydrogeochemical monitoring to identify "hydrosensitive sites" in central-southern Italy

Tutor

Prof. Marco Petitta

PhD student

Francesca Gori

Co-tutors

Prof. Carlo Doglioni

Dr. Marino Domenico Barberio

Index

Monitoraggio idrogeologico e idrogeochimico per individuare siti "idrosensibili" in Italia centro-meridionale

Riassunto

In aree tettonicamente attive, lo studio sistematico delle acque sotterranee ha permesso di osservare variazioni nella chimica e nella circolazione idrica sotterranea potenzialmente legata allo scatenarsi di forti terremoti. Numerosi studi hanno infatti evidenziato la sensibilità dei fluidi in relazione ai complessi equilibri tensionali che si creano durante il ciclo sismico nelle porzioni più superficiali della crosta terrestre. Sono stati ampiamente documentati per esempio cambiamenti nelle portate delle sorgenti, nei livelli piezometrici, nella composizione geochimica e isotopica delle acque e dei gas. Nel corso degli anni, in letteratura sono stati proposti vari meccanismi per spiegare come queste risposte idrogeologiche e idrogeochimiche possano essere il risultato di variazioni della permeabilità crostale e del mixing tra fluidi superficiali e fluidi profondi in risalita lungo le discontinuità tettoniche. Per tale motivo, risulta essenziale non solo studiare il comportamento degli acquiferi superficiali ma anche il contributo apportato dai fluidi profondi in grado di alterarne il chimismo con formazione di nuovi equilibri idrogeochimici. Pertanto, la definizione dell'origine dei fluidi e dei possibili processi di interazione acqua-gas-roccia durante la loro migrazione verso l'alto, può fornire nuove indicazioni per la comprensione dei processi sismogenetici. In molti paesi del mondo è già stata realizzata o è attualmente in corso la realizzazione di reti idrogeochimiche al fine di identificare le risposte ai terremoti e alla risalita di fluidi profondi. Gli sforzi scientifici si stanno ora muovendo in questa direzione per ottenere più osservazioni e costruire modelli idrogeochimici affidabili associati a diversi contesti geotettonici.

Sulla scia di questo filone di ricerca, si inserisce questa tesi di Dottorato il cui scopo è quello di compiere un passo in avanti nella comprensione dell'*Idrosensibilità*. Tale termine indica la capacità di un sistema acquifero di rispondere a perturbazioni naturali esterne (terremoti, mixing tra acque a diverso chimismo e interazione con fluidi profondi). Dunque, questo studio ha sostanzialmente il duplice scopo di (i) identificare potenziali cambiamenti idrogeologici e idrogeochimici nelle acque sotterranee e nei gas indotti dai terremoti (relazione diretta acqua sotterranea-sismicità) e (ii) analizzare approfonditamente il mixing di fluidi profondi in sistemi acquiferi regionali superficiali in aree sismicamente attive.

Partendo dall'adozione di un modello fisico concettuale che descrive il comportamento degli strati più superficiali della crosta terrestre (Doglioni et al., 2014), è stato possibile individuare potenziali criteri geologico-strutturali e idrogeologici in grado di definire le migliori condizioni per il

raggiungimento degli obiettivi prefissati. Tali criteri hanno permesso dunque di contestualizzare il monitoraggio e di scegliere due differenti approcci per ciascuno scopo.

Sulla base delle caratteristiche idrogeologiche e geologico-strutturali, è stato scelto di sottoporre a monitoraggio l'Appennino centro-meridionale che rappresenta una delle aree a maggiore pericolosità sismica, caratterizzata da una sismicità storica e attuale significativa sia in termini di intensità che di frequenza di terremoti. Nel dettaglio sono stati selezionati dei siti di monitoraggio nell'area del Matese, Contursi, Sulmona e San Vittorino.

Attraverso un'analisi sistematica e comparata dei parametri idrogeologici e idrogeochimici potenzialmente influenzati dall'attività sismica, è stato condotto un monitoraggio a lungo termine volto a verificare e comprendere l'esistenza di un rapporto diretto causa-effetto tra i segnali sismici e quelli idrogeologici-idrogeochimici nell'area del Matese e di Sulmona. D'altro canto, presso l'area di Contursi e di San Vittorino, è stata realizzata una caratterizzazione idrogeochimica e isotopica di numerose sorgenti, contraddistinte da composizioni idro- e gas-geochimiche molto differenti, al fine di definire i processi di interazione acqua-gas-roccia, i tempi di residenza delle acque sotterranee e i loro percorsi. L'interpretazione di quest'ultimi è stata possibile attraverso la costruzione di sezioni geologiche.

Nel complesso, i risultati di questo studio confermano il grande potenziale del monitoraggio idrogeologico e idrogeochimico (discreto e continuo) per identificare variazioni indotte dalla sismicità anche per terremoti di magnitudo medio-piccola, laddove il contributo dei fluidi profondi è evidente. Infatti, nonostante l'assenza di forti eventi sismici durante il periodo di monitoraggio, sono stati individuati significativi segnali idrogeochimici presismici nelle acque della sorgente di Grassano (area del Matese) in relazione allo sciame sismico di Benevento, il cui evento più forte è stato registrato a San Leucio del Sannio il 16 dicembre 2019 con una magnitudo pari a 3.9. Nel dettaglio, a partire da cinque mesi prima del mainshock è stato registrato un aumento della CO_2 disciolta e un abbassamento del pH. Inoltre, in corrispondenza della sequenza sismica, sono stati rilevati valori anomali nella concentrazione degli ioni maggiori (Ca^{2+}, Na^+, HCO_3^-), con un lieve aumento della conducibilità elettrica. Tali variazioni idrogeochimiche sono state attribuite a processi di dilatazione crostale presismica che avrebbero permesso alla CO_2 profonda di risalire verso la superficie e mescolarsi con le acque di Grassano, causando un aumento della solubilità ionica. I risultati ottenuti hanno messo in luce la possibilità di avere potenziali segnali presismici simili a quelli ipotizzati per la forte sequenza sismica di Amatrice-Norcia del 2016 (Barberio et al., 2017) anche per terremoti di piccola-media magnitudo. Tuttavia, il rapporto falda-sismicità è

stato approfondito non solo dall'elaborazione dei dati registrati e raccolti attivamente nel corso dei tre anni di ricerca ma anche dal processamento di dati precedenti provenienti dall'area del Matese e di Sulmona. Il monitoraggio gas-geochimico del radon ha evidenziato significativi incrementi del gas disciolto nelle acque di due sorgenti prima di tre eventi sismici (terremoto di Balsorano M_w 4.4, 2019; terremoto de L'Aquila M_w 3.8, 2018; terremoto di San Leucio del Sannio M_w 3.9, 2019). Il comportamento sensibile del Rn in relazione ai processi di deformazione crostale può essere spiegato come il risultato della dilatazione del corpo acquifero che ha causato variazioni nel flusso del gas. Inoltre, l'analisi dei dati piezometrici nell'area di Sulmona presso il pozzo di monitoraggio PF60.3 ha consentito di distinguere impulsive fluttuazioni post-sismiche del livello piezometrico legate al passaggio delle onde sismiche di Rayleigh derivanti da terremoti lontani (fino a 18.000 km). Le risposte idrogeologiche registrate hanno evidenziato ancora una volta la potenziale sensibilità degli acquiferi fratturati alla variazione stato tensionale.

I risultati esposti sono stati oggetto delle seguenti tre pubblicazioni su riviste scientifiche internazionali: *Hydrogeochemical changes before and during the 2019 Benevento seismic swarm in central-southern Italy* - Journal of Hydrology; *Optimization of dissolved Radon monitoring in groundwater to contribute to the evaluation of the seismic activity: an experience in central-southern Ital*y - SN Applied Sciences; *New observations in Central Italy of groundwater responses to the worldwide seismicity* - Scientific Reports.

Infine, questo lavoro conferma che l'idrogeochimica delle acque sotterranee è un potente strumento per valutare il mixing dei fluidi e i processi correlati ad esso in aree sismiche, dove le faglie normali profonde potrebbero rappresentare vie preferenziali di risalita a elevata permeabilità. In dettaglio, nell'area Contursi sono stati definiti percorsi più lunghi e complessi per le acque sotterranee termali "contaminate" da fluidi profondi in risalita altamente mineralizzati, e sistemi di circolazione idrica locale per le acque fredde alimentate dagli acquiferi carbonatici regionali. Inoltre, i risultati idrogeochimici sono in linea con recenti studi geofisici condotti in questo settore appenninico che documentano la presenza di un ingente volume di fluidi profondi al di sotto dell'area di studio. Poiché studi pregressi riconoscono la presenza di fluidi profondi in sovrappressione come meccanismo di attivazione dei terremoti, un'indagine multiparametrica idrogeochimica a lungo termine e ad alta frequenza potrebbe essere una chiave per riconoscere variazioni significative nel rapporto di mixing tra acque superficiali e fluidi profondi durante il ciclo sismico. Nella piana di San Vittorino, l'indagine degli elementi in traccia delle acque sotterranee ha chiarito i processi di interazione acqua-roccia, supportando il modello concettuale basato sulla risalita localizzata di fluidi profondi lungo le faglie ad alto angolo. L'analisi degli

isotopi dei gas ha confermato la presenza di una componente profonda con possibili tracce di elio mantellico. I calcoli geotermometrici hanno consentito di definire le profondità di risalita dei fluidi profondi compatibili con quelle ipocentrali dei terremoti in Appennino. Anche in questo caso, conoscere il grado di mixing delle diverse sorgenti, modulato dall'attività delle faglie, è fondamentale per poter fare considerazioni ed elaborazioni relativamente alle deformazioni crostali e alla sismicità.

I risultati descritti sono stati oggetto di due articoli scientifici, di cui uno pubblicato sulla rivista Journal of Hydrology, dal titolo *Hydrogeochemical multi-component approach to assess fluids upwelling and mixing in shallow carbonate-evaporitic aquifers (Contursi area, southern Apennines, Italy*; il secondo pubblicato su Applied Sciences, intitolato *Understanding the origin and mixing of deep fluids in shallow aquifers and possible implications for crustal deformation studies: San Vittorino plain, Central Apennines*.

Abstract

In the last decades, groundwater and gas responses to seismicity have been widely documented in tectonically active regions. Many studies have highlighted the sensitivity of fluid behaviour related to the seismic activity both in terms of hydrogeological and hydrogeochemical anomalies. For instance, variations, including changes in spring discharge, groundwater level, geochemical content, isotope composition, dissolved and free gases have been observed in sensitive monitoring sites at different distances from epicentres. Through the years, various mechanisms have been proposed in the literature to explain groundwater level and discharge changes such as pore-pressure response to crustal elastic strain, permeability changes caused by seismic waves, and fluid migration along dilatant cracks or deep crustal fractures. Besides, variations in geochemistry and isotopic signature of groundwater have been also defined as the results of the following processes: rock weathering enhancement in new rupturing, mixing of waters from different aquifers, deep and hydrothermal fluid upwelling. Therefore, monitoring deep fluids contribution to shallow aquifer systems has been abundantly used for studies devoted to the understanding of the seismicity-groundwater relationship. Besides, defining fluids origin and possible water-gas-rock interaction processes during their upward migration can provide new constraints aimed at the comprehension of the seismogenic processes. In many countries all over the world, the set-up of hydrogeochemical networks has been already established or is currently in progress in order to identify responses induced by earthquakes and ascending deep fluids. Scientific efforts are now moving in this direction to obtain more observations and to build up reliable hydrogeochemical models associated with different geo-tectonic contexts. The aim of this PhD research activity is to take a step forward for the improvement of the comprehension of the aspect named *Hydrosensitivity* which is the "ability of a hydrogeological system to respond to external perturbations (e.g., earthquakes, groundwater mixing, interaction with deep fluids, etc.) to be further correlated with crustal deformation processes and consequently with micro- and macro-seismicity". In detail, this study has the dual purpose of (i) identifying potential earthquake-induced groundwater and gas changes (i.e., direct groundwater-seismicity relationship), and (ii) analysing in-depth mixing of deep fluids in shallow regional aquifer systems in active seismic areas. To achieve these objectives, by considering hydrogeological and seismological features, monitoring sites in the central-southern Apennines were selected (i.e., Matese, Contursi, Sulmona areas, and San Vittorino plain) for monitoring geofluids as markers of active seismogenic processes. Two different approaches were adopted (i) long-term hydrogeological and hydrogeochemical monitoring was carried out with the seismic characterization of the study area

for the detection of groundwater and gas variations related to the seismicity, (ii) complete hydrogeochemical characterization of groundwater to define shallow and deep fluids flowpaths and their consequent mixing was realized through several elaborations. Overall, the results of this study confirm the great potential of having continuous hydrogeological and hydrogeochemical monitoring to identify variations induced by seismicity also related to the occurrence of small-intermediate earthquake magnitude, at least in the areas where deep fluids contribution to groundwater is evident. In fact, despite the absence of strong seismic events during the monitoring period, significant presismic hydrogeochemical signals, possibly linked to seismic activity, were identified at Grassano spring (Matese area). In particular, observed changes were referred to the Benevento seismic swarm, whose strongest event was recorded in San Leucio del Sannio on December 16th, 2019 with a magnitude of 3.9. In detail, starting from three months before the mainshock, an increase in dissolved CO_2 and a lowering of pH were recorded. Furthermore, in conjunction with the seismic sequence, anomalous values of major ions (Ca^{2+}, Na^+, HCO_3^-) were detected, with a slight increase of the electrical conductivity. These hydrogeochemical variations were attributed to presismic crustal dilation processes that could allow the upwelling of deep CO_2 with the Grassano groundwater, enhancing the ion solubility. The results highlighted the possibility of having potential presismic signals similar to those proposed in literature for the stronger seismic sequence of 2016-2017 Amatrice-Norcia, even for small-intermediate magnitude earthquakes. However, the groundwater-seismicity relationship was deepened not only by processing of data actively collected during the three years of research but also by analyzing previous data from the Matese and Sulmona area. Gas-geochemical monitoring of radon gas showed significant increases in dissolved gas activity in two springs before three seismic events (Balsorano earthquake M_w 4.4, 2019; L'Aquila earthquake M_w 3.8, 2018; San Leucio del Sannio earthquake M_w 3.9, 2019). The sensitive behaviour of Rn in relation to crustal deformation processes can be explained as the result of the dilation of the rocks-bearing aquifer which is expected to drive some changes in the chemical content of groundwater. Furthermore, the analysis of the piezometric data measured at the PF60.3 monitoring well in the Sulmona area allowed to distinguish impulsive post-seismic fluctuations in the piezometric level due to the passage of Rayleigh seismic waves deriving from distant earthquakes (up to 18.000 km). The hydrogeological responses highlighted the potential sensitivity of the fractured aquifers to the stress variation. Additionally, this study highlights once again that the acquisition of long-term hydrogeochemical time series (both discrete and continuous) is a powerful tool for analysing mixing and related processes in active seismic areas, where deep-seated normal faults could represent preferential pathways for the upward migration of fluids due to their high permeability. In detail, in the

Contursi area, longer and more complex flowpaths were defined for thermal groundwater mixed with highly mineralized rising deep fluids, while local groundwater flowpath were supposed for cold groundwater fed by regional carbonate aquifers. Furthermore, the hydrogeochemical results are in line with recent geophysical studies, conducted in this sector of the Apennines, which reported the presence of a large volume of deep CO_2-rich fluids below the study area. Since previous studies recognized the presence of deep overpressure fluids as a mechanism for triggering earthquakes, a long-term, high-frequency hydrogeochemical multiparametric monitoring could be a key to recognize significant variations in the mixing ratio between the shallow end-member and the deep one when earthquakes or energetic seismic sequences take place. Finally, in the San Vittorino plain, the investigation of groundwater trace elements occurrence clarified the water-rock interaction processes, supporting the conceptual model based on the localized uprising of deep fluids which matched the distribution of high-angle faults. The analysis of gas isotopes confirmed the presence of a deep contribution with possible traces of mantle-derived helium. Through the geothermal calculations, fluids depths were estimated where Apennine earthquakes usually occur. Also in this case, knowing the degree of mixing of the different sources, modulated by the fault activity, is essential in order to make considerations and processing relating to crustal deformations and seismicity.

1. Introduction

1.1 Groundwater-seismicity relationship and deep fluids contribution to shallow aquifer systems

Earthquake-induced groundwater and gas responses have been documented in seismogenic areas worldwide (Wakita, 1975; Muir-Wood and King, 1993; King et al., 2006; Manga and Wang, 2015; Wang and Manga, 2021). Several observations revealed the sensitivity of fluids related to pre-, co- and post-seismic phases (Esposito et al., 2001; Cicerone et al., 2009; Wang and Manga, 2010; Amoruso et al., 2011; Ingebritsen and Manga, 2014; Shi and Wang, 2014; Sano et al., 2016; Barberio et al., 2017; Onda et al., 2018; Boschetti et al., 2019; He and Singh, 2019; Nakawaga et al., 2019; Buttitta et al., 2020; Shi et al., 2020). Previous studies pointed out anomalies both in terms of hydrogeology and hydrogeochemistry (Roeloffs et al., 1997; King et al., 2000; Montgomery and Manga, 2003; Yan et al., 2014; Petitta et al., 2018; Kim et al., 2019; Hosono and Masaki, 2020; Lutzky et al., 2020; Sato et al., 2020; Wang and Manga, 2021). In detail, changes including spring discharge (Petitta et al., 2018; Mastrorillo et al., 2020), groundwater level and pressure (Kissin, 2007; De Luca et al., 2018; Kim et al., 2019; Hwang et al., 2020; Lan et al., 2021), geochemical ions content (Perez et al., 2008; Malakootian and Nouri, 2010; Wästeby et al. 2014; Skelton et al., 2019; Kim et al., 2020; Barberio et al., 2017; Barbieri et al., 2021), isotope composition (Skelton et al., 2014; Onda et al., 2018; Hosono et al., 2020), dissolved and free gases (Wakita, 1981; Igarashi et al. 1995; Caracausi and Paternoster, 2015; Kawabata et al., 2020; Buttitta et al., 2020) were recognized in sensitive monitoring sites at different distances from epicentres and for different magnitude ranges. However, a possible correlation was found between the distance at which geofluids anomalies were recorded and the magnitude of the seismic event they were related to (Martinelli et al., 2021). Besides, attempts to unify various hydrogeological responses into a coherent framework were carried out (Wang and Manga, 2010), by considering these two parameters (i.e., epicentral distance and earthquake magnitude) as the most relevant ones in controlling the occurrence of variations both in the near-field and in the far-field of seismicity (up to thousands of kilometres of epicentral distance; Manga and Wang, 2015).

International research teams argue that studying hydrogeological and hydrogeochemical earthquake-related effects is a promising target for seismic investigation. Indeed, in many countries all over the world (e.g., Italy, Iceland, Japan, China, Korea, and Turkey; Claesson et al., 2004; Grant et al., 2011; Huang et al., 2012; Inan et al., 2012; Shi et al., 2013; Orihara et al., 2014; Andren et al., 2016; Barberio et al., 2017; De Luca et al., 2018; Petitta et al., 2018; Skelton et al.,

2019; Li et al., 2019; Hosono and Masaki, 2020; Martinelli et al., 2021; Lee et al., 2021), the set-up of hydrogeochemical networks has been already established or is currently in progress to identify possible responses induced by seismic activity. Scientific efforts are now moving towards this direction to obtain more observations to build up and constrain hydrogeological and hydrogeochemical models associated with different geo-tectonic contexts.

For instance, several studies reported both transient and permanent changes in groundwater level of aquifers, as well as changes in water flow from springs, which are also relevant observations to understand the processes/mechanisms driving the changes (Adinolfi Falcone et al., 2012; Binda et al., 2020). Various mechanisms were proposed to explain groundwater level and discharge changes such as: pore-pressure response to crustal elastic strain (Wakita, 1975), permeability changes caused by the passage of seismic waves (Elkhoury et al., 2006), fluid migration along dilatant cracks or deep crustal fractures (Tsunogai and Wakita, 1995), and co-seismic gas bubble development (Crews and Cooper, 2014). Depending on the mechanism involved, the temporal pattern of hydrogeological variation can vary significantly and, hence, can be symptomatic of a specific geological situation. Besides, variations in hydrogeochemistry and isotopic signature of groundwater were also defined as the results of the following processes: deep and hydrothermal fluid upwelling (Barberio et al., 2017; Hosono et al., 2018; Boschetti et al., 2019; Barbieri et al., 2020) along tectonic discontinuities, mixing of groundwater from different aquifers, and rock weathering enhancement in new rupturing (Claesson et al., 2004).

Therefore, monitoring deep fluids contribution to shallow aquifer systems has been abundantly used for studies devoted to the understanding of the seismicity-groundwater relationship (Toutain and Baubron, 1999; Chiodini et al., 2011; Heinicke et al., 2011; Martini, 2016; Boschetti et al., 2019). In fact, it is reasonable to expect that transient physical phenomena affecting crustal structures in seismogenic processes may also produce perturbations in the circulation of deep fluids and gases (Scholz et al., 1973; Martinelli and Albarello, 1997). The flowpaths and geochemistry of deep hydrothermal fluids are affected by faults involved in earthquake nucleation over variable spatial scales, including microscale fractures in dilated rocks of individual faults and kilometre-scale fault displacements across the lithosphere (Scott et al., 2020; Li et al., 2022). Indeed, crustal degassing is observed to be strictly related with seismic activity. For the above-mentioned considerations, defining fluids origin and possible water-gas-rock interaction processes during their upward migration can provide new constraints aimed at the comprehension of seismogenic processes.

In detail, carbon dioxide (CO_2) emissions have been recognized to be possibly connected on a global scale with areas of intense tectonic activity and/or extensive seismicity (Barnes et al., 1978; Irwin and Barnes, 1980; Italiano et al., 2004; Tamburello et al., 2018; Martinelli et al., 2020). CO_2 plays an important role, especially for its presence in the saturated zone of the aquifers, derived either from deep sources, or from carbonate rock dissolution in the aquifer enhanced through earthquake processes (Binda et al., 2020). These sources of CO_2 can be distinguished by different carbon isotope signature which is considered a powerful tool to investigate the hydro- and gas-geochemical processes in seismically active areas. For example, in order to clarify why some springs showed effects from deep fluid interaction and mixing, carbon isotope ($\delta^{13}C$) was used to trace the deep CO_2 in central Italy (Chiodini et al., 2011; Barbieri et al., 2020). Additionally, spatio-temporal variations of minor and trace gases (e.g., He, Rn, Ar) and their isotopic ratios (e.g., $^3He/^4He$) can be used to evaluate mantle or crustal sources of the observed hydrogeochemical anomalies. Indeed, increases of the upwelling of deep fluids (crustal or mantle-derived) can occur presumably due to the development of higher permeability pathways along lithospheric active fault zones (Zhou et al., 2017). In central Italy as well, where active extensional faults and related seismicity occur, hydrogeochemical anomalies and pH changes have been detected four months before the onset of the Amatrice-Norcia seismic sequence (mainshock M_w 6.0 recorded on August 24th, 2016; Barberio et al., 2017). In detail, a strong increase in the concentrations of trace elements (e.g., As, V, Cr, Sr, and Fe) was observed from April 2016. This amount was associated with the inflow of deep fluids into the hydrogeological system. Also, for a similar case recorded in Iceland (Skelton et al., 2019), hydrogeochemical changes were recorded, likely in relation to the crustal dilation, one to ten weeks before an M_w 5.8 transtensional fault earthquake at about 90 km from the epicenter.

1.2 Conceptual model of fluids behaviour at crustal scale

Geoscience studies focusing on the relationship between fluids and crustal stress field variations are growing through the years (Sibson, 1992; Cox, 1995; Miller et al., 1996; Tenthorey et al., 2003; Micklethwaite and Cox, 2004; Doglioni et al., 2014; Barberio et al., 2017; Barbieri et al., 2020; Wang and Manga, 2021).

Observations of many earthquakes show that, prior to the seismic events, the ratio of seismic velocities Vp/Vs decreased to anomalously low values. Since the 1970s, some scientists (Aggarwal et al., 1973; Nur, 1972) put forward a model that would explain this phenomenon. The model is

based on laboratory fracture studies which show that rock undergoes an inelastic volumetric increase prior to failure. This phenomenon is known as *dilatancy* which is produced by the formation and propagation of cracks within the rock and the diffusion of fluids through the volume of rock in the earthquake source region (Scholz et al., 1973). Laboratory data also indicate that the observed Vp/Vs anomalies can be explained by the assumption that dilatancy precedes the earthquake (Nur and Simmons, 1969).

Moreover, many researchers recognized the dual role of fluids known as "fluids drive faulting" and "faulting drives fluids". In fact, they behave both "actively" and "passively" with respect to the fault mechanism (Sibson, 2000; Doglioni et al., 2014). The first mentioned case means that fluids can decrease fault strength, hence favouring the initial motion of the hangingwall. As pore pressure increases, they can cause the nucleation of the mainshock actively by triggering ruptures of asperities along the fault plane (Miller et al., 2004; Scuderi and Collettini, 2016; Scuderi et al., 2017). This aspect makes them crucial for the mechanics of fault behaviour and its periodic activation. Such changes in pore pressure can be responsible for the variations of groundwater level, chemical content, and deep endogenous fluid flux detected before the onset or during seismic events (Manga and Wang, 2015). However, fault planes may represent preferential conduits or even barriers for fluids whose diffusion in rock voids depends on geological factors, such as: texture, porosity, and connectivity among fractures that control the secondary permeability. Besides, fluids also play a relevant passive role (Tullis et al., 1996; Wannamaker et al., 2002). Indeed, when a variation in the stress state occurs, they are squeezed by pressure gradients and are transported according to the permeability of the crust (Salazar et al., 2002) which is one of the most important parameters controlling fluids behaviour (Wang and Manga, 2021).

A widely accepted geo-structural model proposed by Doglioni et al. (2014) considers a simplified two-layer crustal rheology: the ductile lower crust is characterized by a constant strain rate, whereas the brittle upper crust is characterized by episodic locking-unlocking behaviour (Figure 1.1). Based on this conceptual model, the authors explained the different behaviour of fluids as function of the tectonic setting (e.g., extensional, and compressional environments), where opposite kinematics and mechanical evolutions are generated. Between the two crustal levels, along the so-called "brittle-ductile transition" (hereafter BDT), the stress gradient is created and then released during the earthquake.
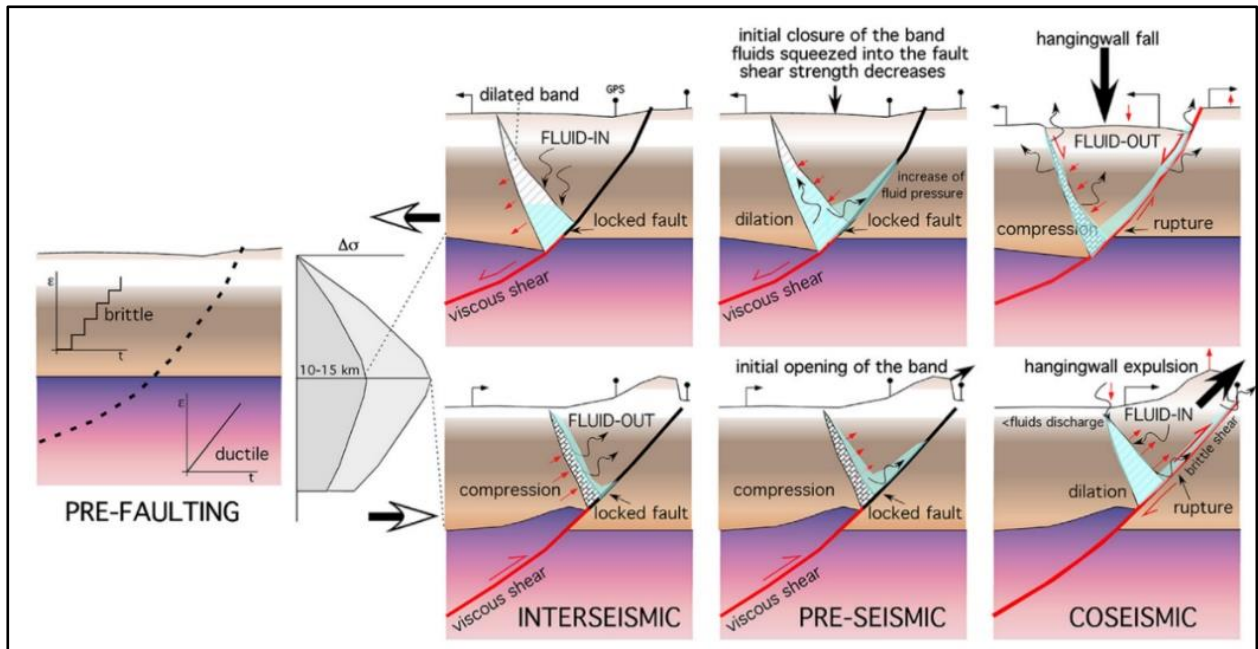
Figure 1.1. Conceptual model of fluid behaviour during interseismic, pre-seismic and coseismic period in case of extensional (top) and compressional (bottom) tectonics (Doglioni et al., 2014).

In the extensional tectonic setting, the triangle of crust above the BDT remains "suspended" while a dilated area forms during the interseismic period (Figure 1.1). This condition allows fluids to enter in the fractured volume and they decrease fault strength causing the beginning of the hangingwall collapse. From a hydrogeological standpoint, it means that during the interseismic period the permeability increases with a consequent decrease in groundwater level. When the triangle of crust above the BDT starts to drop in the pre-seismic period, fractures close and groundwater level starts to rise. This increase culminates in the coseismic period. On the contrary, in the compressional environment, during the interseismic period, along a thrust fault an over-compressed band separates the ductile shear from the overlying locked fault segment. The hangingwall is eventually expelled during the coseismic period (Figure 1.1). For instance, the opposite signs of fluid discharge (i.e., positive, and negative during the coseismic period), were observed along normal faults and thrusts, respectively (Muir-Wood and King, 1993; Jónsson et al., 2003). It has also been demonstrated that the size of groundwater oscillations in a specific well is related to the magnitude of earthquake, and its epicentral distance from the monitoring well (Roeloffs, 1998; Weingarten and Ge, 2014).
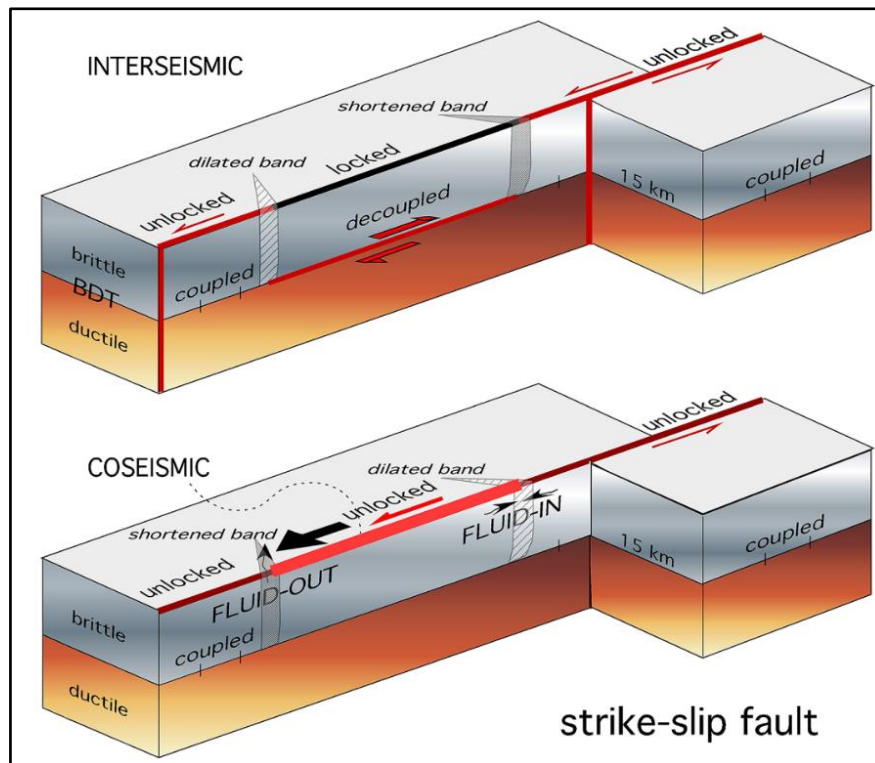
Figure 1.2. Conceptual model of fluid behaviour during interseismic, and coseismic period for an ideal strike-slip fault crossing the BDT (Doglioni et al., 2014).

An interseismic and coseismic model for an ideal strike-slip fault crossing the BDT was also proposed by Doglioni et al. 2014. Strike-slip faults may have coexisting, locked and unlocked (creeping) segments. Along the locked brittle part, basal shear with the ductile lower crust is inferred, and two bands with opposite evolution (i.e., tension and shortening) form at the tip points of the inactive part of the fault. Along the unlocked part, the brittle layer rather moves coherently with the deeper ductile layer. During the coseismic stage, the locked fault moves instantaneously, temporarily reversing the strain in the two bands, i.e., the dilated band is shortened, and the overcompressed band is however rather dilated. This condition means that, during the coseismic stage, fluids are squeezed out in the shortened band, and the opposite behaviour is expected along the dilated band (Figure 1.2). Also, strike-slip earthquakes caused at the same time both uplift and decrease of the groundwater level. For instance, the activated segments of right-lateral strike-slip faults during the 2000 M_w 6.5 seismic events in Iceland, were associated to the coseismic upraise and falling at the two tip lines, followed by opposite trends during post-seismic relaxation (Jónsson et al., 2003).

In this complex hydro-geostructural framework, the upwelling of deep-seated fluids in the shallow crust must be considered too (Chiodini et al., 1995; Italiano et al., 2000). They derive from deeper portions of the lithosphere (e.g., deep crust and/or upper mantle) and are generally characterized by high mineralization and abundance of gaseous content (e.g., chiefly CO_2, and CH_4, Rn, He, N_2, H_2, and H_2S). For example, in the Apennine context, the origin of CO_2 was explained as being the combination of both a mantle source and a product of thermometamorphic reactions within the buried Meso-Cenozoic limestone (Giustini et al., 2013). Deep fluids are often stored in overpressurized reservoirs, upper-confined by low permeability layers, which can be connected to the surface through lithospheric fault systems (Chiodini et al., 2004; Frondini, 2008; Trippetta et al., 2013; Smeraglia et al., 2020). In detail, areas undergoing extension are characterized by CO_2 emissions and a significant deep fluids contribution to groundwater is evident. According to many studies, extensional tectonic regimes in fact would play a key role in creating pathways for the uprising deep fluids, connecting the deep portion of crust to the earth surface (Tamburello et al., 2018; Lamberti et al., 2019). In these areas, where high CO_2 fluxes directly affect regional aquifer, most or part of the deeply generated gas can be dissolved by groundwater because of the relatively high solubility of CO_2 in water. To distinguish the different sources of inorganic carbon in groundwater, the following carbon mass balance in regional aquifers was proposed (Chiodini et al., 2000):

$$TDIC = Ccarb + Cext \quad (1)$$

$$Ccarb = Ca + Mg - SO_4 \quad (2)$$

$$Cext = CTDIC - Ccarb = Cinf + Cdeep \quad (3)$$

TDIC includes the total dissolved inorganic carbon in groundwater, whose origin is ascribable to the presence of different sources of carbon. Indeed, it corresponds to the sum of two components (see Eq. 1). Ccarb is the carbon derived from the water-rock interaction of groundwater with carbonate aquifers. Thus, the Eq. (2) considers the dissolution of calcite and dolomite, and the presence of anhydrite and/or gypsum too. Cext is the carbon derived from "external sources", expressed by the sum of two parameters (see Eq. 3): Cinf is the carbon from atmospheric and biogenic CO_2 (i.e., the infiltrating waters), and Cdeep is deep CO_2 from metamorphic, mantle, or magma sources (Chiodini et al., 2000; Chiodini et al., 2004). As highlighted in recent scientific papers, the progressive inflow of CO_2-rich deep fluids in shallow aquifers and, hence, the consequent mixing, can produce significant changes in groundwater hydrogeochemistry (Barberio et al., 2017; Boschetti et al., 2019; Barbieri et al., 2020).

1.3 Aim of the work

This PhD project aims to characterize hydrogeologically and hydrogeochemically springs in central-southern Apennines with the dual specific goal of (i) identifying potential earthquake-induced groundwater and gas changes (i.e., direct groundwater-seismicity relationship), and (ii) analysing in-depth mixing of deep fluids in shallow regional aquifer systems in active seismic areas. To achieve these objectives, two different approaches were adopted in the selected areas.

Long-term monitoring based on the collection of both discrete and continuous data has been carried out with the seismic characterization of the study area for the detection of groundwater and gas variations related to the seismic activity. In detail, hydrogeological and hydrogeochemical parameters potentially influenced by seismic activity (temperature, pH, electrical conductivity, chemical and isotopic composition of groundwater and dissolved gases) have been analyzed. Thus, the existence and modalities of a cause-effect relationship between the hydrogeological and hydrogeochemical signals with the seismic ones have been detected. This first approach was mainly used in the Matese area, selected within this research activity (whose geo-structural, hydrogeological setting will be in-depth described in Chapter 2), and in the Sulmona area, which is a pre-existing hydrogeological test site developed since 2014 to investigate the groundwater-seismicity relationship (Barberio, 2019). During my PhD activity, I had also the opportunity to analyse continuous data from this latter site and they will be displayed and commented in the Discussion section (see Chapter 5).

On the other hand, hydrogeochemical screenings of springs with different geochemical features have been executed. A complete characterization of the hydrogeochemistry of groundwater, also by determining groundwater-rock interaction, saturation indices, and fluids origin has been defined. Finally, the construction of detailed groundwater flowpaths, by defining mixing between deep and shallow fluids, has been realized through a multi-component approach characterized by several elaborations. This second approach was mainly applied in the Contursi area, selected within this research activity (whose geo-structural, seismo-tectonic and hydrogeological setting will be in-depth described in Chapter 2) and in the San Vittorino plain, where discrete hydrogeochemical and gas-geochemical data were collected before the onset of my PhD. To deepen both deep and meteoric fluid contributions to a regional groundwater circulation model in an active seismic area, also in this case, I had the opportunity to actively work on this latter dataset that will be presented in the Discussion section (see Chapter 5).

Therefore, this research study tries to take a step forward for the improvement of the comprehension of the aspect named *Hydrosensitivity*. This term refers to the "ability of a hydrogeological system to respond to external perturbations (e.g., earthquakes, groundwater mixing, interaction with deep fluids, etc.) to be further correlated with crustal deformation processes and, consequently, with micro- and macro-seismicity".

With the aim to answer the main scientific questions about the earthquake-hydrology and the mixing of deep and shallow fluids, the Hydrosensitivity will be treated in different works reported in the Discussion section which is structured according to a collection of papers organized into two main sections based on each specific goal.

I am the first author of two research articles treating the "core" areas of the PhD project. *"Hydrogeochemical changes before and during the 2019 Benevento seismic swarm in central-southern Italy"* deals groundwater-seismicity relationship, showing possible earthquake-induced effect on groundwater in the Matese area. *"Hydrogeochemical multi-component approach to assess fluids upwelling in shallow carbonate-evaporitic aquifers (Contursi area, southern Apennines, Italy)"* deals mixing processes in shallow carbonate aquifers in the Contursi area, by providing a model for groundwater flowpath and deep-seated fluids inflow through tectonic discontinuities. However, to reach the objectives and to corroborate my thesis, my research activity extended to other areas in central Italy (i.e., the Sulmona area and the San Vittorino Plain) by analyzing and processing retrieved unpublished data from pre-existing monitoring (both discrete and continuous). Thus, I actively worked on these areas, and, for this reason, I am the second author of other three research articles reported in the Discussion section.

Overall, these papers show promising results from ongoing hydrogeological and hydro- and gas-geochemical monitoring. Results obtained during the last three years highlighted the significance of the role of the integrated approach useful for improving groundwater monitoring aimed at identifying hydrogeological signals related to mixing with deep fluids potentially correlated with seismic activity in active tectonic areas.

2. Study area: Why Central-Southern Apennines?

2.1 Site selection

The first step in the building of a hydrogeochemical monitoring network is the proper site selection. With the aim of conducting the research in the best possible conditions, the effort was made to identify areas where two main features (i.e., seismological, and hydrogeological) were optimal to achieve the stated goals (Petitta et al., 2020). Starting from a conceptual physical model that describes the behavior of the shallow layers of the crust (Doglioni et al., 2014; Petricca et al., 2015), the attention was focused on areas presenting the highest earthquake occurrence probability (Slejko et al., 2010).

In detail, the following seismological-geodetical criteria were considered:

• Identification of areas characterized by high seismic hazard from the seismic hazard map (available online: http://zonesismiche.mi.ingv.it/mappa_ps_apr04/italia.html);

• Presence of regional tectonic discontinuities (DISS Working Group, 2021);

• Estimation of the maximum magnitude expected (Riguzzi et al., 2012; Doglioni et al., 2015);

• Paleo-seismological analysis (Pantosti et al., 1993; Galli and Naso, 2009);

• Interseismic GPS velocity field (Esposito et al., 2020);

• Distribution and magnitudes of both historical (i.e., CPTI15 version 4.0, Rovida et al., 2022) and instrumental seismicity of Italy (Latorre et al., 2023).

Concerning the hydrogeological-hydrogeochemical aspects, the main criteria are reported below:

• Availability of water resource and monitoring points;

• Knowledge of underground hydrodynamics;

• Regional representativeness of monitoring sites;

• Identification of areas potentially influenced by deep-seated circuits.

Thus, based on all these geological constraints, and on previous results documented in literature (Martinelli and Albarello, 1997; Barberio et al., 2017; Franchini et al., 2021; Martinelli and Tamburello, 2020), the central-southern Apennines were chosen. They represent a natural promising laboratory for monitoring geofluids as markers of crustal deformation and active seismogenic processes, owing to the great abundance of groundwater resources and the nature of the regional aquifers hosted by fractured Meso-Cenozoic carbonates that enhances the response to deep fluids uplift, allowing fast and concentrate changes in groundwater close to tectonic lines. Additionally, the intense seismic activity affecting this area confirms the relevance of the research to better understand the interactions between seismicity and hydrogeology.

In detail, this study mainly focused on surveys and monitoring (both discrete and continuous) conducted at the Matese, and the Contursi sites. However, in the Discussion section, data from other sites (Sulmona and San Vittorino plain) in central Italy have been processed and discussed aimed at achieving the objectives of this work. According to previous statistical studies, that subdivided the territory of Italy into different areas based on the probability of earthquakes occurrence (e.g., from medium to large magnitude), both the above-mentioned nodes are included in the areas as the ones with the highest probability of earthquake (with $M_w \geq 5.5$) occurrence in the near future (Cinti et al., 2004; Slejko et al., 2010). Furthermore, according to the classification of seismic hazard provided by the National Institute of Geophysics and Volcanology (INGV), they are in the "Zona 1" characterized by the highest seismic hazard (Figure 2.1) (http://zonesismiche.mi.ingv.it/class2004.html).
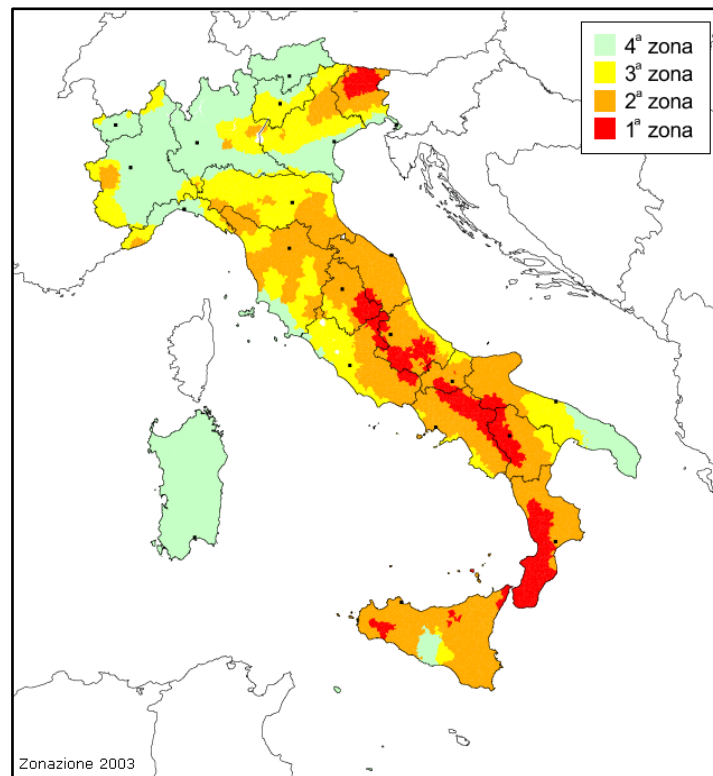
Figure 2.1. Classification of zones based on the seismic hazard in Italy (provided by INGV).

In fact, this sector of the Apennine chain is characterized by the presence of many active tectonic discontinuities (i.e., normal faults) in a regime of tensional stress chiefly NE-SW-oriented. Also, the Italian Database of the Main Seismogenic Sources (DISS Working Group, 2021), identified seismogenic sources in these areas (extensional faults in the NW-SE direction) capable of generating earthquakes with magnitude up to ~ 7. Consistently, Trippetta et al. (2019) identified faults whose seismological potential (maximum expected magnitude) is up to M_w 7.0. Paleoseismological evidence showed that the highest frequency for $6.5 \leq M_w \leq 7$ earthquakes belongs to these areas in the whole Italian peninsula for the past millennium (Chiarabba and Amato, 1997; Galli et al., 2008; Galli et al., 2017; Cinque et al., 2000). Indeed, the Matese area was struck by four strong earthquakes with a periodicity of about 100-150 years. The recent and strongest seismic sequence was recorded in December 2013 with the strongest event of M_w 4.9 (Chiarabba and Amato, 1997; D'Amico et al., 2014; Galli et al., 2017). The Contursi area falls within the epicentral zone of the M_w 6.9 Irpinia earthquake of 23rd November 1980 (Westaway & Jackson, 1987; Bernard and Zollo, 1989; Improta et al., 2003).

Once the seismological criteria were satisfied, hydrogeological and hydrogeochemical features of the two nodes were studied to confirm their selection. The chosen areas are characterized by great availability of water resource, since the wide carbonate ridge and/or massif can store huge volumes of groundwater, acting as the main aquifer systems (Fiorillo and Doglioni, 2010). Besides, deep fluids contributions are very evident: springs located along main tectonic lineaments are characterized by thermalism and intense degassing (Harabaglia et al., 2008; Italiano et al., 2000; Di Luccio et al., 2018; Vannoli et al., 2021).

Therefore, based on annual and seasonal flow rates, and hydro- and gas-geochemical parameters collected in literature data, springs in the two nodes were selected (Celico, 1978; Celico, 1979; Fiorillo, 2009; Cuoco et al., 2017). Sampled groundwater is addressed to many different uses due to the various hydrogeochemical properties. For instance, fresh springs directly fed by carbonate aquifers are tapped for drinking purposes, while the mineralized and thermal ones supply spas. In detail, four springs (named Capovolturno, Rio Freddo, Grassano, and Telese Terme) were selected in the Matese area for hydrogeological, hydrogeochemical and gas-geochemical long-term monitoring. Instead, twenty-two springs with different geochemical features (e.g., from low to high mineralization, abundant or absent degassing) were investigated in the Contursi area (Sele river valley). Once springs were selected, groundwater samples were collected aimed at the characterization of the main chemical-physical characteristics derived from water-rock interaction and potential mixing processes between deep and shallow fluids, and at the assessing the hydrogeochemical feasibility. For more in-depth information about the geodynamics, geo-structural and hydrogeological setting of the selected areas the reader is referred to the following paragraphs.

2.2 Geodynamic setting

The Mediterranean tectonic setting derived from the convergence between Africa and Eurasia plates which took place since the Late Cretaceous (80 Ma). The Mediterranean region underwent many deformation events occurred during two main phases of its geodynamic story (Doglioni et al., 1999). These lithospheric processes produced the current structural setting of the Apennine orogen. The first deformation stage, between the Cretaceous and the Oligocene, was characterized by the relative motion of the above-mentioned plates and the related subduction of the African lithosphere beneath the European one (Scandone, 1980; Doglioni, 1991; Faccenna et al., 2001). The second deformation stage, from the Tortonian age, led to the opening of the Tyrrhenian basin

and the eastward migration of the Apennines chain-foredeep-foreland system (Malinverno and Ryan, 1986; Doglioni, 1991; Patacca and Scandone, 2007). During an intense extensional process, new oceanic crust with a maximum thickness of 10 km was formed in the southern Tyrrhenian basin (Nicolich, 1989). For this reason, due to the different compositional properties between the oceanic Ionian lithosphere (subducting underneath the Calabrian Arc), and the Adriatic continental lithosphere (subducting underneath the central-southern Apennines), the subduction was considered irregular and asymmetrical (Lucente et al., 1999). The differences in composition and thickness of the Apenninic subducting slab are also recorded by the present seismicity (Carminati and Doglioni, 2012; Figure 2.2).
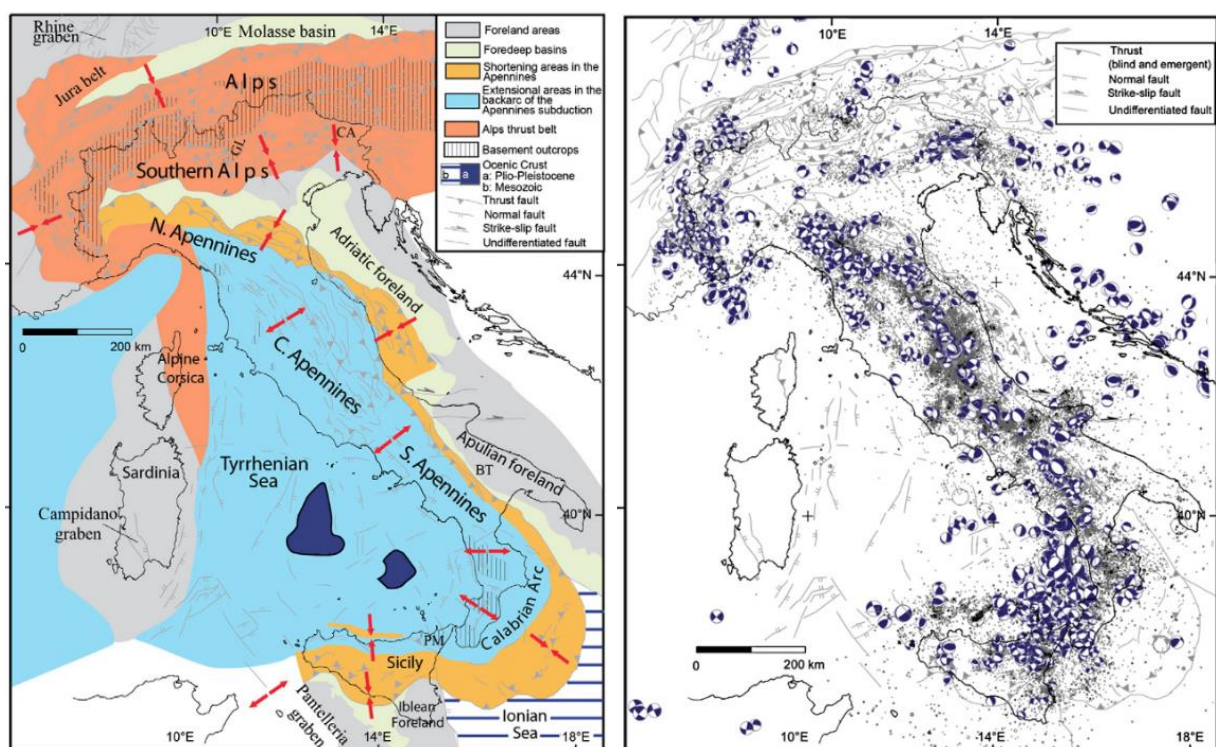

Figure 2.2. On the left, the tectonic map of Italy, showing the major tectonic and geodynamic settings. On the right, the map displays the earthquakes distribution and the CMT solutions (Pondrelli et al., 2006). Instrumental data between 1981 and 2001 are from Catalogo della Sismicità Italiana: http://csi.rm.ingv.it/; and between 2002 and 2010 are from Bollettino Sismico Italiano: http://bollettinosismico.rm.ingv.it and http://iside.rm.ingv.it/ (from Carminati and Doglioni, 2012).

Several studies indicate that at present the crustal extensional regime is seismogenic along the axis of the Apennine belt and it is responsible for most of the current seismicity (Montone et al., 2004). While the compressional regime is active along the eastern margin of the Apennines and the Western Adriatic Sea (Chiarabba et al., 2005).

The extension-compression couple migrated radially, northeastward in the northern Apennines, eastward in the central-southern Apennines, and southeastward in Calabria and Sicily with velocities of 1 to 3 cm/yr and was induced by the eastward retreat of the hinge of the Adriatic subducting slab (Carminati and Doglioni, 2012). Geodetic observations, together with seismological studies, reveal that the Apennine fold-and-thrust belt is undergoing a NE-trending extension, with seismic deformation rates higher in the southern portion (Di Luccio et al., 2005; D'Agostino et al., 2014).

The central-southern Apennines is in fact one of the most seismically active areas in Italy, and in recent centuries it was struck by earthquakes of magnitude $M_w > 6.5$. The study of the distribution of historical earthquakes (Rovida et al., 2022), and the analysis of the focal mechanisms (Mariucci and Montone, 2020; Ciaccio et al., 2021) allow obtaining useful information aimed at in-depth comprehension of the kinematics and active tectonics of the study area.

2.3 Geo-structural and seismo-tectonic setting

The central-southern Apennine is a segment of the circum-Mediterranean orogenic system. Its structural setting is the result of compressive, extensional, and strike-slip events related to the W-dipping subduction and the subsequent flexural retreat of the Apulo-Adriatic microplate, which was followed by the crustal extension linked to the opening of the Tyrrhenian retro-arc basin (Sartori, 1989; Patacca et al., 1990, Doglioni et al., 1991; Bonardi et al., 2009) (Figure 2.3). The spatial-temporal propagation of the compression-extension wave, which began from the internal domains in the Lower-Middle Miocene, continued until the current configuration was reached.
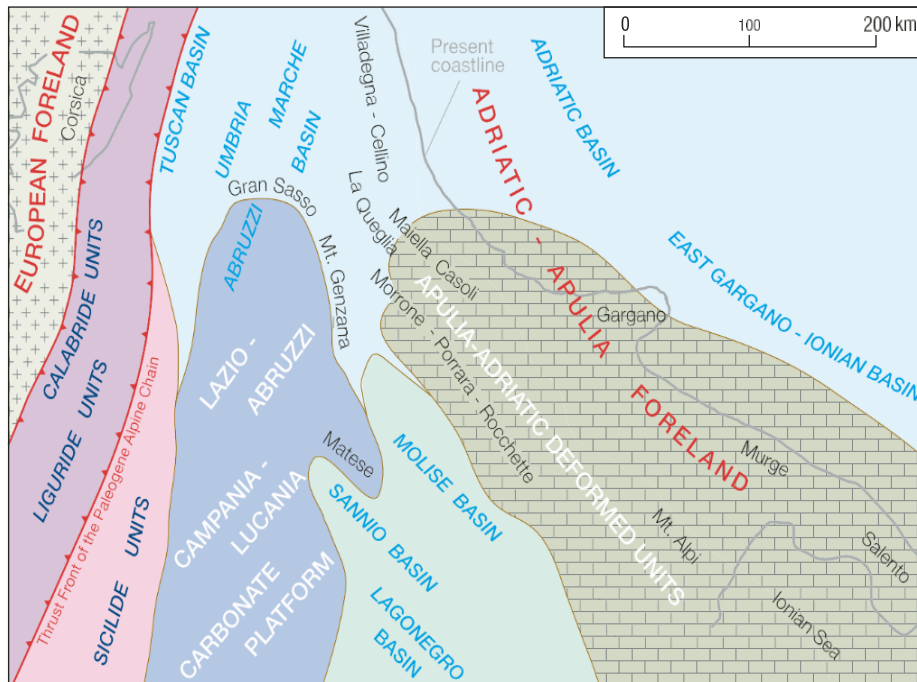
Figure 2.3. The paleogeography of the central-southern Apennines superposed onto the present coastline (from Vezzani et al., 2010). Here, the distribution of carbonate platforms and pelagic basins, from which derive the major tectonic units of the Apenninic fold-and-thrust belt. Main structural domains from west to east: the extensional Tyrrhenian and peri-Tyrrhenian domain; Calabride, Liguride and Sicilide Units, comprising the Lazio-Abruzzi and Campania-Lucania, Abruzzi and Umbria-Marche, Lagonegro-Sannio, and Sannio-Molise Units; the Adriatic-Bradanic Foredeep; and finally, the Adriatic-Apulia Foreland, emergent in the Gargano and Murge promontories.

At the beginning of the Pliocene, a crustal regional extension dissected the internal and axial part of the central-southern Apennines by NW-SE trending normal faults (Cavinato and De Celles, 1999; Patacca and Scandone, 2007; Smeraglia et al., 2020), and by pre-existing structures (e.g., re-utilization of older thrust systems) (Faccenna et al., 1995; Galadini and Galli, 2000). During Pleistocene and Quaternary, the extensional tectonics affected the western flank of the central-southern Apennines producing several sedimentary basins (Campo Imperatore, Fucino, L'Aquila, Sulmona, Campania Plain, Sele River Valley, Vallo di Diano, and Auletta Valley) tectonically controlled by NW-SE and NE-SW normal faults (Barchi et al., 2007; Milia et al., 2017). Here several morphological depressions, close to the sea level, were the location of thick Pliocene-Quaternary deposits (Galadini and Messina, 1994; Cavinato and De Celles, 1999; Ciarcia and Vitale, 2018).

In detail, the geo-structural setting of two carbonate structures that constitute two horst structures in central-southern Apeninnes, as well as their historical seismicity will be described, i.e., the Matese massif (Figure 2.4), and the Picentini mountains (Figure 2.5).

The carbonate Matese massif crops out in the median sector of the Apennine chain and represents a topographic high between the Bojano basin to the east, and the depressions of the middle Volturno river valley to the west (Boncio et al., 2016). It is wide about 1500 km^2 with elevations up to 2050 m (Fiorillo and Pagnozzi, 2015; Rufino et al., 2021). The main lithological units are the Late Triassic-Miocene carbonate sequences (i.e., limestones and dolostone) which reach thickness ranging between 2500 and 3000 m and are intensely fractured and faulted (Fiorillo and Guadagno, 2010; Silverii, 2016). From south to north, the Matese massif is formed by Meso-Cenozoic carbonates of a shallow water platform, a by-pass margin, and slope environments, separated by paleo-geographic boundaries. However, carbonate rocks are locally covered by turbiditic and hemipelagic siliciclastic deposits of the upper Miocene (D'Argenio et al., 1973; Di Bucci et al., 1999; Patacca and Scandone, 2007).
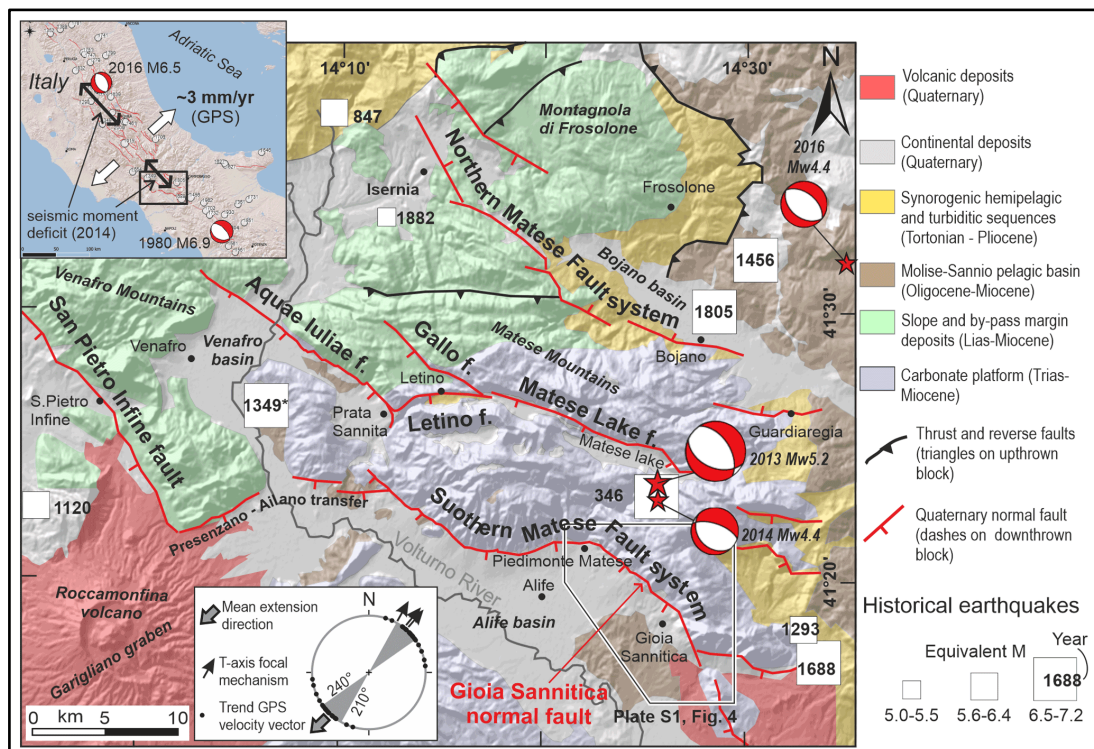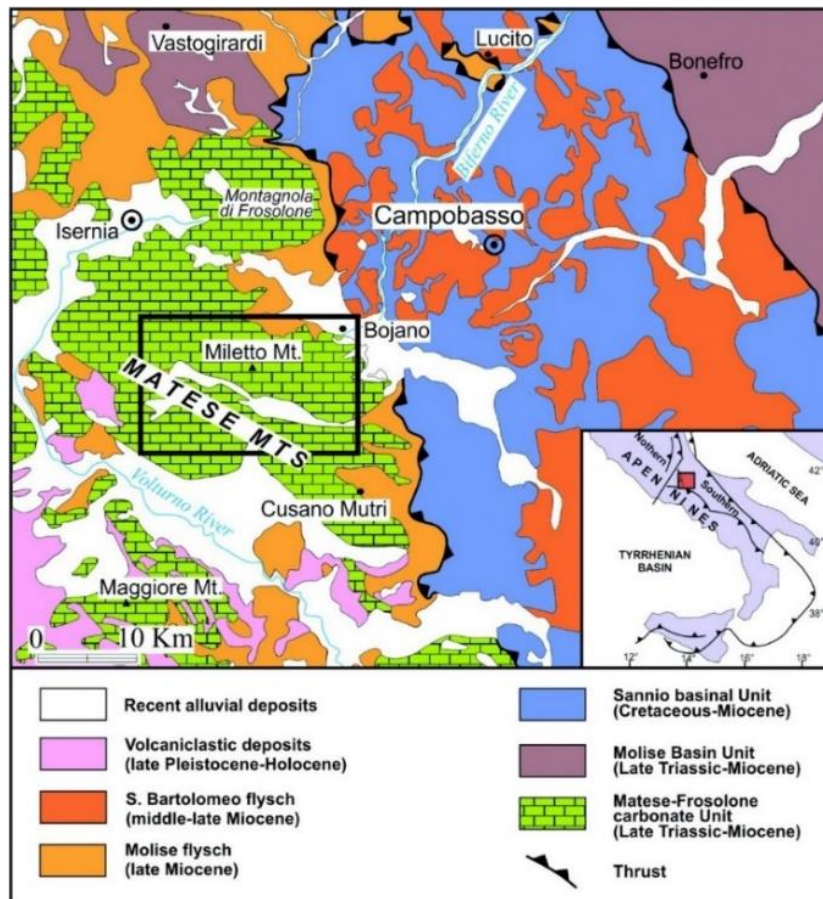
Figure 2.4. Above, the geological sketch map of a portion of Southern Apennines, where the black box shows the Matese massif (from Aucelli et al., 2013). Below, the zoom of the geo-structural setting of the Matese massif is reported (from Boncio et al., 2022).

From a seismological point of view, this area is considered one of the most active sectors of the Apennines, in fact the Matese massif is characterized by the presence of many fault systems (Esposito et al., 2020; Boncio et al., 2022): the Northern Matese fault system, NW-trending and NE-dipping, which borders the Bojano-Isernia basin. Along the Bojano basin, the portion of the Northern Matese fault system is named Bojano Basin fault. This structure was associated with the 1456 and 1805 events (Galli and Galadini, 2003; Galli et al., 2017). Moving toward SE, near Venafro village, the Aquae Iulie fault (NW-trending, SW dipping) has been recognized as active and responsible of the 1349 earthquake (Galli and Naso, 2009). In the inner massif, a secondary SW-dipping fault system is known as the Matese Lake fault, bordering the northern side of the homonymous lake, the San Gregorio Fault, and the Castello Matese Fault. Finally, the SW-dipping normal fault Piedimonte Matese borders the massif toward the Volturno Basin, and the San Pietro Infine fault borders the Venafro Mounts (Ferranti et al., 2015; Boncio et al., 2016). Finally, the southern portion of the carbonate massif is bordered by the Southern Matese fault system.

In past centuries, the Matese area was struck by destructive earthquakes separated by long periods of relative quiescence. The major events occurred in 1349, 1456, 1688 and 1805 (Rovida et al., 2022). For instance, in 1456 the M_w 7.1 earthquake destroyed the villages of Bojano, Frosolone, and Macchiagodena. It consisted of a multiple event with several epicentres linked to different seismogenic sources (i.e., the southern one, in the Benevento area; the central one, in the Bojano plain; the northern one, on the Meta and Mainarde mountains). Nowadays, seismic measurements show that this portion of the Apennines is mainly affected by low magnitude events ($M_w \leq 4$) (http://terremoti.ingv.it/). Larger seismic events are often superimposed to low magnitude seismic swarms, like the ones that occurred after the mainshocks of 1997-98, 2001, 2005, 2013-2014 and 2014-2016 (Milano et al., 2008; Fracassi and Milano, 2014; Di Luccio et al., 2018). On 29th December 2013, the Matese massif was hit by a M_w 5.0 earthquake followed by intense seismic activity (Convertito et al., 2016). A second earthquake occurred on 20th January 2014 (M_w 4.2) and low-level seismic activity continued until February 2014. From the sequence beginning, more than 350 events were recorded, between 10 and 25 km depth, with very few events between 5 and 10 km depth (Di Luccio et al., 2018). At the end of the 2019, a seismic sequence started on 21st November. It included 87 earthquakes whose main seismic event was the M_w 3.9 San Leucio del Sannio earthquake occurred on 16th December.

The Picentini Mts. are located in the inner part of the Southern Apennine and represent one of the main mountain ridges of the chain. They form a WNWESE-trending rectangular block with dimensions of approximately 40 km from east to west, and 30 km from north to south. Their structures resulted from both contractional and extensional tectonics (Pappone and Ferranti, 1995 and references therein). They are formed by Meso-Cenozoic sedimentary deposits deriving from different paleogeographic units of the Mesozoic Apulian passive margin (Patacca and Scandone, 2007; Porreca and Mattei, 2012). These units are now arranged in a complex nappe pile (Patacca and Scandone, 2007). The outcropping rocks of the Picentini Mts. belong to Trias-Miocene calcareous-dolomite series, which are largely fractured and faulted with a thickness of over 2500 m.
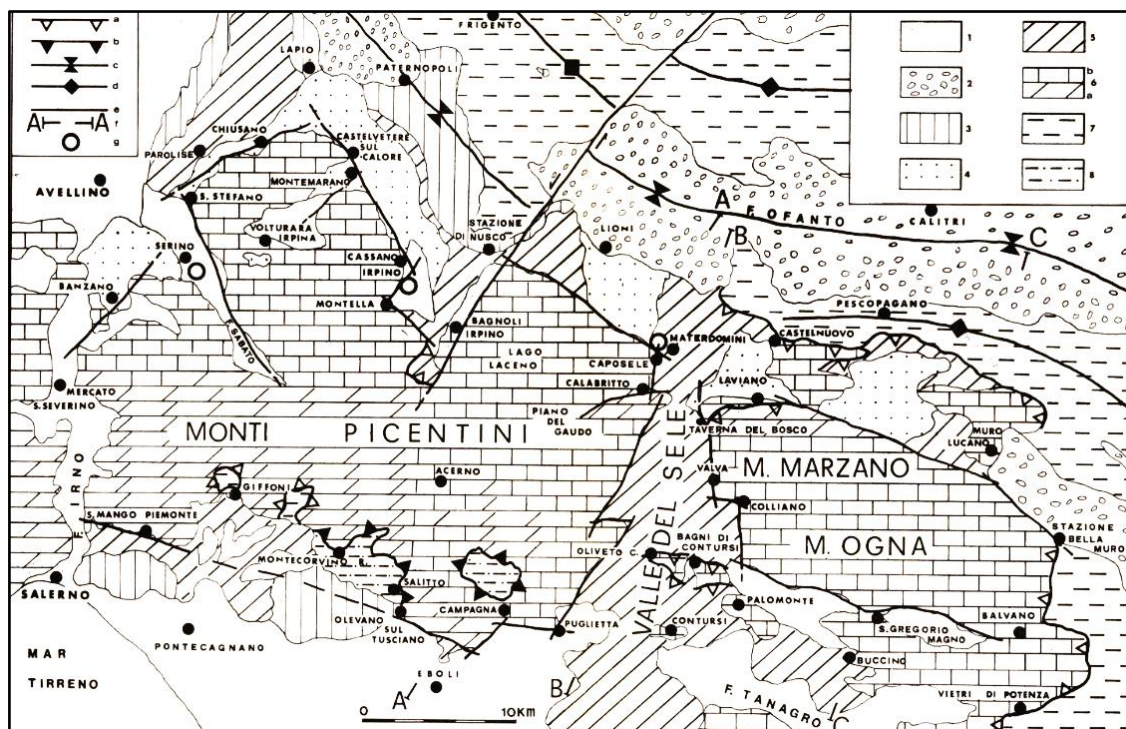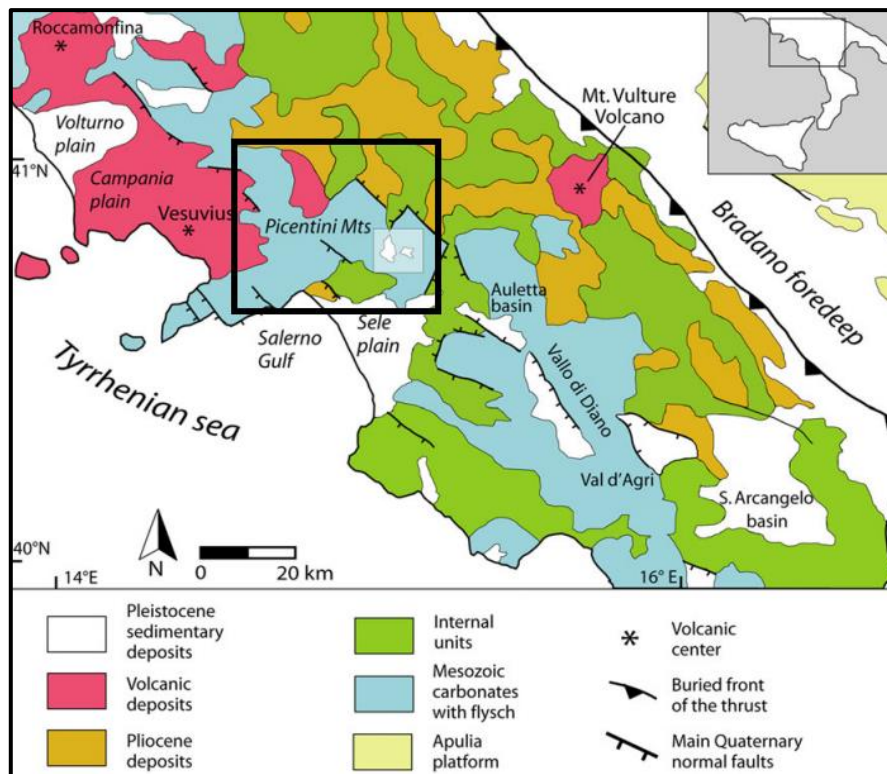
Figure 2.5. Above, the geological sketch map of a portion of Southern Apennines where the black box shows the Picentini Mts. (from Porreca and Mattei, 2010). Below, the zoom of the geo-structural setting of the Picentini Mts. is shown (from Ortolani, 1975).

The carbonate series are tectonically bordered by terrigenous sequences consisting of argillaceous complex and flysch sequences. The geo-structural setting of the Picentini Mts. is quite complex

due to the presence of a marked extensional tectonics that was characterized by two main recognizable phases. The first one occurred between the Upper Pliocene and the Lower Pleistocene and crustal extension was accommodated by low angle normal faults; the more recent second phase, between the Lower and the Middle Pleistocene, was characterized by high-angle normal faults and responsible for the uplift of the massif (Ietto, 1965; D'Argenio et al., 1987; Oldow et al., 1993; Ferranti and Oldow, 1999). The current morpho-structural setting of the Picentini Mts. is controlled by sets of subvertical normal faults, whose late-stage motion is predominantly dip-slip. The tectonic boundary between the northern and southern Picentini is represented by a NW-SE-trending line, the so-called "Accellica-Polveracchio line", which stretches more than 25 km between the upper valleys of the Imo, and Sele Rivers. This line consists of NE-dipping high-angle normal faults which downthrow the northern relative to the southern domain. In the northern Picentini Mts., the Terminio-Accellica unit forms most of the outcrops, and structurally underlie the Lagonegro terrains which outcrop in the Irpinia region (Merlini and Mostardini, 1986; Marsella et al., 1995). In the southern Picentini Mts., several tectonic windows expose the lowest structural units of the thrust stack. In the eastern Picentini Mts., tectonic discontinuities border the upper Sele river valley (Wasowski et al., 2002). This morphologic low is underlain by Upper Cretaceous and Cenozoic terrigenous deposits (i.e., flysch) with variable amounts of clay materials. The overall structural pattern of the upper Sele river valley has been commonly interpreted as a NS-trending graben (Ortolani, 1975; Coppola and Pescatore, 1989). Contrarily, other researchers (Celico and Civita, 1976; Budetta et al., 1988) have argued that the Picentini carbonate block is thrust over the terrigenous rocks which crop out at the foot of the mountain front. Regardless of the tectonic contact nature, most workers agree that the Quaternary neotectonic evolution of the area caused a several hundred-meter uplift and associated intensive erosion (Cinque et al., 1993).

Concerning the seismicity, this area was characterized by many seismic events showing medium to high magnitude. Strong historical events have been well documented since 1500: 1561 - Vallo di Diano; 1694 - Irpinia; 1826 - Tito; 1831 - Rivello; 1836 - Lagonegro; 1851 - Basilicata; 1857 - Val d'Agri; 1930 - Irpinia; 1962 - Irpinia; 1980 - Irpinia (Esposito et al., 1988; Marturano et al., 1988; Porfido et al., 1988; CPTI Working Group, 2004; Pierdominici et al., 2011). For instance, the great M_w 6.9 Irpinia earthquake was characterized by three ruptures on different segments. It was possible to recognize each responsible seismogenic source as follows: the first one concerned the Monti Marzano, Carpineta and Cervialto Fault. The second one spread towards the SE, along the San Gregorio Plain. Finally, the third one involved a fault segment located NE of the first one.

From a geodetical point of view, the investigated sector of the central-southern Apennines represents a complex portion of the chain that undergoes to different extension rate (Giuliani et al., 2009; Boncio et al., 2016; Cowie et al., 2017). According to recent GPS studies, the magnitude of extension and strain seems to vary systematically moving along the axis of the Apennine chain parallel to the main fault systems (Ferranti et al., 2014). Within the Campania-Molise sector in the north, the extension accommodated by faults at the Matese massif is ~ 3.6 mm/yr. Moving to the southeast, extension decreases to ~ 2 mm/yr in Sannio, and then to ~ 2.3 mm/yr in the Picentini Mountains, and ~ 1–1.5 mm/yr in Irpinia. Thus, a 1.5-2 mm/yr decrease in extension rate from ~3.5 mm/yr to ~ 1.5–2 mm/yr characterizes the transition from northern (Matese) to central (Sannio-Picentini-Irpinia) Campania (Ferranti et al., 2014).

2.4 Hydrogeological setting

The central-southern Apennines are characterized by huge amounts of groundwater hosted by carbonate aquifers, whose thickness reaches approximately 2500 m (Allocca et al., 2014; Figure 2.6). In detail, they consist of Triassic-Liassic dolomites, Jurassic limestones, and Paleogene marly limestones of the Mesozoic carbonate platform series that, during Miocene tectonic orogenic deformation phases, were piled up in the Apennine chain (Patacca and Scandone, 2007). Due to the fold-and-thrust belt structure, groundwater flowpath is mainly controlled by the geometry of tectonic and stratigraphic contacts with lower permeability units belonging to pre- and syn-orogenic basinal and flysch series (Celico, 1983; Petitta, 2009).
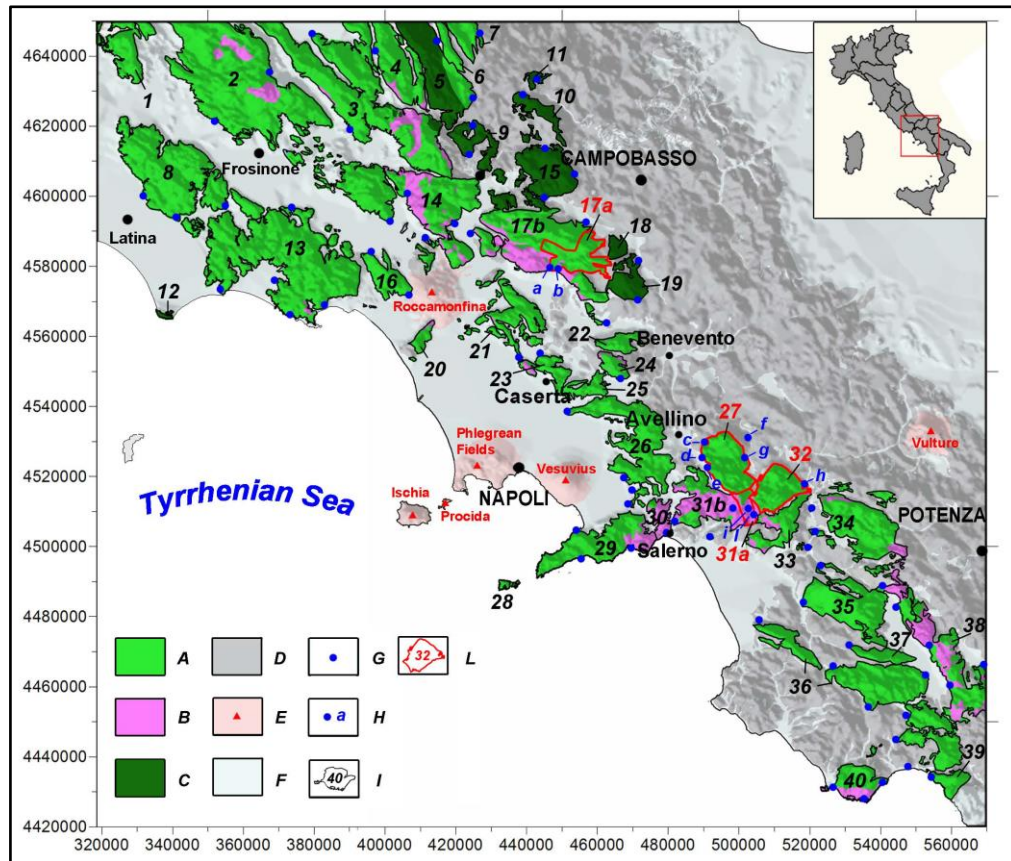
Figure 2.6. Map of the carbonate aquifers of the central-southern Apennines (from Allocca et al., 2014). A) limestone and dolomitic limestone units of the carbonate platform series (Jurassic-Paleogene); B) dolomitic units of the carbonate platform series (Trias-Liassic); C) calcareous-marly units of the outer basin series (Trias-Paleogene); D) pre-, syn- and late-orogenic molasses and terrigenous units (Cretaceous-Pliocene); E) volcanic centers (Pliocene-Quaternary); F) alluvial and epiclastic units (Quaternary); G) main basal springs of karst aquifers; H; I; L) factors considered for the calculation of the hydrogeological budget performed by Allocca et al. (2014).

Also, Triassic evaporites at the base of the Meso-Cenozoic carbonates, as well as the Messinian deposits are known as relevant sealing levels (aquicludes) for groundwater (Franchini et al., 2021). Besides, groundwater circulation is generally oriented towards the lowest point of hydrogeological boundaries, where basal springs are located, having very high discharge rates and steady regimes (Boni et al., 1986). Groundwater is supplied by wide recharge areas, where the infiltration is very high and is mostly driven by fractures and, secondarily, by dissolution features (Petitta et al., 2011). Hence, both fracturing and karstification play a crucial role in recharging aquifers, since carbonate rocks are heavily fractured and faulted (Fiorillo and Guadagno, 2010; Amoruso et al., 2013). The primary fracture pattern is oriented in NW-SE direction (Celico et al., 1994),

perpendicularly to the direction of the tectonic extension that affects this sector of Apennines (D'Agostino, 2014). However, inside carbonate aquifers themselves, groundwater bodies can be compartmentalized in basin-in-series systems (Celico et al., 2006) by the presence of minor stratigraphic or tectonic factors, including faults associated with low-permeability clay-rich gouge zones (Smeraglia et al., 2017).

Recharge processes in carbonate aquifers are chiefly and strongly controlled by climatic characteristics of the central-southern Apennines and their temporal variability. Climate is of the mountain variety of the Mediterranean type, being characterized by rainy/snowy autumn-winters and dry summers. Indeed, the recharge occurs prevalently in winter and spring owing to direct precipitation and snow melt at high altitudes (Romano and Preziosi, 2013; Silverii et al., 2019).

Below, hydrogeological settings of three regional carbonate aquifers will be deepened: the Matese massif, the Picentini Mts. (in detail, the Mt. Polveracchio sub-hydrogeological structure), and also the Mt. Morrone carbonate aquifer, which feeds the Sulmona area.

The Matese carbonate aquifer (Figure 2.7) is formed by a Meso-Cenozoic (mainly Cretaceous) carbonate succession that is about 2500-3000 m thick. It is bounded at the edges by low-permeability deposits that are in contact with the massif itself through normal and thrust faults. In detail, along the northern and eastern sectors, the Matese massif is tectonically joined by a thrust fault to argillaceous complexes and flysch sequences (Petrella and Celico, 2009). Instead, along the southern and western sectors, it is bounded by normal faults and covered by recent Quaternary deposits of the Volturno river plain. The tectono-karstic depressions located at high elevations in the central sector of the massif divide this unit into eastern and western sectors and represent relevant recharge zones of the Matese aquifer. Particularly, the Lago Matese polje is the main one, occupying an area of 45 km^2 between 1000 and 2050 m a.s.l. (Fiorillo and Pagnozzi, 2015).
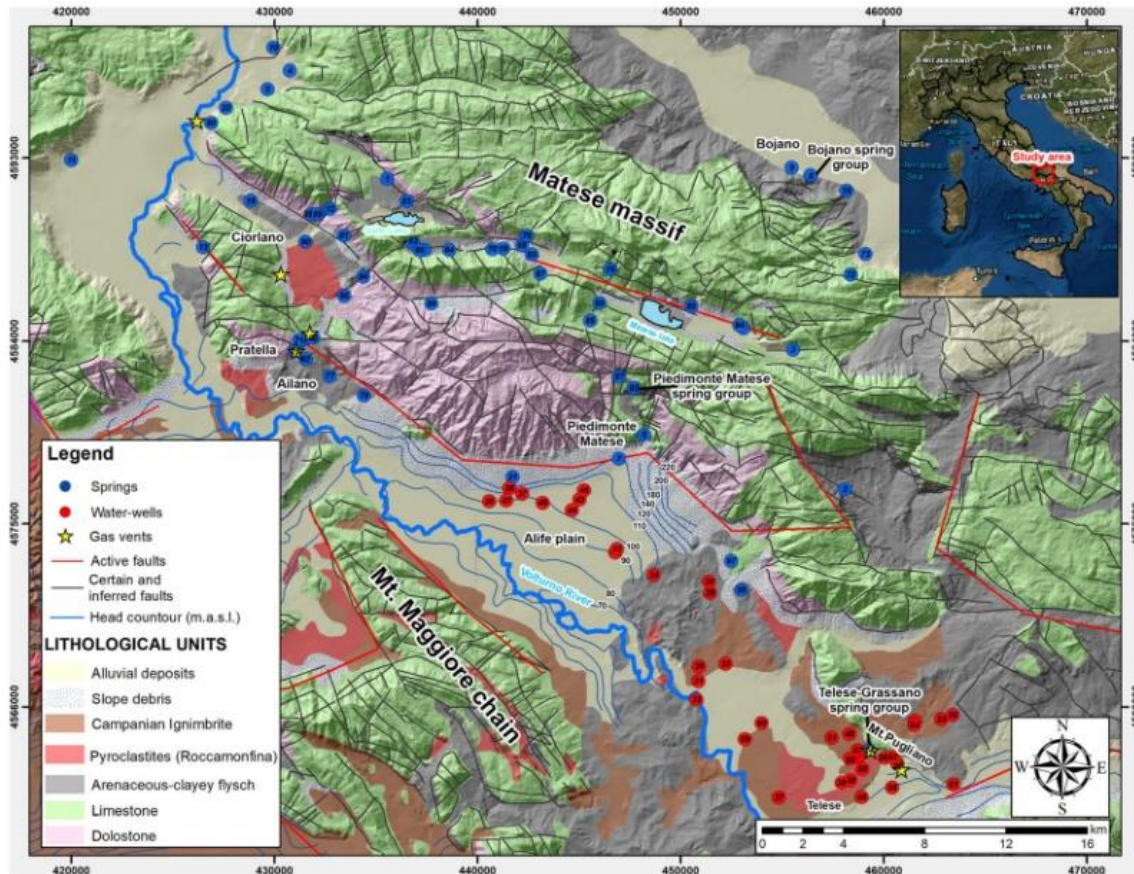
Figure 2.7. Simplified hydrogeological overview of the Matese aquifer (from Rufino et al., 2020). Geological info coming from Istituto Superiore per la Protezione e la Ricerca Ambientale (ISPRA, 2009); Hydrogeological features coming from P.T.R Regione Campania (2007).

Among the main springs, in the northern sector, the Bojano spring group has a total mean discharge of about 2.8 m^3/s. It is chiefly fed by groundwater circulating in the carbonate succession of Mount La Gallinola.

In the southern sector, the Grassano-Telese springs are fed by the eastern sector of the Matese aquifer which is hydraulically connected by buried karst terrains to outcropping karst reliefs as Mt. Monaco, Mt. Acero, and Montepugliano. The latter one represents the main discharge zone of the aquifer and the lowest elevation outflows (54 m a.s.l.) (Leone et al., 2019), where a deep and wide groundwater flowpath locally converge providing an upwelling flow, driven by conduits and fracture networks (Fiorillo et al., 2019). Grassano-Telese springs are located at the southern slope of Montepugliano along the contact between the intensely fractured platform limestones and alluvial deposits. Grassano and Telese springs are cold calcium-bicarbonate waters, and hypothermal sulphurous and CO_2-rich ones, respectively (Corniello and De Riso, 1986; Fiorillo et

al., 2019). This endogenous hydrogeochemical signature is attributable to the upwelling of deep fluids along fault systems, as also testified by the presence of numerous sinkholes (Fiorillo et al., 2019). Grassano spring consists of different outlets with a mean annual discharge of 4.5 m^3/s, while the average discharge of Telese spring is about 1 m^3/s (Corniello et al., 2021). In this study, the Capovolturno spring was also considered, which belongs to a different circuit with respect to the other three springs. It is located at the eastern boundary of Mount Rocchetta, where the contact between the limestone sequence and the terrigenous deposits is found. The ridge of Mount Rocchetta is characterized by a very fractured karst aquifer which is hydraulically connected to the hydrogeological unit of Mount Genzana - Mount Greco. This could explain the considerably high mean annual discharge of about 6.6 m^3/s (Discenza et al., 2011).

The Picentini Mts. represent a karstic system over an area of about 600 km^2 (Figure 2.8). Outcropping rocks, belonging to a Trias-Miocene calcareous-dolomitic succession, have a thickness of 2500 m and are very fractured and faulted, and frequently reduced to fault breccia. This carbonate series is bordered by less permeable sequences consisting of clayey and flysch sequences (Ietto, 1965). The presence of large endorheic areas is fundamental in the recharge processes (Fiorillo et al., 2015). However, they are affected by pyroclastic deposits covering the carbonate rocks that influence the infiltration in the karst substrate. Due to many tectonic discontinuities, groundwater flowpaths is well constrained, and the whole karst system of the Picentini Mts. is divided into four main sub-units, recognized as different hydrogeological basins (Celico and Civita, 1976; Celico, 1978; Coppola et al. 1989) as follows: Terminio-Tuoro, Cervialto, Polveracchio-Raione and Accellica-Licinici-Mai, recognized as different hydrogeological basins (Coppola and Pescatore, 1989; Calcaterra et al., 1994; Fiorillo and Ventafridda, 2010; Corniello et al., 2010).
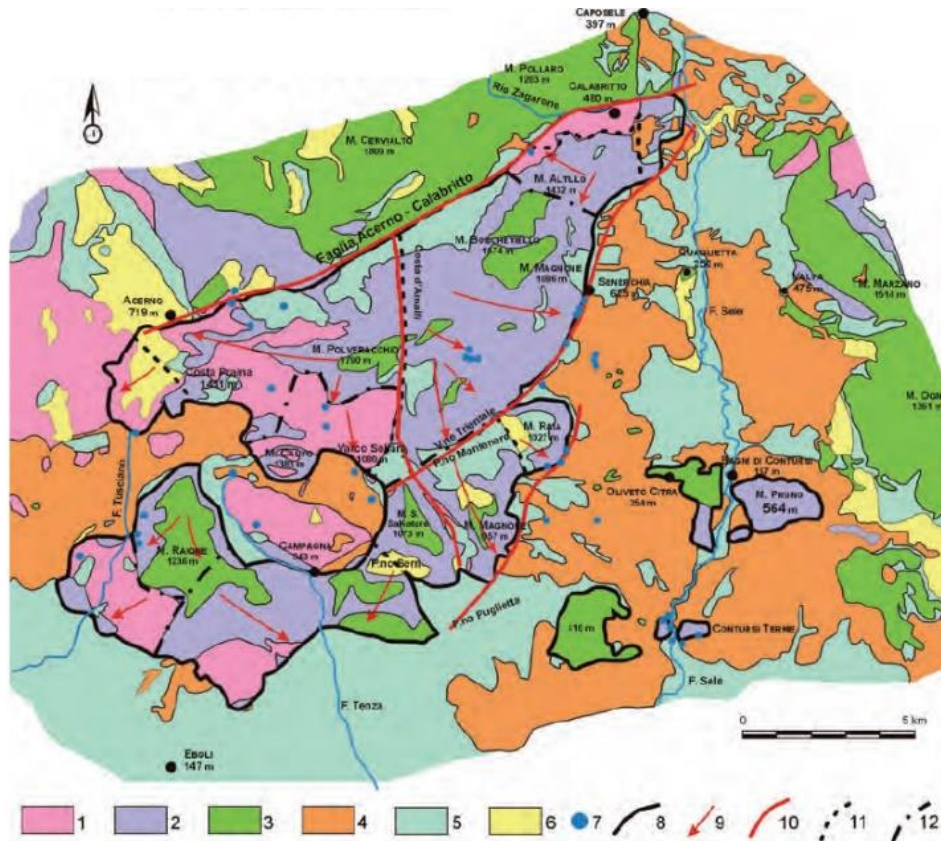
Figure 2.8. Simplified hydrogeological map of the Mt. Polveracchio aquifer (from Del Prete et al., 2004). Legend: 1) dolomitic complex (medium permeability); 2) calcareous dolomitic complex (high permeability); 3) calcareous complex (high permeability); 4) clayey-marly-sandy complex (low permeability); 5) alluvial complex (high permeability); 6) alluvial-lacustrine-pyroclastic complex (medium-low permeability); 7) spring; 8) hydrogeological unit limit; 9) flowpaths direction; 10) border fault of Mt. Polveracchio; 11) groundwater divides; 12) leaky groundwater divide.

In detail, the sub-structure of Mt. Polveracchio-Raione is divided into two independent hydrogeological basins. The complex geo-structural setting of Mt. Polveracchio aquifer affects groundwater flow (Celico et al., 1987). Along the northern and north-eastern margin, the hydrogeological limit consists of a fault between Acerno and Calabritto localities, where the local groundwater outlet is the Acquara-Ponticchio spring. Along the western margin, the boundary is represented by a fault system separating Mt. Accellica from Mt. Polveracchio. Further south, the Polveracchio basin is buffered by impermeable lithotypes of the Lagonegro Units that outcrop in Campagna's tectonic window (Corniello et al., 2010). Finally, along the eastern margin, in the upper Sele river valley, the boundary consists of a tectonic thrusting front. Here, several calcium-bicarbonate springs are located. Through a deeper and longer circuit, groundwater reaches very

mineralized springs in the inner zone of the Sele river valley (i.e., Contursi Terme, and Contursi Bagni springs; Celico, 1979, 1983) by crossing carbonate substrate covered by terrigenous deposits.

Finally, the Sulmona area is located between the Gran Sasso, and the Mt. Morrone carbonate aquifers (Figure 2.9). Regional groundwater flowpaths converge to feed a few base-flow springs in the Sulmona plain with discharges between less than 0.1 m^3/s and more than 1 m^3/s. The Mt. Morrone carbonate aquifer is confined by low permeability layers: i) the thrust zone between the Gran Sasso carbonate unit and the Mt. Morrone carbonate unit, in the northern sector; ii) the thrust zone between the Mt. Morrone unit and the Laga siliciclastic unit, in the eastern sector; and iii) the Mt. Morrone active extensional fault, in the western sector, isolating the carbonate deep aquifer from local shallow aquifers in the Sulmona plain (Salvati, 2002).
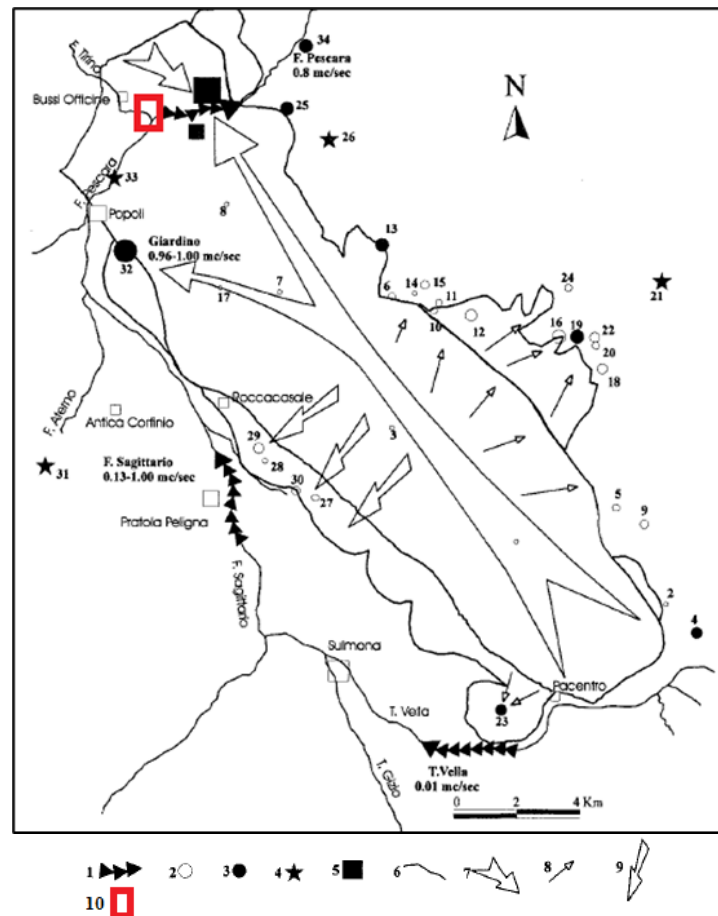
Figure 2.9. Simplified hydrogeological map of the Mt. Morrone aquifer (from Conese et al., 2001). 1) Linear spring; 2-3) Spring; 4) Sulphurous Springs; 5) Wells; 6) Rivers; 7) Main basal groundwater flowpaths; 8) Minor flowpaths; 9) Basal circulation towards the Sulmona plain; 10) Monitoring well (PF 60.3)

Groundwater is mainly of the calcium bicarbonate type due to the carbonate dissolution, but it is occasionally mixed with deep sulphate-calcium-bicarbonate waters. This deep contribution is enhanced by active faults and related deep rock deformation (Miccadei et al., 1992). The Giardino Spring is a main discharge of Mt. Morrone aquifer and is located in its north-western portion, at the intersection with the Mt. Morrone normal fault (Barberio et al., 2018). The spring is characterized by steady flow and chemical regimes, and a high discharge rate of approximately 1 m^3/s (Conese et al., 2001; Barberio et al., 2017). The PF60.3 hydrogeological monitoring station consists of a 100 m deep well, where a multiparametric probe was installed. No active abstractions influencing the groundwater level and spring discharge are ongoing in this aquifer, as documented by previous monitoring (Conese et al., 2001).

3. Monitoring: Material and Methods

In this Chapter, monitoring will be deeply defined to explain and highlight the relevance of every acquired parameter during the research activity. Different methodologies were adopted to obtain a complete overview of the investigated topic. Hence, a hydrogeological, hydrogeochemical, isotopic, gas-geochemical monitoring, and the study of both seismicity rate and its spatial distribution were performed throughout the years of the PhD. By considering both logistic conditions and hydrogeological characteristics, springs in two areas of southern Apennines (i.e., Matese and Contursi) were selected within this research project. However, as already mentioned, two different approaches were used to achieve the main goal of this study. Here, discrete and continuous monitoring carried out in the surveys will be presented. In detail, in the Matese area, long-term monitoring of four springs (i.e., Rio Freddo, Grassano, Telese Terme, and Capovolturno; Figure 3.1) was carried out. In the Contursi area, an in-depth screening of 22 springs with different geochemical features was executed. Finally, also the continuous hydrogeological monitoring in the Sulmona area (run within a pre-existing research activity in central Italy) will be described.

Figure 3.1. Photos of three springs in the Matese area (from left to right: Grassano spring, Telese spring, Rio Freddo spring).

3.1 Hydrogeological monitoring

Continuous hydrogeological monitoring was performed for measurement of physical-chemical parameters at Grassano spring, and it is still ongoing. By using the Hydrolab HL4 Multiparameter

Probe (Figure 3.2), electrical conductivity, temperature, pH, dissolved oxygen, and water level were continuously and simultaneously recorded. The probe is characterized by an EC resolution of 0.001 mS/cm (error ± 0.5% of reading), a temperature resolution of 0.01°C (error ± 0.1°C), a pH resolution of 0.01 (error ± 0.2 pH), a dissolved oxygen resolution of 0.01 mg/L, and a water level resolution of 0.01 m (error ± 0.05 m). The device is equipped with integrated data recording capability. Measurements of parameters are automatically repeated and stored every 15 minutes. Also, data of rainfall were collected from the rain gauge station of Parco del Grassano (http://centrofunzionale.regione.campania.it/). Besides, groundwater level data from the 100 m deep well drilled through the Mt. Morrone regional carbonate aquifer were acquired. Groundwater level in the PF60.3 well was measured by using the OTT ecoLog 800 multiparametric probe (Figure 3.2), equipped with an automatic system for continuous acquisition and remote data transmission (online at: https://h3o.stonebit.it/), including groundwater level, temperature, and electrical conductivity (groundwater level: resolution 0.001 m, error ± 0.05%; temperature: resolution 0.001 °C, error 0.1 °C; electrical conductivity: resolution 0.001 mS/cm, error ± 0.5%). The frequency of data measurements was every five minutes. The barometric pressure of groundwater level measurements was automatically compensated for.
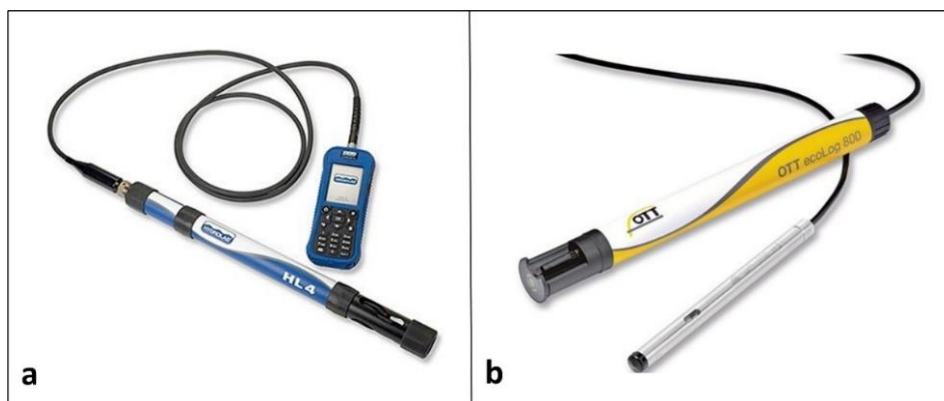
Figure 3.2. a) HL4 probe for continuous monitoring of temperature, pH, electrical conductivity, and dissolved oxygen; b) OTT ecoLog 800 multiparametric probe, for continuous acquisition and remote transmission of data, including groundwater level, temperature, and electrical conductivity.

3.2 Hydrogeochemical monitoring

The sampling is the first step of every analytical process. It is considered a complex and delicate phase since quality of results closely depends on it. Therefore, collecting representative groundwater samples is a fundamental prerequisite for a correct interpretation of data.

Hydrogeochemistry is closely related to (i) the nature of the water (marine, meteoric or magmatic), (ii) the lithology of host rocks, (iii) the hydrodynamics in the aquifer which means both the length and depth of groundwater flowpaths (Goldscheider et al., 2010). Thus, it is strongly affected on the residence time and on possible mixing processes too (Barbieri et al., 2017). Hydrogeochemistry is also deeply affected by the presence of acidic and/or reducing dissolved gases as well as by the thermal condition of the aquifer.

Good preliminary information to hydrogeochemically characterize groundwater can be achieved by measuring temperature, pH, electrical conductivity, and by determining major ions (i.e., cations and anions), useful to assess the hydrogeochemical facies and the occurrence of chemical processes during the groundwater flowpath. Additionally, to complete and get an exhaustive hydrogeochemical characterization, the analysis of minor and trace elements allows an improvement in the comprehension of dissolution/precipitation reactions, anthropogenic pollution phenomena, saline intrusion, and variations in the surrounding conditions (pH-Eh).

Hence, taking into account these considerations, during the sampling survey, the following procedure was performed. At each spring, electrical conductivity, temperature, and pH were directly measured in situ (Figure 3.3) using the multiparametric probe WTW Multi 3420 with accuracies of 1 μS/cm, 0.1 °C, and 0.01 pH unit, respectively. In addition, groundwater samples addressed to analyses aimed at the determination of hydrogeochemical composition (i.e., major ions, minor and trace elements, isotope contents) were collected into sterile polyethylene bottles and stored at low temperatures in ice-filled fridge boxes to avoid alterations of chemical components. However, sampling techniques were different in relation to the type of analysis to be performed (Wilde et al., 1998). Samples for major ions were filtered with 0.45 μm membrane and the ones for trace elements were filtered and acidified with ultrapure HNO_3 (pH = 2) to keep metals in solution. All the hydrogeochemical analyses, except for the isotopic ones, were carried out at the Geochemistry Laboratory of the Department of Earth Sciences at Sapienza University of Rome.

Figure 3.3. Material for survey sampling (i.e., polyethylene bottles for collecting water, and the multiparametric probe WTW Multi 3420 right inside the case) and in situ determination of alkalinity.

Below, the analytical methods used for the determination of major and minor/trace elements are reported:

• Volumetric analysis for the determination of the alkalinity (HCO_3^-) of groundwater. It was measured by titration with 0.05 N HCl solution as titrating agent and methyl orange as indicator which is sensitive to pH changes. In detail, both the methyl orange and HCl were added to the sample. Due to the addition of the hydrochloric acid, the pH was lowered. When it reached the value equal to 4.4, the bicarbonate titration ended, concomitantly with the colour change of the sample itself. As a last step, the following formula was used to calculate the HCO_3^- concentration:

Total alkalinity (meq/L) HCO_3 = [V HCl (mL) × normality / Sample volume (mL)] × 1000

• Ion chromatography to define anionic and cationic compositions. Chromatographs Dionex ICS 5000, and Dionex ICS 1100 were used to analyze anions (F^-, Cl^-, SO_4^{2-}, and NO_3^-), and cations (Ca^{2+}, Mg^{2+}, Na^+, and K^+), respectively (Figure 3.4). This analytical technique allowed to recognize and separate major ions through ion exchange between the mobile phase, consisting of the eluent containing the sample, and the stationary phase represented by the ion exchange resin. At the end of the processing, the chromatogram was obtained, and concentrations of each ion were

calculated. Overall, the accuracy of major ion analyses is based on the principle of electroneutrality. It means that the difference between the sum of the concentrations of cations and anions, expressed in meq/L must be balanced. A widely accepted criterion for the validation of analytical data is that the electroneutrality be within ± 5% (Baird et al., 2017). Based on this principle, the ionic-balance error checked on each sample was within this percentage.

Figure 3.4. The Chromatograph Dionex ICS 1100 for cations analyses and the Chromatograph Dionex ICS 5000 for the anions analyses, equipped with a Dionex AS-DV autosampler.

• Mass Spectrometry for minor and trace elements analyses, by using an ICP-MS spectrometer (Inductively Coupled Plasma Mass Spectrometry, X Series 2 Thermo Fisher Scientific Waltham, MA, USA) (Figure 3.5). Blanks, standard solutions, and sample dilutions were prepared by using ultrapure water (Millipore, Milli-Q, 16 MW cm), and an internal standard (Rh) was added to correct the ICP-MS instrumental drift. This very sensitive technique allowed the determination of various inorganic trace elements commonly found in groundwater. In detail, the plasma torch produced the ionization, while the mass spectrometer separated the produced ions based on their mass/charge ratio. According to this procedure, each ion arrived at different times, producing signal proportional to its concentration. The analytical accuracy of this method ranges between 2% and 5%.

Figure 3.5. Spectrometer ICP-MS (Inductively Coupled Plasma Mass Spectrometry) used for trace element analyses.

3.3 Isotope monitoring

Some characteristics of groundwater do not depend on the chemical-physical parameters or on the ambient conditions, indeed they strictly reflect features of the infiltrating water and the reservoir rock (Clark and Fritz, 2013). With the aim of assessing processes involving groundwater origin and mixing, it was useful to determine the groundwater isotope composition. Physically, isotopes are atoms of the same chemical element, but they differ for the number of neutrons, and therefore for the mass (Barbieri, 2019). The most relevant isotopes for Hydrogeology Science are the stable water isotopes: ^{18}O for oxygen, and ^2H (or Deuterium, D) for hydrogen (Gat, 1996; Mook and Rozanski, 2000). However, also isotopes of other molecules can clarify more in-depth aspects related to water-gas-rock interaction. Therefore, during this research activity, samples addressed to analyses of the following isotope contents: $\delta^{18}O$, δD, and ^3H (H_2O), $\delta^{34}S$ and $\delta^{18}O$ (SO_4), $\delta^{13}C$ (TDIC), were collected into sterile polyethylene bottles without any treatments. The isotope analyses were performed at IT2E Isotope Tracer Technologies Europe Srl in Milan (Italy) and at the National Institute of Geophysics and Volcanology (INGV, section of Palermo, Italy), by using a mass spectrometer equilibrated on 25°C as described by Epstein and Mayeda (1953) for oxygen; hydrogen measurements were carried out by reducing the water sample to hydrogen by passage over hot zinc at about 520 °C according to the procedure described by Coleman et al. (1982). The analytical precision is about ±0.1‰ for $\delta^{18}O$ and ±1‰ for δD. Measurements of stable isotopes of

water (δ^{18}O and δD), dissolved sulphate (δ^{34}S and δ^{18}O), and carbon (δ^{13}C) are expressed in terms of delta units per mil (δ‰) of the sample isotope ratio relative to the same ratio in the standard which are: Vienna Standard Mean Ocean Water (V-SMOW), Vienna Canyon Diablo Troilite (V-CDT), Vienna Pee-Dee Belemnite (V-PDB) standards, respectively.

$$\delta = (R_{Sa}/R_S - 1) \times 1000$$

R_{Sa}: isotope ratio of the sample, and R_S: isotope ratio of the standard.

Tritium (^{3}H) content was determined by an electrolytic enrichment and liquid scintillation counting method, and it is reported in TU (Tritium Unit).

3.3.1 Isotope of Water

Stable isotopes of the water molecule (δ^{18}O and δD) provide useful information about the origin of groundwater, the recharge area, and potential mixing processes (Clark, 2015). They also provide additional information about possible water-rock interaction at high temperatures (generally estimated to be as high as 150 °C), mainly the ^{18}O/^{16}O in carbonate environments and possible exchange between uprising gas phase and groundwater (both O and H) causing isotope fractionations. As mentioned in the previous paragraph, water isotope ratios are expressed in delta units (δ‰) with respect to Standard Mean Ocean Water (SMOW) which represents the average value of the isotopic composition of ocean waters. Stable isotopes can become enriched and depleted through a separation process that is named "isotopic fractionation" which takes place during phase changes such as evaporation, condensation, chemical reactions, or biological processes. The isotope fractionation of the water molecule is due to various causes, including the effects of continentality, latitude, and altitude (Clark and Fritz, 1997). Despite the complexity of processes that concur to modify the isotopic composition of meteoric water, Craig (1961) highlighted the existence of a linear correlation between δD and δ^{18}O that is valid on a global scale, known as the Global Meteoric Waters Line (GMWL). Consequently, other models, correlating the δD and δ^{18}O associated with local geographic regions, were developed. They are the so-called Local Meteoric Water Lines (LMWL). Concerning Italy, based on isotopic measurements carried out in numerous rain gauge stations distributed all over the country Longinelli and Selmo (2003) and Giustini et al. 2016 reported three correlation lines valid for northern, central, and southern Italy. The radioactive isotope of hydrogen is Tritium (^{3}H) whose half-life is 12.4 years. It is an excellent tracer of groundwater because it is incorporated into water molecules of rainfall that

recharges aquifers. Tritium is continually produced in small quantities in the upper atmosphere by the interaction of cosmic rays with gaseous nitrogen. However, its importance as a standard dating tool for groundwater is due to the great amounts of tritium that were produced in the atmosphere between 1952 and 1980 because of the testing of thermonuclear weapons. Since these years, tritium concentrations persisted in the atmosphere for many decades following the cessation of atmospheric nuclear weapons testing. Therefore, the absence of tritium in groundwater samples clearly indicates recharge prior to the period of bomb testing (> 70 years) and it is designated as old groundwater. Conversely, groundwater containing tritium concentrations greater than 1 TU is considered young, having a recharge time between 10 and 50 years (Lindsey et al., 2019).

3.3.2 Isotope of Carbon

Stable isotopes of carbon are ^{12}C and ^{13}C, and carbon isotope ratios are expressed in delta units (δ‰) with respect to the Standard Pee Dee Belemnite standard (PBD) (Craig, 1953). In detail, the measurement of the carbon isotopic signature of CO_2 is useful to distinguish its origin from different sources (Hilton, 1996; Kulongoski et al., 2013). Marine limestones, organic carbon from soils and sedimentary rocks, and the upper-mantle degassing are among the main sources of carbon. They have distinct $δ^{13}C$ end-members, with marine limestone exhibiting $δ^{13}C$ close to 0‰, sedimentary organic matter less than 20‰, and upper-mantle degassing ranging between -4 and -9‰ (Javoy et al., 1986; Sano and Marty, 1995). Besides, Sano & Marty (1995) proposed to assess the mixing relations for carbon of various origins using the combination of $δ^{13}C$ and $^{3}He/^{4}He$ (R/Ra).

3.3.3 Isotope of Sulphate

The major forms of sulphur in the hydrogeological subsurface environment include sulphate (SO_4^{2-}) and sulphide (HS^-) minerals, sulphate and sulphide dissolved in water, and hydrogen sulphide gas (H_2S), and sulphur in organic compounds (Langmuir, 1997; Appelo and Postma, 2004; Porowski et al., 2019). Dissolved sulphates (SO_4^{2-}) are among the most common sulphur species in natural groundwater environments, ranging from a few mg/L in shallow waters up to tens of g/L in fossil brines. They can derive from different sources (i.e., atmospheric, lithosphere, and hydrosphere), whose signatures are distinguishable through the measurements of the isotopic compositions expressed in delta units (δ‰): $δ^{34}S$ with respect to Canyon Diablo Troilite (CDT),

and $\delta^{18}O$ with respect to Standard Mean Ocean Water (SMOW). Sulphate isotope ratios are also strongly influenced by microbial activity as well as by water-rock interactions. They are commonly used as a geochemical tool for tracing reduction processes, fluid mixing, and element cycling under both hydrothermal and low-temperature conditions (Jones and Fike, 2013). Among significant fractionation processes, thermochemical reduction is under hydrothermal conditions, while during bacterial sulphate reduction kinetic fractionation of the sulphur isotopes is at low temperatures (Hoefs, 1997; Canfield, 2001). The isotopic composition of atmospheric sulphate is determined both by marine aerosols and fossil fuels. Instead, lithospheric sulphur is mainly found in sedimentary rocks, as sulphate in evaporite deposits or in reduced form in sulphurous minerals such as pyrite.

3.4 Gas-geochemical monitoring

Over the last decades, many investigations about gas were carried out aimed at deepening their behaviour in relation to different geodynamic and tectonic contexts (Toutain and Baubron, 1999), presence of tectonic discontinuities (i.e., faults and fractures; Mörner and Etiope, 2002; Zhou et al., 2010), earthquakes and volcanic activity (Paudel et al., 2018), petroleum exploration, geothermal areas (Boyle, 2013), and exhalation of greenhouse gases (Etiope, 2015). It is known that according to their origin (i.e., atmospheric, crustal, or mantle-derived), gases show different compositional features which are easily distinguishable. For instance, deep crustal or mantle-derived fluids are characterized by greater amounts of He, Rn, CO_2, and CH_4 (Minissale, 2004; Caracausi and Paternoster, 2015) and by a specific isotopic signature. Through faults and regional lithospheric discontinuities which act as vehicles, they can reach great distances and move upward towards the surface by the aid of gas carrier (Etiope and Martinelli, 2002). During their migration, gas can be stored in aquifers or in reservoir rocks. Hence, the gas composition detected in groundwater can be considered the result of mixing of various degree between shallow and deep gas sources. With the aim of detecting variations in gas concentrations related to the seismicity, groundwater Rn and CO_2 activity were continuously measured by using probes since these gases showed strong sensitivity to crustal deformations worldwide (Salazar et al., 2002; Steinitz et al., 2003; Chiodini et al., 2004; Italiano et al., 2008). In detail, AlphaGUARD Model PQ2000PRO by Saphymo (integrated with a RAM module 7 for gas stripping) was used for dissolved radon measurements at the Rio Freddo and Grassano springs. The same device was also installed at Maro spring (Andalusia, Spain) during my PhD period abroad carried out in the last year of the research activity. Mini CO_2 by Pro-Oceanus Systems Inc was used for CO_2 measurements at Grassano

spring. Moreover, recorded data can be monitored and downloaded in real time, by an online system of data acquisition developed by Digimatic s.r.l. (https://webvision.digimatic.it/).

3.4.1 Dissolved Radon

Radon (^{222}Rn) is an endogenous natural radioactive noble gas whose half-life is of 3.82 days. It is the most commonly occurring radon isotope in nature, produced by α-decay from Radium (^{226}Ra) within the decay chain of Uranium (^{238}U). It is moderately soluble in water and its activity strictly depends on the geological nature of substratum, and on the occurrence of its parent elements (Sundal et al., 2004). Moreover, also other chemical, physical, and geological features (e.g., grain size, porosity, and seasonal variations) influence its behaviour (King et al., 1982; Pinault and Baubron, 1997; Barberio et al, 2018). In particular, the migration of Rn is driven by rock permeability that increases with the presence of fractures, structural discontinuities, and karst cavities (Tanner, 1980). The most important processes for Rn transport in groundwater are diffusion and convection. Since Rn is a heavy element, it preferentially moves upward by way of a fluid carrier. When a nucleus of Ra decays, the nucleus of neoformed Rn undergoes the so-called alpha-recoil effect, therefore it is pushed in the opposite direction to that of the particle α (equivalent to a nucleus of ^{4}He; Sasaki et al., 2004). According to the proposed model (Tanner, 1980), only a fraction of the gas produced inside the solid matrix can leave the rock. To undergo convective transport by fluids that permeate the rock, the radio nuclei must decay at a certain distance from the surface of the rock particles. Due to changes in crustal stress/strain and variations in pore pressure that occur before earthquakes, anomalies in Rn concentrations have been traced in seismogenic areas worldwide (Igarashi et al., 1995). Thus, the use of Rn as a hydrogeochemical tracer found various applications in different fields of the geosciences, especially related to seismic events (Wakita et al., 1980; Ingebritsen and Manga, 2014; Riggio and Santulin, 2015). Based on all these observations, Rn activity in groundwater was continuously detected in two springs in the Matese area (i.e., Rio Freddo and Grassano springs) using the AlphaGUARD probe consisting of a pulse ionization chamber associated with an alpha spectrometer identifying Rn pulses (Barberio et al., 2018) (Figure 3.6). Additionally, thanks to specific sensors, the device simultaneously measured ambient temperature, relative humidity, and atmospheric pressure. The probe ensures a fast and precise response to different Rn concentrations as well as maintenance-free operations due to long-term stable calibration (sensitivity 1 CPM at 20 Bq/m^3, error 3%). The probe is suitable

for continuous monitoring of Rn concentrations between 2 and 2,000,000 Bq/m^3. Measurements are automatically repeated and stored every 10 minutes.

Figure 3.6. The AlphaGUARD device (Model PQ2000PRO) for radon monitoring with a RAM 7 module for stripping gas from the water.

3.4.2 Dissolved Carbon Dioxide

Carbon dioxide is the most abundant and widespread gaseous species in volcanic and hydrothermal environments (Kerrick, 2001). Natural CO_2 degassing occurs through four main sources: (i) mantle, (ii) metamorphism of carbonate rocks, (iii) decomposition of organic matter, (iv) biological activity (Irwin and Barnes, 1980). In seismically active areas, the origin of carbon dioxide is commonly associated with a mixture of these sources (Sugisaki et al., 1983). Through the study of the $\delta^{13}C$ isotopes, it is possible to clearly recognize them (Chiodini et al., 2004; see Chapter 3; paragraph 3.3.2). High CO_2 fluxes appear to be correlated both to areas with high heat flux and to ones affected by intense fault fracturing. Indeed, CO_2-rich springs occur worldwide along major zones of seismicity, and according to a recent global analysis (Tamburello et al., 2018), there is a positive spatial correlation between CO_2 degassing and extensional tectonic regimes. Thus, normal faults, and areas with high structural damage represent the most suitable scenario for CO_2 uprising (Lamberti et al., 2019). To detect potential variations in deep fluids degassing, Grassano spring was also equipped with the Mini CO_2 probe for continuous measurements of dissolved CO_2 (Figure 3.7). The device is a compact in situ submersible pCO_2 sensor designed for broad use in water sciences. The sensor can be deployed in both fresh and seawater. It can be used for long-term monitoring in remote areas, spot-checking specific locations, and in industrial applications (accuracy $\pm2\%$ of maximum range). The Mini CO_2 operates by

stripping the dissolved gas in solution through a semi-permeable membrane to a gas headspace containing a non-dispersive infrared detector (NDIR). The NDIR sensor is factory-calibrated using WMO traceable standards (http://public.wmo.int). With pCO_2 ranges from 0 to 10%, the instrument provided the versatility needed, by allowing the continuous acquisition of carbon dioxide concentrations, and repeating measurements every 15 min.

Figure 3.7. MiniCO$_2$ probe for continuous monitoring of carbon dioxide.

3.5 Seismicity of the study area

All the hydrogeological, hydro- and gas-geochemical data were compared with the background seismicity of the investigated area. Seismic monitoring was substantially based on the retrieval of seismic data, i.e., the recorded seismicity that occurred in the study area of this specific goal (i.e., Matese area) during the monitoring. In detail, as reported in the Aim of the work (see the Introduction section), the groundwater-seismicity relationship was deepened not only by processing of data actively collected during the three years of the PhD but also by analyzing previous data both from the Matese and the Sulmona areas. The main findings of possible earthquake-induced hydrogeological responses (statistically significant and/or supported by further elaborations) will be shown in the Discussion section. In the Results section, the comparison among the acquired times series and seismic events with M > 2 that occurred within a circular spatial window with a diameter of 60 km centred on Telese Terme village (Lat. 41.216667°; Long. 14.533333°) will be shown. This radius of distance was chosen to cover an area comprising all the monitored springs, and the magnitude greater than 2 to filter and thus exclude very low-magnitude earthquakes and microseismic events, which are unlikely to cause a recognizable hydrogeological response. The seismic data are from the online database of Istituto Nazionale di Geofisica e Vulcanologia (available at the website: http://terremoti.ingv.it/).

4. Results and interpretation

In this Chapter, results will be described and interpreted. In detail, the following paragraphs will mainly focus on data from Matese and Contursi area. However, during my PhD, I actively worked on retrieved data from other monitoring sites in central Italy (Sulmona area and San Vittorino plain). These latter data were collected before the onset of my research activity, and for this reason, they are not reported in this section but will be presented and in-depth discussed in the Discussion section. Also, some preliminary results from a new hydrogeochemical monitoring station installed in Andalusia region (southern Spain) during the period abroad of my PhD activity will be presented.

4.1 Matese area

In this section, results of this multidisciplinary investigation will be presented. All the hydrogeochemical and gas-geochemical collected data will be shown to (i) hydrogeochemically characterize selected springs (see location in Figure 4.1) (ii) analyse temporal variations (i.e., construction of time series) to recognize environmental, seasonal, periodic signals, and potential pattern related to occurrence of seismic events.
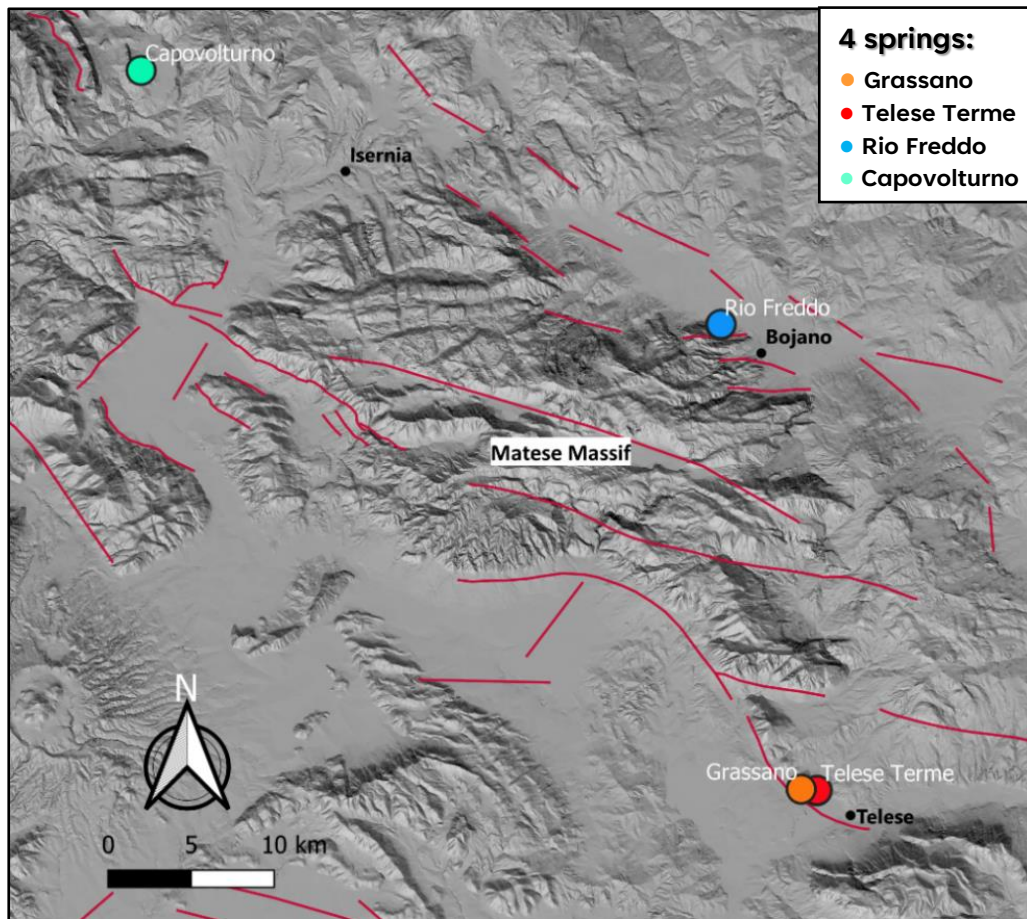
Figure 4.1. Map of the Matese area. Active faults are displayed with red lines from the Ithaca database (https://www.isprambiente.gov.it/en/projects/soil-and-territory/italy-hazards-from-capable-faulting). The base digital elevation model is from the TINITALY DEM (http://tinitaly.pi.ingv.it/). Locations of springs are depicted with coloured circles. This figure has been realized using QGIS 3.16.

4.1.1 Hydrogeochemical characterization

Chemical-physical parameters (e.g., temperature, pH, and electrical conductivity), major ions, trace element concentrations, and isotope contents of each sampling survey are presented in the Annex 1a. The four sampled springs are characterized by low to moderate-high salinity. To better look into their hydrogeochemical features, two different classification diagrams were realized (i.e., Piper and Schoeller diagrams), where data of major ions concentrations in mg/L were suitably converted into meq/L (milliequivalents per liter).

The trilinear Piper diagram shows the relative concentrations of the major cations and anions, which constitute the most significant total dissolved solids in groundwater (Piper, 1944; Figure 4.2). Hence, it allows to graphically represent cation and anion compositions of many samples on

a single graph where major groups or trends can be easily discerned. In the Matese area, the content of major ions (Calcium, Magnesium, Sodium, Potassium, Chlorides, Sulphates, and Bicarbonates) reveals one main hydrogeochemical facies. All the waters are predominantly enriched in bicarbonate and calcium ions (Ca-HCO₃ facies). Despite the same hydrogeochemical domain, it is noteworthy that Telese spring is hypothermal, sulphurous calcium-bicarbonate type (Harabaglia et al., 2002), with a noticeable amount of free gas phase (up to 95-97% v/v).
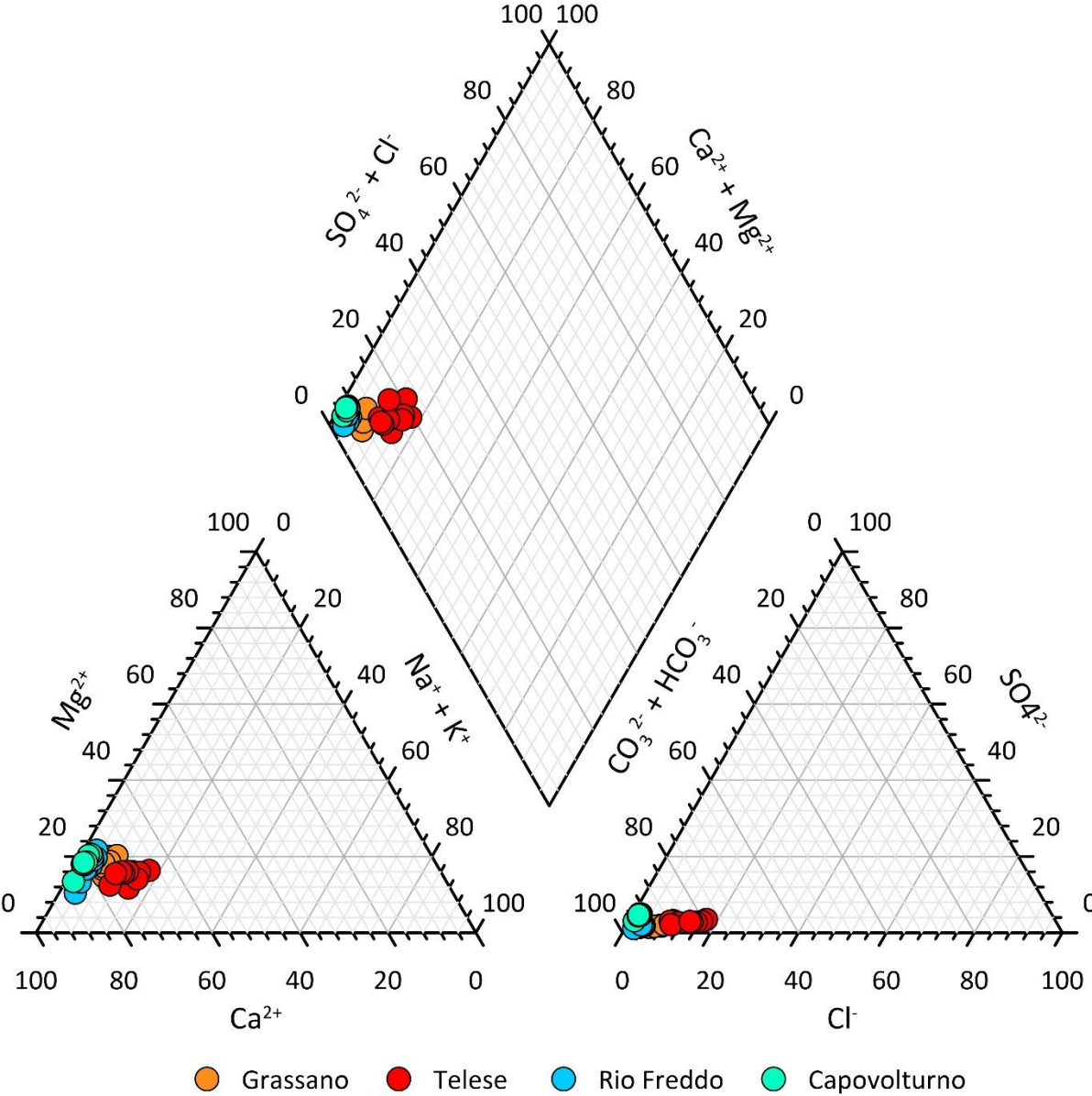

Figure 4.2. Piper diagram for groundwater samples from the Matese area. All samples are included in the calcium-bicarbonate waters domain.

To obtain quantitative information about springs mineralization, the logarithmic Schoeller diagram was used (Figure 4.3). In fact, it presents the major ions on X-axis, and their concentration on Y-axis with a logarithmic scale.
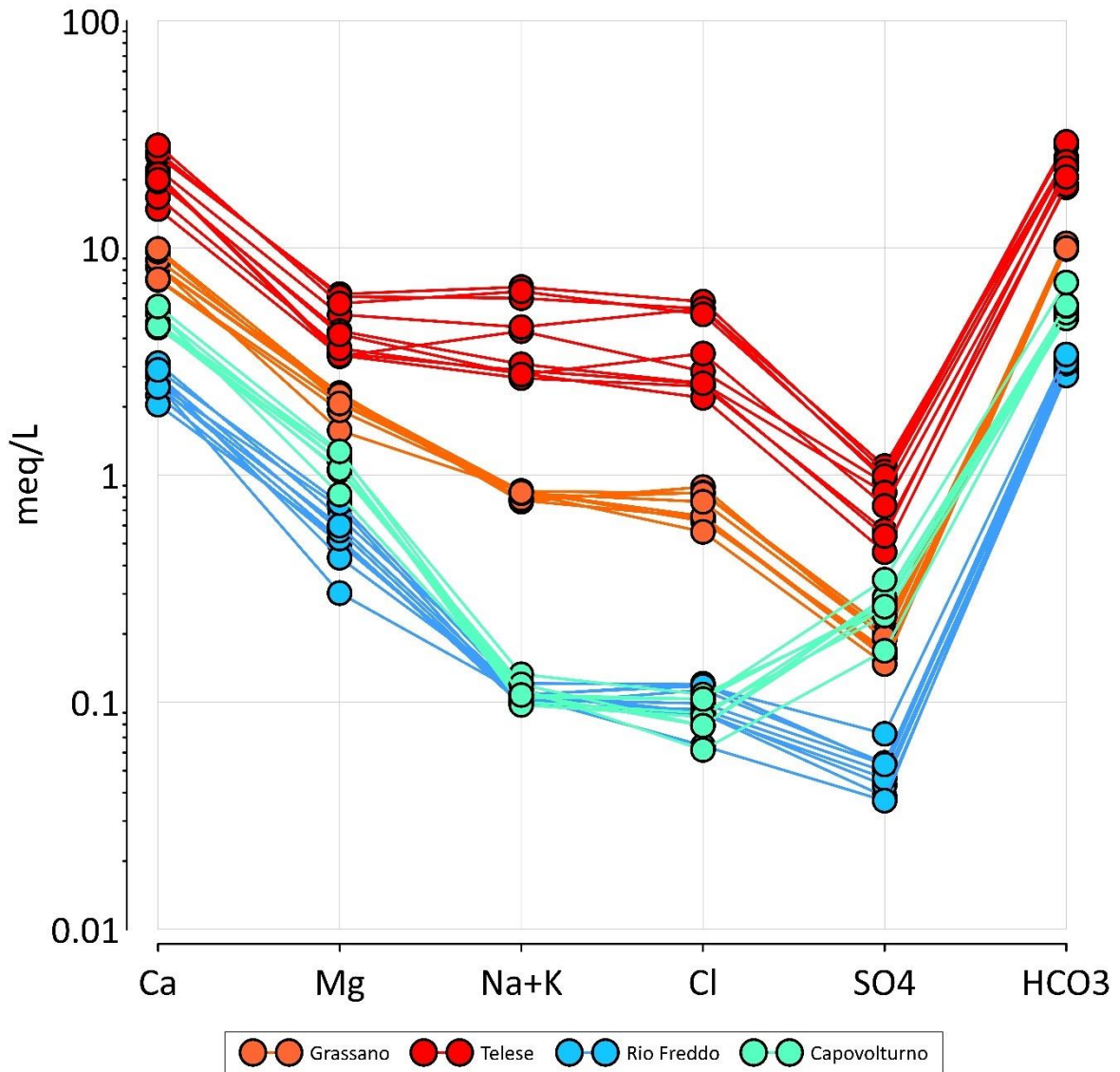
Figure 4.3. Schoeller diagram showing concentration of major ions (Ca, Mg, Na+K, Cl, SO_4, and HCO_3) of groundwater samples from the Matese area.

Based on the Hydrogeological setting of the study area (see Chapter 2; paragraph 2.4), this graph makes it possible to distinguish three groundwater flow systems:

• deep and long groundwater flowpath for Telese spring, which is the most mineralized compared to the other analyzed waters; the detected high concentrations of the major ions agree with results of previous works (Calcaterra et al., 2009; Di Luccio et al., 2018; Corniello et al., 2021), and are

ascribable to deep fluids contributions ascending along fractures and tectonics discontinuities of karst limestones.

• "intermediate" groundwater flowpath is represented by Grassano waters, deriving from the mixing between the shallow regional flowpath, coming from the Matese carbonate aquifer, and the hydrothermal-mineralized and gas-rich fluids upwelling along faults.

• shallow groundwater flowpath consisting of the waters of Bojano and Capovolturno, which has relatively low concentrations of major ions. It is noteworthy that Capovolturno groundwater has higher content of sulphates than Bojano one, owing to the circulation in two different aquifer systems.

These flowpaths imply different geochemical process involving water-rock-gas interaction which can be also studied by the values of stable isotope ($\delta^{18}O$-δD) of spring waters plotted in Figure 4.4. Also, the Global Meteoric Water Line (GMWL), and with the Local Meteoric Water Lines (i.e., Central Italy Meteoric Line and Southern Italy Meteoric Line from Giustini et al., 2016) were displayed. Samples of Capovolturno, and Rio Freddo springs are aligned along the CIMWL and the SIMWL, respectively. Indeed, they represent the meteoric recharge of carbonate aquifers, while Grassano, and Telese springs are characterized by isotopic signatures more enriched in heavy isotopes representing the mixing with ascending deep fluids and are representative of longer circuits. In detail, a positive shift in $\delta^{18}O$ values is observed. This trend is likely due to the mixing with CO_2-rich waters which can produce a horizontal deviation from the LMWL (Pauwels et al., 1997; Cartwright et al., 2000: Karolyte et al., 2017). Indeed, CO_2 can promote low temperature mineral dissolution and secondary mineral precipitation reactions, preferentially consuming ^{18}O and equilibrium oxygen isotope exchange between CO_2 and water, leaving the δD signature unchanged (Corniello et al., 2021).
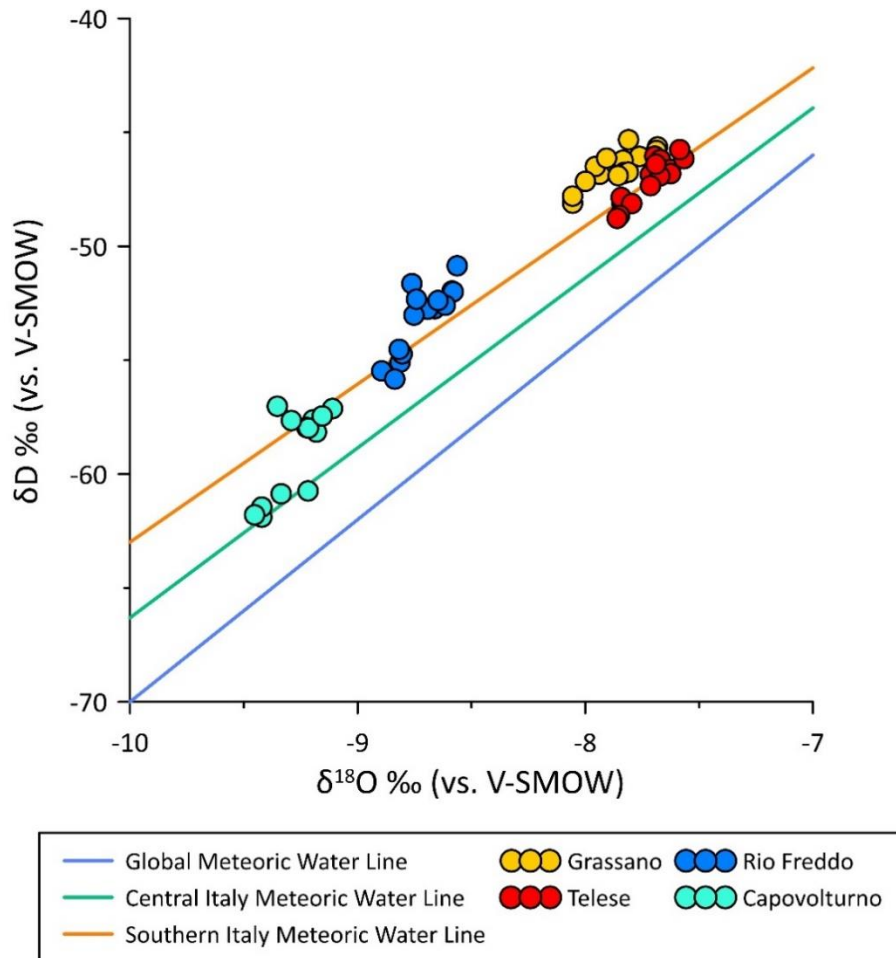
Figure 4.4. Stable isotope (δ^{18}O-δD) of groundwater samples from the Matese area. The Global Meteoric Water Line (Clark and Fritz, 2013), the Central Italy Meteoric Water Line, and the Southern Italy Meteoric Water Line (Giustini et al., 2016) are displayed with light blue, dark green, and orange lines, respectively.

4.1.2 Time series

Detecting temporal variation of the hydrogeological, hydrogeochemical and gas-geochemical parameters represent a crucial factor in achieving the proposed goal. The environmental, local, seasonal signals, and anthropic noises must necessarily be recognized during the processing. In this paragraph, time series (e.g., both discrete and continuous) of chemical-physical parameters, major ions, trace elements, and dissolved gases will be reported. Values of maximum, minimum, mean, standard deviation, and coefficient of variation for each parameter of every spring were calculated and reported in Annex 1b. Besides, the cross analysis of the different variables allows to identify potential interactions among signals, and their typical periodicity.

However, for future research, longer time series need to be acquired and an investigation specifically addressed the comprehension of the possible influence of external sources (i.e., periods of heavy rain/drought, seasonal fluctuation of water table/flow rate) on hydrogeochemical and isotopic composition should be executed to expand our understanding about Hydrosensitivity.

4.1.2.1 Discrete hydrogeochemical time series: chemical-physical parameters, major ions, trace elements

Figure 4.5 shows discrete monitoring of chemical-physical parameters performed during the sampling surveys at each spring of the Matese area (between January 2020 and March 2022). The temperature, electrical conductivity, and pH values for Grassano, Rio Freddo, and Capovolturno springs had good stability over the considered time span having slight annual trends that can be observed. For instance, variations of about 1 °C and 100 µS/cm regarding the temperature and electrical conductivity, respectively. Contrarily, Telese spring has a more variable behaviour. As described before, it is a hypothermal mineralized spring which is influenced by a greater inflow of deep fluids. For this reason, during the recharge period of the aquifer, its waters are influenced by the dilution effect. Indeed, clear decreases in temperature and electrical conductivity were recorded, as shown in Figure 4.5. The pH lowest value (min pH = 6.05: acidic water solution) was observed at Telese spring, consistently with the abundant presence of dissolved CO_2, while the highest pH values (pH max = 8.1) was measured at Rio Freddo spring representing basicity of the waters (similar to Capovolturno spring). Grassano spring also has a basic pH (sometimes slightly acidic), however it presents completely different hydrochemical features with respect Rio Freddo and Capovolturno.

Chemical-physical parameters
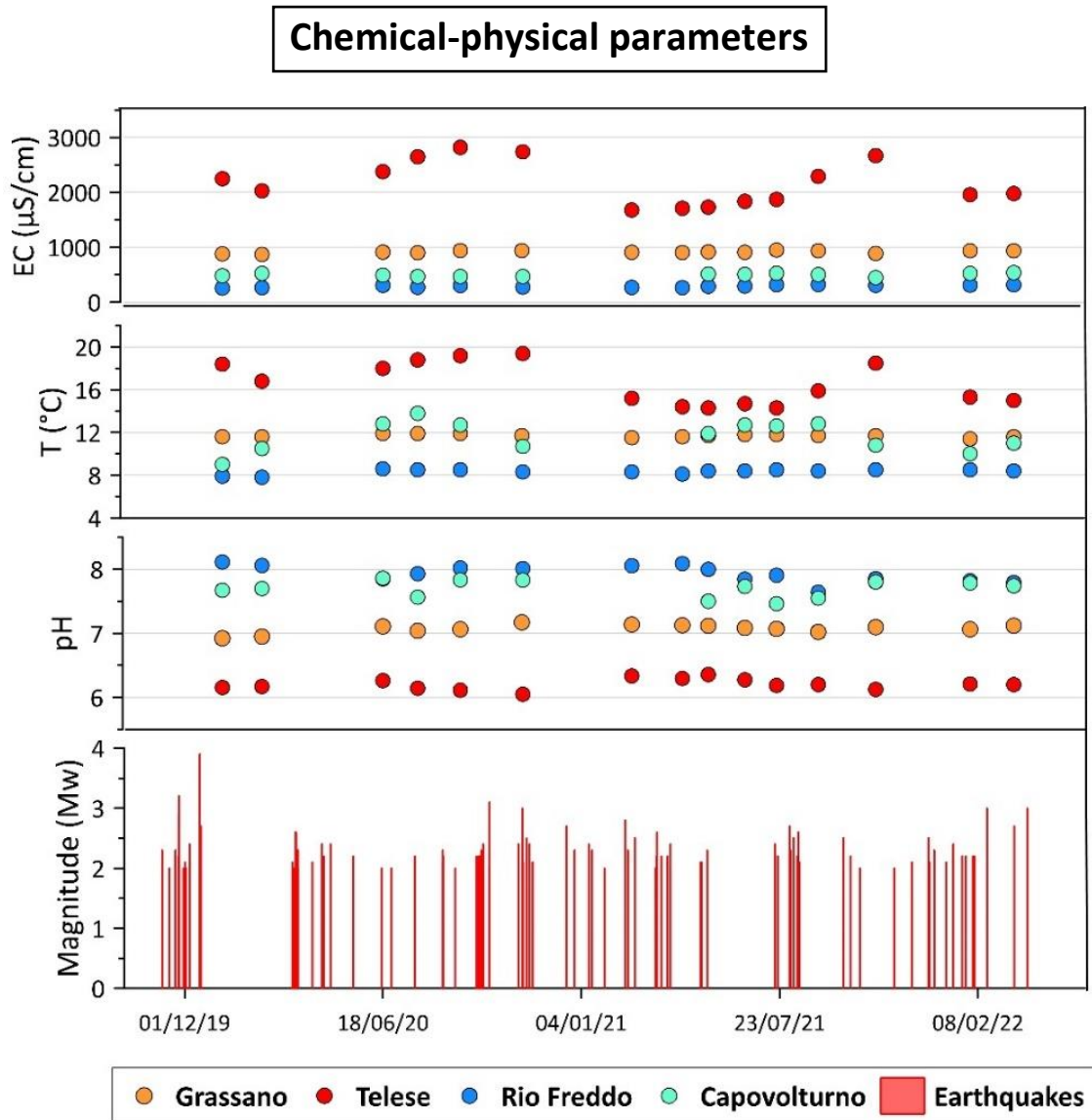
Figure 4.5. Hydrogeological discrete time series: a) electrical conductivity; b) temperature; c) pH; d) seismic events M > 2 within 60 km from Telese Terme.

Figures 4.6a and 4.6b display major ions (cations and anions) concentrations since January 2020. The time series represent the discrete monitoring at the four springs of the Matese area where groundwater samples were collected and addressed to chromatographic analyses. A good stability of the ionic concentrations over time of each single spring can be observed, although a weak seasonal signal is present. Concentrations of the major ions in solution reflects the electrical conductivity values. Therefore, the highest concentrations were found at Telese spring, and the lowest at Rio Freddo one. Seismic events that occurred during the hydrogeochemical period are reported too. Among the "ordinary" background seismicity that characterized this sector of the Apennines, the strongest seismic sequence occurred about 25 km far from the monitoring site of

Grassano spring, near San Leucio del Sannio village. It started on November 21st, 2019 and ended on December 17th, 2019. It included 87 seismic events whose maximum earthquake magnitude was equal to 3.9, recorded on December 16th, 2019. Only at Grassano spring, significant changes in major ion concentrations possibly related to this seismic sequence were detected. In detail, this analysis revealed that Ca^{2+}, Na^+ and HCO_3^- were characterized by anomalous values of concentrations with respect to the whole distribution recorded in a specific monitored period (February 2018 to September 2020). In the Discussion section (paragraph 5.1: Gori and Barberio, 2022), the geochemical process which took place at Grassano spring will be in-depth explained.
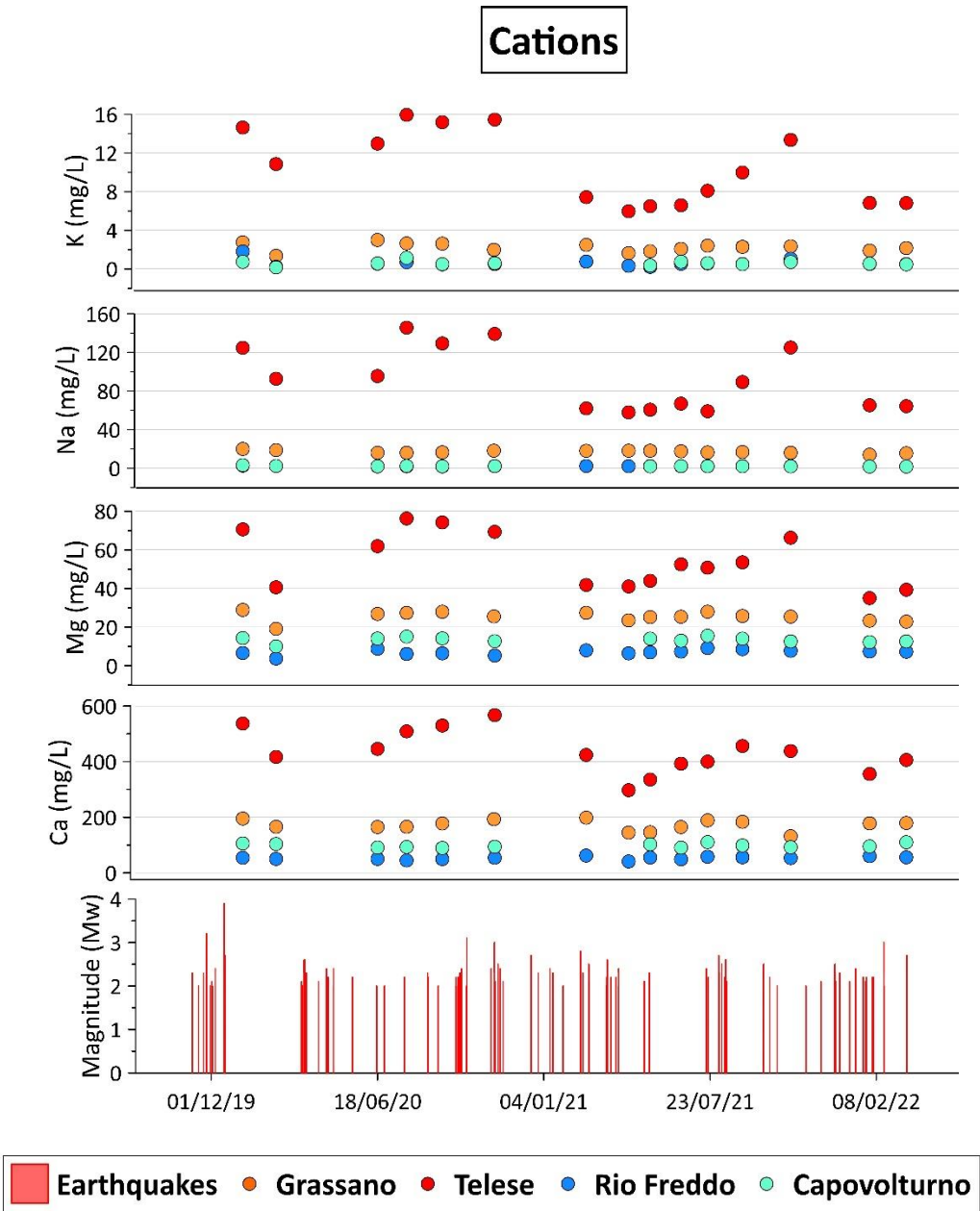
Figure 4.6a. Hydrogeochemical discrete time series: cations (Ca^{2+}, Mg^{2+}, Na^+, and K^+), and seismic events $M_w > 2$ within 60 km from Telese Terme.
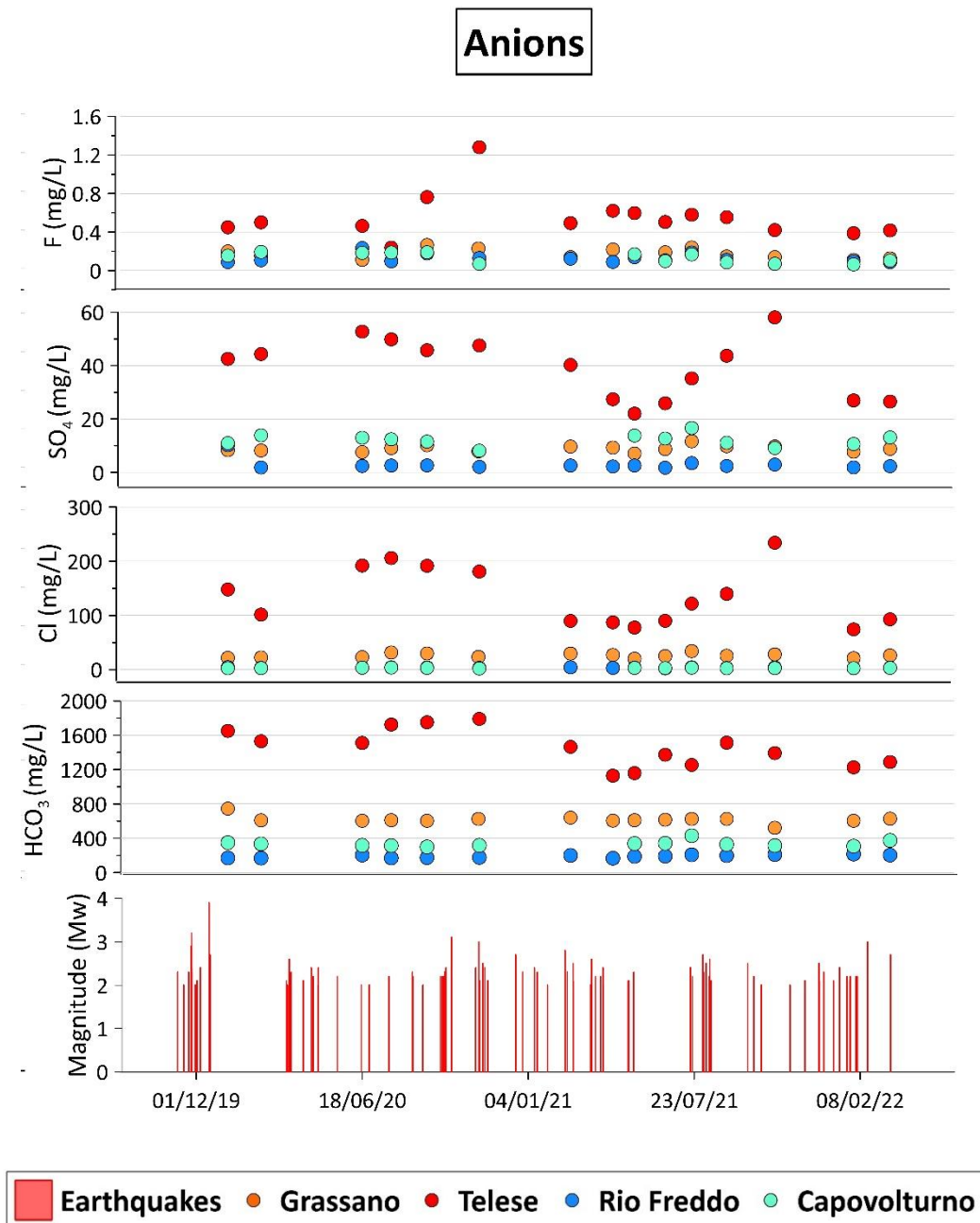
Figure 4.6b. Hydrogeochemical discrete time series: anions (HCO_3^-, Cl^-, SO_4^{2-}, and F^-), and seismic events $M_w > 2$ within 60 km from Telese Terme.

Figure 4.7a and 4.7b include trace elements time series of groundwater samples collected from January 2020 to March 2022. As observed for major ions, trace elements show good stability in time. Evident decreases in Li, B, Cs, Rb, Ba, and Sr were pointed out at Telese spring due to the dilution effect by shallow cold (and low salinity) groundwater. This behaviour was detected also in measurements of chemical-physical parameters, and major ion concentrations and could be attributable to the phases of recharge of the Matese carbonate aquifer. In fact, these minor elements

are typically enriched in evaporite sequences, representing the deep thermal system. Their selection was determined by considering their hydrogeochemical mobility and property with respect to the hydrothermal groundwater flowpath.
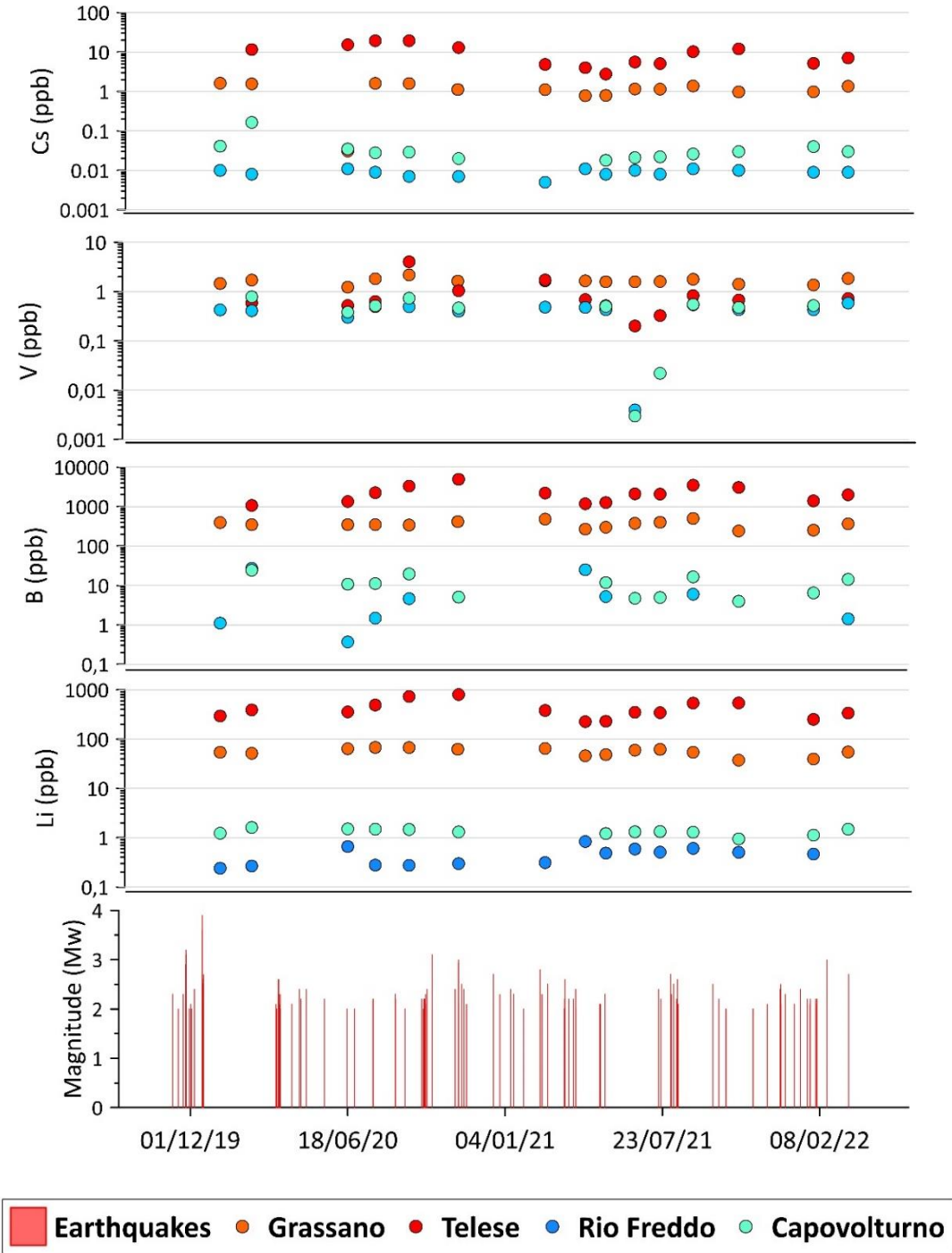
Figure 4.7a. Hydrogeochemical discrete time series: trace elements (Li, B, V, and Cs) concentrations (Y-axis with a logarithmic scale) and seismic events $M_w > 2$ within 60 km from Telese Terme.
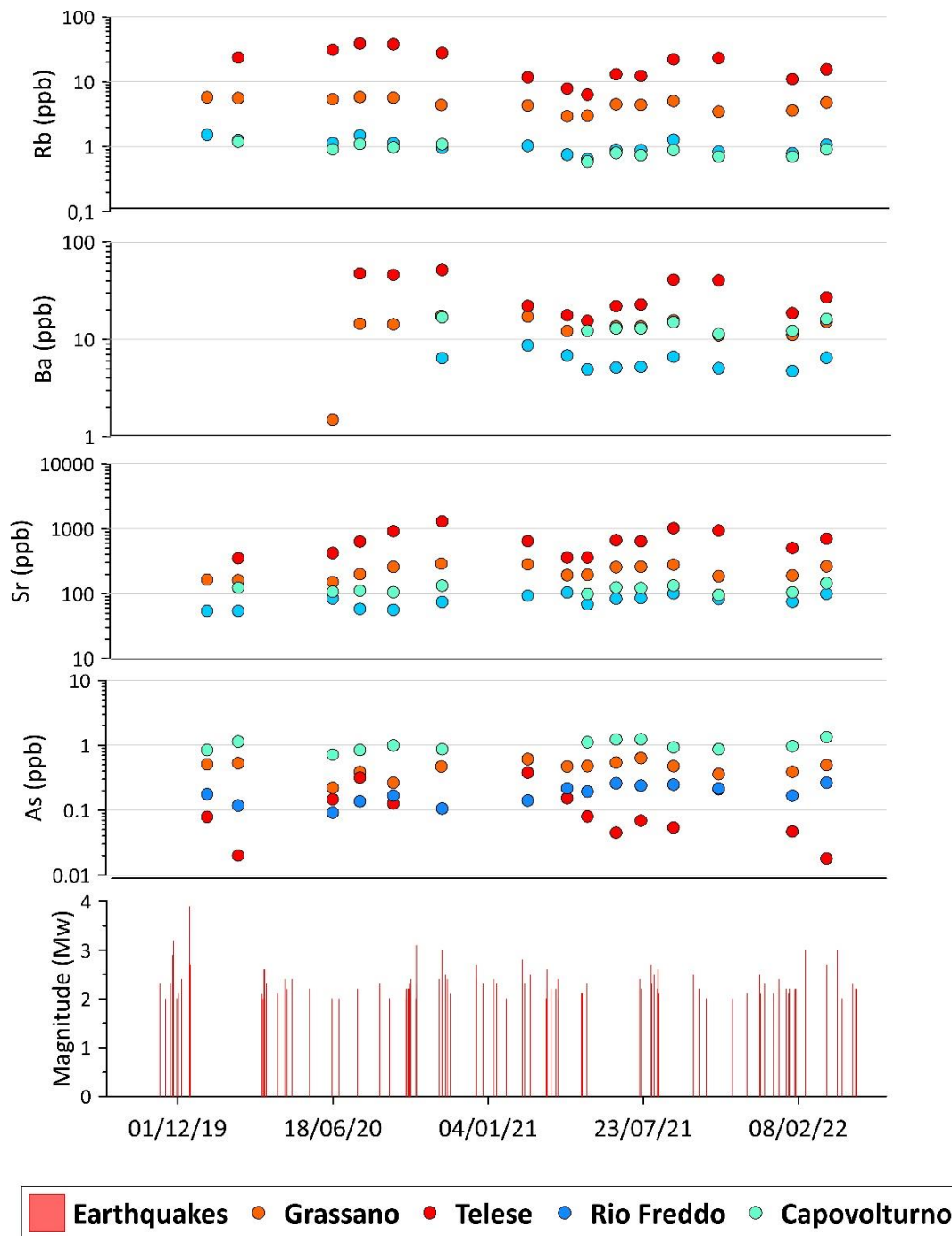
Figure 4.7b. Hydrogeochemical discrete time series: trace elements (As, Sr, Ba, and Rb) concentrations (Y-axis with a logarithmic scale) and seismic events M > 2 within 60 km from Telese Terme.

4.1.2.2 Continuous hydrogeological and hydrogeochemical times series: chemical-physical parameters, and water level

Figure 4.8 shows the continuous hydrogeological time series acquired from March 2019 to December 2021 through the HL4 probe at Grassano spring. For this reason, the parameters consisting of water level, and chemical-physical parameters (i.e., pH, electrical conductivity, and temperature) were all displayed in the same plot. Also, data recorded before the beginning of my PhD were reported because of the significance of hydrogeological variations pointed out in relation to the Benevento seismic swarm (November-December 2019). During this seismic sequence, the strongest earthquake of the whole monitoring period was recorded. Additionally, both rainfall daily data measured by the rain gauge station of Parco del Grassano, and seismic events with magnitude greater than 2 that occurred within an area having a radius of 60 km centred on Telese Terme village are reported. The lack of hydrogeological data between March and June 2020 is due to the shutdown of the device, and the premature end of these time series is owing to its functioning.
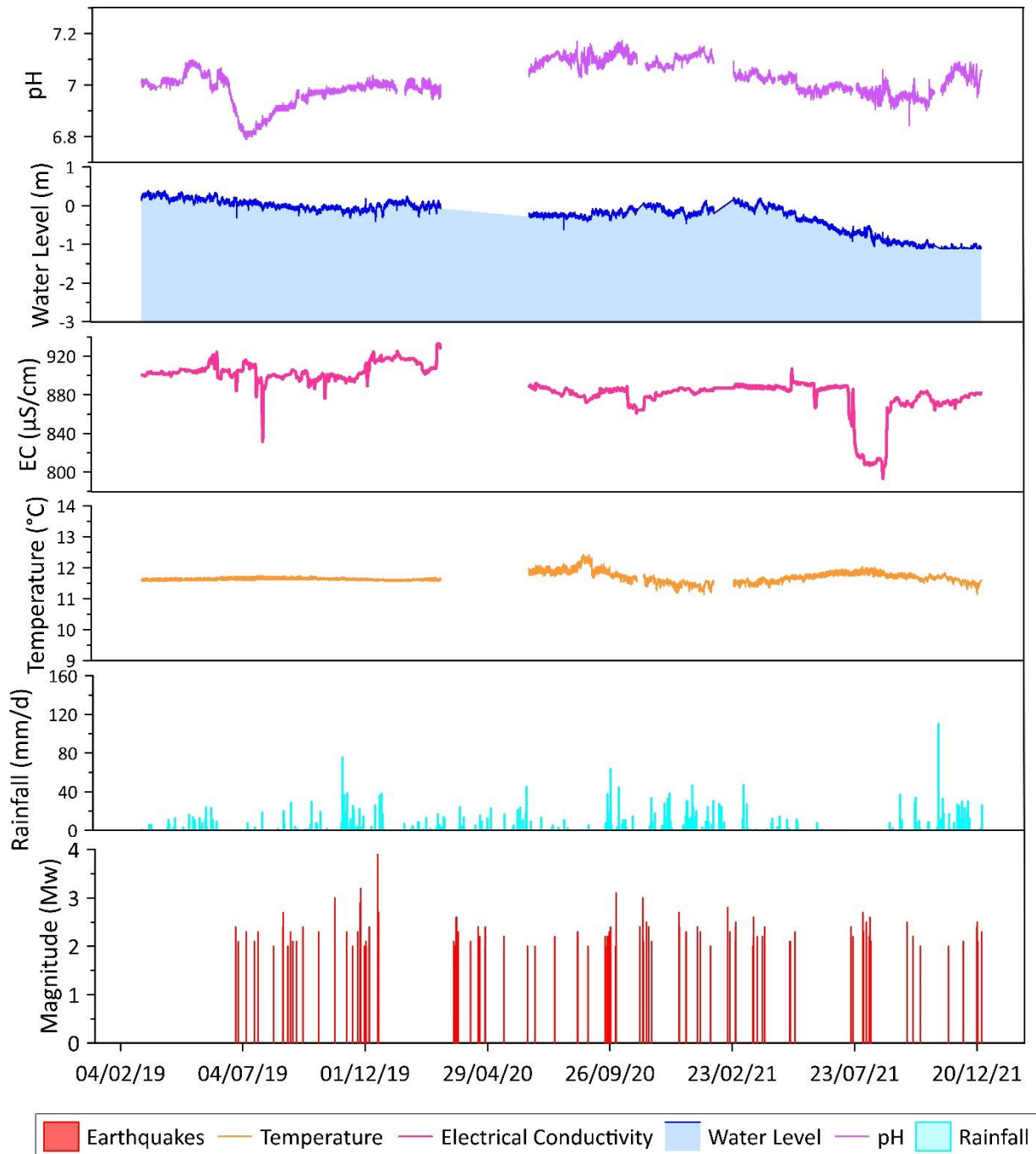
Figure 4.8. Hydrogeological continuous time series: a) pH; b) water level; c) electrical conductivity; d) temperature; e) rainfall at Parco del Grassano; f) seismic events $M_w > 2$ within 60 km from Telese Terme.

The analysis of these time series allows to give the following considerations:

- Seismicity affecting the study area in the investigated period is typical of this sector of Apennines that is characterized by the many low magnitude seismic sequence events mainly with $M_w \leq 3$ (real-time earthquake list provided by INGV: http://terremoti.ingv.it/;

Adinolfi et al., 2015). It is easy recognizable the strongest seismic sequence of the whole monitoring period which started in November 2019 and reached its mainshock on 16th December with M_w 3.9 San Leucio del Sannio earthquake.

- The rainfall is typical of the Mediterranean climate zone characterized by the presence of a dry summer period and a wet autumn-winter period. However, the small detected variations in hydrogeological features (e.g., water temperature and water level) confirm the regional importance of the selected spring which is few influenced by seasonal recharge and depletion cycles. During this specific temporal window of monitoring, a total of 2964 mm of rainfall was measured.

- It is noteworthy that before the gap of data (i.e., between March 2019 and March 2021) the probe was in a different measuring point at Grassano spring with respect to the current one (since June 2020 to December 2021) whose data seem to be more variable. For instance, this aspect is clear by observing temperature and water level time series. Despite the different setting condition, temperature parameter shows a good stability all over the monitored period with an average value of 11.65 °C.

- Electrical conductivity and pH average values are equal to 888 µS/cm and 7.0 unit, respectively. These values agree with those recorded on field by using the multiparametric probe WTW Multi 3420. In detail, pH time series since June to September 2019 was firstly characterized by a sharp decrease and a subsequent increase. Instead, the electrical conductivity time series showed a visible increase of about since November 2019 to January 2020. Both these behaviours were deeply discussed in the Discussion section (see paragraph 5.1: Gori and Barberio, 2022). Another variation of electrical conductivity was observed at the end of July 2021 when an abrupt decrease started. It is difficult to explain as an earthquake response, however, among the factors that could induce this behaviour, the seismicity cannot be excluded, because the change of EC was recorded some days before the onset of the Sassinoro seismic swarm whose strongest seismic event was M_L 2.7. It was about 20 km far from the monitoring station. The possible relationship between groundwater and seismicity should be analyzed more in-depth.

4.1.2.3 Continuous gas-geochemical time series: dissolved CO_2 and Radon concentrations

Figure 4.9 displays dissolved CO_2 time series recorded from May 2019 to June 2022. Unfortunately, it is characterized by several gaps of data due to electrical interruption, and sensor damage. However, like the case of HL4 probe, previous data before the beginning of my PhD (e.g., November 2019) were taken into account since dissolved CO_2 increased in the aquifer system from 6.0% to 6.8% five months before the onset of the Benevento seismic swarm (November-December 2019) causing the above-mentioned sudden pH decrease. The geochemical process that occurred in Grassano spring and involved many hydrogeochemical parameters is widely described and deepened in the Discussion section (paragraph 5.1: Gori and Barberio, 2022). Between May and December 2019, the average value of CO_2 was 6.4%. While between May 2021 and June 2022, it was equal to 4.5%. Furthermore, despite the lower values in this latter second part of the time series, another increase in dissolved CO_2 was detected before the onset of the Sassinoro seismic swarm in August 2022. Besides, another interesting upward changes in concentration from 4.3% to 4.9% was detected two days before the M_L 3.7 earthquake in Campobasso (on May 17th, 2022). Some evident CO_2 spikes are clearly discernible and are attributable both to instrumental, and anthropic noises (i.e., instrument maintenance). Finally, dissolved gas temporal trend did not show a significant correlation with rainfall during the monitoring period.
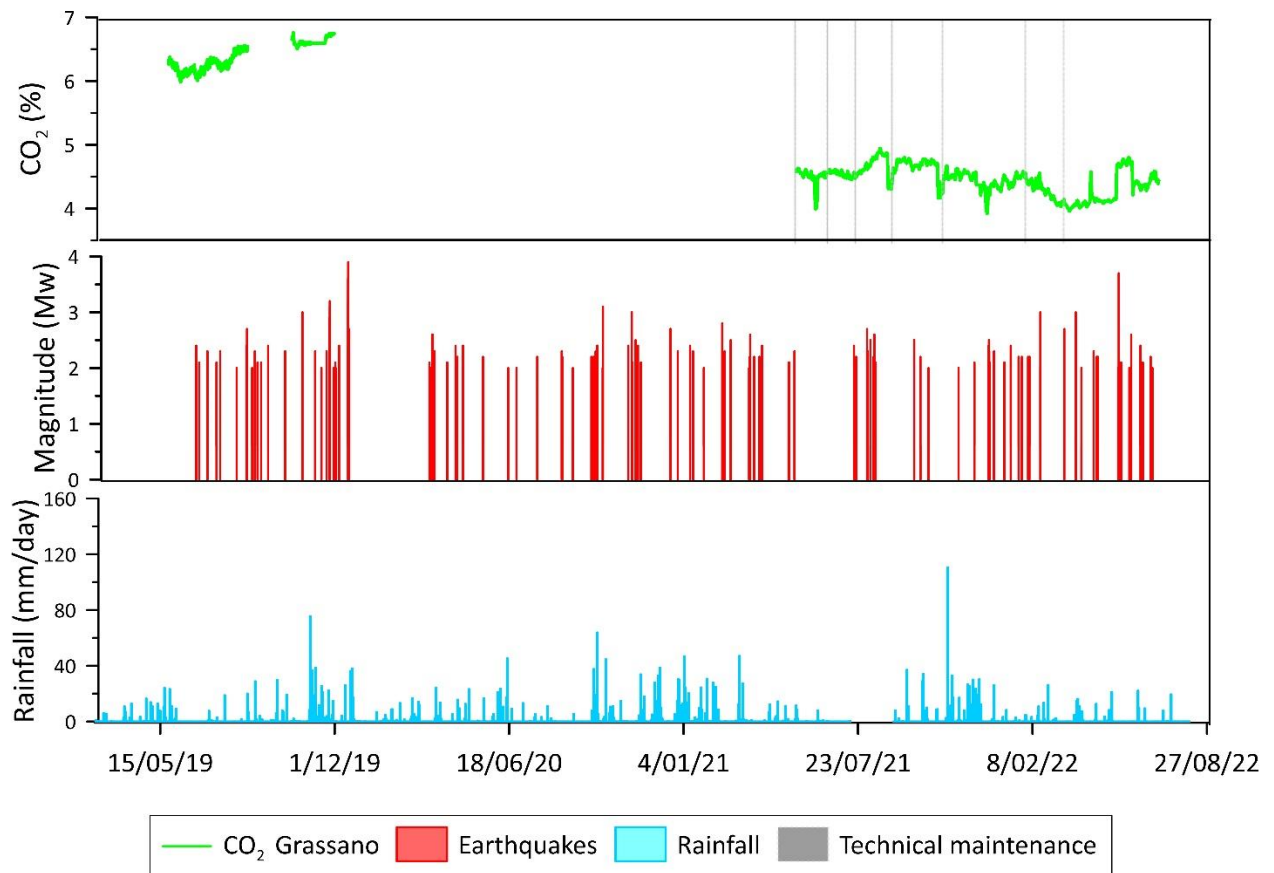
Figure 4.9. Gas-geochemical time series: a) CO_2; b) seismic events $M_w > 2$ within 60 km from Telese Terme; c) rainfall at Parco del Grassano.

Figure 4.10 shows two Radon time series measured at Grassano spring (between July 2020 and June 2022), and at Rio Freddo spring (between January 2020 and June 2022). It is evident that the first time series is shorter than the second one because the probe was installed in July 2020. Furthermore, rainfall data and earthquakes that occurred within an area having a radius of 60 km centred on Telese Terme village are reported. Since groundwater radon signals are very dense and noisy, 10-hour moving averages were calculated for both monitoring sites to make easier the analysis of the time series. Rn average value calculated for all the acquired data at Grassano spring is about 36600 Bq/m^3. During the first year of acquisition (from July 2020 to the end of July 2021), the mean is lower (about 34000 Bq/m^3). Later groundwater Rn concentration started to increase, as pointed out for dissolved CO_2, some days before the Sassinoro seismic sequence, and it recorded higher values until the end of the monitoring period (average value: 39000 Bq/m^3). On the other hand, an opposite behaviour with respect to that of CO_2 gas was observed (i.e., CO_2 increase vs Rn decrease). It is difficult to explain this behaviour and surely it must be deepened by trying to find possible relationships with environmental, hydrogeological, and seismological factors.

Regarding this latter aspect, the possibility that the Rn change represents an earthquake-induced response is not excluded since the M_L 3.7 Campobasso earthquake occurred (on 17th May 2022) some days after the step-like response of gases.

Instead, Rn average value calculated for all the acquired data at Rio Freddo spring is about 4700 Bq/m^3. The concentration of Rn was steady for the first five months (up to May 2020), later it started to decrease, firstly mildly and then drastically probably due to maintenance interventions on the measurement station (depicted as grey lines) which have caused several perturbations in the recorded signal. Since April 2021, Rn data were more stable. However, also groundwater Rn concentrations at Rio Freddo spring, like happened at Grassano spring, showed an increase before the Sassinoro seismic sequence in July 2021. The increase was of approximately 1400 Bq/m^3 (from 4544 Bq/m^3 in the last days of July to the maximum peak of 5952 Bq/m^3) in mid-August. A further Rn variation (i.e., increase) was recorded in the first days of January 2021. Also, in this case, among the potential causes, the seismic sequences of Vinchiaturo (CB) and Gioia Sannitica (CE) which occurred at the end of December 2021 (M_L between 2.1 and 2.4) cannot be excluded but surely this possibility must be validated through more elaborations. Some gaps in data were due to a lack of electricity at the monitoring station. Overall, dissolved Rn did not show a significant correlation with rainfall during the monitoring period too.
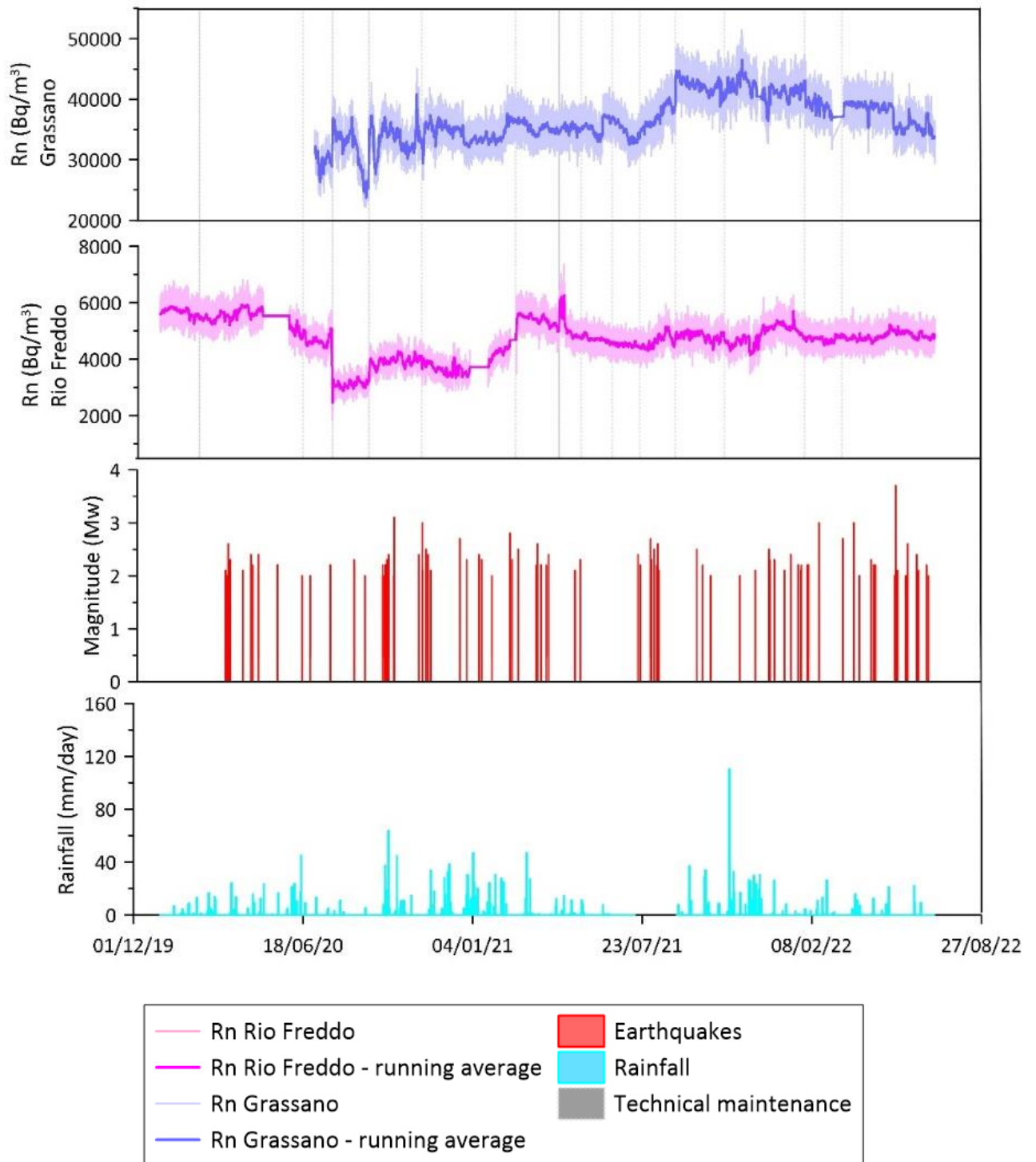
Figure 4.10. Gas-geochemical time series: a) Radon activity at Grassano spring b) Radon activity at Rio Freddo spring; c) seismic events $M_w > 2$ within 60 km from Telese Terme; d) rainfall at Parco del Grassano.

4.2 Contursi area

In this section, hydrogeochemical results of groundwater samples collected in the upper Sele river valley will be presented to in-depth characterize the hydrogeochemistry of the selected twenty-two springs (see location in Figure 4.11). The main aim is to define water-rock interaction processes, fluids origin, and evolution aimed at the construction of a conceptual groundwater flowpath model which can provide useful information on mixing ratio between deep and shallow fluids. The complete database showing all the acquired data is provided in the Annex 2.
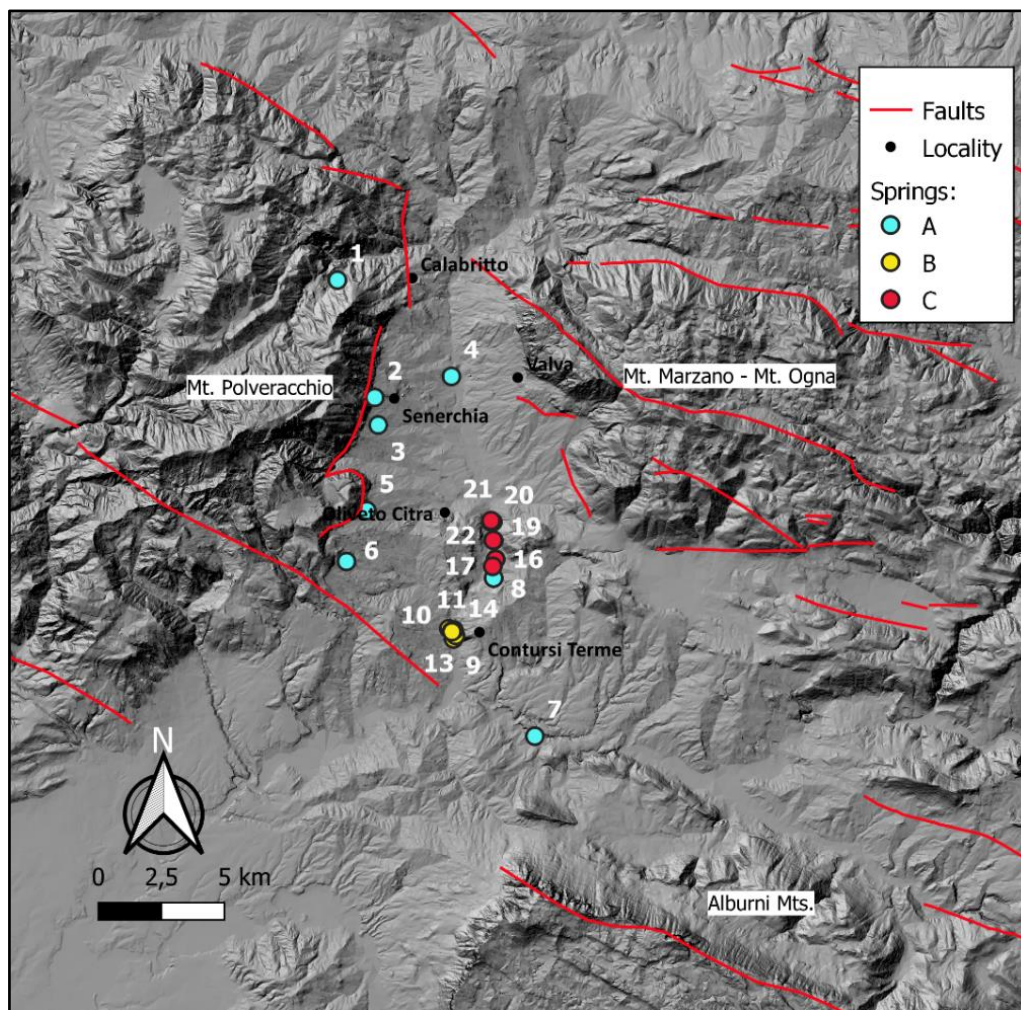
Figure 4.11. Map of the Contursi area. Active faults are displayed with red lines from the Ithaca database (https://www.isprambiente.gov.it/en/projects/soil-and-territory/italy-hazards-from-capable-faulting). The base digital elevation model is from the TINITALY DEM (http://tinitaly.pi.ingv.it/). Investigated springs are displayed with circles of different colours depending on their geochemical features. Relative numbers refer to specific information of each sample site (see Discussion section; paragraph 5.4: Gori et al., 2023). This figure has been realized using QGIS 3.16.

Results of chemical-physical parameters pointed out wide ranges of variation in their measurements that explain the clear difference of hydrogeochemical features of groundwater in the upper Sele river valley. Indeed, values of temperatures, pH, and electrical conductivity, vary between 7.8 and 47 °C, 6.0 and 8.4 unit, and 298 and 6470 µS/cm, respectively.

To make easier and clearer the interpretation of graphical elaborations, springs were classified into three groups (named A, B, and C) according to their temperature, degree of mineralization and TDS. In detail, group A includes cold and low salinity groundwater (from S1 to S8); group B includes the intermediate salinity groundwater (from S9 to S14); group C includes the thermal and saline groundwater (from S15 to S22).

Also, for the Contursi area to better recognise the hydrogeochemical facies, a preliminary characterization by using major ion contents was realized through the Piper diagram (Piper, 1944; Figure 4.12). A linear hydrogeochemical evolutionary mixing trend was observed from the calcium-bicarbonate facies of S1 spring to Na(Ca)-HCO_3 (Cl) water domain of S22 spring.
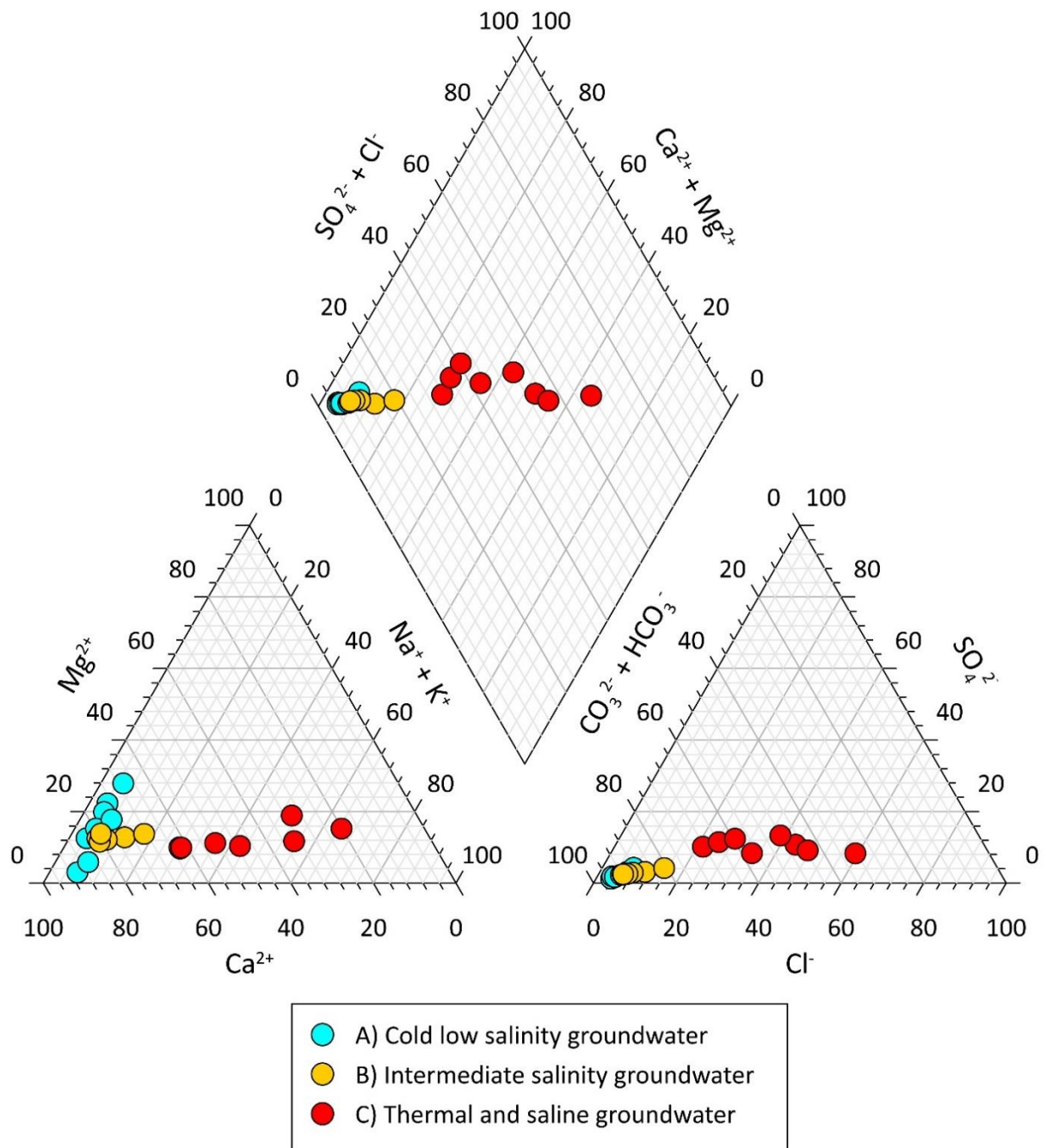
Figure 4.12. Piper diagram for groundwater samples from the Contursi area. Groundwater samples show a hydrogeochemical evolutionary mixing trend from the Ca-Mg-HCO₃ hydrofacies to the Na(Ca)-HCO3(Cl).

Some springs were selected for performing samplings of stable and radioactive isotopes, including the stable isotopes of water (δ^{18}O-δD), sulphate (δ^{34}S-δ^{18}O), and the radioactive isotope of hydrogen (^{3}H).

Figure 4.14 displays the values of Oxygen-18 and Deuterium, expressed in parts per thousand differences (δ ‰) of the isotope ratio of each sample with respect to the same ratio in the standard (V-SMOW). Also, the Southern Italy Meteoric Water Line and the Global Meteoric Water line from literature are reported (Craig, 1961; Giustini et al., 2016). Water isotopic values are from −8.5 to −6.3‰, and from −50 to −38‰ for $\delta^{18}O$ and for δD, respectively. The stable isotope values ($\delta^{18}O$-δD) of nine selected springs reveal that samples have a meteoric origin. As shown in Figure 4.14 groundwater of group A is aligned along the Southern Italy Meteoric Water Line, indicating that local precipitation recharges the aquifer. However, groundwater of group C is characterized by significant deviations both in $\delta^{18}O$ and δD values, potentially affected by different geochemical process and groundwater flowpaths. For instance, shift towards less negative $\delta^{18}O$ values could be characteristic of isotopic water-rock exchange at high temperature, mainly in carbonate environment (Karolyte et al., 2017 and references therein). Furthermore, Figure 4.13 shows that Tritium measurements of groundwater samples are between 1 and 2.3 TU. However, the binary relationship between groundwater tritium and $\delta^{18}O$ does not show a linear correlation. Therefore, for tracing the groundwater movement and for determining the relative ages of groundwater, data will be processed by applying two models (i.e., the piston-flow and well-mixed reservoir) based on tritium isotope (see Discussion section; paragraph 5.4: Gori et al., 2023).
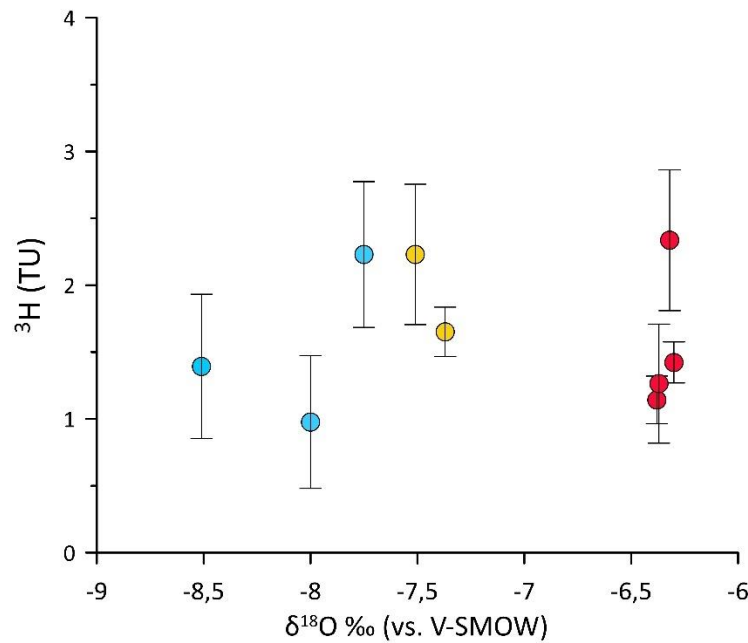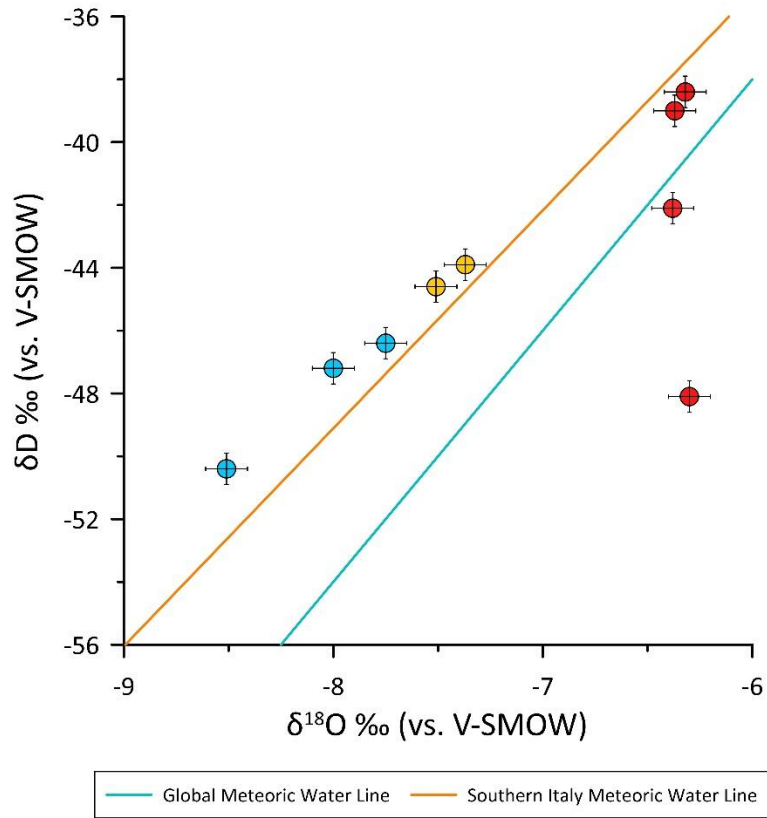
Figure 4.13. a) Stable isotope (δ^{18}O-δD) of groundwater samples from the Contursi area. The Global Meteoric Water Line (Clark and Fritz, 2013), and the Southern Italy Meteoric Water Line (Giustini et al., 2016) are displayed with dark green, and orange lines, respectively. b) Radioactive isotope of hydrogen (^{3}H) vs stable isotope of oxygen (δ^{18}O) of groundwater samples from the Contursi area. Groups of groundwater (i.e., A, B and C) are depicted with different colors.

Figure 4.14 shows the values of the Sulfur-34 and the Oxygen-18 of the dissolved SO_4, expressed in parts per thousand differences (δ ‰) of the isotope ratio of each sample with respect to the same ratio in the standards: V-CDT (Vienna Canyon Diablo Troilite), and V-SMOW (Vienna Standard Mean Ocean Water) for $\delta^{34}S$ and for $\delta^{18}O$, respectively. Only groundwater samples of groups B and C are reported, since groundwater belonging to group A showed low SO_4 content. Dissolved SO_4 isotopes are characterized by the following range values: from 5.3 to 8.4 and, from 9.7 to 21.9 for $\delta^{18}O$ and for $\delta^{34}S$, respectively. Besides, fields of possible sources of the sulphate are also reported with rectangles (Clark and Fritz, 1997). The complete and in-depth discussion of all the isotopic behaviours is reported in the Discussion section (see paragraph 5.4: Gori et al., 2023).
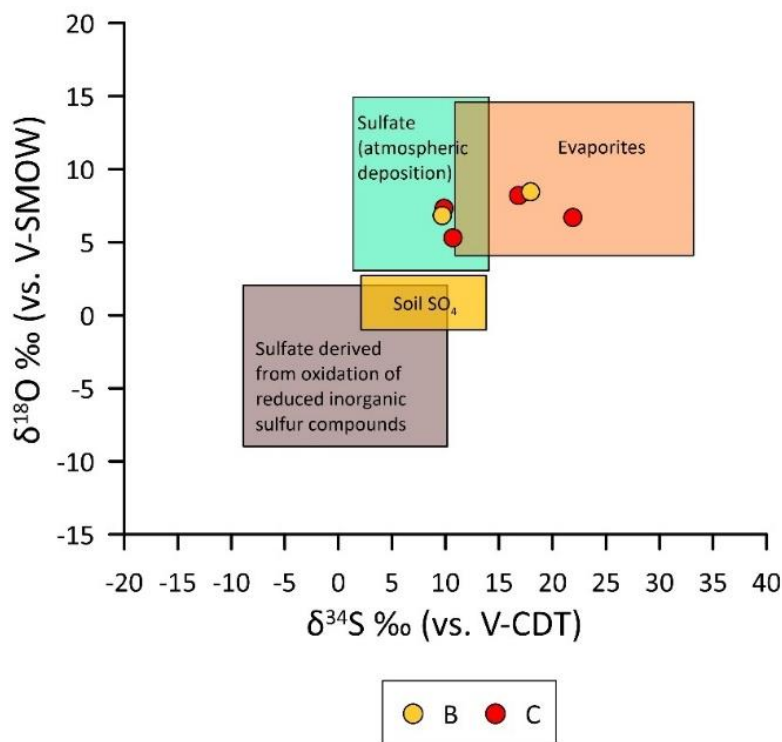
Figure 4.14. Sulphate stable isotopes diagram (from Clark and Fritz, 1997). Isotope ranges for different potential sources of sulphate are displayed with rectangles. $\delta^{18}O$-SO_4 and $\delta^{34}S$-SO_4 isotopic values of some samples from the Contursi area.

Figure 4.15 shows concentrations of trace elements (i.e., B, Sr, Li, Rb, Cs, and Ba) that were selected by considering their hydrogeochemical mobility and property with respect to the hydrothermal groundwater flow. Generally, they act as less reactive and conservative elements in thermal waters and are often used to identify common origins or common deep processes. Plots are reported as box-and-whisker plots to better understand the statistical range distribution of the

elements. Each box represents interquartile ranges (25-75 quartiles) and is separated into two parts by the median. The whiskers are limited by the interquartile range (IQR) with a factor equal to 1.5. All selected elements have wide boxes, meaning that populations are not clustered around the median and show high variability of distribution. Furthermore, only group A has outliers exceeding the whisker in Sr, Li, Rb and B. The overall difference in the minor/trace element concentrations (see ppb on Y-axis) between cold and thermal groundwater indicates that thermal one has a greater reactivity leading to greater weathering of the elements from the host rock during flowpath, also favoured by the acidic environment created by the dissolution of huge quantity of deep-derived CO_2. Additionally, the concentration contrast is presumably amplified by the shorter residence times of the cold groundwater and their dilution by phreatic waters (Wang and Shpeyzer, 1997; Ma et al., 2011).
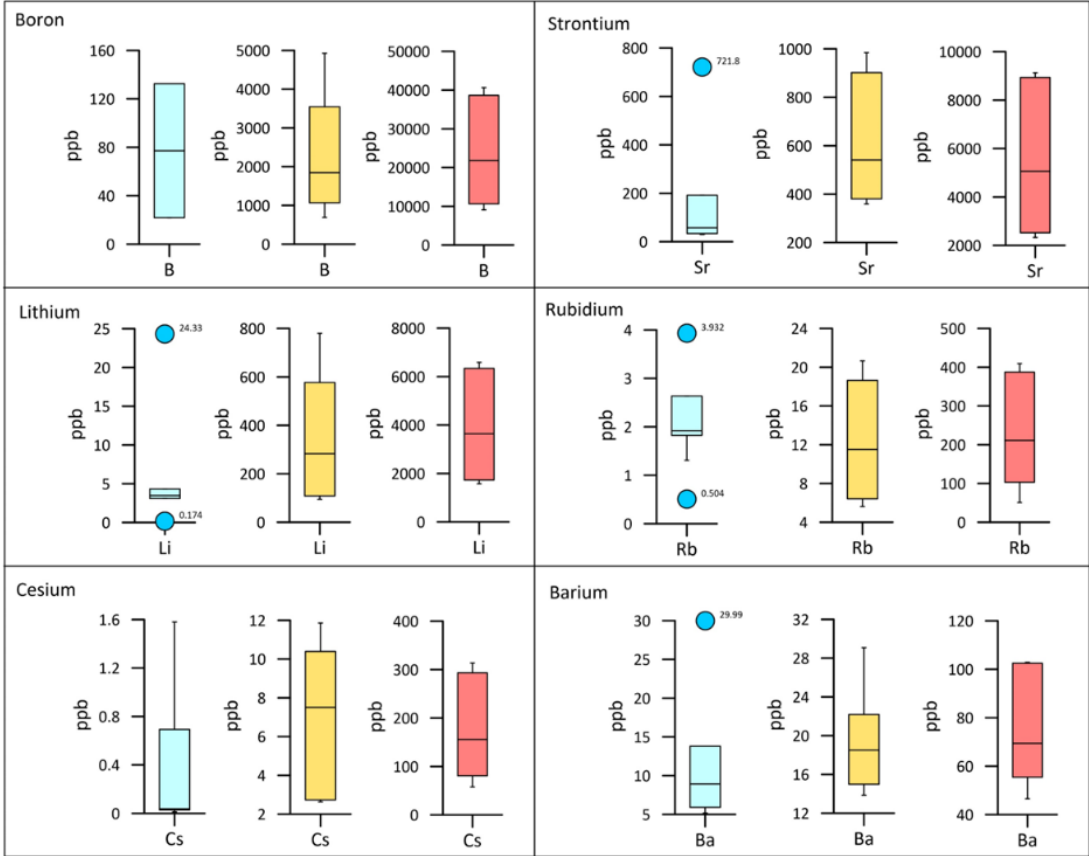
Figure 4.15. Box-and-whisker plots for the selected trace elements (i.e., B, Sr, Li, Rb, Cs, and Ba).

4.3 Maro spring (Andalusia, Spain)

Within my research activity, I started an international collaboration with the University of Málaga (Andalusia, Spain) to monitor hydrogeochemical variations in Maro spring potentially induced by seismic activity. In this paragraph, some characteristics of the investigated spring and some preliminary results of the new ongoing monitoring are briefly presented.

Andalusia, located in southern Spain, is an area of moderate seismic activity in a global context, but one of the Spanish regions with higher seismicity. Maro spring (situated at 120 m a.s.l.; see location in Figure 4.16) is the main discharge point of the Sierra Almijara carbonate aquifer which mainly consists of karstified Triassic calcareous, and dolomite marbles whose high permeability is mainly due to fracturing and karstification (Carrasco et al., 2002; Vadillo et al., 2012). The spring has an average outflow of 250 L/s with a range between 20 and 1600 L/s suggesting a well-developed karstic condition. In fact, it responds very quickly to rainfall with an increasing outflow and dilution of chemical content of water (Liñán et al., 1999; Andreo et al., 2018).

Since December 2021, sampling surveys are ongoing monthly to measure chemical-physical parameters, and to collect groundwater samples (Figure 4.17) addressed to many different hydrogeochemical analyses at the Department of Ecology and Geology of Málaga University. Additionally, a radon probe was installed in June 2022 to measure continuously dissolved gas in groundwater (Figure 4.17).

All the data acquired during these first months of the monitoring are provided in the Annex 3.
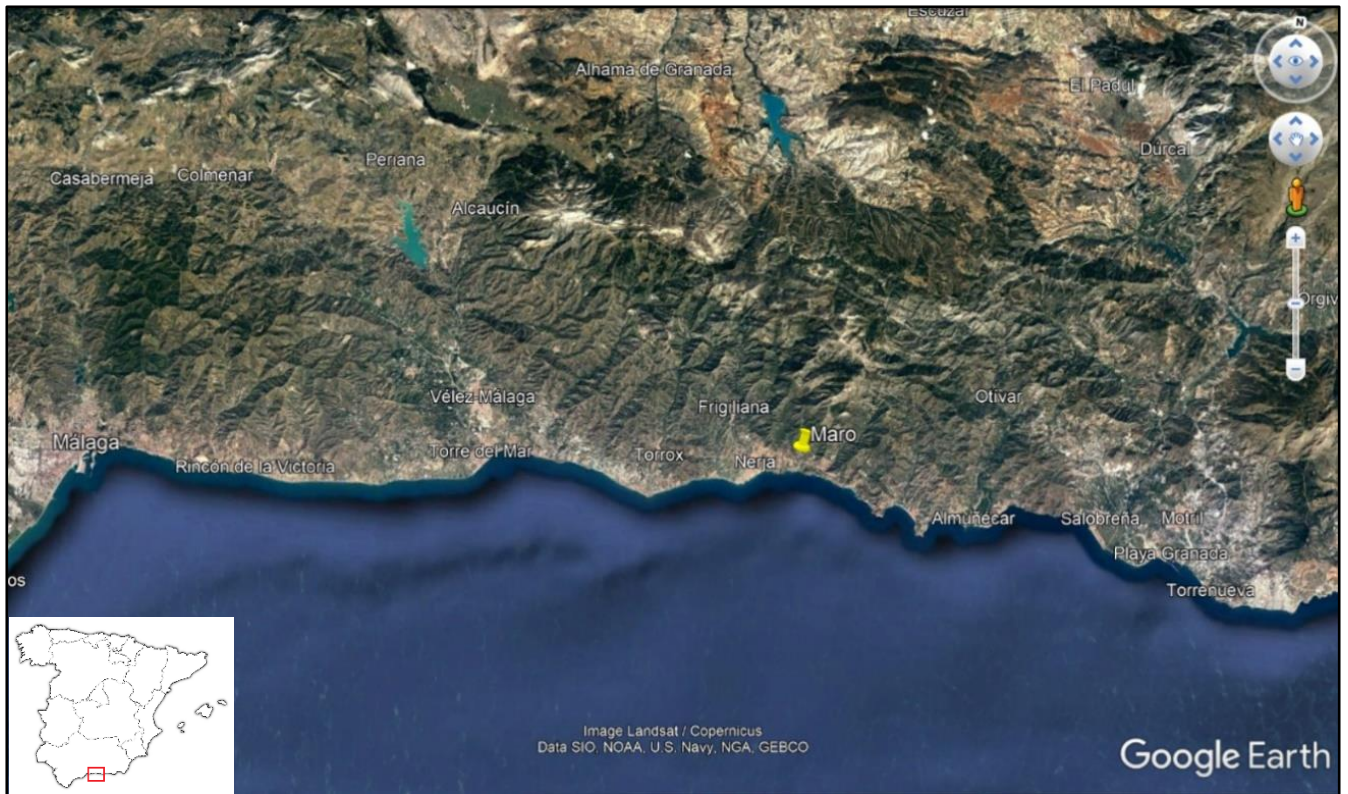
Figure 4.16. The monitoring site at Maro spring is shown with the yellow symbol (see location in lower left inset).

Figure 4.17. On the left, me sampling groundwater; on the right, the AlphaGUARD device for radon monitoring that I installed at Maro spring.

In Figure 4.18, Piper diagram shows that groundwater of Maro spring is included in the calcium-sulphate waters domain (Ca-SO₄ facies). It is characterized by a total mineralization higher than typical expected for carbonate environments. In detail, the high content of sulphate ions is ascribed to the dissolution of Mesozoic gypsum hosted in the carbonate formation (Benavente et al., 2010). The average values of electrical conductivity and pH are 900 µS/cm and 8.1 unit, respectively. Values of maximum, minimum, standard deviation, and coefficient of variation of each parameter were calculated and are reported in the Annex 3.
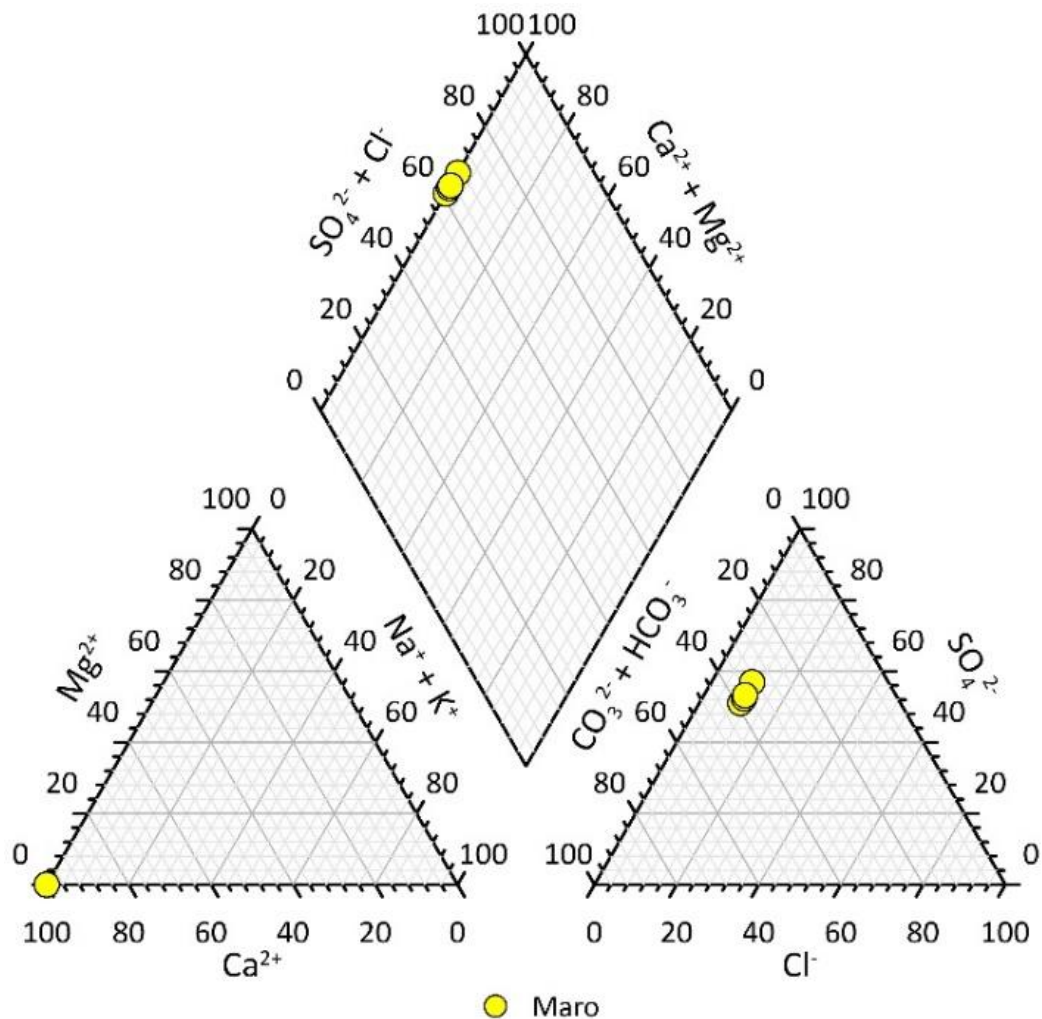
Figure 4.18. Piper diagram showing major ions content of Maro spring.

Figure 4.19 shows the time series of major ions concentration from December 2021 to July 2022. Rainfall data are collected by the rain gauge station "Estación meteorológica Cueva de Nerja - 6313XA" located at the Nerja Cave, approximately 500 m to the W of Maro spring. Seismic data are from the Instituto Geográfico Nacional (online at: https://www.ign.es/web/ign/portal).

In the monitoring period a total of only 151 mm of rainfall was measured. The background seismicity of the study area was characterized by more than 400 seismic events in a radius of about 60 km from Malaga. In detail, 46 earthquakes with $M_w > 2$ were recorded and are displayed in Figure 4.19a and 4.19b.
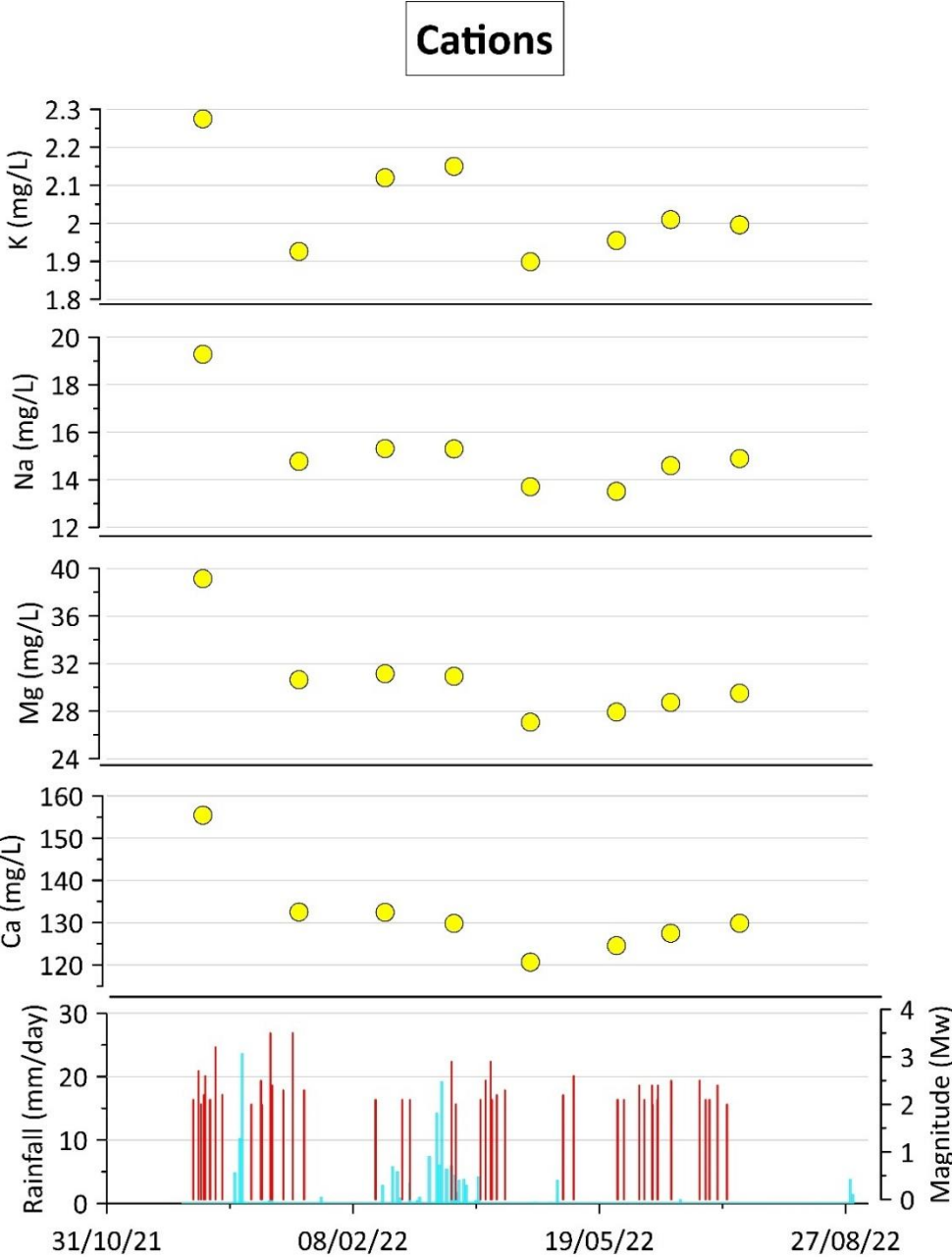
Figure 4.19a. Times series concentrations of major ions (cations: Ca, Mg, Na, and K) are displayed. Also, rainfall and earthquakes recorded in the monitoring period are reported with cyan and red bars, respectively.
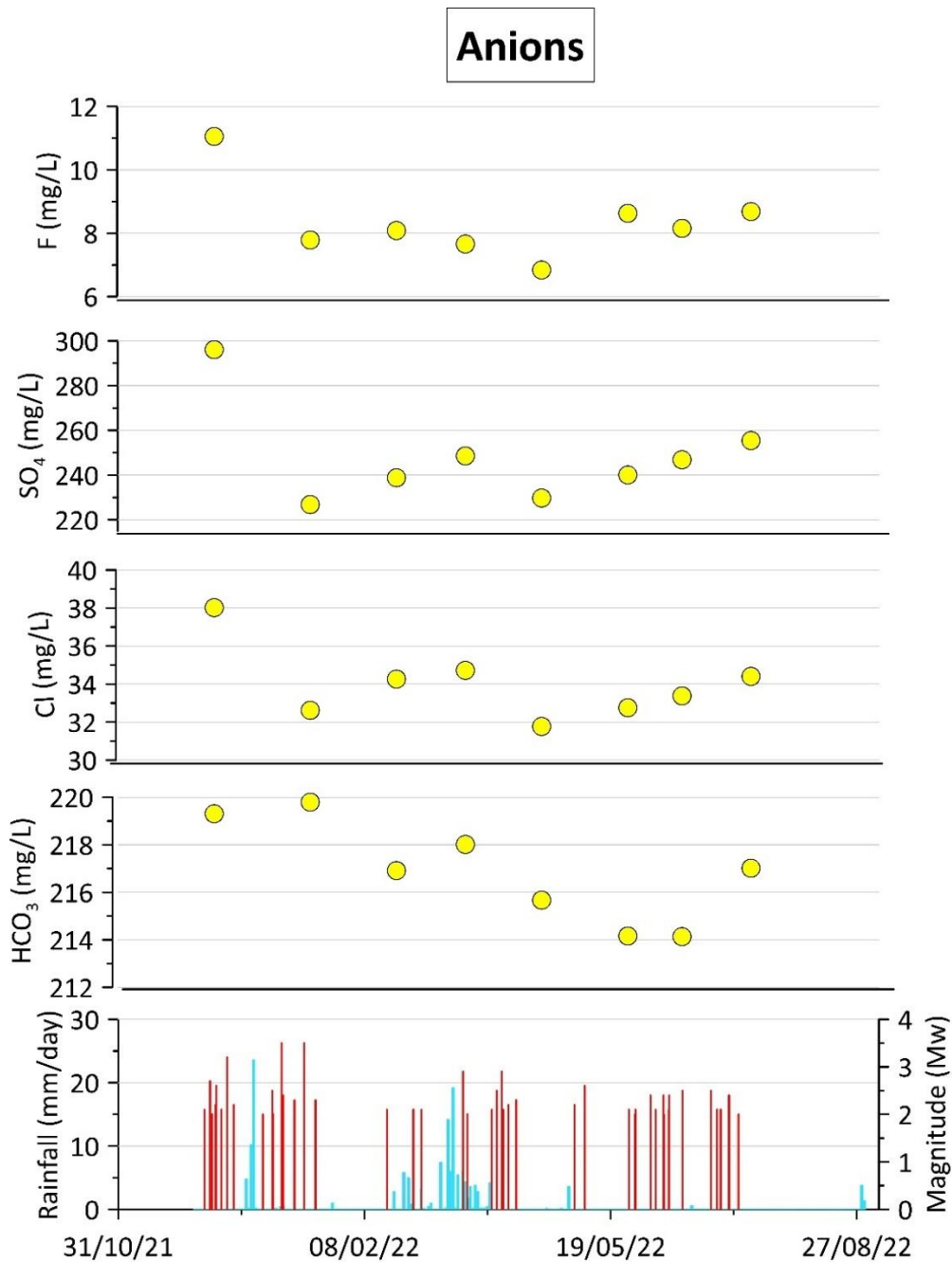
Figure 4.19b. Times series concentrations of major ions (anions: HCO₃, Cl, SO₄, F) are displayed. Also, rainfall and earthquakes recorded in the monitoring period are reported with cyan and red bars, respectively.

At present, the short times series does not allow to point out significant variations of the major ion contents in relation to the seismic activity. Longer times series is needed to define the baseline of every element of the spring in order to detect anomalous signals possibly associated with seismic events.

Below, continuous time series of dissolved radon gas measured in Maro spring between June and July 2022 is shown (Figure 4.20).
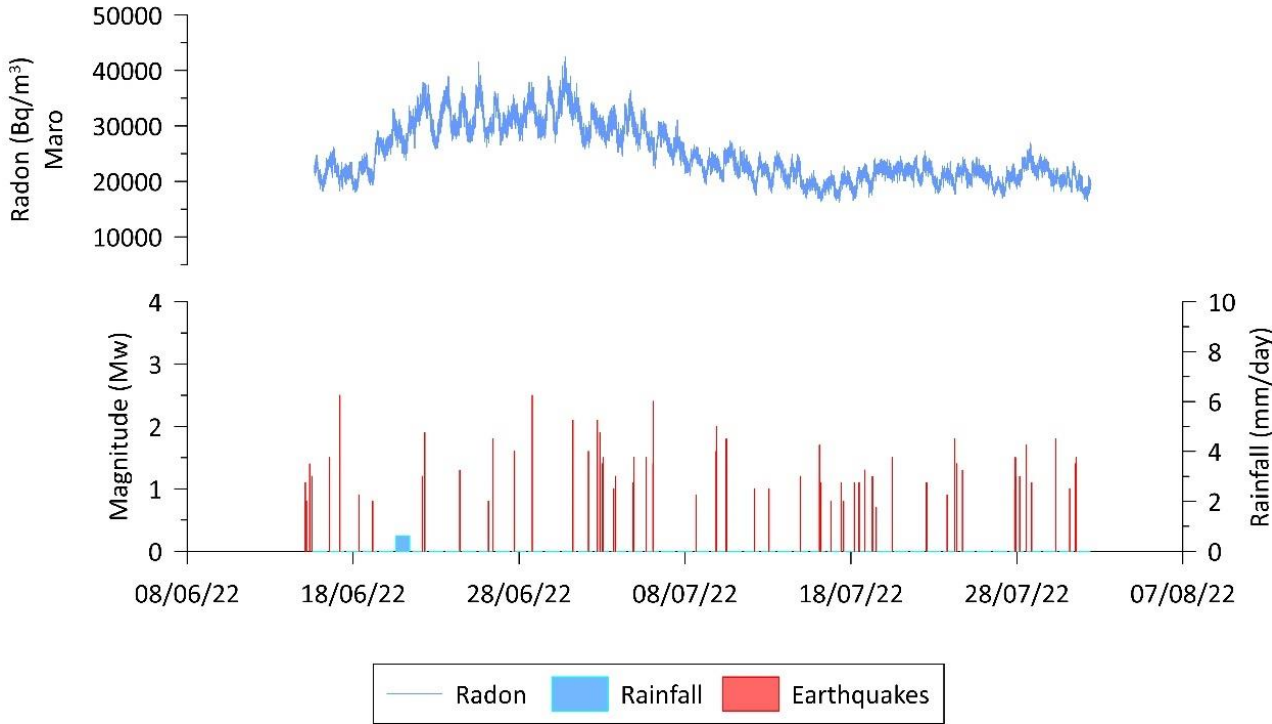
Figure 4.20. Time series of dissolved radon gas measured between June and July 2022.

Despite rainfall was substantially absent during the monitoring period, in the first days of acquisition, an increase in concentration was detected (up to about 40000 Bq/m^3). Later, concentration started to decrease recovering lower values (similar to those recorded at beginning of the time series), and a quite steady trend with values approximately equal to 21000 Bq/m^3. The Rn average value calculated for the whole time series is about 25600 Bq/m^3.

Some clear daily fluctuations were recognized, presumably ascribable to influencing factors linked to solar cycles, such as oscillations of temperature and atmospheric pressure, and also related rock deformations (King et al., 1982; Pinault and Baubron, 1997; Barberio et al., 2018). Also, in this case longer time series will permit to define in-depth the behaviour of the dissolved gas to be further related to seismicity and environmental factors influencing its activity.

5. Discussion

The Discussion is structured according to a collection of published papers where results from the ongoing hydrogeological and hydro- and gas-geochemical monitoring were reported. To reach the proposed goals and to corroborate my thesis, in addition to the areas treated as the "core" of the project (i.e., Matese and Contursi), my research activity extended to other areas in central Italy (i.e., the Sulmona area and the San Vittorino Plain) by analyzing and processing retrieved unpublished data from pre-existing monitoring (both discrete and continuous) run by my colleagues of the Sapienza University of Rome. In detail, the Sulmona area is a monitoring site developed since 2014 in central Apennines to investigate groundwater and seismicity relationship for expanding the understanding of perturbations of fluids in the upper crust due to earthquakes (Barberio et al., 2017; Petitta et al., 2018; Boschetti et al., 2019). On the other hand, the San Vittorino Plain is a suitable site for expanding knowledge about the origin and mixing of deep fluids and the water-rock-gas interactions in shallow aquifer systems leading to an improvement in the comprehension of crustal deformation (Centamore et al., 2009; Petitta et al, 2011; Barbieri et al., 2017).

Paragraphs 5.1, 5.2, and 5.3 deal strictly with the groundwater-seismicity relationship, showing possible earthquake-induced effect on groundwater (e.g., hydro- and gas-geochemical variations in concentration, and groundwater level changes).

Paragraph 5.1 focuses on the hydrogeochemical variations and anomalies detected at Grassano spring (Matese area) before and during the onset of the 2019 Benevento seismic swarm. Results confirm the occurrence of a potential pre-seismic geochemical process in the fractured carbonate aquifers, like the one proposed in literature for the stronger 2016-2017 Amatrice-Norcia seismic sequence.

Paragraph 5.2 shed light on significant correlations between seismic signals and dissolved radon gas concentrations in two springs emerging along two active fault zones in the inner sector of the central-southern Apennines (Matese and Sulmona areas).

Paragraph 5.3 highlights the great hydrosensitivity of the study site in the Sulmona area where groundwater level variations induced by distant earthquakes (i.e., passage of Rayleigh seismic waves) were clearly identified owing to their impulsive character.

Paragraphs 5.4 and 5.5 deal mainly with the deep fluids contribution in shallow aquifer system, by means of a multi-component approach (e.g., calculation of saturation indices, analyses of stable

and radioactive isotopes, application of geothermometers), coupled with the construction of geo-structural cross-sections.

Paragraph 5.4 reports a detailed characterization of groundwater in the Contursi area to assess mixing process in shallow carbonate aquifers and also it provides a conceptual model for groundwater flowpath and deep-seated fluids inflow through deep normal faults acting as preferential pathways.

Paragraph 5.5 investigates the gas-water-rock interaction and the processes that influence aquifer chemistry, providing new insights for understanding hydrogeochemical variations as a function of crustal deformations in the framework of a well-known hydrogeological conceptual model.

A very exhaustive explanation and comprehension of all processes involving groundwater mixing with deep fluids as a function of crustal deformation, micro and macro-seismicity remains a primary objective of analysis and research worldwide. However, this PhD study achieved promising results in the field of hydrogeological and hydrogeochemical monitoring applied for seismic purposes.

Collection of scientific papers:

- **Gori, F.,** & Barberio, M. D. (2022). Hydrogeochemical changes before and during the 2019 Benevento seismic swarm in central-southern Italy. *Journal of Hydrology*, 604, 127250.

- Barberio, M. D., **Gori, F.**, Barbieri, M., Billi, A., Casalati, F., Franchini, S., Lorenzetti, L., & Petitta, M. (2020). Optimization of dissolved Radon monitoring in groundwater to contribute to the evaluation of the seismic activity: an experience in central-southern Italy. *SN Applied Sciences*, 2(8), 1-12.

- Barberio, M. D., **Gori, F.**, Barbieri, M., Billi, A., Caracausi, A., De Luca, G., Franchini, S., Petitta, M., & Doglioni, C. (2020). New observations in Central Italy of groundwater responses to the worldwide seismicity. *Scientific Reports*, 10, 17850.

- **Gori, F.**, Paternoster, M., Barbieri, M., Buttitta, D., Caracausi, A., Parente, F., Sulli, A., & Petitta M. (2023). Hydrogeochemical multi-component approach to assess fluids upwelling in shallow carbonate-evaporitic aquifers (Contursi area, southern Apennines, Italy). *Journal of Hydrology, 129258.*

- Barberio, M.D., **Gori, F.**, Barbieri, M., Boschetti, T., Caracausi, A., Cardello, G.L., Petitta, M. (2021). Understanding the Origin and Mixing of Deep Fluids in Shallow Aquifers and Possible Implications for Crustal Deformation Studies: San Vittorino Plain, Central Apennines. *Applied Sciences*, 11(4), 1353.

5.1 Hydrogeochemical changes before and during the 2019 Benevento seismic swarm in central-southern Italy

Francesca Gori[1] and Marino Domenico Barberio[1,*]

[1] Department of Earth Sciences, Sapienza University of Rome

*Corresponding author: Marino Domenico Barberio, Earth Sciences Department, Sapienza University of Rome, Italy. Piazzale Aldo Moro, 5, Rome, Italy; phone +39 3200443022; e-mail: marinodomenico.barberio@uniroma1.it

Research papers
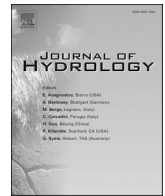
Hydrogeochemical changes before and during the 2019 Benevento seismic swarm in central-southern Italy

Francesca Gori , Marino Domenico Barberio [*]

[1] *Department of Earth Sciences, Sapienza University of Rome, Italy*

ABSTRACT

Insights into seismic precursors have been obtained in the last decades. However, a detailed understanding of hydrogeochemical anomalies prior to earthquakes still remains the aim of many research teams worldwide. In order to investigate the earthquake-groundwater relationship, between 2018 and 2020, we performed sampling surveys coupled with continuous multiparametric monitoring in Grassano spring fed by the Matese aquifer (central-southern Apennines, Italy). Hydrogeochemical changes were observed before the onset and during the 2019 Benevento seismic sequence, including dissolved CO_2 increase, pH lowering, and anomalies in major ions (i.e., Ca^{2+}, Na^+, HCO_3^-) that later recovered to their typical concentrations. We suggest that variations in groundwater geochemistry were induced by dilatative preparatory phases of earthquakes, typical of the extensional setting. This condition allowed the deep CO_2 upwelling along tectonic discontinuities, as testified by the C_{ext} (carbon from external sources) behaviour detected in Grassano groundwater during the 2019 year. Despite the small-intermediate magnitude of the mainshock, results highlight and confirm the occurrence of a potential pre-seismic geochemical process in the fractured carbonate aquifers, similar to the one proposed in literature for the stronger 2016–2017 Amatrice-Norcia seismic sequence.

1. Introduction

Detecting earthquake precursors is one of the most compelling challenges in Earth sciences. Groundwater changes induced by seismic activity have been widely documented all over the world (Wakita, 1975; Muir-Wood and King, 1993; Elkhoury et al., 2006; Manga and Wang, 2015). Many studies shed light on the variation of crustal fluids behaviour after the occurrence of seismic events. However, in the last decades attempts to identify preseismic anomalies have been carried out too (Wakita et al., 1980; Igarashi et al., 1995; Salazar et al., 2002; Ingebritsen and Manga, 2014; Chen et al., 2015). In detail, changes in spring discharge (Petitta et al., 2018; Mastrorillo et al., 2020), groundwater level (Kim et al., 2019; Hwang et al., 2020; Lan et al., 2021), geochemical content (Kim et al., 2020; Nakagawa et al., 2020), isotope composition (Skelton et al., 2014; Onda et al., 2018; Hosono et al., 2020), dissolved and free gases (Pérez et al., 2006; Sano et al., 2016; Kawabata et al., 2020) have been recognized. Several study cases are from China, Japan, Italy, Iceland, and Korea where the set-up of hydrogeochemical networks has been already established or is currently in progress (Shi et al., 2013; Orihara et al., 2014; Andrén et al., 2016;

Barberio et al., 2017; De Luca et al., 2018; Skelton et al., 2019; Li et al., 2019; Hosono and Masaki, 2020; Martinelli et al., 2021; Barbieri et al., 2021; Lee et al., 2021). Most of the interpretations agree in attributing hydrogeochemical anomalies to groundwater mixing between different aquifers driven by crustal dilation prior to seismic events (Tsunogai and Wakita, 1995; Claesson et al., 2004; Doglioni et al., 2014; Skelton et al., 2014; Andrén et al., 2016). In order to deepen understanding of the groundwater-earthquake relationship, related geochemical models have been also developed (Wästeby et al., 2014; Boschetti et al., 2019). Despite these scientific efforts, the knowledge about hydrogeochemical behaviour related to the seismic cycle need more observations to carry out a statistical analysis aimed at identifying a common denominator. In particular, the three main questions that are searching for answers are: When, Where and How the next earthquakes will occur. To achieve this objective, several study cases are necessary to build up appropriate geochemical models, naturally associated with different geo-tectonic contexts. This goal can be reached only through the increase of observations that can help to provide useful constraints on models (Wang and Manga, 2021).

Towards this direction, since 2014, a multiparametric monitoring

network (consisting of two monitoring sites i.e., Sulmona and Matese areas) has been developed in central Italy by our research group, with the main aim of identifying preseismic signals in groundwater (Barberio et al., 2017; Boschetti et al., 2019; Barbieri et al., 2020; Barberio et al., 2020; Franchini et al., 2021; Coppola et al., 2021).

This study had two main objectives: identifying hydrogeochemical changes related to seismicity and putting them in a conceptual geochemical model. Additionally, we tried to achieve these purposes even for small-intermediate earthquake magnitudes ($M_w < 5$). We reported new hydrogeochemical changes induced by the 2019 Benevento seismic swarm (main earthquake: M_w 3.9) recorded in the Matese Node (i.e., Grassano spring). In detail, we measured variations in pH, CO_2, electrical conductivity, and some major elements before and in conjunction with the onset of the seismic swarm. The temporal sequence of hydrogeochemical recorded changes allows us to recognize the potential geochemical mechanism that triggered anomalies as discussed about the 2016–2017 Amatrice-Norcia seismic sequence (main earthquake M_w 6.5; Boschetti et al., 2019). This relationship is surprising and constitutes a novelty, since most of the research on this topic detected geochemical changes only for mainshock stronger than 5 (Inan et al., 2012; Skelton et al., 2014).

We are confident that findings can help geoscientist to better understand the hydrogeochemical responses of shallow aquifer system to deep fluid injection in different geological context (e.g., both seismic and volcanic areas; Amonte et al., 2021; Barbieri et al., 2021).

2. Geological and hydrogeological setting

The central-southern Apennines fold-and-thrust belt developed during Neogene and Quaternary times (Doglioni et al., 1996). The orogenesis is related to the W-dipping subduction of the Apulian lithosphere, whose slab retreat caused the progressive eastward migration of the foreland flexure, thrust fronts, and of the extensional back-arc tectonics (Doglioni, 1991; Cardello et al., 2021). The chain is characterized by NE-verging thrust faults, which dissected the tectonic edifice into several thick tectonic sheets. Since the Late Miocene, the post-orogenic crustal extension has affected the Apennines from west to east, forming half-graben intramountain basins, controlled by high-angle W-dipping normal faults and mostly filled by Pliocene-Quaternary continental deposits (Cavinato and Celles, 1999). At present times, the extensional tectonics is still ongoing, and it is currently strongly seismogenic along the axial region of the Apennines, whereas compressive kinematics is active in the Adriatic front, consistently with the regional stress field (Galli et al., 2008). The main domain is represented by the Meso-Cenozoic carbonate units, formed by limestone, dolomitic limestone, and dolomitic series of carbonate platform facies. The wide carbonate ridges of central-southern Apennines can store huge volumes of groundwater, acting as the main aquifer systems. Their hydrogeological complexity is essentially defined by the high transmissivity due to fracturing and locally karstification. Generally, groundwater is drained by large discharge springs with steady flow rate at the boundaries of the aquifers, where carbonate rocks are in contact with low-permeability deposits (aquicludes or aquitards), such as pre- and *syn*-orogenic basinal and flysch clayey series (Allocca et al., 2014).

In detail, the wide karst area of the Matese Massif, about 1500 km², crops out in the median sector of the Apennine chain, with elevations up to 2050 m (Fiorillo and Pagnozzi, 2015; Rufino et al., 2021). The main lithological units are the Late Triassic-Miocene carbonate sequences (i. e., limestones and dolostone) which reach thickness ranging between 2500 and 3000 m and are heavily fractured and faulted (Fiorillo and Guadagno, 2010; Silverii, 2016). From a seismological point of view, this area is considered one of the most active sectors of the Apennines, characterized by the presence of two main fault systems: one within the core of the massif, i.e., fault system of Matese-Gallo-Letino lakes (MGLF) and the Aquae Iuliae normal fault (AIF), and a second one at its western side i.e., the Ailano-Piedimonte Matese normal faults, (AIPMF) (Boncio

et al., 2016).

The basal groundwater flowpath of the Matese aquifer is constrained by tectonic discontinuities, as well as geometric relationships between stratigraphical units (Celico and Petrella, 2008; Fiorillo et al., 2019; Rufino et al., 2021). Along the northern and eastern sectors, the Matese massif is tectonically joined by a thrust fault to low permeability argillaceous complexes and flysch sequences (Petrella and Celico, 2009). Instead, along the southern and western sectors, it is bounded by normal faults and covered by recent Quaternary deposits of the Volturno river plain. The Matese massif is characterized by many endorheic areas located at high elevations, whose formation is associated with the upper Pliocene-Pleistocene tectonic activity. These areas play a crucial role in recharge processes. Particularly, the Lago Matese polje represents the main recharge zone of the aquifer, occupying an area of 45 km² between 1000 and 2050 m a.s.l. (Fiorillo and Pagnozzi, 2015). Grassano-Telese springs are fed by the eastern sector of the Matese aquifer which is hydraulically connected by buried karst terrains and outcropping karst reliefs as Mt. Monaco, Mt. Acero, and Montepugliano (Fig. 1. Montepugliano relief is the discharge zone of a wide portion of the Matese aquifer, where a deep and wide groundwater circulation locally converge providing a general upwelling flow, driven by conduits and fracture networks (Fiorillo et al., 2019). Indeed, among the three main spring groups, Grassano-Telese springs, located at the southern slope of Montepugliano relief, represent the main discharge zone of the aquifer and the lowest elevation outflows (54 m a.s.l.) (Leone et al., 2019). These springs are characterized by both cold calcium-bicarbonate waters (Grassano spring) and hypothermal sulphurous and CO_2-rich ones (Telese spring) (Corniello and De Riso, 1986; Fiorillo et al., 2019). Grassano spring consists of different outlets with a mean annual discharge of 4.5 m³/s, while the average discharge of Telese spring is about 1 m³/s (Corniello et al., 2021). Besides, the isotopic signature of these springs reveals the same catchment area. Therefore, mineralization occurs in the final part of the groundwater flowpath, where uprising of deep gases (CO_2 and H_2S) occurs along the faults of Montepugliano relief (Corniello et al., 2021).

3. Material and methods

In this study, we analysed hydrogeochemical, gas-geochemical, isotopic and seismic data in order to investigate earthquake-induced effects on groundwater. Between February 2018 to September 2020, we performed twenty sampling campaigns at Grassano spring (Lat. 41.225040°, Long. 14.514426°, altitude 54 m) to look into groundwater hydrogeochemistry. Additionally, we carried out sampling at Telese spring (Lat. 41.223350°, Long. 14.525977°, altitude 57 m) and specifically, in June 2020 we executed a sampling survey addressed to collect data useful for the calculation of the groundwater carbon mass balance (e.g., major ions, chemical-physical parameter and isotope composition of CO_2).

In detail, chemical-physical parameters were measured on-site through the multiparametric probe WTW Multi 3420: temperature (resolution 0.1 °C), pH (resolution 0.001), and electrical conductivity (EC). Standard analytical methods were applied to characterize the chemical composition (Bridgewater et al., 2017). For the determination of major (anions and cations) elements, groundwater samples (filtered in situ through a 0.45 μm filter) were collected into polyethylene bottles. Firstly, they were kept at low temperature in ice-filled fridge boxes to avoid alterations of water components, and then they were analyzed by ion chromatography at the Geochemistry Laboratory of the Department of Earth Sciences at Sapienza University of Rome. Specifically, chromatographs Dionex ICS 5000 and Dionex ICS 1100 were used to determine the anionic content (F^-, Cl^-, SO_4^{2-}, and NO_3^-) and the cationic one (Ca^{2+}, Mg^{2+}, Na^+, and K^+), respectively. As testified by the cation–anion balance checked on each sample, the analytical error associated with these instruments was less than 5%. Alkalinity was measured on-site by titration with 0.05 N HCl solution and methyl-orange as indicator. Data
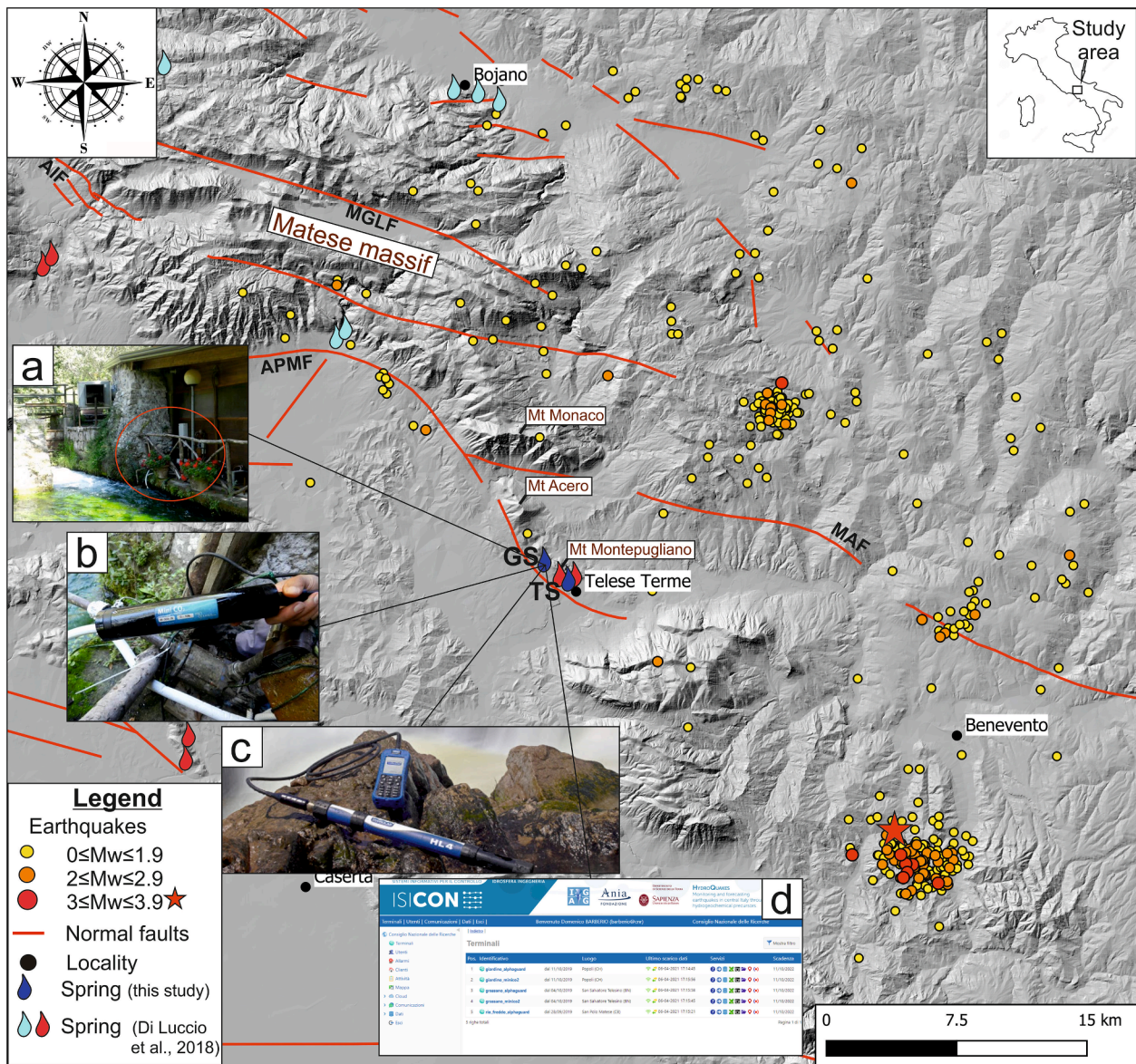
Fig. 1. Map of the study area (central-southern Apennines, see location in upper right inset). Active faults are from the Ithaca database (https://www.isprambiente. gov.it/en/projects/soil-and-territory/italy-hazards-from-capable-faulting). Base digital elevation model is from the ISPRA database SINAnet (https://www.sinanet. isprambiente.it/it). Locations of Grassano spring and Telese spring are displayed with blue drops and are reported as GS and TS, respectively. Springs (both of shallow, and hydrothermal systems, from Di Luccio et al., 2018), fed by the Matese aquifer and considered in the Result and Discussion section, are depicted with cyan and red drops, respectively. Earthquakes that occurred in the monitoring period (2018–2020) within a radial distance of 30 km from Telese Terme are shown with circles of different colors depending on the magnitude. The M_w 3.9 earthquake is displayed with a red star (http://terremoti.ingv.it/); Main faults are also displayed (MAF: Miranda Apice Fault, APMF: Ailano-Piedimonte Matese Fault; AIF: Aquae Iuliae Fault; MGLF: Matese-Gallo-Letino Fault). (a) Monitoring site; (b) MiniCO₂ probe for continuous monitoring of carbon dioxide; (c) HL4 probe for continuous monitoring of temperature, pH, and electrical conductivity, and dissolved oxygen; (d) Online system of data acquisition (https://webvision.digimatic.it/) used to investigate and download acquired time-series in real-time. (For interpretation of the references to colour in this figure legend, the reader is referred to the web version of this article.)

of major ions since February 13th, 2018 to January 8th, 2020 were also published in Franchini et al. (2021).

We performed continuous monitoring by installing two multiparametric probes (HL4 and Mini CO₂). The Hydrolab HL4 Multiparameter Probe measured continuously and simultaneously temperature, pH, and electrical conductivity, and dissolved oxygen. The device was equipped with integrated data recording capability. Measurements of parameters were automatically repeated and stored every 15 min, since July 19th, 2018 to October 29th, 2020. The Mini CO₂ Submersible Sensor (produced by Pro-Oceanus Systems Inc) was installed on May 24th, 2019, for the continuous monitoring of dissolved CO₂ concentrations. The gas was stripped from the water through a gas-permeable

membrane and subsequently sent to the non-dispersive infrared detector (NDIR). With pCO₂ ranges from 0 to 10%, the instrument provided the versatility needed, by allowing the continuous acquisition of carbon dioxide concentrations, and repeating measurements every 15 min. Unfortunately, the firmware of the probe was damaged by a power surge on December 10th, 2019, therefore the sensor stopped acquiring data. Moreover, recorded data can be monitored and downloaded in realtime, by an online system of data acquisition developed by Digimatic s.r.l. (https://webvision.digimatic.it/).

Furthermore, thermodynamic calculations were carried out by using Phreeqc Interactive software for Windows (version 3), precisely the *prheeqc.dat* thermodynamic dataset (Parkhurst and Appelo, 2013).

Sample water conditions of T, pH, major ions, and alkalinity were used as input data to calculate the molality concentrations of the water content. In detail, the total molality of Ca, Mg, SO_4, and TDIC (mol/kg H_2O) was used for the calculation of C_{carb} and C_{ext} parameters in the following carbon mass balances (Chiodini et al., 2000):

$$TDIC = C_{carb} + C_{ext} \quad (1)$$

$$C_{carb} = Ca + Mg - SO_4 \quad (2)$$

$$C_{ext} = C_{TDIC} - C_{carb} = C_{inf} + C_{deep} \quad (3)$$

TDIC includes the total dissolved inorganic carbon in groundwater, whose origin is ascribable to the presence of different sources of carbon. Hence, it corresponds to the sum of these components (see Eq. 1). C_{carb} is the carbon derived from the water–rock interaction of groundwater with carbonate aquifers. Thus, the Eq. (2) considers the dissolution of calcite and dolomite, and also the presence of anhydrite and/or gypsum. C_{ext} is the carbon derived from "external sources", indeed it is expressed by the sum of two parameters (see Eq. 3): where C_{inf} is the carbon from atmospheric and biogenic CO_2 (i.e., the infiltrating waters), and C_{deep} is deep CO_2 from metamorphic, mantle, or magma sources (Chiodini et al., 2000; Chiodini et al., 2004).

The $\delta^{13}C$ isotope composition of deep CO_2 of Grassano spring was from Barbieri et al. (2020), while the one of Telese spring was obtained in this study. In detail, it was analysed by using a Thermo Scientific Delta V Plus isotope ratio mass spectrometer. The $\delta^{13}C$-CO_2 value is in terms of δ‰ units (expressed as V-PDB, Vienna Pee Dee Belemnite international standard), with analytical error of ± 0.15‰. Analytical devices were provided by the National Institute of Geophysics and Volcanology (INGV, Palermo, Italy).

Finally, we selected all earthquakes (~370) that occurred in the same period of the hydrogeochemical monitoring within a radial distance of 30 km from Telese Terme (Lat. 41.216729°, Long. 14.526261°). This area was selected according to the strain radius-epicentral distance relationship proposed by Dobrovolsky et al. (1979). Seismic data come from the database run by National Seismic Network (available on the website: http://terremoti.ingv.it/). The amount of energy released (E) was estimated from the earthquake magnitude M_w through the magnitude-energy relationship (see Eq. 4; Gutenberg, 1956):

$$Log\ E = 1.5 \times M_w + 11.8$$

4. Results and discussion

Collected data at Grassano spring refer both to continuous and discrete sampling, and are represented by chemical-physical parameters, major ions, and dissolved CO_2. We also considered seismic data. All discrete measurements are reported in the Table S1. In this section we present and discuss only the data that we considered relevant with respect to the aim of this work. Table 1 displays the maximum, average, and minimum values of all main parameters recorded during 2018–2020 monitoring.

The hydrogeochemical facies of Grassano spring is shown in the Piper diagram (Fig. 2a, by clear calcium-bicarbonate facies with minimal variations during the study period.

To better understand the geochemical features of the analysed groundwater, we considered data published in a previous study (Di Luccio et al., 2018). Grassano groundwater are located between two

end-members represented by the shallow system and the hydrothermal one (depicted as the blue ellipse and the red one, respectively in Fig. 2b. This observation agrees with the results of a recent research (Corniello et al., 2021) which points out the mixing between shallow regional flowpath, coming from Matese carbonate aquifer (Fig. 1, and the deep mineralized and gas-rich groundwater upwelling along faults (e.g., Telese spring, Fig. 1.

Fig. 3 shows parameters having a potential correlation with seismic activity. In detail, we displayed the whole time series, both discrete and continuous of CO_2, pH, electrical conductivity, and Calcium (Ca^{2+}), Sodium (Na^+) and Alkalinity (HCO_3^-) concentrations. Other measured parameters (i.e., temperature) and ions did not show any potential evidence of relationship with seismicity, and for this reason, based on the main purpose of this work, they are not discussed but they are reported in the Table S1. Stream discharge of the spring was not recorded in this study.

Fig. 3b displays CO_2 time series recorded from May 24th, 2019 to December 10th, 2019, which was characterized by several lacks of data due to electrical interruption. Besides, it is noteworthy that such time series is shorter than other continuous data because the probe was installed in May 2019 and it turned off in December 2019 owing to sensor damage. The average value was 6.4%. In the first period (since June to September 2019) the CO_2 values recorded a general increase from 6.0% to 6.8%. Later the trend was approximately steady around 6.7%. Evident CO_2 spikes are clearly discernible and are attributable to instrumental noises. Fig. 3c includes continuous pH time series recorded from July 19th, 2018 to October 29th, 2020, with missing data from March 2020 to June 2020. In addition, discrete pH measurements recorded during our campaign surveys were reported with circles. During five surveys, we had some problems with pH sensor of the portable WTW Multi 3420 probe. Therefore, for these cases, we recalculated pH value through the arithmetic mean of daily continuous values provided by the HL4 probe. Direct and recalculated data were displayed with cyan and green circles, respectively (Fig. 3c. Both continuous and discrete average values were about equal to 7.0. The time series were quite steady within a minimum value of 6.8 and a maximum one of 7.3 during the monitoring period. Despite this limited range of variation (0.5), a notable decrease was recorded since August 2018 to October 2018 (about 0.25), followed by 2 months of instrumental noises owing to some problems of the setting station on-field. Since June 7th, 2019 to September 10th, 2019, the series was firstly characterized by a sharp decrease equal to 0.3 and a subsequent clear increase of 0.2. Fig. 3d contains the electrical conductivity time series, both discrete and continuous, with the same interval and inconsistences of pH series (e.g., setting of the station and data lack). Again, recorded spikes in the signal were attributable to instrumental noises. Continuous and discrete average values were 905 μS/cm and 901 μS/cm, respectively. The time series values were quite steady around the mean, however a visible increase of about 45 μS/cm was detected since November 20th, 2019 to January 9th, 2020. Finally, time series of Ca^{2+}, Na^+ and HCO_3^-, consisting of the surveys performed between February 2018 and September 2020, are plotted in Fig. 3e, 3f, and 3 g. The average values of the analysed major ions (mg/L) were 174.5, 16.6, and 658, respectively (Table 1. Statistical distribution of ions concentrations was analysed through box-and-whiskers plots (Fig. 4. The box, separated into two parts by the median, represents the interquartile range (first and third quartiles). The whiskers are limited by the interquartile range

Table 1
Maximum, average and minimum values of major ions and chemical-physical parameters.

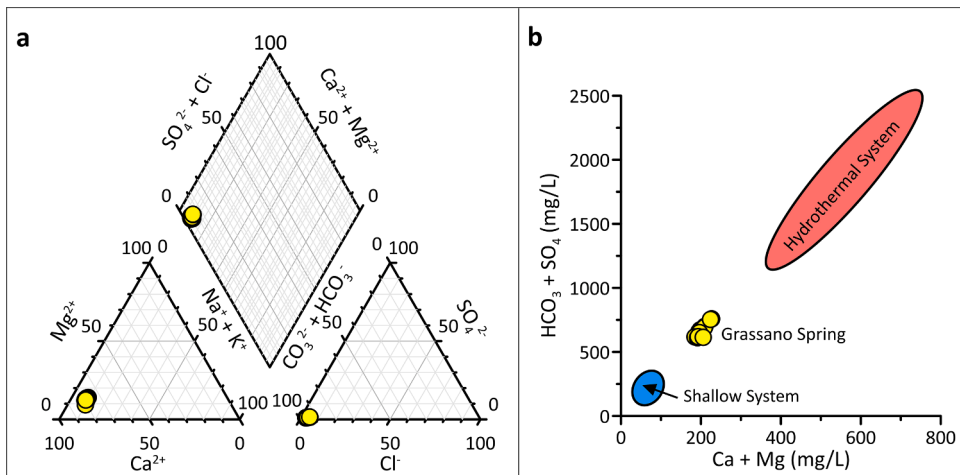|	Ca	Mg	Na	K	Cl	SO4	HCO3	F	NO3	EC	T	pH
	mg/L	mg/L	mg/L	mg/L	mg/L	mg/L	mg/L	mg/L	mg/L	μS/cm	°C	
Max	198.3	30.4	20.0	3.0	31.5	10.2	751.3	0.4	4.7	973.0	12.3	7.1
Average	174.5	27.4	16.6	2.4	23.8	8.2	658.0	0.1	2.8	901.1	11.7	7.0
Min	164.5	19.1	14.7	1.3	18.9	7.0	604.1	0.1	1.9	869.0	11.2	6.8

Fig. 2. (a) Piper diagram for the hydro-geochemical classification of groundwater samples, resulting enriched in bicarbonate and calcium ions (Ca-HCO₃ facies); (b) The major ion ratio (Ca + Mg/HCO₃ + SO₄) suggests that the hydrogeochemistry of Grassano spring (yellow circles) derives from the mixing between the shallow system (blue ellipse) and the hydrothermal one (red ellipse). Data of shallow and hydrothermal systems are from Di Luccio et al. (2018). (For interpretation of the references to colour in this figure legend, the reader is referred to the web version of this article.)

(IQR) with a factor equal to 1.5. This analysis revealed that all three ions were characterized by anomalous values (dots in Fig. 4 of concentrations (ppm) with respect to the whole distribution recorded in the three-years monitoring. Since "outliers" exceed the whiskers only in the surveys performed on November 19th, 2019, and on January 8th, 2020, they (and associated changes in electrical conductivity, pH values and dissolved CO_2) did not represent seasonal and/or natural hydrogeochemical variations.

During the monitoring period three main seismic sequences (see location in Fig. 1 and time series in Fig. 3a were clearly recognized among the typical background seismicity that characterized this sector of the Apennines (Milano et al., 2006). The first one was represented by 72 seismic events occurred since August 31st, 2018 to September 16th, 2018, about 15 km far from Grassano spring. The maximum earthquake had $M_w = 2.8$. The second, and the third seismic sequences occurred in the same area, about 25 km far from the monitoring site, near San Leucio del Sannio village. The first of these two sequences started on November 21st, 2019 and ended on December 17th, 2019. It included 87 seismic events and the maximum earthquake magnitude was equal to 3.9, recorded on December 16th, 2019. The same area was struck by a second and smaller swarm in March 2020, composed by 54 seismic events (maximum earthquake magnitude $M_w = 2.6$). The calculation of the Cumulated Energy (shown with the green line in Fig. 3a highlighted the strongest energy release in conjunction with the second seismic swarm.

Fig. 5 displays the time chart with the temporal sequence of significant detected variations. Changes in pH, electrical conductivity, and major ions concentrations are supposed to be related to the previously observed CO_2 increase in the aquifer system. To sum up, the CO_2 increase would induce a sudden pH decrease that was followed by a mild increase. In conjunction with the pH recovery to the previous values (e. g., values of May 2019), it was recorded an electrical conductivity increase coupled with anomalous high values of Ca^{2+}, Na^+, and HCO_3^- concentrations, exactly two days before the onset of the seismic sequence, and about one month before the main seismic event (i.e., the M_w 3.9 San Leucio del Sannio earthquake occurred on December 16th, 2019). However, discrete sampling did not allow to recognise exactly the moment in which concentrations of these ions started to increase. Anyway, this process was attributed to the reaction of the hosting aquifer system, the so-called "buffering effect" (Langmuir, 1997; Drever, 2005). In order to re-equilibrate the original chemical conditions after being hit by a CO_2 increase, the aquifer system naturally reacts through the following equations (Eq. 5, 6):

CO_2 (aq) + H_2O (aq) → H_2CO_3 → H^+ + HCO_3^- (induce pH decreasing) (5)

Dissolved HCO_3^- (groundwater) + H^+ (released) ⇌ H_2CO_3 (aq) (pH buffer) (6)

In detail, the addition of CO_2 to karst fractured carbonate aquifer dissolved both the carbonate fraction (Ca^{2+} and HCO_3^-) and weathered the silica one of the reservoir rocks (Minissale, 2004; Clark, 2015). Due to the buffering effect of the carbonate-bicarbonate ($CO_3^{2-} - HCO_3^-$) pair, the pH stabilizes when CO_2 is dissolved or exsolved (Amonte et al., 2021). Indeed, an ion exchange process could have involved the Na ions adsorbed onto clay minerals. In fact, cations have different tendencies to be adsorbed or desorbed. Their tendency for adsorption in natural waters is as follows: (strongly adsorbed) $Ca^{2+} > Mg^{2+} > K^+ > Na^+$ (weakly adsorbed), which means that sodium ions are much more likely to be desorbed from surfaces and then to be ejected and transferred into groundwater (Rajmohan and Elango, 2004; Manahan, 2017; Chen et al., 2021). Alternatively, such increase in Na concentrations could be just explained as deep fluid upwelling, in fact, high sodium concentration is certain feature of deeply originated fluids in deep reservoir in crust. Similar geochemical changes in groundwater were also recognized in other studies (Bourg and Loch, 1995; Malakootian and Nouri, 2010; Barberio et al., 2017; Paudel et al., 2018). For instance, the 2016–2017 Amatrice-Norcia seismic sequence, which occurred about 80 km far from the studied monitoring site, caused the CO_2 inflow in the shallow regional aquifer and consequently the pH variation, with consequent trace element mobilization (i.e., As, V, Cr, Fe; Barberio et al., 2017).

In addition, the geochemical modelling, conducted by Boschetti et al. (2019), confirmed that the variation in the CO_2 fugacity can change the adsorption/desorption process of some elements in the rock aquifer. In the present study, we suppose that a similar geochemical process could be inferred at Grassano spring. Indeed, Grassano spring is characterized by the presence of high dissolved CO_2 concentration, whose source is attributable to crustal deep degassing (Di Luccio et al., 2018). Hence, following previous studies (Frondini et al., 2019; Barbieri et al., 2020), a calculation of the carbon mass balance has been carried out to define the C_{ext} component useful to quantify and distinguish the carbon related to the deep source from the biogenic (C_{inf}) and carbonate (C_{carb}) ones.

Fig. 6a, shows the C_{ext} value versus the $\delta^{13}C_{ext}$ isotopic composition of Grassano spring (yellow circle), resulting between infiltrating waters (blue ellipse) and the CO_2 rich-springs (red rectangle) of the Matese aquifer. However, it is clear that the Grassano groundwater is closer to the deep end-member which corresponds to our sampling of Telese spring performed in June 2020 (red circle). Moreover, this evidence suggests the mixing between CO_2-rich deep groundwater, such as Telese spring, and Grassano spring that could be enhanced by dilatative preparatory phases of earthquakes, typical of the extensional setting (Sibson, 2000; Doglioni et al., 2014). Indeed, the $\delta^{13}C_{ext}$ isotopic ratio of Grassano spring is heavier compared to that of other carbonate springs of the Matese aquifer (data taken from Di Luccio et al., 2018), showing an endogenous signature (Barbieri et al., 2020). The contribution of
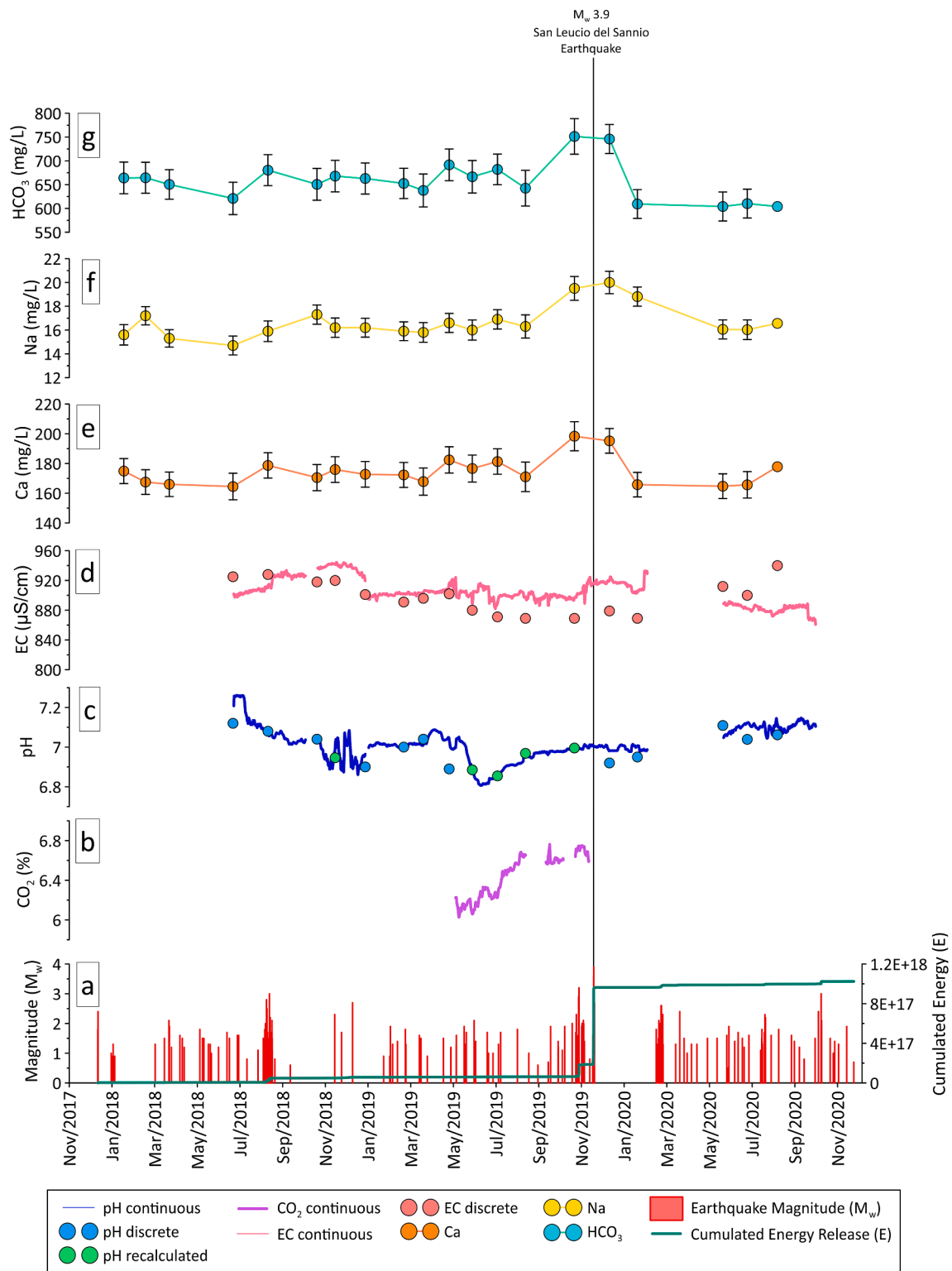
Fig. 3. (a) Time series (January 1st, 2018 – December 31st, 2020) of seismic activity: earthquakes occurred in the same period of the hydrogeochemical monitoring are shown with red bars, and the calculated cumulated energy release (Gutenberg, 1956) is displayed by a green line; Seismic data are from the INGV database (http://terremoti.ingv.it/); (b) Time series (May 24th, 2019 – December 10th, 2019) of CO_2 continuously recorded is shown by the purple line; (c) Time series (July 19th, 2018 – October 29th, 2020) of pH continuously recorded is shown with the blue line, while pH discrete sampling is displayed with cyan (direct measurements) and green (recalculated values) circles; (d) Time series (July 19th, 2018 – October 29th, 2020) of electrical conductivity both continuous and discrete are shown with pink line and circles, respectively; (e, f, g) Time series of major ions (i.e., Ca^{2+}, Na^+, and HCO_3^-), are shown with orange, yellow, and turquoise circles, respectively. (For interpretation of the references to colour in this figure legend, the reader is referred to the web version of this article.)
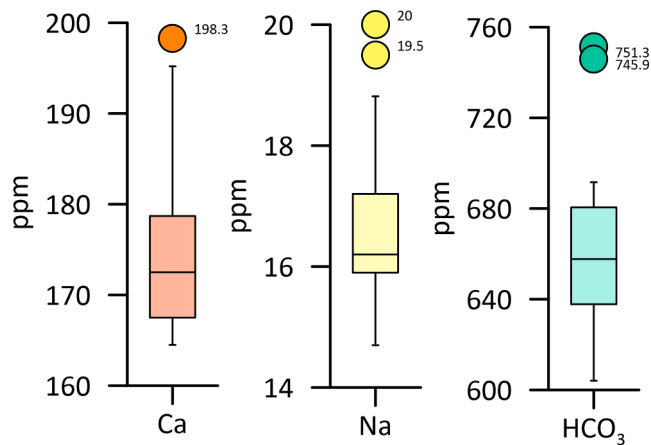
Fig. 4. Box-and-whiskers plots of major ions (Ca^{2+}, Na^{+}, and HCO$_3^{-}$) point out anomalous values (outliers) in November 2019 and January 2020.

deep CO$_2$ confirms the influence and the mixing with a deep circulation system, widely hidden by the large contribution to the discharge of the shallow carbonate circulation system. The calculation of the carbon mass balance of groundwater samples allows to obtain the C$_{ext}$ time series shown in Fig. 6b. In detail, we recorded a progressive increase of C$_{ext}$ through the entire 2019 year that reached the maximum value at the end of the seismic sequence, precisely in the survey performed in January 2020. The C$_{ext}$ values of the last three surveys were among the minima measurements of the monitoring period. Also, pH, continuous electrical conductivity, major ions concentration recovered their

preseismic values, consistently with our interpretation of geochemical processes.

We speculate that the increase of C$_{ext}$ value during 2019 was due to deep pre-seismic geological processes (i.e., variation in dilation) that allowed the upwelling of the deep CO$_2$ flux along tectonic discontinuities. Through this multiparametric approach, it is possible to provide a description of a complex geochemical process that potentially induced the hydrogeochemical changes in Ca^{2+}, Na^{+}, and HCO$_3^{-}$ just a few days before the onset of the seismic sequence. Apart from furnishing a potential hydrogeochemical model, it is also necessary to take a step forward to identify possible geo-structural mechanism that could induce the recorded geochemical responses.

It is noteworthy that fluids have an "active" role in decreasing fault strength, thereby they can influence fault mechanics, and the cyclic activation. Fluids can also act "passively" (e.g., Tullis et al., 1996; Wannamaker et al., 2002; Doglioni et al., 2014), being squeezed by pressure gradients, and transported depending on rock permeability (Salazar et a., 2002). Their migration, whatever the origin is (e.g., meteoric, crustal, or mantle-derived), is influenced by variation in the state of the stress. For example, as consequence of dilatancy and fluid-diffusion mechanism, fluids are rapidly redistributed in the crust (Sibson et al., 1975). Besides, also fluid discharges of opposite sign (i.e., negative and positive during the coseismic phase) have been documented along thrust and normal faults, respectively (Muir-Wood and King, 1993). Also, changes in hydrogeochemical content of groundwater may be expected because earthquake-induced groundwater flow is effective in transporting solutes, and seismic events may open new passageways to connect fluids from different reservoirs, and thus facilitating such exchange (Wang and Manga, 2021). Most variations in geochemical composition are consistent with the model of earthquake-
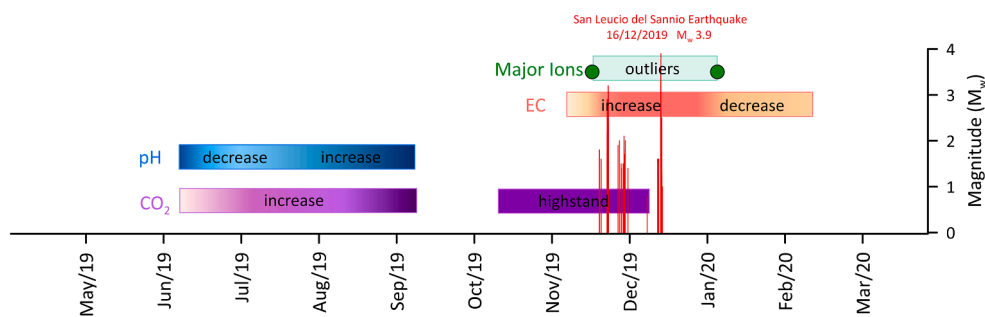
Fig. 5. Fig. 5. Time chart resuming the relevant hydrogeochemical variations. Outliers measured in major ions are depicted with two green points, while the horizontal light green bar shows the period in which we assume that concentration values presumably have remained high. (For interpretation of the references to colour in this figure legend, the reader is referred to the web version of this article.)
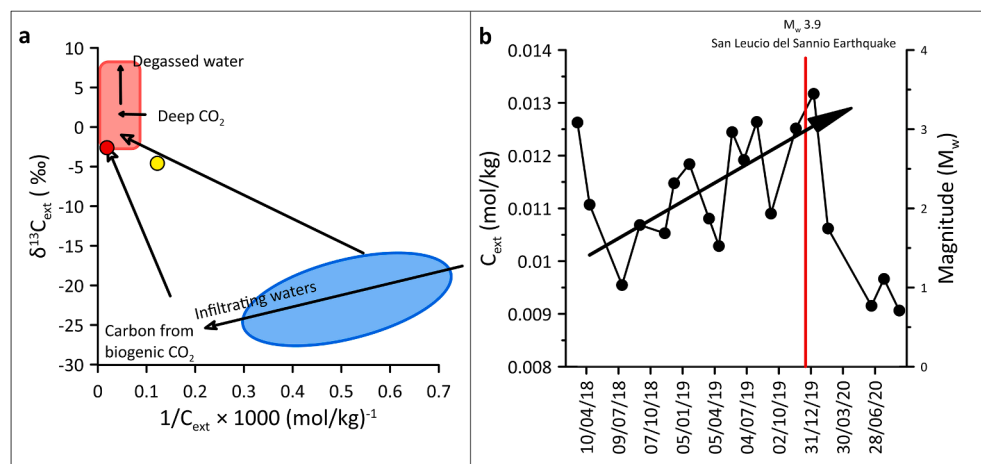
Fig. 6. (a) δ^{13}C$_{ext}$ versus 1/C$_{ext}$ diagram. Grassano spring is displayed with the yellow circle and Telese spring is represented by the red one. Data of other springs of the Matese carbonate aquifer (from Di Luccio et al., 2018) are displayed with the blue ellipse and the red rectangle, corresponding to infiltrating waters and to CO$_2$-rich springs, respectively. (b) Time series of C$_{ext}$ (2018 – 2020) at Grassano springs calculated through the carbon mass balance (Chiodini et al., 2000). The M$_w$ 3.9 mainshock is shown with a red bar. (For interpretation of the references to colour in this figure legend, the reader is referred to the web version of this article.)

enhanced groundwater transport through basin-wide or local enhanced permeability (Wang et al., 2013; Wang and Manga, 2021). It may breach hydrologic barriers (e.g., aquitards), connecting otherwise isolated aquifers or other fluid sources, and then causing fluid source switching and/or mixing (Wang and Manga, 2021). Studies of these processes can represent another step to improve the comprehension both about natural transport processes, and earthquake-induced hydrogeochemical responses. Despite data concerning hydrogeochemical changes are less abundant than those regarding changes in groundwater level and discharge, through the years they allowed to get useful information to constrain models of hydrogeological processes induced by seismicity (Wang and Manga, 2021).

According to a recent global analysis (Tamburello et al., 2018), there is a positive spatial correlation between CO_2 degassing and extensional tectonic regimes that would play a key role in creating pathways for the uprising deep fluids and connecting the deep portion of crust to the earth surface. Thus, normal faults, strike-slip faults and areas with high structural damage represent the most suitable scenario for CO_2 uprising (Lamberti et al., 2019). A widely accepted geo-structural model is based on the concept of stick–slip fault behaviour in the upper crust and on the presence of a stable sliding fault in the middle-lower crust (Doglioni et al., 2015; Petricca et al., 2015). The development of fault zone fracturing, together with hanging-wall dilation and initial collapse in the preseismic phase, produce high fluid pressure (e.g., CO_2), and consequently migration of fluids from the high pressure zone to the low pressure one (Doglioni et al., 2014).

During the 2019 Benevento seismic swarm, the seismicity delineated the existence of a subvertical WNW-ESE striking fault plane between 7 and 18 km depth. The estimated focal mechanism highlighted a right lateral strike-slip kinematics of the fault structure which accommodates differential extensional deformation and represents a potential source of $M_w > 5$ damaging earthquakes (Ciaccio et al., 2021). In this context, presumably, in the preseismic preparatory phase the deep fluids uprising in shallow regional aquifers could be enhanced due to the generation of high pore pressure along fault plane and fractures (Cardello and Mancktelow, 2015; Barberio et al., 2021).

Findings like those reported in our work are relevant because they confirmed, in similar geological and tectonic setting, a common geochemical process able to cause the same pattern of hydrogeochemical anomalies. In fact, we argue that the recorded geochemical responses were induced by a similar geochemical process that caused the anomalies prior to the 2016–2017 Amatrice-Norcia seismic sequence (main earthquake: M_w 6.5; Chiaraluce et al., 2017). The proposed tectonic model reconstructed for the two different study areas is the same too. Implications derived from our study can be applied to cases in other countries and in other geological contexts. For example, variations in groundwater hydrogeochemical content were also observed before and during volcanic activity in Iceland, and in Tenerife Island as consequence of pulses of fluid injection from volcanic and/or hydrothermal system (Barberio et al., 2021; Amonte et al., 2021)

5. Conclusion

In this study, hydrogeochemical monitoring, both discrete and continuous, of chemical-physical parameters, major ions and dissolved CO_2 was performed in Grassano spring (central-southern Italy), with the aim of identifying in groundwater potential precursors of nearby earthquakes.

We conclude that:

- Anomalous concentrations of Ca^{2+}, Na^+ and HCO_3^- were recorded in one sample before and in another one after the 2019 Benevento seismic sequence (main earthquake on December 16th, 2019: M_w 3.9 San Leucio del Sannio).
- Changes in groundwater chemical content are attributable to the progressive increase of deep CO_2 in the aquifer system, which temporarily lowered pH and enhanced the solubility of the above-mentioned major ions.
- The deep pre-seismic dilatational processes are supposed to be responsible for enhancing the influx and ascent of CO_2 in the regional carbonate aquifer. In fact, the increase of CO_2 in the studied aquifer and spring started before the related seismic sequence.
- The geochemical process that occurred in Grassano groundwater prior to the seismic sequence was similar to that defined for the 2016–2017 Amatrice-Norcia seismic sequence, despite the seismicity during our monitoring period was characterized by small-intermediate magnitude.
- The obtained results shed light on the possibility of having pre-seismic hydrogeochemical signals in springs and groundwater also for small-intermediate earthquake magnitude, at least in the areas where deep fluids contribution to groundwater is evident.
- This study highlights also the crucial role of the multiparametric approach to expand the knowledge about the relationship between the geochemical process in groundwater and seismic activity. However, also other parameters as for example discharge rates as well as the groundwater level are needed to clarify some hydrogeological aspects.
- The setup of a standardized and diffuse monitoring network of groundwater, like that of this study, would produce significant and useful information towards the solving of the three main questions When, Where, and How the release of seismic energy will occur.

CRediT authorship contribution statement

Francesca Gori: Conceptualization, Methodology, Investigation, Formal analysis, Software, Data curation, Visualization, Writing – review & editing. **Marino Domenico Barberio:** Conceptualization, Methodology, Investigation, Formal analysis, Data curation, Software, Visualization, Writing – review & editing.

Declaration of Competing Interest

The authors declare that they have no known competing financial interests or personal relationships that could have appeared to influence the work reported in this paper.

Appendix A. Supplementary data

Supplementary data to this article can be found online at https://doi.org/10.1016/j.jhydrol.2021.127250.

References

Allocca, V., Manna, F., De Vita, P., 2014. Estimating annual groundwater recharge coefficient for karst aquifers of the southern Apennines (Italy). Hydrol. Earth Syst. Sci. 18, 803–817. https://doi.org/10.5194/hess-18-803-2014.

Amonte, C., Asensio-Ramos, M., Melián, G.V., Pérez, N.M., Padrón, E., Hernández, P.A., Rodríguez, F., D'Auria, L., López, D., 2021. Hydrogeochemical temporal variations related to changes of seismic activity at Tenerife, Canary Islands. Bull. Volcanol. 83 (4), 1–18.

Andrén, M., Stockmann, G., Skelton, A., Sturkell, E., Mörth, C.M., Guðrúnardóttir, H.R., Keller, N.S., Odling, N., Dahrén, B., Broman, C., Balic-Zunic, T., Hjartarson, H., Siegmund, H., Freund, F., Kockum, I., 2016. Coupling between mineral reactions, chemical changes in groundwater, and earthquakes in Iceland. J. Geophys. Res. Solid Earth 121 (4), 2315–2337.

Barberio, M.D., Barbieri, M., Billi, A., Doglioni, C., Petitta, M., 2017. Hydrogeochemical changes before and during the 2016 Amatrice-Norcia seismic sequence (central Italy). Sci. Rep. 7, 11735. https://doi.org/10.1038/s41598-017-11990-8.

Barberio, M.D., Gori, F., Barbieri, M., Billi, A., Caracausi, A., De Luca, G., Franchini, S., Petitta, M., Doglioni, C., 2020. New observations in Central Italy of groundwater responses to the worldwide seismicity. Sci. Rep. 10, 1–10.

Barberio, M.D., Gori, F., Barbieri, M., Boschetti, T., Caracausi, A., Cardello, G.L., Petitta, M., 2021. Understanding the Origin and Mixing of Deep Fluids in Shallow Aquifers and Possible Implications for Crustal Deformation Studies: San Vittorino Plain, Central Apennines. Appl. Sci. 11 (4), 1353.

Barbieri, M., Boschetti, T., Barberio, M.D., Billi, A., Franchini, S., Iacumin, P., Selmo, E., Petitta, M., 2020. Tracing deep fluid source contribution to groundwater in an active seismic area (central Italy): A combined geothermometric and isotopic (δ13C) perspective. J. Hydrol. 582, 124495. https://doi.org/10.1016/j.jhydrol.2019.124495.

Barbieri, M., Franchini, S., Barberio, M. D., Billi, A., Boschetti, T., Giansante, L., Gori, F., Jónsson, S., Petitta, M., Skelton, A., Stockmann, G., 2021. Changes in groundwater trace element concentrations before seismic and volcanic activities in Iceland during 2010–2018. Sci. Total Environ. 148635.

Boncio, P., Dichiarante, A. M., Auciello, E., Saroli, M., Stoppa, F. 2016. Normal faulting along the western side of the Matese Mountains: Implications for active tectonics in the Central Apennines (Italy). J. Struct. Geol. 82, 16–36.

Boschetti, T., Barbieri, M., Barberio, M.D., Billi, A., Franchini, S., Petitta, M., 2019. CO_2 Inflow and Elements Desorption Prior to a Seismic Sequence, Amatrice-Norcia 2016, Italy. Geochem. Geophys. Geosyst. 20(5), 2303–2317. 10.1029/2018GC008117.

Bourg, A. C. M., Loch, J. G. 1995. Mobilization of heavy metals as affected by pH and redox conditions. In Biogeodynamics of pollutants in soils and sediments (pp. 87–102). Springer, Berlin, Heidelberg.

Bridgewater, L.L., Baird, R.B., Eaton, A.D., Rice, E.W., Association, A.P.H., Association, A.W.W., Federation, W.E. (Eds.), 2017. Standard methods for the examination of water and wasterwater, 23rd ed. American Public Health Association, Washington, DC.

Cardello, G.L., Mancktelow, N.S., 2015. Veining and post-nappe transtensional faulting in the SW Helvetic Alps (Switzerland). Swiss J. Geosci. 108 (2–3), 379–400.

Cardello, G.L., Vico, G., Consorti, L., Sabbatino, M., Carminati, E., Doglioni, C., 2021. Constraining the Passive to Active Margin Tectonics of the Internal Central Apennines: Insights from Biostratigraphy, Structural, and Seismic Analysis. Geosciences 11 (4), 160.

Cavinato, G.P., Celles, P.D., 1999. Extensional basins in the tectonically bimodal central Apennines fold-thrust belt, Italy: Response to corner flow above a subducting slab in retrograde motion. Geology 27 (10), 955–958.

Celico, F., Petrella, E., 2008. Evoluzione delle conoscenze idrogeologiche del settore nord-occidentale del massiccio carbonatico del Matese-nota preliminare. Mem. Descr. Carta Geol. d'Italia 77, 177–2182.

Chen, C.H., Tang, C.C., Cheng, K.C., Wang, C.H., Wen, S., Lin, C.H., Wen, Y.Y., Meng, G., Yeh, T.K., Jan, J.C., Yen, H.Y., Liu, J.Y., 2015. Groundwater–strain coupling before the 1999 Mw 7.6 Taiwan Chi-Chi earthquake. J. Hydrol. 524, 378–384. https://doi.org/10.1016/j.jhydrol.2015.03.006.

Chen, X., Jiang, C., Zheng, L., Zhang, L., Fu, X., Chen, S., Chen, Y., Hu, J., 2021. Evaluating the genesis and dominant processes of groundwater salinization by using hydrochemistry and multiple isotopes in a mining city. Environ. Pollut. 283, 117381.

Chiaraluce, L., Di Stefano, R., Tinti, E., Scognamiglio, L., Michele, M., Casarotti, E., Cattaneo, M., De Gori, P., Chiarabba, C., Monachesi, G., Lombardi, A., Valoroso, L., Latorre, D., Marzorati, S., 2017. The 2016 Central Italy Seismic Sequence: A First Look at the Mainshocks, Aftershocks, and Source Models. Seismo. Res. Lett. 88 (3), 757–771. https://doi.org/10.1785/0220160221.

Chiodini, G., Frondini, F., Cardellini, C., Parello, F., Peruzzi, L., 2000. Rate of diffuse carbon dioxide Earth degassing estimated from carbon balance of regional aquifers: The case of central Apennine, Italy. J. Geophys. Res. 105 (B4), 8423–8434. https://doi.org/10.1029/1999JB900355.

Chiodini, G., Cardellini, C., Amato, A., Boschi, E., Caliro, S., Frondini, F., Ventura, G., 2004. Carbon dioxide Earth degassing and seismogenesis in central and southern Italy. Geophys. Res. Lett. 31 (7), n/a–n/a.

Ciaccio, M. G., Improta, L., Marchetti, A., Nardi, A., BSI Working Group. 2021. The 2019-2020 repeated small swarms in the Benevento area, Southern Apennines, Italy. GNGTS 2021-39° Convegno Nazionale.

Claesson, L., Skelton, A., Graham, C., Dietl, C., Mörth, M., Torssander, P., Kockum, I., 2004. Hydrogeochemical changes before and after a major earthquake. Geology 32 (8), 641. https://doi.org/10.1130/G20542.110.1130/2004110.

Clark, I., 2015. Groundwater geochemistry and isotopes. CRC Press.

Coppola, M., Correale, A., Barberio, M.D., Billi, A., Cavallo, A., Fondriest, M., Nazzari, M., Paonita, A., Romano, C., Stagno, V., Viti, C., Vona, A., 2021. Meso-to

nano-scale evidence of fluid-assisted co-seismic slip along the normal Mt. Morrone Fault, Italy: Implications for earthquake hydrogeochemical precursors. Earth Planet. Sci. Lett. 568, 117010. https://doi.org/10.1016/j.epsl.2021.117010.

Corniello, A., De Riso, R., 1986. Idrogeologia e idrochimica delle sorgenti dell'Agro Telesino (BN). Geologia applicata e Idrogeologia 21, 53–84.

Corniello, A., Guida, M., Stellato, L., Trifuoggi, M., Carraturo, F., Del Gaudio, E., Del Giudice, C., Forte, G., Giarra, A., Iorio, M., Marzaioli, F., Toscanesi, M., 2021. Hydrochemical, isotopic and microbiota characterization of telese mineral waters (Southern Italy). Environ. Geochem. Health. https://doi.org/10.1007/s10653-021-00806-4.

De Luca, G., Di Carlo, G., Tallini, M., 2018. A record of changes in the Gran Sasso groundwater before, during and after the 2016 Amatrice earthquake, central Italy. Sci. Rep. 8, 15982. https://doi.org/10.1038/s41598-018-34444-1.

Di Luccio, F., Chiodini, G., Caliro, S., Cardellini, C., Convertito, V., Pino, N.A., Tolomei, C., Ventura, G., 2018. Seismic signature of active intrusions in mountain chains. Sci. Adv. 4, e1701825. https://doi.org/10.1126/sciadv.1701825.

Doglioni, C., 1991. A proposal for the kinematic modelling of W-dipping subductions-possible applications to the Tyrrhenian-Apennines system. Terra Nova 3 (4), 423–434.

Doglioni, C., Harabaglia, P., Martinelli, G., Mongelli, F., Zito, G., 1996. A geodynamic model of the Southern Apennines accretionary prism. Terra Nova 8 (6), 540–547.

Doglioni, C., Barba, S., Carminati, E., Riguzzi, F., 2014. Fault on–off versus coseismic fluids reaction. Geosci. Front. 5 (6), 767–780. https://doi.org/10.1016/j.gsf.2013.08.004.

Doglioni, C., Carminati, E., Petricca, P., Riguzzi, F., 2015. Normal fault earthquakes or graviquakes. Sci. Rep. 5 (1), 1–12.

Drever, J. I. 2005. Surface and Ground Water, Weathering, and Soils: Treatise on Geochemistry, Volume 5 (Vol. 5). Elsevier.

Elkhoury, J.E., Brodsky, E.E., Agnew, D.C., 2006. Seismic waves increase permeability. Nature 441 (7097), 1135–1138. https://doi.org/10.1038/nature04798.

Fiorillo, F., Guadagno, F.M., 2010. Karst Spring Discharges Analysis in Relation to Drought Periods, Using the SPI. Water Resour. Manage. 24 (9), 1867–1884. https://doi.org/10.1007/s11269-009-9528-9.

Fiorillo, F., Pagnozzi, M., 2015. Recharge processes of Matese karst massif (southern Italy). Environ. Earth Sci. 74 (12), 7557–7570. https://doi.org/10.1007/s12665-015-4678-y.

Fiorillo, F., Leone, G., Pagnozzi, M., Catani, V., Testa, G., Esposito, L., 2019. The Upwelling Groundwater Flow in the Karst Area of Grassano-Telese Springs (Southern Italy). Water 11, 872. https://doi.org/10.3390/w11050872.

Franchini, S., Agostini, S., Barberio, M.D., Barbieri, M., Billi, A., Boschetti, T., Pennisi, M., Petitta, M., 2021. HydroQuakes, central Apennines, Italy: Towards a hydrogeochemical monitoring network for seismic precursors and the hydro-seismo-sensitivity of boron. J. Hydrol. 598, 125754. https://doi.org/10.1016/j.jhydrol.2020.125754.

Frondini, F., Cardellini, C., Caliro, S., Beddini, G., Rosiello, A., Chiodini, G., 2019. Measuring and interpreting CO_2 fluxes at regional scale: the case of the Apennines, Italy. J. Geol. Soc. 176 (2), 408–416. https://doi.org/10.1144/jgs2017-169.

Galli, P., Galadini, F., Pantosti, D., 2008. Twenty years of paleoseismology in Italy. Earth-Sci. Rev. 88, 89–117. https://doi.org/10.1016/j.earscirev.2008.01.001.

Gutenberg, B., 1956. The energy of earthquakes. Quarter. J. Geol. Soc. 112 (1–4), 1–14.

Hosono, T., Masaki, Y., 2020. Post-seismic hydrochemical changes in regional groundwater flow systems in response to the 2016 Mw 7.0 Kumamoto earthquake. J. Hydrol. 580, 124340. https://doi.org/10.1016/j.jhydrol.2019.124340.

Hosono, T., Yamada, C., Manga, M., Wang, C.-Y., Tanimizu, M., 2020. Stable isotopes show that earthquakes enhance permeability and release water from mountains. Nat. Commun. 11, 2776. https://doi.org/10.1038/s41467-020-16604-y.

Hwang, H.S., Hamm, S.Y., Cheong, J.Y., Lee, S.H., Ha, K., Lee, C., Woo, N.C., Yun, S.M., Kim, K.H., 2020. Effective time-and frequency-domain techniques for interpreting seismic precursors in groundwater level fluctuations on Jeju Island. Korea. Sci. Rep. 10 (1), 1–14.

Igarashi, G., Saeki, S., Takahata, N., Sumikawa, K., Tasaka, S., Sasaki, Y., Takahashi, M., Sano, Y., 1995. Ground-Water Radon Anomaly Before the Kobe Earthquake in Japan. Science 269 (5220), 60–61. https://doi.org/10.1126/science:269.5220.60.

Inan, S., Balderer, W.P., Leuenberger-West, F., Yakan, H., Ozvan, A., Freund, F.T., 2012. Springwater chemical anomalies prior to the Mw = 7.2 Van eathquake (Turkey). Geochem. J. 46, 11–16.

Ingebritsen, S.E., Manga, M., 2014. Hydrogeochemical precursors. Nat. Geosci. 7 (10), 697–698.

Kawabata, K., Sato, T., Takahashi, H.A., Tsunomori, F., Hosono, T., Takahashi, M., Kitamura, Y., 2020. Changes in groundwater radon concentrations caused by the 2016 Kumamoto earthquake. J. Hydrol. 584, 124712.

Kim, J., Lee, J., Petitta, M., Kim, H., Kaown, D., Park, I.W., Lee, S., Lee, K.K., 2019. Groundwater system responses to the 2016 ML 5.8 Gyeongju earthquake. South Korea. J. Hydrol. 576, 150–163.

Kim, J., Joun, W. T., Lee, S., Kaown, D., Lee, K. K. 2020. Hydrogeochemical Evidence of Earthquake-Induced Anomalies in Response to the 2017 MW 5.5 Pohang Earthquake in Korea. Geochemistry, Geophys. Geosystems 21(12), e2020GC009532.

Lamberti, M.C., Vigide, N., Venturi, S., Agusto, M., Yagupsky, D., Winocur, D., Barcelona, H., Velez, M.L., Cardellini, C., Tassi, F., 2019. Structural architecture releasing deep-sourced carbon dioxide diffuse degassing at the Caviahue – Copahue Volcanic Complex. J. Volcanol. Geotherm. Res. 374, 131–141. https://doi.org/10.1016/j.jvolgeores.2019.02.004.

Lan, S., Gu, H., Yu-Liu, 2021. Changes in groundwater level and tidal response caused by the Wenchuan earthquake, China. Hydrogeol. J. 10.1007/s10040-021-02302-6.

Langmuir, D., 1997. Aqueous Environmental Geochemistry. Prentice-Hall, Inc., Upper Saddle River, NJ.

Lee, H. A., Hamm, S. Y., Woo, N. C. 2021. Pilot-Scale Groundwater Monitoring Network for Earthquake Surveillance and Forecasting Research in Korea. Water, 13(17), 2448.

Leone, G., Pagnozzi, M., Catani, V., Testa, G., Esposito, L., Fiorillo, F., 2019. Hydrogeology of the Karst Area of the Grassano and Telese Springs. AS-ITJGW. https://doi.org/10.7343/as-2019-415.

Li, B., Shi, Z., Wang, G., Liu, C., 2019. Xianshuihe Fault zone, Western China. J. Hydrol. 11.

Malakootian, M., Nouri, J., 2010. Chemical variations of ground water affected by the earthquake in bam region. Int. J. Environ. Res. 4 (3), 443–454.

Manahan, S.E., 2017. Environmental chemistry. CRC Press.

Manga, M., Wang, C.Y., 2015. Earthquake Hydrology. Treatise on. Geophysics 4, 25.

Martinelli, G., Ciolini, R., Facca, G., Fazio, F., Gherardi, F., Heinicke, J., Pierotti, L., 2021. Tectonic-Related Geochemical and Hydrological Anomalies in Italy during the Last Fifty Years. Minerals 11, 107. https://doi.org/10.3390/min11020107.

Mastrorillo, L., Saroli, M., Viaroli, S., Banzato, F., Valigi, D., Petitta, M., 2020. Sustained post-seismic effects on groundwater flow in fractured carbonate aquifers in Central Italy. Hydrol Process. 34 (5), 1167–1181.

Milano, G., Di Giovambattista, R., Ventura, G., 2006. Seismicity and stress field in the Sannio-Matese area. Ann. Geophys.

Minissale, A., 2004. Origin, transport and discharge of CO_2 in central Italy. Earth Sci. Rev. 66, 89–141.

Muir-Wood, R., King, G.C.P., 1993. Hydrological signatures of earthquake strain. J. Geophys. Res. 98 (B12), 22035–22068. https://doi.org/10.1029/93JB02219.

Nakagawa, K., Yu, Z.-Q., Berndtsson, R., Hosono, T., 2020. Temporal characteristics of groundwater chemistry affected by the 2016 Kumamoto earthquake using self-organizing maps. J. Hydrol. 582, 124519. https://doi.org/10.1016/j.jhydrol.2019.124519.

Onda, S., Sano, Y., Takahata, N., Kagoshima, T., Miyajima, T., Shibata, T., Pinti, D.L., Lan, T., Kim, N.K., Kusakabe, M., Nishio, Y., 2018. Groundwater oxygen isotope anomaly before the M6.6 Tottori earthquake in Southwest Japan. Sci. Rep. 8, 4800. https://doi.org/10.1038/s41598-018-23303-8.

Orihara, Y., Kamogawa, M., Nagao, T., 2014. Preseismic changes of the level and temperature of confined groundwater related to the 2011 Tohoku earthquake. Sci. Rep. 4 (1), 1–6.

Parkhurst, D. L., Appelo, C. A. J. 2013. Description of input and examples for PHREEQC version 3: a computer program for speciation, batch-reaction, one-dimensional transport, and inverse geochemical calculations (No. 6-A43). US Geological Survey.

Paudel, S.R., Banjara, S.P., Wagle, A., Freund, F.T., 2018. Earthquake chemical precursors in groundwater: a review. J. Seismol. 22 (5), 1293–1314. https://doi.org/10.1007/s10950-018-9739-8.

Pérez, N.M., Hernández, P.A., Padrón, E., Cartagena, R., Olmos, R., Barahona, F., Melián, G., Salazar, P., López, D.L., 2006. Anomalous diffuse CO_2 emission prior to the January 2002 short-term unrest at San Miguel Volcano, El Salvador, Central America. Pure Appl. Geophys. 163 (4), 883–896.

Petitta, M., Mastrorillo, L., Preziosi, E., Banzato, F., Barberio, M.D., Billi, A., Cambi, C., De Luca, G., Di Carlo, G., Di Curzio, D., Di Salvo, C., Nanni, T., Palpacelli, S., Rusi, S., Saroli, M., Tallini, M., Tazioli, A., Valigi, D., Vivalda, P., Doglioni, C., 2018. Water-table and discharge changes associated with the 2016–2017 seismic sequence in central Italy: hydrogeological data and a conceptual model for fractured carbonate aquifersChangements du niveau piézométrique et des débits associés à la séquence sismique 2016–2017 en Italie centrale: données hydrogéologiques et modèle conceptuel pour des aquifères carbonatés fracturésCambios en el nivel freático y en la descarga asociados con la secuencia sísmica 2016–2017 en el centro de Italia: datos hidrogeológicos y un modelo conceptual para acuíferos carbonatados fracturados意大利中部2016–2017年地震序列有关的水位和流量变化:水文地质数据和裂隙碳酸盐含水层的概念模型Mudanças no nível freático e na descarga associadas com a sequência sísmica 2016–2017 no centro da Itália: dados hidrológicos e um modelo conceitual para aquíferos carbonáticos fraturados. Hydrogeol. J. 26 (4), 1009–1026. https://doi.org/10.1007/s10040-017-1717-7.

Petrella, E., Celico, F., 2009. Heterogeneous aquitard properties in sedimentary successions in the Apennine chain: case studies in southern Italy. Hydrol. Process.: Int. J. 23 (23), 3365–3371.

Petricca, P., Barba, S., Carminati, E., Doglioni, C., Riguzzi, F., 2015. Graviquakes in Italy. Tectonophysics 656, 202–214.

Rajmohan, N., Elango, L.J.E.G., 2004. Identification and evolution of hydrogeochemical processes in the groundwater environment in an area of the Palar and Cheyyar River Basins, Southern India. Environ. Geol. 46 (1), 47–61.

Rufino, F., Cuoco, E., Busico, G., Caliro, S., Maletic, E.L., Avino, R., Darrah, T.H., Tedesco, D., 2021. Deep carbon degassing in the Matese massif chain (Southern Italy) inferred by geochemical and isotopic data. Environ. Sci. Pollut. Res. 28 (34), 46614–46626. https://doi.org/10.1007/s11356-020-11107-1.

Salazar, J.M.L., Pérez, N.M., Hernández, P.A., Soriano, T., Barahona, F., Olmos, R., Cartagena, R., López, D.L., Lima, N., Melián, G., Castro, L., Galindo, I., Notsu, K., 2002. Precursory diffuse carbon dioxide degassing signature related to a 5.1 magnitude earthquake in El Salvador, Central America. Earth Planet. Sci. Lett. 205 (1–2), 81–89.

Sano, Y., Takahata, N., Kagoshima, T., Shibata, T., Onoue, T., Zhao, D., 2016. Groundwater helium anomaly reflects strain change during the 2016 Kumamoto earthquake in Southwest Japan. Sci. Rep. 6, 37939. https://doi.org/10.1038/srep37939.

Shi, Z., Wang, G., Liu, C., 2013. Advances in research on earthquake fluids hydrogeology in China: a review. Earthq. Sci. 26 (2), 415–425.

Sibson, R.H., Moore, J.M.M., Rankin, A.H., 1975. Seismic pumping—a hydrothermal fluid transport mechanism. Journal of the Geological Society 131 (6), 653–659.

Sibson, R.H., 2000. Fluid involvement in normal faulting. J. Geodyn. 29 (3–5), 469–499.

Silverii, F., 2016. Study of the transient deformation of Central and Southern Apennines from GPS observations. Doctoral. Dissertation.

Skelton, A., Andrén, M., Kristmannsdóttir, H., Stockmann, G., Mörth, C.-M., Sveinbjörnsdóttir, Á., Jónsson, S., Sturkell, E., Guðrúnardóttir, H.R., Hjartarson, H., Siegmund, H., Kockum, I., 2014. Changes in groundwater chemistry before two consecutive earthquakes in Iceland. Nat. Geosci. 7 (10), 752–756. https://doi.org/10.1038/ngeo2250.

Skelton, A., Liljedahl-Claesson, L., Wästeby, N., Andrén, M., Stockmann, G., Sturkell, E., Mörth, C.-M., Stefansson, A., Tollefsen, E., Siegmund, H., Keller, N., Kjartansdóttir, R., Hjartarson, H., Kockum, I., 2019. Hydrochemical Changes Before and After Earthquakes Based on Long-Term Measurements of Multiple Parameters at Two Sites in Northern Iceland—A Review. J. Geophys. Res. Solid Earth 124 (3), 2702–2720. https://doi.org/10.1029/2018JB016757.

Tamburello, G., Pondrelli, S., Chiodini, G., Rouwet, D., 2018. Global-scale control of extensional tectonics on CO_2 earth degassing. Nat. Commun. 9 (1), 1–9.

Tsunogai, U., Wakita, H., 1995. Precursory chemical changes in ground water: Kobe earthquake, Japan. Science 269 (5220), 61–63.

Tullis, J., Yund, R., Farver, J., 1996. Deformation-enhanced fluid distribution in feldspar aggregates and implications for ductile shear zones. Geology 24 (1), 63–66.

Wakita, H., 1975. Water Wells as Possible Indicators of Tectonic Strain. Science 189 (4202), 553–555. https://doi.org/10.1126/science:189.4202.553.

Wakita, H., Nakamura, Y., Notsu, K., Noguchi, M., Asada, T., 1980. Radon anomaly: a possible precursor of the 1978 Izu-Oshima-kinkai earthquake. Science 207 (4433), 882–883.

Wang, C.Y., Wang, L.P., Manga, M., Wang, C.H., Chen, C.H., 2013. Basin-scale transport of heat and fluid induced by earthquakes. Geophys. Res. Lett. 40 (15), 3893–3897.

Wang, C.Y., Manga, M., 2021. Water and Earthquakes. Springer Nature.

Wannamaker, P.E., Jiracek, G.R., Stodt, J.A., Caldwell, T.G., Gonzalez, V.M., McKnight, J.D., Porter, A.D., 2002. Fluid generation and pathways beneath an active compressional orogen, the New Zealand Southern Alps, inferred from magnetotelluric data. J. Geophys. Res. Solid Earth 107 (B6), ETG-6.

Wästeby, N., Skelton, A., Tollefsen, E., Andrén, M., Stockmann, G., Claesson Liljedahl, L., Sturkell, E., Mörth, M., 2014. Hydrochemical monitoring, petrological observation, and geochemical modeling of fault healing after an earthquake: Fault healing after an earthquake. J. Geophys. Res. Solid Earth 119 (7), 5727–5740. https://doi.org/10.1002/2013JB010715.

5.2 Optimization of dissolved Radon monitoring in groundwater to contribute to the evaluation of the seismic activity: an experience in central-southern Italy

Marino Domenico Barberio*[,1], Francesca Gori[1], Maurizio Barbieri[1], Andrea Billi[2], Flaminia Casalati[1], Stefania Franchini[1], Lucrezia Lorenzetti[1], Marco Petitta[1]

[1] Earth Sciences Department, Sapienza University of Rome, Rome, Italy,

[2] Consiglio Nazionale delle Ricerche, IGAG, Rome, Italy

* Corresponding author: Marino Domenico Barberio, Earth Sciences Department, Sapienza University of Rome, P.le Aldo Moro 5, 00185, Rome, Italy; email: marinodomenico.barberio@uniroma1.it tel. (+39) 3200443022

Optimization of dissolved Radon monitoring in groundwater to contribute to the evaluation of the seismic activity: an experience in central-southern Italy

M. D. Barberio[1] · F. Gori[1] · M. Barbieri[1] · A. Billi[2] · F. Casalati[1] · S. Franchini[1] · L. Lorenzetti[1] · M. Petitta[1]

Abstract

Anomalies in Radon (^{222}Rn) concentrations prior to earthquakes have been widely documented in seismogenic areas worldwide, but questions about their predictability remain largely unanswered. Even if it is not universally accepted, the analysis of the high-resolution time series of Rn (^{222}Rn) concentrations in groundwater, air and soil has been proposed as a suitable method to identify seismic precursors. This study, which is aimed at identifying potential gas-geochemical precursors to nearby earthquakes, analyses groundwater Rn concentrations, which were continuously measured between April 2017 and December 2019. We conducted a detailed time series analysis of dissolved Rn in two springs emerging along two active fault zones in the inner sector of the central-southern Apennines (i.e. the Matese and Morrone fault zones) in Italy. We used a simple statistical method to identify seismic precursor anomalies in Rn concentrations. Anomalies are commonly assumed as values exceeding $\pm 2\sigma$. Furthermore, we calculated the strain radius (for which a gas-geochemical precursor was expected) and the epicentral distance (from both our monitoring stations) of each seismic event of $M_w \geq 3.5$ that occurred in the monitoring area. Results from our ongoing research are promising and show significant correlations between seismic signals and Rn concentrations. However, longer time series data that include more energetic earthquakes are needed to shed light on the behaviour of this gas in relation to crustal deformation processes.

Keywords Radon · Earthquakes · Precursors · Geochemistry · Groundwater · Springs

1 Introduction

Studies about earthquake-induced natural processes have always fascinated scientists all over the world. To date, scientific research has produced several results [1–4], which in most cases are represented by the detection of geophysical or geochemical anomalies in acquired long time series data. These anomalies have been highlighted in different geoscience disciplines and concern variations in: foreshock sequences [5], ratios of seismic wave velocities Vp/Vs [6], electromagnetic fields [7], surface deformations [8], groundwater flow and chemistry [9–14] and gas emissions [15–18]. In particular, Radon (^{222}Rn) has been widely

investigated over the last few decades as a potential seismic precursor candidate [10, 19–21].

However, despite these studies, there are still several significant gaps in adopting Rn as an earthquake precursor. According to a previous study [22], there are many reasons for poor understanding of possible precursor activity, such as inadequate statistical evidence, the lack of long-term measurements and the difficulty in distinguishing between seasonal variations and anomalies at the same magnitude. Acquiring a solid understanding of the chemical and physical processes occurring in the Earth's upper crust requires a substantial number of measurements. ^{222}Rn is an endogenous natural noble gas with

a radioactive half-life of 3.82 days produced by α-decay from Radium (^{226}Ra). It is highly soluble in water, and the behaviour of Rn in groundwater is influenced by the geological nature of the substratum. The concentration of Rn in soil depends strongly on chemical, physical and geological factors, such as grain size, porosity and permeability along with seasonal variations, including temperature and atmospheric pressure [23, 24]. The migration of Rn is driven by rock permeability, which increases with the presence of fractures, structural discontinuities and karst cavities [25, 26]. Both mechanisms of Rn transport (diffusion and advection) depend on rock porosity and permeability, which at the same time vary as a function of the stress field [27]. Due to changes in crustal stress/strain and variations in pore pressure that occur before earthquakes, anomalies in Rn concentrations have been traced and analysed in seismogenic areas worldwide [28, 29]. This evidence is associated with changes in water–rock interactions, which is commonly explained as the strong ability of gas migration promoted by the creation of highly permeable zones, such as microcracks and fractures.

Since 2014, with the aim of establishing new hydrogeological, hydrogeochemical, and gas-geochemical monitoring sites, a few pilot sites for the research of seismic precursors have been installed in the central–southern Apennines (Italy), where they have been continuously monitored and updated [12–14, 30, 31]. This study presents the results obtained from the investigation of Rn gas concentrations in groundwater that were continuously measured in two springs fed by regional carbonate aquifers in Italy. The aim of this paper is to evaluate whether the high-frequency monitoring of Rn dissolved in groundwater can be correlated with regional seismic activity, hence contributing to the identification of potential seismic precursors. Furthermore, the creation and development of regional monitoring networks comprising a large number of sensors for the measurement of dissolved Rn will allow a better understanding of the behaviour of this gas in relation to seismic activity and hydrogeological factors.

2 Geological and hydrogeological settings

The central-southern Apennine chain is an east-verging fold-thrust belt related to the west-dipping subduction of the Apulian lithosphere [32], which was developed during the Neogene and Quaternary periods. This mountain chain is characterized by NE-verging thrust faults, which dissected the tectonic edifice into several thick tectonic sheets. The post-orogenic crustal extensional regime has progressively cut across these thrust sheets from the Messinian-Pliocene onwards [33, 34] (Fig. 1). In particular,

systems of NW-striking normal faults have created half-graben intramountain basins mostly filled by Pliocene-Quaternary continental deposits [35]. At present, the extensional regime is strongly seismogenic along the axis of the central Apennines, while the compressional regime is active along the eastern margin of the Apennines and beneath the western Adriatic Sea [36–38] (Fig. 1).

The Apennine belt is characterized by huge fractured aquifers hosted by Meso-Cenozoic carbonate sequences. Due to the fold–thrust belt structure, the groundwater flowpath of the fractured aquifers is controlled at their base by the geometry of tectonic and stratigraphic contacts with low-permeability layers (aquicludes), such as pre- and syn-orogenic basinal and flysch clayey series [39]. The aquifer systems are characterized by high transmissivity, which is mostly due to fractures and karst cavities. Significant flow through springs is usually both stable and huge.

In this work, we performed continuous monitoring of Rn in two springs: the Giardino spring (SG) and the Rio Freddo spring (SRF) located at Lat. 42.162819° and Long. 13.841160° and at Lat. 41.472902° and Long. 14.496860°, respectively; the springs are fed by two regional carbonate aquifers: Mt. Morrone and the Matese Mts (Fig. 2A). In the northern sector, the Mt. Morrone aquifer is bounded by the thrust zone between the Gran Sasso carbonate unit and the Mt. Morrone carbonate unit. In the eastern sector, it is bounded by the thrust zone between the Mt. Morrone unit and the Laga siliciclastic unit, while in the western sector, it is bounded by the Mt. Morrone active extensional fault [40]. The SG (Fig. 2A) is a main discharge outlet of the Mt. Morrone aquifer and is characterized by steady flow and chemical regimes with a high discharge rate of approximately 1 m^3/s [12, 31]. Its waters are predominantly tapped by the local drinking water company (ACA Pescara). This spring is located at the north-western boundary of the aquifer at the intersection with the Mt. Morrone normal fault (striking NW–SE by approximately 25 km and dipping towards the SW: Fig. 2A). This fault triggered pre-historical earthquakes up to M_w 6.5 or stronger. The current rate of extension in this area assessed through GPS measurements is 3–4 mm/a [8].

The wide karst area of the Matese Mts aquifer crops out in the median sector of the Apennine chain and presents high slopes and elevations up to 2050 m [41]. Carbonate sequences are represented by limestone and limestone-dolostone (late Triassic-Miocene) series with a thickness ranging between 2500 and 3000 m. Along the northern and eastern sectors, the Matese massif (hanging wall) is tectonically bounded by a thrust fault onto younger low-permeability argillaceous complexes and flysch sequences (footwall). Along the southern and
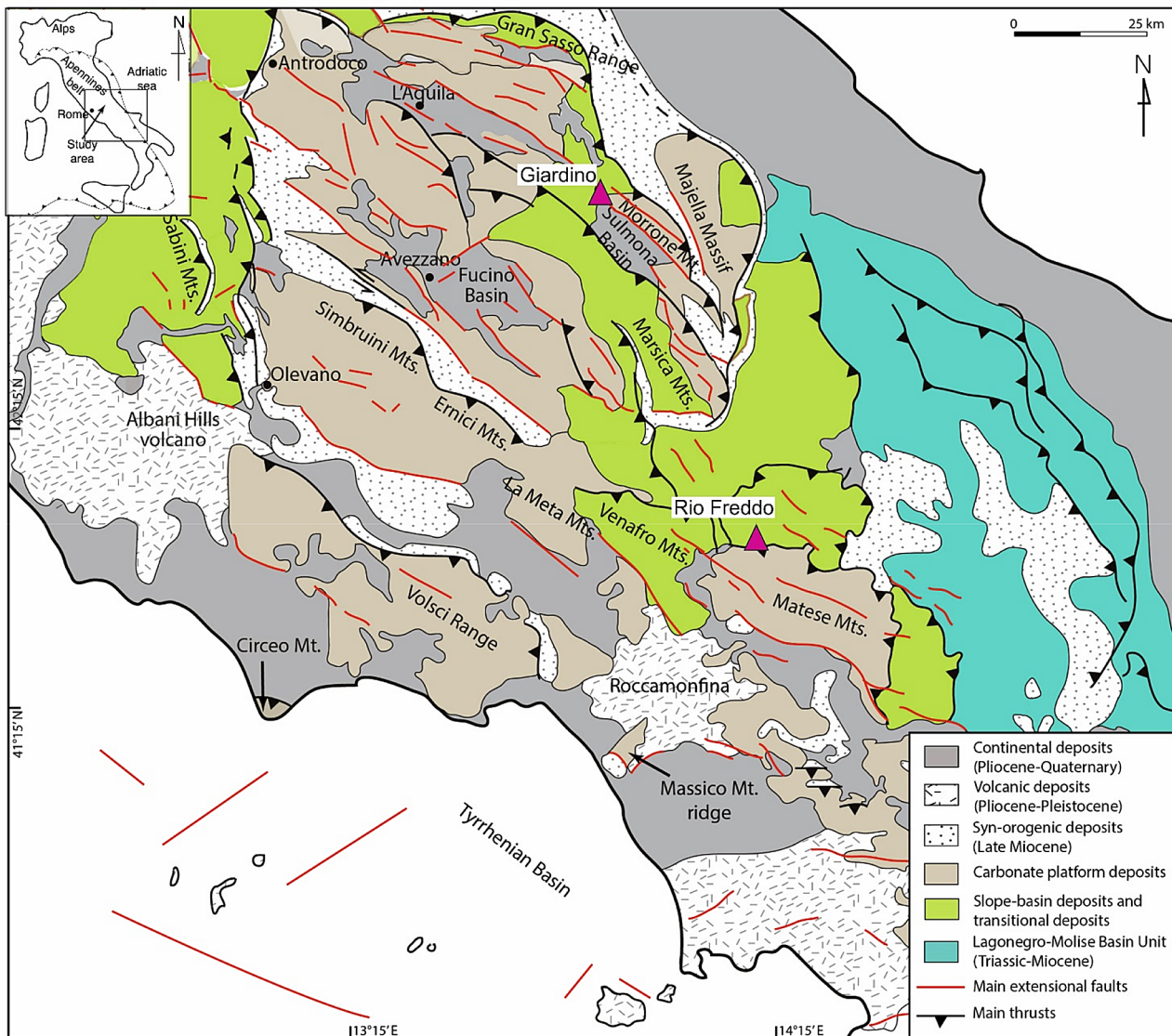
Fig. 1 Regional geological map of central-southern Apennines, Italy. Modified from [34]

western sectors, the massif is bounded by normal faults, and it is covered by recent Quaternary deposits of the Volturno river plain. Three main groups of springs are fed along the northern side of the massif near the village of Bojano [42]. These springs are fed by the karst system of the north-central sector of the Matese massif and have a total mean discharge of about 2.8 m³/s. Most of them are tapped by A.S.R. Molise Acque for drinking purposes. The SRF (Fig. 2A) is located east of the village of Bojano along debris deposits that cover the fault between the limestone and flysch sequences [43]. The Matese area is a region characterized by high seismicity with a NE–SW extension rate of 2.0 ± 0.2 mm/a estimated via GPS data [44].

3 Materials and methods

To investigate the relationship between Rn gas in groundwater and seismic activity, Rn concentrations were continuously measured between April 2017 and December 2019 in the SG and between June 2018 and December 2019 in the SRF. To strip gas from the water, the study used an AlphaGUARD probe (Model PQ2000PRO: see Fig. 2B, C) with high-capacity storage equipped with a RAM 7 module. The gas was subsequently sent to the detector for measurements through a low-flow pump. Moreover, in addition to Rn water concentrations, the device simultaneously recorded ambient temperature, relative humidity, and atmospheric pressure thanks to additional sensors. The AlphaGUARD detector consists
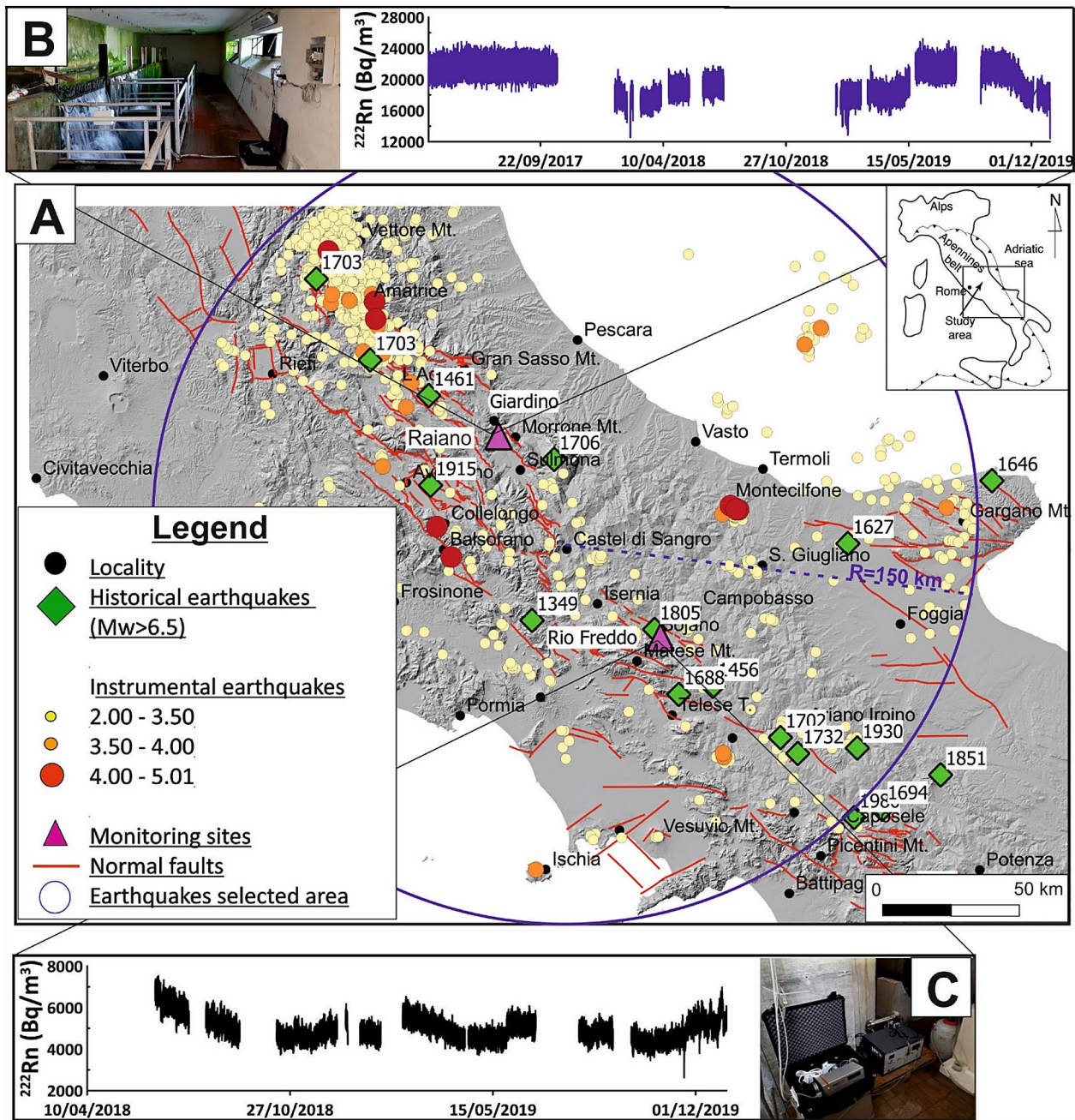
Fig. 2 A Map of central-southern Apennines, Italy. Location of springs is displayed with cyan triangular symbols. Earthquakes (1 April 2017–31 December 2019) occurred in the study area are displayed with circles of different size and colour depending of their magnitude. Historical earthquakes ($M_w \geq 6.5$) are shown with green rhombuses. Seismic data are from the INGV database (available online at http://terremoti.ingv.it/). **B** AlphaGUARD probe (left) and time series (1 April 2017–31 December 2019) of Rn concentrations (right) at SG. **C** AlphaGUARD probe (right) and time series (1 June 2018–31 December 2019) of Rn concentrations (left) detected at SRF

of a pulse ionization chamber associated with an alpha spectrometer that recognizes the specific pulses caused by Rn. The probe guarantees a fast and precise response to different concentrations and maintenance-free operation, owing to its long-term stable calibration (sensitivity 1 CPM at 20 Bq/m³: error of 3%) and is suitable for the

continuous measurement of Rn concentrations between 2–2,000,000 Bq/m³. The automatic data-sampling frequency was set to every 10 min. The two instruments were installed in the surplus flow at the exit of the two collected springs. To identify potential seismic precursors, these springs were also sampled monthly together with

other selected springs [12, 14] to determine their chemical–physical parameters, major ions, trace elements and stable water isotopes.

4 Results

The Rn concentrations in the groundwater were measured between April 2017 and December 2019 in the SG (Fig. 2B) and between June 2018 and December 2019 in the SRF (Fig. 2C). The waters of the SG and SRF are mainly enriched in bicarbonate and calcium ions (Ca-HCO$_3$ facies) due to carbonate dissolution. In terms of chemical–physical parameters (e.g. pH, temperature and electrical conductivity), both springs are characterized by a slightly basic pH of 7.85, temperatures ranging from 7.8 to 11.9 °C, and limited mineralization defined by electrical conductivity values of 315 and 263 µs/cm for the SG and the SRF, respectively. Both Rn time series included missing data that corresponded to periods of probe maintenance or periods of low water flow when the probe emerged, thus measuring atmospheric Rn concentration. Acquisition disturbances were also caused during monthly data download operations. The Rn concentration maximum values were 25,216 and 7520 Bq/m^3, while the minimum ones were 12,416 and 2624 Bq/m^3 for the SG and SRF, respectively. In the time series shown in Fig. 2B, C, the dissolved Rn concentrations appear to be variable around the average values of 20,068.83 and 5038.3 Bq/m^3, respectively. However, it is possible to observe seasonal variations or rapid changes in Rn content commonly linked to the hydrogeological and hydrological cycles [22].

Figure 2A shows the background seismicity of the study area (available online: http://terremoti.ingv.it/), which was recorded in the same period of the gas-geochemical monitoring. Earthquakes that occurred in an area with a radius of 150 km centred on Castel di Sangro (Lat. 41.783991°, Long. 14.108032°) were selected. This locality is the midpoint between the two monitoring stations (i.e. the SG and SRF in Fig. 2A). The M_w 5.1 Montecilfone earthquake, which occurred in Molise on August 16, 2018, was the main seismic event during the monitoring period (2017–2019).

5 Time series processing and interpretation

This study conducted some simple data processing to identify potential anomalies in Rn concentrations related to seismic activity. In particular, some simple elaborations were adopted, which were similar to those that allowed other researchers to identify significant evidence of correlations between gas anomalies and seismic activity in tectonically active areas [2, 21, 45, 46]. The frequency of Rn activity for both springs is described by the typical Gaussian distribution (Fig. 3). Hence, the recorded fluctuations (whether temporal, diurnal or seasonal) are within the range included in $M \pm 2\sigma$, where M and σ are the mean and standard deviations of the time series, respectively, [47]. Instead, anomalies in Rn concentrations are defined as significant deviations from the mean value; specifically, it is commonly assumed that signals related to earthquakes fall outside the so-called 2-σ confidence interval [48].

Based on these studies, the mean values and the standard deviations of Rn activity, which are useful for
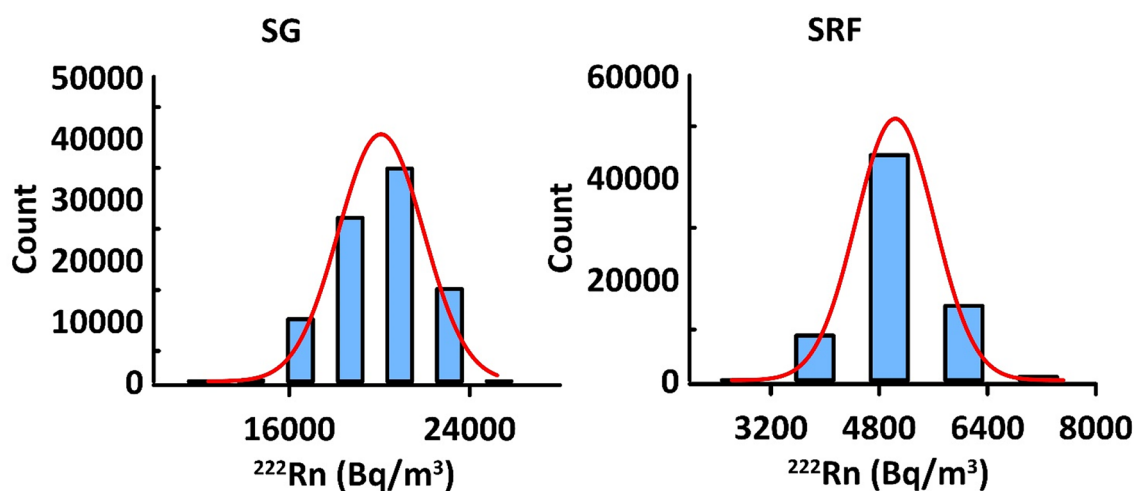
Fig. 3 On the X-axis, the Rn activity is shown (Bq/m^3); on the Y-axis the count is displayed. The frequency of Rn activity for both springs (SG on the left and SRF on the right) is described by the typical Gaussian distribution, represented as the symmetric "bell curve" shape with a red line

the detection of outliers, have been calculated for the SG (SG0, Fig. 4) and for the SRF (Fig. 5). The acquired time series are shown in Figs. 4 and 5 with three-hour moving averages, which were adopted to eliminate data noise. The mean values and the $\pm\sigma$ and $\pm 2\sigma$ thresholds are also displayed in graphs by solid and dashed lines, respectively. These graphs also show seismic events of $M_w \geq 3.5$ (taken from the previously described database).

In Fig. 4, SG0 represents the entire SG time series recorded between April 2017 and December 2019. Since this series is uneven, the sequence has been separated into four sections (SG1–SG4 in Fig. 4) to improve the accuracy of the processing. No intervals exceeding the $\pm 2\sigma$ thresholds in relation to the seismicity of the study area are observed. However, decomposing the SRF time series is not necessary, as the data show a relatively limited variation from the mean value of about 5000 Bq/
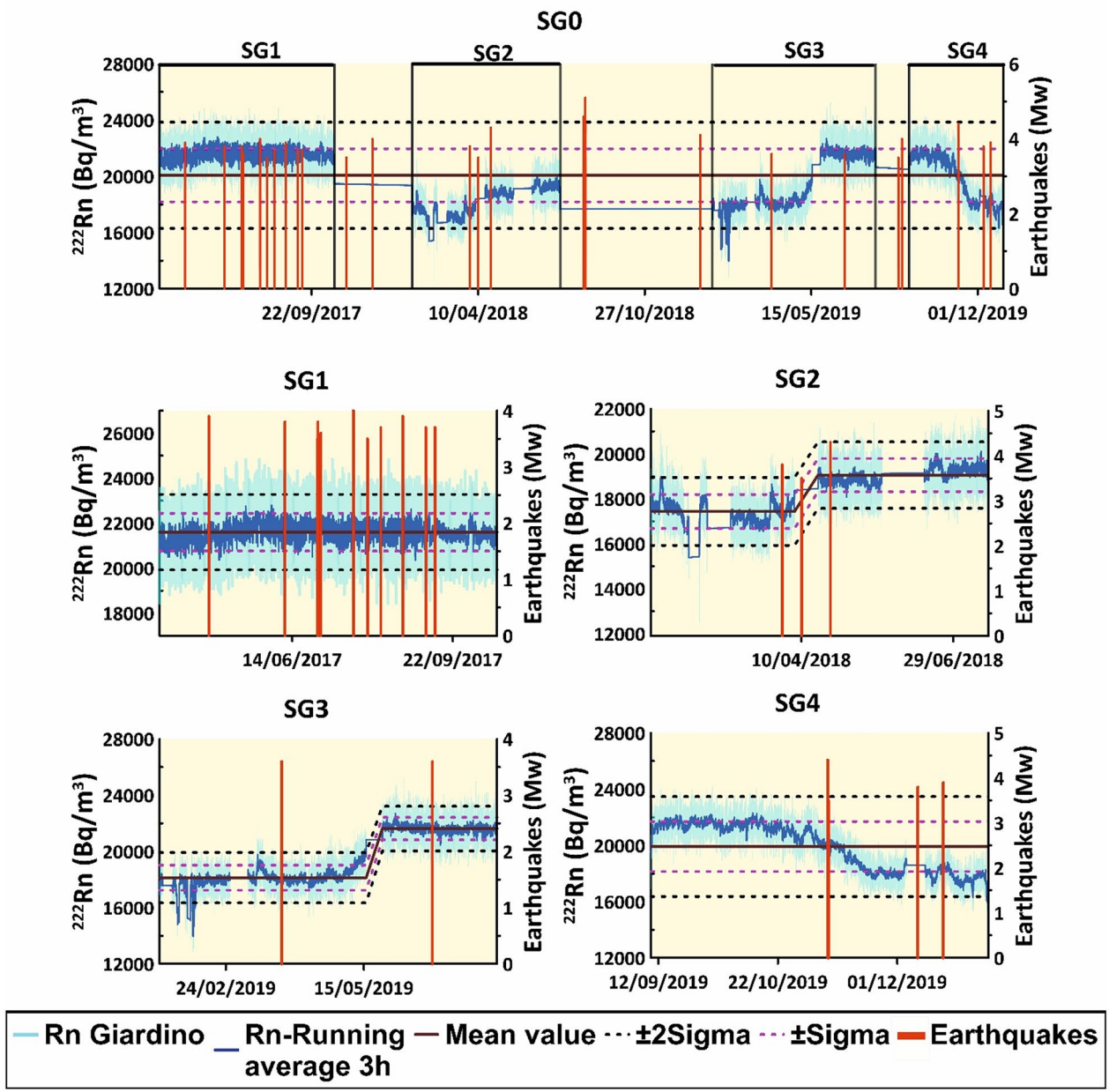
Fig. 4 Time series (1 April 2017–31 December 2019) of Rn concentrations recorded at SG (SG0). SG1, SG2, SG3, and SG4 are the four segments into which the sequence was divided. Rn activity is displayed with cyan lines, while its moving averages of 3 h are shown with blue lines. Mean values and the $\pm\sigma$ and $\pm 2\sigma$ thresholds are displayed with solid lines and with dashed ones, respectively. Seismic events with $M_w \geq 3.5$ (from the INGV database, available online at http://terremoti.ingv.it/) are shown with red bars

SRF
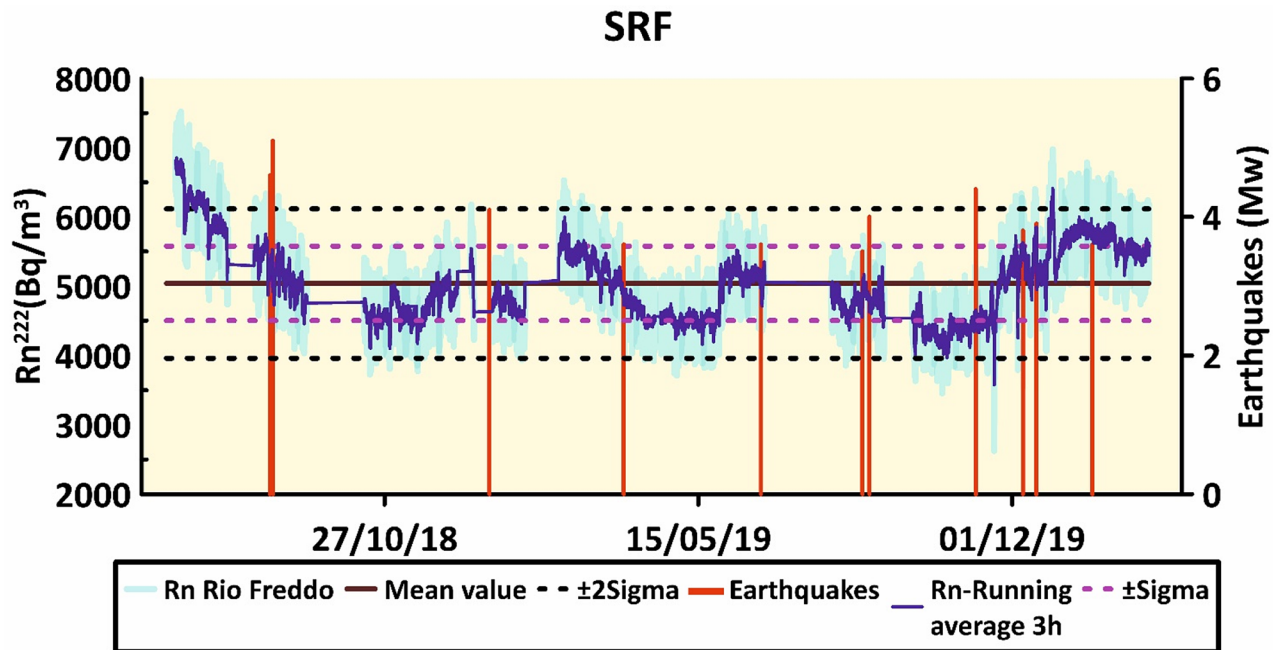
Fig. 5 Time series (1 June 2018–31 December 2019) of Rn concentrations recorded at RFS. Rn activity is displayed with cyan line, while its moving averages of 3 h are shown with blue line. Mean value and the $\pm\sigma$ and $\pm 2\sigma$ thresholds are displayed with solid line and with dashed ones, respectively. Seismic events with $M_w \geq 3.5$ (from the INGV database, available online at http://terremoti.ingv.it/) are shown with red bars

m^3 (Fig. 5). Additionally, in this case, as for the SG, there are no intervals exceeding the $\pm 2\sigma$ thresholds in relation to seismic activity. The values exceeding $\pm 2\sigma$ are due to different conditions: (1) at the SG, they are related to sensor emersions above the water surface (Fig. 4), while (2) at the SRF, they are represented by the initial values of the time series that are presumably attributable to another condition (before the start of monitoring), whose course is not known (Fig. 5).

Additionally, a different data processing procedure was considered. According to Dobrovolsky et al. [49], two parameters must be treated together to calculate the strain radius (R in km) of the effective precursory manifestation zone: the magnitude of the earthquake (M_w) and the distance between the epicentre and the measuring site (D in km). In this way, these authors defined a relationship to identify the interactions between gas-geochemical and seismic signals using the following empirical equation:

$$R = 10^{0.43 \times M} \tag{1}$$

where R is the strain radius of the precursory manifestation zone and M is the moment magnitude (M_w).

The conceptual basis of Eq. (1) is that an approximately circular region around the epicentre of the earthquake should undergo elastic crustal deformation prior to earthquakes [50]. Therefore, precursory signals were expected for events where $R \geq D$. Considering two earthquakes of the same magnitude, a closer seismic event affects the Rn activity in the monitoring site more significantly than a distant one.

Equation (1) was applied to $M_w \geq 3.5$ earthquakes that occurred at the two study sites (between April 2017 and December 2019). Epicentral distances from the two sites were also determined (Fig. 6). This processing allowed the identification of five seismic events for the SG and six seismic events for the SRF, in which a possible Rn response was expected in terms of geochemical precursor signals.

The response could not be verified for three of the five seismic events identified at the SG due to the lack of Rn data, while no interaction was observed for the four Montecilfone seismic events at the SRF. The non-interaction between the gas content and the Montecilfone earthquakes has a geodynamic explanation; these seismic events occurred in a different plate (i.e. in the Adria plate subducting towards the SW beneath the Apennines) from the Apennine belt where the monitoring sites are located [51]. Therefore, it is not surprising that the Montecilfone seismic sequence did not cause anomalies in the inner sector of the Apennines.

Overall, three seismic events produced expected Rn activity responses as presented in Fig. 7. Specifically, the M_w 3.8 L'Aquila earthquake, which occurred on March 31st,
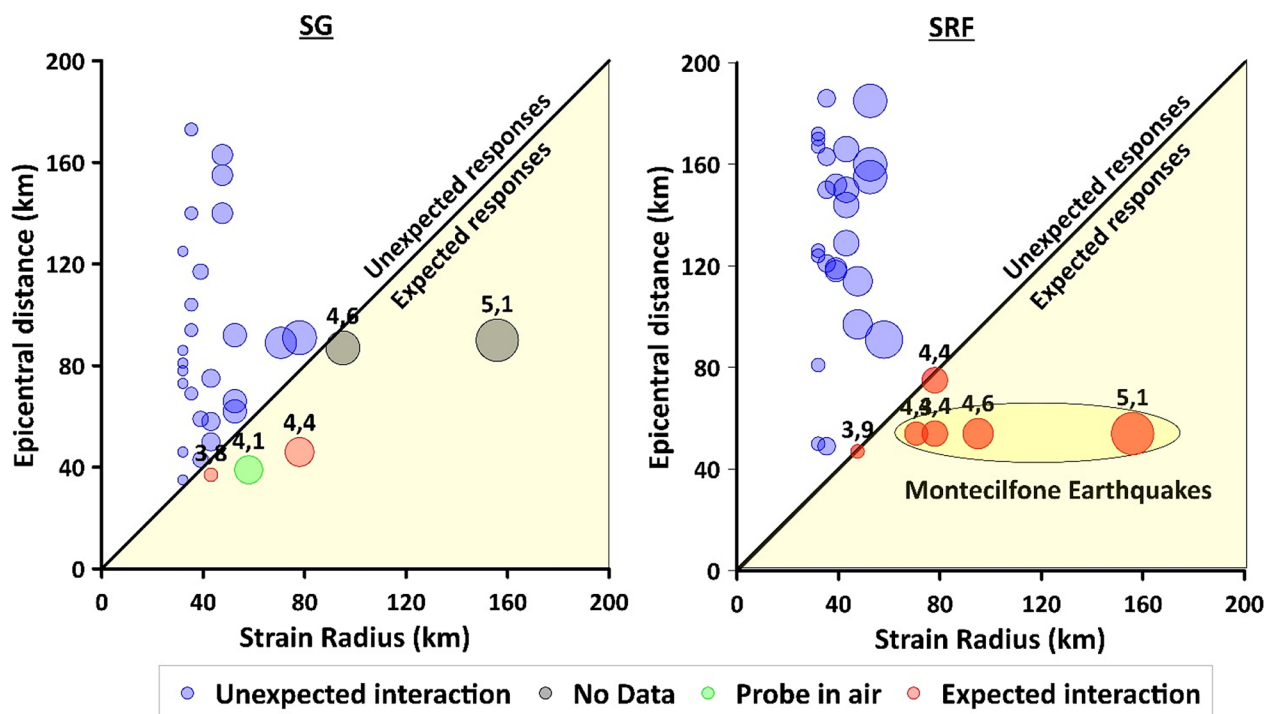
Fig. 6 Seismic events with $M_w \geq 3.5$ in the $R–D$ plane, where R is the strain radius of the precursory manifestation zone, and D is the epicentral distance (km) from the two springs [49, 50]. Earthquakes, for which an interaction between gas-geochemical and seismic signals was supposed, fall into the "expected responses" area (the label indicates the M_w earthquake). Only red circles are taken into consideration due to lack of Rn data, sensor emersions, and unexpected interactions that are displayed with black, green and blue circles, respectively

2018, was detected at the SG; the M_w 4.4 Balsorano earthquake, which occurred on 7 November 2019, produced responses at both springs; and the M_w 3.9 San Leucio del Sannio earthquake, which occurred on 16 December 2019, produced a response at the SRF. These two latter events present comparable R and D values at the SRF. For this reason, they fall on the straight line (Fig. 6, SRF) that separates the expected interaction area ($R \geq D$) from the unexpected interaction area ($R < D$). Specifically, an increase in Rn concentration (which lasted for about 12 h) of ≈ 1200 Bq/m^3 (7% with respect to the average value) and another one of ≈ 1500 Bq/m^3 (8% with respect to the average value) were observed at the SG seven and 11 days before the L'Aquila and the Balsorano earthquakes, respectively (the black arrow in the SG, Fig. 7A, B). For the latter earthquake, a decrease of approximately 2000 Bq/m^3 (after the peak) was also observed. Another increase in Rn concentration of ≈ 500 Bq/m^3 (10% with respect to the average value, which lasted about six hours) was recorded at the SRF about 17 days before the Balsorano earthquake (the black arrow on the left in the SRF, Fig. 7C). A different Rn behaviour was identified at the SRF before the San Leucio del Sannio earthquake. The preparation phase of this seismic event is illustrated by a clear increasing trend

during the month of November of ≈ 1000 Bq/m^3 (20% with respect to the average value: the black arrow at the SRF on the right, Fig. 7). In all the observed cases, it can be inferred that changes in the strain field before seismic activity may have affected gas and fluid migration, causing an increase in Rn content ranging from 7 to 20% with respect to (background) pre-anomaly values. Therefore, the recorded pre-seismic signals could be explained as the result of dilation and/or contraction of fracture systems that led to changes in the gas flow behaviour; however, it is believed that a more accurate analysis of time lags between the Rn signals and the occurrence of earthquakes is necessary, as the identified interactions are too limited in number to clarify this aspect. Additionally, processes of dilation and/or contraction are expected to drive some changes in the chemical content of groundwater, whose intensity would be inversely correlated with the groundwater resource volume in the corresponding aquifers due to different dilution rates. Furthermore, some transient and evident perturbations in Rn concentrations before the San Leucio del Sannio earthquake were detected, but these were attributed to the users' field interventions. The sampling frequency of 10 min allowed the acquisition of accurate data through which it was possible to measure
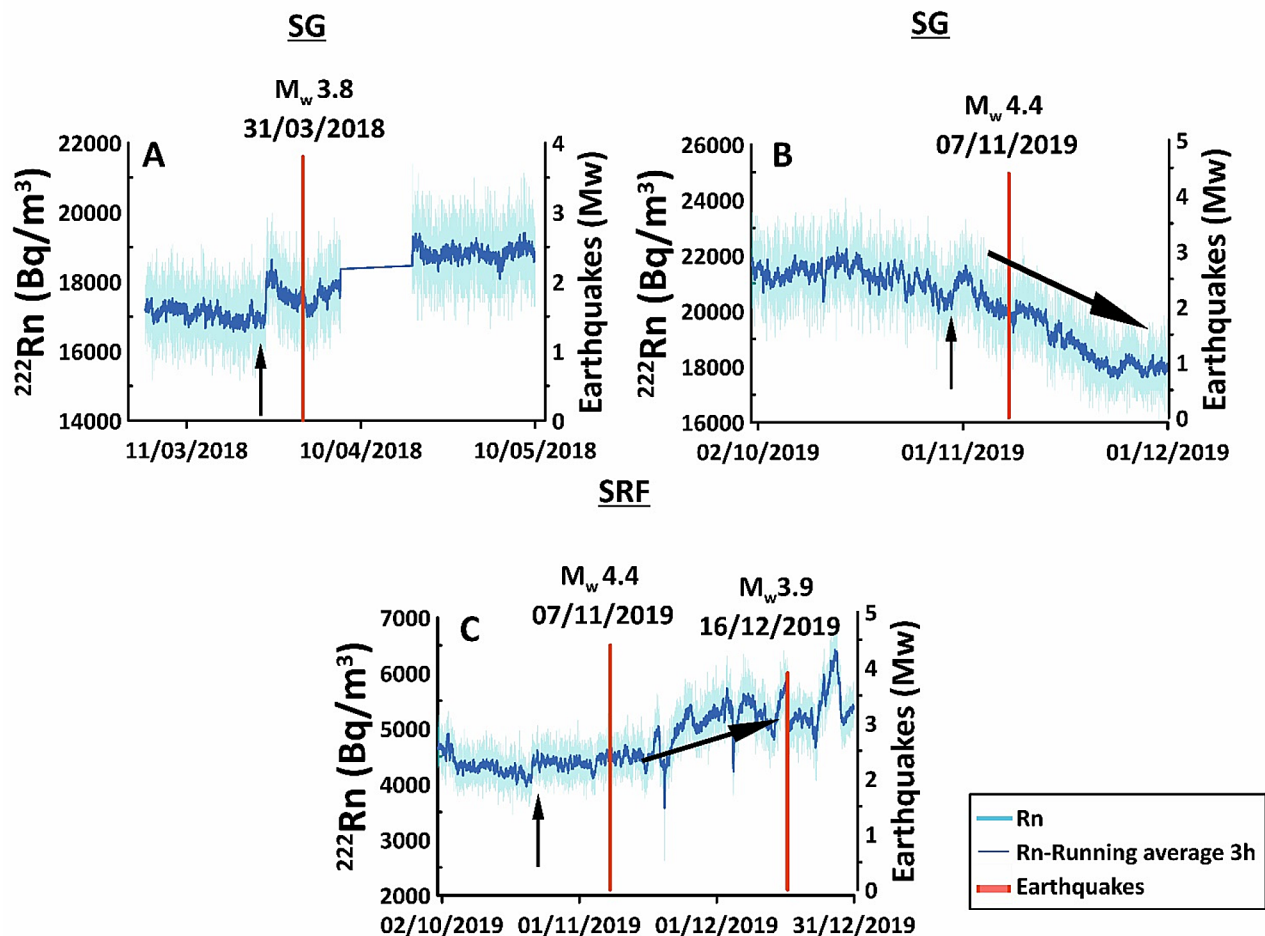
Fig. 7 Time series of Rn concentrations in relation to seismic activity. The seismic events that produced expected Rn activity responses are shown with red bars. **A** M_w 3.8 L'Aquila earthquake occurred on March 31st, 2018, detected at SG; **B** M_w 4.4 Balsorano earthquake occurred on 7 November 2019, detected at SG; **C** M_w 3.9 San Leucio del Sannio earthquake occurred on 16 December 2019 and M_w 4.4 Balsorano earthquake occurred on 7 November 2019, both recorded at SRF. The black arrows show the identified anomalies

the duration of the anomalies until the signals returned to stable background values.

Considering the anomalies recorded on the Rn time series at the two sites, the correlation between the selected events (for which a response was expected) and the hydrogeochemical time series acquired in the SG and SRF areas was investigated. Indeed, the monthly sampling of some selected springs in the two areas made it possible to detect some anomalies in springs with deeper input [12, 14]. Box-and-whiskers statistical analyses performed on the hydrogeochemical data of these springs revealed anomalous values (outliers) in Li, V, Cr and Cs concentrations in the Raiano spring (Fig. 2A) before the Balsorano earthquake, for which anomalies in Rn content were recorded at both stations (i.e. the SG and SRF in Fig. 7).

The recorded variations and trends identified in the hydrogeochemical time series of the Rn-monitored SG and SRF did not show clear relationships with seismic events. Nevertheless, a potential response could exist that is represented by the behaviour of some elements and ions, such as Cl, SO_4 and Fe, and parameters such as electrical conductivity and temperature at the SG, where limited changes were recorded. Moreover, the sampling frequency of the water chemistry (every month) did not allow comparisons with the Rn time series (one measurement every 10 min). Therefore, the availability of longer time series data is essential for the correct evaluation of the variations in the acquired series.

6 Conclusions

The properties of Rn as an extremely mobile and nonreactive gas makes it an ideal tracer in water with the potential use in the short-term forecast of earthquakes. When used

in conjunction with other chemical and physical parameters, its prediction significance is greatly enhanced. This study performed continuous monitoring of dissolved Rn in two springs (the SG and the SRF) in central–southern Italy. This monitoring was and remains aimed at identifying potential gas-geochemical precursors to nearby earthquakes. Despite the absence of intermediate–strong seismic events during the monitoring period, some preliminary results can be drawn from the ongoing research:

- The first three years of gas-geochemical monitoring (April 2017 to December 2019) highlighted a good stability of Rn concentrations in two springs fed by regional carbonate aquifers in central–southern Italy.
- Significant Rn increases recorded before three small seismic events ($M_w < 4$) confirm that the preliminary results achieved are promising and are in line with the international known approaches and results [10, 18, 21, 45]. Indeed, significant Rn anomalies were found for all monitored seismic events that were expected to influence the Rn concentration in groundwater based on the strain radius (R in km) of the effective precursory manifestation zone.
- Specifically, the M_w 4.4 Balsorano earthquake, which occurred on 7 November 2019, produced significant responses in Rn concentrations in both springs as well as hydrogeochemical anomalies before this seismic event in concentrations of Li, V, Cr and Cs that were recorded at the nearby Raiano spring.
- The hydrogeochemical time series acquired at SG and SRF showed no significant relationship to seismic events. The difference between the sampling frequencies of the gas-geochemical and hydrogeochemical monitoring did not allow comparisons to be made between the recorded Rn anomalies and the geochemical time series.
- On the basis of the above-mentioned results, we are confident that the expansion of the monitoring network through the installation of additional sensors for the measurement of dissolved Rn in water will allow geoscientists to shed light on the behaviour of this gas in relation to crustal deformation processes, depending on the earthquake's magnitude and epicentral distance.

Compliance with ethical standards

References

1. Wakita H, Nakamura Y, Notsu K, Noguchi M, Asada T (1980) Radon anomaly: a possible precursor of the 1978 Izu-Oshima-kinkai earthquake. Science 207(4433):882–883. https://doi. org/10.1126/science.207.4433.882

2. Toutain JP, Baubron JC (1999) Gas geochemistry and seismo-tectonics: a review. Tectonophysics 304(1–2):1–27. https://doi. org/10.1016/S0040-1951(98)00295-9

3. Montgomery DR, Manga M (2003) Streamflow and water well responses to earthquakes. Science 300(5628):2047–2049. https ://doi.org/10.1126/science.1082980

4. King CY, Zhang W, Zhang Z (2006) Earthquake-induced groundwater and gas changes. Pure Appl Geophys 163(4):633–645. https://doi.org/10.1007/s00024-006-0049-7

5. Reasenberg PA (1999) Foreshock occurrence before large earthquakes. J Geophys Res Solid Earth 104(B3):4755–4768. https:// doi.org/10.1029/1998JB900089

6. Lucente FP, De Gori P, Margheriti L, Piccinini D, Di Bona M, Chiarabba C, Piana Agostinetti N (2010) Temporal variation of seismic velocity and anisotropy before the 2009 MW 6.3 L'Aquila earthquake, Italy. Geology 38(11):1015–1018. https://doi. org/10.1130/G31463.1

7. Fraser-Smith AC, Bernardi A, McGill PR, Ladd M, Helliwell RA, Villard OG Jr (1990) Low-frequency magnetic field measurements

near the epicenter of the Ms 7.1 Loma Prieta earthquake. Geophys Res Lett 17(9):1465–1468. https://doi.org/10.1029/GL017i009p01465

8. Riguzzi F, Crespi M, Devoti R, Doglioni C, Pietrantonio G, Pisani AR (2012) Geodetic strain rate and earthquake size: new clues for seismic hazard studies. Phys Earth Planet Inter 206:67–75. https://doi.org/10.1016/j.pepi.2012.07.005

9. Roeloffs EA (1988) Hydrologic precursors to earthquakes: a review. Pure Appl Geophys 126:177–209. https://doi.org/10.1007/BF00878996

10. King CY, Koizumi N, Kitagawa Y (1995) Hydrogeochemical anomalies and the 1995 Kobe earthquake. Science 269(5220):38–40

11. Skelton A, Andrén M, Kristmannsdóttir H, Stockmann G, Mörth CM, Sveinbjörnsdóttir Á, Jónsson S, Sturkell E, Guðrúnardóttir HR, Hjartarson H, Siegmund H, Kockum I (2014) Changes in groundwater chemistry before two consecutive earthquakes in Iceland. Nat Geosci 7(10):752–756. https://doi.org/10.1038/ngeo2250

12. Barberio MD, Barbieri M, Billi A, Doglioni C, Petitta M (2017) Hydrogeochemical changes before and during the 2016 Amatrice-Norcia seismic sequence (central Italy). Sci Rep 7(1):1–12. https://doi.org/10.1038/s41598-017-11990-8

13. Boschetti T, Barbieri M, Barberio MD, Billi A, Franchini S, Petitta M (2019) CO_2 inflow and elements desorption prior to a seismic sequence, Amatrice-Norcia 2016, Italy. Geochem Geophys Geosyst 20(5):2303–2317. https://doi.org/10.1029/2018GC008117

14. Barbieri M, Boschetti T, Barberio MD, Billi A, Franchini S, Iacumin P, Selmo E, Petitta M (2020) Tracing deep fluid source contribution to groundwater in an active seismic area (central Italy): a combined geothermometric and isotopic (δ13C) perspective. J Hydrol 582:124495. https://doi.org/10.1016/j.jhydrol.2019.124495

15. Martini C (2016) Signals in water-the deep originated CO_2 in the Peschiera-Capone acqueduct in relation to monitoring of seismic activity in central Italy. Acque Sotterranee-Ital J Groundw. https://doi.org/10.7343/as-2016-246

16. Sano Y, Takahata N, Kagoshima T, Shibata T, Onoue T, Zhao D (2016) Groundwater helium anomaly reflects strain change during the 2016 Kumamoto earthquake in Southwest Japan. Sci Rep 6:37939. https://doi.org/10.1038/srep37939

17. Buttitta D, Caracausi A, Chiaraluce L, Favara R, Morticelli MG, Sulli A (2020) Continental degassing of helium in an active tectonic setting (northern Italy): the role of seismicity. Sci Rep 10(1):1–13. https://doi.org/10.1038/s41598-019-55678-7

18. Kawabata K, Sato T, Takahashi HA, Tsunomori F, Hosono T, Takahashi M, Kitamura Y (2020) Changes in groundwater radon concentrations caused by the 2016 Kumamoto earthquake. J Hydrol. https://doi.org/10.1016/j.jhydrol.2020.124712

19. Riggio A, Santulin M (2015) Earthquake forecasting: a review of radon as seismic precursor. B Geofis Teor Appl. https://doi.org/10.4430/bgta0148

20. Ching-Chou F, Walia V, Yang TF, Lou-Chuang L, Liu TK, Cheng-Hong C, Arvind K, Shih-Jung L, Tzu-Hua L, Kuo-Liang W (2017) Preseismic anomalies in soil-gas radon associated with 2016 M 6.6 Meinong earthquake, Southern Taiwan. TAO Terr Atmos Ocean Sci 28(5):7. https://doi.org/10.3319/TAO.2017.03.22.01

21. Kuo T, Chen W, Ho C (2018) Anomalous decrease in groundwater radon before 2016 Mw 6.4 Meinong earthquake and its application in Taiwan. Appl Radiat Isot 136:68–72. https://doi.org/10.1016/j.apradiso.2018.02.015

22. Morales-Simfors N, Wyss RA, Bundschuh J (2019) Recent progress in radon-based monitoring as seismic and volcanic precursor: a critical review. Crit Rev Environ Sci Technol 50:979–1012. https://doi.org/10.1080/10643389.2019.1642833

23. King PT, Michel J, Moore WS (1982) Groundwater geochemistry of 228Ra, 226Ra, 222Rn. Geochim Cosmochim Acta 46:1173–1182. https://doi.org/10.1016/0016-7037(82)90003-5

24. Pinault JL, Baubron JC (1997) Signal processing of diurnal and semidiurnal variations in Radon and atmospheric pressure: a new tool for accurate in situ measurement of soil gas velocity, pressure gradient, and tortuosity. J Geophys Res 102:18101–18120. https://doi.org/10.1029/97JB00971

25. Tanner AB (1980) Radon migration in the ground: a supplementary review. Nat Radiat Environ III 1:5–56

26. Adinolfi Falcone R, Carucci V, Falgiani A, Manetta M, Parisse B, Petitta M, Rusi S, Spizzico M, Tallini M (2012) Changes on groundwater flow and hydrochemistry of the Gran Sasso carbonate aquifer after 2009 L'Aquila earthquake. Ital J Geosci 131(3):459–474. https://doi.org/10.3301/IJG.2011.34

27. Holub RF, Brady BT (1981) The effect of stress on radon emanation from rock. J Geophys Res Solid Earth 86(B3):1776–1784. https://doi.org/10.1029/JB086iB03p01776

28. Hauksson E (1981) Radon content of groundwater as an earthquake precursor: evaluation of worldwide data and physical basis. J Geophys Res Solid Earth 86(B10):9397–9410. https://doi.org/10.1029/JB086iB10p09397

29. Igarashi G, Saeki S, Takahata N, Sumikawa K, Tasaka S, Sasaki Y, Takahashi M, Sano Y (1995) Ground-water radon anomaly before the Kobe earthquake in Japan. Science 269:60–61. https://doi.org/10.1126/science.269.5220.60

30. Barberio MD, Gori F, Barbieri M, Billi A, Devoti R, Doglioni C, Petitta M, Riguzzi F, Rusi S (2018) Diurnal and semidiurnal cyclicity of Radon (222Rn) in groundwater, Giardino spring, central Apennines, Italy. Water 10(9):1276. https://doi.org/10.3390/w10091276

31. Petitta M, Mastrorillo L, Preziosi E, Banzato F, Barberio MD, Billi A, Cambi C, De Luca G, Di Carlo G, Di Curzio D, Di Salvo C, Nanni T, Palpacelli S, Rusi S, Saroli M, Tallini M, Tazioli A, Valigi D, Vivalda P, Doglioni C (2018) Water-table and discharge changes associated with the 2016–2017 seismic sequence in central Italy: hydrogeological data and a conceptual model for fractured carbonate aquifers. Hydrogeol J 26(4):1009–1026. https://doi.org/10.1007/s10040-017-1717-7

32. Doglioni C, Harabaglia P, Martinelli G, Mongelli F, Zito G (1996) A geodynamic model of the Southern Apennines accretionary prism. Terra Nova 8(6):540–547. https://doi.org/10.1111/j.1365-3121.1996.tb00783.x

33. Scrocca D (2010) Southern Apennines: structural setting and tectonic evolution. J Virtual Explor 36:13

34. Curzi M, Aldega L, Bernasconi SM, Berra F, Billi A, Boschi C, Franchini S, Van der Lelij R, Viola G, Carminati E (2020) Architecture and evolution of an extensionally-inverted thrust (Mt. Tancia Thrust, Central Apennines): Geological, structural, geochemical, and K–Ar geochronological constraints. J Struct Geol. https://doi.org/10.1016/j.jsg.2020.104059

35. Cavinato GP, Celles PD (1999) Extensional basins in the tectonically bimodal central Apennines fold-thrust belt, Italy: response to corner flow above a subducting slab in retrograde motion. Geology 27(10):955–958. https://doi.org/10.1130/0091-7613(1999)027%3c0955:EBITTB%3e2.3.CO;2

36. Galadini F, Galli P (2000) Active tectonics in the central Apennines (Italy)—input data for seismic hazard assessment. Nat Hazards 22(3):225–268. https://doi.org/10.1023/A:1008149531980

37. Galli P, Galadini F, Pantosti D (2008) Twenty years of paleoseismology in Italy. Earth-Sci Rev 88(1–2):89–117. https://doi.org/10.1016/j.earscirev.2008.01.001

38. Trippetta F, Petricca P, Billi A, Collettini C, Cuffaro M, Lombardi AM, Scrocca D, Ventura G, Morgante A, Doglioni C (2019) From mapped faults to fault-length earthquake magnitude (FLEM): a

test on Italy with methodological implications. Solid Earth. https://doi.org/10.5194/se-10-1555-2019

39. Allocca V, Manna F, De Vita P (2014) Estimating annual groundwater recharge coefficient for karst aquifers of the southern Apennines (Italy). Hydrol Earth Syst Sci 18(2):803–817. https://doi.org/10.5194/hess-18-803-2014

40. Conese M, Nanni T, Peila C, Rusi S, Salvati R (2001) Idrogeologia della Montagna del Morrone (Appennino abruzzese): Dati preliminari. Mem Soc Geol Ital 56:181–196

41. Fiorillo F, Pagnozzi M (2015) Recharge processes of Matese karst massif (southern Italy). Environ Earth Sci 74(12):7557–7570. https://doi.org/10.1007/s12665-015-4678-y

42. Civita M (1969) Valutazione analitica delle riserve in acque sotterranee alimentanti alcune tra le principali sorgenti del massiccio del Matese (Italia meridionale). Boll Soc Nat Napoli 78:133–163

43. Petrella E, Celico F (2009) Heterogeneous aquitard properties in sedimentary successions in the Apennine chain: case studies in southern Italy. Hydrol Process 23(23):3365–3371. https://doi.org/10.1002/hyp.7441

44. Esposito A, Galvani A, Sepe V, Atzor S, Brandi G, Cubellis E, De Martino P, Dolce M, Massucci A, Obrizzo F, Riguzzi F, Tammaro U, Pietrantonio G (2020) Concurrent deformation processes in the Matese massif area (Central-Southern Apennines, Italy). Tectonophysics 774:228234. https://doi.org/10.1016/j.tecto.2019.228234

45. Igarashi G, Wakita H (1990) Groundwater radon anomalies associated with earthquakes. Tectonophysics 180(2–4):237–254. https://doi.org/10.1016/0040-1951(90)90311-U

46. Heinicke J, Koch U, Martinelli G (1995) CO_2 and radon measurements in the Vogtland Area (Germany)—a contribution to earthquake prediction research. Geophys Res Lett 22(7):771–774. https://doi.org/10.1029/94GL03074

47. Chaudhuri H, Barman C, Iyengar AS, Ghose D, Sen P, Sinha B (2013) Network of seismo-geochemical monitoring observatories for earthquake prediction research in India. Acta Geophys 61(4):1000–1025. https://doi.org/10.2478/s11600-013-0134-0

48. Hauksson E, Goddard JG (1981) Radon earthquake precursor studies in Iceland. J Geophys Res Solid Earth 86(B8):7037–7054. https://doi.org/10.1029/JB086iB08p07037

49. Dobrovolsky IP, Zubkov SI, Miachkin VI (1979) Estimation of the size of earthquake preparation zones. Pure Appl Geophys 117(5):1025–1044. https://doi.org/10.1007/BF00876083

50. Silva HG, Bezzeghoud M, Oliveira MM, Reis AH, Rosa RN (2013) A simple statistical procedure for the analysis of radon anomalies associated with seismic activity. Ann Geophys 56(1):0106. https://doi.org/10.4401/ag-5570

51. Pinter N, Grenerczy G, Weber J, Medak D, Stein S (2006) The Adria microplate: GPS geodesy, tectonics and hazards. Springer, Berlin

5.3 New observations in Central Italy of groundwater responses to the worldwide seismicity

Marino Domenico Barberio[1,*], Francesca Gori[1], Maurizio Barbieri[1], Andrea Billi[2], Antonio Caracausi[3], Gaetano De Luca[4], Stefania Franchini[1], Marco Petitta[1], Carlo Doglioni[1,5]

[1] Earth Sciences Department, Sapienza University of Rome, Rome, Italy

[2] Consiglio Nazionale delle Ricerche, IGAG, Rome, Italy

[3] National Institute of Geophysics and Volcanology, Palermo, Italy

[4] National Institute of Geophysics and Volcanology, National Earthquake Observatory, L'Aquila, Italy

[5] National Institute of Geophysics and Volcanology, Rome, Italy

[*] Corresponding author: Marino Domenico Barberio, Earth Sciences Department, Sapienza University of Rome, P.le Aldo Moro 5, 00185, Rome, Italy; email: marinodomenico.barberio@uniroma1.it tel. (+39) 320 0443022

scientific reports

Check for updates

OPEN

New observations in Central Italy of groundwater responses to the worldwide seismicity

Marino Domenico Barberio[1]✉, Francesca Gori[1], Maurizio Barbieri[1], Andrea Billi[2], Antonio Caracausi[3], Gaetano De Luca[4], Stefania Franchini[1], Marco Petitta[1] & Carlo Doglioni[1,5]

Chemical and physical responses of groundwater to seismicity have been documented for thousands of years. Among the waves produced by earthquakes, Rayleigh waves can spread to great distances and produce hydrogeological perturbations in response to their passage. In this work, the groundwater level, which was continuously recorded in a monitoring well in Central Italy between July 2014 and December 2019, exhibited evident responses to dynamic crustal stress. In detail, 18 sharp variations of the groundwater level due to worldwide $M_w \geq 6.5$ earthquakes were observed. Apart from earthquakes that occurred in Papua New Guinea and those with a hypocentral depth > 150 km, all far away $M_w \geq 7.6$ earthquakes produced impulsive oscillations of groundwater. As the earthquake magnitude decreased, only some earthquakes with $6.5 \leq M_w < 7.6$ caused groundwater level perturbations, depending on the data acquisition frequency and epicentral distance from the monitoring well. A clear correlation between earthquake distance and magnitude in hydrogeological responses was found. Our results shed light on the hydrosensitivity of the study site and on the characteristics of fractured aquifer systems. Detecting the water table variations induced by distant earthquakes is another step towards a correct identification of (preseismic) hydrogeological changes due to near-field seismicity.

Earthquakes are among the main natural processes that can cause the strongest perturbations in the Earth's crust. Seismic events can change crustal stress, both static and dynamic, in the co-seismic and post-seismic phases. Static stress is generated by fault loading and its release mostly occurs in the near-field whereas dynamic stress is triggered by fault slip, generating the migration of seismic waves and, for this reason, its perturbation also spreads to the far-field. Many studies have highlighted the sensitivity of fluid behaviour related to the modification of the stress field, both the static and the dynamic one[1,2]. In particular, hydrogeological and geochemical responses include: changes in groundwater level[3–5], temperature[6,7], water chemistry[8–10], stream flow[11–13], and gas geochemistry[14–18]. Among these parameters, a change in groundwater level is more commonly recorded due to the simplicity of doing so through the use of inexpensive devices. In fractured high-permeability aquifers, like the one studied in this work, impulsive changes in the water table are frequent, also due to classical hydrogeological causes. Various mechanisms have been proposed to explain groundwater level responses to earthquakes including: (1) poroelastic response to co-seismic static strain[19]; (2) undrained consolidation of sediments[20]; (3) clogging–unclogging of pores and fractures by oscillatory flows produced by the passage of seismic waves[3,21,22]; (4) co-seismic gas bubble development[23,24]; (5) shaking-induced compaction or dilatation[25]. Depending on the mechanism involved, the temporal pattern of groundwater level variation can vary significantly and, hence, can be symptomatic of specific mechanisms. Previous studies have highlighted permanent and transient signals that are characterized by step-like and/or spike-like temporal changes both upward and/or downward[26–28]. Only a few studies have reported groundwater level variations induced by earthquakes that are very far away from the observation point, known as 'teleseism'[3,25,26,29,30]. According to the USGS a teleseism is a tremor related to seismic events occurring more than 1000 km away[31]. To investigate the relationship between groundwater characteristics and the seismic cycle, two multiparameter probes were installed in a 50 m and a 100 m deep groundwater wells (PF60.2 and PF60.3) in the Central Apennines (Italy, Fig. 1, see "Material and methods" section) in 2014.

These wells were part of a monitoring test site in fractured carbonate aquifers, developed for the identification of potential hydrogeochemical precursors of earthquakes[5,9]. After their installation (July 2014 for PF60.3

[1]Earth Sciences Department, Sapienza University of Rome, P.le Aldo Moro 5, 00185 Rome, Italy. [2]Consiglio Nazionale Delle Ricerche, IGAG, Rome, Italy. [3]National Institute of Geophysics and Volcanology, Palermo, Italy. [4]National Institute of Geophysics and Volcanology, National Earthquake Observatory, L'Aquila, Italy. [5]National Institute of Geophysics and Volcanology, Rome, Italy. ✉email: marinodomenico.barberio@uniroma1.it
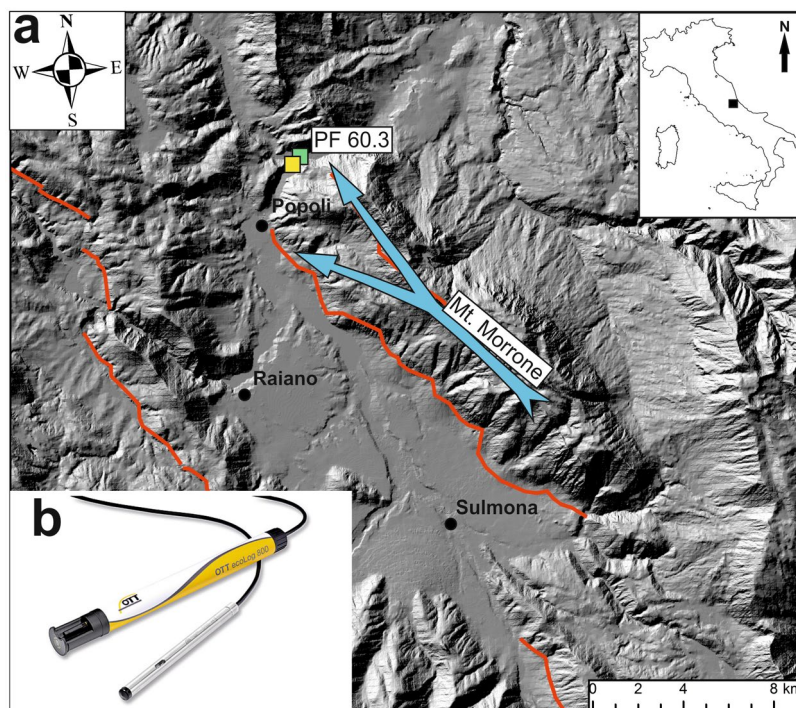
Figure 1. Study area. This figure has been drawn using CorelDRAW[32]. (**a**) Map of Central Apennines (see location in upper right inset). Active faults (all extensional) are from the Ithaca database (available online at https://www.isprambiente.gov.it/en/projects/soil-and-territory/italy-hazards-from-capable-faulting). Base digital elevation model is from the ISPRA database SINAnet (available online at https://www.sinanet.ispra mbiente.it/it). Locations of the PF60.2 and PF60.3 wells monitored in this work are displayed with yellow and green symbols, respectively. The blue arrow indicates the principal groundwater flow path of the Mt. Morrone aquifer; (**b**) OTT ecoLog800 multiparametric probe for continuous acquisition and remote transmission of data, including groundwater level, temperature, and electrical conductivity.

and November 2014 for PF60.2) the probe in the PF60.3 well recorded significant changes in groundwater level following the occurrence of many high magnitude earthquakes around the world ($M_w \geq 6.5$). In this paper, we present the results of the water level monitoring with a view to expanding the understanding of perturbations of fluids in the upper crust due to earthquakes, with a focus on groundwater–earthquake physical relationships. Since these or similar probes are used by us and other geoscientists to identify potential hydrogeochemical precursors to nearby earthquakes[2,5,9,20,33,34], identifying and thus filtering the effect on (and also the cause of) the groundwater level induced by distant earthquakes is a pre-requisite to understanding the possible effect induced by the seismic cycle of nearby faults.

Geological and hydrogeological settings

The Central Apennines fold-and-thrust belt was formed by tectonic accretion and the following backarc extension during the Oligocene-Quaternary 'westward' subduction and 'eastward' retreat of the Adriatic plate beneath the European plate. This segment of mountain chain is characterized by NE-verging thrusts, which dissect the tectonic edifice into several thick tectonic sheets[35]. The post-accretion extensional regime, which has dominated the Central Apennines from the Pliocene onwards, has segmented the orogenic edifice and determined the current structural setting. The development, in particular, of NW-striking extensional faults has been responsible of intra-mountain basin formation (e.g. the Campo Imperatore, L'Aquila, Fucino, and Sulmona basins). These basins are mostly half-grabens filled by Upper Pliocene and Pleistocene continental deposits. At present, the extensional regime is particularly seismogenic along the axis of the Central Apennines, while the compressional regime is active along the eastern margin of the Apennines and the Western Adriatic Sea. The monitoring wells are located in the hanging wall of the Mt. Morrone normal fault system (Fig. 1), where the current rates of extension measured by the GPS network are 3–4 mm/years[36]. The Apennines belt is characterized by huge fractured aquifers hosted by Meso-Cenozoic carbonate sequences forming the Apennines thrust sheets. The aquifer systems, characterized by high transmissivity and huge flow through springs with a stable and huge discharge, are often separated and sealed by low-permeability layers (aquicludes), such as siliciclastic marine and continental deposits. The study site, in particular, is located between the Gran Sasso and the Mt. Morrone carbonate aquifers (Fig. 1). Groundwater flow feeds base-flow springs in the gorges of the Pescara River[9] [references therein].
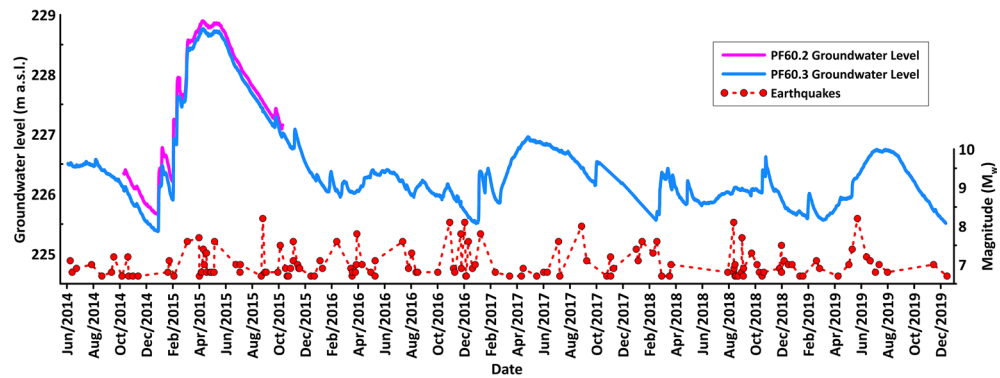
Figure 2. Time series. This figure has been realized using Grapher 7. (**a**) Time series (July 1st, 2014–December 31st, 2019) of groundwater level recorded in the PF60.3 well (100 m deep; Fig. 1a) is shown with the blue line; time series (October 1st, 2014–November 30th, 2015) of groundwater level recorded in the PF60.2 well (50 m deep; Fig. 1a) is shown with the pink line. (**b**) Time series (July 1st, 2014–December 31st, 2019) of magnitude ($M_w \geq 6.5$) for earthquakes occurred worldwide in the same period of the hydrogeological monitoring is shown with red dots. Seismic data are from the INGV database (available online at https://terremoti.ingv.it/).

Results

The groundwater level data were continuously recorded (every five minutes) from July 2014 to December 2019 in PF60.3 and from November 2014 to October 2015 in PF60.2 (Fig. 2). The acquired data highlight that the water table is characterized by a typical seasonal variation of about 1.5 m and a maximum oscillation of about 3.40 m (i.e. the change between minimum and maximum values, February 2015–June 2015), which is a very limited variation in agreement with the base-flow conditions in the observed discharge area (Fig. 2). No active withdrawals influencing the groundwater level are ongoing in this aquifer, as documented by previous monitoring[9]. This monitoring also showed that local rainfall has a negligible effect on the groundwater level due to the location in the discharge zone of the aquifer[9]. In Fig. 2, we show the earthquakes with $M_w \geq 6.5$ that occurred worldwide in the same period of hydrogeological monitoring. Detailed analyses of groundwater level data corresponding to all 218 seismic events were processed, and 18 characteristic groundwater level behaviours were found and are shown in Fig. 3 together with the seismic trace of the vertical component recorded by two nearby seismometers (the number on the top of each diagram corresponds to the earthquake ID in the Supplementary Table 1). All the 18 cases selected are characterized by anomalous groundwater level changes recorded only in the PF60.3 well within one hour, at most, from the occurrence of the seismic event, depending on the epicentral distance. Moreover, these variations are described by upward, downward or both spike changes because of the data acquisition moment of the probe (every five minutes) in relation to the arrival of Rayleigh waves. Hence, the gap between two consecutive recordings implies that the acquisition of groundwater level data can occur at any time of the seismic wave passage. In addition, other trends and smaller spikes (e.g. in diagrams 11 and 203) can be attributed to further hydrological perturbations, such as the recharge and discharge of the aquifer. However, the main impulsive peaks induced by distant earthquakes are clearly discernible and related to the ground motion as also shown by the vertical component of the seismic trace. When the counts (directly proportional to the velocity of ground motion) were less of about 20,000, the groundwater level exhibited less evident responses (this condition was found for example in diagrams 3 and 9 in Fig. 3). The maximum amplitude and the duration of the groundwater level perturbation range between the maxima of 8.7 cm and 35 min, respectively, and the minima of 0.8 cm and 5 min, respectively (see Supplementary Table 1). The worldwide distribution of earthquakes (with $M_w \geq 6.5$) is shown in Fig. 4, where the abovementioned 18 seismic events are displayed with red circles (other colours in Fig. 4 refer to the classification of Fig. 5 in the "Discussion" section).

Discussion

The results suggest that, in the aquifer where the PF60.3 well is located, the passage of seismic waves due to the strongest earthquakes worldwide ($M_w \geq 6.5$) produced abrupt fluctuations in groundwater level in the Central Apennines. No other classical hydrological process has indeed involved the study area (e.g. local and anthropic perturbation or near-field earthquakes). Two simultaneous mechanisms can be recognized as the main cause for the observed fluctuations: (1) rapid pressure changes in the aquifer as the body rock is dilated and compressed by earthquake waves passing through it, and (2) amplification by the water column momentum moving in the well, due to the fractured system[30,38–40]. Previous works[30,38] proposed that groundwater level fluctuations in a well can be induced only by those waves that produce rock body volume changes, the so-called 'dilatational waves. Both P waves and the later arriving Rayleigh waves own this property, with the latter being expected to generate the larger dilatational oscillations owing to their long periods (typically ~ 20 s, with wavelength ~ 100 km)[41–44]. On the contrary, S and Love waves, which produce shear motion as they propagate through rocks, are not expected to produce significant volume changes. Moreover, the groundwater response to P waves cannot be determined by our monitoring system due to a measurement frequency (once every five minutes) that is not high enough to accurately record P waves, which have frequencies of several cycles per second[38,40]. Hence, it is commonly
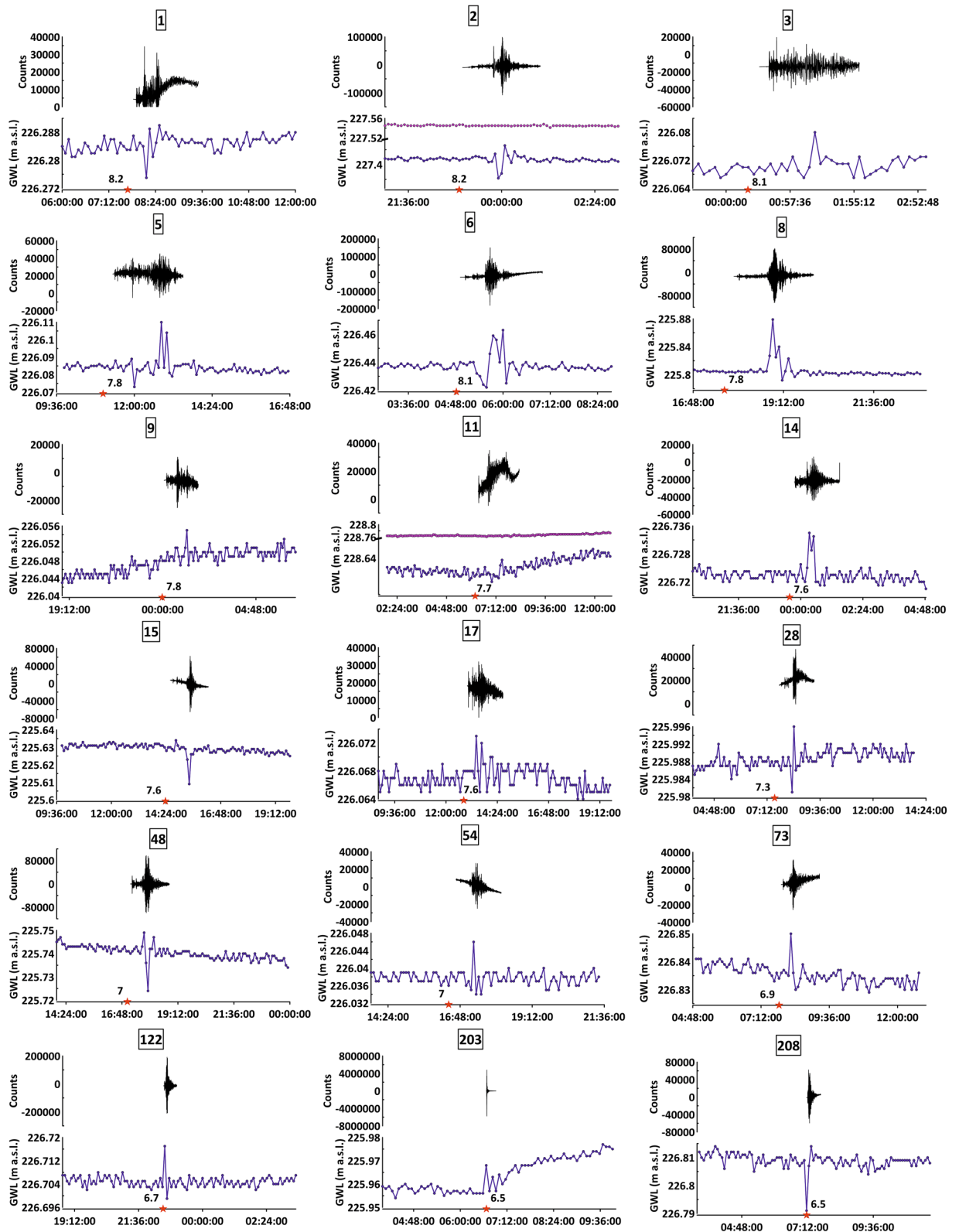
Figure 3. Groundwater level, seismic trace, and earthquakes. This figure has been realized using Grapher 7. 18 cases of interaction between signals are exhibited. The groundwater level is shown with the blue line (recorded in PF60.3) and the pink line (recorded in PF60.2), the vertical component of ground motion from local seismic stations (T0110 and INTRodacqua) is displayed with the black line and seismic events are shown with red stars. On the Y axis of the seismic trace, counts are directly proportional to the ground velocity. Seismic data are from the INGV database (available online at https://terremoti.ingv.it/). The numbers on the top of each diagram refer to the earthquake ID reported in the Supplementary Table 1.
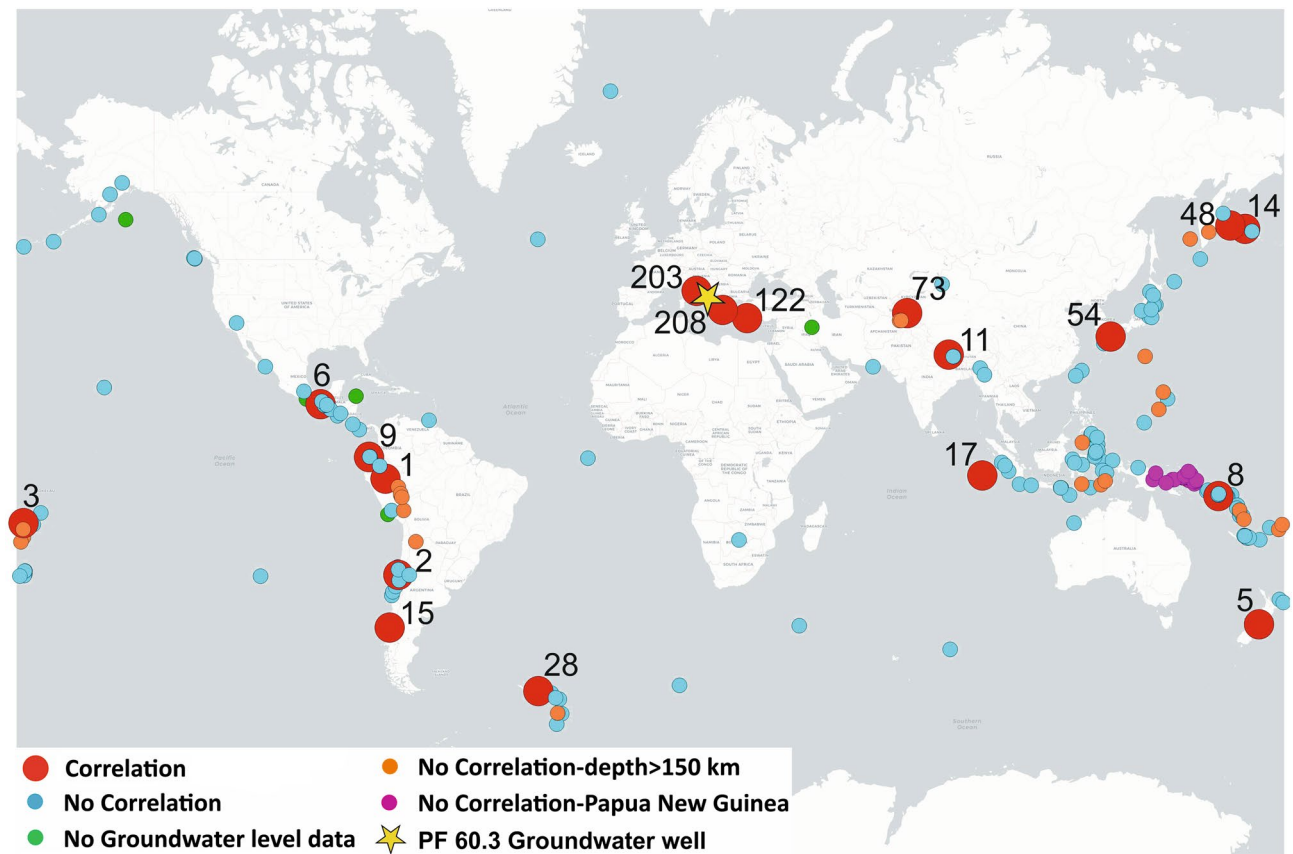
Figure 4. The worldwide distribution of earthquakes ($M_w \geq 6.5$). This figure has been realized using QGIS 3.6[37]. The 218 seismic events are displayed with circles (the different colours refer to the classification of Fig. 5 in the "Discussion" section) and are reported with the respective number of the Supplementary Table 1. Seismic data are from the INGV database (available online at https://terremoti.ingv.it/).

assumed that, in the far-field (>1000 km), water level responds only to long-period surface Rayleigh waves[3,30,39,45]. Based on these previous studies, we interpreted the recorded groundwater level changes as driven by the passage of remotely-generated Rayleigh waves (teleseisms) through the aquifer.

In our temporal series (Fig. 2), we identified 18 main events where the groundwater level in the PF60.3 well exhibited an anomalous spike change both/either upward and/or downward (Figs. 3 and 4 red circles). Given the above consideration about the acquisition gap of five minutes, the shape and the amplitude of the perturbation did not reflect the real waveform. Thus, the physical insignificance of the recorded upward and/or downward spikes did not allow us to group these effects into different classes. To understand the interaction between groundwater level and far-field seismicity, the relationships between earthquake magnitude, distance from the well, and hypocentral depth were analysed (Fig. 5). We observed a significant response to all the strongest seismic events in the world with a $M_w \geq 7.6$ (Fig. 5 red circles), except for those that occurred in Papua New Guinea (Fig. 5 pink circles) and for those occurring at depths greater than 150 km (Fig. 5 orange circles). The hypocentral depths of the 18 events under consideration reached a maximum of 150 km, except one that was deeper (depth 574 km for the M_w 8.1 of Fiji Islands on August 19, 2018 see Supplementary Table 1). Among the correlations observed, 11 events were characterized by M_w between 7.6 and 8.2, whereas the other seven seismic events had an earthquake M_w between 6.5 and 7.5. Thus, as the distance between the monitoring well and the earthquake epicentre decreases, a relationship was observed even for earthquake magnitudes less than 7.6 (Fig. 5 smaller red circles). Among these seismic events that induced groundwater responses, only two were located within the near-field seismicity (Figs. 3 and 5). For example, the 2016 M_w 6.5 Norcia earthquake is the sole case within the near-field where a step change was observed, with a water table increase lasting for several days after the earthquake[5,9,22,46]. However, a correlation between epicentral distance from the wells and earthquake magnitude is evident (Fig. 5 yellow box), confirming that these two parameters are the two most relevant factors in controlling the responses of groundwater level at a specific site[6,47]. It is not surprising that earthquakes with magnitudes close to our lower limit ($M_w = 6.5$), occurring at great distances, did not have an effect on the groundwater level data. The remaining seismic events did not cause appreciable variation in the water table (Fig. 5, blue circles) and six of them occurred in periods of a gap in groundwater level monitoring due to probe maintenance work (Fig. 5, green circles). The relationship observed between the epicentral distance and the duration of perturbation on groundwater level data is indeed directly proportional (Fig. 5, black numbers). Moreover, during the period of hydrogeological monitoring, transient changes induced by the passage of seismic waves did not produce any variation in chemical parameters (temperature and electrical conductivity) at the PF60.3 well, in addition to the piezometric level.

114
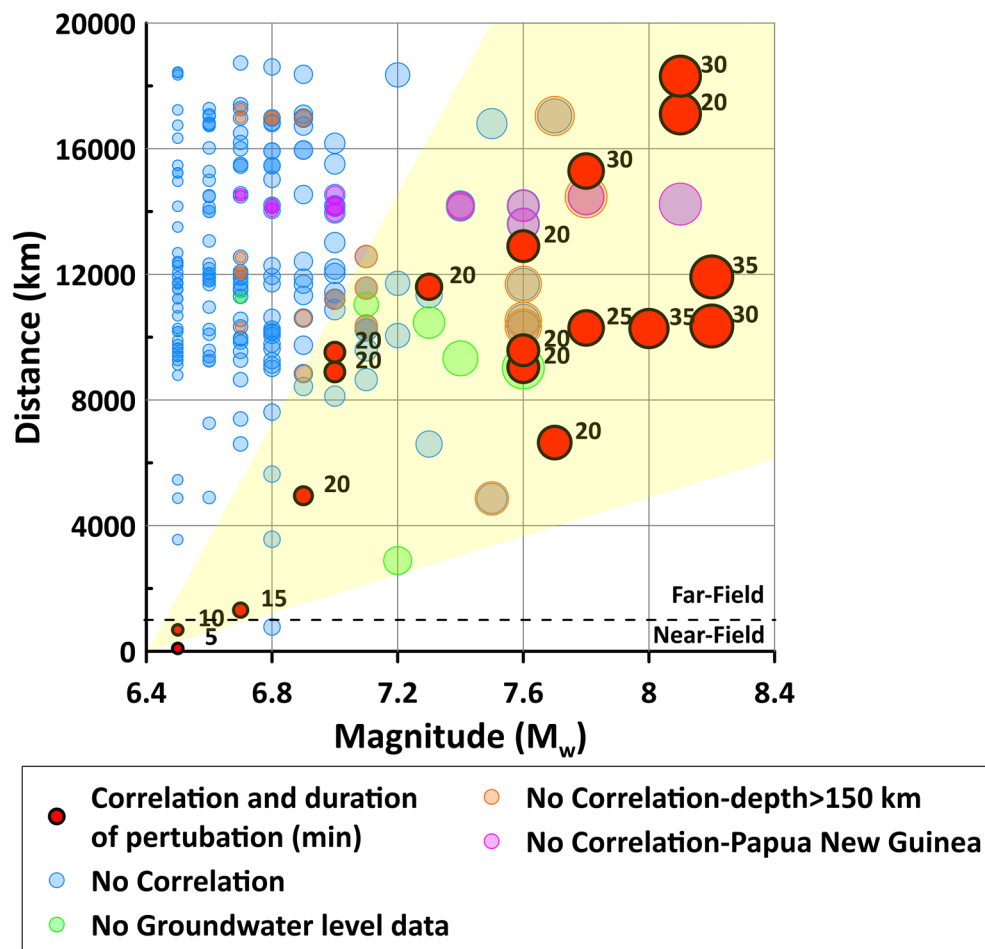
Figure 5. Distance from wells vs earthquake magnitude. This figure has been realized using Grapher 7. On the Y axis, epicentral distance from the monitoring wells (PF60.2 and PF60.3) is shown; on the X axis, the magnitude of the seismic events ($M_w \geq 6.5$) occurred in the same period of our hydrogeological monitoring is shown. Seismic data are from the INGV database (available online at https://terremoti.ingv.it/). 18 earthquakes, for which a correlation with groundwater level changes has been identified, are displayed with red circles of different sizes depending on the magnitude. A number is also reported indicating the duration of perturbation. The remaining earthquakes are displayed with blue, green, orange, and pink circles and did not cause appreciable variation in the groundwater level. Correlation between magnitude and distance is displayed with the yellow box.

Indeed, the perturbations derived from teleseismic waves are not able to produce a rock–water–gas interaction strong enough to consequently cause hydrogeochemical changes (e.g. variations in chemical-physical parameters, gas content, and/or mixing between deep and shallow fluids), because the static stress does not involve the aquifer, which simply hosts the seismic waves propagation from far seismic events. The absence of any geochemical variations confirms that fluids moving within the well and the surrounding rocks have an impulse that is negligible to the kinetic of reaction (e.g. water–rock).

Furthermore, a significant exception of non-relationship between groundwater level and far-seismicity is represented by strong earthquakes in Papua New Guinea (Fig. 5, pink circles). It is worth noticing that an 'anomalous' absence of groundwater level variation corresponding to this seismicity was found for all the seismic events that occurred in Papua New Guinea, about 14,000 km away from the monitoring wells. Tectonically, Papua New Guinea is located at the triple junction of the Eurasian, Indo-Australian, and Pacific plates. It presents some of the most complex tectonic activity, including oceanic crust subduction and arc continent collision[48]. A wide Bouguer gravity anomaly is caused by the uneven density distribution in the crust and upper mantle. Therefore, this gravitational anomaly and a surrounding larger anelasticity of the lithosphere can provide a comprehensive explanation for this unrecorded event[49]. The variation in the crustal structure within Papua New Guinea could cause the dispersion of Rayleigh waves[50] affecting their potential perturbation at a great distance, as in our monitoring site. This hypothesis was supported by ground velocity data from two considered local seismometers (e.g. counts less of about 20,000).

We also observed a few cases of no manifest interaction occurring between the groundwater level and earthquakes even with a magnitude larger than 7.0 and regardless of the epicentral distance from the monitored site.

A plausible explanation could be connected with low ground velocity variations induced by these seismic events and/or with the monitoring frequency of the probe (5 mins), which may have been insufficient to detect some high-frequency signals. This latter aspect would apply to those seismic events that occurred close to the monitoring well and were consequently characterized by short travel-time intervals of possibly lower than five minutes.

In order to assess the significance of the observed peaks owing to the arrival of Rayleigh seismic waves, where it was possible, groundwater level data were processed. In detail, groundwater time series, from a minimum of 3 to a maximum of 15 days around the seismic events (depending on the time series suitability) were detrended. Furthermore, mean values and the $\pm 2\sigma$ thresholds of groundwater level were calculated. Anomalous signals (e.g. groundwater level peaks recognized as results of interaction with seismic events) exceeding the $\pm 2\sigma$ confidence interval due to the occurrence of 14 out of the 18 earthquakes were pointed out (See Supplementary Table 2).

Another recent study[29] conducted in China has corroborated our results and strengthened the relationship between teleseismic waves and groundwater level responses. Despite only having one monitored well, these authors observed 61 responses from distant earthquakes. In their study, in contrast to our work, the sampling frequency rate is 1 sample/s. For this reason, they detected more interactions and identified also nearby earthquakes with a faster perturbation and a lower magnitude. However, it is noteworthy that 10 out of our 18 identified interactions were also recorded by the monitoring well in China.

We also analysed possible relationships between the following parameters: the amplitude of groundwater level perturbation vs. earthquake magnitude and the duration of groundwater level perturbation vs. earthquake magnitude. As already discussed, a five-minute gap between every groundwater level acquisition implies that the real maximum amplitude of oscillations could be bigger than that recorded. Consequently, the expected relationship between the amplitude of groundwater level perturbation vs. earthquake magnitude has not been found. On the contrary, the relationship between the duration of groundwater level perturbation and earthquake magnitude follows a direct linear correlation, described by a Pearson's coefficient $r = 0.83$ with p value < 0.05. Thus, the relationship has been statistically verified. As observed, the strongest earthquakes produced the longest perturbations. At the same time the hypocentral depth influenced the seismic wave propagation. Indeed, the M_w 8.1 Fiji Islands earthquake with a hypocentral depth of 574 km produced a shorter perturbation (20 min) than other earthquakes of a similar magnitude (see Supplementary Fig. 1 and Supplementary Table 1).

The results also highlighted the aspect named "Hydrosensitivity" of the monitoring site[5,9,51,52]. With the term hydrosensitivity we refer to the ability of a hydrogeological system to respond to external perturbations (e.g. discharge and recharge period, earthquakes, tides). Other hydrogeological monitoring stations in Central Italy, equipped with the same instrumentation and the same sampling frequency, have not so far recorded any correlation between groundwater level variation and far-field seismicity. For instance, we have previously mentioned that in the November 2014 to October 2015 period the groundwater level response to seismicity recorded in the 100 m deep well PF60.3 did not match with that recorded in the 50 m deep well PF60.2, which was only 3 m away from the PF60.3. The main difference between these two wells is their depth and the lithology of the drilled rock bodies: the PF60.3 well is instated into the fractured carbonate bedrock hosting the Mt. Morrone aquifer, whereas the PF60.2 well is instated into the alluvial deposits. Furthermore, other monitoring sites also located in fractured aquifers in Central Italy did not show such water table oscillations. Consequently, the possibility of observing groundwater level response to far-field seismicity is strongly related to the selection of the monitoring site, and should take into consideration several criteria[52], the first of which is the difference between porous and fractured aquifers, where the latter can clearly show responses to teleseismic activity.

Other similar research carried out by international teams in Iceland, Japan, China, and Korea[19,34,53,54] has been aimed at identifying potential changes in groundwater level and in chemical content due to the occurrence of earthquakes. Unlike our work, these studies were not specifically devoted to far-field seismic events. They focused on fluid behaviour during the seismic cycle, which is mainly defined by the groundwater level decreasing prior to the earthquake in connection with fracture opening and permeability change[54]. For example, three phases of groundwater level were recorded since 230 days before the M_w 7.6 Chi-Chi earthquake in Taiwan. These variations were characterized by a sharp and significant decrease (phase 1), a subsequent rise (phase 2), and a stop of groundwater level uplift about 13 days prior to the earthquake (phase 3)[53]. Furthermore, in southern Iceland, coseismic and post-seismic water level changes in geothermal wells located in a seismic zone were detected, following two M_w 6.5 earthquakes[19]. Finally, in the Central Apennines (Central Italy), significant hydraulic pressure and electrical conductivity anomalies were identified five days before the M_w 6.0 Amatrice earthquake[46]. Apart from these trends, the hydraulic pressure data showed coseismic effects related to the M_w 8.2 Chile earthquake (on September 16th, 2015) where the arrival of long-period Rayleigh waves was very clear[55]. As shown in our study (Fig. 3), the typical impulsive peak-like response of groundwater level to the passage of Rayleigh waves in the monitoring site is easily discernible because of its characteristics, which differ from other perturbations (e.g. the effects of rainfall, the recharge and discharge of the aquifer, the effects of near-field seismicity). In particular, this work allowed us to recognize these transient perturbations and exclude them as a potential signal caused by near-field seismicity. Knowing about and discerning the effect of all the parameters (including teleseism) that can influence the hydrogeological and hydrogeochemical features is a fundamental pre-requisite for the investigation of the potential effects of nearby earthquakes.

Conclusions

- The PF60.3 monitoring well, equipped with a multiparametric probe OTT ecoLog800 in a fractured carbonate aquifer, allowed us to identify groundwater level fluctuations related to the passage of Rayleigh seismic waves deriving from distant earthquakes.

- Owing to their impulsive character, the oscillations induced by teleseismic waves are clearly recognisable with respect to classical water table changes correlated with the hydrogeological cycle and/or human induced changes.
- The peculiar responses of the monitoring well PF60.3 highlighted once again the potential sensitivity of the fractured aquifers to the strain variation in pre-selected hydrogeological conditions.
- Since many groups in seismic regions of the world are now running monitoring stations to identify potential hydrogeological precursors to large near-field earthquakes (e.g. Italy, China, Iceland, Japan, and Korea), the characterization and identification of teleseismic effects on these monitoring stations are a pre-requisite for the correct recognition of near-field seismic effects. This recognition may be due to the typically impulsive peak-like response of the groundwater level to strong teleseisms, which is markedly different from that driven by near-field earthquakes.

Material and methods

In this study, we used both hydrogeological and seismic data to identify interactions between groundwater levels and distant earthquakes. The hydrogeological monitoring data are from the PF60.2 and PF60.3 wells, which are 50 m and 100 m deep boreholes drilled through alluvial deposits and the Mt. Morrone regional carbonate aquifer, respectively (Fig. 1). The PF60.2 and the PF60.3, which are located at Lat. 42.196875°, Long. 13.852316°, altitude 238.90 m, and Lat. 42.196910°, Long. 13.852372°, altitude 238.95 m, respectively, were equipped with multiparametric probes (OTT ecoLog800) to measure the groundwater levels in 2014. These probes are equipped by an automatic system for continuous data acquisition and remote data transmission, concerning groundwater level, temperature, and electrical conductivity (groundwater level: resolution 0.001 m, error ± 0.05%; temperature: resolution 0.001 °C, error 0.1 °C; electrical conductivity: resolution 0.001 mS/cm, error ± 0.5%). The sample frequency of data measurement was set to five minutes. The barometric pressure of groundwater level measurements was automatically compensated for. With respect to the seismic data, we used the database run by the National Seismic Network (from the website https://terremoti.ingv.it/). Data were filtered to select the main seismic events (n. 218 events with $M_w \geq 6.5$, see Supplementary Table 1), which occurred worldwide in the same period of our hydrogeological monitoring at the PF60.2 and PF60.3 wells (July 2014–December 2019, Fig. 2b). Supplementary Table 1 summarises the main parameters for every recorded seismic event (i.e. time (UTC), latitude, longitude, depth (km), magnitude (M_w), event location name, the occurrence of groundwater level change, epicentral distances from the monitoring wells, maximum amplitude (cm) and duration (min) of perturbation on groundwater level). For the 18 seismic events that caused groundwater level responses, data from two local seismic stations were also considered. Specifically, the T0110 seismic station, located about 10 km from the PF60.3 well, was used. This station belongs to the National Seismic Network of the Centro Nazionale Terremoti of the Istituto Nazionale di Geofisica e Vulcanologia (CNT-INGV) and is equipped with a broadband Trillium 120 s compact seismometer (see online at https://terremoti.ingv.it/instruments/station/T0110). Only during the occurrence of two teleseismic events (n. 48 and 122) the T0110 seismic station was out of order. Hence, for these two latter cases, the reported data are from another station named INTRodacqua, which is located about 20 km from our monitoring site and it is equipped with a Trillium 40 s seismometer (see online at https://terremoti.ingv.it/instruments/station/INTR). For the elaboration, only the vertical seismic component of ground motion was used.

References

1. Lay, T. & Wallace, T. C. *Modern Global Seismology* (Academic Press, Cambridge, 1995).
2. Manga, M. & Wang, C. Y. Earthquake hydrology. *Treatise on Geophysics*, 305–328 (2015).
3. Brodsky, E. E., Roeloffs, E., Woodcock, D., Gall, I. & Manga, M. A mechanism for sustained groundwater pressure changes induced by distant earthquakes. *J. Geophys. Res. Solid Earth* **108**, 88 (2003).
4. Roeloffs, E. *et al.* Water-level changes induced by local and distant earthquakes at Long Valley caldera, California. *J. Volcanol. Geotherm. Res.* **127**, 269–303 (2003).
5. Petitta, M. *et al.* Water-table and discharge changes associated with the 2016–2017 seismic sequence in central Italy: hydrogeological data and a conceptual model for fractured carbonate aquifers. *Hydrogeol. J.* **26**, 1009–1026 (2018).
6. Shi, Z. & Wang, G. Hydrological response to multiple large distant earthquakes in the Mile well, China. *J. Geophys. Res. Earth Surf.* **119**, 2448–2459 (2014).
7. He, A. & Singh, R. P. Coseismic groundwater temperature response associated with the Wenchuan earthquake. *Pure Appl. Geophys.* **177**, 109–120 (2020).
8. Skelton, A. *et al.* Changes in groundwater chemistry before two consecutive earthquakes in Iceland. *Nat. Geosci.* **7**, 752 (2014).
9. Barberio, M. D., Barbieri, M., Billi, A., Doglioni, C. & Petitta, M. Hydrogeochemical changes before and during the 2016 Amatrice-Norcia seismic sequence (central Italy). *Sci. Rep.* **7**, 11735 (2017).
10. Boschetti, T. *et al.* CO_2 inflow and elements desorption prior to a seismic sequence, Amatrice-Norcia 2016, Italy. *Geochem. Geophys. Geosyst.* **20**, 2303–2317 (2019).
11. Muir-Wood, R. & King, G. C. Hydrological signatures of earthquake strain. *J. Geophys. Res. Solid Earth* **98**, 22035–22068 (1993).
12. Manga, M., Brodsky, E. E. & Boone, M. Response of streamflow to multiple earthquakes. *Geophys. Res. Lett.* **30**, 5 (2003).
13. Montgomery, D. R. & Manga, M. Streamflow and water well responses to earthquakes. *Science* **300**, 2047–2049 (2003).
14. Wakita, H., Nakamura, Y., Notsu, K., Noguchi, M. & Asada, T. Radon anomaly: a possible precursor of the 1978 Izu-Oshima-kinkai earthquake. *Science* **207**, 882–883 (1980).
15. Chiodini, G. *et al.* Carbon dioxide earth degassing and seismogenesis in central and southern Italy. *Geophys. Res. Lett.* **31**, 1–12 (2004).
16. Caracausi, A. & Paternoster, M. Radiogenic helium degassing and rock fracturing: a case study of the southern Apennines active tectonic region. *J. Geophys. Res. Solid Earth* **120**, 2200–2211 (2015).

17. Sano, Y. *et al.* Groundwater helium anomaly reflects strain change during the 2016 Kumamoto earthquake in Southwest Japan. *Sci. Rep.* **6**, 37939 (2016).
18. Buttitta, D. *et al.* Continental degassing of helium in an active tectonic setting (northern Italy): the role of seismicity. *Sci. Rep.* **10**, 1–13 (2020).
19. Jónsson, S., Segall, P., Pedersen, R. & Björnsson, G. Post-earthquake ground movements correlated to pore-pressure transients. *Nature* **424**, 179 (2003).
20. Wang, C. Y. & Chia, Y. Mechanism of water level changes during earthquakes: near field versus intermediate field. *Geophys. Res. Lett.* **35**, 12 (2008).
21. Elkhoury, J. E., Brodsky, E. E. & Agnew, D. C. Seismic waves increase permeability. *Nature* **441**, 1135 (2006).
22. Mastrorillo, L. *et al.* Sustained post-seismic effects on groundwater flow in fractured carbonate aquifers in Central Italy. *Hydrol. Process.* **34**, 1167–1181 (2019).
23. Linde, A. T., Sacks, I. S., Johnston, M. J., Hillt, D. P. & Bilham, R. G. Increased pressure from rising bubbles as a mechanism for remotely triggered seismicity. *Nature* **371**, 408–410 (1994).
24. Crews, J. B. & Cooper, C. A. Experimental evidence for seismically initiated gas bubble nucleation and growth in groundwater as a mechanism for coseismic borehole water level rise and remotely triggered seismicity. *J. Geophys. Res. Solid Earth* **119**, 7079–7091 (2014).
25. Zhang, Y., Fu, L. Y., Huang, F. & Chen, X. Coseismic water-level changes in a well induced by teleseismic waves from three large earthquakes. *Tectonophysics* **651**, 232–241 (2015).
26. Sil, S. & Freymueller, J. T. Well water level changes in Fairbanks, Alaska, due to the great Sumatra-Andaman earthquake. *Earth Planets Space* **58**, 181–184 (2006).
27. Chadha, R. K., Singh, C. & Shekar, M. Transient changes in well-water level in bore wells in Western India due to the 2004 Mw 9.3 Sumatra Earthquake. *B. Seismol. Soc. Am.* **98**, 2553–2558 (2008).
28. Shi, Z., Wang, G., Manga, M. & Wang, C. Y. Mechanism of co-seismic water level change following four great earthquakes–insights from co-seismic responses throughout the Chinese mainland. *Earth Planet. Sci. Lett.* **430**, 66–74 (2015).
29. He, A., Deng, W., Singh, R. P. & Lyu, F. Characteristics of hydroseismograms in Jingle well, China. *J. Hydrol.* **582**, 124529 (2020).
30. Cooper, H. H. Jr., Bredehoeft, J. D., Papadopulos, I. S. & Bennett, R. R. The response of well-aquifer systems to seismic waves. *J. Geophys. Res.* **70**, 3915–3926 (1965).
31. Anderson, D. N., Fagan, D. K., Tinker, M. A., Kraft, G. D. & Hutchenson, K. D. A mathematical statistics formulation of the teleseismic explosion identification problem with multiple discriminants. *B. Seismol. Soc. Am.* **97**, 1730–1741 (2007).
32. CorelDRAW Graphics Suite X4. Copyright (c) 200–5T8TGCN [Sapienza University Campus Uniroma1]. All rights reserved. https://www.coreldraw.com/.
33. Wakita, H. Geochemical challenge to earthquake prediction. *Proc. Natl. Acad. Sci. USA* **93**, 3781–3786 (1996).
34. Orihara, Y., Kamogawa, M. & Nagao, T. Preseismic changes of the level and temperature of confined groundwater related to the 2011 Tohoku earthquake. *Sci. Rep.* **4**, 6907 (2014).
35. Vezzani, L., Festa, A. & Ghisetti, F. C. Geology and tectonic evolution of the Central-Southern Apennines. *Italy. Geol. Soc. Am.* https://doi.org/10.1130/SPE469 (2010).
36. Riguzzi, F. *et al.* Geodetic strain rate and earthquake size: new clues for seismic hazard studies. *Phys. Earth Planet. Int.* **206**, 67–75 (2012).
37. QGIS Development Team. QGIS Geographic Information System. Open Source Geospatial Foundation Project. https://qgis.osgeo.org. (2019).
38. Eaton, J. P. & Takasaki, K. J. Seismological interpretation of earthquake-induced water-level fluctuations in wells. *B. Seismol. Soc. Am.* **49**, 227–245 (1959).
39. Liu, L. B., Roeloffs, E. & Zheng, X. Y. Seismically induced water level fluctuations in the Wali well, Beijing, China. *J. Geophys. Res. Solid Earth* **94**, 9453–9462 (1989).
40. Woodcock, D. Seismically induced water-level oscillation in a fractured-rock aquifer well near Grants Pass. *Oreg. Geol.* **58**, 27–33 (1996).
41. Stein, S. & Wysession, M. *An Introduction to Seismology, Earthquakes, and Earth Structure* (Wiley, Hoboken, 2009).
42. Levshin, A. L., Barmin, M. P. & Ritzwoller, M. H. Tutorial review of seismic surface waves' phenomenology. *J. Seismol.* **22**, 519–537 (2018).
43. MacDonald, G. J. *The Earth's Free Oscillations* (National Aeronautics and Space Administration, New York, 1962).
44. Alterman, Z., Jarosch, H. & Pekeris, C. L. Propagation of Rayleigh Waves in the Earth. *Geophys. J. Int.* **4**, 219–241 (1961).
45. Shih, D. C. F., Wu, Y. M. & Chang, C. H. Significant coherence for groundwater and Rayleigh waves: evidence in spectral response of groundwater level in Taiwan using 2011 Tohoku earthquake. *J. Hydrol.* **486**, 57–70 (2013).
46. De Luca, G., Di Carlo, G. & Tallini, M. A record of changes in the Gran Sasso groundwater before, during and after the 2016 Amatrice earthquake, central Italy. *Sci. Rep.* **8**, 1–16 (2018).
47. Weingarten, M. & Ge, S. Insights into water level response to seismic waves: A 24 year high-fidelity record of global seismicity at Devils Hole. *Geophys. Res. Lett.* **41**, 74–80 (2014).
48. Baldwin, S. L., Fitzgerald, P. G. & Webb, L. E. Tectonics of the new guinea region. *Annu. Rev. Earth Planet. Sci.* **40**, 495–490 (2012).
49. Yang, G. *et al.* Isostatic anomaly characteristics and tectonism of the New Britain Trench and neighboring Papua New Guinea. *Geod. Geodyn.* **9**, 404–410 (2018).
50. Brooks, J. A. Rayleigh wave dispersion studies of crustal and upper mantle structure in New Guinea. *Doctoral dissertation, University of Tasmania* (1969).
51. Barberio, M. D. *et al.* Diurnal and semidiurnal cyclicity of radon (222Rn) in groundwater, Giardino Spring, Central Apennines, Italy. *Water* **10**, 1276 (2018).
52. Petitta, M. *et al.* Groundwater monitoring in regional discharge areas selected as "Hydrosensitive" to seismic activity in Central Italy. in *Advances in Natural Hazards and Hydrological Risks: Meeting the Challenge* 21–25 (Springer, New York, 2020).
53. Chen, C. H. *et al.* Groundwater–strain coupling before the 1999 Mw 7.6 Taiwan Chi-Chi earthquake. *J. Hydrol.* **524**, 378–384 (2015).
54. Kim, J. *et al.* Groundwater system responses to the 2016 ML 58 Gyeongju earthquake, South Korea. *J. Hydrol.* **576**, 150–163 (2019).
55. De Luca, G., Di Carlo, G. & Tallini, M. Hydraulic pressure variations of groundwater in the Gran Sasso underground laboratory during Amatrice earthquake of August 24th, 2016. *Ann. Geophys.* **59**, 1 (2016).

Acknowledgements

Author contributions

M.D.B., C.D., and M.P. designed and supervised experiments. M.D.B., F.G., S.F. performed hydrogeological survey. M.D.B., F.G., and M.P. performed hydrogeological analyses. A.B., A.C. G.D.L. and M.B. contributed to the data processing, result discussion, and final interpretation. M.D.B. and F.G. wrote the manuscript with significant contributions by all the Authors. M.D.B. drew all figures with significant contributions by all the Authors. Eventually, all Authors reviewed the manuscript and figures and approved their submission to Scientific Reports.

Competing interests

The authors declare no competing interests. However, three of the authors are members of the editorial board: Carlo Doglioni, Andrea Billi and Maurizio Barbieri.

Additional information

Supplementary information is available for this paper at https://doi.org/10.1038/s41598-020-74991-0.

Correspondence and requests for materials should be addressed to M.D.B.

Reprints and permissions information is available at www.nature.com/reprints.

Publisher's note Springer Nature remains neutral with regard to jurisdictional claims in published maps and institutional affiliations.

5.4 Hydrogeochemical multi-component approach to assess fluids upwelling and mixing in shallow carbonate-evaporitic aquifers (Contursi area, southern Apennines, Italy)

Francesca Gori[1,*], Michele Paternoster[2,3], Maurizio Barbieri[4], Dario Buttitta[2,3], Antonio Caracausi[3], Fabrizio Parente[5], Attilio Sulli[5], Marco Petitta[1]

[1] Department of Earth Sciences, Sapienza University of Rome, Rome, Italy

[2] Department of Sciences, University of Basilicata, Potenza, Italy

[3] Istituto Nazionale di Geofisica e Vulcanologia, Sezione di Palermo, Palermo, Italy

[4] Department of Chemical Engineering and Environmental Materials, Sapienza University of Rome, Rome, Italy

[5] Department of Earth and Marine Sciences, University of Palermo, Palermo, Italy

*Corresponding author: Francesca Gori, Department of Earth Sciences, Sapienza University of Rome, Italy, Piazzale Aldo Moro, 5, Rome, Italy.

Phone: (+39) 06 49914156; e-mail: francesca.gori@uniroma1.it
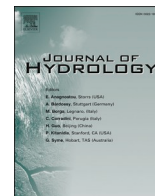
Research papers

Hydrogeochemical multi-component approach to assess fluids upwelling and mixing in shallow carbonate-evaporitic aquifers (Contursi area, southern Apennines, Italy)

Francesca Gori [a,*], Michele Paternoster [b,c], Maurizio Barbieri [d], Dario Buttitta [b,c], Antonio Caracausi [c], Fabrizio Parente [e], Attilio Sulli [e], Marco Petitta [a]

[a] Department of Earth Sciences, Sapienza University of Rome, Rome, Italy
[b] Department of Sciences, University of Basilicata, Potenza, Italy
[c] Istituto Nazionale di Geofisica e Vulcanologia, Sezione di Palermo, Palermo, Italy
[d] Department of Chemical Engineering and Environmental Materials, Sapienza University of Rome, Rome, Italy
[e] Department of Earth and Marine Sciences, University of Palermo, Palermo, Italy

ABSTRACT

With the aim of deepening our understanding of deep-seated fluids upwelling and mixing in large regional aquifers, we performed a hydrogeochemical study of twenty-two springs in the Contursi area (upper Sele river valley, southern Apennines) by means of the measurements of chemical-physical parameters, major ions, trace elements, and stable and radioactive isotopes. Besides, we realized two updated geo-structural cross-sections in order to reconstruct the groundwater flowpath in the study area. The hydrogeochemical composition, as well as the water temperature allow to identify three main groups of groundwater: Cold and Low salinity Groundwater (CLGW), Intermediate Salinity Groundwater (ISGW), and Thermal Salinity Groundwater (TSGW). The CLGW group, mostly emerging at the boundary of carbonate aquifers, is characterized by alkaline earth-bicarbonate hydrofacies. Instead, ISGW and TSGW, situated in the inner zone of the valley, show gradually a hydrogeochemical evolution towards sodium-chloride type hydrofacies domain with the highest salinity value. Stable isotope (δ^{18}O-δD) of CLGW reveal the local meteoric origin of groundwater, while isotopic signatures of ISGW and TSGW is associated with the deep fluids inflow. CLGW hydrogeochemistry is clearly related to dissolution of carbonate rocks. On the other hand, for ISGW and TSGW an additional contribution from evaporitic rocks is supported by saturation indices values (gypsum and anhydrite) and validated by isotopic signature of dissolved sulphate (δ^{34}S-δ^{18}O). The application of two models based on tritium data (i.e., the piston-flow and well-mixed reservoir) attributes longer and deeper groundwater flowpaths to TSGW. Through geothermometric calculations (e,g., K-Mg and SiO$_2$-quartz), the equilibrium temperature of deep fluids reservoir is also extrapolated (i.e., 75–96 °C). The results of the adopted hydrogeochemical multi-component approach allowed us to propose an interpretative model of groundwater flowpath for the Contursi area, where deep-seated tectonic discontinuities play a significant role for the upwelling of saline deep thermal fluids in shallow aquifers.

1. Introduction

The investigation of crustal-scale groundwater flow is one of the most demanding challenges for hydrogeochemistry and hydrogeological scientists. Groundwater hydrogeochemistry is the result of many simultaneous processes, involving the water–rock-gas system, that include weathering, dissolution/precipitation, ion exchange, redox reactions, sorption, gas generation and consumption, and other

mechanisms (Freeze and Cherry, 1979; Matthess, 1982; Deutsch, 2020). The occurrence of these processes and their extent are strictly related to some hydrogeological factors such as (i) the nature of the aquifer system (e.g., both the lithology of host rocks, and the water-type. i.e., meteoric, marine, or magmatic), (ii) the length and depth of groundwater flowpath, (iii) the groundwater residence time, (iv) the presence and the location of tectonic features (e.g., faults and fractures) which can enhance groundwater mixing and deep fluids upwelling (Andreo et al.,

2016; Gil-Márquez et al., 2017). Therefore, water geochemistry is telling us a long and complex story that groundwater undergoes in the brittle crust (Sibson et al., 1975; Goldscheider et al., 2010; Doglioni et al., 2014; Smeraglia et al., 2018). The scale of groundwater flow both in terms of depth and width is mainly affected by the continuity of aquifer systems, hydraulic gradient between the recharge area and the discharge one, and by the presence of regional tectonic structures (Toth, 1995; De Vries and Simmers, 2002; Cook, 2003; Chen and Goldscheider, 2014). In detail, high hydraulic gradient can cause deepening of flowpaths in the aquifer that can lead groundwater up to some kilometres below the topographic surface. According to the local geothermal gradient, groundwater gets higher temperature and thus can rise convectively, mainly along faults (Minissale, 1991; Qiu et al., 2018; Yang et al., 2019). In this complex hydro-geostructural framework, the ascending of endogenous fluids (e.g., chiefly CO_2-dominant) must be considered too (Chiodini et al., 1995a, Chiodini et al., 1995b; Italiano et al., 2000; Paternoster et al., 2017; Barbieri et al., 2020; Barberio et al., 2021; Gori and Barberio, 2022). Deep fluids are generally characterized by high mineralization and abundance of gaseous content (e.g., CO_2, CH_4, Rn, He, N_2, H_2, and H_2S). These fluids are often stored in overpressurized reservoirs, upper-confined by low permeability layers, which can be connected to the surface through lithospheric fault systems (Chiodini et al., 2004; Frondini, 2008; Chiocchini et al., 2010; Trippetta et al., 2013; Smeraglia et al., 2020).

In this study, we performed a multi-component hydrogeochemical characterization of 22 springs in the Contursi area, in the inner zone of the Sele river valley (southern Apennines, Italy), where groundwater flowpaths from regional carbonate aquifers converge. Additionally, springs located along main tectonic lineaments are affected by thermalism and intense degassing with a mantle-related geochemical signatures (e.g., in Bagni di Contursi village; Panichi and Tongiorgi, 1975; Celico et al., 1979; Ghiara et al., 1994; Italiano et al., 2000; Minissale, 2004; Vannoli et al., 2021). Furthermore, recent geophysical studies furnished seismic imaging of this area from P and S waves velocity models, suggesting a fluid accumulation in a wide rock volume below the study area (Amoroso et al., 2014; Improta et al., 2014). Also, the presence of brackish and brine waters was supposed (Duchi et al., 1995; Improta et al., 2014; Amoroso et al., 2017; De Landro et al., 2022).

Owing to the various hydrogeochemical characteristics, groundwater in the Sele river valley is addressed to many different uses. For instance, fresh springs directly fed by carbonate aquifers are tapped for drinking purposes, and the mineralized and thermal ones supply spas.

The goal of this work is: a) to define water–rock interaction processes affecting the chemical composition of the investigated groundwater; b) to determine fluids origin and evolution (the mechanism of water salinization); c) to calculate the reservoir temperature using classical geothermometric approaches; d) to propose a conceptual model of fluids flowpath through the construction of two updated geological cross-sections. The results of this study may find important applications, such as exploitation of low-enthalpy geothermal resources, use of thermal waters for therapeutic purposes, and offer a relevant preliminary tool in order to define the relationship between stress field variations, pore-pressure evolution at depth in a seismically active area.

2. Geological and hydrogeological setting

The study area is located in the southern Apennines which is part of a mountain chain that develops from the Southern Abruzzi-Alto Molise region to Sicily, crossing the Calabrian arc (Malinverno and Ryan, 1986; Doglioni, 1991; Patacca and Scandone, 2007). From a geodynamic point of view, the southern Apennines are an east-verging fold-and-thrust belt related to the subduction of the Apulian lithosphere towards West (Doglioni, 1995; Faccenna et al., 2001). Starting from middle-upper Pleistocene, the axial zone of the chain raised and an extensional tectonic developed in NW-SE direction, responsible of the formation of seismogenic faults up to 15 km deep. The southern Apennines are

characterized by a series of superimposed tectonic units, constituted by a deep-seated carbonate duplex system belonging to the so-called Apennine Carbonates, characterized by shallow water deformed carbonates and overlained by basinal sequences belonging to Lagonegro units (Patacca and Scandone, 2007; Ciarcia et al., 2009; Pierdominici et al., 2011; Vitale and Ciarcia, 2018). Low angle thrust faults separate the Apennine Carbonates in the hanging wall, from the Lagonegro units in the footwall. The Apennine accretionary wedge is tectonically superimposed onto the buried Apulian Platform which is characterized by the presence of folds that form hydrocarbon and CO_2 geological traps (Shiner et al., 2004) generating overpressured reservoirs. Geophysical studies carried out in this sector of Apennines (Amoroso et al., 2014; Improta et al., 2014) shed light on a diffused high V_P/v_S ratio within the fractured Apulian Platform carbonates between 5 and 10 km depth, where intense microseismicity occurs. This seismic imaging from P and S waves velocity models suggests deep-seated fluid accumulation (i.e., mixtures of brine and or CO_2) in a wide rock volume below the study area (Amoroso et al., 2017; De Landro et al., 2022).

This study focuses on the Sele river valley situated in the central portion of the southern Apennine, precisely in the Irpinia region. Commonly, the structural pattern of the upper Sele river valley has been interpreted as a NS-trending graben (Ortolani, 1975; Cotecchia, 1986; Coppola and Pescatore, 1989), where the main tectonic discontinuities border the high relief massifs made of Mesozoic carbonate rocks, located to the West and East of the Sele river valley (i.e., the Picentini Mts. and Mt. Marzano-Ogna, respectively) (Merlini and Mostardini, 1986, Wasowski et al., 2002). From a seismological standpoint, the ongoing crustal extension regime is responsible for the high seismicity of the southern Apennines. In particular, the study area represents an interesting site for seismologists since it is considered one of the areas in southern Apennines with the highest seismogenic potential (Slejko et al., 1998). It was struck by the recent strong 1980 M_w 6.9 Irpinia earthquake (Bernard and Zollo, 1989; Ascione et al., 2020) that occur few kilometres away from Contursi village. The area is currently affected by background seismicity with the most of seismic events occurring along the 1980 Irpinia deep-seated ruptures (De Matteis et al., 2012) with prevailing normal faulting focal mechanisms (Pierdominici et al., 2011).

The hydrogeological setting of the southern Apennines is characterized by *meso*-Cenozoic carbonates that act as huge karst aquifers bounded by low permeability deposits (i.e., aquitards and/or aquicludes), such as *syn*-orogenic siliciclastic marine deposits or Messinian evaporites (Boni et al., 1986; Celico et al., 2006). The upper Sele river valley is bordered to East and West by two carbonate mountain ranges: Mt. Marzano-Ogna and Picentini Mts., respectively (Fig. 1). They constitute two main aquifers of the study area because of their large volume and high hydraulic conductivity enhanced by diffuse fracturing and intense karst processes (Celico and Civita, 1976; Wasowski et al., 2002). They fed several springs located along their fault boundaries, where aquicludes of turbidite deposits are in direct contact with carbonate rocks (Budetta et al., 1988). The Picentini Mts. constitute a 600 km^2 wide large karst system and encompass four large mountain groups (Corniello et al., 2010), recognized as different hydrogeological basins. Among these basins, the Mt. Polveracchio aquifer (Fig. 1) is characterized by a complex geo-structural setting that affects groundwater flowpaths strictly constrained by tectonic discontinuities (Celico et al., 1987). Along the northern and north-eastern margin, the hydrogeological limit consists of a fault between Acerno and Calabritto localities, where the main groundwater outlet is the Acquara-Ponticchio spring (S1). Along the western margin, the boundary is represented by a fault system separating Mt. Accellica from Mt. Polveracchio. Further south, the Polveracchio basin is buffered by impermeable lithotypes of the Lagonegro units (Fig. 1; see legend: unit #7) (Corniello et al., 2010). Finally, along the eastern margin, in the upper valley of the Sele river, the boundary consists of a tectonic thrusting front, where many cold springs (i.e., S2, S3, S5, S6) are located. Through a deeper and longer circuit, groundwater feeds very mineralized springs in the inner zone of
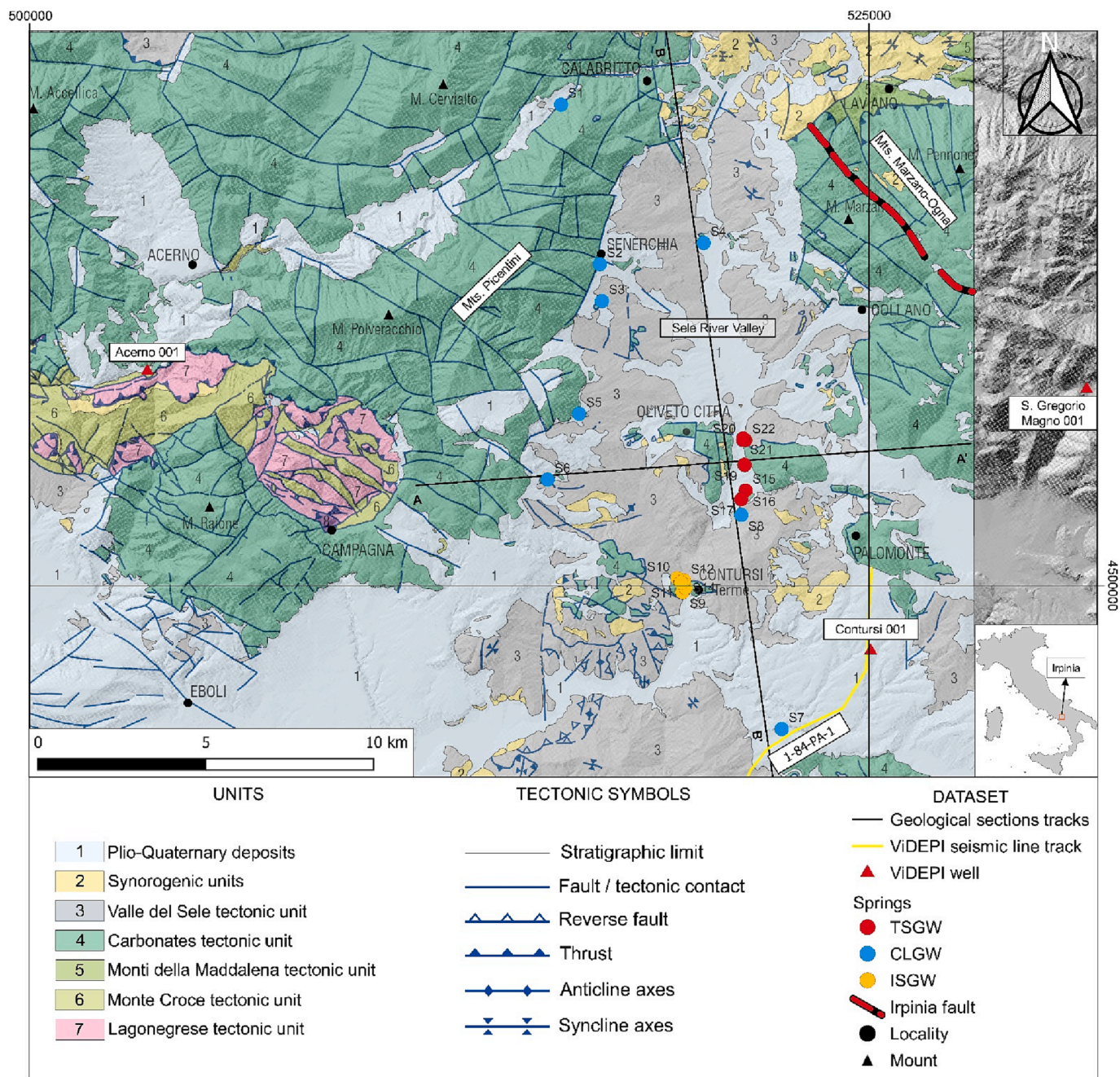
Fig. 1. Simplified tectonic map (modified after Di Nocera et al., 2016) of the Sele river valley and the dataset used for this study. In the bottom right corner, the location of the study area is reported (Irpinia region; see the red square). Lithologies of the tectonic units are described in the section 4.2.

the Sele river valley (i.e., Contursi Terme and Bagni di Contursi springs (from S15 to S22; Celico et al., 1979, Celico, 1983) by crossing carbonate substrate covered by terrigenous deposits.

3. Material and analytical Methods

3.1. Sampling, field and laboratory analysis

A sampling survey of twenty-two springs was carried out in May 2021 (Fig. 1). Water samples for major, minor and trace elements analyses were filtered with 0.45 μm membrane filters and, to keep metals in solution, the latter were acidified on-site (with ultrapure HNO_3 to pH = 2). Water samples for isotopic analyses ($\delta^{18}O$-H_2O, δD-H_2O, ^3H-H_2O, $\delta^{34}S$-SO_4, and $\delta^{18}O$-SO_4) were collected without treatments. They were sampled into high-density polyethylene bottles and stored at low

temperatures in ice-filled fridge boxes to avoid alterations of chemical components.

Electrical conductivity (EC) measured at 25 °C, Temperature (T), and pH were directly measured in situ using the multiparametric probe WTW Multi 3420 with accuracies of 1 μS/cm, 0.1 °C, and 0.01 pH unit, respectively.

Anions and cations were determined by ion chromatography at the Geochemistry Laboratory of the Department of Earth Sciences at Sapienza University of Rome. Chromatographs Dionex ICS 5000, and Dionex ICS 1100 were used to analyse anions (F^-, Cl^-, SO_4^{2-}, and NO_3^-), and cations (Ca^{2+}, Mg^{2+}, Na^+, and K^+), respectively. Bicarbonate ions were measured by titration with 0.05 N HCl solution as titrating agent and methyl orange as indicator. Ionic-balance error checked on each sample was within ± 5 % (Baird et al., 2017). Dissolved SiO_2 was measured by VIS spectrophotometry upon reaction with ammonium molybdate in

acid media (and treatment with oxalic acid) to form a yellow silico-molybdate complex, whose absorbance was read at 410 nm (Nollet, 2007).

Samples for trace elements were analysed using an ICP-MS spectrometer (X Series 2 Thermo Fisher Scientific Waltham, MA, USA). Blanks, standard solutions, and sample dilutions were prepared by using ultrapure water (Millipore, Milli-Q, 16 MW cm), and an internal standard (Rh) was added to correct the ICP-MS instrumental drift. The analytical accuracy of this method ranges between 2 % and 5 %.

Measurements of the water stable isotope ratios ($\delta^{18}O$ and δD), and the sulphur and oxygen isotopic composition in dissolved sulphate ($\delta^{34}S$-SO_4 and $\delta^{18}O$-SO_4) are expressed in terms of delta units (‰) units relative to the Vienna Standard Mean Ocean Water (V-SMOW) and Vienna Canyon Diablo Troilite (V-CDT) standards, respectively. Tritium (^3H) content was determined by an electrolytic enrichment and liquid scintillation counting method, and it is reported in TU (Tritium Unit). These analyses were performed only on some springs (i.e., S2, S4, S7, S9, S10, S16, S17, S18, S21) at IT2E Isotope Tracer Technologies Europe Srl in Milan (Italy).

The speciation software PHREEQC Interactive 3.6.2 (Parkhurst and Appelo, 2013) was used to calculate Saturation Index (S.I.).

3.2. Calculation of mean residence time of groundwater

Tritium (^3H) is a natural radioactive isotope of hydrogen (its short half-life is of 12.32 years) that can be used as a tracer for determining the groundwater age. Due to the increase and decrease of this radionuclide in rainwater during atmospheric nuclear-weapons testing in the 1945–1963 s, it is often used to differentiate groundwater recharged before and after the early 1950 s (McMahon, 2012). Groundwater age is useful to estimate recharge rates (Wang et al., 2008), to propose hydrogeochemistry models on the fluid circulation (Sanford, 2011, Apollaro et al, 2015) and to infer information on the vulnerability of aquifers to contamination by anthropogenic activities at the land surface (Raco et al., 2022). The dating of groundwater assumes that the tritium activity at the time of recharge is known and that the measured value in water sample corresponds only to the radioactive decay. The estimation of the mean residence time of groundwater was obtained by adopting two end-member models, i.e., the piston-flow and the well-mixed reservoir. The piston-flow model assumes absence of mixing along the whole water flowpath, from the recharge area to discharge one. Contrarily, the well-mixed reservoir model assumes complete mixing between the water entering the reservoir and the water already stored into it (Shevenell and Goff, 1995; Apollaro et al., 2015; Apollaro et al., 2016). To link tritium content of groundwater to its mean residence time, it was necessary to take into account tritium data of local rainwaters from the IAEA-WMO stations (IAEA/WMO, 2013) and from the Global Network of Isotopes in Precipitation (GNIP) in Italy and Europe. About 2000 values of rainwaters from 1953 to 2019 have been used in order to define tritium contents as a function of time. The dataset shows a sudden increase in tritium values in 1961–1963 and then a gradual decrease until reaching constant values (around 8.5 Tritium Unit) in recent years (tritium-time plot is reported in Fig. S1) As described by Apollaro et al. (2015, 2016), the required input functions, calculated in the dataset in different number of segments, have been defined and applied for two different models (the piston-flow and the well-mixed reservoir) in the equations proposed by Shevenell and Goff (1995), linking the output tritium concentration at time *t* to the mean residence time of water in the geothermal reservoir.

3.3. Geothermometers

The classical method used to calculate the reservoir temperature is chemical geothermometry consisting of the use of different empiric or experimental calibrations based on temperature dependent heterogeneous chemical reactions. Many geothermometric techniques have been proposed through the years for different geochemical and geological settings (Fournier, 1977; Fournier and Potter, 1979; Fouillac and Michard, 1981; Arnórsson et al., 1983; Marini et al., 1986; Giggenbach, 1988; Chiodini et al., 1995a, Chiodini et al., 1995b; Battistel et al., 2014). It is known that chemical geothermometers are based on some theoretical assumptions: (i) water is in equilibrium with host rocks, as such water is saturated by the mineral phases governing the geothermometer, and (ii) the waters neither re-equilibrate nor mix with shallow circulating fluids during the ascent towards the surface. The silica geothermometers (SiO_2- chalcedony, and SiO_2-quartz; Truesdell, 1976; Fournier, 1977), and cation geothermometers (K-Mg; Giggenbach, 1988; Fournier, 1979; Fournier and Truesdell, 1973) were employed in this study.

3.4. Geological cross-section construction

To achieve the goal of this study, also two orthogonal schematic geological sections were made in order to reconstruct the fluids flow-paths down to 5 km depth below the surface. Both the cross sections fall within the Sele river valley: the first one is a W-E section (A-A') and the second one is a N—S section (B-B') (see Fig. 1). These sections have been realized by using as reference the "Foglio 468 – Eboli", which is a geological map of the CARG (CARtografia Geologica) project, on a scale of 1:50.000 (Fig. 1 shows the tectonic scheme obtained from the above-mentioned map). Regarding the reference elevation model, the DEM provided by the TINITALY portal (Tarquini et al., 2007) was used. Based on ViDEPI database, wells "Acerno 001", "Contursi 001", and "S. Gregorio Magno 001" were studied in order to calibrate the geological sections. All the data were imported and elaborated both in QGIS (v. 3.22.5) and in MOVE^{TM} software (v. 2022.1).

4. Results

4.1. Hydrogeochemical characterization

The chemical-physical parameters, major ions, minor and trace elements, saturation indices, and isotopic data ($\delta^{18}O$-H_2O, δD-H_2O, ^3H-H_2O, $\delta^{34}S$-SO_4, and $\delta^{18}O$-SO_4) are listed in Table 1, Table 2, and Table 3.

According to the EC and T values, three main groups can be clearly recognized (see Fig. 3). Also, the multivariate statistical approach of Principal Component Analyses (PCA) was performed (Maćkiewicz and Ratajczak, 1993) using R software to support and validate the hydrogeochemical classification of samples based on chemical compositional similarities. The first two principal component resolve 96.5 % of the total data variance (see Fig. S2).

A first group, represented by Cold and Low salinity Groundwater (hereafter CLGW) includes samples from S1 to S8 (see Table 1). These waters have the lowest EC (≤ 700 μS/cm) and T values (from 7.8 to 14.3 °C). The pH values are alkaline between 7.2 and 8.4, and these waters are in oxidizing condition (average value of 247 mV). They show a Ca-Mg-HCO_3 hydrofacies (Fig. 4). A second group with Intermediate Salinity Groundwater (hereafter ISGW) includes samples from S9 to S14 (see Table 1). They show T values between 13.8 and 18.5 °C, EC values from 1090 to 1981 μS/cm. The pH values are slightly acidic (from 6.0 to 6.8), while Eh values are between –197 and 229 mV. ISGW belongs to Ca-Mg-HCO_3 hydrofacies like CLGW. A third group of Thermal and Saline Groundwater (hereafter TSGW) includes samples from S15 to S22 (see Table 1). In detail, TSGW group is brackish-type water, according to the classification of Drever (1997), having EC values from 2560 to 6470 μS/cm. The latter are thermal with T values between 25 and 47 °C, slightly acidic (pH values from 6.2 to 6.4) and have negative Eh values (up to –285 mV). Furthermore, they are characterized by a Na-HCO_3-Cl composition (Fig. 4) and show a marked enrichment in sulphate respect to other groups (Table 1). These waters show a bubbling gas phase and have high dissolved CO_2 values too (Italiano et al., 2000). NO_3 values are generally very low, at times ranging from below the detection limit,

Table 1

Chemical-physical parameters, and major ions composition of groundwater from the study area are shown (numbers of springs correspond to the sites shown in Fig. 1).

Spring	Location		Chemical-physical parameters and Major Ions											
	Latitude UTM 33T	Longitude UTM 33T	T °C	pH	EC µS/cm	Eh mV	Ca mg/L	Mg mg/L	Na mg/L	K mg/L	Cl mg/L	SO4 mg/L	HCO3 mg/L	F mg/L
S1	4514317.88	515823.1	7.8	7.8	354	272.4	78.7	7.2	4.0	1.0	5.7	3.2	250.2	0.07
S2	4509575.13	516,989	7.9	7.7	300	252.7	55.2	10.2	3.2	1.0	5.1	2.4	228.8	0.05
S3	4508475.04	517046.1	9.7	8.4	298	206.5	48.1	12.2	3.9	1.0	5.7	3.0	213.6	0.05
S4	4510201.66	520069.8	10.5	7.4	518	298.7	92.5	14.8	5.9	1.4	7.9	5.7	357.0	0.12
S5	4505117.4	516,361	10.1	7.8	352	301.8	74.1	8.6	4.9	1.0	6.6	3.5	247.1	0.08
S6	4503164.03	515417.3	12.1	7.5	398	178.3	97.0	1.9	7.6	1.3	9.5	5.3	274.6	0.07
S7	4495742.24	522392.7	12.8	7.2	664	299.01	121.2	17.5	12.9	2.3	18.5	11.9	433.2	0.22
S8	4502107.15	521191.1	14.3	7.5	613	166.3	132.6	5.5	13.5	0.9	19.4	14.9	387.5	0.16
S9	4499811.48	519441.4	14.1	6.5	1090	85.8	243.4	22.8	21.5	3.9	28.7	16.1	771.9	0.25
S10	4500221.41	519281.3	17.3	6.1	1981	−197.3	454.3	47.8	88.1	9.8	102.1	40.0	1388.2	0.40
S11	4500115.23	519383.4	14.7	6.5	1435	228.9	329.9	31.0	41.4	5.8	52.5	25.9	1000.7	0.24
S12	4500159.22	519482.9	18.5	6.0	1924	−147.8	407.5	49.6	112.3	12.2	136.8	52.0	1266.2	0.27
S13	4500097.7	519399.5	14.4	6.6	1298	213.6	295.4	25.7	30.3	4.9	40.3	20.8	909.2	0.24
S14	4499940.76	519529.2	13.8	6.8	1054	198	239.6	25.4	21.9	4.1	28.9	16.4	765.8	0.25
S15	4502838.02	521319.4	26.4	6.3	2570	−224.5	427.9	40.4	206.0	31.4	252.1	162.7	1385.2	1.12
S16	4502837.92	521317.3	26.4	6.3	2560	−219.2	440.4	43.1	210.0	31.0	320.6	202.3	1434.0	1.51
S17	4502573.69	521,185	24.8	6.2	2770	−197.5	455.4	44.5	223.9	30.3	397.0	238.1	1446.2	1.15
S18	4503593.2	521292.7	36.8	6.2	4460	−273.2	248.7	94.3	438.5	67.8	795.4	266.3	1434.0	0.61
S19	4503601.13	521280.3	37.5	6.3	4640	−258.5	608.9	78.4	444.5	56.2	769.4	254.6	2224.2	1.49
S20	4504333.49	521,240	34.3	6.2	5240	−273.9	639.1	85.5	617.4	73.7	1027.1	479.5	2196.7	1.84
S21	4504385.25	521241.9	46.7	6.4	6380	−285	288.4	132.9	995.8	115.7	1694.0	321.9	1592.6	1.39
S22	4504331.3	521308.4	47	6.4	6470	−263	598.2	127.3	1063.0	113.4	1485.9	389.3	2349.3	1.69

Table 2

Trace elements concentrations, stable and radioactive isotopic contents of groundwater from the study area are shown (numbers of springs correspond to the sites shown in Fig. 1).

Spring	Minor elements and Isotopes										
	Li µg/L	B µg/L	Rb µg/L	Sr µg/L	Cs µg/L	Ba µg/L	δ^2H-H$_2$O ‰ V-SMOW	δ^{18}O-H$_2$O ‰ V-SMOW	^{3}H TU	δ^{18}O-SO$_4$ ‰ V-SMOW	δ^{34}S-SO$_4$ ‰ V-CDT
S1	3.1	<0.002	3.9	33.8	1.6	8.2					
S2	<0.002	<0.002	2.0	29.9	0.04	5.2	−50.4	−8.5	1.4		
S3	0.2	<0.002	1.3	33.7	0.02	5.9					
S4	4.3	<0.002	1.8	114.9	0.04	13.2	−47.2	−8.0	1.0		
S5	<0.002	<0.002	1.8	32.9	0.03	5.6					
S6	<0.002	<0.002	2.5	81.4	0.01	9.6					
S7	24.3	132.5	2.6	191.7	0.7	13.8	−46.4	−7.8	2.2		
S8	3.5	21.8	0.5	721.8	0.04	30					
S9	94.4	688.7	5.6	359.1	2.6	13.9	−44.6	−7.5	2.2	6.8	9.7
S10	576.9	3545	18.6	902.0	10.4	22.2	−43.9	−7.4	1.7	8.4	18.0
S11	302.7	1818	13.6	566.1	11.9	21.3					
S12	779.9	4925	20.7	984	10.1	29.1					
S13	263.3	1871	9.4	516.4	4.9	15.8					
S14	108.7	1067	6.4	380.5	2.7	15.0					
S15	1602	9107	50.8	2331.0	57.7	53.4					
S16	1574	9176	52.7	2425.0	60.6	55.4	−38.4	−6.3	2.3	7.3	9.9
S17	1730	10,620	103.3	2524.0	80.9	46.6	−39.0	−6.4	1.3	5.3	10.7
S18	3434	20,470	203.1	4867.0	149.3	67.0	−42.1	−6.4	1.1	8.2	16.8
S19	3846	23,230	219.1	5247.0	162.1	71.8					
S20	4737	28,360	288.5	6810.0	214.5	78.2					
S21	6588	40,650	409.5	9130.0	313.6	102.9	−48.1	−6.3	1.4	6.7	21.9
S22	6342	38,640	387.5	8936.0	293.2	102.5					

from 0.18 to 4.15 mg/L (S20) and did not show significant differences among the three groups. Among minor and trace elements (F, Li, B, Rb, Sr, Cs, SiO$_2$, and Ba), TSGW show the highest concentrations, up to three orders of magnitude higher than CLGW and ISGW groups. The δ^{18}O-H$_2$O and δD-H$_2$O values measured in nine samples (three of CLGW group, two of ISGW group and four of TSGW group, Table 2) range from − 8.5 to − 6.3 ‰, and from − 50 to − 38 ‰, respectively. The δ^{34}S-SO$_4$ and δ^{18}O-SO$_4$ values measured in six samples, belonging to ISGW and TSGW groups, show the following range values: from 5.3 to 8.4 and, from 9.7 to 21.9 for δ^{18}O and for δ^{34}S, respectively. Finally, tritium content is between 1 and 2.3 TU (see Table 2) measured in nine water samples.

4.2. Geo-structural interpretation

With the aim of furnishing a model for groundwater and deep fluids flowpaths, and to reconstruct the geological scheme of the Sele river Valley, we realized two schematic geological cross-sections both longitudinally and transversally with respect to the location of thermal springs and to the vergence of the Apennines fold-and-thrust belt, as well as a stratigraphic column down to a depth of about 5 km (Fig. 2).

In the central part of the A-A' section (Fig. 2), the so-called Valle del Sele tectonic unit results to be the geometrically highest unit in the area, overlying the Carbonate tectonic unit, with a maximum thickness of about 400 m. The Valle del Sale tectonic unit is characterized, from

Table 3

Calculated saturation indices of groundwater from the study area are shown (numbers of springs correspond to the sites shown in Fig. 1).

Saturation Indices				
Spring	Anhydrite	Calcite	Dolomite	Gypsum
S1	−3.47	0.46	−0.04	−2.96
S2	−3.7	0.24	−0.17	−3.2
S3	−3.66	0.84	1.21	−3.18
S4	−3.17	0.29	−0.09	−2.7
S5	−3.43	0.43	0.05	−2.95
S6	−3.14	0.35	−0.85	−2.69
S7	−2.77	0.32	−0.02	−2.33
S8	−2.61	0.66	0.14	−2.18
S9	−2.48	0.1	−0.64	−2.05
S10	−1.97	0.13	−0.47	−1.58
S11	−2.22	0.28	−0.27	−1.8
S12	−1.88	0.01	−0.63	−1.5
S13	−2.33	0.29	−0.28	−1.9
S14	−2.48	0.38	−0.02	−2.05
S15	−1.34	0.39	0.12	−1.05
S16	−1.24	0.4	0.17	−0.96
S17	−1.19	0.39	0.12	−0.88
S18	−1.31	0.21	0.46	−1.13
S19	−1.06	0.82	1.23	−0.89
S20	−0.83	0.67	0.91	−0.63
S21	−1.19	0.57	1.31	−1.12
S22	−0.89	1	1.83	−0.81

bottom to top, by the presence of clayey units interspersed with marly limestones, clayey-limestones, and arenaceous-marl (Di Nocera et al., 2016). The lower unit is the so-called Carbonate tectonic unit with a maximum thickness of about 3500 m. It outcrops in Picentini Mts. and in Mt. Castello (the western and eastern part of the A-A' cross section, respectively), and also in the structural highs of Oliveto Citra and Mt. Pruno. It consists of Mesozoic carbonates deposited in an interval between the Triassic and the Cretaceous and generated in a transition sector between the carbonate shelf edge and the Lagonegro Basin (Di Nocera et al., 2016). At the bottom of the carbonates, there are dolomitic successions. The Picentini Mts. were generated by the E-verging thrust front, while the back thrust and the respective splays, that dissects the Carbonate units in the eastern part, are responsible for the presence of the Oliveto Citra and Mt. Pruno highs (see Fig. 2). These tectonic structures have been also recognized in the ViDEPI seismic line "1–84-PA-1" (see location in Fig. 1). The unresolved western part of the A-A' section is due to the uncertainty given by the huge vertical displacement that involved the Lagonegrese tectonic unit (Fig. 2).

In the B-B' section, both the Valle del Sele tectonic unit and the Carbonate tectonic unit are covered, at times, by the synorogenic unit in erosive and disconformable contact (Fig. 2). In the northern part of the section, a lateral ramp, tectonically underlying to the Carbonate tectonic unit, is constituted by the carbonates of Monti della Maddalena tectonic unit (Di Nocera et al., 2016) with a maximum thickness of about 2000 m (Fig. 2). At the bottom, it is constituted by the presence of an intensely fractured dolomitic succession (from Upper Triassic to Lower Jurassic). At the top, it consists of a carbonate platform succession (from the Lower Jurassic to the Upper Miocene). The Lagonegrese tectonic unit is mainly represented by Mesozoic clayey deposits of deep-sea environment, and, at the top, by flysch deposits. In this area, the maximum thickness of the Lagonegrese tectonic unit is about 2000 m. The tectonic contact between the Lagonegrese unit and the Apulian carbonates is found at a depth of 4286 m in the "Acerno 001" well (see location in Fig. 1). This well falls in the Campagna tectonic window, which testifies the presence of a tectonic doubling of the Lagonegrese units (Patacca, 2007) that could justify the shallow depth of these units in the western part of the cross section. The doubling of the Lagonegrese units is also due to the sandwiching of the Mt. Croce tectonic unit, which outcrops in the western part of the study area (Fig. 1), but it is not in the area of sampling and is not crossed by the geological sections. The presence of the evaporitic Messinian Gessoso-Solfifera Formation, mainly constituted by gypsum and clays, with a thickness of about 80 m, is also reported. The geometrically deepest tectonic unit recognizable in the area is represented by the Apulian carbonates up to, at least, 5 km in depth. It is constituted by shallow water Mesozoic-Tertiary platform carbonates. As shown in both sections, regarding the tectonic discontinuities, a deep normal fault crosses both the Messinian Gessoso-Solfifera Formation and the Apulian carbonates. It is supposed to be responsible for playing a crucial role in the uprising of deep fluids towards the surface in the area of Bagni di Contursi (Fig. 2). Overall, carbonate units are the most common in the area and represent both the edge and the central part of the carbonate platform. At the bottom of these units, intensely fractured dolomitic successions are present and classified as cataclasites and ultra-cataclasites (Di Nocera et al., 2016). It is worthy of note that Montanari et al. (2017) analyzed drill-stem-tests performed in Mesozoic carbonate units, whose physical features are comparable with the ones of the Sele River valley, and they also measured porosity and permeability values, over 6 km depth. On fine-grained dolostones and vuggy dolomicrites, they measured an average permeability $<1.0 \cdot 10^{-18}$ m^2 and equal to 7.7 $\cdot 10^{-13}$ m^2, respectively. In carbonate units, permeability varies from 1.9 $\cdot 10^{-16}$ m^2 to 1.2 $\cdot 10^{-13}$ m^2. Besides, taking into account the P waves velocity provided by Valoroso et al. (2011), the density of the main
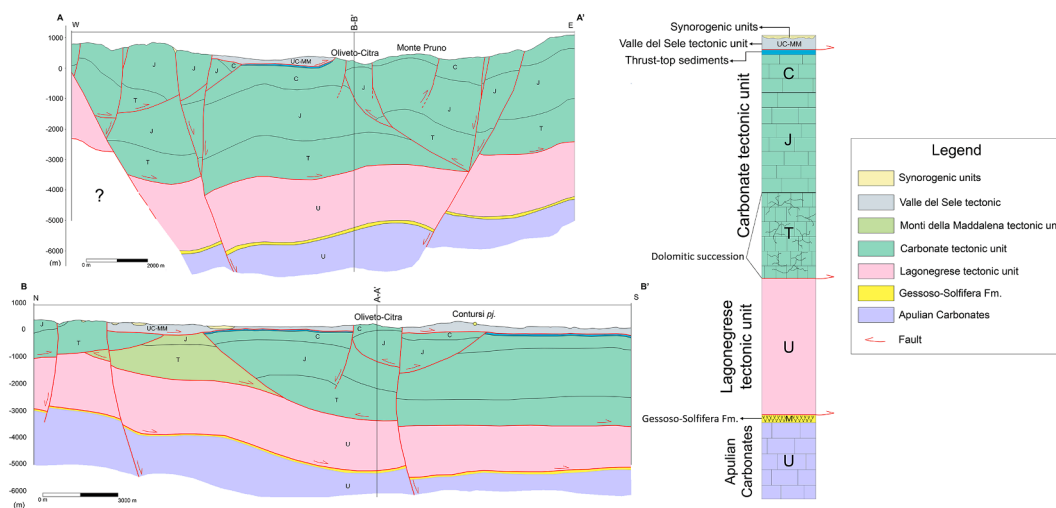

Fig. 2. Schematic cross sections (A-A' and B-B'; see Fig. 1 for location) and the lithostratigraphic column. UC-MM: Upper Cetaceous-Middle Miocene; C: Cretaceous; J: Jurassic; T: Triassic; M: Messinian; U: Undefined age.
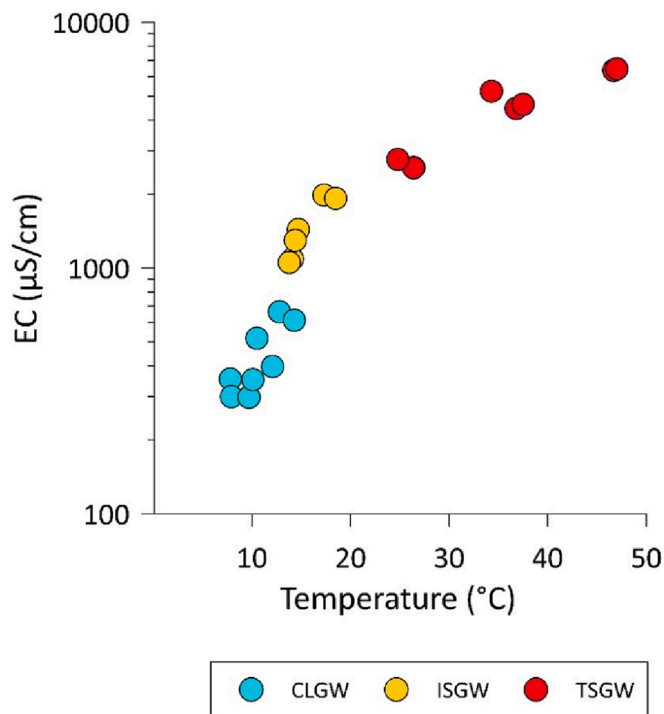
Fig. 3. Electrical conductivity (μS/cm) vs temperature (°C). Three groups of groundwater (i.e., CLGW, ISGW, and TSGW) are identified and displayed with different colours.

tectonic units was calculated and also the lithostatic pressure at 5 km depth was set at about 1.3 Kbar.

5. Discussion

5.1. Water-Rock interaction processes

The Langelier-Ludwig diagram (Fig. 4) clarifies that T and EC increase (Fig. 3) is related to a gradual enrichment of the Cl-SO$_4$ and Na contents, starting from Ca(Mg)–HCO$_3$ composition of cold samples (CLGW type) up to Na-HCO$_3$-Cl composition of thermal samples (TSGW type). In this latter hydrogeochemical facies, the composition of brine waters both in the Apennine context (Toscani et al., 2007; Boschetti et al., 2011a; Boschetti et al., 2011b), and in the volcanic/geothermal one (Minissale et al., 2016) were reported (Fig. 4). The separation between CLGW and TSGW groups is well-marked, while most springs of ISGW group show an intermediate composition, suggesting the presence of mixing processes between the cold end-member and the thermal one.

To evaluate both the role of the lithologies involved in the main geochemical processes, and the related mixing process, the relationships between the main solutes have been investigated. The Ca/(Ca + Mg) ratios have been plotted against HCO$_3$/(HCO$_3$ + SO$_4$) ratios (Fig. 5) in order to verify if the aquifers are dominated by carbonate-evaporite rocks. The CLGW and ISGW groups fall along calcite and dolomite dissolution line, indicating that the dissolution of carbonate rocks (mainly calcite) is the main process. Conversely, TSGW is more shifted towards an anhydrite end-member than CLGW. The relative increase in Mg^{2+} goes on with an increase of SO$_4^{2-}$, suggesting that TSGW are affected by dedolomitization driven by dissolution of gypsum or anhydrite. This process is quite common in aquifers containing dolostones associated with gypsiferous layers (Capaccioni et al., 2001; Appelo and Postma, 2005; Ma et al., 2011; Capecchiacci et al., 2015). The gypsum dissolution determines an increase in Ca^{2+} which in turn allows calcite to precipitate. Consequently, the decrease in CO$_3^{2-}$ causes the dolomite dissolution and the Mg^{2+} increase in solution (Gil-Márquez et al., 2017;

Apollaro et al., 2020). These constraints are confirmed by saturation indices of calcite, dolomite and gypsum, representative of the carbonate and evaporite components (Table 2). Fig. 6a shows that CLGW and ISGW groups are in equilibrium with calcite, slightly undersaturated in dolomite, and strongly undersaturated with respect to gypsum. TSGW is in equilibrium with calcite, supersaturated or in equilibrium with dolomite, and slightly undersaturated with a trend towards saturation with respect to gypsum (Fig. 6b).

The mixing processes between cold end-member and thermal one is also well represented by Na-Cl diagram (see Fig. S3). All investigated waters align along the Na/Cl ratio ~ 1 with TSGW having higher values than ISGW and CLGW. For the latter ones, the Na/Cl ratio is linked to seawater spray while for thermal waters (TSGW), it can be associated to deep fluids uprising produced by halite dissolution from evaporitic layers.

TSGW shows also high F$^-$ concentrations (from 0.61 to 1.84 mg/L) that are probably linked to the presence of fluorine-containing minerals, such as fluorapatite, fluorite and phlogopite in the lithology through which the water flows. The precipitation of calcite and subordinately dolomite could cause the removal of Ca^{2+} and enhance fluorite dissolution and F$^-$ enrichment, as proposed by Apollaro et al. (2020) for carbonate aquifers.

In the TSGW, the high B concentrations and the positive correlation with Cl$^-$ content (conservative element) supports the occurrence of evaporitic-water interaction process, since this element is typically enriched in evaporite sequences (Battistel et al., 2016; Holser, 2018). Similarly to B, also Li and Rb show a good positive correlation with Cl$^-$ (high Pearson's "r" correlation coefficient greater than 0.9; see Fig. S4 and Table S1) suggesting a contribution from water-rock interaction (Wang et al., 2019).

5.2. Oxygen and hydrogen isotope composition

The δD and δ^{18}O values are displayed in Fig. 7, together with Southern Italy Meteoric Water Line (SIML; Longinelli and Selmo, 2003) and Global Meteoric Water Line (GMWL; Clark and Fritz, 2013). CLGW is enriched in lighter isotopes and falls on SIML representing the shallow component (i.e., the current meteoric recharge of the aquifer). Similar to CLGW type, ISGW samples fall on meteoric water line and are located between the shallow cold end-member (CLGW type) and the inflowing thermal and brackish fluids (TSGW type) with oxygen isotopic signature more enriched in heavy isotopes. TSGW type has a narrow range of δ^{18}O values (from –6.38 ‰ to –6.30 ‰), and conversely a wide variability for δD. They move away from SIML with a positive δ^{18}O-shift, more marked for S18 and S21 showing the highest T and salinity value. Generally, saline waters (brackish, brine, connate, formation water, metamorphic water, etc.) fall on the right of the local meteoric water line, though scattered with an increase in both δ^{18}O and δD values with increasing salinity and T (Kharaka and Hanor, 2003; Hoefs, 2009; Toscani et al. 2007; Boschetti et al., 2011a; Boschetti et al., 2011b; Sharp, 2017), and their origin cannot be related to present-day precipitation. From an isotopic point of view, the composition of TSGW may be interpreted as a mixture between brine-type waters, originated from deep aquifer flowing upward, and cold water. In order to verify this hypothesis, the δ^{18}O values are plotted against Cl$^-$ contents together with mixing lines between cold water (representing local meteoric water line) and average values of brine-type from literature (Fig. 8). For shallow end-member we used the average values of cold water (Cl = 10.4 mg/L and δ^{18}O = –8.09 ‰) while for brine end-member Cl$^-$ contents between 70 and 120 g/L and δ^{18}O value of + 5 ‰ (Toscani et al., 2007; Boschetti et al., 2011a; Boschetti et al., 2011b; Yan et al., 2013) has been taken into account. Thermal waters do not fall on the mixing lines, showed an enrichment in heavy oxygen isotope linked probably to secondary processes responsible for the modification of the chemical and isotopic composition.

Additionally, thermal waters in Contursi area are characterized by bubbling gases with high CO$_2$ content (Duchi et al., 1995; Italiano et al.,
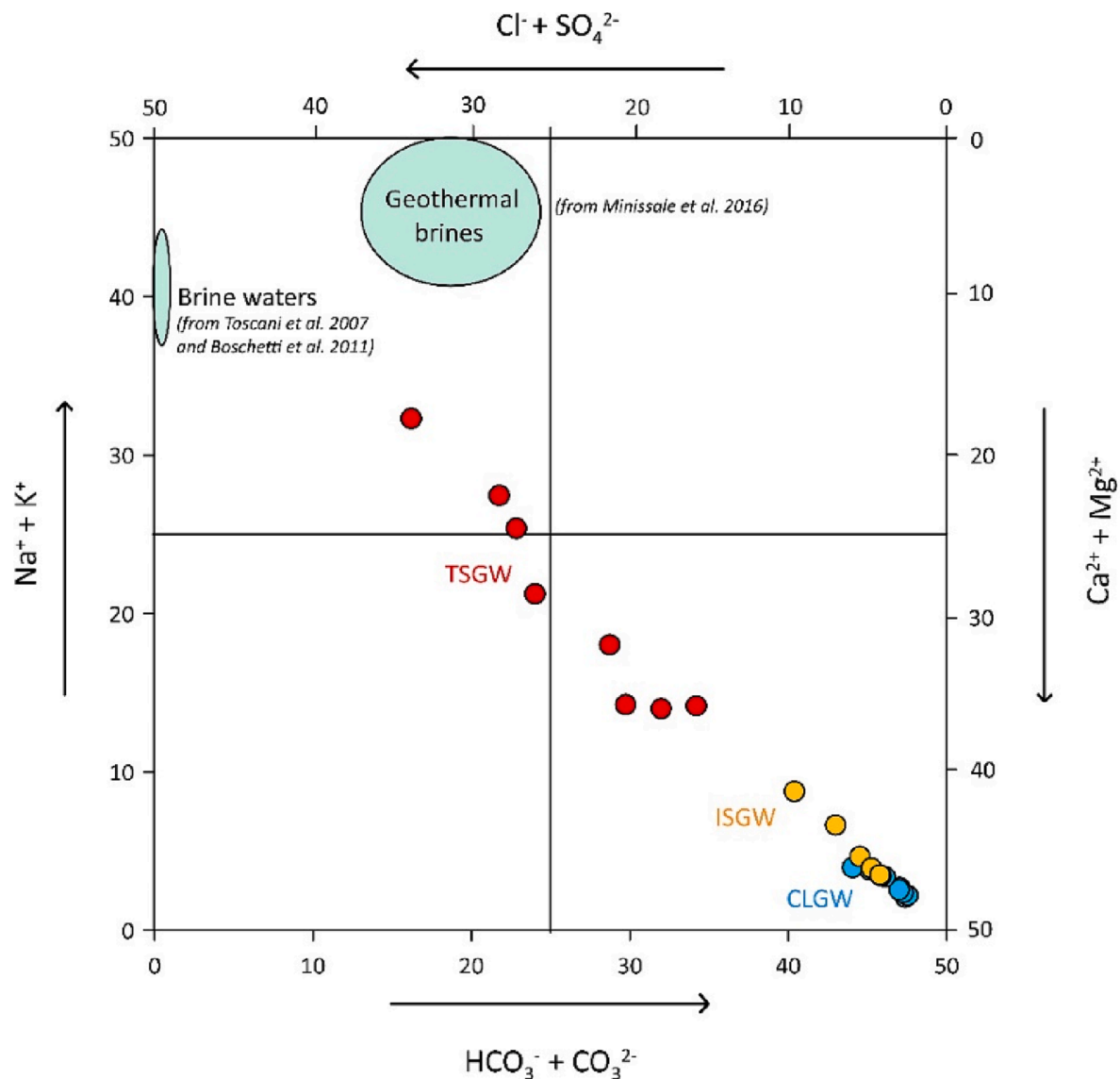
Fig. 4. Langelier-Ludwig diagram (Langelier and Ludwig, 1942) for groundwater samples from the Sele river valley. Most of samples are enriched in bicarbonate and calcium-magnesium ions (Ca-Mg-HCO$_3$ hydrofacies). Only mineralized springs of the Contursi area are included in the sodium-chloride waters domain (Na-Cl hydrofacies). In detail, Cold Low salinity Groundwater (CLGW), Intermediate Salinity Groundwater (ISGW), and Thermal Saline Groundwater (TSGW) are displayed with cyan, yellow, and red circles, respectively; Literature data of brine waters and geothermal brines are also displayed (Toscani et al., 2007; Boschetti et al., 2011; Minissale et al., 2016).

2000; Minissale, 2004). It is known that for CO$_2$-rich waters various natural processes may deviate the δ^{18}O e δD values in reservoir waters from equilibrium values on the meteoric water line. Generally, ^{18}O enrichment, with no change in the hydrogen isotope ratio, has been associated with oxygen isotope exchange with bedrock minerals or water-steam separation in geothermal conditions (Clayton and Steiner, 1975; Matsuhisa et al., 1979; Giggenbach, 1992), while ^{18}O depletion is proposed to be due to CO$_2$-water interaction at lower temperatures. Recently, Karolite et al. (2017) have verified that for CO$_2$-rich springs the equilibration with CO$_2$-dominat gas can result in ^{18}O enrichment and depletion in waters and therefore geothermal conditions are not necessary to produce ^{18}O-enriched waters. The ^{18}O enrichment is facilitated if the starting δ^{18}O value of CO$_2$ is significantly higher than that of the water and if high gas–water ratios are present (Karolyte et al., 2017). Our samples show these conditions linked to CO$_2$, nevertheless thermal waters are characterized from a big range of δD values, too. The δD enrichment without an effect on δ^{18}O can be justified from fractionation between degassing H$_2$, H$_2$S, CH$_4$, and water in active magmatic systems

(Richet et al., 1977). However, the chemical geothermometers indicate roughly that Contursi area is characterized by a low temperature geothermal system, not comparable to an active magmatic one. Alternatively, it is possible that the big range of δD values can be attributed to recharge in past at different temperatures, higher than the current one. A further explanation for this variability of isotopic data (positive δ^{18}O-shift and the value range in δD) can be linked to evaporative processes. In fact, during evaporation the lighter isotopes (^{16}O and ^{1}H) enter the vapour phase, and consequently water vapour is depleted in ^{18}O and ^{2}H, whereas the remaining water is enriched in both heavier isotopes (^{18}O and ^{2}H). The d-excess (d = δD – 8 δ^{18}O) is an important parameter for evaluating the effect of evaporation (Hoefs, 2009) and its value decreases during the evaporations process. The deuterium excesses of investigated groundwater, calculated using the SIML, range from 11.8 ‰ (S2) to – 2.05 ‰ (S21). Plotting the d-excess vs EC values (Fig. 9), it is possible to verify if the evaporation process is occurred. CLGW and ISGW are located along the dissolution line, while TSGW shows a negative correlation falling into the area linked to evaporative
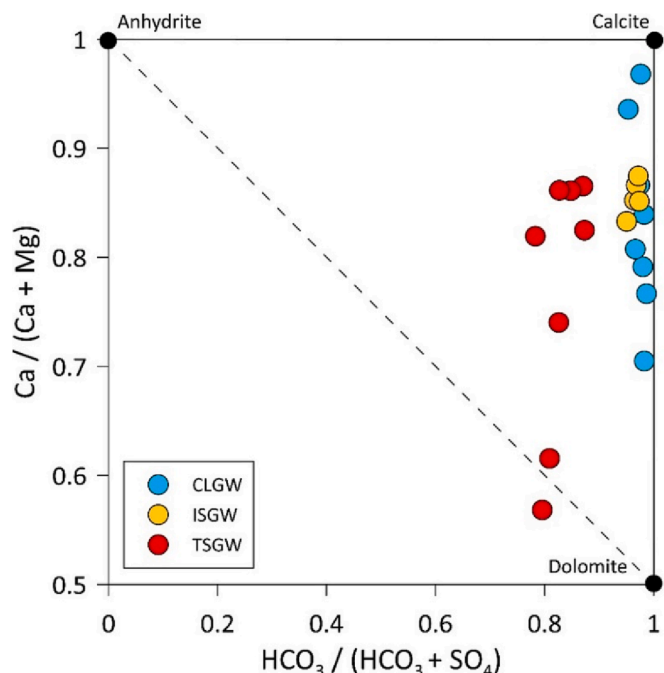
Fig. 5. Binary diagram: Ca/(Ca + Mg) vs HCO$_3$/(HCO$_3$ + SO$_4$) (Apollaro et al., 2020).

processes. In addition, all waters are well-correlated (R^2 = 0.94) highlighting that the mixing processes between cold end-member and thermal deep one, evaporated in depth, can be occurred.

5.3. Tritium data

Based on the above-mentioned hydrogeochemical and isotopic considerations, different flowpaths can be supposed for the analysed groundwater. In order to estimate different residence times, the binary relationship between groundwater tritium and Cl$^-$ contents was investigated. However, it did not show a linear correlation (Fig. S5). Based on

the assumptions reported in the Methods section, the piston-flow model was applied only to the CLGW group, while the well-mixed reservoir model to ISGW and TSGW, according to the approach adopted by Apollaro et al. (2015, 2016). CLGW show tritium contents between 0.98 TU and 2.23, the two water samples of ISGW have tritium values of 1.7 TU and 2.2 TU respectively, and the tritium contents of TSGW are between 1.1 TU and 2.3 TU.

Based on the first above-mentioned model (i.e., piston-flow) with the uncertainties caused by the input functions of tritium data of rainwaters, a mean residence time of about 20 years has been estimated for CLGW. This residence time value indicates that these springs are discharged from a relatively young and shallow aquifer behaving as a piston-flow circuit of a high flow rate, as evidenced by their chemical composition too. Alternatively, for other groundwater groups by adopting the well-mixed reservoir model, the mean residence is greater than 100 years, with maximum values associated with TSGW. These values indicate that thermal waters are conditioned by longer circuits affecting the geothermal reservoir in depth, while ISGW is due to the mixing of meteoric water (same as CLGW) and thermal and brackish water uprising.

5.4. Reservoir temperature estimation

Considering the physical–chemical composition of the investigated groundwater and the geological-hydrogeological framework, the geothermal reservoir feeding the Contursi area thermal systems was expected to be hosted in carbonate-evaporitic rocks. Only TSGW type has been treated with geothermometric calculations, since these waters are the least affected by dilution and thus, they are the most representative of the thermal deep end-member. The SiO$_2$-quartz geothermometers (Truesdell, 1976; Fournier, 1977; Michard, 1979) show temperatures in the range 80–96 °C, while SiO$_2$-chalcedony geothermometers provide temperatures between 50 and 68 °C. The latter temperature range is slightly higher than the discharge temperature and therefore, quartz is likely the most phase controlling the dissolved silica contents in the studied area. The K-Mg geothermometers yields temperatures (from 75° to 96 °C) similar to those obtained with the SiO$_2$-quartz geothermometers. In previous studies (e.g., Apollaro et al., 2012; Pastorelli et al., 1999; Wang et al., 2015) these two geothermometers
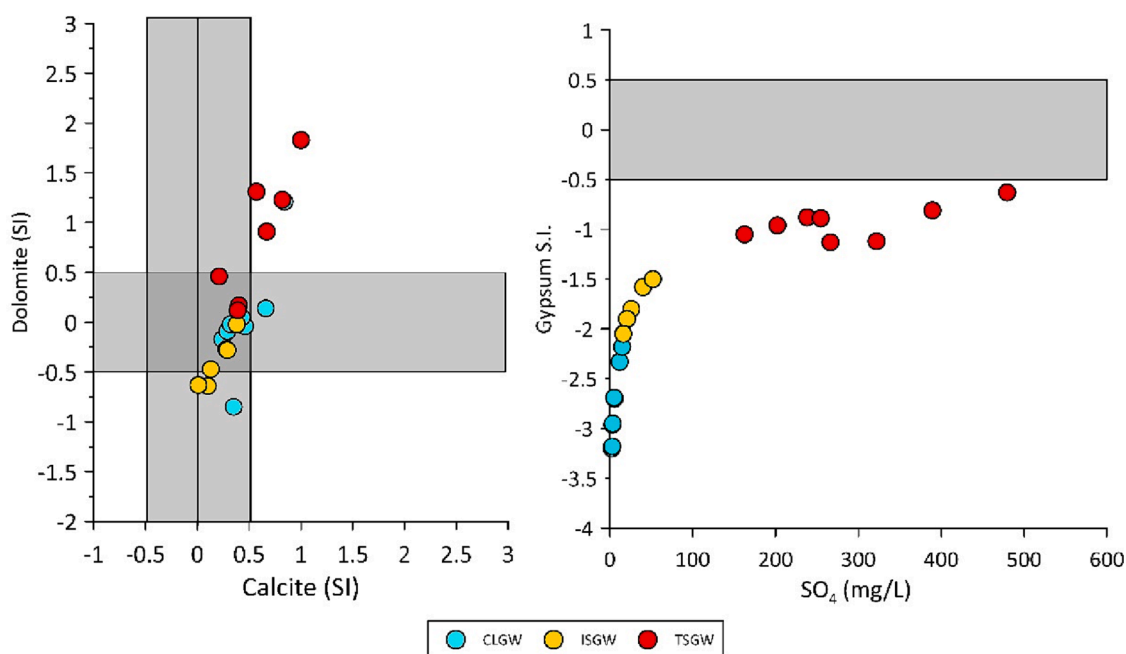
Fig. 6. A) Saturation indices: Calcite (SI) vs Dolomite (SI); b) Gypsum (SI) vs SO$_4$. Grey bars show ranges of equilibrium values (i.e., saturation state).
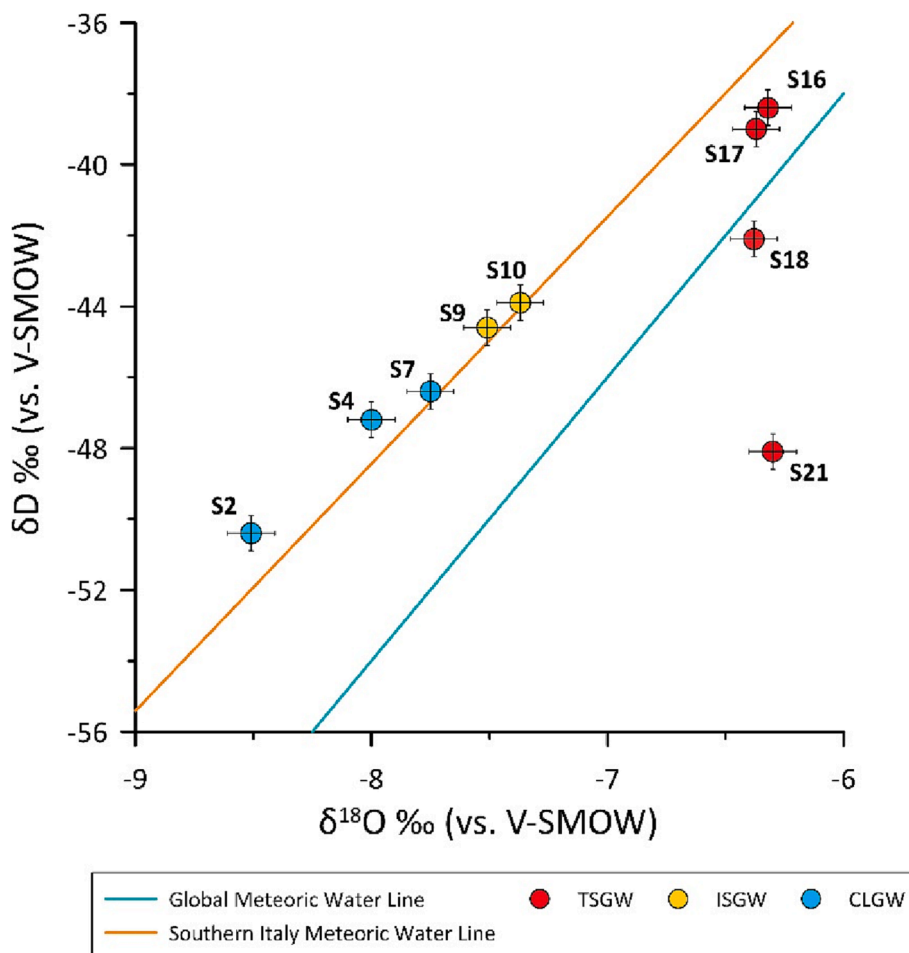
Fig. 7. Water stable isotopes diagram. $\delta^{18}O$ vs δD values of some samples from Sele river valley are shown with error bars. The Global Meteoric Water Line (Clark and Fritz, 2013), and the Southern Italy Meteoric Water Line ($\delta D = 6.97\ \delta18O + 7.32$; Longinelli and Selmo, 2003) are displayed with green, and orange lines, respectively.
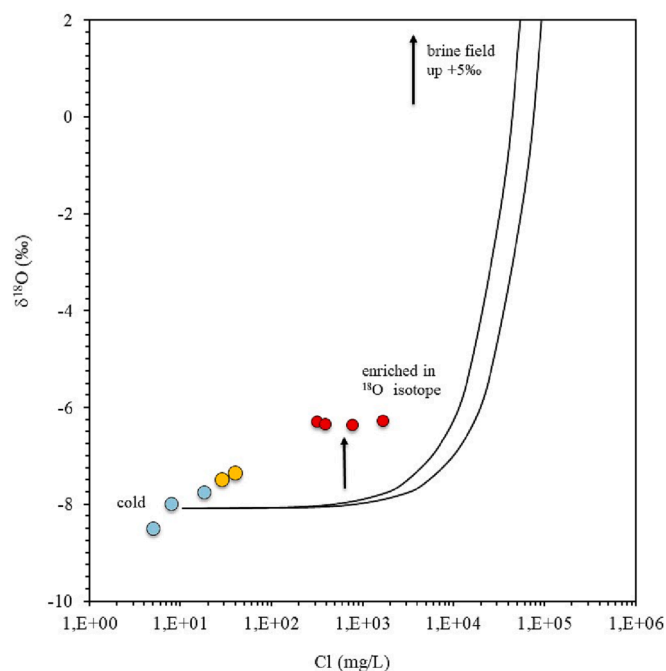
Fig. 8. The binary diagram displays the relationship between $\delta^{18}O$ and Cl^- contents (mg/L) of nine samples from the Sele river valley.

have been considered as the most suitable for low temperature carbonate-evaporitic systems. Considering all these results and excluding the higher values previously mentioned, a thermal reservoir temperature range of 75–95 °C can be considered representative for the investigated area. Taking into account the geothermometric estimations and the trend of geotherm proposed by Boncio et al., 2008, thermal reservoir can be estimated at the depth between 2 and 3 km.

5.5. $\delta^{34}S$ and $\delta^{18}O$ values in dissolved sulphate

The isotope composition of dissolved sulphate in groundwater has been analysed in order to constrain the sulphate origin in some water samples belonging to the ISGW and TSGW groups. The CLGW samples have not been analysed as they show low SO_4 values. The $\delta^{34}S$-SO_4 and $\delta^{18}O$-SO_4 values of the investigated groundwater samples fall into and very close to the field of evaporites (Fig. 10; Clark and Fritz, 1997; Paternoster et al., 2010; Petitta et al., 2011). Geological data indicate the presence of the Messinian Gessoso-Solfifera Formation at the top of the Apulian carbonates at a depth of about 4 km in "Acerno 001" well (Fig. 2). To ascertain that isotopic signature of studied waters is attributable to these evaporitic Messinian deposits, the $\delta^{34}S$-SO_4 values and SO_4 concentration of the water samples have been plotted together with mixing lines between rainwater and Messinian marine sulphate minerals (values from Boschetti et al., 2011a; Boschetti et al., 2011b; Vespasiano et al. 2021; Fig. 11). Three water samples (S9, S10 and S21) fall along the mixing lines, suggesting that the Messinian deposits are the mainly source of dissolved sulphate for the thermal systems of Contursi area.
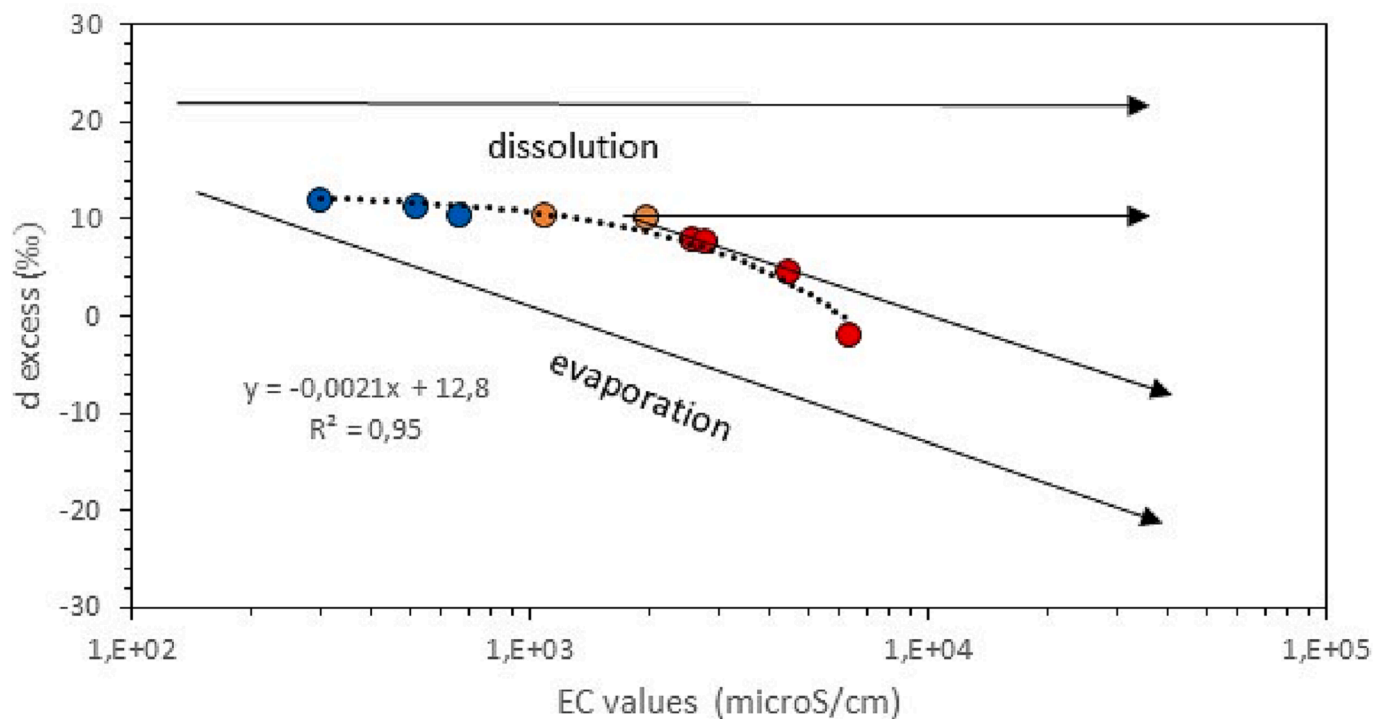
Fig. 9. Relationship between deuterium excess and EC (µS/cm) of nine samples from the Sele river valley.
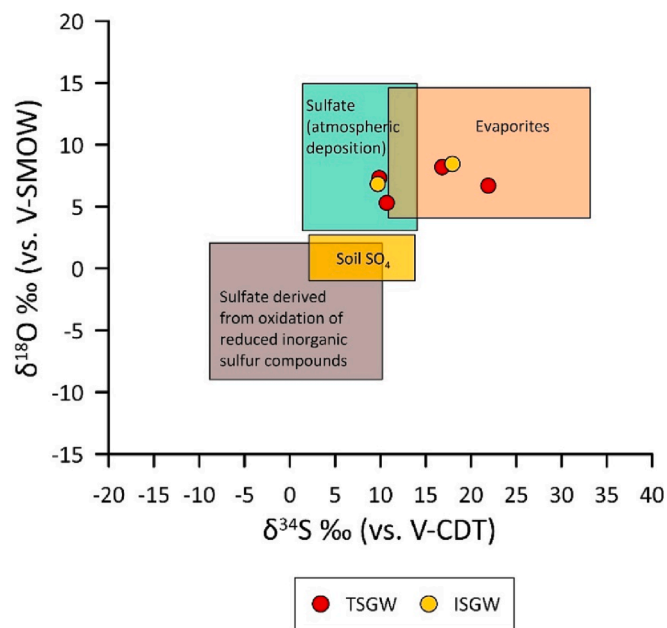
Fig. 10. Sulphate stable isotopes diagram (from Clark and Fritz, 1997). Isotope ranges for different potential sources of sulphate are displayed with rectangles. $\delta^{18}O$-SO_4 and $\delta^{34}S$-SO_4 isotopic values of some samples of ISGW and TSGW are shown.

Fig. 11. $\delta^{34}S$-SO_4 (vs V-CDT) vs SO_4 concentration (mg/L) of groundwater samples are plotted together with mixing lines between rainwater and Messinian marine sulphate minerals.

Nevertheless, three samples (S16, S17 and S18) do not match the mixing model and show an ^{32}S-enrichment in the dissolved sulphate. Known that thermal waters are characterised by bubbling gases with high CO_2 and H_2S contents (Italiano et al., 2000; Minissale, 2004), it is possible that part of the H_2S of the gas phase is rapidly oxidized when it comes into contact with shallow meteoric water. The irreversible oxidation of H_2S, much faster kinetically than the reduction of sulphate to sulphide (Ohmoto and Rye, 1979), determines an ^{32}S-enrichment in the dissolved

sulphate whose entity is function of the degree of oxidation in non-equilibrium condition as stated by Martinez Serrano et al. (1996). Therefore, for these samples the dissolved sulphate may be due to the contribution of oxidation of H_2S, and the Messinian deposits leaching at depth.

5.6. Interpretative model of fluids flow

This hydrogeochemical multi-approach allows to draw a hydrogeological model of the fluid circulation with the aid of cross-sections

11

(see Fig. 2). Hydrogeochemical and isotopic data (both stable and radioactive) indicate the existence of more complex and regional groundwater hydrodynamics for the ISGW and TSGW, which are characterized by longer and deeper flowpaths emerging in the inner zone of the Sele river valley. Instead, a local flow system with a shorter residence time of water is supposed for the CLGW shallow carbonate groundwater mostly emerging at the boundary of carbonate aquifers.

Besides, as shown in the geological schematic sections (Fig. 2), tectonic discontinuities (e.g., deep-seated faults) play a crucial role in the circulation, acting as pathways for the upward migration of deep contributions to reach the shallow regional aquifers that are totally recharged by meteoric infiltration (as stated by δD and $\delta^{18}O$ values). The mixing between deep-seated thermal fluids and colder shallow groundwater fed by regional carbonate aquifers occurs with different degree for ISGW and TSGW springs. Particularly, the latter ones show hydrogeochemical features directly connected with deep tectonic structures of the Contursi area (see Fig. 2). We speculate that deep inputs ascend from the Apulian Platform, where combinations of brine and or CO_2 mixtures are supposed (Duchi et al., 1995; Amoroso et al., 2017; De Landro et al., 2022), and crossing the Messinian deposits, they acquire the above-mentioned isotopic signature of evaporites. In the shallower portion of the crust (i.e., within the Carbonate tectonic unit), these mineralized fluids mix with fresh groundwater hosted in regional carbonate aquifers.

Our results are in line with recent geophysical studies carried out in this sector of Apennines that detected deep-seated fluid accumulation i.e., mixtures of brine and or CO_2 (Amoroso et al., 2014; Improta et al., 2014; Amoroso et al., 2017; De Landro et al., 2022). It is noteworthy also that De Landro et al., 2022 observed spatiotemporal seismic velocity changes that are caused by different mechanisms in the shallow and in the deep crust. In the shallower volume, they are associated with meteoric water recharge processes, and in the deeper volume they are related to pore pressure pulsations. Since previous works invoked overpressured fluids at depth as primary mechanism of interaction between fluid dynamic and earthquake triggering (Chiarabba et al., 2020; Chiodini et al., 2020), for future research the hydrogeochemical investigation in active seismic areas could be based on high-frequency and long-term multiparametric hydrogeochemical monitoring to quantify these pulsations as function of changes in mixing ratio between shallow groundwater and deep contributions.

6. Conclusion

In complex and active tectonic areas, the multi-component approach combining hydrogeochemistry to geo-structural setting and isotopic study is a powerful tool for analysing mixing and related processes between shallow groundwater and ascending deep fluids along main fault systems. The application of this tool to the Contursi area in the upper Sele river valley (southern Apennines, southern Italy) results to be appropriate to monitor this hydrogeochemical process, owing to its hydrogeological and geo-structural features. In fact, the study area is characterized by groundwater resources converging from shallow carbonate aquifers to several springs showing different geochemical signatures (e.g., degree of mineralization and thermalism), and by the presence of deep-seated tectonic discontinuities acting as preferential pathways for fluids upwelling.

A significant hydrogeochemical evolutionary trend from the Ca-Mg-HCO$_3$ hydrofacies to the Na-HCO$_3$-Cl one was found in the analysed groundwater samples. Thus, according to the geochemical composition as well as to the thermal trend and to the EC, three main groups of groundwater have been identified as follows: Cold and Low salinity Groundwater (CLGW), Intermediate Salinity Groundwater (ISGW), and Thermal and Saline Groundwater (TSGW). This classification was validated by stable isotopes ($\delta^{18}O$-δD). In fact, isotopic values of CLGW corresponding to the shallow end-member fall on the local meteoric water line (i.e., $\delta^{18}O$: from − 8.51 to − 7.75 ‰; δD: −50.4 to −46.4 ‰),

while ISGW and TSGW are characterized by isotopic signatures more enriched in heavy isotopes (i.e., $\delta^{18}O$: from − 7.51 to − 6.30 ‰; δD: −48.1 to − 38.4 ‰) attributed to the inflow of deep fluids which have undergone natural processes modifying the pristine isotopic signature.

Therefore, CLGW chemistry is clearly related to carbonate rocks (calcite and dolomite)-water interaction. In contrast, for ISGW and TSGW an additional contribution from evaporitic rocks can be proposed as shown by chemical composition, SI values (gypsum and anhydrite) and sulphur isotopic signature of dissolved sulphate, whose values are associated with the evaporitic Messinian Gessoso-Solfifera Formation.

Our geo-structural review provided a structural sketch down to a depth of approximately 5 km. The geological cross-sections highlighted the presence of deep-seated normal faults which could represent the best network of pathways for deep fluids migration towards the surface allowing the mixing between deep and shallow end-members.

Additionally, through the application of two models (i.e., the piston-flow and well-mixed reservoir) based on tritium isotope, deeper and longer circuits have been pointed out for TSGW flowpaths. Also, by selecting geothermometers for medium–low geothermal systems, the equilibrium reservoir temperature of deep contributions between 75 and 96 °C was extrapolated for springs where evidence of significant deep contributions was found. Hence, applying the geothermal gradient of the study area, an estimation of depth of fluids reservoir at about 3 km was inferred.

Moreover, our results agree with recent geodetical and seismological studies in the selected area that reported an intensely fractured deep fluid-saturated volume of the crust. The same studies shed light on the spatiotemporal evolution of pore pressure pulsations at depth in highly sensitive fault system zones. At the same time, in the shallow crust, transient deformations were attributable to phases of recharge of wide aquifers. Consequently, recording changes in hydrogeological mixing ratio by long-lasting hydrogeochemical multi-component approach could be crucial to analyse and discern both the pore pressure pulsations in the deep crust and hydrogeological variations in the shallow crust.

CRediT authorship contribution statement

Francesca Gori: Conceptualization, Methodology, Investigation, Formal analysis, Software, Data curation, Writing – original draft. **Michele Paternoster:** Conceptualization, Methodology, Investigation, Data curation, Validation, Writing – original draft, Writing – review & editing. **Maurizio Barbieri:** Conceptualization, Methodology, Validation, Supervision. **Dario Buttitta:** Methodology, Investigation. **Antonio Caracausi:** Conceptualization, Methodology, Investigation, Validation, Supervision. **Fabrizio Parente:** Methodology, Investigation, Software, Data curation, Writing – original draft. **Attilio Sulli:** Conceptualization, Methodology, Validation, Supervision, Writing – review & editing. **Marco Petitta:** Conceptualization, Methodology, Supervision, Project administration, Writing – review & editing.

Data availability

All data are freely available

Appendix A. Supplementary data

Supplementary data to this article can be found online at https://doi.org/10.1016/j.jhydrol.2023.129258.

References

Amoroso, O., Ascione, A., Mazzoli, S., Virieux, J., Zollo, A., 2014. Seismic imaging of a fluid storage in the actively extending Apennine mountain belt, southern Italy. Geophys. Res. Lett. 41 (11), 3802–3809.

Amoroso, O., Russo, G., De Landro, G., Zollo, A., Garambois, S., Mazzoli, S., Parente, M., Virieux, J., 2017. From velocity and attenuation tomography to rock physical modeling: Inferences on fluid-driven earthquake processes at the Irpinia fault system in southern Italy. Geophys. Res. Lett. 44 (13), 6752–6760.

Andreo, B., Gil-Márquez, J.M., Mudarra, M., Linares, L., Carrasco, F., 2016. Hypothesis on the hydrogeological context of wetland areas and springs related to evaporitic karst aquifers (Málaga, Córdoba and Jaén provinces, Southern Spain). Environ. Earth Sci. 75 (9), 1–19.

Apollaro, C., Dotsika, E., Marini, L., Barca, D., Bloise, A., De Rosa, R., Doveri, M., Lelli, M., Muto, F., 2012. Chemical and isotopic characterization of the thermomineral water of Terme Sibarite springs (Northern Calabria, Italy). Geochem. J. 46 (2), 117–129.

Apollaro, C., Vespasiano, G., De Rosa, R., Marini, L., 2015. Use of mean residence time and flowrate of thermal waters to evaluate the volume of reservoir water contributing to the natural discharge and the related geothermal reservoir volume. Application to Northern Thailand hot springs. Geothermics 58, 62–74.

Apollaro, C., Vespasiano, G., Muto, F., De Rosa, R., Barca, D., Marini, L., 2016. Use of mean residence time of water, flowrate, and equilibrium temperature indicated by water geothermometers to rank geothermal resources. Application to the thermal water circuits of Northern Calabria. J. Volcanol. Geotherm. Res. 328, 147–158.

Apollaro, C., Caracausi, A., Paternoster, M., Randazzo, P., Aiuppa, A., De Rosa, R., Fuoco, I., Mongelli, G., Muto, F., Vanni, E., Vespasiano, G., 2020. Fluid geochemistry in a low-enthalpy geothermal field along a sector of southern Apennines chain (Italy). J. Geochem. Explor. 219, 106618.

Appelo, C.A.J., Postma, D., 2005. Geochemistry. Groundwater and pollution 536.

Arnórsson, S., Gunnlaugsson, E., Svavarsson, H., 1983. The chemistry of geothermal waters in Iceland. III. Chemical geothermometry in geothermal investigations. Geochim. Cosmochim. Acta 47 (3), 567–577.

Ascione, A., Nardò, S., Mazzoli, S., 2020. The MS 6.9, 1980 Irpinia Earthquake from the basement to the surface: a review of tectonic geomorphology and geophysical constraints, and new data on postseismic deformation. Geosciences 10 (12), 493.

Baird R.B., Eaton A.D., Rice, E.W., 2017. Standard methods for examination of water and wastewater, 23rd edn. American Public Health Association (APHA), American Water Works Association (AWWA), Water Environment Federation (WEF), Washington DC.

Barberio, M.D., Gori, F., Barbieri, M., Boschetti, T., Caracausi, A., Cardello, G.L., Petitta, M., 2021. Understanding the origin and mixing of deep fluids in shallow aquifers and possible implications for crustal deformation studies: San Vittorino plain. Central Apennines. Appl. Sci. 11 (4), 1353.

Barbieri, M., Boschetti, T., Barberio, M.D., Billi, A., Franchini, S., Iacumin, P., Selmo, E., Petitta, M., 2020. Tracing deep fluid source contribution to groundwater in an active seismic area (central Italy): A combined geothermometric and isotopic (δ13C) perspective. J. Hydrol. 582, 124495.

Battistel, M., Hurwitz, S., Evans, W., Barbieri, M., 2014. Multicomponent geothermometry applied to a medium-low enthalpy carbonate-evaporite geothermal reservoir. Energy Procedia 59, 359–365.

Battistel, M., Hurwitz, S., Evans, W.C., Barbieri, M., 2016. The chemistry and isotopic composition of waters in the low-enthalpy geothermal system of Cimino-Vico Volcanic District. Italy. J. Volcanol. Geotherm. Res. 328, 222–229.

Bernard, P., Zollo, A., 1989. The Irpinia (Italy) 1980 earthquake: detailed analysis of a complex normal faulting. J. Geophys. Res. Solid Earth 94 (B2), 1631–1647.

Boni, C., Bono, P., Capelli, G., 1986. Schema Idrogeologico dell'Italia Centrale. Mem. Soc. Geol. It. 991–1012.

Boschetti, T., Toscani, L., Shouakar-Stash, O., Iacumin, P., Venturelli, G., Mucchino, C., Frape, S.K., 2011a. Salt waters of the Northern Apennine Foredeep Basin (Italy): origin and evolution. Aquat. Geochem. 17 (1), 71–108.

Boschetti, T., Cortecci, G., Toscani, L., Iacumin, P., 2011b. Sulfur and oxygen isotope compositions of Upper Triassic sulfates from Northern Apennines (Italy): palaeogeographic and hydrochemical implications. Geol. Acta 9, 129–147.

Budetta, P., Celico, P., Corniello, A., De Riso, R., Ducci, D., Nicotera, P., 1988. Carta idrogeologica del F. 186 (S. Angelo dei Lombardi). Memoria illustrativa. Mem. Soc. Geol. It. 41, 1029–1038.

Capaccioni, B., Didero, M., Paletta, C., Salvadori, P., 2001. Hydrogeochemistry of groundwaters from carbonate formations with basal gypsiferous layers: an example from the Mt Catria–Mt Nerone ridge (Northern Appennines, Italy). J. Hydrol. 253 (1–4), 14–26.

Capecchiacci, F., Tassi, F., Vaselli, O., Bicocchi, G., Cabassi, J., Giannini, L., Nisi, B., Chioccioria, G., 2015. A combined geochemical and isotopic study of the fluids discharged from the Montecatini thermal system (NW Tuscany, Italy). Appl. Geochem. 59, 33–46.

Celico, P.B., 1983. Idrogeologia dei massicci carbonatici, delle piane quaternarie e delle aree vulcaniche dell'Italia centro-meridionale: Marche e Lazio meridionali, Abruzzo. Molise e Campania, Cassa per il Mezzogiorno.

Celico, P., Civita, M., 1976. Sulla tettonica del Massiccio del Cervialto (Campania) e le implicazioni idrogeologiche ad essa connesse. Boll. Soc. Natur. in Napoli 85, 555–580.

Celico, P., De Gennaro, M., Ghiara, M.R., Stanzione, D., 1979. Le sorgenti termominerali della valle del Sele (SA): indagini strutturali, idrogeologiche e Geochimiche. Rend. Soc. Ital. Mineral. Petrol. 31, 389–409.

Celico, P., Guadagno, F.M., Luise, G., Tescione, M., Vallario, A., 1987. Idrogeologia del Monte Polveracchio – Monte Raione (Monti Picentini - Campania). Mem. Soc. Geol. It. 37, 341–362.

Celico, F., Petrella, E., Celico, P., 2006. Hydrogeological behaviour of some fault zones in a carbonate aquifer of Southern Italy: an experimentally based model. Terra Nova 18 (5), 308–313.

Chen, Z., Goldscheider, N., 2014. Modeling spatially and temporally varied hydraulic behavior of a folded karst system with dominant conduit drainage at catchment scale, Hochifen-Gottesacker. Alps. J. Hydrol. 514, 41–52.

Chiarabba, C., Buttinelli, M., Cattaneo, M., De Gori, P., 2020. Large earthquakes driven by fluid overpressure: The Apennines normal faulting system case. Tectonics 39 (4), e2019.

Chiocchini, U., Castaldi, F., Barbieri, M., Eulilli, V., 2010. A stratigraphic and geophysical approach to studying the deep-circulating groundwater and thermal springs, and their recharge areas, in Cimini Mountains-Viterbo area, central Italy. Hydrogeol. J. 18, 1319–1341.

Chiodini, G., Frondini, F., Marini, L., 1995a. Theoretical geothermometers and PCO2 indicators for aqueous solutions coming from hydrothermal systems of medium-low temperature hosted in carbonate-evaporite rocks. Application to the thermal springs of the Etruscan Swell, Italy. Appl. Geochem. 10 (3), 337–346.

Chiodini, G., Frondini, F., Ponziani, F., 1995b. Deep structures and carbon dioxide degassing in central Italy. Geothermics 24 (1), 81–94.

Chiodini, G., Cardellini, C., Amato, A., Boschi, E., Caliro, S., Frondini, F., Ventura, G., 2004. Carbon dioxide Earth degassing and seismogenesis in central and southern Italy. Geophys. Res. Lett. 31 (7).

Chiodini, G., Cardellini, C., Di Luccio, F., Selva, J., Frondini, F., Caliro, S., Rosiello, A., Beddini, G., Ventura, G., 2020. Correlation between tectonic CO$_2$ Earth degassing and seismicity is revealed by a 10-year record in the Apennines, Italy. Sci. Adv. 6 (35), eabc2938.

Ciarcia, S., Vitale, S., Di Staso, A., Iannace, A., Mazzoli, S., Torre, M., 2009. Stratigraphy and tectonics of an Internal Unit of the southern Apennines: implications for the geodynamic evolution of the peri-Tyrrhenian mountain belt. Terra Nova 21 (2), 88–96.

Clark, I.D., Fritz, P., 1997. Environmental Isotopes in Hydrogeology. Lewis Publishers, New York.

Clark, I.D., Fritz, P., 2013. Environmental isotopes in hydrogeology. CRC Press.

Clayton, R.N., Steiner, A., 1975. Oxygen isotope studies of the geothermal system at Wairakei. New Zealand. Geochim. Cosmochim. Acta 39 (8), 1179–1186.

Cook, P.G., 2003. A guide to regional groundwater flow in fractured rock aquifers. Seaview Press, Henley Beach, South Australia, p. 151.

Coppola, L., Pescatore, T., 1989. Lineamenti di neotettonica dei Monti Terminio-Tuoro, Cervialto e Marzano (Appennino meridionale). Bollettino Società Geologica Italiana 108 (1), 105–119.

Corniello, A., Ducci, D., Aquino, A., 2010. Hydrogeological map of the Monti Picentini Regional Park (southern Italy) at 1: 50,000 scale. Bollettino Geofisica Teorica ed Applicata 51 (4).

Cotecchia, V., 1986. Ground deformation and slope instability produced by the earthquake slope of 23 November 1980 in Campania and Basilicata. Geol. Appl. Idrogeol. 21, 31–100.

De Landro, G., Amoroso, O., Russo, G., D'Agostino, N., Esposito, R., Emolo, A., Zollo, A., 2022. Decade-long monitoring of seismic velocity changes at the Irpinia fault system (southern Italy) reveals pore pressure pulsations. Sci. Rep. 12 (1), 1–9.

De Matteis, R., Matrullo, E., Rivera, L., Stabile, T.A., Pasquale, G., Zollo, A., 2012. Fault delineation and regional stress direction from the analysis of background microseismicity in the southern Apennines, Italy. Bulletin of the Seismological Society of America 102 (4), 1899–1907.

De Vries, J.J., Simmers, I., 2002. Groundwater recharge: an overview of processes and challenges. Hydrogeol. J. 10 (1), 5–17.

Deutsch, W.J., 2020. Groundwater Geochemistry: Fundamentals And Applications To Contamination. CRC Press.

Di Nocera S., Iannace A., Torre M., Basso C., Caiazzo C., Ciarcia S., Cinque A., Gasparrini M., Matano F., Mazzoli S., Mitrano T., Pagliaro S. Parente M., 2016. Note illustrative della Carta Geologica d'Italia alla scala 1: 50.000, foglio 468 Eboli. ISPRA Istituto Superiore per la Protezione e la Ricerca Ambientale, Servizio Geologico d'Italia.

Doglioni, C., 1991. A proposal for the kinematic modelling of W-dipping subductions-possible applications to the Tyrrhenian-Apennines system. Terra Nova 3 (4), 423–434.

Doglioni, C., 1995. Geological remarks on the relationships between extension and convergent geodynamic settings. Tectonophysics 252 (1–4), 253–267.

Doglioni, C., Barba, S., Carminati, E., Riguzzi, F., 2014. Fault on–off versus coseismic fluids reaction. Geosci. Front. 5 (6), 767–780.

Drever, J.I., 1997. The geochemistry of natural waters: surface and groundwater environments, 3rd edn. Prentice Hall, Upper Saddle River.

Duchi, V., Minissale, A., Vaselli, O., Ancillotti, M., 1995. Hydrogeochemistry of the Campania region in southern Italy. J. Volcanol. Geotherm. Res. 67 (4), 313–328.

Faccenna, C., Becker, T.W., Lucente, F.P., Jolivet, L., Rossetti, F., 2001. History of subduction and back arc extension in the Central Mediterranean. Geophys. J. Int. 145 (3), 809–820.

Fouillac, C., Michard, G., 1981. Sodium/lithium ratio in water applied to geothermometry of geothermal reservoirs. Geothermics 10 (1), 55–70.

Fournier, R.O., 1977. Chemical geothermometers and mixing models for geothermal systems. Geothermics 5 (1–4), 41–50.

Fournier, R.O., 1979. A revised equation for the Na/K geothermometer. Transactions of the Geothermal Resources Council 3, 221–224.

Fournier, R.O., Potter, I., R. w., 1979. Magnesium correction to the Na K Ca chemical geothermometer. Geochim. Cosmochim. Acta 43 (9), 1543–1550.

Fournier, R.O., Truesdell, A.H., 1973. An empirical Na K Ca geothermometer for natural waters. Geochim. Cosmochim. Acta 37 (5), 1255–1275.

Freeze, R.A., Cherry, J.A., 1979. Groundwater. PrenticeHall, Englewood, Cliffs, New Jersey, p. 604.

Frondini, F., 2008. Geochemistry of regional aquifer systems hosted by carbonate-evaporite formations in Umbria and southern Tuscany (central Italy). Appl. Geochem. 23 (8), 2091–2104.

Ghiara, M.R., Stanzione, D., Petti, C., 1994. Chemical and isotope characteristics of the deep waters of the high valley of the River Sele (Italy); correlations between geochemical parameters and seismic activity. Bollettino Società Geologica Italiana 113 (3), 521–537.

Giggenbach, W.F., 1988. Geothermal solute equilibria. derivation of Na-K-Mg-Ca geoindicators. Geochim. Cosmochim. Acta 52 (12), 2749–2765.

Giggenbach, W.F., 1992. Isotopic shifts in waters from geothermal and volcanic systems along convergent plate boundaries and their origin. Earth Planet. Sci. Lett. 113 (4), 495–510.

Gil-Márquez, J.M., Barberá, J.A., Andreo, B., Mudarra, M., 2017. Hydrological and geochemical processes constraining groundwater salinity in wetland areas related to evaporitic (karst) systems. A case study from Southern Spain. J. Hydrol. 544, 538–554.

Goldscheider, N., Mádl-Szőnyi, J., Erőss, A., Schill, E., 2010. Thermal water resources in carbonate rock aquifers. Hydrogeol. J. 18 (6), 1303–1318.

Gori, F., Barberio, M.D., 2022. Hydrochemical changes before and during the 2019 Benevento seismic swarm in central-southern Italy. J. Hydrol. 604, 127250.

Hoefs, J., 2009. Stable isotope geochemistry, 6th ed. Springer.

Holser, W.T., 2018. Trace elements and isotopes in evaporites. In: Marine Minerals. De Gruyter, pp. 295–346.

IAEA/WMO, 2013. Global network of isotopes in precipitation. The GNIP database. (Accessible at: http://www.iaea.org/water).

Improta, L., De Gori, P., Chiarabba, C., 2014. New insights into crustal structure, Cenozoic magmatism, CO₂ degassing, and seismogenesis in the southern Apennines and Irpinia region from local earthquake tomography. J. Geophys. Res. Solid Earth 119 (11), 8283–8311.

Italiano, F., Martelli, M., Martinelli, G., Nuccio, P.M., 2000. Geochemical evidence of melt intrusions along lithospheric faults of the Southern Apennines, Italy: geodynamic and seismogenic implications. J. Geophys. Res. Solid Earth 105 (B6), 13569–13578.

Karolytė, R., Serno, S., Johnson, G., Gilfillan, S.M., 2017. The influence of oxygen isotope exchange between CO₂ and H₂O in natural CO₂-rich spring waters: Implications for geothermometry. Appl. Geochem. 84, 173–186.

Kharaka, Y.K., Hanor, J.S., 2003. Deep fluids in the continents: I. Sedimentary basins. Treat. Geochem. 5, 605.

Langelier, W.F., Ludwig, H.F., 1942. Graphical methods for indicating the mineral character of natural waters. Journal (American water works association) 34 (3), 335–352.

Longinelli, A., Selmo, E., 2003. Isotopic composition of precipitation in Italy: a first overall map. J. Hydrol. 270 (1–2), 75–88.

Ma, R., Wang, Y., Sun, Z., Zheng, C., Ma, T., Prommer, H., 2011. Geochemical evolution of groundwater in carbonate aquifers in Taiyuan, northern China. Appl. Geochem. 26 (5), 884–897.

Maćkiewicz, A., Ratajczak, W., 1993. Principal components analysis (PCA). Comput. Geosci. 19 (3), 303–342.

Malinverno, A., Ryan, W.B., 1986. Extension in the Tyrrhenian Sea and shortening in the Apennines as result of arc migration driven by sinking of the lithosphere. Tectonics 5 (2), 227–245.

Marini, L., Chiodini, G., Cioni, R., 1986. New geothermometers for carbonate—evaporite geothermal reservoirs. Geothermics 15 (1), 77–86.

Martinez Serrano, R.G., Jacquier, B., Arnold, M., 1996. The δ34S composition of sulfates and sulfides at the Los Humeros geothermal system, Mexico and their application to physicochemical fluid evolution. J. Volcanol. Geotherm. Res. 73, 99–118.

Matsuhisa, Y., Goldsmith, J.R., Clayton, R.N., 1979. Oxygen isotopic fractionation in the system quartz-albite-anorthite-water. Geochim. Cosmochim. Acta 43 (7), 1131–1140.

Matthess, G., 1982. The Properties Of Groundwater. Wiley, New York, p. 498.

McMahon, P.B., 2012. Use of classes based on redox and groundwater age to characterize the susceptibility of principal aquifers to changes in nitrate concentrations. 1991 to 2010: U.S. Geological Survey Scientific Investigations Report 2012–5220.

Merlini, S., Mostardini, F., 1986. Appennino centro-meridionale: sezioni geologiche e proposta di modello strutturale. Geologia dell'Italia centrale. Congresso nazionale. 73, 147–149.

Michard, G., 1979. Géothermomètres chimiques. Bull de BRGM III (2), 183–189.

Minissale, A., 1991. Thermal springs in Italy: their relation to recent tectonics. Appl. Geochem. 6 (2), 201–212.

Minissale, A., 2004. Origin, transport and discharge of CO₂ in central Italy. Earth-Sci. Rev. 66 (1–2), 8–141.

Minissale, A., Donato, A., Procesi, M., Giammanco, S., Pizzino, L., 2016. Dati e Carte geochimiche del Mezzogiorno d'Italia.

Montanari, D., Minissale, A., Doveri, M., Gola, G., Trumpy, E., Santilano, A., Manzella, A., 2017. Geothermal resources within carbonate reservoirs in western Sicily (Italy): A review. Earth-Sci. Rev. 169, 180–201.

Nollet, L.M.L., 2007. Handbook of Water Analysis 2nd Ed, The Journal of Nutrition, Health Aging.

Ohmoto, H. and Rye, R.O., 1979. Isotopes of sulfur and carbon. In: H.L. Barnes (Editor), Geochemistry of Hydrothermal Ore Deposits, 2nd edition. Publisher? New York. ch. IO: 509–567.

Ortolani, F., 1975. Assetto strutturale dei Monti Picentini, della Valle del Sele e del Gruppo di Monte Marzano – Monte Ogna (Appennino Meridionale). Implicazioni idrogeologiche. Boll. Soc. Geol. It. 94, 209–230.

Panichi, C., Tongiorgi, E., 1975. Carbon isotopic composition of CO₂ from springs, fumaroles, mofettes, and travertines of central and southern Italy. Proc. 2nd U.N. Symp. Devel. Use Geothermal Resources, San Francisco 1, 815–825.

Parkhurst, D.L., Appelo, C.A.J., 2013. Description of input and examples for PHREEQC version 3—a computer program for speciation, batch-reaction, one-dimensional transport, and inverse geochemical calculations. US Geol. Survey Techniq. Methods 6 (A43), 497.

Pastorelli, S., Marini, L., Hunziker, J.C., 1999. Water chemistry and isotope composition of the Acquarossa thermal system, Ticino, Switzerland. Geothermics 28 (1), 75–93.

Patacca, E., Scandone, P., 2007. Geology of the southern Apennines. Bollettino Società Geol. Ital. 7, 75–119.

Paternoster, M., Parisi, S., Caracausi, A., Favara, R., Mongelli, G., 2010. Groundwaters of Mt. Vulture volcano, southern Italy: chemistry and sulfur isotope composition of dissolved sulfate. Geochem. J. 44 (2), 125–135.

Paternoster, M., Oggiano, G., Sinisi, R., Caracausi, A., Mongelli, G., 2017. Geochemistry of two contrasting deep fluids in the Sardinia microplate (western Mediterranean): Relationships with tectonics and heat sources. J. Volcanol. Geotherm. Res. 336, 108–117.

Petitta, M., Primavera, P., Tuccimei, P., Aravena, R., 2011. Interaction between deep and shallow groundwater systems in areas affected by Quaternary tectonics (Central Italy): a geochemical and isotope approach. Environ. Earth Sci. 63 (1), 11–30.

Pierdominici, S., Mariucci, M.T., Montone, P., 2011. A study to constrain the geometry of an active fault in southern Italy through borehole breakouts and downhole logs. J. Geodyn. 52 (3–4), 279–289.

Qiu, X., Wang, Y., Wang, Z., Regenauer-Lieb, K., Zhang, K., Liu, J., 2018. Determining the origin, circulation path and residence time of geothermal groundwater using multiple isotopic techniques in the Heyuan Fault Zone of Southern China. J. Hydrol. 567, 339–350.

Richet, P., Bottinga, Y., Javoy, M., 1977. A review of hydrogen, carbon, nitrogen, oxygen, sulphur, and chlorine stable isotope fractionation among gaseous molecules. Annu. Rev. Earth Planet. Sci. 5 (1), 65–110.

Sanford, W., 2011. Calibration of models using groundwater age. Hydrogeol. J. 19 (1), 13–16.

Sharp, Z. (2017). Principles of stable isotope geochemistry.

Shevenell, L., Goff, F., 1995. The use of tritium in groundwater to determine fluid mean residence times of Valles caldera hydrothermal fluids, New Mexico. USA. J. Volcanol. Geotherm. Res. 67 (1–3), 187–205.

Shiner, P., Beccacini, A., Mazzoli, S., 2004. Thin-skinned versus thick-skinned structural models for Apulian carbonate reservoirs: constraints from the Val d'Agri Fields, S Apennines. Italy. Mar. Pet. Geol. 21 (7), 805–827.

Sibson, R.H., Moore, J.M.M., Rankin, A.H., 1975. Seismic pumping—a hydrothermal fluid transport mechanism. Journal of the Geological Society 131 (6), 653–659.

Slejko, D., Peruzza, L., Rebez, A., 1998. Seismic hazard maps of Italy.

Smeraglia, L., Bernasconi, S.M., Berra, F., Billi, A., Boschi, C., Caracausi, A., Carminati, E., Castorina, F., Doglioni, C., Italiano, F., Rizzo, L.A., Uysal, I.T., Zhao, J. X., 2018. Crustal-scale fluid circulation and co-seismic shallow comb-veining along the longest normal fault of the central Apennines. Italy. Earth Planet. Sci. Lett. 498, 152–168.

Smeraglia, L., Aldega, L., Bernasconi, S.M., Billi, A., Boschi, C., Caracausi, A., Carminati, E., Franchini, S., Rizzo, A.L., Rossetti, F., Vignaroli, G., 2020. The role of trapped fluids during the development and deformation of a carbonate/shale intra-wedge tectonic mélange (Mt. Massico, Southern Apennines, Italy). J. Struct. Geol. 138, 104086.

Tarquini, S., Isola, I., Favalli, M., Mazzarini, F., Bisson, M., Pareschi, M.T., Boschi, E., 2007. TINITALY/01: a new triangular irregular network of Italy. Ann, Geophys.

Toscani, L., Boschetti, T., Maffini, M., Barbieri, M., Mucchino, C., 2007. The groundwaters of Fontevivo (Parma Province, Italy): redox processes and mixing with brine waters. Geochem.: Explor. Environ. Anal. 7 (1), 23–40.

Toth, J., 1995. Hydraulic continuity in large sedimentary basins. Hydrogeol. J. 3 (4), 4–16.

Trippetta, F., Collettini, C., Barchi, M.R., Lupattelli, A., Mirabella, F., 2013. A multidisciplinary study of a natural example of a CO₂ geological reservoir in central Italy. Int. J. Greenh. Gas Control. 12, 72–83.

Truesdell, A. H. 1976. Summary of section III-geochemical techniques in exploration. In Proc. 2nd UN Symp. on the Development and Use of Geothermal Resources (Vol. 1, pp. 1iii-1xxix).

Valoroso, L., Improta, L., De Gori, P., Chiarabba, C., 2011. Upper crustal structure, seismicity and pore pressure variations in an extensional seismic belt through 3-D and 4-D VP and VP/VS models: The example of the Val d'Agri area (southern Italy). J. Geophys. Res. Solid Earth 116 (B7).

Vannoli, P., Martinelli, G., Valensise, G., 2021. The seismotectonic significance of geofluids in Italy. Front. Earth Sci. 9, 25.

Vespasiano, G., Marini, L., Muto, F., Auqué, L.F., Cipriani, M., De Rosa, R., Critelli, S., Gimeno, M.J., Blasco, M., Dotsika, E., Apollaro, C., 2021. Chemical, isotopic and geotectonic relations of the warm and cold waters of the Cotronei (Ponte Coniglio), Bruciarello and Repole thermal areas (Calabria-Southern Italy). Geothermics 96, 102228.

Vitale, S., Ciarcia, S., 2018. Tectono-stratigraphic setting of the Campania region (southern Italy). J. Maps 14 (2), 9–21.

Wang, H.Y., Guo, H.M., Xiu, W., Bauer, J., Sun, G.X., Tang, X.H., Norra, S., 2019. Indications that weathering of evaporite minerals affects groundwater salinity and As mobilization in aquifers of the northwestern Hetao Basin. China. Appl. Geochem. 109, 104416.

Wang, B., Jin, M., Nimmo, J.R., Yang, L., Wang, W., 2008. Estimating groundwater recharge in Hebei Plain, China under varying land use practices using tritium and bromide tracers. J Hydrol. 356 (1–2), 209–222.

Wang, J., Jin, M., Jia, B., Kang, F., 2015. Hydrochemical characteristics and geothermometry applications of thermal groundwater in northern Jinan, Shandong, China. Geothermics 57, 185–195.

Wasowski, J., Pierri, V., Pierri, P., Capolongo, D., 2002. Factors controlling seismic susceptibility of the Sele valley slopes: the case of the 1980 Irpinia earthquake re-examined. Surv. Geophys. 23 (6), 563–593.

Yan, Q., Gao, Z., Ni, S., Shi, Z., Yin, G., 2013. Evolution of isotopic composition and deuterium excess of brines in the Sichuan Basin. China. Chinese J. Chem. 32 (1), 69–77.

Yang, P., Luo, D., Hong, A., Ham, B., Xie, S., Ming, X., Wang, Z., Pang, Z., 2019. Hydrogeochemistry and geothermometry of the carbonate-evaporite aquifers controlled by deep-seated faults using major ions and environmental isotopes. J. Hydrol. 579, 124116.

15

5.5 Understanding the origin and mixing of deep fluids in shallow aquifers and possible implications for crustal deformation studies: San Vittorino Plain, Central Apennines

Marino Domenico Barberio[1], Francesca Gori[1], Maurizio Barbieri[1], Tiziano Boschetti[2], Antonio Caracausi[3], Giovanni Luca Cardello[1,4], Marco Petitta[1,*]

[1] Earth Sciences Department, Sapienza University of Rome, Italy;

[2] Department of Chemistry, Life Sciences and Environmental Sustainability, University of Parma, Italy;

[3] National Institute of Geophysics and Volcanology, Palermo, Italy;

[4] Department of Chemistry and Pharmacy, University of Sassari, Italy;

* Corresponding author: Marco Petitta, Earth Sciences Department, Sapienza University of Rome, P.le Aldo Moro 5, 00185, Rome, Italy; email: marco.petitta@uniroma1.it tel. (+39) 064991 4834

Understanding the Origin and Mixing of Deep Fluids in Shallow Aquifers and Possible Implications for Crustal Deformation Studies: San Vittorino Plain, Central Apennines

Marino Domenico Barberio [1], Francesca Gori [1], Maurizio Barbieri [1], Tiziano Boschetti [2], Antonio Caracausi [3], Giovanni Luca Cardello [4] and Marco Petitta [1,*]

1 Earth Sciences Department, Sapienza University of Rome, 00185 Rome, Italy; marinodomenico.barberio@uniroma1.it (M.D.B.); francesca.gori@uniroma1.it (F.G.); maurizio.barbieri@uniroma1.it (M.B.)
2 Department of Chemistry, Life Sciences and Environmental Sustainability, University of Parma, 43124 Parma, Italy; tiziano.boschetti@unipr.it
3 National Institute of Geophysics and Volcanology, 90146 Palermo, Italy; antonio.caracausi@ingv.it
4 Department of Chemistry and Pharmacy, University of Sassari, 07100 Sassari, Italy; glcardello@uniss.it
* Correspondence: marco.petitta@uniroma1.it; Tel.: +39-064991-4834

Abstract: Expanding knowledge about the origin and mixing of deep fluids and the water–rock–gas interactions in aquifer systems can represent an improvement in the comprehension of crustal deformation processes. An analysis of the deep and meteoric fluid contributions to a regional groundwater circulation model in an active seismic area has been carried out. We performed two hydrogeochemical screenings of 15 springs in the San Vittorino Plain (central Italy). Furthermore, we updated the San Vittorino Plain structural setting with a new geological map and cross-sections, highlighting how and where the aquifers are intersected by faults. The application of Na-Li geothermometers, coupled with trace element and gas analyses, agrees in attributing the highest temperatures (>150 °C), the greatest enrichments in Li (124.3 ppb) and Cs (>5 ppb), and traces of mantle-derived He (1–2%) to springs located in correspondence with high-angle faults (i.e., S5, S11, S13, and S15). This evidence points out the role of faults acting as vehicles for deep fluids into regional carbonate aquifers. These results highlight the criteria for identifying the most suitable sites for monitoring variations in groundwater geochemistry due to the uprising of deep fluids modulated by fault activity to be further correlated with crustal deformation and possibly with seismicity.

Keywords: groundwater mixing; deep fluids; earthquake-hydrology; isotope; geochemistry

1. Introduction

Groundwater hydrogeochemistry is closely related to the nature of the aquifer and to the length and depth of the groundwater flow paths, and it strongly depends on the residence time [1,2]. However, structural-geological features (e.g., faults and the tectonic pattern distribution) can also affect the water chemistry, as they allow and facilitate the mixing of groundwater of different origins [3,4]. While down-going fluids may be of meteoric (or even karstic) origin, uprising fluids may connect the lowermost parts of a stratified aquifer to the surface. Direct field evidence of exhumed seismogenic zones in carbonate rocks furnishes a fossilized example of how high pore-fluid pressure currently is at depth [5,6]. In these contexts, the vein and fault record demonstrated that isotopic equilibrium can be interrupted during exhumation by transient thoroughgoing faulting, allowing meteoric fluids to reach otherwise rock-buffered fluid systems [7–9]. Additionally, deep fluids play an active role in the seismic cycle and fault activation mechanisms, which are increasingly highlighted in geoscience studies [10–18]. For this reason, in recent decades, works aimed at identifying signals that can anticipate strong seismic events in field and laboratory activities have been intensified [3,19–25]. These studies have

identified variations in the concentration of gases such as He, Rn, CO_2, H, and CH_4 [26,27], groundwater chemical content [3,21,22], and the physical properties of rocks [28,29].

However, determining the origin of fluids in shallow aquifers and answering the questions of where and how these fluids originate, and determining the possible water–gas–rock interaction processes during their migration, can provide new constraints for understanding the processes related to seismogenic processes. Research in this direction has mainly deepened the understanding of fluid origins, focusing on the determination of quantities useful to define their origin and mixing. In detail, some conservative elements in waters (e.g., As, V, Fe, Li, Cs, and Rb) and isotopes of some gaseous species (e.g., He and Ar) have been recognized and used as tracers that are often not bound to a circulation model [21,30–33]. In this frame, the central Apennines mountain belt in central Italy represents a natural laboratory to efficiently examine these topics, both for its tectonic-structural framework [34], the abundance of groundwater resources [35], and the rise of deep fluids along normal faults [11–13,36,37].

In addition, the nature of the regional aquifers hosted by fractured Meso–Cenozoic carbonates with limited karst development [38] enhances the response to deep fluids uprising through the shallow crustal layers, possibly allowing fast and concentrated changes in groundwater close to high-angle faults, coupled with smoothed and aquifer-wide less evident effects on hydrogeochemistry. Thus, to improve the comprehension of the relationships of both deep and shallow fluids in regional aquifers, we conducted an integrated study of the regional hydrostructures and water composition in the San Vittorino Plain, an intramontane basin in the central Apennines. In fact, this plain is characterized by an abundance of water resources [38,39] and large diffuse active degassing focused along high-angle faults [36]. Overall, the area is defined by different fault systems related to the different steps of the regional structural history [40], and there are traces of Quaternary volcanism [41,42]. In addition, according to a recent study [37] which aimed to evaluate the aquifer's potential susceptibility to be affected by detectable chemical-physical anomalies during seismogenic processes, the San Vittorino Plain has been placed at the "top-ranking position" as one of the most suitable areas for the monitoring of seismic activity in central Italy by groundwater monitoring.

By sampling and analyzing 15 springs with different degrees of mineralization and gaseous contents, combined data of the chemical composition (chemical-physical parameters, major and minor elements, and free and dissolved gases), isotopic ratios ($\delta D/\delta^{18}O$-H_2O, $\delta^{13}C$-CO_2, He, and Ar), and Na/Li geothermometry were used to establish first the origin and then the mixing extent of the deep and shallow fluids into the San Vittorino Plain aquifers. We investigated the role of thermodynamic balance, established among gas, water, and rock, and the secondary processes that influence aquifer chemistry, providing new insights for understanding hydrogeochemical variations as a function of crustal deformations in the framework of a well-known hydrogeological conceptual model [38,43].

In summary, the aim of this research was to improve the comprehension of the mechanisms of deep fluid rise and mixing in large regional aquifers to better understand: (i) the role of the different local fault systems and regional crustal structures in spreading deep fluids in aquifers and related springs; and (ii) the identification of criteria for establishing useful groundwater monitoring of the changes in mixing of these fluids with time and space as a function of crustal deformation and, consequently, their correlation with micro- and possibly macro-seismicity of the area.

2. Geological and Hydrogeological Setting

2.1. Apennines Tectonics Summary

The fold-and-thrust belt structure between the northern and central Apennines has developed since the Oligocene, with a main east to northeastward vergence (Figure 1) [34,44–46]. Generally, the carbonate domains of the Apennines were affected during the late Triassic, early Jurassic, and early Cretaceous by syn- to late-rift tectonic effects, which determined sedimentary successions with long-living platforms to the east of the study area and the

basinal domains to the west and north of it [47,48]. The Reatini Mountains (Mts) are composed of Mesozoic carbonate pelagic successions (basinal units), while the Giano Mt. and Nuria Mt. are made of thick shallow water carbonate successions (Figure 1). During the late Cretaceous, shallow water platforms were further fragmented and drowned at their rims. Until the early Miocene, this allowed the deposition of basinal to escarpment sediments (e.g., Navegna Basin, Figure 1). In the middle Miocene, outer to inner carbonate ramp units were deposited on the different downstepped blocks that were then invaded by thick synorogenic successions during the late Miocene [49]. Further, during the late Miocene orogenic phase, these units piled up towards East-North-East in the fold-thrust belt [50]. The postorogenic extensional tectonics and erosion started from the Pliocene and are still ongoing [51,52]. This crustal regime enhanced the development of intramontane plains and alluvial valleys among the carbonate ridges (Figure 1) [53]. The deep structure of the study area is poorly constrained due to the scarcity of available wells and absence of seismic lines, and the uncertainty of the thickness and continuity of the structural units.
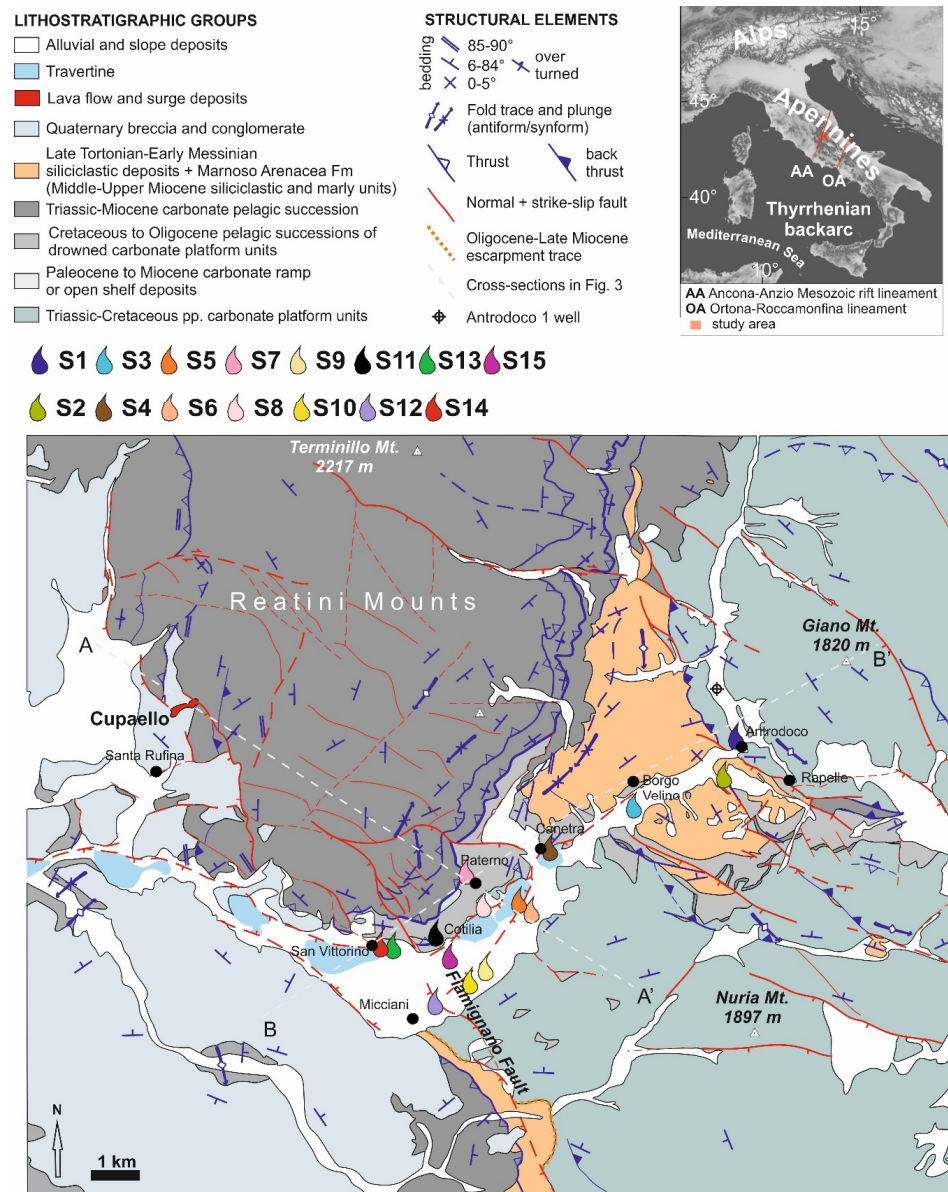
Figure 1. Simplified tectonic map of the study area modified after the compared review of Foglio "L'Aquila" and "Rieti" (https://www.isprambiente.gov.it/ accessed on 3 February 2021) [40,49,50,54,55]. The map shows the location of the selected springs.

2.2. The San Vittorino Plain Structure

The San Vittorino Plain is one of the intramontane basins of the Apennines (elevation of 400–425 m a.s.l.) and is defined as a complex graben with a length of approximately 4 km and a width of approximately 2 km, hosting the Velino River. The plain is located between the Latium–Abruzzi neritic carbonate platform domain (Giano Mt. and Nuria Mt. ridge, on the east; Figure 1) and the Umbria–Marche–Sabina basinal domain on the west (Reatini Mounts) [39,40]. The area has recorded regional polyphase tectonic activity. In particular, traditionally, the Ancona–Anzio lineament ([56,57] and references therein) was reactivated during the late Miocene as a transpressive front that subdivides the northern from the central Apennines (i.e., the Olevano–Antrodoco–Sibillini line) [58]. These factors allowed the basinal domain to overthrust the platform together with its late Miocene synorogenic deposits (e.g., siliciclastic deposits). The fold-and-thrust structure was later affected by regional uplift and was passively cross-cut by Quaternary transtensive structures allowing the sedimentation of thick lower-middle Pleistocene breccia and conglomerates within tight continental graben-like basins [46,59–61]. Lateral and vertical heteropic stratigraphic contacts occur within the clastic deposits of the plain subsoil, while several fault systems define the tectonic network in this area [40] (Figure 1). Among these faults, the Fiamignano Fault is one of the most relevant normal faults and related paleoescarpments. It trends NW–SE and dips to the SW (Figure 1), showing polyphase activity during the Cenozoic and later also during the Quaternary [40,47,49]. Further, NE-striking faults occur in the San Vittorino Plain, downthrowing the Meso–Cenozoic carbonates in the graben. Nearly N-striking transtensive faults occur at the western edge of the Reatini Mounts, bounding continental clastic successions. Near their top, the Cupaello eruptive center (melilititic ultrapotassic kamafugites and carbonatites: the last activity 0.64 Myr ago; Figure 1), occurs at a major fault [41,42].

2.3. Hydrogeological Setting

The carbonate ridges in the central Apennines correspond to wide recharge areas of the main fractured regional aquifers that can store large quantities of groundwater. Groundwater flow in fractured carbonate aquifers is laterally limited by continental depositional sequences in the intramontane plains, and tectonic activity induces continuous base-level changes in the aquifers [39,62]. These conditions have possibly hindered the development of a mature karst network in the discharge areas of the aquifers [63]. Therefore, in such wide aquifers (up to 1000 km^2), an impulsive response to seasonal recharge is not recognizable, as stated by very high and steady spring discharges [39], located at the boundaries of the carbonate aquifers limited by recent clastic and alluvial deposits. The San Vittorino Plain hosts the discharge of large carbonate aquifers; for example, the Giano–Nuria–Velino Mts hydrogeological system [38,39] (Figure 1). These fractured ridges, belonging to the carbonate platform domain, are highly permeable due to fracturing and karst processes in the recharge zone, with a total recharge area of approximately 1016 km^2, and effective infiltration of 880 mm/yr vs. the average precipitation of over 1200 mm/yr [35,64]. These carbonate aquifers feed spring groups with a total discharge of approximately 30 m^3/s [39]. The main springs are located on the southern and northern boundaries of the San Vittorino Plain and include the Peschiera springs (S10 (Figure 1), 18 m^3/s), partially exploited for drinking purposes; the streambed springs of Antrodoco (approximately 2 m^3/s), the spring group of Canetra (S4, 4.5 m^3/s), San Vittorino (S14, 0.5 m^3/s), and the highly mineralized springs of Terme di Cotilia (S11, 0.25 m^3/s). On the other hand, the Paterno perched spring, located on the right slope of the Velino River, is fed by the Mt. Paterno–Canetra ridge (S7, Figure 1). This minor hydrogeological unit also contributes to regional groundwater recharge.

In addition, spring locations and hydrogeochemistry are influenced by tectonics and the different permeabilities of the alluvial/clastic layers of the plain, having variable widths, up to approximately 200 m. Groundwater from carbonate aquifers can undergo chemical-physical variations upon its transfer towards the alluvial shallow aquifer. Consequently,

the springs of the area have different hydrogeochemical characteristics that are also the result of active degassing in the middle valley of the Velino River [31,36,38,39,43,65]. Hence, mixing induced by deep fluid inputs, whose upward movements occur along tectonic discontinuities and are partially buried by recent clastic deposits, may cause progressive and significant hydrogeochemical changes in the springs.

Although the San Vittorino Plain is far from having any evidence of active volcanism, it is characterized by relevant gas emissions, with a maximum CO_2 flux of 5.7×10^{-5} kg m^{-2} d^{-1} [31,38,66]. In some cases, the aggressiveness of the waters conferred by gaseous contributions can promote the development of collapse phenomena, so-called sinkholes [67]. Through the assessment of the chemical composition of the fluids associated with the sinkholes of the plain, the origin of this CO_2 was explained as being the combination of both a mantle source and a product of thermometamorphic reactions within the buried Meso–Cenozoic limestone [68].

3. Methods

3.1. Sampling and Analysis

To characterize the hydrogeochemistry of groundwater in the study area, 15 of the most representative springs with different geochemical features were selected (e.g., from low to high mineralization, the presence and/or absence of free gases and bubbling) from among approximately 80 springs measured in previous studies [39]. Water samples were collected during two surveys performed in October 2018 and January 2019. In each sampling campaign, chemical-physical parameters (temperature, pH, and electrical conductivity) were also measured on-site through the multiparametric probe WTW Multi 3620 IDS.

The collected samples for several analyses (including major and trace elements, stable isotope of water, dissolved and free gases, and noble gas isotope ratio) were kept at low temperatures in ice-filled fridge boxes to avoid alterations of components prior to the laboratory analyses. Samples for the determination of major (anions and cations) and trace element concentrations were analyzed at the Geochemistry Laboratory of Earth Sciences Department of Sapienza University (Rome, Italy). Samples for analysis of the stable isotopes ($\delta^{18}O$-H_2O and δD-H_2O), gaseous contents, and isotopic ratios were sent to the geochemistry laboratories of the National Institute of Geophysics and Volcanology of Palermo.

Samples for the major and trace element analyses were filtered in situ through a 0.45 µm filter into polyethylene bottles. In addition, waters collected for trace element analysis were acidified with added concentrated ultrapure HNO_3 to prevent the precipitation of metals. Samples for the analyses of stable isotopes and dissolved gases were collected in glass bottles. Gas samples were collected in Pyrex bottles with vacuum valves at both ends, taking care to prevent air contamination.

For the determination of major ions, samples were analyzed by ion chromatography. Waters with a high electrical conductivity (greater than 800 µS/cm) were diluted with ultrapure water before inserting them into the chromatograph.

To determine the anionic content (F$^-$, Cl$^-$, SO$_4^{2-}$, and NO$_3^-$), a Dionex ICS 5000 chromatograph was used, while the cationic content (Ca^{2+}, Mg^{2+}, Na$^+$, and K$^+$) was determined by a Dionex ICS 1100 chromatograph. The analytical error associated with these instruments is less than 5%, as also testified by the cation–anion balance checked on each sample [69]. The software Dionex Chromeleon, connected to both chromatographs, allowed us to know the concentrations of each major ion of the sampled waters in terms of ppm (mg/L). Alkalinity was measured by titration with 0.05 N HCl on site.

Analysis of the trace elements was carried out using an ICP-MS spectrometer (X Series 2 Thermo Fisher Scientific Waltham, MA, USA). Ultrapure water (Millipore, Milli-Q, 16 MΩ cm) was used to prepare blanks, standard solutions, and sample dilutions, and an internal standard, Rh, was added to correct the ICP-MS instrumental drift. The analytical accuracy of this method ranges between 2% and 5% [21,70].

Measurement of the stable isotopes of water ($\delta^{18}O$ and δD) was carried out on samples collected in the first campaign (October 2018) to improve the hydrogeochemical model and to understand the mixing processes between the waters of the regional karst system and those of deep origin. These analyses were performed at the Istituto Nazionale di Geofisica e Vulcanologia of Palermo, Sicily, Italy.

The isotopic ratio of oxygen was measured using a Thermo Delta V Plus mass spectrometer coupled to a GasBench II, exploiting the equilibration technique between H_2O and CO_2 [71]. For the determination of the hydrogen isotopic ratio, a Delta Plus XP mass spectrometer coupled with a TC/EA reactor was utilized. The isotopic values for the waters are expressed in δ‰ vs V-SMOW (Vienna Standard Mean Oceanic Water). The uncertainties were $\pm$ 0.1% for $\delta^{18}O$ and $\pm$ 1% for δD. A fast and completely automated procedure to determine the $\delta^{13}C$ (as V-PDB, Vienna Pee Dee Belemnite) of total inorganic carbon dissolved in water ($\delta^{13}C_{DIC}$) was utilized [72]. This method is based on the acidification of water samples transforming the whole dissolved inorganic carbon species into CO_2. Water samples are directly injected with a syringe into vials with screw caps that have a pierceable rubber septum. A GasBench II was used both to flush pure helium into the vials and to automatically dispense a fixed amount of H_3PO_4. Full-equilibrium conditions between the produced CO_2 and water are reached at a temperature of 70 °C ($\pm$ 0.1 °C) in less than 24 h. Carbon isotope ratios ($^{13}C/^{12}C$) were measured on a Delta V Plus mass spectrometer connected online with GasBench II.

The dissolved gas content was determined with a gas chromatograph (Perkin Elmer 8500) with an Ar carrier on a 4 m column (Carbosieve SII) and double detector (TCD and FID – Thermal and Flame Ionization Detector, respectively) [73]. The analytical error was evaluated to be approximately $\pm$ 3% for all gaseous species. Based on the solubility data of gaseous species in water, the concentrations of the dissolved gases in the water were calculated [74] and also corrected for atmospheric contamination, taking into account the N_2/O_2 ratio in the samples and comparing it with the same ratio in the atmosphere.

He isotopes were analyzed with a static vacuum mass spectrometer (GVI Helix SFT), characterized by a double collector that allows the simultaneous detection of the ^3He and ^4He ion beams (isotopic precision ratio within $\pm$ 0.5%). The $^3He/^4He$ ratio was obtained by measuring ^3He and ^4He in an electron multiplier detector and in an axial Faraday detector, respectively. Ne isotopes were measured by a multi-collector mass spectrometer (model Thermo-Helix MC plus) after standard purification procedures ([17] and references therein). He isotopic ratios are reported as R/Ra values, where Ra is the He-isotope ratio in the atmosphere (1.39×10^{-6}). Overall, analyses of gases (free, dissolved, and isotopes) were provided in the noble gases laboratory at the Istituto Nazionale di Geofisica e Vulcanologia of Palermo.

3.2. Thermodynamic and Isotopic Calculations

The mineral saturation indices and the partial pressure of dissolved carbon dioxide as $logP(CO_2)$ were calculated using the PHREEQC Interactive code (PHREEQCi version 3) and the llnl.dat/thermo.com.v8.dat thermodynamic databases [75]. To check the uncertainty related to different data sets and calculation methods of the activity coefficients (i.e., Debye–Hückel, B-Dot), the parameters for selected samples with the Spec8 tool of The Geochemist's Workbench's® code (release 12) [76] and the thermo.dat thermodynamic datasets were also calculated. The same codes were used to calculate the molality of the so-called C_{ext} parameter, i.e., the carbon from external sources derived from processes other than the interaction with carbonate rocks (C_{carb}) [33,77]. In addition, to evaluate the $\delta^{13}C$ isotope composition of CO_2 ($\delta^{13}C_{ext}$) in the inspected water samples [33], the NetpathXL 1.5 code was used [78,79]. The input data for this latter code were the $\delta^{13}C_{DIC}$ values, chemical-physical parameters (pH, T) and chemical composition of the water samples. During calculation, the value of $\delta^{13}C_{carb}$ = +2.2‰ was assumed to be the isotopic composition of the carbonate aquifer [80,81]. The obtained $\delta^{13}C_{ext}$ results are substantially the same if we also take into account the difference in the isotope composition of the Mesozoic

carbonate minerals in the Antrodoco area [82]: $\delta^{13}C_{dolomite}$ = +2.7‰ and $\delta^{13}C_{calcite}$ = +1.6‰. However, in comparison with the similar approach of [36], the $\delta^{13}C_{ext}$ calculated by Netpath showed an enrichment of approximately +1.13 ‰, because the code takes into account the fractionation effect related to carbon dioxide solubilization: $CO_2(g) \rightarrow CO_2(aq)$ [33]. Finally, the statistical significance of the ordinary least square (OLS) regressions was checked using both the OriginLab code [83] and the table of critical values for Pearson's r correlation coefficient from the N parameter (two-tailed test).

3.3. Map Review and Cross-Section Construction

The lithostratigraphic architecture of the carbonate succession has been reviewed into a new geological map (Figure 1) that was produced after the grouping of the different lithostratigraphic units reported in the ISPRA dataset and in the literature [49,50,54,84]. We have thus harmonized the stratigraphic and tectonic information published in the 1:100,000 maps (L'Aquila, Rieti; https://www.isprambiente.gov.it/ accessed on 3 February 2021), and we also considered the distribution of the Quaternary deposits [55].

To build the geological cross-sections, bibliographic and available stratigraphic information were compared. The basal decollement was extrapolated from the position of the evaporites in [84]. Cross-sections were drawn perpendicular to the main direction of transport during convergence and subparallel to the strike to provide a 3D sketch overview of the deep circulation of the fluids. The thickness of the units is virtually constant. The attitude of the layers at the surface guides the interpretation of the deeper structures. The Antrodoco 001 well stratigraphy has been reported, as it is available from a public data set (available online: https://www.videpi.com accessed on 3 February 2021).

4. Results

The 15 sampled springs are characterized by moderate to high salinity. The hydrogeochemical facies are Ca-HCO$_3$ and Ca-SO$_4$ types [38,39,43]. In addition, some springs show continuous bubbling of free gases [31,68].

4.1. Hydrogeochemical Results: Chemical-Physical Parameters, Major and Trace Elements, and H$_2$O Stable Isotope Ratio

The chemical-physical parameters (e.g., temperature, pH, and electrical conductivity) and trace element concentrations of each survey are presented in Supplementary File Table S1.

The Piper diagram [85] (Figure 2) shows two main hydrogeochemical facies. As expected, waters are predominantly enriched in bicarbonate and calcium ions (Ca-HCO$_3$ facies). The freshwater endmember is represented by S7. The other springs, despite showing the same hydrogeochemical facies, are progressively enriched in SO$_4$ and Mg. This condition is attributable to the increase in the water–rock interaction due to the flow path in the main aquifer and/or the progressive mixing with groundwater that has different chemical compositions. Only springs of the Antrodoco area (i.e., S1 and S2) are included in the calcium-sulphate waters domain (Ca-SO$_4$ facies). This evidence suggests the circulation of this groundwater in Triassic carbonate-evaporitic formations and limited dilution with Ca-HCO$_3$ water.
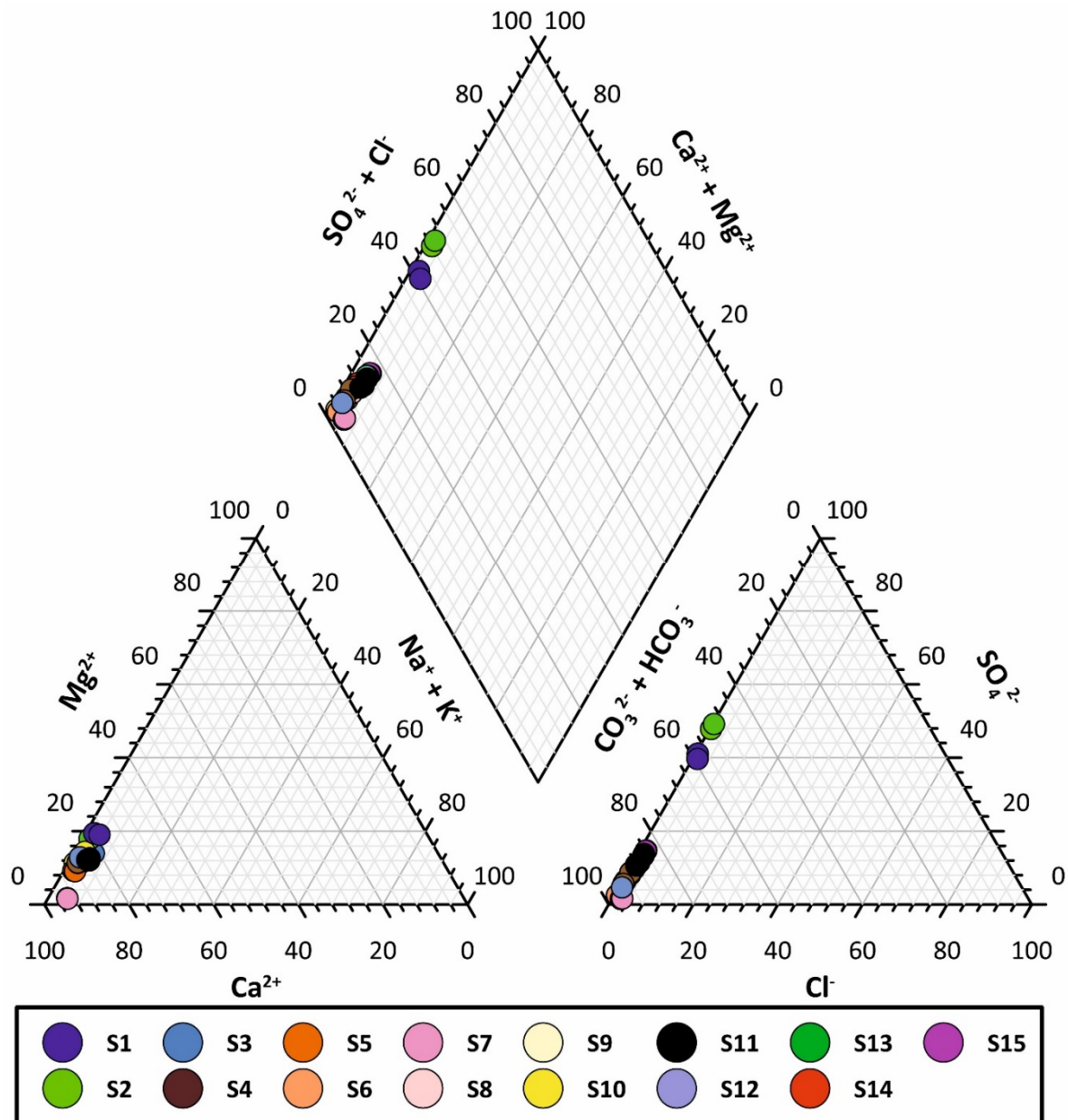
Figure 2. Piper diagram of groundwater samples from the San Vittorino Plain. All samples are predominantly enriched in bicarbonate and calcium ions (fresh waters and mixing waters; Ca-HCO$_3$ facies). Only springs of the Antrodoco area (i.e., S1 and S2) are included in the calcium-sulphate waters domain (mineralized waters; Ca-SO$_4$ facies). For spring location see Figure 1.

Stable isotopic analyses of water sampled in October 2018 were carried out to investigate their origin and groundwater flow paths, as well as to eventually determine the physical processes and chemical reactions that take place during groundwater flow. The springs are characterized by isotopic values from −8.9 to −9.8‰ and from −53 to −62‰ for δ^{18}O and for δ^2H, respectively (see Supplementary File Table S1).

4.2. Gas Geochemical Results: Dissolved and Free Gases, Noble Gas, and Isotope Ratio

The collected samples refer to both free and dissolved gases depending on the presence/absence of bubbling in the water of selected springs in each survey. Only four samples for free gases were taken in January 2019.

The results of the performed gas analyses (both free and dissolved gases) are reported in Supplementary File Table S1. Almost all water samples are CO$_2$ dominated with

concentrations ranging from 3.1 to 663.7 ccSTP/L. Some springs (e.g., S3, S6, and S12) recorded concentrations that were lower than the detection limit. Similarly, CH_4 was also measured only in some springs (Supplementary File Table S1) with concentrations between 5.21×10^{-5} and 1.52×10^{-3} ccSTP/L. Helium concentrations vary from 3.19×10^{-4} to 3.92×10^{-3} ccSTP/L. He-isotope composition in the collected fluids ranges from 0.07 Ra to 0.15 Ra. The $^4He/^{20}Ne$ ratios of all investigated fluids are generally higher than 0.318 (i.e., the value of the atmosphere) [86], indicating that air contamination was negligible [73]. The only exception is the sample collected at S11, in which $^4He/^{20}Ne$ is lower than 1, showing that this sample is affected by air contamination. All the samples have $^{40}Ar/^{36}Ar$ ratios that are indistinguishable from the ratio in the atmosphere.

4.3. Deep Structural Interpretation

In light of our structural review, we hereby present two geological cross-sections (Figure 3), aiming at providing a structural sketch for the possible paths of fluid circulation within the studied complex aquifer down to a depth of approximately 5–6 km. Field evidence allows us to trace at depth a persistent Jurassic–Miocene carbonate pelagic succession that crops out in the west and includes Triassic evaporites and dolomites, and early Jurassic fractured and porous carbonates (Reatini Unit). In the east, we also distinguish two Triassic–Cretaceous carbonate platform units (i.e., Nuria Mt and Giano Mt). Additionally, the Reatini Unit is internally affected by several thrusts. The overall structural set is dominated by imbricated thrust sheets that involve pre-existing normal faults (orange lines) with associated syn-sedimentary units of variable thickness and facies distribution. These transitional units consist of Cretaceous to Oligocene pelagic successions with resediments shedding out the platform that deposited on top of drowned carbonate platform units. North of the Nuria Mt., they are further topped by middle Miocene carbonate ramp deposits. More to the SW, the Nuria Mt. succession consists of Paleocene to Miocene open shelf to basinal deposits, possibly deposited onto transitional Mesozoic carbonate units. By inverting the basin structures, thrust tectonics determined the occurrence of a thick thrust zone that displays a transpressive lateral ramp with the overturned Reatini Unit on the hanging wall and the Nuria Unit at its footwall (Figure 3). The transitional units within the thrust zone are further imbricated with tectonic lenses of more competent carbonate units, S/C shear fabrics (schistosity/cisaillement), and folds in the more marly units. The oldest fold-and-thrust structure is further crosscut by two major backthrusts that cross-cut both the pelagic succession and, possibly, the Nuria Mt. (cross-section AA', Figure 3). At Antrodoco, the high-angle contact between the Triassic dolomites and the late Tortonian–early Messinian siliciclastic units is interpreted as being intercepted by the Antrodoco 001 well. This suggests that a major backthrust accompanies the formation of a triangular zone (cross-section BB', Figure 3). Finally, to the southwest and to the west, stepwise segments of the normal oblique faults bound the Reatini Mounts and the Nuria Mt. normal fault systems are characterized by lateral strike deviation and offset reduction to a few hundred meters at the fault tips. In our interpretation, these faults, bounding also the San Vittorino Plain, cross-cut the entire fold-and-thrust structure.
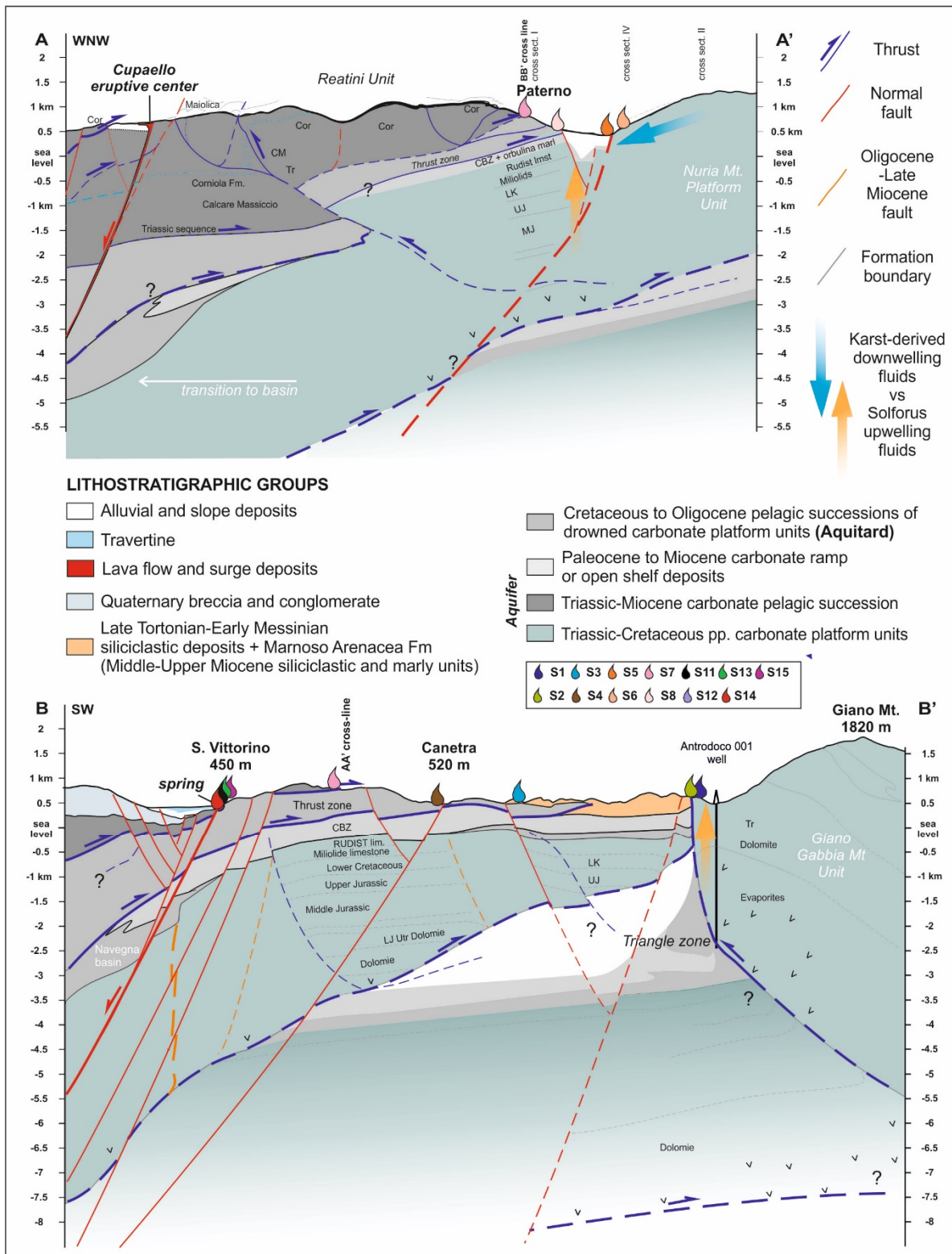
Figure 3. Geological cross-sections showing a sketched reconstruction of the fold-and-thrust belt architecture, which is cross-cut by high-angle transtensive faults. The figure also shows the projection of the Antrodoco 001 well, which intercepts the backthrust tilting the Giano–Gabbia Mt. unit. See Figure 1 for the trace of the cross-sections and relative intersection from [54].

5. Discussion

Previous investigations based on the hydrogeochemistry of the fluids [43,65] highlighted that the groundwater hydrogeochemistry of the San Vittorino Plain is the result of the addition of deep fluids (i.e., mantle-derived and crustal fluids) to the shallow groundwater circulating in a regional carbonate fractured aquifer. All of the selected springs represent the main discharge points and are not affected by surface runoff.

Based on chemical parameters, in the Piper diagram, the groundwater of the 15 selected springs seems to be aligned along a single mixing trend or evolutionary path, whose end-members are Ca-HCO$_3$ and Ca-SO$_4$ types (Figure 2). However, a closer look at the bicarbonate corner of the Langelier–Ludwig diagram, which has the same meaning as the central diamond in Piper's plot (Figure S1), reveals at least two possible evolutionary trends: (i) an increase of the sulphate concentration in the Antrodoco area (i.e., S1 and S2) due to dissolution of Upper Triassic gypsum/anhydrite; and (ii) a trend from samples with higher HCO$_3$ relative concentrations, Peschiera/Paterno areas (S10, S7, S8), towards the S11 and S15 samples. Furthermore, the comparison with the historical data of the selected springs showed that the systematic enrichments of alkali elements Na and K, relative to alkaline earth metals Ca and Mg, occurred in the past (Figure S1) [36,37,43,87–90]. Regardless, the main chemical constituents alone are not enough to explain the hydrogeochemical processes to quantify deep components and their influence on each spring.

With the aim of identifying both chemically and physically the deep fluid end-member, in this paragraph, we will focus on: (i) the reconstruction of thermodynamic balances through the application of different geothermometers; (ii) the study of the possible water–rock interaction processes through the analysis of some conservative elements; (iii) the determination of the origin of free and dissolved gases; and (iv) the connection between deep and shallow aquifer systems through the study of the relationship between the geochemistry of groundwater and neotectonics. Some relevant chemical data are reported in Table 1.

The evaluation of the deep temperature in low enthalpy carbonate-evaporitic systems (T < 150 °C) is frequently a demanding challenge [91]. Regarding central Italy, several approaches using chemical geothermometry have been proposed [91–95]. Recently, the temperatures inferred by the Na-Li ratio offered results consistent with those obtained from multicomponent geochemical models [33]. In this study, the Na-Li inferred temperatures by the [96] equation gradually increase as the contribution of deep inorganic carbon, traceable by the $\delta^{13}C_{ext}$ parameter, increases (Figure 4; Figure S2). Taking into account the absolute uncertainties of this kind of geothermometer ($\pm$ 20 °C) [96], negative results on waters with shallower circulation in the heterothermic zone of a karst system such as S7 are not as astonishing (Figure 4) [97]. In contrast, most of the spring samples at $\delta^{13}C_{ext}$ > −5‰ seem to have a relevant deep contribution and/or circulation in the deep homothermic zone affected by the local geothermal gradient, with a temperature that can be inferred by the Na-Li geothermometer and clustering around the low-high enthalpy limit [33] (T = 150 °C, see Supplementary File Table S1). We did not measure the $\delta^{13}C$(DIC) parameter in some springs (S6, S8, S10, S12, S13, and S15). However, an analysis of historical data reveals how the S10 spring (Peschiera) falls close to the abovementioned $\delta^{13}C_{ext}$ divide of −5‰ ($\delta^{13}C_{ext}$ = −6.6 ± 1.2‰) (Figure 4; Figure S2), confirming the involvement of both shallow and deep fluids [33,36,43,89]. The involvement of a deeper fluid having an increasing amount of CO$_2$ with a geogenic signature is also confirmed by the significant regression between the Na-Li temperature and the CO$_2$ partial pressure parameter logPCO$_2$ calculated under sampling conditions (Figure 5). The SO$_4$-F geothermometer was adopted to verify the reliability of the results obtained by the Na-Li geothermometer. However, as already found in other geothermal systems [98,99], the SO$_4$-F geothermometer gave systematically negative temperature values using the equation calibrated for the temperature range of 75–150 °C [95]. Otherwise, the extrapolation of the equation calibrated for the range 150–300 °C [94] offers consistent results with those from Na-Li, but only for the springs showing fewer negative values of the saturation index for gypsum/anhydrite and fluorite.

For example, Antrodoco: T(SO$_4$-F) = 112 $\pm$ 13 °C and T(Na-Li) = 119 $\pm$ 14 °C (N = 18). In this study, using the Na-Li temperatures as the most likely temperature at depth and the equations of [94], for S11 (which has a mean T(Na-Li) = 196 $\pm$ 25 °C, N = 8), we obtained the highest logPCO$_2$ = 3.5 value (logPCO$_2$ = 0.7 $\pm$ 0.2 for Antrodoco). Such a relatively high temperature in S11 was also supposed to explain the boron isotope composition of this water that resembles a tourmaline-equilibrated fluid [100]. In contrast, the obtained logPCO$_2$ values are higher than those obtained with the PHREEQCi code under sampling conditions (Figure 5) but are in the order of magnitude with those of other deep crustal fluids in the Apennine [101]. Therefore, the adoption of the Na-Li geothermometer allowed us to evaluate the temperatures of the San Vittorino system (up to 150–200 °C), where evidence of springs with significant deep contributions was found. Applying the geothermal gradient of the area (66 °C at 3 km depth in the Antrodoco 1 borehole) [102] at these temperatures, an estimation of the depth of fluids ranging between 2.2 and 8.8 km was carried out.

Table 1. Chemical results used in this paragraph. Same spring analyses (location in Figure 1) refer to subsequent samplings.

	Li	Rb	Cs	δ^{13}Cext(g)	Na/Li	logP(CO$_2$)	δD	δ^{18}O	R/Ra	He/Ne	R/Ra	He/Ne
	ppb	ppb	ppb	‰ (vs. V-PDB)	°C		‰ (vs. V-SMOW)	‰ (vs. V-SMOW)	Dissolved	Dissolved	Free	Free
S1	16.46	4.09	1.23	6.38×10^{-1}	125	−0.95	−60	−9.7				
S1	12.50	3.17	0.90	-2.26×10^{0}	86	−1.00			0.11	28.98		
S2	22.73	5.18	1.69	7.86×10^{-1}	144	−0.69	−61	−9.8				
S2	21.20	4.83	1.38	-1.76×10^{0}	127	−0.64			0.11	38.56		
S3	5.60	2.36	0.17		94	−1.34						
S3	4.81	1.53	0.07	-1.71×10^{-1}	58	−1.41			0.08	1.82		
S4	4.95	2.33	0.27	-2.45×10^{0}	94	−1.21	−62	−9.8				
S4	3.96	1.72	0.18	-4.96×10^{0}	80	−1.27			0.10	12.54		
S5	48.73	7.15	7.45	1.93×10^{0}	193	−0.26	−60	−9.8				
S5	47.15	6.54	6.44	-2.51×10^{0}	172	−0.10			0.07	8.35	0.11	121.50
S6	2.81	1.53	0.24		69	−1.18						
S7	0.43	0.58	0.00	-2.00×10^{1}	2	−2.75	−53	−8.9				
S7	0.35	0.60	0.00	-2.81×10^{1}	−5	−2.98						
S8	9.32	2.61	1.10		112	−1.44	−61	−9.8				
S9	1.88	1.38	0.07	-3.37×10^{0}	52	−0.92			0.12	9.12	0.17	20.57
S10	1.53	1.53	0.06		48	−1.68	−60	−9.8				
S11	98.11	9.64	5.36	2.14×10^{0}	193	0.00	−55	−9				
S11	83.65	7.82	3.78		179	−0.19			0.08	0.59		
S11	100.70	9.66	5.14	6.44×10^{0}	148	−0.07					0.10	198.57
S12	5.86	2.29	0.27		99	−1.12						
S13	68.46	7.82	2.02		160	−0.21						
S14	19.81	3.32	0.62	-8.44×10^{-1}	133	−0.76	−59	−9.7				
S14	8.28	1.92	0.49	-3.69×10^{0}	100	−1.12			0.10	13.27	0.15	37.97
S15	105.30	10.45	5.08		167	0.02						
S15	124.30	11.16	5.98		184	0.02	−59	−9.4				
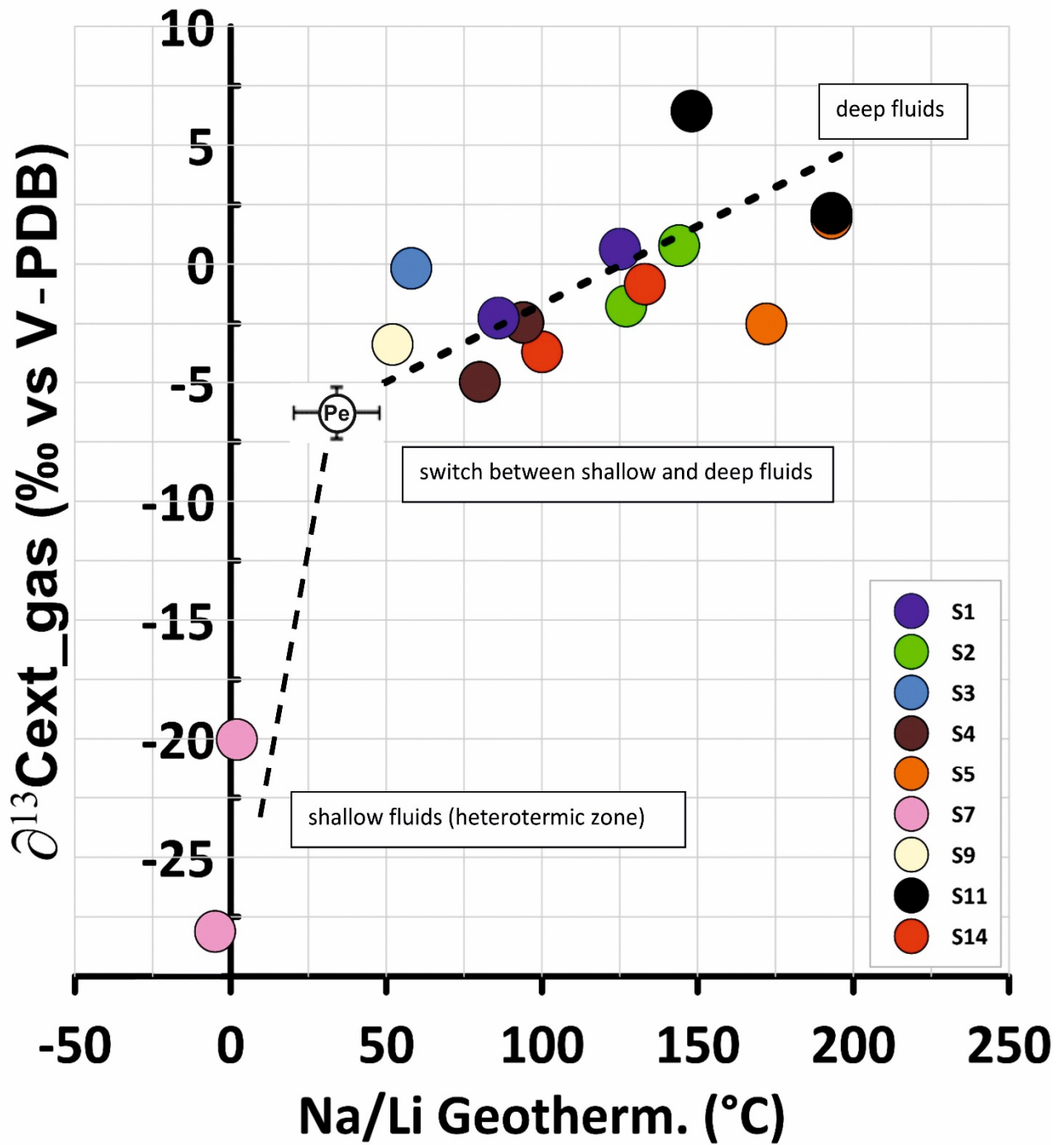
Figure 4. δ^{13}Cext versus T, where T = temperature in $°$C obtained from an Na-Li geothermometer [96]. δ^{13}Cext was calculated only for some groundwater samples from the San Vittorino Plain (displayed with circles), whose (δ^{13}C$_{DIC}$) was measured. Historical data from the S10 Peschiera "Pe" spring are also shown for comparison (see also Figure S2). See Figure 1 for spring location.
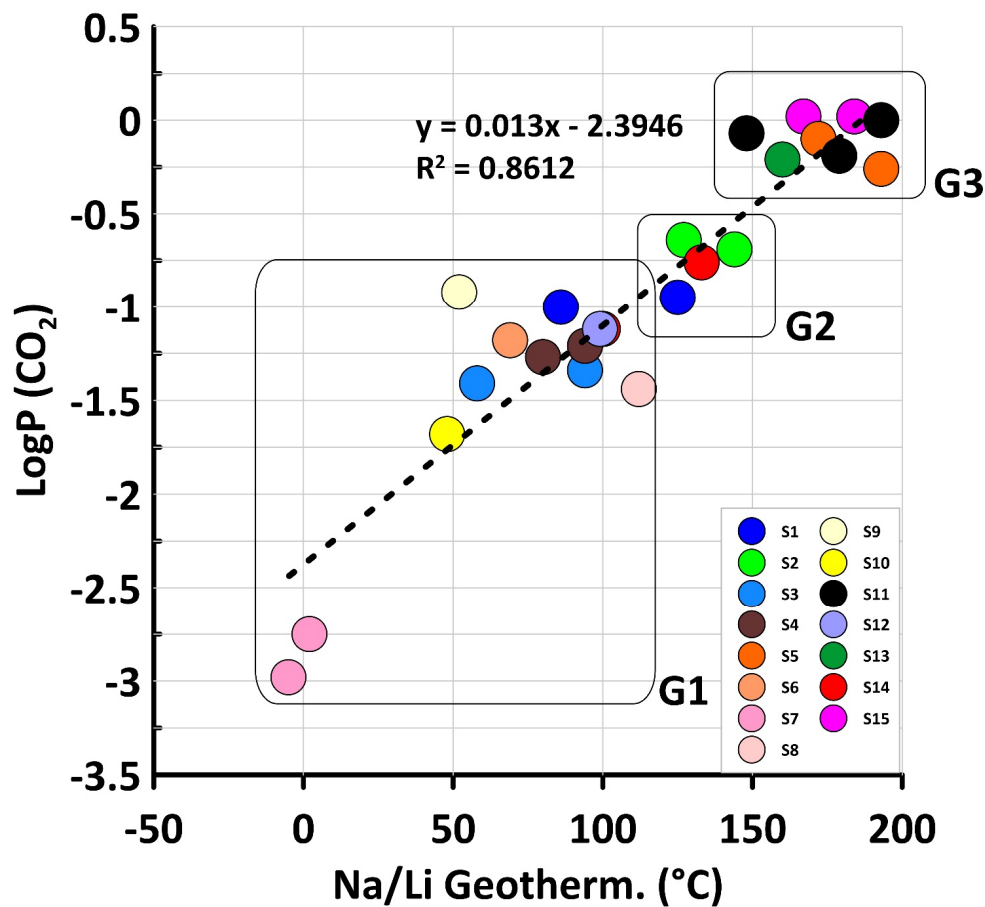
Figure 5. LogP(CO_2) at sampling conditions calculated by PHREEQCi [75] versus T, where T = temperature in °C obtained from an Na-Li geothermometer [96]. A high coefficient of determination (R-squared value = 0.86) for the groundwater samples from the San Vittorino Plain was found. See Figure 1 for spring location. G1, G2 and G3 refer to new spring groups.

Given the correlation between the temperatures inferred by the Na-Li geothermometer, the isotopic composition of CO_2 gas ($\delta^{13}C_{ext}$), logPCO2, and some dissolved element concentrations (e.g., Li, As, Cs, and Rb), the Li-Rb-Cs ternary diagram was also developed [103] (Figure 6). Indeed, these elements generally act as less reactive and conservative elements in thermal waters, and they are often used to identify common origins or common deep processes starting from the chemical composition of waters [104,105]. Li is incorporated in secondary quartz and chlorite minerals and can be acquired directly in the dissolution process [106]. Rb and Cs are vicariants of K; therefore, they move into water solution following the leaching of minerals or alteration products rich in K (e.g., zeolites or clays). Since the Rb atomic radius is more similar to the K radius, it is a favorable vicariant with respect to Cs, which is often adsorbed on the mineral surface [107]. The analyzed groundwater covers a large area of the Li-Rb-Cs ternary diagram, as shown in Figure 6. However, three different groups of springs (G1, G2, and G3) can be clearly evidenced. The first one (G1), located close to the composition of mean limestone (the "L" field in Figure 6) [108], includes springs clearly belonging to the calcium-bicarbonate facies (S3, S4, S6, S7, S9, S10, and S12), where the water chemistry is dominated by simple interactions with the calcites and dolomites of the Mesozoic limestones (Figure 6). In central Italy, the median composition of carbonate aquifers with shallow circulation falls on the Li-Rb side of the diagram, due to a relatively low Cs concentration (0.02 ppb) [109]. Most of the Cs of the mean limestone composition is retained in low solubility impurities of the carbonate rocks. In contrast, limited enrichments in Li in some of the abovementioned springs (S3, S4, and S12) are possibly due to the mixing with groundwater circulating in the bedrock evaporitic deposits, as supported by the increase in sulphates in the same springs or eventually the uprising of

H₂S. The second group (G2) is represented by groundwater of the calcium-sulphate domain (S1, S2 and, to a lesser extent, S14; Figure 6), whose chemical compositions are attributable to a more extensive dissolution of the sulphate minerals [33,38,88]. Finally, the third group (G3) is characterized by groundwater with the highest concentrations of Li and Cs (S5, S11, S13, and S15) that suggests a different circulation model with respect to the other two groups. It is noteworthy that the samples of the second and third clusters are within or close to the ratios 1.2 < Rb/Cs < 3.0, typical of waters interacting with Upper Triassic Burano Formations [110–112], where the higher ratio is common of sulphate waters such as those from the Antrodoco area (S1, S2). In addition, the Li-Rb-Cs contents of the carbonatitic and silicate fractions of Cupaello rocks display red pentagons [41,42]. The Rb/Cs ratio seems to be similar to that of the G2 and G3 groups; however, the Li content is very different. Indeed, the Cupaello unit consists of ultrapotassic rocks, and their dissolution should give K/Na > 1, but this condition is not verified in our sampled groundwater. This fact allows to us to exclude a direct influence of magmatic rocks in the rising fluids of the San Vittorino Plain. The three groups (G1, G2, and G3) recognized through this analysis are the same as those we obtained with the geothermometric analysis (Na-Li geothermometer vs. logPCO₂ in Figure 5).
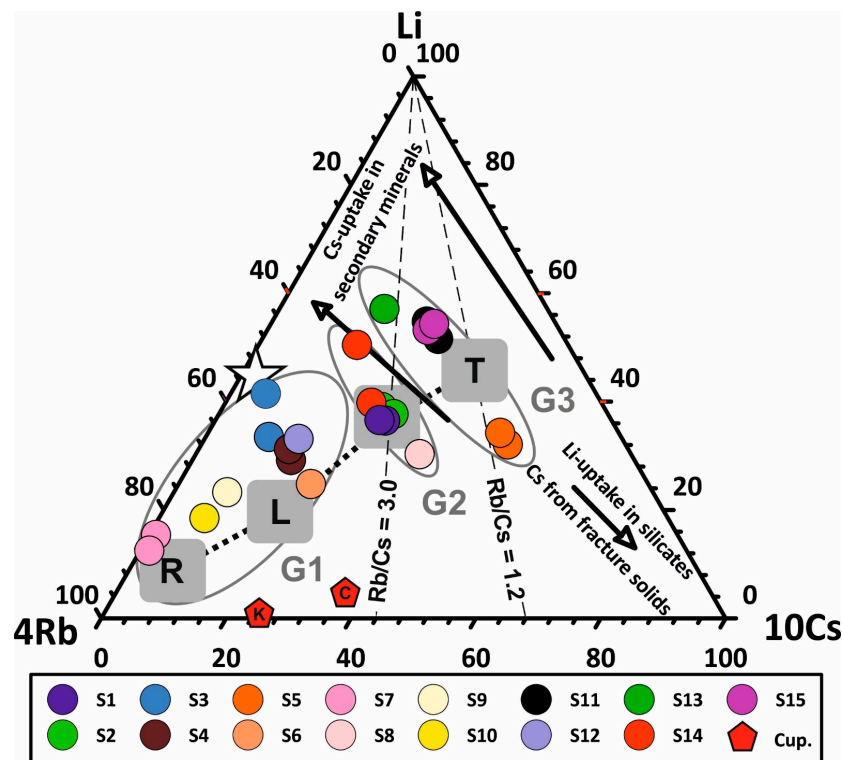
Figure 6. Li-Rb-Cs ternary diagram of the water samples (weight basis), modified after [103]. Three different groups of springs that correspond to the different steps of the water–rock interaction path (dotted line), are evidenced: (G1) groundwater of the calcium-bicarbonate water domain in the "limestone area" including S3, S4, S6, S7, S9, S10, and S12 whose water chemistry is dominated by simple interactions with calcites and dolomites of the Mesozoic limestones; that cluster contains: the "R" gray field (isochemical dissolution of mean crustal rocks) [103], the white star that depicts the median composition of carbonate aquifers with shallow circulation from central Italy [109], and the mean limestones composition "L" [108]; (G2) groundwater of the calcium-sulphate domain in the "evaporites area" including S1, S2, and S14 whose chemical compositions are attributable to a more extensive dissolution of the first groups of the sulphate minerals; and (G3) groundwater with the highest concentrations of Li and Cs including S5, S11, S13, and S15, whose geochemistry suggests a deep-seated circulation with respect to the first two groups. However, groups 2 and 3 are enclosed between 1.2 < Rb/Cs < 3.0, typical of thermal waters interacting with the Upper Triassic Burano Formations ("T" = Tuscany thermal waters [110]). The Li-Rb-Cs contents of the carbonatitic (C) and silicate (K) fractions of Cupaello rocks are shown with red pentagons (Cup.) [41,42]. See Figure 1 for spring location.

Despite this evidence of deep circulation and mixing between shallow and deep groundwater, the water stable isotopes measured only for some springs of the San Vittorino Plain (S1, S2, S4, S5, S7, S8, S10, S11, S14, and S15) did not record any significant fractionation due to upwelling of deep fluids. Indeed, the oxygen and hydrogen stable isotope compositions of central Italy's groundwater could be compared with the meteoric water lines available in the literature. Among these, the global and Mediterranean meteoric water lines, with an excess of deuterium equal to d = 10 (GMWL) [113] and d = 22 (MMWL), respectively, are the most commonly used [38,114–116]. However, it should be made clear that the value of d = 22 was inferred for the eastern Mediterranean area [117], which has very different climatic conditions from those of this study. Specifically, for central Italy, and in particular for the Latium region, the monitored meteorological events were included between water lines with a deuterium excess of between d = 12 and d = 17 [118,119]. Moreover, the central Italy meteoric water line (CIMWL) [120] and the central Italian limestone aquifer water line (LAWL) [121] are within the ribbon and have extreme lines of d = 12 and d = 17 (Figure 7). Therefore, the deuterium excess range of 12 < d < 17 could be comparable with the so-called "uncertainty wings" of meteoric waters in this area [122].
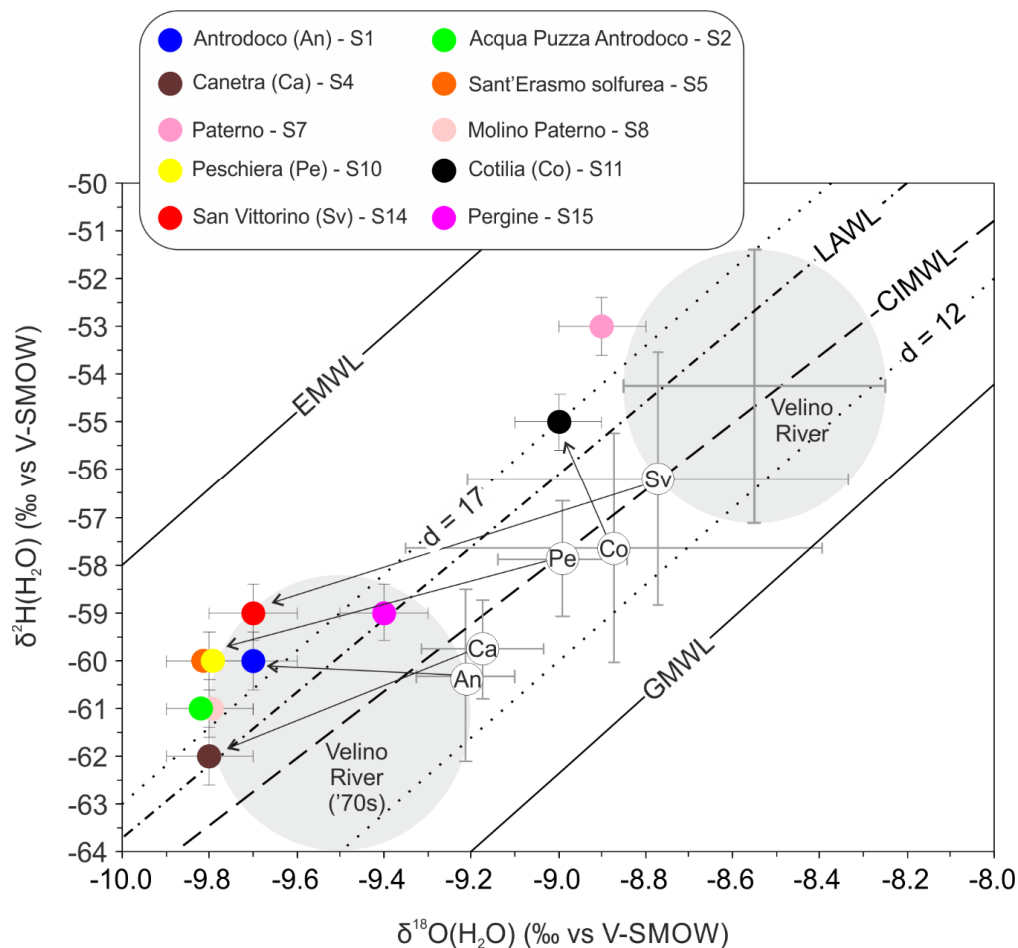
Figure 7. δ^2H-δ^{18}O (H$_2$O) isotope values of some samples from the San Vittorino Plain. The global and Mediterranean meteoric water lines, with excess deuterium equal to d = 10 (GMWL) [113] and d = 22 (MMWL), respectively, are used. The central Italy meteoric water line (CIMWL) [120] and the central Italy limestone aquifer water line (LAWL) [121] are also displayed within the ribbon with extreme lines of d = 12 and d = 17. Historical analyses of the isotope composition of the Velino River fall within the deuterium excess variation range of the water lines. Similarly, the groundwater of the San Vittorino Plain also falls within the compositional variation range of local rainwater. The white circles with the abbreviations Ca, An, Pe, Co, and Sv are historical data of springs with the largest standard deviation variations on historical data. See Figure 1 for spring location.

Indeed, the historical analyses of the isotope compositions of the Velino River, although showing rather significant variations over time from $\delta^{18}O = -9.5 \pm 0.3‰$ (N = 12) during the seventies [123] and $\delta^{18}O = -8.6 \pm 0.3‰$ (N = 4) in recent times [116], fall within the deuterium excess variation range of the water lines (Figure 7). Similarly, the groundwater of the San Vittorino Plain also falls within the compositional variation range of local rainwater. Figure 7 also highlights the different local recharge areas for S7 and S11, which show less negative isotopic values, indicating the lower altitude of the recharge area. All other springs show more negative isotopic values corresponding to different and higher altitudes of the recharge area, including the possible contribution of snow melting (mean $\delta^{18}O = -11‰$) [114], which was probably more significant during past meteoric recharge periods. This hypothesis is supported by the shift with time of the mean isotopic composition of surface waters, such as the Velino River (Figure 7), which shows increased isotopic values (approximately +1‰ for $\delta^{18}O$). Obviously, this shift with time is not due to a change in recharge area; consequently, this increase is due to a minor influence of high elevation areas on aquifer recharge, which can be attributed to a lower persistence of snow coverage during recent years, in line with regional climatic studies [124]. Hence, the water isotopes confirm that S7 is fed by shallow and fast-flow meteoric events infiltrating Mt. Paterno (Reatini Mts). Therefore, it represents the "shallow" end-member of our study area, comparable with the modern composition of the Velino River water (Figure 7). A similar origin can be attributed to the meteoric contribution to the S11 discharge. It should also be noted that historical analyses of some springs (e.g., S11) show considerable standard deviations both as oxygen ($\pm 0.6‰$) and as hydrogen ($\pm 3‰$) ratios (Figure 7). This significant standard deviation for S11 is probably related to the bubbling and high pressure of the dissolved gases that could enhance the evaporation effect and the variability over time of the isotopic composition of the water at the sampling site. Finally, neither ^{18}O-depletion nor ^{18}O-enrichment, due to a dominant role of CO_2 exchange with water or a significant contribution of high-temperature magmatic fluids, are distinguishable, respectively.

Differently, the analyses of free and dissolved gases in the groundwater of the San Vittorino Plain highlighted the presence of components of some volatiles different from those that are atmosphere-sourced (CO_2, CH_4, and He). In detail, He is a good tracer for recognizing the outgassing of deep-derived (mantle or crust) volatiles in continental regions, even where evidence of volcanic activity is lacking [11,125–127] because He is mainly sourced by the mantle, crust, and atmosphere, and the isotopic signatures of these three end-member reservoirs are strongly different ($^3He/^4He = 1.4 \times 10^{-6}$ in air; $\approx 10^{-5}$ mantle; $\approx 10^{-8}$ crust). In this work, the percentages of mantle-derived He and crustal He (produced by U and Th decay in the crust) were evaluated by using the approach proposed by [128], which is based on both He isotope ratios and $^4He/^{20}Ne$ ratios. Here, we assumed convective upper mantle MORB-Type (Mid Oceanic Ridge Basalts, 8 Ra) for the mantle end-member, He isotopic ratios of 0.01–0.03 Ra for the crust end member, and the atmospheric He isotope signature (1 Ra). The $^4He/^{20}Ne$ ratios of the same end-members are >1000 for the mantle and the crust and 0.318 for the atmosphere. Mainly, the reliably considered results are characterized by $^4He/^{20}Ne$ ratios higher than 10, as they do not suffer from relevant He air contamination. The samples of the San Vittorino Plain have very low contributions of mantle-derived He, which is no higher than ~1–2% (Figure 8). However, the mantle below Italy is contaminated by subduction processes, decreasing the pristine signature of the He isotopic ratio [129]. Hence, if we assume a He isotopic signature lower than the typical MORB value (8 ± 1 Ra), the mantle contribution would be higher than the above estimated values. Considering the existence of the local tectonic discontinuities that were able to drive magma batches towards the surface [130], (Figure 1), the San Vittorino graben can still act as an efficient structure that allows bottom-up interconnections for the transfer of deep-sourced volatiles to stratified regional aquifers. However, we cannot determine whether He is sourced by shallow reservoirs of mantle He stored in crustal layers [131] or directly by mantle ([73] and references therein).
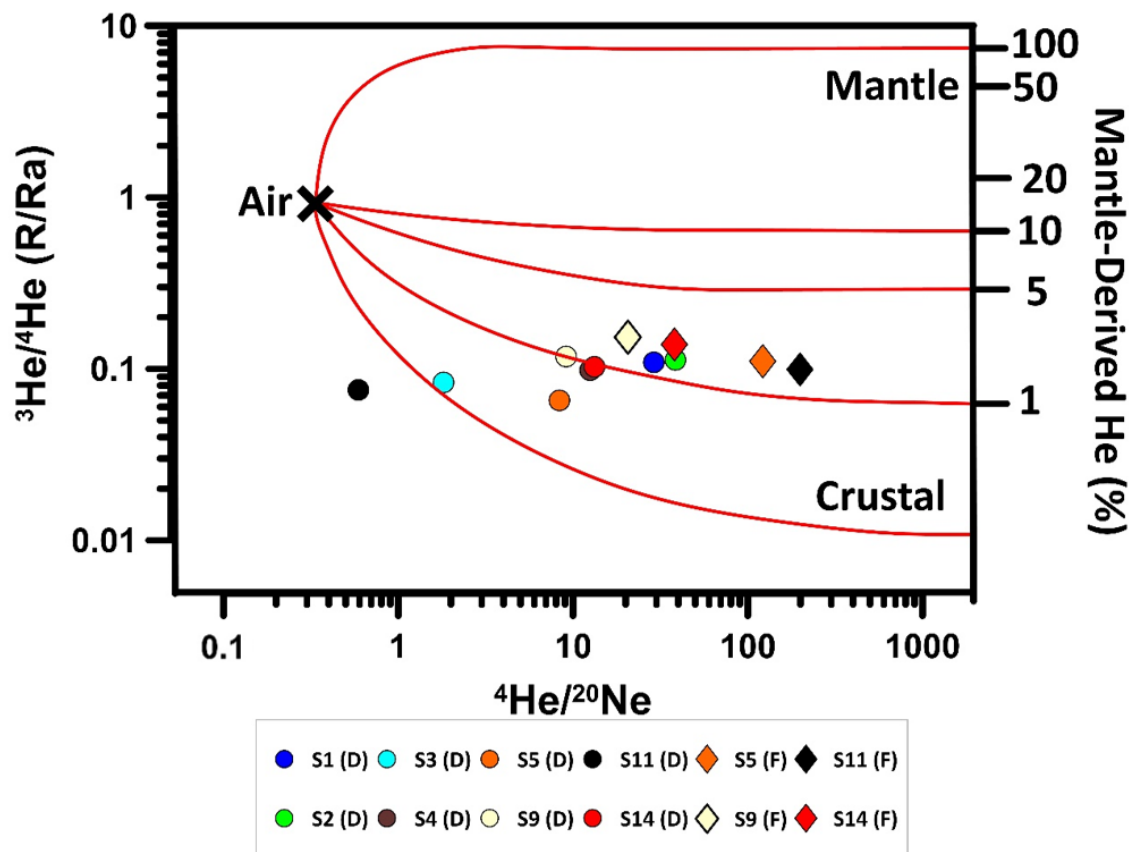
Figure 8. Diagram of ^{3}He/^{4}He (R/Ra) versus ^{4}He/^{20}Ne ratios. Mixing lines between the atmosphere and upper mantle, and the atmosphere and crust were calculated using the end members: air (^{3}He/^{4}He = 1.4 × 10^{-6}, ^{4}He/^{20}Ne = 0.318) [86], upper mantle (^{3}He/^{4}He = 12 × 10^{-6}, ^{4}He/^{20}Ne = 100,000) [132], and old continental crust (^{3}He/^{4}He = 0.02 × 10^{-6}, ^{4}He/^{20}Ne = 100,000) [131]. Samples of dissolved and free gases are named (D) and (F), respectively. See Figure 1 for spring location.

Overall, the mixing of prevailing crustal components with mantle-derived volatiles at the regional scale has also been evidenced by previous studies [11,13,20,31,32,36,65] based on He isotopes and the δ^{13}C of CO_2. This isotopic ratio can be ascribed to different sources: limestone (δ^{13}C = 0‰), organic matter (δ^{13}C = −30‰), or mantle (δ^{13}C = −6.5‰) [133]. Most of the sampled groundwater exhibits $\delta^{13}C_{ext}$ values between −5‰ and +5 ‰, which are near the values proper of the deep fluid contribution ($\delta^{13}C_{ext} = \delta^{13}C_{deep} = -0.35$‰; Figure S2), which is different from spring S7, which shows a mean value of approximately −25‰ and is confirmed to be represented only by "infiltrating waters" ($\delta^{13}C_{inf}$) (Figure S2). Concerning the more negative values of the deep source CO_2, while $\delta^{13}C_{ext}$ values near −6‰ might result from the simple infiltration of magmatic carbon, they do not prove the existence of a mantle-derived fluid [134]. In contrast, according to [31,36], the highest/positive calculated $\delta^{13}C_{ext}$ is due to a fractionation effect related to degassing, which in the study area could reach values close to +8‰ (Figure S2). The effect of diffuse CO_2 degassing in the study area is also detectable in the Peschiera spring, where $\delta^{13}C_{ext}$ and the alkali/alkaline earth metal ratio showed concomitant variations (Figures S3 and S4). The highest value of $\delta^{13}C_{ext} = -4.7$‰, corresponding to $\delta^{13}C_{deep} = +8.8$‰ [36], was calculated on a sample collected just a day after the main shock occurred in Norcia (30 October 2016, magnitude moment M_w = 6.5; Figures S3 and S4 show the recalculated data of the Pe spring from [90]).

In summary, the groundwater in the San Vittorino Plain derives from complex geochemical balances that are established between water, rock, and gas. Each component of this ternary system substantially and differently affects the final geochemistry of the

groundwater, depending on the concentration of rising gases, the lithology of the aquifer, and the chemical-physical characteristics of the infiltrating water. No contributions of surface runoff to groundwater hydrogeochemistry were detected. The elaborations concerning geothermometers (Figure 5 and Supplementary File Table S1), trace elements (Figure 6 and Supplementary File Table S1), and gases (Figure 8 and Supplementary File Table S1) converge in attributing the highest temperatures (>150 °C), the greatest enrichments in Li and Cs, and traces of mantle-derived He (1–2%) to S5, S11, S13, and S15. These springs are located in peculiar sites within the San Vittorino Plain. Indeed, the waters of S11, S13, and S15 flow precisely in correspondence with the main and deeper structural elements in the area (i.e., the Fiamignano Fault and its conjugate structures; see Figures 1 and 3BB'). In addition, the water of S5 is fed by a flow influenced by the uprising of deep fluids along one of the main normal faults (orange arrow in Figure 3AA'). This observation is also corroborated by the depths inferred by geothermometric analyses that are in line with those identified in the cross-section construction. The Cs (S5) and Li (S11, S13, and S15) enrichments (or Li and Cs impoverishments, respectively) shown in Figure 6 are often related to deep processes involving silicates (clays, zeolites, quartz, or chalcedony) that often produce temperature-dependent distributions of these elements [103,135,136]. In the same area of this study, Cs enrichment up to 6.5 ppb was also detected in the "Paulla Bassa" and "Paulla 3" springs [89], which are brackish and reduced (sulphurous), similar to S5. Such a relatively high Cs concentration in old, deep-seated, and saline groundwater could also be ascribed to the long-term weathering of micaceous minerals, typically enriched in Cs, in fracture coatings and wall rock [137]. In addition, the presence of deep sourced He and CO_2 found in the same springs confirms the detailed influence of a deep circulation system, largely hidden by the huge contribution to the discharge of the shallow carbonate circulation system (as highlighted by the stability of the water isotopes). In our interpretation, the pressurized nappes can be connected via high-angle transtensive faults, which represent a preferred bottom-up connection path. The remaining two groups of springs (G1 and G2) show a degree of "deep contribution", gradually decreasing with respect to the deep fluids uprising. These springs are located at the intersection with secondary structural elements that are probably not able to allow a relevant uprising of deep fluids. In some cases (e.g., S10), the great abundance of shallow waters may hinder the deep signal.

Although this area is characterized by intense degassing and evident chemical and isotopic features of mixing of shallow and deep fluids, there are only some springs whose hydrogeochemical features are directly connected with deep structures. In detail, their depth corresponds to the common hypocenters of earthquakes in the Apennine chain (7–10 km) because of the direct connection of the tectonic lines allowing the upward migration of fluids along high-angle faults. Furthermore, the springs of potential interest are those least affected by shallow circulation (also in terms of seasonal variations). For future research, the investigations should be based on high-frequency multiparametric monitoring at different sites and on data cross analysis, through which the dynamics and time evolution of processes in relation to the seismicity of the central Apennines region could be characterized in more detail [100].

In addition, for the management and exploitation of water resources, sites such as the San Vittorino Plain require careful monitoring of the huge quantities of available high-quality water resources, as they could undergo alterations in their chemical-physical properties induced by uprising deep fluids rich in CO_2 and heavy metals. For example, the groundwaters of S5, S11, S13, and S15 show concentrations of As between 4 and 60 ppb, probably owing to the greater amount of dissolved CO_2. These factors can become relevant for future scenarios of climate change, which can increase heavy metal concentrations. Similarly, the large quantities of dissolved CO_2 make the waters more aggressive towards calcium carbonate, increasing the already high sinkhole risk in the area [68].

6. Conclusions

The San Vittorino Plain, an intramontane plain where a large amount of groundwater resources converges from large mountain fractured aquifers to several springs affected by different degrees of mineralization, represents one of the more interesting areas for evaluating groundwater mixing of direct rainfall recharge components with deep fluids uprising along high-angle faults reaching a depth of at least 5 km b.s.l. In our study, we suggest a methodological approach useful for improving groundwater monitoring aimed at identifying geochemical signals related to crustal deformation and potentially to seismic activity.

Analysis of the results of major and trace elements, stable isotopes of water, chemistry and isotopes of dissolved and free gases, coupled with an updated geo-structural setting and very detailed knowledge of the hydrogeology, allowed us to build a robust conceptual model where all elements converge into a coherent framework. By applying different geothermometers, a reliable thermodynamic balance reveals the Na-Li geothermometer as an affordable tool for calculating the equilibrium temperature of the deep contributions, established at approximately 150–200 °C. Such deep fluids show a hydrogen and oxygen isotope composition typical of meteoric water, whereas the ^{18}O-enriched component typical of high-temperature magmatic fluids is substantially absent. However, the analysis of He and CO_2 isotopes confirms the presence of a deep component with possible traces of mantle-derived helium (1–2%). Trace element occurrence clarifies the water–rock interaction processes and supports the conceptual model based on the localized uprising of deep fluids that do not casually match the distribution of high-angle faults that are capable of connecting different reservoirs delimited by less permeable thrust zones. The distribution and concentration of deep fluids uprising and spreading into the aquifers cause significant changes in the classical calcium-bicarbonate equilibrium of the basal springs, allowing the subdivision of the sampled selected springs into three groups showing different degrees of deep contribution (G1, G2, and G3).

On the basis of the reviewed structural map, the geological setting shown in the cross-sections presented herein could also make possible the uprising of deep-derived gases in the Velino Valley. In this sketched model, it is now clear that these high-angle faults work as a network of pathways through which deep fluids reach the shallow regional aquifers that are otherwise totally recharged by meteoric infiltration. Based on geothermometrical analysis and structural cross sections, we inferred the origin of the deep fluid portion at a depth of approximately 7–10 km, where Apennine earthquakes usually occur. Consequently, this integrated approach can help identify the most suitable sites aimed at analyzing the relationships between groundwater and seismicity. Indeed, knowing the mixing degree among different springs, it is possible to recognize whether and where the flux of the deep portion, modulated by fault activity, increases or decreases with respect to permeability variations along the uprising zones.

A list of possible criteria found within this study for the optimization of future groundwater hydrogeochemical monitoring aimed at correlating crustal deformation along faults and related (micro- and perhaps macro-) seismicity can be summarized as follows: (a) discharge areas with concentrations of different hydrochemical spring characteristics; (b) steady base flow from regional aquifers recharged by meteoric infiltration; (c) selection of the most representative sampling sites on the basis of a complete hydrochemical/isotopic analysis; and (d) review of fault geometries at the surface and depth. We consider the future possible establishment of a groundwater monitoring network based on the abovementioned criteria to be very useful for improving the contribution of groundwater monitoring to the wide research field of earthquake precursors.

Supplementary Materials: The following are available online at https://www.mdpi.com/2076-3417/11/4/1353/s1: Table S1: Chemical data; Figure S1: Detail of Langelier–Ludwig diagram; Figure S2: δ^{13}Cext versus 1/Cext diagram; Figure S3: Time series of the Y-coordinate of the Langelier–

Ludwig diagram and $\delta^{13}C_{ext}$ parameter at Peschiera spring (Pe); Figure S4: Moving averages on Figure S3 data

References

1. Edmunds, W.M.; Smedley, P.L. Residence time indicators in groundwater: The East Midlands Triassic sandstone aquifer. *Appl. Geochem.* **2000**, *15*, 737–752. [CrossRef]
2. Goldscheider, N.; Mádl-Szőnyi, J.; Erőss, A.; Schill, E. Review: Thermal water resources in carbonate rock aquifers. *Hydrogeol. J.* **2010**, *18*, 1303–1318. [CrossRef]
3. Skelton, A.; Liljedahl-Claesson, L.; Wästeby, N.; Andrén, M.; Stockmann, G.; Sturkell, E.; Mörth, C.M.; Stefansson, A.; Tollefsen, E.; Siegmund, H.; et al. Hydrochemical Changes Before and After Earthquakes Based on Long-Term Measurements of Multiple Parameters at Two Sites in Northern Iceland—A Review. *J. Geophys. Res. Solid Earth* **2019**, *124*, 2702–2720. [CrossRef]
4. Singh, P.; Mukherjee, S. Chemical signature detection of groundwater and geothermal waters for evidence of crustal deformation along fault zones. *J. Hydrol.* **2020**, *582*, 124459. [CrossRef]
5. Cardello, G.L.; Mancktelow, N.S. Veining and post-nappe transtensional faulting in the SW Helvetic Alps (Switzerland). *Swiss J. Geosci.* **2015**, *108*, 379–400. [CrossRef]
6. Clemenzi, L.; Storti, F.; Balsamo, F.; Molli, G.; Ellam, R.; Muchez, P.; Swennen, R. Fluid pressure cycles, variations in permeability, and weakening mechanisms along low-angle normal faults: The Tellaro detachment, Italy. *Geol. Soc. Am. Bull.* **2015**, *127*, 1689–1710. [CrossRef]
7. Agosta, F.; Kirschner, D.L. Fluid conduits in carbonate-hosted seismogenic normal faults of central Italy: Fluid conduits in seismogenic normal faults. *J. Geophys. Res.* **2003**, *108*. [CrossRef]
8. Cardello, G.L. The Rawil Depression: Its Structural History from Cretaceous to Neogene. Ph.D. Thesis, ETH Zurich, Zürich, Switzerland, 2013; p. 1 Band.
9. Smeraglia, L.; Aldega, L.; Bernasconi, S.M.; Billi, A.; Boschi, C.; Caracausi, A.; Carminati, E.; Franchini, S.; Rizzo, A.L.; Rossetti, F.; et al. The role of trapped fluids during the development and deformation of a carbonate/shale intra-wedge tectonic mélange (Mt. Massico, Southern Apennines, Italy). *J. Struct. Geol.* **2020**, *138*, 104086. [CrossRef]
10. Miller, S.A.; Nur, A. Permeability as a toggle switch in fluid-controlled crustal processes. *Earth Planet. Sci. Lett.* **2000**, *183*, 133–146. [CrossRef]
11. Italiano, F.; Martelli, M.; Martinelli, G.; Nuccio, P.M. Geochemical evidence of melt intrusions along lithospheric faults of the Southern Apennines, Italy: Geodynamic and seismogenic implications. *J. Geophys. Res.* **2001**, *105*, 13569–13578. [CrossRef]
12. Chiodini, G.; Cardellini, C.; Amato, A.; Boschi, E.; Caliro, S.; Frondini, F.; Ventura, G. Carbon dioxide Earth degassing and seismogenesis in central and southern Italy: Carbon dioxide earth degassing and seismogenesis. *Geophys. Res. Lett.* **2004**, *31*. [CrossRef]
13. Italiano, F.; Bonfanti, P.; Ditta, M.; Petrini, R.; Slejko, F. Helium and carbon isotopes in the dissolved gases of Friuli Region (NE Italy): Geochemical evidence of CO_2 production and degassing over a seismically active area. *Chem. Geol.* **2009**, *266*, 76–85. [CrossRef]
14. Doglioni, C.; Barba, S.; Carminati, E.; Riguzzi, F. Fault on–off versus coseismic fluids reaction. *Geosci. Front.* **2014**, *5*, 767–780. [CrossRef]

15. Smeraglia, L.; Bernasconi, S.M.; Berra, F.; Billi, A.; Boschi, C.; Caracausi, A.; Carminati, E.; Castorina, F.; Doglioni, C.; Italiano, F.; et al. Crustal-scale fluid circulation and co-seismic shallow comb-veining along the longest normal fault of the central Apennines, Italy. *Earth Planet. Sci. Lett.* **2018**, *498*, 152–168. [CrossRef]

16. Collettini, C.; Tesei, T.; Scuderi, M.M.; Carpenter, B.M.; Viti, C. Beyond Byerlee friction, weak faults and implications for slip behavior. Earth Planet. *Sci. Lett.* **2019**, *519*, 245–263. [CrossRef]

17. Buttitta, D.; Caracausi, A.; Chiaraluce, L.; Favara, R.; Gasparro, M.; Sulli, A. Evidences of the role of seismicity on degassing of volatile through the crust. *Sci. Rep.* **2020**, *10*, 1–13. [CrossRef]

18. Italiano, F.; Solecki, A.; Martinelli, G.; Wang, Y.; Zheng, G. New Applications in Gas Geochemistry. *Geofluids* **2020**, *2020*, 1–3. [CrossRef]

19. Caracausi, A.; Italiano, F.; Martinelli, G.; Paonita, A.; Rizzo, A. Long-term geochemical monitoring and extensive/compressive phenomena: Case study of the Umbria Region (Central Apennines, Italy). *Ann. Geophys.* **2005**, *48*, 43–53.

20. Italiano, F.; Caracausi, A.; Favara, R.; Innocenzi, P.; Martinelli, G. Geochemical monitoring of cold waters during seismicity: Implications for earthquake-induced modification in shallow aquifers. *Terr. Atmos. Ocean. Sci.* **2005**, *16*, 709. [CrossRef]

21. Barberio, M.D.; Barbieri, M.; Billi, A.; Doglioni, C.; Petitta, M. Hydrogeochemical changes before and during the 2016 Amatrice-Norcia seismic sequence (central Italy). *Sci. Rep.* **2017**, *7*, 11735. [CrossRef]

22. Boschetti, T.; Barbieri, M.; Barberio, M.D.; Billi, A.; Franchini, S.; Petitta, M. CO_2 Inflow and Elements Desorption Prior to a Seismic Sequence, Amatrice-Norcia 2016, Italy. *Geochem. Geophys. Geosyst.* **2019**, *20*, 2303–2317. [CrossRef]

23. Cappa, F.; Scuderi, M.M.; Collettini, C.; Guglielmi, Y.; Avouac, J.-P. Stabilization of fault slip by fluid injection in the laboratory and in situ. *Sci. Adv.* **2019**, *5*, eaau4065. [CrossRef]

24. Hosono, T.; Masaki, Y. Post-seismic hydrochemical changes in regional groundwater flow systems in response to the 2016 Mw 7.0 Kumamoto earthquake. *J. Hydrol.* **2020**, *580*, 124340. [CrossRef]

25. Shi, Z.; Zhang, H.; Wang, G. Groundwater trace elements change induced by M5.0 earthquake in Yunnan. *J. Hydrol.* **2020**, *581*, 124424. [CrossRef]

26. Hartmann, J.; Levy, J.K. Hydrogeological and Gasgeochemical Earthquake Precursors? A Review for Application. *Nat. Hazards* **2005**, *34*, 279–304. [CrossRef]

27. Uysal, I.T.; Feng, Y.; Zhao, J.; Isik, V.; Nuriel, P.; Golding, S.D. Hydrothermal CO_2 degassing in seismically active zones during the late Quaternary. *Chem. Geol.* **2009**, *265*, 442–454. [CrossRef]

28. Tesei, T.; Collettini, C.; Barchi, M.R.; Carpenter, B.M.; Di Stefano, G. Heterogeneous strength and fault zone complexity of carbonate-bearing thrusts with possible implications for seismicity. *Earth Planet. Sci. Lett.* **2014**, *408*, 307–318. [CrossRef]

29. Scuderi, M.M.; Collettini, C. The role of fluid pressure in induced vs. triggered seismicity: Insights from rock deformation experiments on carbonates. *Sci. Rep.* **2016**, *6*, 24852. [CrossRef]

30. Italiano, F.; Martinelli, G.; Plescia, P. CO_2 Degassing over Seismic Areas: The Role of Mechanochemical Production at the Study Case of Central Apennines. *Pure Appl. Geophys.* **2008**, *165*, 75–94. [CrossRef]

31. Giustini, F.; Blessing, M.; Brilli, M.; Lombardi, S.; Voltattorni, N.; Widory, D. Determining the origin of carbon dioxide and methane in the gaseous emissions of the San Vittorino plain (Central Italy) by means of stable isotopes and noble gas analysis. *Appl. Geochem.* **2013**, *34*, 90–101. [CrossRef]

32. Caracausi, A.; Paternoster, M. Radiogenic helium degassing and rock fracturing: A case study of the southern Apennines active tectonic region. *J. Geophys. Res. Solid Earth* **2015**, *120*, 2200–2211. [CrossRef]

33. Barbieri, M.; Boschetti, T.; Barberio, M.D.; Billi, A.; Franchini, S.; Iacumin, P.; Selmo, E.; Petitta, M. Tracing deep fluid source contribution to groundwater in an active seismic area (central Italy): A combined geothermometric and isotopic ($\delta13C$) perspective. *J. Hydrol.* **2020**, *582*, 124495. [CrossRef]

34. Carminati, E.; Doglioni, C. Alps vs. Apennines: The paradigm of a tectonically asymmetric Earth. *Earth Sci. Rev.* **2012**, *112*, 67–96. [CrossRef]

35. Boni, C.; Bono, P.; Capelli, G. Schema Idrogeologico Dell'Italia Centrale. *Mem. Soc. Geol.* **1986**, *35*, 991–1012.

36. Chiodini, G.; Cardellini, C.; Di Luccio, F.; Selva, J.; Frondini, F.; Caliro, S.; Rosiello, A.; Beddini, G.; Ventura, G. Correlation between tectonic CO_2 Earth degassing and seismicity is revealed by a 10-year record in the Apennines, Italy. *Sci. Adv.* **2020**, *6*, eabc2938. [CrossRef]

37. Madonia, P.; Cangemi, M.; Oliveri, Y.; Germani, C. Hydrogeochemical Characters of Karst Aquifers in Central Italy and Relationship with Neotectonics. *Water* **2020**, *12*, 1926. [CrossRef]

38. Petitta, M.; Primavera, P.; Tuccimei, P.; Aravena, R. Interaction between deep and shallow groundwater systems in areas affected by Quaternary tectonics (Central Italy): A geochemical and isotope approach. *Environ. Earth Sci.* **2011**, *63*, 11–30. [CrossRef]

39. Petitta, M. Idrogeologia della media valle del fiume velino e della piana di s. Vittorino (Rieti, Italia centrale) / hydrogeology of the middle valley of the velino river and of the s. Vittorino plain (Rieti, Central Italy). *Ital. J. Eng. Geol. Environ.* **2009**, 157–181. [CrossRef]

40. Centamore, E.; Nisio, S.; Rossi, D. The San Vittorino Sinkhole Plain: Relationships between bedrock structure, sinking processes, seismic events and hydrothermal springs. *Ital. J. Geosci.* **2009**, *128*, 629–639.

41. Stoppa, F.; Cundari, A. A new Italian carbonatite occurrence at Cupaello (Rieti) and its genetic significance. *Contrib. Mineral. Petrol.* **1995**, *122*, 275–288. [CrossRef]

42. Peccerillo, A. *Plio-Quaternary Volcanism in Italy*; Springer: Berlin/Heidelberg, Germany; New York, NY, USA, 2005; Volume 365, ISBN 978-3-540-25885-8.

43. Barbieri, M. Groundwater mixing in the discharge area of San Vittorino Plain (Central Italy): Geochemical characterization and implication for drinking uses. *Environ. Earth. Sci.* **2017**, *76*, 393. [CrossRef]

44. Doglioni, C. A proposal for the kinematic modelling of W-dipping subductions—possible applications to the Tyrrhenian-Apennines system. *Terra Nova* **1991**, *3*, 423–434. [CrossRef]

45. Patacca, E.; Scandone, P. Geology of the southern Apennines. *Boll. Della Soc. Geol. Ital.* **2007**, *7*, 75–119.

46. Carminati, E.; Fabbi, S.; Santantonio, M. Slab bending, syn-subduction normal faulting, and out-of-sequence thrusting in the Central Apennines: Effects of slab bending in the Apennines. *Tectonics* **2014**, *33*, 530–551. [CrossRef]

47. Centamore, E.; Nisio, S. Tettonica e sedimentazione (Lias-Pleistocene) nella media Valle del Salto (Rieti, Italia Centrale). *Stud. Geol. Camerti* **2002**, *2*, 53–70.

48. Cardello, G.L.; Doglioni, C. From Mesozoic rifting to Apennine orogeny: The Gran Sasso range (Italy). *Gondwana Res.* **2015**, *27*, 1307–1334. [CrossRef]

49. Bigi, S.; Costa Pisani, P. From a deformed Peri-Tethyan carbonate platform to a fold-and-thrust-belt: An example from the Central Apennines (Italy). *J. Struct. Geol.* **2005**, *27*, 523–539. [CrossRef]

50. Deiana, G.; Pasqualini, L.; Salvucci, R.; Stroppa, P.; Tondi, E. Il sistema dei sovrascorrimenti dei Monti Reatini: Analisi geometrica e cinematica. *Stud. Geol. Camerti* **1995**, 199–206.

51. Chiarabba, C.; Jovane, L.; DiStefano, R. A new view of Italian seismicity using 20 years of instrumental recordings. *Tectonophysics* **2005**, *395*, 251–268. [CrossRef]

52. D'Agostino, N. Complete seismic release of tectonic strain and earthquake recurrence in the Apennines (Italy). *Geophys. Res. Lett.* **2014**, *41*, 1155–1162. [CrossRef]

53. Cavinato, G.P.; Celles, P.D. Extensional basins in the tectonically bimodal central Apennines fold-thrust belt, Italy: Response to corner flow above a subducting slab in retrograde motion. *Geology* **1999**, *27*, 955–958. [CrossRef]

54. Centamore, E.; Nisio, S.; Rossi, D. Aspetti geologico-strutturali in relazione alla formazione della 'sinkhole plain' di S. Vittorino. In Proceedings of the State of the Art on the Study of Sinkhole Phenomena and Role of the National and Local Government in the Territory Administration, Rome, Italy, 20–21 May 2004.

55. Carrara, C.; Brunamonte, F.; Ferreli, L.; Lorenzoni, P.; Margheriti, L.; Michetti, A.M.; Raglione, M.; Rosati, M.; Serva, L. I terrazzi della medio-bassa Valle del Fiume Velino. *Stud. Geol. Camerti* **1993**, *1992*, 97–102.

56. Castellarin, A.; Colacicchi, R.; Praturlon, A.; Cantelli, C. The jurassic-lower pliocene history of the Ancona-Anzio Line (Central Italy). *Mem. Della Soc. Geol. Ital.* **1982**, *24*, 325–336.

57. Butler, R.W.H.; Tavarnelli, E.; Grasso, M. Structural inheritance in mountain belts: An Alpine–Apennine perspective. *J. Struct. Geol.* **2006**, *28*, 1893–1908. [CrossRef]

58. Pizzi, A.; Galadini, F. Pre-existing cross-structures and active fault segmentation in the northern-central Apennines (Italy). *Tectonophysics* **2009**, *476*, 304–319. [CrossRef]

59. Dramis, F. Il ruolo dei sollevamenti tettonici a largo raggio nella genesi del rilievo appenninico. *Stud. Geol. Camerti* **1993**, *1*, 9–15.

60. Faccenna, C.; Florindo, F.; Funiciello, R.; Lombardi, S. Tectonic setting and Sinkhole Features: Case histories from western Central Italy. In *Neotectonics: Recent Advances. Quaternary Proceedings*; Owen, L.A., Stewart, I., Vita-Finzi, C., Eds.; Quaternary Research Association: Cambridge, UK, 1993; Volume 3, pp. 47–56.

61. Centamore, E.; Nisio, S. Effects of uplift and tilting in the Central-Northern Apennines (Italy). *Quat. Int.* **2003**, *101–102*, 93–101. [CrossRef]

62. D'Agostino, N.; Jackson, J.A.; Dramis, F.; Funiciello, R. Interactions between mantle upwelling, drainage evolution and active normal faulting: An example from the central Apennines (Italy). *Geophys. J. Int.* **2001**, *147*, 475–497. [CrossRef]

63. Fiorillo, F.; Petitta, M.; Preziosi, E.; Rusi, S.; Esposito, L.; Tallini, M. Long-term trend and fluctuations of karst spring discharge in a Mediterranean area (central-southern Italy). *Environ. Earth Sci.* **2015**, *74*, 153–172. [CrossRef]

64. Boni, C.; Petitta, M. Sorgenti lineari e valutazione dell'infiltrazione efficace in alcuni bacini dell'Italia Centrale. *Quad. Geol. Appl.* **1994**, *1*, 99–113.

65. Chiodini, G.; Cardellini, C.; Caliro, S.; Chiarabba, C.; Frondini, F. Advective heat transport associated with regional Earth degassing in central Apennine (Italy). *Earth Planet. Sci. Lett.* **2013**, *373*, 65–74. [CrossRef]

66. Lombardi, S.; Annunziatellis, A.; Beaubien, S.E.; Ciotoli, G. Near-surface gas geochemistry techniques to assess and monitor CO2 geological sequestration sites. In *Advances in the Geological Storage of Carbon Dioxide*; Lombardi, S., Altunina, L.K., Beaubien, S.E., Eds.; Kluwer Academic Publishers: Dordrecht, The Netherlands, 2006; Volume 65, pp. 141–156. ISBN 978-1-4020-4469-4.

67. Salvati, R.; Sasowsky, I.D. Development of collapse sinkholes in areas of groundwater discharge. *J. Hydrol.* **2002**, *264*, 1–11. [CrossRef]

68. Annunziatellis, A.; Beaubien, S.E.; Ciotoli, G.; Lombardi, S.; Nisio, S.; Nolasco, F. Studio dei parametri geologici e geochimici per la comprensione dei meccanismi genetici degli sprofondamenti nella piana di S. Vittorino (Rieti). In Proceedings of the State of the Art on the Study of Sinkhole Phenomena and Role of the National and Local Government in the Territory Administration, Rome, Italy, 20–21 May 2004.

69. Bridgewater, L.L.; Baird, R.B. *Standard Methods for the Examination of Water and Wasterwater*, 23rd ed.; American Public Health Association, American Water Works Association, Water Environment Federation, Eds.; American Public Health Association: Washington, DC, USA, 2017; ISBN 978-0-87553-287-5.

70. Nigro, A.; Sappa, G.; Barbieri, M. Application of boron and tritium isotopes for tracing landfill contamination in groundwater. *J. Geochem. Explor.* **2017**, *172*, 101–108. [CrossRef]

71. Epstein, S.; Mayeda, T. Variation of O18 content of waters from natural sources. *Geochim. Cosmochim. Acta* **1953**, *4*, 213–224. [CrossRef]

72. Capasso, G.; Favara, R.; Grassa, F.; Inguaggiato, S.; Longo, L. On-line technique for preparing and measuring stable carbon isotope of total dissolved inorganic carbon in water samples (d13CTDIC). *Ann. Geophys.* **2005**, *48*, 159–166.

73. Caracausi, A.; Sulli, A. Outgassing of Mantle Volatiles in Compressional Tectonic Regime Away From Volcanism: The Role of Continental Delamination. *Geochem. Geophys. Geosyst.* **2019**, *20*, 2007–2020. [CrossRef]

74. Capasso, G.; Inguaggiato, S. A simple method for the determination of dissolved gases in natural waters. An application to thermal waters from Vulcano Island. *Appl. Geochem.* **1998**, *13*, 631–642. [CrossRef]

75. Parkhurst, D.L.; Appelo, C.A.J. Description of Input and Examples for PHREEQC Version 3—A Computer Program for Speciation, Batch-Reaction, One-Dimensional Transport, and Inverse Geochemical Calculations, (USGS). 2013. Available online: https://pubs.usgs.gov/tm/06/a43/ (accessed on 10 April 2020).

76. Bethke, C. *Geochemical and Biogeochemical Reaction Modeling*, 2nd ed.; Oxford University Press: Cambridge, UK; New York, NY, USA, 2008; ISBN 978-0-521-87554-7.

77. Chiodini, G.; Frondini, F.; Cardellini, C.; Parello, F.; Peruzzi, L. Rate of diffuse carbon dioxide Earth degassing estimated from carbon balance of regional aquifers: The case of central Apennine, Italy. *J. Geophys. Res.* **2000**, *105*, 8423–8434. [CrossRef]

78. Plummer, L.N.; Prestemon, E.C.; Parkhurst, D.L. An interactive code (NETPATH) for modeling net geochemical reactions along a flow path, version 2.0. *Water Resour. Investig. Rep.* **1994**, *94*, 4169.

79. Parkhurst, D.L.; Charlton, S.R. *NetpathXL—An Excel Interface to the Program NETPATH*; U.S. Geological Survey Techniques and Methods 6–A26; USGS: Reston, VA, USA, 2008.

80. Di Luccio, F.; Chiodini, G.; Caliro, S.; Cardellini, C.; Convertito, V.; Pino, N.A.; Tolomei, C.; Ventura, G. Seismic signature of active intrusions in mountain chains. *Sci. Adv.* **2018**, *4*, e1701825. [CrossRef]

81. Frondini, F.; Cardellini, C.; Caliro, S.; Beddini, G.; Rosiello, A.; Chiodini, G. Measuring and interpreting CO 2 fluxes at regional scale: The case of the Apennines, Italy. *J. Geol. Soc.* **2019**, *176*, 408–416. [CrossRef]

82. Masi, U.; Tucci, P.; Azzaro, E. Chemiostratigrafia e petrografia della formazione dolomitica triassica di Antrodoco (Rieti, Lazio settentrionale). *Geol. Romana* **1995**, *31*, 307–318.

83. OriginLab. *Origin User Guide*; OriginLab Corporation: Northampton, MA, USA, 2018.

84. Capotorti, F.; Fumanti, F.; Mariotti, G. Carta geologica del settore compreso tra il M. Nuria, il M. Gabbia e l'alta valle del F. Velino (Appennino Centrale)—scala 1: 50000. *Stud. Geol. Camerti* **1996**. Available online: http://193.204.8.201:8080/jspui/handle/1336/763 (accessed on 10 April 2020).

85. Piper, A.M. A graphic procedure in the geochemical interpretation of water-analyses. *Trans. AGU* **1944**, *25*, 914. [CrossRef]

86. Ozima, M.; Podosek, F.A. *Noble Gas Geochemistry*, 2nd ed.; Cambridge University Press: Cambridge, UK; New York, NY, USA, 2002; ISBN 978-0-521-80366-3.

87. Defennu, L.; Lombardi, S.; Federici, C. An introductory note on statistical analysis of physio-chemical characteristics of natural waters. Application to some Central Apennines spring waters. Atti della Accademia Nazionale dei Lincei. Classe di Scienze Fisiche, Matematiche e Naturali. *Rendiconti* **1975**, *59*, 125–139.

88. Governa, M.E.; Masciocco, L.; Riba, M.; Zuppi, G.M.; Lombardi, S. Karst and geothermal water circulation in the Central Apennines (Italy). In *Isotope Techniques in the Study of the Hydrology of Fractured and Fissured Rocks*; International Atomic Energy Agency: Vienna, Austria, 1989.

89. Civita, M.V.; Fiorucci, A. The recharge-discharge process of the Peschiera spring system (central Italy). *Aqua Mundi* **2010**, *1*, 161–178.

90. Rosen, M.R.; Binda, G.; Archer, C.; Pozzi, A.; Michetti, A.M.; Noble, P.J. Mechanisms of Earthquake-Induced Chemical and Fluid Transport to Carbonate Groundwater Springs After Earthquakes. *Water Resour. Res.* **2018**, *54*, 5225–5244. [CrossRef]

91. Battistel, M.; Hurwitz, S.; Evans, W.; Barbieri, M. Multicomponent Geothermometry Applied to a Medium-low Enthalpy Carbonate-evaporite Geothermal Reservoir. *Energy Procedia* **2014**, *59*, 359–365. [CrossRef]

92. Marini, L.; Chiodini, G.; Cioni, R. New geothermometers for carbonate—evaporite geothermal reservoirs. *Geothermics* **1986**, *15*, 77–86. [CrossRef]

93. Minissale, A.A.; Duchi, V. Geothermometry on fluids circulating in a carbonate reservoir in north-central Italy. *J. Volcanol. Geotherm. Res.* **1988**, *35*, 237–252. [CrossRef]

94. Chiodini, G.; Cioni, R.; Guidi, M.; Marini, L. Chemical geothermometry and geobarometry in hydrothermal aqueous solutions: A theoretical investigation based on a mineral-solution equilibrium model. *Geochim. Cosmochim. Acta* **1991**, *55*, 2709–2727. [CrossRef]

95. Chiodini, G.; Frondini, F.; Marini, L. Theoretical geothermometers and PCO2 indicators for aqueous solutions coming from hydrothermal systems of medium-low temperature hosted in carbonate-evaporite rocks. Application to the thermal springs of the Etruscan Swell, Italy. *Appl. Geochem.* **1995**, *10*, 337–346. [CrossRef]

96. Sanjuan, B.; Millot, R.; Ásmundsson, R.; Brach, M.; Giroud, N. Use of two new Na/Li geothermometric relationships for geothermal fluids in volcanic environments. *Chem. Geol.* **2014**, *389*, 60–81. [CrossRef]

97. Ford, D.; Williams, P.W. *Karst Hydrogeology and Geomorphology*; John Wiley & Sons: Chichester, UK; Hoboken, NJ, USA, 2007; ISBN 978-0-470-84996-5.

98. Awaleh, M.O.; Boschetti, T.; Adaneh, A.E.; Daoud, M.A.; Ahmed, M.M.; Dabar, O.A.; Soubaneh, Y.D.; Kawalieh, A.D.; Kadieh, I.H. Hydrochemistry and multi-isotope study of the waters from Hanlé-Gaggadé grabens (Republic of Djibouti, East African Rift System): A low-enthalpy geothermal resource from a transboundary aquifer. *Geothermics* **2020**, *86*, 101805. [CrossRef]

99. Blasco, M.; Gimeno, M.J.; Auqué, L.F. Low temperature geothermal systems in carbonate-evaporitic rocks: Mineral equilibria assumptions and geothermometrical calculations. Insights from the Arnedillo thermal waters (Spain). *Sci. Total Environ.* **2018**, *615*, 526–539. [CrossRef]

100. Franchini, S.; Agostini, S.; Barberio, M.D.; Barbieri, M.; Billi, A.; Boschetti, T.; Pennisi, M.; Petitta, M. HydroQuakes, central Apennines, Italy: Towards a hydrogeochemical monitoring network for seismic precursors and the hydro-seismo-sensitivity of boron. *J. Hydrol.* **2020**, 125754. [CrossRef]

101. Collettini, C.; Cardellini, C.; Chiodini, G.; De Paola, N.; Holdsworth, R.E.; Smith, S.A.F. Fault weakening due to CO_2 degassing in the Northern Apennines: Short- and long-term processes. *Geol. Soc. Lond. Spec. Publ.* **2008**, *299*, 175–194. [CrossRef]

102. Trumpy, E.; Manzella, A. Geothopica and the interactive analysis and visualization of the updated Italian National Geothermal Database. *Int. J. Appl. Earth Obs. Geoinf.* **2017**, *54*, 28–37. [CrossRef]

103. Giggenbach, W.F. Chemical Techniques in Geothermal Exploration. In *D'Amore, F. Applications of Geochemistry in Geothermal Reservoir Development*; UNITAR/UNDP Publication: Rome, Italy, 1991; pp. 119–142.

104. Chatterjee, S.; Sarkar, A.; Deodhar, A.S.; Biswal, B.P.; Jaryal, A.; Mohokar, H.V.; Sinha, U.K.; Dash, A. Geochemical and isotope hydrological characterisation of geothermal resources at Godavari valley, India. *Environ. Earth. Sci.* **2017**, *76*, 97. [CrossRef]

105. Hou, Y.; Shi, Z.; Mu, W. Fluid Geochemistry of Fault Zone Hydrothermal System in the Yidun-Litang Area, Eastern Tibetan Plateau Geothermal Belt. *Geofluids* **2018**, *2018*, 1–13. [CrossRef]

106. Shakeri, A.; Moore, F.; Kompani-Zare, M. Geochemistry of the thermal springs of Mount Taftan, southeastern Iran. *J. Volcanol. Geotherm. Res.* **2008**, *178*, 829–836. [CrossRef]

107. Göb, S.; Loges, A.; Nolde, N.; Bau, M.; Jacob, D.E.; Markl, G. Major and trace element compositions (including REE) of mineral, thermal, mine and surface waters in SW Germany and implications for water–rock interaction. *Appl. Geochem.* **2013**, *33*, 127–152. [CrossRef]

108. Reimann, C.; de Caritat, P. *Chemical Elements in the Environment*; Springer: Berlin/Heidelberg, Germany, 1998; ISBN 978-3-642-72018-5.

109. Morgantini, N.; Frondini, F.; Cardellini, C. Natural trace elements baselines and dissolved loads in groundwater from carbonate aquifers of central Italy. *Phys. Chem. Earth* **2009**, *34*, 520–529. [CrossRef]

110. Bencini, A. Considerazioni sulla distribuzione geochimica del cesio nelle acque termali toscane. *Rend. Della Soc. Ital. Mineral. e Petrologia* **1984**, *39*, 449–454.

111. Boschetti, T.; Venturelli, G.; Toscani, L.; Barbieri, M.; Mucchino, C. The Bagni di Lucca thermal waters (Tuscany, Italy): An example of $CaSO_4$ waters with high Na/Cl and low $CaSO_4$ ratios. *J. Hydrol.* **2005**, *307*, 270–293. [CrossRef]

112. Capecchiacci, F.; Tassi, F.; Vaselli, O.; Bicocchi, G.; Cabassi, J.; Giannini, L.; Nisi, B.; Chioccciora, G. A combined geochemical and isotopic study of the fluids discharged from the Montecatini thermal system (NW Tuscany, Italy). *Appl. Geochem.* **2015**, *59*, 33–46. [CrossRef]

113. Craig, H. Isotopic Variations in Meteoric Waters. *Science* **1961**, *133*, 1702–1703. [CrossRef]

114. Spadoni, M.; Brilli, M.; Giustini, F.; Petitta, M. Using GIS for modelling the impact of current climate trend on the recharge area of the S. Susanna spring (central Apennines, Italy). *Hydrol. Process.* **2010**, *24*, 50–64. [CrossRef]

115. Minissale, A.; Vaselli, O. Karst springs as "natural" pluviometers: Constraints on the isotopic composition of rainfall in the Apennines of central Italy. *Appl. Geochem.* **2011**, *26*, 838–852. [CrossRef]

116. Archer, C.; Noble, P.; Kreamer, D.; Piscopo, V.; Petitta, M.; Rosen, M.R.; Poulson, S.R.; Piovesan, G.; Mensing, S. Hydrochemical determination of source water contributions to Lake Lungo and Lake Ripasottile (central Italy). *J. Limnol.* **2016**. [CrossRef]

117. Gat, J.R.; Carmi, I. Effect of climate changes on the precipitation patterns and isotopic composition of water in a climate transition zone: Case of the Eastern Mediterranean Sea area. In *The Influence of Climate Change and Climatic Variability on the Hydrologic Regime and Water Resources*; International Association Hydrological Sciences Publication Vancouver: Wallingford, UK, 1987; Volume 168, pp. 513–523.

118. Bono, P.; Gonfiantini, R.; Alessio, M.; Fiori, C.; D'Amelio, L. Stable isotopes (d18O, d2H) and tritium in precipitation: Results and comparison with groundwater perched aquifers of Central Italy. In *Isotopic Composition of Precipitation in the Mediterranean Basin in Relation to Air Circulation Patterns and Climate*; TECDOC Series; International Atomic Energy Agency: Vienna, Austria, 2005; Volume 1453, pp. 115–124.

119. Gherardi, F.; Bono, P.; Fiori, C.; Tejeiro, M.D.; Gonfiantini, R. Modeling the altitude isotope effect in precipitations and comparison with the altitude effect in groundwater. In Proceedings of the International Symposium on Advances in Isotope Hydrology and its Role in Sustainable Water Resources Management (IHS-2007), Vienna, Austria, 21–25 May 2007; Volume 21, p. 269.

120. Longinelli, A.; Selmo, E. Isotopic composition of precipitation in Italy: A first overall map. *J. Hydrol.* **2003**, *270*, 75–88. [CrossRef]

121. Celico, P.; Gonfiantini, R.; Koizumi, M.; Mangano, F. Environmental isotope studies of limestone aquifers in central Italy. *Isot. Hydrol.* **1983**, *6*, 173–192.

122. Boschetti, T.; Cifuentes, J.; Iacumin, P.; Selmo, E. Local Meteoric Water Line of Northern Chile (18° S–30° S): An Application of Error-in-Variables Regression to the Oxygen and Hydrogen Stable Isotope Ratio of Precipitation. *Water* **2019**, *11*, 791. [CrossRef]

123. Zuppi, G.M.; Bortolami, G. Hydrogeology: A privileged field for environmental stable isotopes applications. *Some Italian examples. Rend. Della Soc. Ital. Mineral. Petrologia* **1982**, *38*, 1197–1212.

124. Romano, E.; Preziosi, E. Precipitation pattern analysis in the Tiber River basin (central Italy) using standardized indices: Precipitation pattern analysis in the tiber river basin. *Int. J. Climatol.* **2013**, *33*, 1781–1792. [CrossRef]

125. Burnard, P.; Bourlange, S.; Henry, P.; Geli, L.; Tryon, M.D.; Natal'in, B.; Sengör, A.M.C.; Özeren, M.S.; Çagatay, M.N. Constraints on fluid origins and migration velocities along the Marmara Main Fault (Sea of Marmara, Turkey) using helium isotopes. *Earth Planet. Sci. Lett.* **2012**, *341–344*, 68–78. [CrossRef]

126. O'Nions, R.K.; Oxburgh, E.R. Helium, volatile fluxes and the development of continental crust. *Earth Planet. Sci. Lett.* **1988**, *90*, 331–347. [CrossRef]

127. Caracausi, A.; Martelli, M.; Nuccio, P.M.; Paternoster, M.; Stuart, F.M. Active degassing of mantle-derived fluid: A geochemical study along the Vulture line, southern Apennines (Italy). *J. Volcanol. Geotherm. Res.* **2013**, *253*, 65–74. [CrossRef]

128. Sano, Y.; Gamo, T.; Williams, S.N. Secular variations of helium and carbon isotopes at Galeras volcano, Colombia. *J. Volcanol. Geotherm. Res.* **1997**, *77*, 255–265. [CrossRef]

129. Martelli, M.; Nuccio, P.M.; Stuart, F.M.; Di Liberto, V.; Ellam, R.M. Constraints on mantle source and interactions from He-Sr isotope variation in Italian Plio-Quaternary volcanism: Italian plio-quaternary volcanism. *Geochem. Geophys. Geosyst.* **2008**, *9*, 1–16. [CrossRef]

130. Cardello, G.L.; Consorti, L.; Palladino, D.M.; Carminati, E.; Carlini, M.; Doglioni, C. Tectonically controlled carbonate-seated maar-diatreme volcanoes: The case of the Volsci Volcanic Field, central Italy. *J. Geodyn.* **2020**, *139*, 101763. [CrossRef]

131. Ballentine, C.J.; Marty, B.; Lollar, B.S.; Cassidy, M. Neon isotopes constrain convection and volatile origin in the Earth's mantle. *Nature* **2005**, *433*, 6. [CrossRef] [PubMed]

132. Graham, D.W. Noble Gas Isotope Geochemistry of Mid-Ocean Ridge and Ocean Island Basalts: Characterization of Mantle Source Reservoirs. *Rev. Mineral. Geochem.* **2002**, *47*, 247–317. [CrossRef]

133. Sano, Y.; Marty, B. Origin of carbon in fumarolic gas from island arcs. *Chem. Geol.* **1995**, *119*, 265–274. [CrossRef]

134. Sharp, Z. *Principles of Stable Isotope Geochemistry*, 2nd ed.; The University of New Mexico: Albuquerque, NM, USA, 2017. [CrossRef]

135. Pistiner, J.S.; Henderson, G.M. Lithium-isotope fractionation during continental weathering processes. *Earth Planet. Sci. Lett.* **2003**, *214*, 327–339. [CrossRef]

136. Teng, F.Z.; McDonough, W.F.; Rudnick, R.L.; Wing, B.A. Limited lithium isotopic fractionation during progressive metamorphic dehydration in metapelites: A case study from the Onawa contact aureole, Maine. *Chem. Geol.* **2007**, *239*, 1–12. [CrossRef]

137. Mathurin, F.A.; Drake, H.; Tullborg, E.-L.; Berger, T.; Peltola, P.; Kalinowski, B.E.; Åström, M.E. High cesium concentrations in groundwater in the upper 1.2km of fractured crystalline rock—Influence of groundwater origin and secondary minerals. *Geochim. Cosmochim. Acta* **2014**, *132*, 187–213. [CrossRef]

6. Conclusion

Earthquakes are among the main natural processes that can produce the strongest perturbations in the Earth's crust. The seismic cycle causes strain which changes fluid pressure and alters hydrogeological properties. Chemical and physical responses to seismicity have been abundantly observed in tectonic active areas all over the world. Hydrogeological and geochemical responses include changes in groundwater level, chemical-physical parameters (e.g., temperature, electrical conductivity, pH), groundwater chemistry (e.g., contents of major ions and minor elements), isotope composition, stream flow, and gas-geochemistry. In detail, changes in groundwater level and discharge are interpreted as pore-pressure response to crustal elastic strain and permeability changes, while variations in hydrogeochemistry and isotopic signature of groundwater are explained as the results of mixing of groundwater, rock weathering enhancement in new rupturing, and deep hydrothermal fluid upwelling along regional tectonic discontinuities. Thus, defining fluids origin and possible water-gas-rock interaction processes during the upward migration of deep fluids can provide new constraints aimed at the comprehension of seismogenic processes. Scientific efforts are moving towards this direction to obtain and also to compare many observations in different geo-tectonic contexts, to build and constrain reliable hydrogeological and hydrogeochemical models.

Therefore, this research project aimed at taking a step forward in the comprehension of the *Hydrosensitivity* of shallow regional aquifers to respond to external natural perturbations. In the study, the attention was mainly focused on (i) groundwater-seismicity direct relationship, and (ii) mixing with ascending deep fluids to be further correlated with crustal deformation processes.

The first relevant step was to identify the study area with the aim of conducting the research activity in the best possible geological conditions. Thus, based on some fundamental geological-structural, and hydrological-hydrogeochemical criteria, the central-southern Apennines (central-southern Italy) were selected. They represent a natural promising laboratory for monitoring geofluids as markers of active seismogenic processes. Regional aquifers are hosted by fractured Meso-Cenozoic carbonates that are characterized by a great abundance of groundwater resources and their nature enhances the response to deep fluids uplift, allowing fast and concentrate changes in groundwater close to tectonic lines. Additionally, the intense seismic activity affecting this area, confirms the relevance of the research to better understand the direct interactions between seismicity and hydrogeology. In fact, in the central-southern Apennines, crustal tectonic extension is active and seismogenic, and significant deep fluids contributions to shallow groundwater are

associated with this crustal tectonic regime. Tensional tectonic environment creates pathways for the uprising deep fluids connecting the deep portion of crust to the shallow one. The origin of deep fluids (mainly CO_2) was explained as being the combination of both a mantle source and a product of thermometamorphic reactions within the buried Meso-Cenozoic limestone.

Following the above-consideration, active tectonic areas characterized by evident deep fluids contributions and regional groundwater circulations were chosen (i.e., Matese and Contursi sites) to conduct hydrogeological and hydrogeochemical monitoring performed through the three years of research activity. Additionally, retrieved data from pre-existing hydrogeological test sites (i.e., Sulmona and San Vittorino plain) in central Italy were considered and processed in order to study simultaneously the investigated geological processes in different sites with similar features in the Apennine context.

The work was carried on through two different approaches:

1) To investigate the groundwater-seismicity relationship, a long-term hydrogeological and hydrogeochemical monitoring was adopted. It consisted of the collection of both discrete (i.e., periodical sampling surveys) and continuous data (i.e., measurements with probes installed at springs and wells) with the seismic characterization of the study area for the detection of groundwater and gas variations possibly related to the seismicity. In detail, hydrogeological and hydrogeochemical parameters potentially influenced by seismic activity (i.e., temperature, pH, electrical conductivity, major and trace elements contents, isotopic composition of groundwater and dissolved gases) were analysed. The existence and modalities of a cause-effect relationship between the hydrogeological and hydrogeochemical signals with the seismic ones were detected. In the Matese area, four basal springs of carbonate aquifers were identified to conduct this multidisciplinary investigation and surveys were regularly carried out. Also, hydrogeological and gas-geochemical data from continuous monitoring performed in the Sulmona area were analyzed in relation to seismicity.

2) To assess mixing and upwelling of deep fluids in shallow groundwater, detailed integrated analyses of groundwater with very different geochemical features were executed. A complete characterization of the hydrogeochemistry of groundwater was realized, by determining groundwater-rock interaction processes, saturation indices, fluids origin, residence times, trace elements content, gas origin and abundance. Additionally, an interpretative deep fluids and groundwater flowpath was drawn with the aid of the construction of schematic cross-sections. In the Contursi area, 22 springs were chosen for this investigation (i.e., discrete collection of

samples for several analyses, and measurements of hydrogeochemical parameters). Also, data of groundwater samples from the San Vittorino plain were addressed to many hydrogeochemical analyses. Data were processed in order to define relationship between the shallow and deep end-members.

In the light of the obtained results, it is possible to state that the following prerogatives are essential for verifying the interactions between groundwater and earthquakes, and for the assessing of deep fluids upwelling and mixing with shallow groundwater:

• The acquisition of a geological-structural conceptual model for the identification of the monitoring area, and for the selection of parameters to be measured during the hydrogeological and hydrogeochemical monitoring.

• The identification of discharge areas characterized by the presence of different hydrogeochemical springs which could be representative of monitoring points on the basis of a complete hydrogeochemical/isotopic analysis. It is essential to make the acquired data useful to correctly interpret the complex chemical-physical processes and dynamics occurring in the crust.

• The identification of hydrosensitive areas, characterized by a long and deep flowpath in regional aquifers, influenced by the upwelling of deep hydrothermal fluids, and with low anthropic noises.

• The systematic monitoring to carry out a comparative analysis of the many parameters according to reliable methods and professional tools.

Concerning the possible earthquake-induced responses in groundwater, the achieved results allow to define the following significant conclusions:

- Despite the absence of strong seismic events during the monitoring period, the discrete and continuous hydrogeological and hydrogeochemical monitoring shed light on the possibility of having pre-seismic hydrogeochemical signals in springs also for small-intermediate earthquake magnitude, at least in the areas where deep fluids contribution to groundwater is evident.

- Anomalous concentrations of Ca^{2+}, Na^+ and HCO_3^- were recorded in one sample before and in another one after the 2019 Benevento seismic sequence (main earthquake on December 16th, 2019: M_w 3.9 San Leucio del Sannio) at Grassano spring (in the Matese area).

- Changes in groundwater chemical content are attributable to the progressive increase of CO_2 in the aquifer system continuously measured at Grassano spring. This increase of

dissolved gas temporarily lowered pH (discretely and continuously measured) and enhanced the solubility of the above-mentioned major ions, that define the hydrochemical facies recognised at this site.

- The behaviour of fractured aquifers in relation to the seismic activity is compatible with the geological-structural conceptual model considered in this study. Deep pre-seismic dilatational processes produced the observed behaviour of pH during the pre-seismic phases owing to the inflow of deep CO_2 into the shallow carbonate system. This condition could be linked to a variation of the pore pressure at depth in the months before the onset of the seismic sequence (variations of the fluids flowpaths: from areas with higher pore pressure to areas with lower pore pressure).

- Isotopic signature of $\delta^{13}C$ and carbon mass balance confirm the deep origin of carbon dioxide whose influx and ascent in the regional carbonate aquifer were continuously detected by using CO_2 probe.

The large amount of data collected in the Matese area through these three years, as shown in Chapter 4, requires much more developed processing than reported. In fact, the attention here has focused on the hydrogeological and hydrogeochemical anomalies pointed out at Grassano spring related to the Benevento seismic sequence at the end of 2019. It is worthy of note that this seismic swarm was the most energetic that occurred a few kilometres from the monitoring site during the whole studied period. A more in-depth and detailed study of the time series acquired over the PhD will be accomplished in a desirable continuation of the research project.

However, groundwater-seismicity relationship was also deepened by the in-depth study and the processing of retrieved data in the Matese and Sulmona areas which allow to detect other significant hydrogeological and hydrogeochemical changes possibly related to the seismic activity (both in the near-field, as well as in the far-field):

- Gas-geochemical Radon monitoring highlighted significant Rn increases recorded before three seismic events ($M_w < 4.5$: i.e., M_w 4.4 Balsorano earthquake occurred on November 7th, 2019; M_w 3.8 L'Aquila earthquake occurred on March 31st, 2018; M_w 3.9 San Leucio del Sannio earthquake occurred on 16th December 2019) at two springs (Matese and Sulmona area). Rn anomalies were found for all monitored seismic events that were expected to influence the Rn concentration in groundwater based on the strain radius (R in km) of the effective precursory manifestation zone (from Barberio et al. 2020 in the Discussion section, paragraph 5.2).

- The sensitive behaviour of the dissolved gas in relation to crustal deformation processes, depended on the earthquake's magnitude and epicentral distance. The pre-seismic signals pointed out in the gas dissolved concentration could be explained as the result of dilation and/or contraction of fracture systems that led to changes in the gas flow. Pre-seismic signals could be linked both to deep processes (i.e., deep CO_2 acting as a carrier for radon) or shallow (due to fracturing and opening of new fractures).

- The study and the analysis of the hydrogeological data (i.e., piezometric level) acquired through the years in the Sulmona area at the PF60.3 monitoring well allow to identify groundwater level post-seismic fluctuations characterized by an impulsive character related to the passage of Rayleigh seismic waves (i.e., dynamic stress) produced by distant earthquakes (up to 18.000 km far).

- The peculiar responses of the monitoring well PF60.3 highlighted once again the potential sensitivity of the fractured aquifers to the strain variation.

Furthermore, this research activity confirms and highlights once again that groundwater hydrogeochemistry is a powerful tool for analysing mixing and related processes. Both case studies shed light on the role of deep-seated normal faults that could represent the best network of pathways for deep fluids migration towards the surface allowing the mixing between deep fluids and groundwater of shallow aquifers.

In detail, the following conclusions were drawn for the Contursi area:

- The processing of all the hydrogeochemical data allows to define water-rock interaction processes (by the calculation of saturation indices, main ion ratios and trace element distributions), groundwater origin (by stable isotope signatures), residence times (by tritium radioactive isotope), and fluids flowpaths at depth, were recognised.

- The identification of existence of more complex and regional groundwater hydrodynamics for thermal and mineralized groundwater. Instead, local flow systems fed by cold groundwater at the boundary of the regional carbonate aquifers.

- Hydrogeochemical results are in line with recent geophysical studies carried out in this sector of Apennines that shed light on a diffused high V_P/V_S ratio within the deep fractured carbonates (i.e., Apulian Platform) due to the presence of deep-seated fluid accumulation (e.g., mixtures of brine-CO_2).

Other and similar conclusions were made for the San Vittorino plain:

- Trace element occurrence clarifies the water-rock interaction processes and supports the conceptual model based on the localized uprising of deep fluids along high-angle faults.
- Knowing the mixing degree among different springs, it is possible to recognize whether and where the flux of the deep portion, modulated by fault activity, increases, or decreases with respect to permeability variations along the uprising zones.
- The analysis of He and CO_2 isotopes confirms the presence of a deep component with possible traces of mantle-derived helium (1–2%). These values are particularly remarkable since San Vittorino Plain is located in the inner part of the chain, where ^4He largely dominate in groundwater due to water-rock interaction and large residence time of fluids in the crust.
- Based on geothermometrical analysis, the origin of the deep fluid portion at a depth of approximately 7–10 km was inferred, where Apennine earthquakes usually occur.

Ultimately, the promising results obtained during the last three years shed light on the role of the integrated approach in hydrogeological and hydrogeochemical monitoring to expand the knowledge about the relationship between the geochemical process in groundwater due to the mixing with deep fluids to be possibly correlated with seismicity in active tectonic areas. Since previous works invoked overpressured fluids at depth as primary mechanism of interaction between fluid dynamic and earthquake triggering, for future research the hydrogeological and hydrogeochemical investigation could be based on high-frequency and long-lasting multiparametric monitoring to quantify these pulsations as function of changes in mixing ratio between shallow groundwater and deep contributions.

References

Adinolfi Falcone, R., Carucci, V., Falgiani, A., Manetta, M., Parisse, B., Petitta, M., ... & Tallini, M. (2012). Changes on groundwater flow and hydrochemistry of the Gran Sasso carbonate aquifer after 2009 L'Aquila earthquake. Italian Journal of Geosciences, 131(3), 459-474.

Adinolfi, G. M., De Matteis, R., Orefice, A., Festa, G., Zollo, A., de Nardis, R., & Lavecchia, G. (2015). The September 27, 2012, ML 4.1, Benevento earthquake: A case of strike-slip faulting in Southern Apennines (Italy). Tectonophysics, 660, 35-46.

Allocca, V., Manna, F., & De Vita, P. (2014). Estimating annual groundwater recharge coefficient for karst aquifers of the southern Apennines (Italy). Hydrology and Earth System Sciences, 18(2), 803-817.

Amoruso, A., Crescentini, L., Petitta, M., Rusi, S., & Tallini, M. (2011). Impact of the 6 April 2009 L'Aquila earthquake on groundwater flow in the Gran Sasso carbonate aquifer, Central Italy. Hydrological Processes, 25(11), 1754-1764.

Andreo, B., Barberá, J. A., Mudarra, M., Marín, A. I., García-Orellana, J., Rodellas, V., & Pérez, I. (2018). A multi-method approach for groundwater resource assessment in coastal carbonate (karst) aquifers: the case study of Sierra Almijara (southern Spain). Hydrogeology journal, 26(1), 41-56.

Aucelli, P. P., Cesarano, M., Di Paola, G., Filocamo, F., & Rosskopf, C. M. (2013). Geomorphological map of the central sector of the Matese Mountains (Southern Italy): an example of complex landscape evolution in a Mediterranean mountain environment. Journal of Maps, 9(4), 604-616.

Baird R.B., Eaton A.D., & Rice, E.W. (2017). Standard methods for examination of water and wastewater, 23rd edn. American Public Health Association (APHA), American Water Works Association (AWWA), Water Environment Federation (WEF), Washington DC

Barberio, M. D., Barbieri, M., Billi, A., Doglioni, C., & Petitta, M. (2017). Hydrogeochemical changes before and during the 2016 Amatrice-Norcia seismic sequence (central Italy). Scientific reports, 7(1), 1-12.

Barberio, M. D., Gori, F., Barbieri, M., Billi, A., Devoti, R., Doglioni, C., Petitta, M., Riguzzi, F., & Rusi, S. (2018). Diurnal and semidiurnal cyclicity of radon (222rn) in groundwater, Giardino spring, central Apennines, Italy. Water, 10(9), 1276.

Barberio, M.D. (2019). Monitoraggio idrogeologico come potenziale metodologia d'indagine dei precursori sismici. PhD Thesis.

Barbieri, M., Nigro, A., & Petitta, M. (2017). Groundwater mixing in the discharge area of San Vittorino Plain (Central Italy): geochemical characterization and implication for drinking uses. Environmental Earth Sciences, 76(11), 1-14.

Barbieri, M. (2019). Isotopes in hydrology and hydrogeology. Water, 11(2), 291.

Barbieri, M., Boschetti, T., Barberio, M. D., Billi, A., Franchini, S., Iacumin, P., ... & Petitta, M. (2020). Tracing deep fluid source contribution to groundwater in an active seismic area (central Italy): A combined geothermometric and isotopic (δ13C) perspective. Journal of Hydrology, 582, 124495.

Barchi, M., Amato, A., Cippitelli, G., Merlini, S., & Montone, P. (2007). Extensional tectonics and seismicity in the axial zone of the Southern Apennines. Bollettino della Societa Geologica Italiana, Spec. Issue 7, 47-56

Bernard, P., & Zollo, A. (1989). The Irpinia (Italy) 1980 earthquake: detailed analysis of a complex normal faulting. Journal of Geophysical Research: Solid Earth, 94(B2), 1631-1647.

Bonardi, G., Ciarcia, S., Di Nocera, S., Matano, F., Sgrosso, I., & Torre, M. (2009). Main kinematic units map of the southern Apennines. Explanatory notes.

Boncio, P., Dichiarante, A. M., Auciello, E., Saroli, M., & Stoppa, F. (2016). Normal faulting along the western side of the Matese Mountains: Implications for active tectonics in the Central Apennines (Italy). Journal of Structural Geology, 82, 16-36.

Boncio, P., Auciello, E., Amato, V., Aucelli, P., Petrosino, P., Tangari, A. C., & Jicha, B. R. (2022). Late Quaternary faulting in the southern Matese (Italy): implications for earthquake potential and slip rate variability in the southern Apennines. Solid Earth, 13(3), 553-582.

Boni, C. F., Bono, P., & Capelli, G. (1987). Schema idrogeologico dell'Italia centrale. Società Geologica Italiana.

Boschetti, T., Barbieri, M., Barberio, M. D., Billi, A., Franchini, S., & Petitta, M. (2019). CO2 inflow and elements desorption prior to a seismic sequence, Amatrice-Norcia 2016, Italy. Geochemistry, Geophysics, Geosystems, 20(5), 2303-2317.

Boyle, R. W. (2013). Geochemical prospecting for thorium and uranium deposits. Elsevier.

Budetta, P., Celico, P., Corniello, A., De Riso, R., Ducci, D., & Nicotera, P. (1988). Carta idrogeologica del F. 186 (S. Angelo dei Lombardi). Memoria illustrativa. Memorie della Società Geologica Italiana, 41, 1029-1038.

Buttitta, D., Caracausi, A., Chiaraluce, L., Favara, R., Gasparo Morticelli, M., & Sulli, A. (2020). Continental degassing of helium in an active tectonic setting (northern Italy): the role of seismicity. Scientific reports, 10(1), 1-13.

Caiazzo, C., Giovine, G., Ortolani, F., Pagliuca, S., Schiattarella, M., & Vitale, C. (1992). Genesi ed evoluzione strutturale della depressione tettonica dell'Alta Valle del Fiume Sele (Appennino Campano-Lucano).

Calcaterra, D., De Riso, R., Ducci, D., Santo, A., & Aquino, S. (1994). Analisi dell'idrodinamica di massicci carsici mediante uso integrato di dati: un esempio nel settore SE del M. Te Terminio (Appennino Meridionale). In Atti IV Geoengineering International Congress: Soil and Groundwater Protection, Geda, Torino (Vol. 2, pp. 587-596).

Calcaterra, D., Esposito, A., Fuschini, V., Galluccio, F., Giulivo, I., Nardò, S., ... & Terranova, C. (2009, December). L'utilizzo della tecnica Psinsar™ per l'individuazione ed il monitoraggio di sinkholes in aree urbanizzate della Campania: i casi di Telese Terme (Bn) e Sarno (Sa). In Atti 2 Workshop internazionale Sinkholes Roma (pp. 3-4).

Canfield D. E. (2001). Biogeochemistry of sulfur isotopes. In Stable isotope in geochemistry. Reviews in mineralogy and geochemistry, eds Valley J. W. and Cole D. R., 607-36. Washington, DC: The mineralogy Society of America.

Caracausi, A., & Paternoster, M. (2015). Radiogenic helium degassing and rock fracturing: A case study of the southern Apennines active tectonic region. Journal of Geophysical Research: Solid Earth, 120(4), 2200-2211.

Carminati, E., & Doglioni, C. (2012). Alps vs. Apennines: the paradigm of a tectonically asymmetric Earth. Earth-Science Reviews, 112(1-2), 67-96.

Carrasco, F., Vadillo, I., Liñán, C., Andreo, B., & Durán, J. J. (2002). Control of environmental parameters for management and conservation of Nerja Cave (Malaga, Spain). Acta carsologica, 31(1).

Cartwright, I., Weaver, T., Tweed, S., Ahearne, D., Cooper, M., Czapnik, K., & Tranter, J. (2002). Stable isotope geochemistry of cold CO_2-bearing mineral spring waters, Daylesford, Victoria,

Australia: sources of gas and water and links with waning volcanism. Chemical Geology, 185(1-2), 71–91.

Cavinato, G. P., & Celles, P. D. (1999). Extensional basins in the tectonically bimodal central Apennines fold-thrust belt, Italy: response to corner flow above a subducting slab in retrograde motion. Geology, 27(10), 955-958.

Celico, P., & Civita, M. (1976). Sulla tettonica del massiccio del Cervialto (Campania) e le implicazioni idrogeologiche ad essa connesse [On the tectonics of the Cervialto Massif (Campania) and related hydrogeological issues], Boll. Soc. Natur, Naples, 85.

Celico, P. (1978). Schema idrogeologico dell'Appennino carbonatico centro-meridionale. Memorie e Note Istituto di Geologia Applicata, Napoli, 14, 1-97.

Celico, P. (1979). Considerazioni sull'idrogeologia di alcune zone dell'Italia centro-meridionale alla luce dei risultati di recenti indagini geognostiche. Memorie e Note Istituto Geologia Applicata, 15, 1-43.

Celico, P. (1983). Le risorse idriche sotterranee dell'Appennino carbonatico centro-meridionale. Idrotecnica, 1, 3-18.

Celico, P., Guadagno, F., Luise, G., Tescione, M., & Vallario, A. (1987). Idrogeologia del Monte Polveracchio-Monte Raione (Monti Picentini, Campania).

Celico, P., Pelella, L., Stanzione, D., & Aquino, S. (1994). Sull'idrogeologia e l'idrogeochimica dei Monti Alburni (SA). Geologica Romana, 30, 687-698.

Celico, F., Petrella, E., & Celico, P. (2006). Hydrogeological behaviour of some fault zones in a carbonate aquifer of Southern Italy: an experimentally based model. Terra Nova, 18(5), 308-313.

Centamore, E., Nisio, S., & Rossi, D. (2009). The San Vittorino Sinkhole Plain: relationships between bedrock structure, sinking processes, seismic events and hydrothermal springs. Bollettino della Societa Geologica Italiana, 128(3), 629-639.

Chiarabba, C., & Amato, A. (1997). Upper-crustal structure of the Benevento area (southern Italy): fault heterogeneities and potential for large earthquakes. Geophysical Journal International, 130(1), 229-239.

Chiarabba, C., Jovane, L., & Di Stefano, R. (2005). A new view of Italian seismicity using 20 years of instrumental recordings. Tectonophysics, 395(3-4), 251-268.

Chiodini, G., Frondini, F., & Ponziani, F. (1995). Deep structures and carbon dioxide degassing in central Italy. Geothermics, 24(1), 81-94.

Chiodini, G., Frondini, F., Cardellini, C., Parello, F., & Peruzzi, L. (2000). Rate of diffuse carbon dioxide Earth degassing estimated from carbon balance of regional aquifers: The case of central Apennine, Italy. Journal of Geophysical Research: Solid Earth, 105(B4), 8423-8434.

Chiodini, G., Cardellini, C., Amato, A., Boschi, E., Caliro, S., Frondini, F., & Ventura, G. (2004). Carbon dioxide Earth degassing and seismogenesis in central and southern Italy. Geophysical Research Letters, 31(7).

Chiodini, G., Caliro, S., Cardellini, C., Frondini, F., Inguaggiato, S., & Matteucci, F. (2011). Geochemical evidence for and characterization of CO_2 rich gas sources in the epicentral area of the Abruzzo 2009 earthquakes. Earth and Planetary Science Letters, 304(3-4), 389-398.

Ciaccio MG, Di Stefano R, Improta L, Mariucci MT and BSI Working Group (2021). First-Motion Focal Mechanism Solutions for 2015–2019 M $\geq$ 4.0 Italian Earthquakes. Front. Earth Sci. 9:630116.

Cicerone, R. D., Ebel, J. E., & Britton, J. (2009). A systematic compilation of earthquake precursors. Tectonophysics, 476(3-4), 371-396.

Cinque, A., Patacca, E., Scandone, P., & Tozzi, M. (1993). Quaternary kinematic evolution of the Southern Appennines. Relationships between surface geological features and deep lithospheric structures. Annals of Geophysics, 36(2).

Cinque, A., Ascione, A., & Caiazzo, C. (2000). Distribuzione spazio-temporale e caratterizzazione della fagliazione quaternaria in Appennino meridionale. Le ricerche del GNDT nel campo della pericolosità sismica, 203-218.

Cinti, F. R., Faenza, L., Marzocchi, W., & Montone, P. (2004). Probability map of the next M$\geq$ 5.5 earthquakes in Italy. Geochemistry, Geophysics, Geosystems, 5(11).

Claesson, L., Skelton, A., Graham, C., Dietl, C., Mörth, M., Torssander, P., & Kockum, I. (2004). Hydrogeochemical changes before and after a major earthquake. Geology, 32(8), 641-644.

Clark, I.D., Fritz, P., (1997). Environmental Isotopes in Hydrogeology. Lewis Publishers, New York.

Clark, I. D., & Fritz, P. (2013). Environmental isotopes in hydrogeology. CRC press.

Clark, I. (2015). Groundwater geochemistry and isotopes. CRC press.

Coleman, M. L., Shepherd, T. J., Durham, J. J., Rouse, J. E., & Moore, G. R. (1982). Reduction of water with zinc for hydrogen isotope analysis. Analytical chemistry, 54(6), 993-995.

Conese, M., Nanni, T., Peila, C., Rusi, S., & Salvati, R. (2001). Idrogeologia della Montagna del Morrone (Appennino abruzzese): dati preliminari.

Convertito, V., Pino, N. A., & Di Luccio, F. (2016). Investigating source directivity of moderate earthquakes by multiple approach: the 2013 Matese (southern Italy) M w = 5 event. Geophysical Journal International, 207(3), 1513-1528.

Coppola, L., & Pescatore, T. (1989). Lineamenti di neotettonica dei Monti Terminio-Tuoro, Cervialto e Marzano (Appennenino meridionale). Bollettino della Societa Geologica Italiana, 108(1), 105-119.

Corniello, A., & De Riso, R. (1986). Idrogeologia e idrochimica delle sorgenti dell'Agro Telesino (BN). Geologia applicata e Idrogeologia, 21, 53-84.

Corniello, A., Ducci, D., & Aquino, A. (2010). Hydrogeological map of the Monti Picentini Regional Park (southern Italy) at 1: 50,000 scale. Bollettino di Geofisica Teorica ed Applicata, 51(4).

Corniello, A., Guida, M., Stellato, L., Trifuoggi, M., Carraturo, F., Del Gaudio, E., ... & Toscanesi, M. (2021). Hydrochemical, isotopic and microbiota characterization of telese mineral waters (Southern Italy). Environmental Geochemistry and Health, 1-22.

Cowie, P. A., Phillips, R. J., Roberts, G. P., McCaffrey, K., Zijerveld, L. J. J., Gregory, L. C., ... & Wilkinson, M. (2017). Orogen-scale uplift in the central Italian Apennines drives episodic behaviour of earthquake faults. Scientific reports, 7(1), 1-10.

CPTI (2004). Catalogo Parametrico dei Terremoti Italiani, versione 2004 (CPTI04). http://emidius. mi. ingv. it/CPTI/.

Craig, H. (1953). The geochemistry of the stable carbon isotopes. Geochimica et cosmochimica acta, 3(2-3), 53-92.

Craig, H. (1961). Isotopic variations in meteoric waters. Science, 133(3465), 1702-1703.

Crews, J. B., & Cooper, C. A. (2014). Experimental evidence for seismically initiated gas bubble nucleation and growth in groundwater as a mechanism for coseismic borehole water level rise and remotely triggered seismicity. Journal of Geophysical Research: Solid Earth, 119(9), 7079-7091.

Cuoco, E., Minissale, A., Di Leo, A., Tamburrino, S., Iorio, M., & Tedesco, D. (2017). Fluid geochemistry of the Mondragone hydrothermal systems (southern Italy): water and gas compositions vs. geostructural setting. International Journal of Earth Sciences, 106(7), 2429-2444.

D'Agostino, N. (2014). Complete seismic release of tectonic strain and earthquake recurrence in the Apennines (Italy). Geophysical Research Letters, 41(4), 1155-1162.

D'Agostino, N., England, P., Hunstad, I., & Selvaggi, G. (2014). Gravitational potential energy and active deformation in the Apennines. Earth and Planetary Science Letters, 397, 121-132.

D'Amico, S., Cammarata, L., Cangemi, M., Cavallaro, D., Di Martino, R. M., & Carlino, M. F. (2014). Seismic moment tensors and regional stress in the area of the December 2013–January 2014, Matese earthquake sequence (Italy). Journal of geodynamics, 82, 118-124.

D'Argenio, B., Ortolani, F., & Pescatore, T. (1986). Geology of the Southern Apennines. A brief outline. Geologia Applicata e Idrogeologia, 21, 135-161.

D'Argenio, B., Pescatore, T., & Scandone, P. (1973). Schema geologico dell'Appennino meriodionale (Campania e Lucania).

De Luca, G., Di Carlo, G., & Tallini, M. (2018). A record of changes in the Gran Sasso groundwater before, during and after the 2016 Amatrice earthquake, central Italy. Scientific reports, 8(1), 1-16.

Del Prete, S., De Riso, R., & Santo, A. (2004). Primo contributo sui sinkholes di origine naturale in Campania. Atti Conv.: "Stato dell'arte sullo studio dei fenomeni di sinkhole e ruolo delle Amministrazioni statali e locali nel governo del territorio", 20-21 maggio 2004, APAT, 361-376, Roma.

Di Bucci, D., Naso, G., Corrado, S., & Villa, I. M. (2005). Growth, interaction and seismogenic potential of coupled active normal faults (Isernia Basin, central-southern Italy). Terra Nova, 17(1), 44-55.

Di Luccio, F., Fukuyama, E., & Pino, N. A. (2005). The 2002 Molise earthquake sequence: What can we learn about the tectonics of southern Italy?. Tectonophysics, 405(1-4), 141-154.

Di Luccio, F., Chiodini, G., Caliro, S., Cardellini, C., Convertito, V., Pino, N. A., Tolomei, C., & Ventura, G. (2018). Seismic signature of active intrusions in mountain chains. Science Advances, 4(1), e1701825.

Discenza, M. E., Esposito, C., Martino, S., Petitta, M., Prestininzi, A., & Scarascia Mugnozza, G. (2011). The gravitational slope deformation of Mt. Rocchetta ridge (central Apennines, Italy): geological-evolutionary model and numerical analysis. Bulletin of Engineering Geology and the Environment, 70(4), 559-575

DISS Working Group (2021). Database of Individual Seismogenic Sources (DISS), Version 3.3.0: A compilation of potential sources for earthquakes larger than M 5.5 in Italy and surrounding areas. Istituto Nazionale di Geofisica e Vulcanologia (INGV).

Doglioni, C. (1991). A proposal for the kinematic modelling of W-dipping subductions-possible applications to the Tyrrhenian-Apennines system. Terra Nova, 3(4), 423-434.

Doglioni, C., Harabaglia, P., Merlini, S., Mongelli, F., Peccerillo, A. T., & Piromallo, C. (1999). Orogens and slabs vs. their direction of subduction. Earth-Science Reviews, 45(3-4), 167-208.

Doglioni, C., Barba, S., Carminati, E., & Riguzzi, F. (2014). Fault on–off versus coseismic fluids reaction. Geoscience Frontiers, 5(6), 767-780.

Doglioni, C., Carminati, E., Petricca, P., & Riguzzi, F. (2015). Normal fault earthquakes or graviquakes. Scientific Reports, 5(1), 1-12.

Elkhoury, J. E., Brodsky, E. E., & Agnew, D. C. (2006). Seismic waves increase permeability. Nature, 441(7097), 1135-1138.

Epstein, S., & Mayeda, T., 1953. Variation of O18 content of waters from natural sources. Geochimica et cosmochimica acta, 4(5), 213-224.

Esposito, E., Luongo, G., Marturano, A., & Porfido, S. (1988). I terremoti recenti dal 1980 al 1986 nell'Appennino meridionale. Memorie della Società Geologica Italiana, 41, 1117-1128.

Esposito, E., Pece, R., Porfido, S., & Tranfaglia, G. (2001). Hydrological anomalies connected to earthquakes in southern Apennines (Italy). Natural Hazards and Earth System Sciences, 1(3), 137-144.

Esposito, A., Galvani, A., Sepe, V., Atzori, S., Brandi, G., Cubellis, E., De Martino, P., Dolce, M., Massucci, A., Obrizzo, F., Pietrantonio, G., Riguzzi, F., & Tammaro, U. (2020). Concurrent

deformation processes in the Matese massif area (Central-Southern Apennines, Italy). Tectonophysics, 774, 228234.

Etiope, G., & Martinelli, G. (2002). Migration of carrier and trace gases in the geosphere: an overview. Physics of the earth and planetary interiors, 129(3-4), 185-204.

Etiope, G. (2015). Natural gas seepage. The Earth's hydrocarbon degassing.

Faccenna, C., Nalpas, T., Brun, J. P., Davy, P., & Bosi, V. (1995). The influence of pre-existing thrust faults on normal fault geometry in nature and in experiments. Journal of Structural Geology, 17(8), 1139–1149.

Faccenna, C., Becker, T. W., Lucente, F. P., Jolivet, L., & Rossetti, F. (2001). History of subduction and back arc extension in the Central Mediterranean. Geophysical Journal International, 145(3), 809-820.

Ferranti, L., & Oldow, J. S. (1999). History and tectonic implications of low-angle detachment faults and orogen parallel extension, Picentini Mountains, Southern Apennines fold and thrust belt, Italy. Tectonics, 18(3), 498-526.

Ferranti, L., Palano, M., Cannavò, F., Mazzella, M. E., Oldow, J. S., Gueguen, E., Mattia, M., & Monaco, C. (2014). Rates of geodetic deformation across active faults in southern Italy. Tectonophysics, 621, 101-122.

Ferranti, L., Milano, G., Burrato, P., Palano, M., & Cannavò, F. (2015). The seismogenic structure of the 2013–2014 Matese seismic sequence, Southern Italy: implication for the geometry of the Apennines active extensional belt. Geophysical Journal International, 201(2), 823-837.

Fiorillo, F. (2009). Spring hydrographs as indicators of droughts in a karst environment. Journal of Hydrology, 373(3-4), 290-301.

Fiorillo, F., & Doglioni, A. (2010). The relation between karst spring discharge and rainfall by cross-correlation analysis (Campania, southern Italy). Hydrogeology Journal, 18(8), 1881-1895.

Fiorillo, F., & Guadagno, F. M. (2010). Karst spring discharges analysis in relation to drought periods, using the SPI. Water resources management, 24(9), 1867-1884.

Fiorillo, F., & Ventafridda, G. (2010). Le portate sorgive delle sorgenti di Cassano Irpino e Caposele (Campania) durante periodi siccitosi.

Fiorillo, F., & Pagnozzi, M. (2015). Recharge processes of Matese karst massif (southern Italy). Environmental Earth Sciences, 74(12), 7557-7570.

Fiorillo, F., Petitta, M., Preziosi, E., Rusi, S., Esposito, L., & Tallini, M. (2015). Long-term trend and fluctuations of karst spring discharge in a Mediterranean area (central-southern Italy). Environmental Earth Sciences, 74(1), 153-172.

Fiorillo, F., Leone, G., Pagnozzi, M., Catani, V., Testa, G., & Esposito, L. (2019). The upwelling groundwater flow in the karst area of Grassano-Telese springs (Southern Italy). Water, 11(5), 872.

Fracassi, U., & Milano, G. (2014). A soft linkage between major seismogenic fault systems in the central-southern Apennines (Italy): Evidence from low-magnitude seismicity. Tectonophysics, 636, 18-31.

Franchini, S., Agostini, S., Barberio, M. D., Barbieri, M., Billi, A., Boschetti, T., Pennisi, M., & Petitta, M. (2021). HydroQuakes, central Apennines, Italy: Towards a hydrogeochemical monitoring network for seismic precursors and the hydro-seismo-sensitivity of boron. Journal of Hydrology, 598, 125754.

Galadini, F., & Messina, P. (1994). Plio-Quaternary tectonics of the Fucino basin and surrounding areas (central Italy). Giornale di Geologia, 56(2), 73-99.

Galadini, F., & Galli, P. (2000). Active tectonics in the central Apennines (Italy)–input data for seismic hazard assessment. Natural Hazards, 22(3), 225-268.

Galli, P., & Galadini, F. (2003). Disruptive earthquakes revealed by faulted archaeological relics in Samnium (Molise, southern Italy). Geophysical Research Letters, 30(5).

Galli, P., Galadini, F., & Pantosti, D. (2008). Twenty years of paleoseismology in Italy. Earth-Science Reviews, 88(1-2), 89-117.

Galli, P. A. C., & Naso, J. A. (2009). Unmasking the 1349 earthquake source (southern Italy): paleoseismological and archaeoseismological indications from the Aquae Iuliae fault. Journal of Structural Geology, 31(2), 128-149.

Galli, P., Giaccio, B., Messina, P., Peronace, E., Amato, V., Naso, G., Nomade, S., Pereira, A., Piscitelli, S., Bellanova, J., Billi, A., Blamart, D., Galderisi, A., Giocoli, A., Stabile, T., Thile, F., (2017). Middle to Late Pleistocene activity of the northern Matese fault system (southern Apennines, Italy). Tectonophysics, 699, 61-81.

Gat, J. R. (1996). Oxygen and hydrogen isotopes in the hydrologic cycle. Annual Review of Earth and Planetary Sciences, 24(1), 225-262.

Giuliani, R., D'Agostino, N., D'Anastasio, E., Mattone, M., Bonci, L., Calcaterra, S., Gambino, P., & Merli, K. (2009). Active crustal extension and strain accumulation from GPS data in the Molise region (central-southern Apennines, Italy). Bollettino di Geofisica Teorica ed Applicata.

Giustini, F., Blessing, M., Brilli, M., Lombardi, S., Voltattorni, N., & Widory, D. (2013). Determining the origin of carbon dioxide and methane in the gaseous emissions of the San Vittorino plain (Central Italy) by means of stable isotopes and noble gas analysis. Applied geochemistry, 34, 90-101.

Giustini, F., Brilli, M., & Patera, A. (2016). Mapping oxygen stable isotopes of precipitation in Italy. Journal of Hydrology: Regional Studies 8, 162-181.

Grant, R. A., Halliday, T., Balderer, W. P., Leuenberger, F., Newcomer, M., Cyr, G., & Freund, F. T. (2011). Ground water chemistry changes before major earthquakes and possible effects on animals. International Journal of Environmental Research and Public Health, 8(6), 1936-1956.

Harabaglia, P., Mongelli, G., & Paternoster, M. (2002). A geochemical survey of the Telese hypothermal spring, Southern Italy: sulfate anomalies induced by crustal deformation. Environmental Geosciences, 9(3), 89-101.

He, A., & Singh, R. P. (2020). Coseismic groundwater temperature response associated with the Wenchuan earthquake. Pure and Applied Geophysics, 177(1), 109-120.

Hilton, D. R. (1996). The helium and carbon isotope systematics of a continental geothermal system: results from monitoring studies at Long Valley caldera (California, USA). Chemical Geology, 127(4), 269-295.

Hoefs, J. (1997). Stable isotope geochemistry (Vol. 201). Berlin: springer.

Hosono, T., Hartmann, J., Louvat, P., Amann, T., Washington, K. E., West, A. J., ... & Gaillardet, J. (2018). Earthquake-induced structural deformations enhance long-term solute fluxes from active volcanic systems. Scientific reports, 8(1), 1-12.

Hosono, T., & Masaki, Y. (2020). Post-seismic hydrochemical changes in regional groundwater flow systems in response to the 2016 Mw 7.0 Kumamoto earthquake. Journal of Hydrology, 580, 124340.

Hosono, T., Yamada, C., Manga, M., Wang, C. Y., & Tanimizu, M. (2020). Stable isotopes show that earthquakes enhance permeability and release water from mountains. Nature communications, 11(1), 1-9.

Huang, F., Li, M., Ma, Y., Han, Y., Tian, L., Yan, W., & Li, X. (2017). Studies on earthquake precursors in China: A review for recent 50 years. Geodesy and Geodynamics, 8(1), 1-12.

Hwang, H. S., Hamm, S. Y., Cheong, J. Y., Lee, S. H., Ha, K., Lee, C., ... & Kim, K. H. (2020). Effective time-and frequency-domain techniques for interpreting seismic precursors in groundwater level fluctuations on Jeju Island, Korea. Scientific Reports, 10(1), 1-14.

Ietto, A. (1965). Su alcune particolari strutture connesse alla tettonica di sovrascorrimenti dei Monti Picentini (Appennino meridionale). Stabilimento tipografico Genovese.

Igarashi, G., Saeki, S., Takahata, N., Sumikawa, K., Tasaka, S., Sasaki, Y., ... & Sano, Y. (1995). Ground-water radon anomaly before the Kobe earthquake in Japan. Science, 269(5220), 60-61.

Improta, L., Bonagura, M., Capuano, P., & Iannaccone, G. (2003). An integrated geophysical investigation of the upper crust in the epicentral area of the 1980, Ms= 6.9, Irpinia earthquake (Southern Italy). Tectonophysics, 361(1-2), 139-169.

Inan, S., Balderer, W. P., Leuenberger-West, F., Yakan, H., Özvan, A., & Freund, F. T. (2012). Springwater chemical anomalies prior to the Mw= 7.2 Van earthquake (Turkey). Geochemical Journal, 46(1), e11-e16.

Ingebritsen, S. E., & Manga, M. (2014). Hydrogeochemical precursors. Nature Geoscience, 7(10), 697-698.

Irwin, W. P., & Barnes, I. (1980). Tectonic relations of carbon dioxide discharges and earthquakes. Journal of Geophysical Research: Solid Earth, 85(B6), 3115-3121.

Istituto Superiore per la Protezione e la Ricerca Ambientale (ISPRA), CARG project, Carta geologica d'Italia alla scala 1:50000 (2009): https://www.isprambiente.gov.it/Media/carg/. Accessed Jun 2022

Italiano, F., Martelli, M., Martinelli, G., & Nuccio, P. M. (2000). Geochemical evidence of melt intrusions along lithospheric faults of the Southern Apennines, Italy: geodynamic and seismogenic implications. Journal of Geophysical Research: Solid Earth, 105(B6), 13569-13578.

Italiano, F., Martinelli, G., & Plescia, P. (2008). CO2 degassing over seismic areas: the role of mechanochemical production at the study case of Central Apennines. In Terrestrial Fluids, Earthquakes and Volcanoes: The Hiroshi Wakita Volume III (pp. 75-94). Birkhäuser Basel.

Javoy, M., Pineau, F., & Delorme, H. (1986). Carbon and nitrogen isotopes in the mantle. Chemical geology, 57(1-2), 41-62.

Jones, D. S., & Fike, D. A. (2013). Dynamic sulfur and carbon cycling through the end-Ordovician extinction revealed by paired sulfate–pyrite δ34S. Earth and Planetary Science Letters, 363, 144-155.

Jónsson, S., Segall, P., Pedersen, R., & Björnsson, G. (2003). Post-earthquake ground movements correlated to pore-pressure transients. Nature, 424(6945), 179-183.

Karolyte, R., Serno, S., Johnson, G., & Gilfillan, S.M. (2017). The influence of oxygen isotope exchange between CO2 and H2O in natural CO2-rich spring waters: Implications for geothermometry. Applied Geochemistry 84, 173-176.

Kerrick, D. M. (2001). Present and past nonanthropogenic CO2 degassing from the solid Earth. Reviews of Geophysics, 39(4), 565-585.

Kim, J., Lee, J., Petitta, M., Kim, H., Kaown, D., Park, I. W., ... & Lee, K. K. (2019). Groundwater system responses to the 2016 ML 5.8 Gyeongju earthquake, South Korea. Journal of Hydrology, 576, 150-163.

King, P. T., Michel, J., & Moore, W. S. (1982). Ground water geochemistry of 228Ra, 226Ra and 222Rn. Geochimica et Cosmochimica Acta, 46(7), 1173-1182.

King, C. Y., Azuma, S., Ohno, M., Asai, Y., He, P., Kitagawa, Y., ... & Wakita, H. (2000). In search of earthquake precursors in the water-level data of 16 closely clustered wells at Tono, Japan. Geophysical Journal International, 143(2), 469-477.

King, C. Y., Zhang, W., & Zhang, Z. (2006). Earthquake-induced groundwater and gas changes. Pure and Applied Geophysics, 163(4), 633-645.

Kissin, I. G. (2007). New data on crustal sensitive zones and formation of precursors and postseismic responses to earthquakes. Russian Geology and Geophysics, 48(5), 429-441.

Kulongoski, J. T., Hilton, D. R., Barry, P. H., Esser, B. K., Hillegonds, D., & Belitz, K. (2013). Volatile fluxes through the Big Bend section of the San Andreas Fault, California: Helium and carbon-dioxide systematics. Chemical Geology, 339, 92-102.

Lamberti, M. C., Vigide, N., Venturi, S., Agusto, M., Yagupsky, D., Winocur, D., ... & Tassi, F. (2019). Structural architecture releasing deep-sourced carbon dioxide diffuse degassing at the Caviahue–Copahue Volcanic Complex. Journal of Volcanology and Geothermal Research, 374, 131-141.

Lan, S. S., & Gu, H. B. (2021). Changes in groundwater level and tidal response caused by the Wenchuan earthquake, China. Hydrogeology Journal, 29(3), 1329-1341.

Langmuir, D. (1997). Solutions Manual: Aqueous Environmental Geochemistry. Prentice Hall.

Latorre, D., Di Stefano, R., Castello, B., Michele, M., & Chiaraluce, L. (2023). An updated view of the Italian seismicity from probabilistic location in 3D velocity models: The 1981–2018 Italian catalog of absolute earthquake locations (CLASS). Tectonophysics, 846, 229664.

Leone, G., Pagnozzi, M., Catani, V., Testa, G., Esposito, L., & Fiorillo, F. (2019). Hydrogeology of the Karst Area of the Grassano and Telese Springs. Acque Sotterranee-Italian Journal of Groundwater, 8(4).

Li, C., Zhou, X., Li, J., Liu, L., Su, H., Li, Y., ... & Luo, Z. (2022). Hydrogeochemical Characteristics of Thermal Springs in the Qilian-Haiyuan Fault Zone at northeast Tibetan Plateau: Role of fluids and seismic activity. Frontiers in Earth Science, 1676.

Liñán Baena, C., Andreo Navarro, B., & Carrasco Cantos, F. (1999). Caracterización hidrodinámica e hidroquímica del manantial de Maro (Sierra Almijara, provincia de Málaga).

Lindsey, B. D., Jurgens, B. C., & Belitz, K. (2019). Tritium as an indicator of modern, mixed, and premodern groundwater age (No. 2019-5090). US Geological Survey.

Longinelli, A., & Selmo, E. (2003). Isotopic composition of precipitation in Italy: a first overall map. Journal of Hydrology, 270(1-2), 75-88.

Lucente F.P., Chiarabba, C., & Cimini G. (1999). Tomographic constraints on the geodynamic evolution of the Italian region. Journal of Geophys. Research, 104, B9, 20, 307-20, 327.

Lutzky, H., Lyakhovsky, V., Kurzon, I., & Shalev, E. (2020). Hydrological response to the Sea of Galilee 2018 seismic swarm. Journal of Hydrology, 582, 124499.

Ma, R., Wang, Y., Sun, Z., Zheng, C., Ma, T., & Prommer, H. (2011). Geochemical evolution of groundwater in carbonate aquifers in Taiyuan, northern China. Applied Geochemistry, 26(5), 884-897.

Malakootian, M., & Nouri, J. (2010). Chemical variations of ground water affected by the earthquake in bam region Malakootian, M. International Journal of Environmental Research, 4(3), 443-454.

Malinverno, A., & Ryan, W. B. (1986). Extension in the Tyrrhenian Sea and shortening in the Apennines as result of arc migration driven by sinking of the lithosphere. Tectonics, 5(2), 227-245.

Manga, M., & Wang, C. Y. (2015). 4.12. Earthquake hydrology. Treatise on geophysics, 305-328.

Mariucci, M.T., & Montone, P. (2020) Database of Italian present-day stress indicators, IPSI 1.4. Sci Data 7, 298.

Marsella, E., Bally, A. W., Cippitelli, G., D'Argenio, B., & Pappone, G. (1995). Tectonic history of the Lagonegro Domain and Southern Apennine thrust belt evolution. Tectonophysics, 252(1-4), 307-330.

Martinelli, G., & Albarello, D. (1997). Main constraints for siting monitoring networks devoted to the study of earthquake related hydrogeochemical phenomena in Italy. Annals of Geophysics, 40(6).

Martinelli, G., & Tamburello, G. (2020). Geological and geophysical factors constraining the occurrence of earthquake precursors in geofluids: A review and reinterpretation. Frontiers in Earth Science, 650.

Martini, C. (2016). Signals in water-the deep originated CO2 in the Peschiera-Capone acqueduct in relation to monitoring of seismic activity in central Italy. Acque Sotterranee-Italian Journal of Groundwater, 5(4).

Marturano, A., Esposito, E., Porfido, S., & Luongo, G. (1988). Il terremoto del 4 ottobre 1983 (Pozzuoli): Attenuazione dell'intensita con la distanza e relazione magnitudino-intensita. Zonazione della Citta di Napoli. Memorie della Società Geologica Italiana, 41, 941-948.

Mastrorillo, L., Saroli, M., Viaroli, S., Banzato, F., Valigi, D., & Petitta, M. (2020). Sustained post-seismic effects on groundwater flow in fractured carbonate aquifers in Central Italy. Hydrological Processes, 34(5), 1167-1181.

Merlini, S., & Mostardini, F. (1986). Appennino centro-meridionale: sesioni geologiche e proposta di modello strutturale. In Geologia dell'Italia centrale. Congresso nazionale. 73 (pp. 147-149).

Micklethwaite, S., & Cox, S. F. (2004). Fault-segment rupture, aftershock-zone fluid flow, and mineralization. Geology, 32(9), 813-816.

Milano, G., Di Giovambattista, R., & Ventura, G. (2008). Seismic activity in the transition zone between Southern and Central Apennines (Italy): Evidences of longitudinal extension inside the Ortona–Roccamonfina tectonic line. Tectonophysics, 457(1-2), 102-110.

Milia, A., Torrente, M. M., & Iannace, P. (2017). Pliocene-Quaternary orogenic systems in Central Mediterranean: The Apulia-Southern Apennines-Tyrrhenian Sea example. Tectonics, 36(8), 1614-1632.

Miller, S. A., Nur, A., & Olgaard, D. L. (1996). Earthquakes as a coupled shear stress-high pore pressure dynamical system. Geophysical Research Letters, 23(2), 197-200.

Miller, S. A., Collettini, C., Chiaraluce, L., Cocco, M., Barchi, M., & Kaus, B. J. (2004). Aftershocks driven by a high-pressure CO_2 source at depth. Nature, 427(6976), 724-727.

Minissale, A. (2004). Origin, transport and discharge of CO_2 in central Italy. Earth-Science Reviews, 66(1-2), 89-141.

Montgomery, D. R., & Manga, M. (2003). Streamflow and water well responses to earthquakes. Science, 300(5628), 2047-2049.

Montone, P., Amato, A., & Pondrelli, S. (1999). Active stress map of Italy. Journal of Geophysical Research: Solid Earth, 104(B11), 25595-25610.

Mook, W., & Rozanski, K. (2000). Environmental isotopes in the hydrological cycle. IAEA Publish, 39.

Mörner, N. A., & Etiope, G. (2002). Carbon degassing from the lithosphere. Global and Planetary Change, 33(1-2), 185-203.

Muir-Wood, R., & King, G. C. (1993). Hydrological signatures of earthquake strain. Journal of Geophysical Research: Solid Earth, 98(B12), 22035-22068.

Nakagawa, K., Yu, Z. Q., Berndtsson, R., & Hosono, T. (2020). Temporal characteristics of groundwater chemistry affected by the 2016 Kumamoto earthquake using self-organizing maps. Journal of Hydrology, 582, 124519.

Nicolich, R. (1989). Crustal structures from seismic studies in the frame of the European Geotraverse (southern segment) and CROP projects.

Oldow, J. S., D'Argenio, B., Ferranti, L., Pappone, G., Marsella, E., & Sacchi, M. (1993). Large-scale longitudinal extension in the southern Apennines contractional belt, Italy. Geology, 21(12), 1123-1126.

Onda, S., Sano, Y., Takahata, N., Kagoshima, T., Miyajima, T., Shibata, T., ... & Nishio, Y. (2018). Groundwater oxygen isotope anomaly before the M6. 6 Tottori earthquake in Southwest Japan. Scientific reports, 8(1), 1-7.

Ortolani, F. (1975). Assetto strutturale dei Monti Picentini, della valle del Sele e del gruppo di Monte Marzano-Monte Ogna (Appennino Meridionale) implicazioni idrogeologiche. Bollettino della Società geologica italiana, 94(1-2), 209-230.

Pantosti, D., Schwartz, D. P., & Valensise, G. (1993). Paleoseismology along the 1980 surface rupture of the Irpinia fault: implications for earthquake recurrence in the southern Apennines, Italy. Journal of Geophysical Research: Solid Earth, 98(B4), 6561-6577.

Pappone, G., & Ferranti, L. (1995). Thrust tectonics in the Picentini mountains, southern Apennines, Italy. Tectonophysics, 252(1-4), 331-348.

Patacca, E., Sartori, R., & Scandone, P. (1990). Tyrrhenian basin and Apenninic arcs: kinematic relations since Late Tortonian times.

Patacca, E., & Scandone, P. (2007). Geology of the southern Apennines. Bollettino della Società Geologica Italiana, 7, 75-119.

Paudel, S. R., Banjara, S. P., Wagle, A., & Freund, F. T. (2018). Earthquake chemical precursors in groundwater: a review. Journal of Seismology, 22(5), 1293-1314.

Pauwels, H., Fouillac, C., Goff, F., & Vuataz, F. D. (1997). The isotopic and chemical composition of CO2-rich thermal waters in the Mont-Dore region (Massif-Central, France). Applied geochemistry, 12(4), 411-427.

Perez, N. M., Hernández, P. A., Igarashi, G., Trujillo, I., Nakai, S., Sumino, H., & Wakita, H. (2008). Searching and detecting earthquake geochemical precursors in CO2-rich groundwaters from Galicia, Spain. Geochemical Journal, 42(1), 75-83.

Petitta, M. (2009). Hydrogeology of the middle valley of the Velino River and of the S. Vittorino Plain (Rieti, Central Italy). Ital J Eng Geol Environ, 1, 157-182.

Petitta, M., Primavera, P., Tuccimei, P., & Aravena, R. (2011). Interaction between deep and shallow groundwater systems in areas affected by Quaternary tectonics (Central Italy): a geochemical and isotope approach. Environmental Earth Sciences, 63(1), 11-30.

Petitta, M., Mastrorillo, L., Preziosi, E., Banzato, F., Barberio, M. D., Billi, A., ... & Doglioni, C. (2018). Water-table and discharge changes associated with the 2016–2017 seismic sequence in central Italy: hydrogeological data and a conceptual model for fractured carbonate aquifers. Hydrogeology Journal, 26(4), 1009-1026.

Petitta, M., Barberio, D. M., Barbieri, M., Billi, A., Doglioni, C., Passaretti, S., & Franchini, S. (2020). Groundwater monitoring in regional discharge areas selected as "Hydrosensitive" to seismic activity in Central Italy. In Advances in Natural Hazards and Hydrological Risks: Meeting the Challenge (pp. 21-25). Springer, Cham.

Petrella, E., & Celico, F. (2009). Heterogeneous aquitard properties in sedimentary successions in the Apennine chain: case studies in southern Italy. Hydrological Processes: An International Journal, 23(23), 3365-3371.

Petricca, P., Barba, S., Carminati, E., Doglioni, C., & Riguzzi, F. (2015). Graviquakes in Italy. Tectonophysics, 656, 202-214.

Pierdominici, S., Mariucci, M. T., & Montone, P. (2011). A study to constrain the geometry of an active fault in southern Italy through borehole breakouts and downhole logs. Journal of Geodynamics, 52(3-4), 279-289.

Pinault, J. L., & Baubron, J. C. (1997). Signal processing of diurnal and semidiurnal variations in radon and atmospheric pressure: a new tool for accurate in situ measurement of soil gas velocity, pressure gradient, and tortuosity. Journal of Geophysical Research: Solid Earth, 102(B8), 18101-18120.

Piper, A. M. (1944). A graphic procedure in the geochemical interpretation of water-analyses. Eos, Transactions American Geophysical Union, 25(6), 914-928.

Pondrelli, S., Salimbeni, S., Ekström, G., Morelli, A., Gasperini, P., & Vannucci, G. (2006). The Italian CMT dataset from 1977 to the present. Physics of the Earth and Planetary Interiors, 159(3-4), 286-303.

Porfido, S., Esposito, E., Luongo, G., & Marturano, A. (1988). I terremoti del XIX secolo dell'Appennino Campano-Lucano. Memorie della Società Geologica Italiana, 41, 1105-1116.

Porowski, A., Porowska, D., & Halas, S. (2019). Identification of sulfate sources and biogeochemical processes in an aquifer affected by Peatland: Insights from monitoring the isotopic composition of groundwater sulfate in Kampinos National Park, Poland. Water, 11(7), 1388.

Porreca, M., & Mattei, M. (2010). Tectonic and environmental evolution of Quaternary intramontane basins in Southern Apennines (Italy): insights from palaeomagnetic and rock magnetic investigations. Geophysical Journal International, 182(2), 682-698.

Porreca, M., & Mattei, M. (2012). AMS fabric and tectonic evolution of Quaternary intramontane extensional basins in the Picentini Mountains (Southern Apennines, Italy). International Journal of Earth Sciences, 101(3), 863-877.

Preziosi, E., & Romano, E. (2013, April). Are large karstic springs good indicators for Climate Change effects on groundwater?. In EGU General Assembly Conference Abstracts (pp. EGU2013-9367).

Regione Campania (2007). La pianificazione territoriale in Campania – Piano Territoriale Regionale. http://www.difesa.suolo.regione.campania.it/content/category/6/46/71/. Accessed Apr 2022

Riggio, A., & Santulin, M. (2015). Earthquake forecasting: a review of radon as seismic precursor. Bollettino di Geofisica Teorica ed Applicata, 56(2).

Riguzzi, F., Crespi, M., Devoti, R., Doglioni, C., Pietrantonio, G., & Pisani, A. R. (2012). Geodetic strain rate and earthquake size: New clues for seismic hazard studies. Physics of the Earth and Planetary Interiors, 206, 67-75.

Roeloffs, E., Quilty, E., & Scholtz, C. H. (1997). Case 21 water level and strain changes preceding and following the August 4, 1985 Kettleman Hills, California, earthquake. Pure and Applied Geophysics, 149(1), 21-60.

Roeloffs, E. A. (1998). Persistent water level changes in a well near Parkfield, California, due to local and distant earthquakes. Journal of Geophysical Research: Solid Earth, 103(B1), 869-889.

Rovida A., Locati M., Camassi R., Lolli, B., Gasperini P., Antonucci A. (2022). Catalogo Parametrico dei Terremoti Italiani (CPTI15), versione 4.0. Istituto Nazionale di Geofisica e Vulcanologia (INGV).

Rufino, F., Cuoco, E., Busico, G., Caliro, S., Maletic, E.L., Avino, R., Darrah, T.H., & Tedesco, D. (2021). Deep carbon degassing in the Matese massif chain (Southern Italy) inferred by geochemical and isotopic data. Environmental Science and Pollution Research, 28(34), 46614-46626.

Salazar, J. M. L., Pérez, N. M., Hernández, P. A., Soriano, T., Barahona, F., Olmos, R., ... & Notsu, K. (2002). Precursory diffuse carbon dioxide degassing signature related to a 5.1 magnitude earthquake in El Salvador, Central America. Earth and Planetary Science Letters, 205(1-2), 81-89.

201.   Salvati, R. (2002). Natural hydrogeological laboratories: a new concept in regional hydrogeology studies. A case history from central Italy. Environmental Geology, 41(8), 960-965.

Sano, Y., & Marty, B. (1995). Origin of carbon in fumarolic gas from island arcs. Chemical Geology, 119(1-4), 265-274.

Sano, Y., Takahata, N., Kagoshima, T., Shibata, T., Onoue, T., & Zhao, D. (2016). Groundwater helium anomaly reflects strain change during the 2016 Kumamoto earthquake in Southwest Japan. Scientific reports, 6(1), 1-7.

Sartori, R. (1989). Evoluzione neogenico-recente del bacino tirrenico e suoi rapporti con la geologia delle aree circostanti. Giorn. Geologia, ser. 3, 51 (2), 1-39

Sasaki, T., Gunji, Y., & Okuda, T. (2004). Mathematical modeling of radon emanation. Journal of nuclear science and technology, 41(2), 142-151.

Sato, T., Takahashi, H. A., Kawabata, K., Takahashi, M., Inamura, A., & Handa, H. (2020). Changes in the nitrate concentration of spring water after the 2016 Kumamoto earthquake. Journal of Hydrology, 580, 124310.

Scandone, P. (1980). Origin of the Tyrrhenian Sea and Calabrian arc. Bollettino della Società Geologica Italiana, 98(1), 27-34.

Scholz, C. H., Sykes, L. R., & Aggarwal, Y. P. (1973). Earthquake Prediction: A Physical Basis: Rock dilatancy and water diffusion may explain a large class of phenomena precursory to earthquakes. Science, 181(4102), 803-810.

Scott, B. E., Newell, D. L., Jessup, M. J., Grambling, T. A., & Shaw, C. A. (2020). Structural Controls on Crustal Fluid Circulation and Hot Spring Geochemistry Above a Flat-Slab Subduction Zone, Peru. Geochemistry, Geophysics, Geosystems, 21(7).

Scuderi, M. M., & Collettini, C. (2016). The role of fluid pressure in induced vs. triggered seismicity: Insights from rock deformation experiments on carbonates. Scientific reports, 6(1), 1-9.

Scuderi, M. M., Collettini, C., & Marone, C. (2017). Frictional stability and earthquake triggering during fluid pressure stimulation of an experimental fault. Earth and Planetary Science Letters, 477, 84-96.

Shi, Z., & Wang, G. (2014). Hydrological response to multiple large distant earthquakes in the Mile well, China. Journal of Geophysical Research: Earth Surface, 119(11), 2448-2459.

Shi, Z., Zhang, H., & Wang, G. (2020). Groundwater trace elements change induced by M5. 0 earthquake in Yunnan. Journal of Hydrology, 581, 124424.

Sibson, R. H. (1992). Implications of fault-valve behaviour for rupture nucleation and recurrence. Tectonophysics, 211(1-4), 283-293.

Sibson, R. H. (2000). Fluid involvement in normal faulting. Journal of Geodynamics, 29(3-5), 469-499.

Silverii, F. (2016). Study of the transient deformation of Central and Southern Apennines from GPS observations.

Silverii, F., D'Agostino, N., Borsa, A. A., Calcaterra, S., Gambino, P., Giuliani, R., & Mattone, M. (2019). Transient crustal deformation from karst aquifers hydrology in the Apennines (Italy). Earth and Planetary Science Letters, 506, 23-37.

Skelton, A., Andrén, M., Kristmannsdóttir, H., Stockmann, G., Mörth, C. M., Sveinbjörnsdóttir, Á., ... & Kockum, I. (2014). Changes in groundwater chemistry before two consecutive earthquakes in Iceland. Nature Geoscience, 7(10), 752-756.

Skelton, A., Liljedahl-Claesson, L., Wästeby, N., Andrén, M., Stockmann, G., Sturkell, E., ... & Kockum, I. (2019). Hydrochemical changes before and after earthquakes based on long-term measurements of multiple parameters at two sites in northern Iceland—a review. Journal of Geophysical Research: Solid Earth, 124(3), 2702-2720.

Slejko, D., Caporali, A., Stirling, M., & Barba, S. (2010). Occurrence probability of moderate to large earthquakes in Italy based on new geophysical methods. Journal of seismology, 14(1), 27-51.

Smeraglia, L., Billi, A., Carminati, E., Cavallo, A., & Doglioni, C. (2017). Field-to nano-scale evidence for weakening mechanisms along the fault of the 2016 Amatrice and Norcia earthquakes, Italy. Tectonophysics, 712, 156-169.

Smeraglia, L., Aldega, L., Bernasconi, S. M., Billi, A., Boschi, C., Caracausi, A., Carminati, E., Franchini, S., Rizzo, A. L., Rossetti, F., & Vignaroli, G. (2020). The role of trapped fluids during the development and deformation of a carbonate/shale intra-wedge tectonic mélange (Mt. Massico, Southern Apennines, Italy). Journal of Structural Geology, 138, 104086.

Steinitz, G., Begin, Z. E. B., & Gazit-Yaari, N. (2003). Statistically significant relation between radon flux and weak earthquakes in the Dead Sea rift valley. Geology, 31(6), 505-508.

Stucchi M., Meletti C., Montaldo V., Akinci A., Faccioli E., Gasperini P., Malagnini L., Valensise G. (2004). Pericolosità sismica di riferimento per il territorio nazionale MPS04 [Data set]. Istituto Nazionale di Geofisica e Vulcanologia (INGV). https://doi.org/10.13127/sh/mps04/ag

Sugisaki, R., Ido, M., Takeda, H., Isobe, Y., Hayashi, Y., Nakamura, N., ... & Mizutani, Y. (1983). Origin of hydrogen and carbon dioxide in fault gases and its relation to fault activity. The Journal of Geology, 91(3), 239-258.

Sundal, A. V., Henriksen, H., Soldal, O., & Strand, T. (2004). The influence of geological factors on indoor radon concentrations in Norway. Science of the Total Environment, 328(1-3), 41-53.

Tamburello, G., Pondrelli, S., Chiodini, G., & Rouwet, D. (2018). Global-scale control of extensional tectonics on CO2 earth degassing. Nature communications, 9(1), 1-9.

Tanner, A. B. (1980). Radon migration in the ground: A supplementary review. Nat. Radiat. Environ. III, 1, 5-56.

Tenthorey, E., Cox, S. F., & Todd, H. F. (2003). Evolution of strength recovery and permeability during fluid–rock reaction in experimental fault zones. Earth and Planetary Science Letters, 206(1-2), 161-172.

Toutain, J. P., & Baubron, J. C. (1999). Gas geochemistry and seismotectonics: a review. Tectonophysics, 304(1-2), 1-27.

Trippetta, F., Petricca, P., Billi, A., Collettini, C., Cuffaro, M., Lombardi, A. M., ... & Doglioni, C. (2019). From mapped faults to fault-length earthquake magnitude (FLEM): a test on Italy with methodological implications. Solid Earth, 10(5), 1555-1579.

Tsunogai, U., & Wakita, H. (1995). Precursory chemical changes in ground water: Kobe earthquake, Japan. Science, 269(5220), 61-63.

Tullis, J., Yund, R., & Farver, J. (1996). Deformation-enhanced fluid distribution in feldspar aggregates and implications for ductile shear zones. Geology, 24(1), 63-66.

Vadillo, I., Benavente, J., Neukum, C., Grützner, C., Carrasco, F., Azzam, R., ... & Reicherter, K. (2012). Surface geophysics and borehole inspection as an aid to characterizing karst voids and vadose ventilation patterns (Nerja research site, S. Spain). Journal of Applied Geophysics, 82, 153-162.

Vannoli, P., Martinelli, G., & Valensise, G. (2021). The seismotectonic significance of geofluids in Italy. Frontiers in Earth Science, 9, 25.

Vezzani, L., Festa, A., & Ghisetti, F. C. (2010). Geology and tectonic evolution of the Central-Southern Apennines, Italy (Vol. 469). Geological Society of America.

Vitale, S., & Ciarcia, S. (2018). Tectono-stratigraphic setting of the Campania region (southern Italy). Journal of Maps, 14(2), 9-21.

Wakita, H., Nakamura, Y., Notsu, K., Noguchi, M., & Asada, T. (1980). Radon anomaly: a possible precursor of the 1978 Izu-Oshima-kinkai earthquake. Science, 207(4433), 882-883.

Wakita, H. (1981). Precursory changes in groundwater prior to the 1978 Izu-Oshima-Kinkai earthquake. Earthquake Prediction: An International Review, 4, 527-532.

Wang, Y., & Shpeyzer, G. M. (1997). Genesis of thermal groundwaters from Siping'an district, China. Applied geochemistry, 12(4), 437-445.

Wang, C. Y., & Manga, M. (2010). Hydrologic responses to earthquakes and a general metric. Geofluids, 10(1-2), 206-216.

Wang, C. Y., & Manga, M. (2021). Water and Earthquakes (p. 387). Springer Nature.

Wannamaker, P. E., Jiracek, G. R., Stodt, J. A., Caldwell, T. G., Gonzalez, V. M., McKnight, J. D., & Porter, A. D. (2002). Fluid generation and pathways beneath an active compressional orogen, the New Zealand Southern Alps, inferred from magnetotelluric data. Journal of Geophysical Research: Solid Earth, 107(B6), ETG-6.

Wasowski, J., Pierri, V., Pierri, P., & Capolongo, D. (2002). Factors controlling seismic susceptibility of the Sele valley slopes: the case of the 1980 Irpinia earthquake re-examined. Surveys in Geophysics, 23(6), 563-593.

Wästeby, N., Skelton, A., Tollefsen, E., Andrén, M., Stockmann, G., Claesson Liljedahl, L., ... & Mörth, M. (2014). Hydrochemical monitoring, petrological observation, and geochemical modeling of fault healing after an earthquake. Journal of Geophysical Research: Solid Earth, 119(7), 5727-5740.

Weingarten, M., & Ge, S. (2014). Insights into water level response to seismic waves: A 24 year high-fidelity record of global seismicity at Devils Hole. Geophysical Research Letters, 41(1), 74-80.

Westaway, R., & Jackson, J. (1987). The earthquake of 1980 November 23 in Campania—Basilicata (southern Italy). Geophysical Journal International, 90(2), 375-443.

Yan, R., Woith, H., & Wang, R. (2014). Groundwater level changes induced by the 2011 Tohoku earthquake in China mainland. Geophysical Journal International, 199(1), 533-548.

Zhou, X., Du, J., Chen, Z., Cheng, J., Tang, Y., Yang, L., ... & Li, Y. (2010). Geochemistry of soil gas in the seismic fault zone produced by the Wenchuan Ms 8.0 earthquake, southwestern China. Geochemical transactions, 11(1), 1-10.

Zhou, X., Liu, L., Chen, Z., Cui, Y., & Du, J. (2017). Gas geochemistry of the hot spring in the Litang fault zone, Southeast Tibetan Plateau. Applied Geochemistry, 79, 17-26.

Online website list

https://www.isprambiente.gov.it

https://www.ign.es/web/ign/portal

http://terremoti.ingv.it

https://webvision.digimatic.it/

http://tinitaly.pi.ingv.it/

https://www.videpi.com

http://www.difesa.suolo.regione.campania.it/

http://centrofunzionale.regione.campania.it/

https://h3o.stonebit.it/

https://www.ign.es/web/ign/portal

https://www.coreldraw.com/

Appendix

Other scientific papers

- "Changes in groundwater trace element concentrations before seismic and volcanic activities in Iceland during 2010–2018"

- "Climate change and its effect on groundwater quality"

Changes in groundwater trace element concentrations before seismic and volcanic activities in Iceland during 2010–2018

Maurizio Barbieri [a,*], Stefania Franchini [a], Marino Domenico Barberio [a], Andrea Billi [b], Tiziano Boschetti [c], Livio Giansante [a], Francesca Gori [a], Sigurjón Jónsson [d], Marco Petitta [a], Alasdair Skelton [e], Gabrielle Stockmann [f]

[a] Earth Sciences Department, Sapienza University of Rome, Rome, Italy
[b] Consiglio Nazionale delle Ricerche, IGAG, Rome, Italy
[c] Department of Chemistry, Life Sciences and Environmental Sustainability, University of Parma, Italy
[d] King Abdullah University of Science and Technology (KAUST), Saudi Arabia
[e] Department of Geological Sciences, Stockholm University, Stockholm, Sweden
[f] Institute of Earth Sciences, University of Iceland, Reykjavík, Iceland

HIGHLIGHTS

- Boron appears to be a good indicator of water-rock interaction in a geothermal system.
- PCA was used to identify the specific role of elements in different geologic events.
- CPD used to statistically validate of the trend variability in the time series
- Trace elements are promising to identify potential precursors of geological events.

GRAPHICAL ABSTRACT
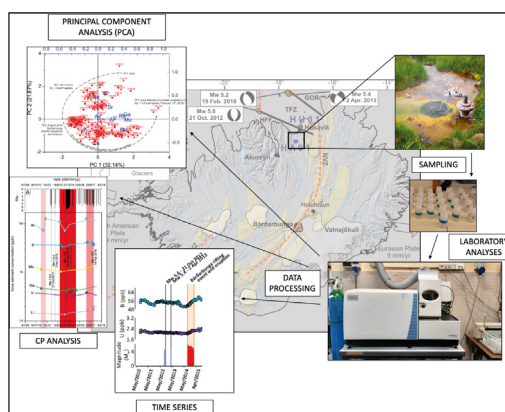
ABSTRACT

We analysed temporal variations of trace element concentrations in groundwater from a 101 m-deep borehole (HA01) in northern Iceland during 2010–2018 and compared them with seismic and volcanic events that occurred in the same period to identify potential hydrogeochemical precursors. An increase of B, Al, V, Li and Mo concentrations started from eight months to one month before the 2014 Bárðarbunga eruption (~115 km from HA01), a major rifting event in central Iceland, while Ga and V concentrations began to increase one day and one month after the onset of the event, respectively. We also found that concentrations of some trace elements (Li, B, Ga, Mo, Sr, Rb and Fe) significantly increased before an M_w 5.0 earthquake that occurred ~80 km from the borehole in 2018. However, other notable hydrogeochemical changes were detected during the monitoring period without apparent correlation with the seismic and volcanic events in the region. This study shows that the systematic long-term hydrogeochemical monitoring in seismic and volcanic areas is critical to advance the science of seismic and eruptive precursors. Furthermore, the use of statistical tools, such as Principal Component Analysis (PCA) and Change Point (CP) detection can help identify the most useful chemical elements and validate the trend variability of those elements in the time series, reducing arbitrary choices of pre-seismic and pre-volcanic hydrogeochemical anomalies as potential precursors.

© 2021 Published by Elsevier B.V.

* Corresponding author.
E-mail address: maurizio.barbieri@uniroma1.it (M. Barbieri).

1. Introduction

Hydrogeochemical changes related to earthquakes have been documented throughout history (Manga and Wang, 2015; Wang and Manga, 2021). Most of these changes were recorded in conjunction with and/or after seismic events (Scholz et al., 1973; Wakita, 1975; Igarashi et al., 1995; Montgomery and Manga, 2003; Manga et al., 2003; Cucci, 2019; Kim et al., 2019; Barberio et al., 2020; Chiodini et al., 2020; Barbieri et al., 2020; Hosono and Masaki, 2020; Kawabata et al., 2020; Sato et al., 2020); however, recent anomalous hydrogeochemical variations before $M_w \geq \sim 5$ earthquakes have been systematically measured and documented (Claesson et al., 2004; Chen et al., 2013; Skelton et al., 2014, 2019; Chen et al., 2015; Barberio et al., 2017; Petitta et al., 2018; De Luca et al., 2018; Onda et al., 2018; Boschetti et al., 2019; Sano et al., 2020). Until recently, the lack or paucity of continuous and long-term hydrogeochemical monitoring aimed at investigating the seismic cycle (Ingebritsen and Manga, 2014; Skelton et al., 2019; Zhou et al., 2020) have significantly limited the ability of scientists to identify and fully understand any seismic precursors of a hydrogeochemical nature. While seismological and geodetic (GPS) networks have been globally active for many years and have provided important information about crustal deformation and seismic cycles (e.g., Chiarabba et al., 2020), hydrogeochemical networks for seismic precursor identification have only recently started to emerge in China, Iceland, Italy, Japan, western USA and a few other countries (Chaudhuri et al., 2013; Hosono and Masaki, 2020; Franchini et al., 2020). These new networks, or single monitoring stations, have produced significant results on pre-seismic hydrogeochemical changes likely connected with the dilatative preparatory phases of intermediately strong earthquakes. In particular, pre-earthquake changes in groundwater temperature (Shi and Wang, 2014; He and Singh, 2019), chemical composition (Claesson et al., 2004; Barberio et al., 2017; Onda et al., 2018; Boschetti et al., 2019; Skelton et al., 2019; Hosono et al., 2020; Nakagawa et al., 2020; Shi et al., 2020; Franchini et al., 2020) and changes in natural gas geochemistry (Wakita et al., 1980; King et al., 2006; Sano et al., 2016; Barbieri, 2019; Buttitta et al., 2020; Martinelli et al., 2020) have been properly documented and interpreted as potential seismic precursors. Fossil instances of seismic precursors are also starting to be documented in fault-related mineralization (Andrén et al., 2016; Coppola et al., 2021) near where hydrogeochemical precursors of strong earthquakes had previously documented in northern Iceland and central Italy (Skelton et al., 2014; Barberio et al., 2017).

Hydrogeochemical monitoring networks are now emerging for seismic precursor identification, whereas volcanic eruption precursors are mainly searched for and identified through seismic and geodetic monitoring (Patanè et al., 2003; Sparks, 2003; McNutt and Roman, 2015) or through geochemical measurements often (but not only) on proximal emissions, such as fumaroles, hot springs and volcanic lakes (Aiuppa et al., 2007; De Moor et al., 2016). Conversely, the intermediate or remote hydrogeochemical monitoring of volcanoes for eruption precursor identification, although used, is rarer (Armienta and De la Cruz-Reyna, 1995; Caracausi et al., 2003). Below, we will show that this remote method could be more suitable, more reliable, and easier than sampling proximal volcanic fluid emissions.

Since 2002, a hydrogeochemical monitoring system has been running in northern Iceland with the main aim of identifying potential precursors to earthquakes. One monitoring station was set up at Húsavík (HU01) and the other at Hafralækur (HA01) (Claesson et al., 2004, 2007; Skelton et al., 2014, 2019; Andrén et al., 2016). The samples from this study come from HA01 that consists of a 101 m-deep borehole located at Lat. 65.8722°N and Long. 17.4528°W (Fig. 1). HA01 has been continuously monitored since 2008. The monitoring system has allowed geoscientists to identify hydrogeochemical changes (interpreted as potential seismic precursors) before three large earthquakes ($M_w > 5.0$) that occurred off northern Iceland on 16 September 2002, 21 October 2012 and 2 April 2013. Before the 2012 M_w 5.6 and the 2013 M_w 5.4

earthquakes, significant anomalies in groundwater concentrations of Na, Ca, Si, $\delta^{18}O$ and δ^2H were recorded at the HA01 hydrogeochemical station (Skelton et al., 2014). These studies were then followed by geochemical modelling and statistical studies to explain and verify previous interpretations (Andrén et al., 2016; Skelton et al., 2019). Moreover, before the 2002 M_w 5.8 earthquake, significant anomalies of Cu, Zn, Mn and Cr were detected in groundwater from the HU01 borehole (20 km from the HA01 borehole) at Húsavík (Skjálfandi Bay; Fig. 1) together with pre- and post-seismic shifts of groundwater concentrations of B, Ca, K, Li, Mo, Na, Rb, S, Si, Sr, Cl, SO_4, $\delta^{18}O$ and δ^2H (Claesson et al., 2004).

In 2018, to expand the hydrogeochemical analyses of the monitored HA01 groundwater and identify further potential precursors of earthquakes in northern Iceland, international collaboration was established between Stockholm University, the University of Iceland at Reykjavík, Sapienza University of Rome and CNR-IGAG in Rome. Within this collaboration, we analysed trace element concentrations in the groundwater sampled from the HA01 borehole between 2010 and 2018 together with earthquake and volcanic data in the same period.

We then used geochemical-thermodynamic computations to constrain the origin of the observed elements. The results show new potential hydrogeochemical precursors of $M_w \geq \sim 5$ earthquakes and remote hydrogeochemical precursors of volcanic eruptions. These results are integrated with previous hydrogeochemical findings obtained from the same monitoring system (Skelton et al., 2019) for a better comprehension of the hydrogeochemical and physical processes that occur during the preparatory phases of intermediately strong earthquakes and volcanic eruptions in Iceland.

Our main aim is to advance the science of hydrogeochemical precursors of earthquakes and volcanic eruptions. Our results are part of a tentative first step towards forming the background necessary to formulate national protocols aimed at seismic and volcanic precursor identification and related hazard mitigation.

2. Geological and hydrogeological settings

Iceland is located on the Mid-Atlantic Ridge between the divergent plate margins of Eurasia to the east, North America to the west, the Reykjanes ridge to the south and the Kolbeinsey ridge to the north (Einarsson, 1991; Einarsson et al., 2008; Árnadottir et al., 2008; Fig. 1). The tectonic setting of Iceland is dominated by an eastward shift of the Mid-Atlantic Ridge due to a hot spot currently located under the Vatnajökull glacier in southeastern Iceland (Thordarson and Larsen, 2007). Two transform zones connect the shifted ridge segment to the Mid-Atlantic Ridge: the South Iceland Seismic Zone (SISZ) to the south and the Tjörnes Fracture Zone (TFZ) to the north (Fig. 1). The TFZ cuts across the area investigated in this work in northern Iceland.

The TFZ is a 120 km-long and 70 km-wide oceanic oblique transform zone linking the Northern Volcanic Rift Zone to the south and the southern end of the submarine Kolbeinsey ridge to the north (Einarsson, 1991; Einarsson et al., 2008; Stefansson et al., 2008). This WNW-ESE-trending fracture zone includes two main transform structures: the Grímsey Oblique Rift (GOR) and the Húsavík-Flatey Fault (HFF) (Gudmundsson et al., 1993; Gudmundsson, 2007; Rögnvaldsson et al., 1998; Stefansson et al., 2008; Wästeby et al., 2014; Tibaldi et al., 2020; Fig. 1).

Seismic activity in Iceland is mainly linked to the extensional and lateral transfer dynamics associated with Mid-Atlantic Ridge kinematics. Therefore, seismic activity is mainly located along the ridge segments, but it is rarer in intraplate areas. Earthquakes in northern Iceland occur mainly in the TFZ (Gudmundsson, 2007) along the HFF and GOR (IMO, 2016; Fig. 1). Strike-slip and normal fault motions in the TFZ are responsible for the high level of seismic activity in this zone, which has hosted more than 10 $M_w > 6$ earthquakes in the past 300 years (Gudmundsson et al., 1993; Gudmundsson, 2007; Rögnvaldsson et al., 1998; Stefansson et al., 2008; Wästeby et al., 2014; Skelton et al., 2019). Additionally, moderately strong earthquakes have been recorded
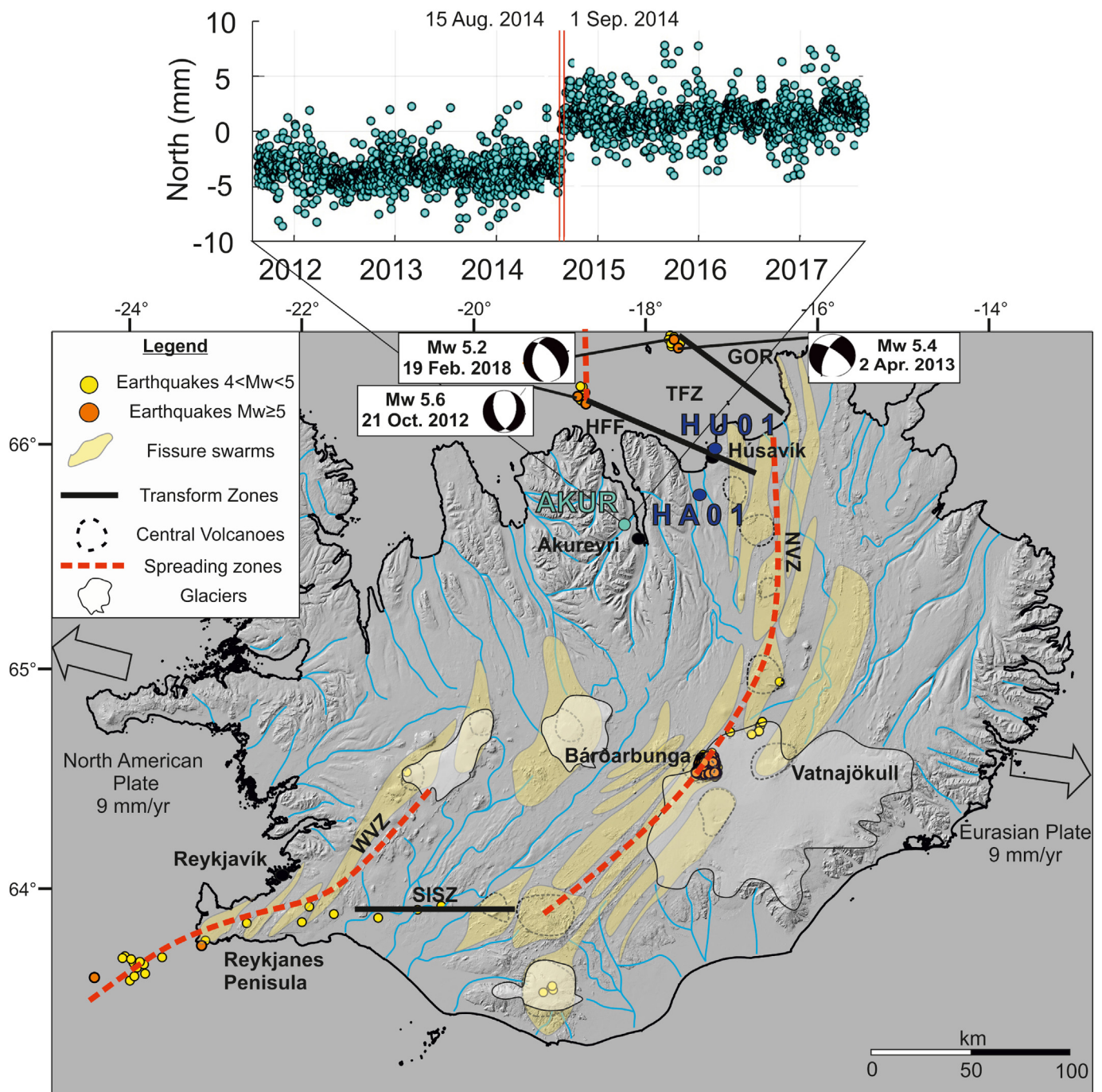
Fig. 1. Map of Iceland. Groundwater sampling sites in Hafralækur (HA01) and Húsavík (HU01), northern Iceland, are displayed with blue symbols. CGPS station (AKUR) in northern Iceland and the relative time series of the detrended north component are displayed with turquoise circles (see the diagram on top of the map; modified after Jónsson et al., 2019). The CGPS time series shows a ~5 mm transient signal due to the Bárðarbunga-Holuhraun dike intrusion. The red vertical lines mark 15 August and 1 September 2014, just before and after the diking activity. In the map, the Bárðarbunga volcano and glaciers (e.g., Vatnajökull) are also shown. Spreading zones and main transform zones are represented with red dotted lines and black solid lines, respectively. Fissure swarms are displayed as yellow shaded areas (from Árnason, 2020). Earthquake epicenters (2010–2018) are represented with orange and yellow dots depending on the magnitude (https://en.vedur.is/). Focal mechanisms of selected earthquakes (October 21st, 2012, Mw 5.6; April 2nd, 2013, Mw 5.4; August 16th, 2014, Mw 4.0; February 19th, 2018, Mw 5.2) are also shown (https://en.vedur.is/). (For interpretation of the references to color in this figure legend, the reader is referred to the web version of this article.)

along with volcanic activity, such as at Katla, Krafla and Bárðarbunga (Einarsson and Björnsson, 1979; Einarsson et al., 2008).

During our monitoring period (2010–2018), the main seismic and volcanic events that occurred in central and northern Iceland were four $M_w \geq 5.0$ earthquakes in the TFZ and one volcanic eruption (a rifting event). The earthquakes occurred off northern Iceland along the western HFF on 21 October 2012 (M_w 5.4 and 5.6 earthquakes occurred at

Lat. 66.333°N and Long. -18.805°W and at Lat. 66.299°N and Long. -18.714°W, respectively), along the GOR on 2 April 2013 (an M_w 5.4 earthquake occurred at Lat. 66.547°N and Long. -17.661°W) and on 19 February 2018 (an M_w 5.2 earthquake occurred at Lat. 66.586°N and Long. -17.708°W) (https://en.vedur.is/; Fig. 1).

A volcanic eruption occurred in Holuhraun, just north of the Vatnajökull glacier, and was part of a rifting event that originated in

3

the Bárðarbunga volcano (Fig. 1). The rifting event started on 16 August 2014, with a magmatic dike gradually propagating 48 km northeastward from the Bárðarbunga volcano until 27 August 2014. The dike propagation and emplacement were followed by eruptive activity beginning on 29 August 2014 and ending on 27 February 2015 (Sigmundsson et al., 2015; Andrén et al., 2016). The Bárðarbunga (dike) intrusion has been estimated ~5 m in thickness (Sigmundsson et al., 2015; Ruch et al., 2016) and it caused strain changes all over northern Iceland, as indicated by ~5 mm of GPS-determined displacements at distances beyond 100 km from the intrusion (Jónsson et al., 2019, Fig. 1).

The HA01 hydrogeochemical monitoring borehole, which is the source of the water samples analysed in this paper, is located in the Hafralækur area (Fig. 1) in a low-temperature geothermal district just south of the TFZ and ~ 20 km to the south of Húsavík (Andrén et al., 2016). In the Hafralækur–Húsavík area, the bedrock mainly consists of mafic and intermediate lavas from the Tertiary to Holocene ages with intercalated sediments (Jóhannesson, 2014). The HA01 borehole is 101 m deep and penetrates a layer of basalt-derived sediments beneath the Younger Laxá Lava, producing three lava flows (Andrén et al., 2016). From the borehole, artesian water naturally flows out after circulating into basalts and basalt-derived sediments. The borehole is cased to a depth of 35 m with filters for water inlets located at 65, 82 and 96 m, yielding a total of 7.7 L/s. The groundwater from the borehole is between 71 and 76 °C with a pH of ~10.2 (at 25 °C). The groundwater has a low dissolved solid content (240 ppm), which is typical of fresh low-temperature geothermal groundwater on the flanks of the active rift zone in Iceland (Kristmannsdóttir et al., 2010; Skelton et al., 2014, 2019; Andrén et al., 2016).

3. Data and methods

Water samples have been collected from the HA01 borehole every week from October 2008 (Skelton et al., 2019). The time window for this study is from September 2010 to June 2018. Two samples from the borehole were collected weekly to determine major (cations and anions) and trace element contents and for isotope analysis. Before sampling, to mitigate the borehole casing oxidation effects, we removed the stagnant water (shallow), then purged a fixed number of borehole volumes, generally between three to five (Trick et al., 2008). Both groundwater samples were filtered in situ through a 0.2 μm filter into acid-washed polyethylene bottles. One sample was filled leaving as little air as possible, and it was not opened again until the analysis stage. This latter sample was used for isotope analysis (Skelton et al., 2019). On the day of sampling, the sample was cooled for around one hour before pH and temperature were measured. In the second sample, Suprapur® HNO3 (Merck KGaA, Darmstadt, Germany) was added to make it 1% acidified. After a period of storage in Iceland, the samples were sent to and stored cold at the University of Stockholm and the University of Iceland in Reykjavík to analyse stable isotopes ($\delta^{18}O$ and δ^2H) and major element concentrations, respectively (Skelton et al., 2019). Finally, the acidified water samples were sent to Rome for trace element concentration analysis (Franchini et al., 2020). This latter analysis used the same sample aliquots that had been previously analysed for the major elements (Skelton et al., 2014, 2019; Andrén et al., 2016). We measured the concentration of dissolved trace elements (lithium (Li), beryllium (Be), boron (B), aluminium (Al), vanadium (V), chromium (Cr), manganese (Mn), iron (Fe), cobalt (Co), nickel (Ni), copper (Cu), zinc (Zn), gallium (Ga), arsenic (As), rubidium (Rb), strontium (Sr), molybdenum (Mo), cadmium (Cd), indium (In), antimony (Sb), caesium (Cs), lead (Pb) and uranium (U); Table S1) at the Geochemistry Laboratory of Sapienza University of Rome with an inductively coupled plasma mass spectrometry ICP-MS (X Series 2 Thermo Fisher Scientific) (Ricolfi et al., 2020). To keep trace element stability in the solutions until analysis, in the ICP-MS laboratory, we re-checked the pH of the acidified water samples and added Suprapur® HNO3 till to pH < 2, if needed (Marcovecchio et al., 2014). We used ultrapure water (Millipore, Milli-Q, 16 MΩ cm) to prepare blanks, standard solutions, sample dilutions and an internal standard, Rh, to correct the ICP-MS instrumental drift. The analytical accuracy of this method ranged between 2% and 5% (Barberio et al., 2017; Nigro et al., 2017). After each tenth sample, we analysed blank and two standard reference materials (SRM1640a purchased from the National Institute of Standards and Technology, United States) as water samples. The parameters for water analyses by ICP-MS (X Series II Thermo Fisher Scientific Inc.) are reported in Table S2. We measured and controlled for uncertainties for all constraints using a regular laboratory replica of samples and by confirming the precision/calibration of the instrument over regular runs with standard solutions. The recoveries of analytes of interest were in the range 98.4–106.3%, whereas recoveries of the SRM1640a were in the range 91.2–111.6%. We added 206Pb, 207Pb and 208Pb isotopes to measure the concentration of lead (Ricolfi et al., 2020).

To analyse and assess the trace element temporal series, and to avoid human influence or an arbitrary choice of anomalies, we used both Principal Component Analysis (PCA) and Change Point (CP) detection. In long-term borehole monitoring, such as for HA01, PCA is useful to identify which elements (components) and samples (loadings) deserve particular attention. After such a selection, CP detection is helpful to identify significant changes in the time-series, particularly when compared to seismic or volcanic events.

The PCA is a statistical tool that can discover unsuspected relationships that could reduce the dimensionality of the dataset while retaining the information present in the data structure. It has been successfully applied to explain the hydrogeochemical composition of geothermal waters in different geological settings (Nicholson, 1993; Boschetti et al., 2003; Awaleh et al., 2020). Different codes from OriginPro version 2019b (OriginLab Corporation, Northampton, MA, USA) and SPSS version 16 (Armonk, NY: IBM Corp; IBM, 2019) were used for classic PCA. Before PCA extraction, the sampling adequacy of the data matrix was checked for the subject-to-variables ratio (Bryant and Yarnold, 1995; Hutcheson and Sofroniou, 1999; Hatcher and O'Rourke, 2013; Garson, 2018), Kaiser-Meyer-Olkin (KMO) and Bartlett's test of sphericity (IBM, 2019). Results were also compared with categorical PCA (CATPCA) and robust PCA (RPCA) (Filzmoser and Todorov, 2013; Hubert et al., 2016). Other details are discussed below in the dedicated section.

We also used CP analysis on the temporal series of chemical data. A CP is a point in which an ordered sequence of data (y1, y2, …, yn) changes its statistical properties (Skalska, 2017). Some freely available codes can solve the detection and statistical evaluation of changes in data trends (Skalska, 2017). The Joinpoint Regression Program (JRP), version 4.8.0.1, is a software package that fits data into joinpoint models (Joinpoint Regression Program, 2020). The software enables the user to test whether an apparent change in trend is statistically significant. A sequence of permutation tests (the Monte Carlo method) identifies the CPs between trends. The procedure is based on a sequential application of likelihood ratio-type tests (Kim et al., 2000). Once the minimum (k_{min}) and maximum (k_{max}) number of CPs is set, choosing the number of statistically significant CPs is performed via a scheme of hypothesis tests that compares a simpler model, called the null model, and a more complicated model called the alternative model. This brief description does not attempt to be mathematically or statistically exhaustive; therefore, the reader is referred to the Joinpoint Regression Program (2020) for more details. In this study, we used the following operative code conditions: i) to obviate the fact that the sampling dates of the trace elements do not have regular periodicity, we used a standard error of 5% (i.e. higher than the real 2%) for each raw data concentration before elaboration; ii) we chose weighted Bayesian information criteria (WBIC) as the model elaboration, which combines both traditional Bayesian information criteria (BIC) and its modification with a harsher penalty (BIC3) using a weighted penalty term based on data characteristics (Joinpoint Regression Program, 2020). The WBIC

was considered the default in the Joinpoint software, particularly for a large dataset (N > 160 samples), because it is more computationally efficient than the permutation tests and maintains a relatively high probability of correct selection (Kim and Kim, 2016; Joinpoint Regression Program, 2020).

Concerning seismic data, we considered earthquakes from 1 September 2010 to 31 December 2018, which included ~800 seismic events ($M_w \geq 4$) in Iceland (see Fig. 1; Table S3). These earthquakes were mostly linked to the volcanic activity and caldera collapse of Bárðarbunga in 2014–2015 (indeed, these earthquakes mainly occurred between August 2014 and February 2015) and to the seismic activity of the HFF and GOR in northern Iceland (Fig. 1). All earthquake data are from the IMO catalogue (https://en.vedur.is/).

4. Results and discussion

4.1. Elemental variability of the HA01 groundwater

Before comparing the chemical data (Table S1) of the monitored HA01 borehole against the seismic and volcanic activities during this study's time window, we computed the coefficients of variation associated with HA01 groundwater trace elements in Fig. 2a (Table S4).

The coefficient of variation corresponds to the ratio between the standard deviation (σ) and the absolute value of the mean ($|\mu|$) of results from the physical-chemical measurements and analyses realized in situ and in the laboratories on the groundwater samples collected during the considered period. The coefficient of variation is a measure
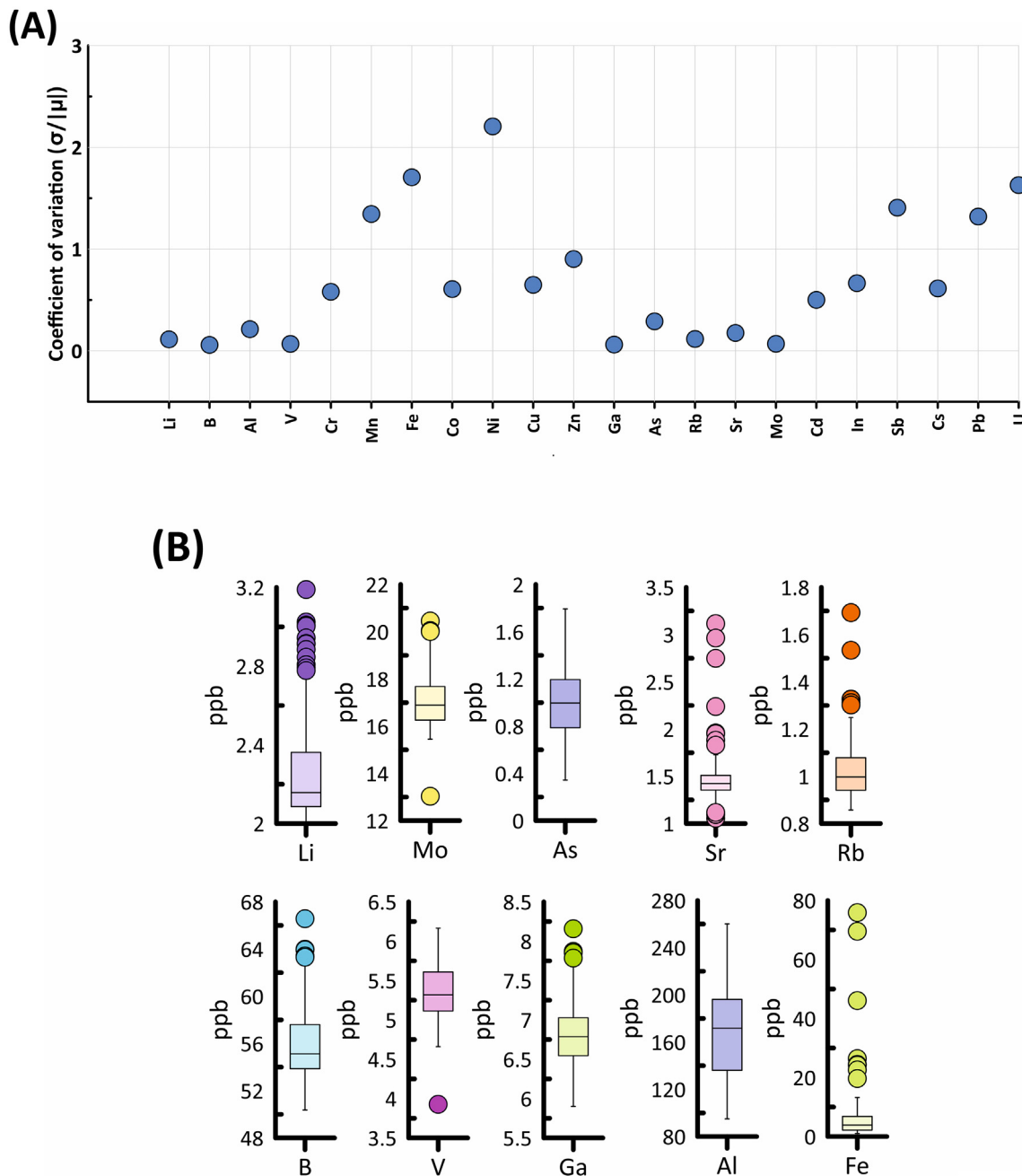

Fig. 2. Variability of elements in the HA01 groundwater. (A) Coefficients of variation for all the trace elements (Table S4). (B) Box-and-whisker plots for the selected trace elements where dots represent "anomalous values" of concentrations (ppb) compared to the median and the associated box as they exceed the whiskers.

of dispersion of a frequency distribution and shows the extent of variability in relation to the mean of the population.

The low variability range (coefficient of variation <0.5) includes Li, B, Al, V, Ga, As, Rb, Sr and Mo. The intermediate variability range (≥0.5 to <1.0) includes Cr, Co, Cu, Zn, Cd, In and Cs. The high variability range (≥1.0) includes Mn, Fe, Ni, Sb, Pb and U (Fig. 2a).

Most elements with coefficients of variation >0.5 have very low average concentrations over the sampling period, namely, less than 1 ppb or even below the quantification limit of the instrument (Table S4). For this reason, we excluded these elements (Co, Cd, In, Cs, Cr, Mn Ni, Cu, Sb, Pb, U and Zn) from our subsequent analyses and elaborations. In terms of Zn, despite an average concentration of 6.42 ppb, it was only detected in 29 out of 166 analysed samples. Although the Fe concentration was often below the instrument detection limit (in 54 samples out of a total of 166), we considered it the same because of its documented role in pre-seismic processes elsewhere (Barberio et al., 2017; Boschetti et al., 2019). The remaining elements (Li, B, Al, V, Ga, As, Rb, Sr and Mo) were mostly characterised by low coefficients of variation (<0.5), which, over a long time series (8–9 years) corroborate their suitability as good indicators for changes connected with environmental events. In other words, anomalies in groundwater concentrations are emphasised by the stability of the time series expressed by the low coefficient of variation.

To better understand the statistical distribution of the analysed populations, we also graphed concentrations of the selected elements (Li, Mo, As, Sr, Rb, B, V, Ga, Al and Fe) as box-and-whisker plots (Fig. 2b). Each box represents interquartile ranges (25–75 quartiles) and is separated into two parts by the median. The whiskers are limited by the interquartile range (IQR) with a factor equal to 1.5. All selected elements had small boxes, meaning that populations were clustered around the median. Furthermore, all elements, except As and Al, had outliers (dots in Fig. 2b), which are anomalous values compared to the median and associated box as they exceed the whiskers (Fig. 2b).

4.2. Time series of trace elements in the HA01 groundwater

The time series of previously selected (Li, Mo, As, Sr, Rb, B, V, Ga, Al and Fe) trace element concentrations (Table S1) are shown in Fig. 3. The graphic representation of the time series allowed us to appreciate the extraordinary stability found in the concentrations of Li, B, Mo, V, Ga, As, Rb, Sr and Al over nine years (Table S1), which is confirmed by the low variability of the sample around the average values (Table S1). Instead, Fe and Zn showed a very high standard deviation, which is a symptom of higher intrinsic variability and/or potential instrumental difficulties in their determination (Fig. 3 and Table S1).

Fig. 3 demonstrates that two groups can be identified based on the trends of concentration over time. The first group is represented by Li, Ga and Mo, while the second group is represented by B, V and Al. These two groups of elements exhibit similar behaviours where comparable trends of concentrations are recognised.

Sr, Rb and Fe concentrations were stable around their average values, only significantly departing between January 2018 and the end of study period (Fig. 3).

The As time series was characterised with very low and variable (but within a very narrow concentration interval of about 1 ppb) concentration values. No clear trends were visible in this narrow distribution within the monitoring period (Fig. 3).

4.3. Preliminary observations on hydrogeochemical changes vs seismic and volcanic events

To identify possible correlations between trace elements of the analysed groundwater and geological events, such as earthquakes and volcanic activity, we compared our hydrogeochemical time series with a time series of seismic events with $M_w \geq 4$ and main volcanic episodes (i.e. from the Bárðarbunga volcano) for the period of monitoring in

selected areas of Iceland (Figs. 1 and 3). We identified the following possible temporal correlations:

(1) An apparent increase in B, Al and V concentrations (HA01) started about five months (May 2012) before the M_w 5.6 seismic event off northern Iceland on 21 October 2012, around 75 km from the HA01 borehole. From July 2012, the concentrations of these three elements returned to background values (Fig. 3). Different hydrogeochemical potential precursors for this earthquake were previously identified (Skelton et al., 2014, 2019; Andrén et al., 2016).

(2) From January 2014, B, Al and V exhibited a substantial decrease in their concentrations (HA01) until August 2014, when a quick inversion and increase of all three elements were recorded. This increase started about one week before the Bárðarbunga seismic sequence and rifting event (16 August 2014), which, in turn, heralded the volcanic eruption (on 29 August 2014) by about two weeks (Gudmundsson et al., 2016). Hence, the elemental inversion and increase of B, Al and V (HA01) occurred about three weeks before the Bárðarbunga eruption in Holuhraun, which occurred at around 115 km from the HA01 borehole (Bárðarbunga is located 140 km away from the borehole). Moreover, in September 2014 (after the onset of the volcanic eruption), Li, Ga and Mo concentrations started to increase. B, Al, V, Li, Ga and Mo returned to background values in February 2015 (Fig. 3).

(3) All the considered trace elements (Li, B, Ga, Mo, Sr, Rb and Fe concentrations in the HA01 groundwater), except for Al, V and As, exceeded the $+2\sigma$ threshold (Table S1) from January 2018, about seven weeks before the M_w 5.2 earthquake off northern Iceland on 19 February 2018, approximately 70 km from the HA01 borehole (Fig. 3). Concentrations of these elements remained high until the end of our study period (June 2018).

(4) Some hydrogeochemical variations occurred in 2016–2017 (HA01) when no significant seismic and volcanic activities occurred. In particular, Li, Ga and Mo exhibited a substantial increase in groundwater concentration (HA01) from December 2016 to November 2017, whereas B, Al and V exhibited a substantial increase from January to June 2017 (Fig. 3). In the same period, the concentration of some major chemical elements in the HA01 water showed anomalous changes (Skelton et al., 2019).

The aforementioned potential correlations between hydrogeochemical trends and seismic-volcanic events are statistically tested below.

4.4. Trace element hydrogeochemistry and volcanic events

As mentioned above and observed in Fig. 3, hydrogeochemical changes before the 2014 Bárðarbunga activity were the most obvious over the recorded time series. We propose some geochemical-thermodynamic computations to understand the possible sources of trace elements (and their pre-volcanic concentration changes) in Icelandic volcanic environments.

Earthquakes are among the most important signals in forecasting eruptions because magma movement enhances the stress of the surrounding rocks. However, seismic activity in volcanic areas can be characterised with wide variability depending on the large range of elastic behaviour and rheology of the rising magma and surrounding rocks (Marzocchi and Bebbington, 2012). Among the main volcanic precursors, geochemical signals may be important in forecasting volcanic eruptions (Marzocchi and Bebbington, 2012). Monitoring methods based on chemical changes related to volcanic activity have been used to detect changes within the volcanic system. Geochemical monitoring has mainly focused on gas emissions from fumaroles or craters and, less frequently, the studies have addressed changes in remote groundwater geochemistry before volcanic eruptions (Armienta et al., 2008).
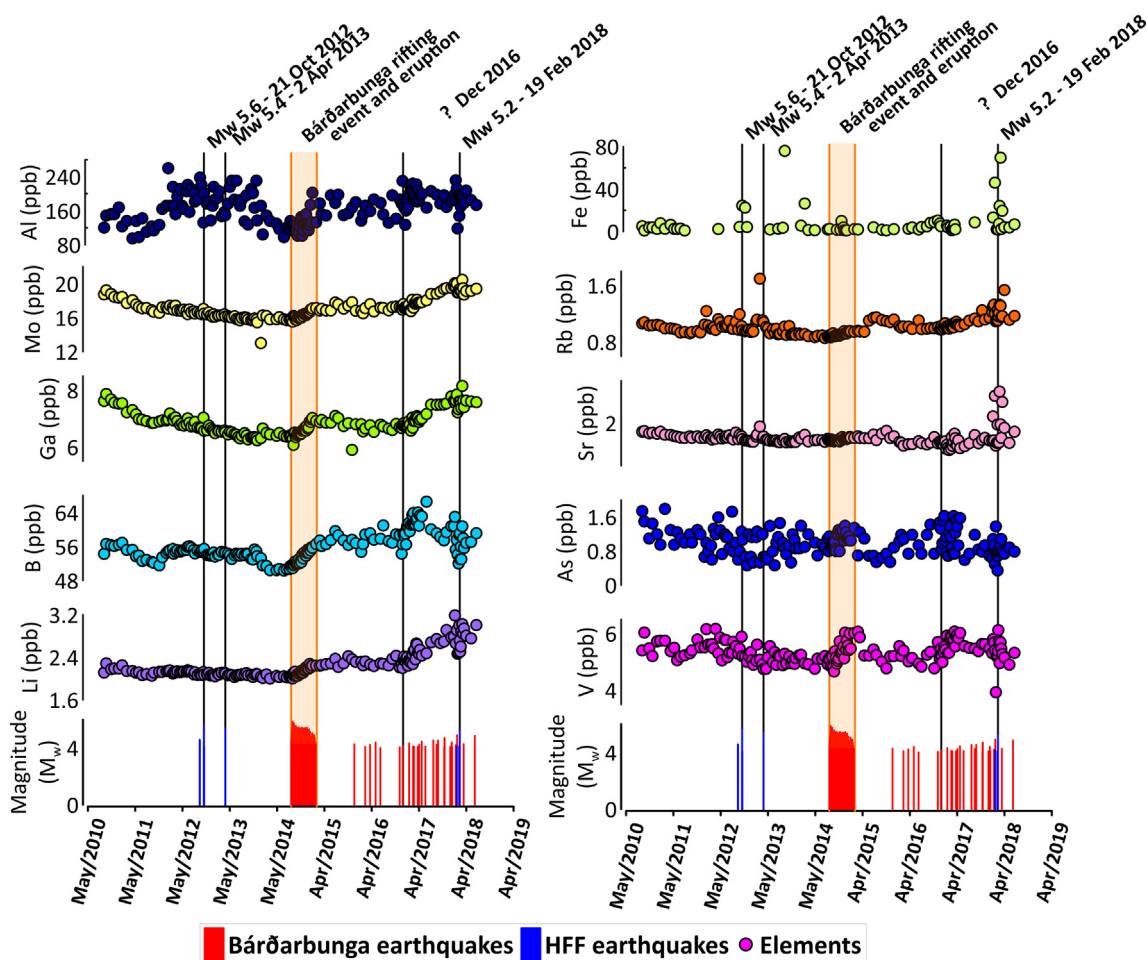
Fig. 3. Time series of trace element concentrations and major earthquakes and volcanic eruptions. Trace elements concentrations in the HA01 groundwater (ppb; September 22nd, 2010 – June 25th, 2018; Table S1) are shown with circles of different colors. Seismic events (M$_w$ ≥ 4; January 13rd, 2011 – February 23rd, 2019; Table S3) related to the Bárðarbunga Volcano and Húsavík-Flatey Fault (HFF) activities are displayed with red and blue bars, respectively. Earthquake data are from the IMO catalogue (https://en.vedur.is/). (For interpretation of the references to color in this figure legend, the reader is referred to the web version of this article.)

Nonetheless, the application of geochemical monitoring methods to water (springs, streams, etc.) associated with volcanism has proven to be productive in understanding mechanisms related to volcanic activity (Armienta and De la Cruz-Reyna, 1995). In an active geothermal system, as is this case study in Iceland, fluids can remotely transport or deposit metals that originate from source water, magmatic volatiles and via rock dissolutions (Kaasalainen et al., 2015; Blomgren et al., 2019). For example, B is highly mobile during water–rock interaction in a basaltic-hosted geothermal system and, therefore, is a good indicator of rock leaching. B is a chemical species that is more sensitive to changes in volcanic activity. Indeed, magma displacement can lead to dome or dike emplacement facilitating the leaching of the host rock. For this reason, the hydrogeochemical composition of springs varies with the changes in volcanic stress pattern (Armienta et al., 2008; Arnórsson and Andrésdóttir, 1995; Kaasalainen et al., 2015).

The calculation of the trace elements' relative mobility (Gislason et al., 1996; Aiuppa et al., 2000; Koh et al., 2016), i.e. the normalised-to-sodium ratio between the trace concentrations detected in the HA01 borehole and basalt (Kokfelt et al., 2006; Kaasalainen and Stefánsson, 2012; Shorttle et al., 2013), definitively confirms that B is the most mobile element in the studied area (Supplementary File RM). Therefore, to examine the volcanic hydro-sensitivity of B, we analysed the relationship between B and trace element concentrations in the geothermal aquifer fluids of the Hafralækur area (Fig. 4). We compared our water samples (black dots) with data from previous studies on snow samples from the Vatnajökull glacier and highland NE of the glacier during the 2014–2015 Bárðarbunga

eruption (white rhombuses; Galeczka et al., 2017), water samples from the Jökulsá á Fjöllum River (JFR) during the 2014–2015 Bárðarbunga eruption (light blue squares; Galeczka et al., 2016), Icelandic cold groundwater (green triangles; Kristmannsdóttir and Klemensson, 2007; Kristmannsdóttir et al., 2009; Kristmannsdóttir, 2011) and Icelandic thermal groundwater (orange triangles; Arnórsson, 1969; Kristmannsdóttir and Klemensson, 2007; Kristmannsdóttir, 2008; Kristmannsdóttir et al., 2009; Kristmannsdóttir, 2011; Kaasalainen and Stefánsson, 2012; Kaasalainen et al., 2015). The transition temperature between cold and thermal waters was 10 °C (Kristmannsdóttir and Klemensson, 2007; Kristmannsdóttir et al., 2009; Kristmannsdóttir, 2011), in agreement with Schoeller's (1962) definition of thermal waters (air or surface water temperature over 4 °C). In Húsavík, the mean annual temperature of surface water was approximately 5.6 °C, and the transition between cold and thermal waters occurred at around logB = 1. The logarithmic values tended to fade the temporal element variability, particularly in samples with a lower coefficient of variation values. However, it was possible to have some indication of the origin of the trace constituents by comparing them with the concentration of median trace elements in Icelandic basalts (Kaasalainen and Stefánsson, 2012) and with the data from Icelandic thermal waters at temperatures lower than or equal to 100 °C (Arnórsson, 1969; Kaasalainen and Stefánsson, 2012; Kaasalainen et al., 2015). Geochemical-thermodynamic codes can be used to model the equilibria of major and trace elements during water–rock interaction (e.g. reaction-path modelling; Marini, 2013; Kaasalainen et al., 2015). However, the low concentration of trace
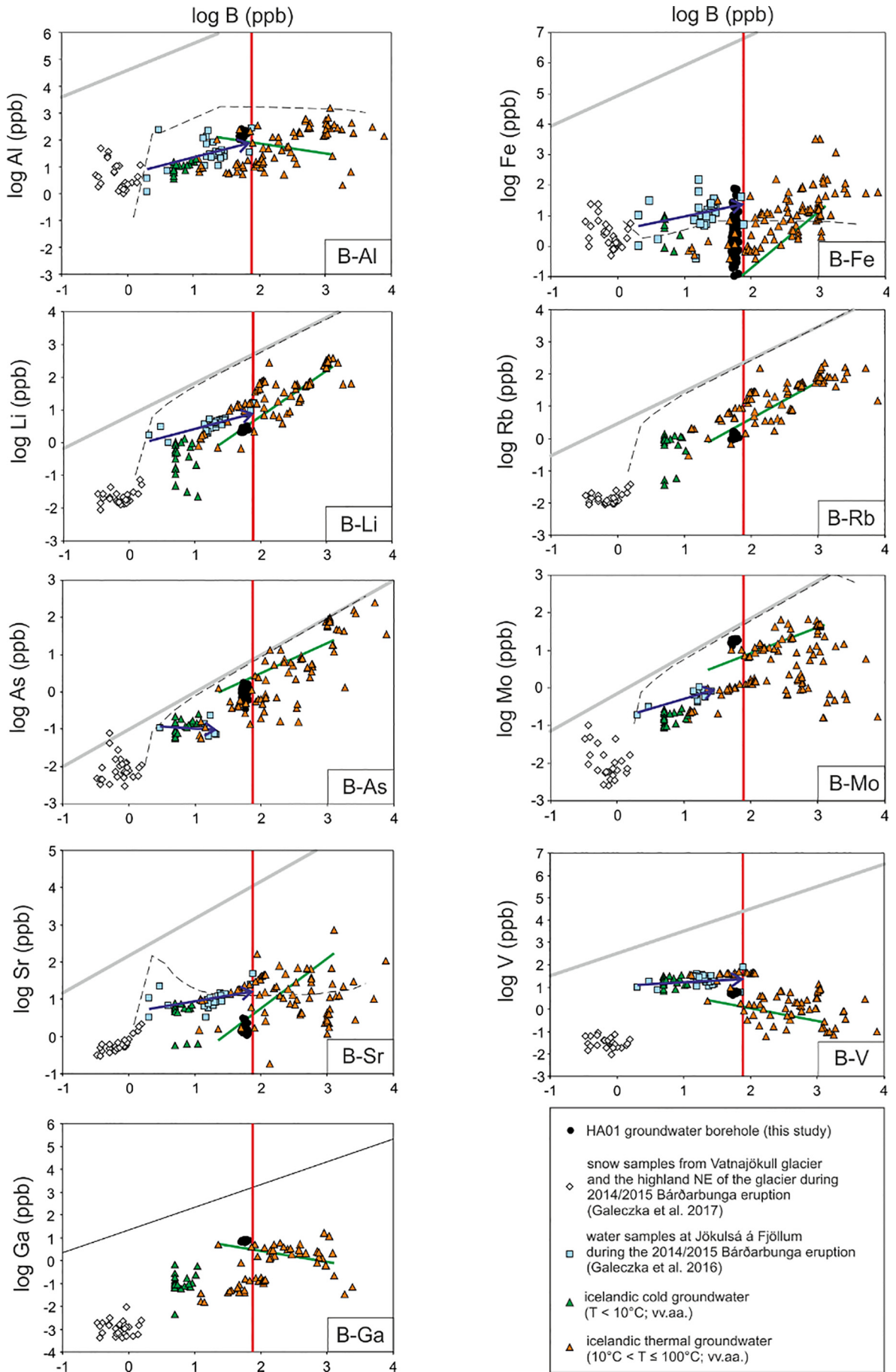
elements in T ≤ 100 °C groundwater combined with the difficulty in taking other phenomena into account, such as adsorption/absorption in minerals (in particular oxides and hydroxides), co-precipitation in complex phases (such as the solid solutions or mixed layered clays) and the incompleteness of the thermodynamic data on solution species, mean that these models must be used with extreme caution when applied to trace elements (Oelkers et al., 2009; Marini, 2013). This is evident in Fig. 4, especially in the case of Li and Rb, where the borehole waters were positioned below the reaction path model created by Kaasalainen et al. (2015). That model was calculated for high-temperature geothermal waters in Iceland; however, the first stretch of the path (low B content) can be compliant for waters at T ≤ 100 °C, as in the case of the HA01 borehole. It is relevant to observe how the HA01 samples are clustered at the switch domain between the surface waters of JFR (Galeczka et al., 2016) and Icelandic thermal waters, which are approximated by the maximum boron content detected in JFR during the 2014–2015 Bárðarbunga eruption (logB = 1.8) (Fig. 4). The samples tend to be closer to the reaction path model in the case of Sr, Al and Fe, with the first one being quite immobile compared to boron. The HA01 borehole groundwater samples have lower contents in Sr compared to the reaction path model and Icelandic thermal waters, probably due to the high pH of the HA01 groundwater (i.e. faster calcite precipitation especially close to the surface conditions) and/or co-precipitation in calcic zeolites (Andrén et al., 2016).

The Al and partial Fe concentrations in HA01 groundwater align with the trend of JFR samples towards Icelandic thermal waters. These two elements are geochemically similar and can be classified as immobile trace elements (Supplementary File RM), probably due to their tendency to form oxide-hydroxide colloids. However, Fe has the greatest variability in the parity of B concentration, probably due to variable redox conditions and/or the fact that iron resides in the structures of nano- to micron-scale clay mineral particles undergoing cycling between Fe(II) and Fe(III) (Ilgen et al., 2019). In contrast, Mo is the second more mobile trace element after B (Supplementary File RM). Its concentration in the HA01 groundwater is also noteworthy because, similarly to basalts, it is much higher than in surface waters and slightly shifts towards higher concentrations compared to other Icelandic thermal waters (Fig. 4). Mo does not have a very high basalt concentration, but it tends to accumulate in water proportionally to the time and temperature of interaction (Arnórsson and Óskarsson, 2007). This confirms that the HA01 groundwater is ancient and probably originated from glacial melting; it is roughly datable to the pre-early Holocene era as suggested by the low stable isotope ratio value of hydrogen, $\delta^2H(H_2O)$ (Skelton et al., 2014). Therefore, it is clear that the analogy of the B content between JFR waters and the HA01 borehole before and during the 2014–2015 volcanic crisis is a mere coincidence, even if the position of the borehole on the growth trend of the trace elements in the water is compatible with its origin from glacial melting. Indeed, in Iceland, early Holocene (12–8.2 cal ka) deglaciation and pulsed warming were associated with two major generations of *jökulhlaups* (glacier outburst mega-floods) around the Vatnajökull icecap at 11.4–11.2 cal ka and 10.4–9.9 cal ka and major tephra emissions from the Grímsvötn and Bárðarbunga subglacial volcanoes (Van Vliet-Lanoë et al., 2020).

We indicated the evolution of the JFR during the 2014–2015 event (purple arrow) along with a less-marked line representative of the correlation of the samples typical of the thermal waters of north Iceland (among which there is also the HU01 borehole; Kristmannsdóttir,

2008) (Fig. 4). As well as the HA01 borehole, these samples have a more basic pH (median equal to 9.7) compared to the others (8.37 in Kristmannsdóttir and Klemensson, 2007; Kristmannsdóttir et al., 2009; Kristmannsdóttir, 2011; 8.66 in NaCl waters in Kaasalainen and Stefánsson, 2012). It is noteworthy that basic pH values are typically measured from water originating from glaciers and are caused by the isolation of groundwater atmospheric CO_2 (Vigier et al., 2006). The correlation line (green line) is always close to the HA01 samples (Fig. 4). Therefore, this line can be representative of the evolutionary trend of the waters in the Hafralækur area. However, water samples from the HA01 borehole represent the transition between JFR and thermal waters (vertical red line) that are especially evident in the Al and Fe graphs. Moreover, trends of HA01 and other basic samples are similar for elements with geochemical affinities, such as Al and Ga (different mobility but with a similar dissolved species behaviour due to the pH; Elmi, 2009), As and Mo (similar high mobility and affinity with sulphides) and Li and Rb (similar moderate mobility and parallel trend to the ratio B/alkali metal in basalts) (Fig. 4; Supplementary File RM). Finally, the concentration of alkali metals Li, Rb and Cs in geothermal fluids increased with increasing temperature (Kaasalainen et al., 2015). This also explains why the trend is different from the high-temperature geochemical model (dotted line), given that the HA01 borehole has a deep T equal to ca. 100 °C (Fig. 4). In Fig. 5, most of the HA01 borehole samples are clustered between the mean composition of meteoric water and a Li/Rb = 2.26 weight ratio, which is between that of basaltic glass (Li/Rb = 2.33 in Berger et al., 1988, which is also similar to MORB, Li/Rb = 2.26 in Gale et al., 2013) and the median ratio of Icelandic tholeiitic basalts (Li/Rb = 2.18; Kaasalainen and Stefánsson, 2012), the latter also being enriched with more Cs (Fig. 5). Generally, processes related to the distribution of these elements in thermal waters are particularly evident at high temperatures in the following range: 150 < T < 350 °C (Seyfried Jr and Bischoff, 1979; Seyfried Jr., 1987; Giggenbach, 1991; Kaasalainen et al., 2015). In such a temperature range, the absorption of Li on quartz or Cs on zeolites is more pronounced (Giggenbach, 1991).

The calculation of the relative mobility of trace elements confirms that B is highly mobile during water–rock interaction in a basaltic-hosted geothermal system (Supplementary File RM). In particular, the analysis of the relationship between B and trace element concentrations in the geothermal aquifer fluids of the Hafralækur area allows us to confirm that water samples from the HA01 borehole represent the transition between JFR and thermal waters (Fig. 4). Furthermore, the noteworthy concentration of Mo confirms that the HA01 groundwater is ancient, probably originating from glacial melting and roughly datable to early Holocene (Arnórsson and Óskarsson, 2007; Skelton et al., 2014).

4.5. Principal Component Analysis (PCA)

In this study, some previously investigated major constituents such as Ca, Na, Si and K (Skelton et al., 2014, 2019) were added to the trace element database (Li, B, Al, V, Ga, As, Rb, Sr, Mo) to elicit as much information as possible from PCA. This addition also helped compensate for the lack of some trace elements that were not considered in PCA processing as they were below the quantification limit. A data matrix of 13 variables (the elements) and 156 subjects (the samples) was obtained that agreed with the subject-to-variables ratio of Bryant and

Fig. 4. Relationships between B and trace element concentrations in the HA01 groundwater. Solid black line depicts the boron/element ratios according to Kaasalainen and Stefánsson (2012, and references therein), except for Ga (median Ga value from Arnórsson, 1969; De Argollo and Schilling, 1978; Willis, 1979; Reimann and De Caritat, 1998). Purple arrow shows the trend line of the trace elements in the Jökulsá á Fjöllum River samples (white squares) during 2014–2015 Bárðarbunga eruption (Galeczka et al., 2016); vertical red line shows the maximum boron concentration detected in the river during that period (log B = 1.8). Snow samples during the same periods are also shown for comparison (white diamonds; Galeczka et al., 2017). Dashed lines depict the reaction-path modelling for high temperature geothermal water (meteoric water – basalt interaction at 260 °C; Kaasalainen et al., 2015). Green and orange triangles are Icelandic cold (T < 10 °C) and thermal waters (10 °C < T ≤ 100 °C) (see the main text for a complete reference list), respectively; green line depicts the best fit of high-pH thermal waters in northern Iceland. (For interpretation of the references to color in this figure legend, the reader is referred to the web version of this article.)
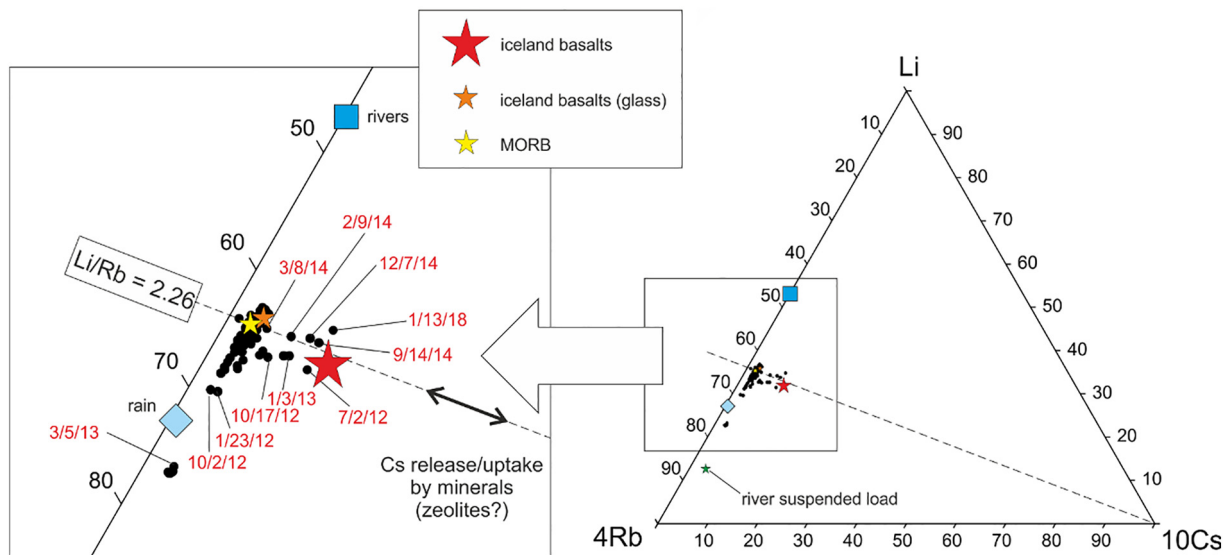
Fig. 5. Li-Rb-Cs ternary diagram. Element percentage from ppb (waters) or ppm (rocks) concentration values are reported over the diagram sides. Black dots show HA01 borehole monitoring trace dataset (this work, Table S1; Li/Rb = 2.26 is the median value of that dataset). Median basalt (Kaasalainen and Stefánsson, 2012), basaltic glass (Berger et al., 1988), MORB (Gale et al., 2013), river and rain waters (Kaasalainen and Stefánsson, 2012) are also shown for comparison. Black dots with sampling date labels as MM/DD/YY.

Yarnold (1995), STV > 5 and other rules of thumb related to the dimension of the subjects (Garson, 2018): subjects = variables x 5 or subjects >100 (Hatcher and O'Rourke, 2013); subjects >150 (Hutcheson and Sofroniou, 1999). The principal components were extracted using the correlation matrix in OriginPro code (Supplementary File 1). Similar results were obtained using the SPSS code, which had the additional option to rotate the extracted components using Varimax (IBM, 2019). With this latter code, both the KMO measure of sampling adequacy (KMO = 0.746) and Bartlett's test of sphericity (significance level ≪ 0.05) indicated that PCA was useful for interpreting the dataset. As suggested by the scree plot's elbow, the right number of components was four, which explains 75% of the cumulative variance of the data (OriginLab, 2019; Supplementary File 1). However, considering that the variance associated with the fourth component (PC4) was less than 10% and that the third component (PC3) was mainly associated with one trace element (As; see the 3D vector plot of the first three components in Supplementary File 1), the PCA results were interpreted using a binary plot, which shows both the variable eigenvectors and the PC1 and PC2 scores related to the samples (Fig. 6). In that plot, As is represented on the centroid of the diagram. Three main associations of the other variables are evident: i) a correlation between Na and Si vectors mainly represented by the positive side of PC2 (Y-axis); ii) the relationship between K and Ca vectors oriented towards the negative quadrant of Fig. 6; iii) the grouping of the trace elements' vectors on the positive side of PC1. Moreover, the sample scores showed a counter-clockwise distribution starting from 2010 (up/right quadrant, Y-axis, PC2). After that, the 2012–2013 samples are distributed just above the positive side of PC2, which is mainly represented by Na and Si variable vectors. This pattern agrees with the chemical variations detected during the swarm events of that period (Skelton et al., 2014), which were related to the labradorite–analcime reactions reported in Andrén et al. (2016). The subsequent clustering of the samples is on the negative (left) side of PC1, which seems to be related to a period of lower chemical concentration of most trace elements described by PC1 (from June 2013 to June 2014). After that, the chemical variability of samples collected in the second half of 2014 progressively shifts towards the K vector. In particular, the samples collected after the seismic swarms at the Bárðarbunga volcano (August 2014) seem not only related to that seismic event but also to the heat flow variations in that area (Reynolds et al., 2019). Indeed, the November 2014 samples, which correspond to the maximum thermal power in the cauldrons

produced by new magma inflow in the volcanic system (Li et al., 2021; Reynolds et al., 2019), are exactly at the top of the K vector (Fig. 6; Supplementary File 2). The samples collected from late 2014 to late 2017/early 2018 migrate gradually towards the lower right quadrant near the apex of the B and Li vectors and subsequently, towards the upper-right quadrant of Fig. 6 (January/February 2018). This might be related to post-eruptive changes after the Bárðarbunga-Holuhraun rifting event (Li et al., 2021; Reynolds et al., 2019). Accordingly, the time-series variation of the deep temperatures inferred by Na/K (Verma and Santoyo, 1997) and Na-K-Ca (Fournier and Truesdell, 1973; Fournier and Potter II, 1979; Fournier, 1989) geothermometric equations applied to the HA01 samples show a maximum temperature at the end of 2014 and other minor jumps in the second half of 2016 (Supplementary File 3). Finally, the progressive temporal shifting of the samples towards the trace element vectors mainly related to the positive side of PC1 (Fig. 6) agrees with the fact that the pre-seismic/seismic events related to 2018 (i.e. the M_w 5.2 earthquake on 19 February 2018) are detectable only with trace elements.

A second PCA used the correlation matrix of the trace elements and aimed to better interpret their behaviour. The KMO (0.721) and Bartlett's test (significance level ≪ 0.05) results certified once again the suitability of the data for structure detection. The main characteristics of this analysis are i) the two main components that explain the 60% of cumulative variance confirm the V, B, Al and Li, Ga, Mo clustering mentioned in the previous section (the latter group is mainly explained by the PC1 axis); ii) at the extreme of the negative side of PC1, samples collected before the Bárðarbunga eruption are grouped, confirming their concentration decreased before the event; iii) on the opposite side of PC1, early 2018 samples are well distinguished as outliers not only by Li, Ga and Mo but also by Rb. The samples collected during the 2012–2013 seismic swarms are indistinguishable from the others because they fall in the centroid of the diagram, confirming that the seismic events during that period are not highlighted by trace elements. Considering that PC1 explains most of the cumulative variance, it could be used as a single variable encompassing all trace elements and reducing unnecessary background information. Both the Varimax rotation and alternative methods of component extraction, such as CATPCA (Ma et al., 2016) or RPCA (Jung et al., 2014), do not increase either the percentage of variance explained by PC1 or the discrimination capacity of its scores (Supplementary File 4). Indeed, it is evident that the scores related to PC1 extracted by classic PCA have a higher peak close to the

date of the 2014 Bárðarbunga eruption and a lower peak in late 2017/early 2018 events compared to those obtained by Varimax-rotated, CATPCA or RPCA (Supplementary File 4).

In summary, the PCA indicates that the seismic events during 2012–2013 were not preceded by significant changes in trace element concentrations, while the 2018 seismic event was preceded by only trace element changes, but not by major element changes. Furthermore, the chemical variability of the groundwater samples collected after the pre-eruptive seismic swarm of the Bárðarbunga volcano (August 2014) is not simply related to seismic events but rather might be connected to post-rifting changes after the Bárðarbunga-Holuhraun rifting event (Reynolds et al., 2019).

4.6. CP detection in the time series

Change Point (CP) detection in the time-series data of the six trace element clusters detected by the PC1 axis (B, Al, V, Li, Ga and Mo; Fig. 7) reveals that each cluster has at least one CP within a central period, which is characterised by seismic events that occurred before and during the Bárðarbunga eruption (Fig. 7; Supplementary File CP). Compared to the first earthquake, the main eruption and following seismic events in the period marked by CPs have a broader date range. The dates marked by CPs span from 10 November 2013 for Al until 22 November 2015 for Ga, with the start of pre-volcanic seismicity (16 August 2014) and eruptive events of the Bárðarbunga (29 August 2014) approximately in the middle of the time series (Fig. 7). The CPs of Al should be taken with caution because it is an element with low mobility. However, the first Al CP is followed by a CP in boron (the most mobile of all

trace elements) on 1 December 2013, which marks the beginning of a declining trend in concentration, which then reverses on 8 March 2014. Element by element, it is difficult to explain the causes of these variations. However, it is interesting to note how the first CPs coeval with the stress accumulation detected in the north Iceland BRE seismic station, which is located immediately above the fault-plane of the Húsavík-Flatey transform fault, and it monitors shear-wave splitting (Hong et al., 2020). At BRE, the stress accumulation connected to the Bárðarbunga event was related to the overpressure of the microfractures' fluid, which began in August 2013, a year before the first pre-volcanic seismic shock at Bárðarbunga (Hong et al., 2020). Therefore, the first detected CPs described here could be linked to fluid overpressure in the microfractures before the main seismic event. In contrast, we speculate that late thermal variations connected to the Bárðarbunga eruption, which persist until the end of 2015 (Reynolds et al., 2019), may have been marked by the CPs of V and Ga, K in the PCA (Fig. 7) and geothermal analysis using the main chemical constituents as described in the previous section.

The second period, characterised by at least one CP in all elements except Ga, is positioned just before the M_w 5.2 earthquake on 19 February 2018 (Fig. 7). Before that seismic event, mobile elements had two (Mo) or three (B, Li) CPs. In particular, after an increasing trend, B starts to decline in concentration on 23 April 2017, approximately one month earlier than the other elements. Then, both B and Li start an abrupt decline on 1 January 2018, followed by an increase on 3 February 2018, i.e. two weeks before the seismic event. It should be noted that the alkali elements ternary diagram (Fig. 5) also shows an outlier on 13 January 2018. The precursor trends and related CPs, although not supported by all trace
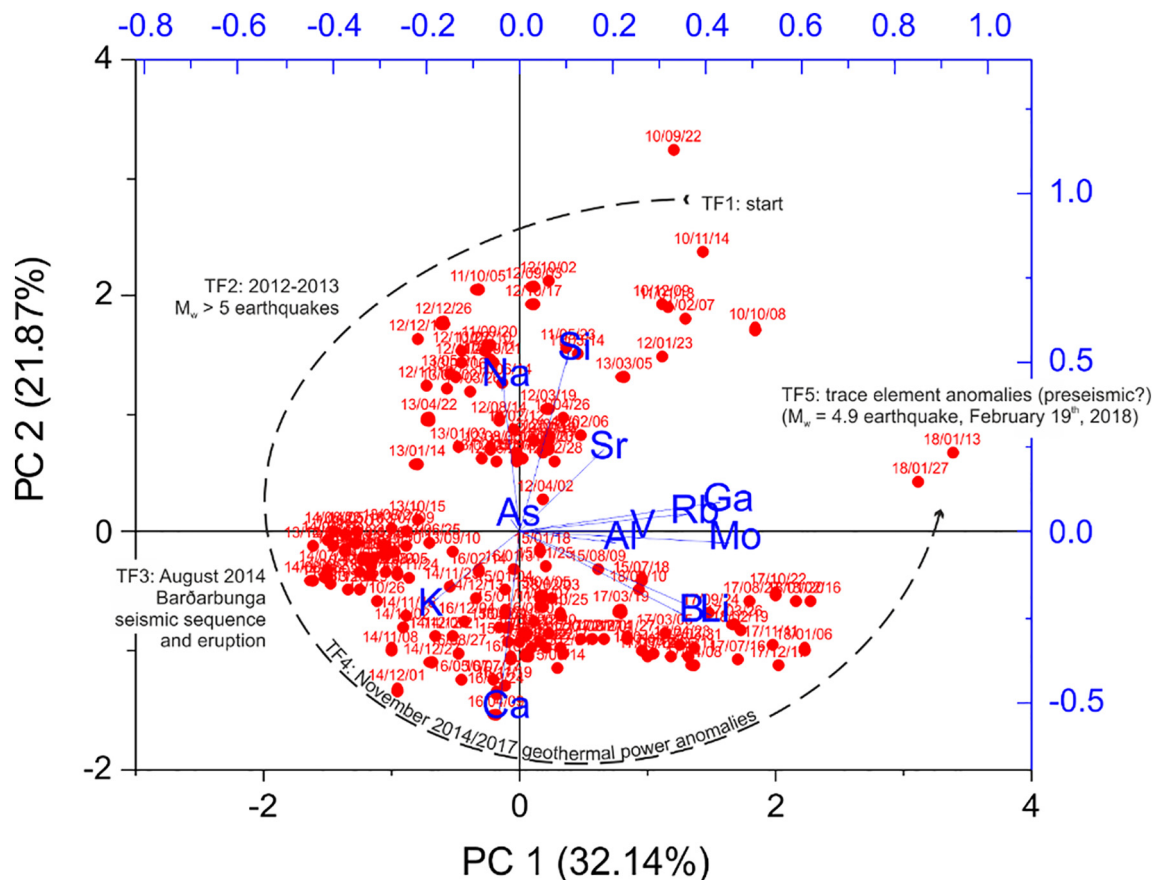
Fig. 6. Principal Component Analysis (PCA) plot. Both the loadings of the variables (eigenvectors, in blue) and the scores assigned to the sampling points (red dots with sampling date labels as YY/MM/DD) are shown, in relation to the first two component (PC1 and PC2). Preliminary data (e.g., correlation matrix) and full results of the PCA are in the Supplementary File 1. The dashed curve depicts an approximated temporal evolution path of the distribution of the sample scores, which seems marked by 5-time frames (TF#). A closer look to the diagram is reported in the Supplementary File 2, showing a magnification of time frames and labels of the sampling data. (For interpretation of the references to color in this figure legend, the reader is referred to the web version of this article.)
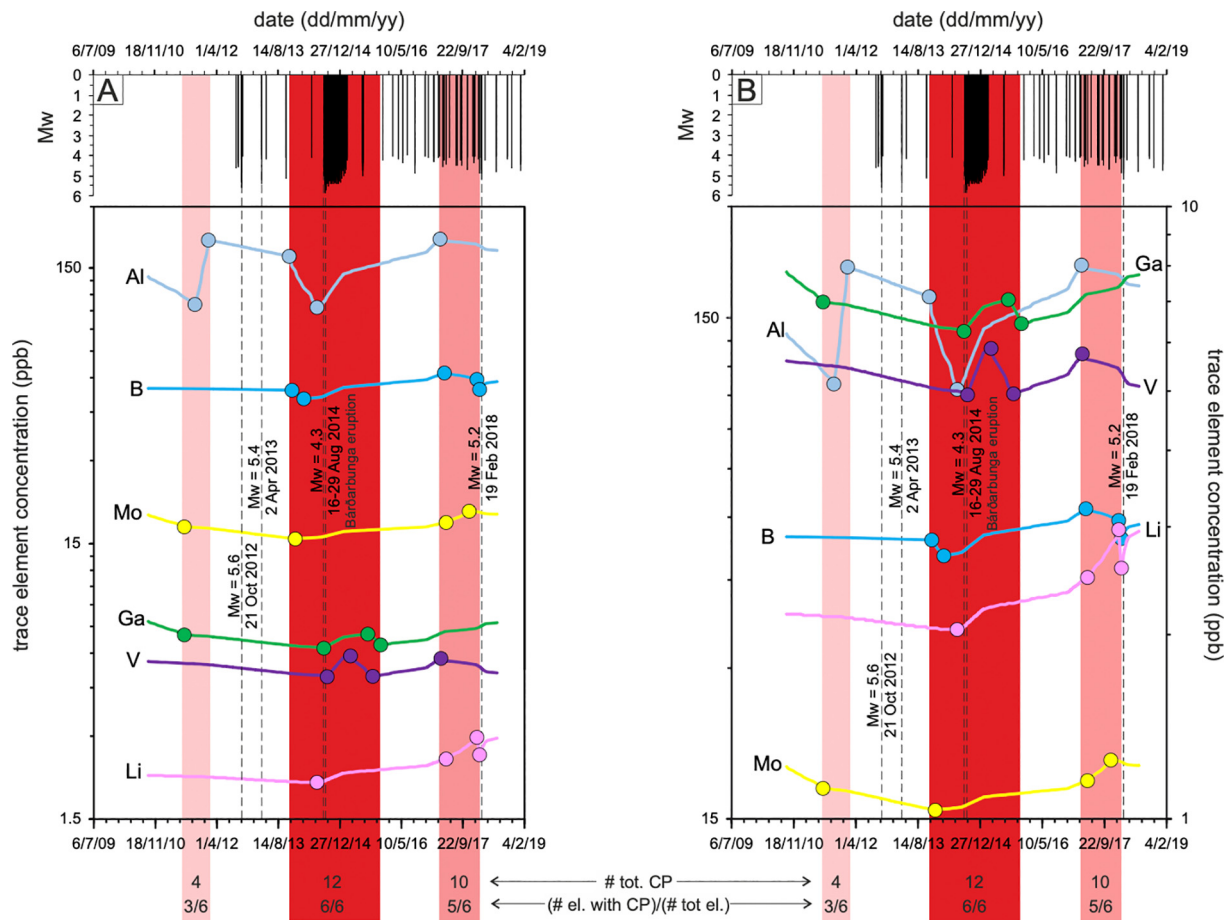
Fig. 7. Change Point (CP) diagram. Comparison between earthquake dates (top of the diagrams, vertical black bars and dashed lines; magnitude moment scale Mw) and the statistically significant change points (CPs) and trends analysed by the JRP code (colored circles and paths, respectively; Joinpoint Regression Program, 2020) related to the six elements clustered on PC1 (Al, B, Ga, Li, Mo and V). In (A), the ppb concentration scale of the elements is referred to the left $\log_{10}$ axis. In (B), to better show the slope of each element trend between the CPs, the elemental concentration within the first decade was splitted to the secondary axis on the right. Along the paths, elbows not marked by circles are statistically not-significant variations in the trends. In both diagrams, the vertical periods shaded in red highlight three different time frames having a different density of change points (bottom of the diagrams): the greater the number of change points (# tot CP) or the elements with CP to the total (# el. CP/6), the darker the red tone. (For interpretation of the references to color in this figure legend, the reader is referred to the web version of this article.)

elements (5–6), could be due to a more significant role of water–rock in-teraction, particularly in the different solubility and chemical composition between the glass and crystalline phase of the rock (Fig. 5) or because of the role of adsorption/desorption carried out by the secondary mineral phases in the aquifer fractures (clays, zeolites).

Finally, Mo and Ga have a CP on 10 July 2011, while Al shows two CPs, the first on 5 October 2011 and the second on 23 January 2012 (Fig. 7). As they are not confirmed by other highly mobile elements, such as B and Li, the supposed time frame has a low significance or low probability (4 CPs in 3/6 elements; Fig. 7). This was confirmed by PCA, which did not find any structure in the trace element data of that period (Fig. 6). From Octo-ber 2008 to September 2012, abrupt changes were detected in $\delta^{18}O$, ac-companied by steadily decreasing concentrations of the main constituents (Na, Si, Ca) (Skelton et al., 2014). These were connected to a progressive decrease in the proportion of groundwater affected by water–rock interaction (Skelton et al., 2014). Therefore, in the absence of a better explanation of their origin, these CPs could be classified as false positives or not directly related to seismic events.

4.7. Pre-eruptive and pre-seismic hydrogeochemical changes: a closer look at the results obtained by statistical analyses

The hydrogeochemical changes recorded before and immediately after the onset of the 2014 Bárðarbunga eruption are the most evident

over the recorded time series (Fig. 3); this is also demonstrated in the PCA and CP statistical analyses (Figs. 6 and 7, respectively). In particular, B and Al concentrations show significant decreases, and Mo has a flat-tening trend due to its stable concentration from eight months before the Bárðarbunga eruption (Fig. 7). Later, the same elements start to increase in concentration before the rifting event and the following volcanic eruption. Moreover, Li, V and Ga concentrations recorded a similar temporal pattern, with the inversion of concentrations occurring circa two months (Li) or one day (Ga) before the start of the rifting event and one month (V) after it (Fig. 7). We interpret these hydrogeo-chemical signals as connected with the large Bárðarbunga rifting event and eruption and, therefore, the changes in B, Al, Mo and Li, V, Ga con-centrations are considered as potential remote volcanic precursors.

As mentioned above, previous studies documented the hydrogeo-chemical sensitivity to earthquakes of the HA01 borehole groundwater, at least for some major constituents (mainly Na and Si) and stable iso-tope ratios of water molecules (Skelton et al., 2014, 2019). In this study, neither PCA nor CP analyses detected significant concentration anomalies or trend variations in trace elements before and after the 21 October 2012 M_w 5.6 seismic event.

In contrast, pre-seismic hydrogeochemical changes occurred before the M_w 5.2 earthquake on 19 February 2018. All the considered trace ele-ments (Li, B, Ga, Mo, Sr, Rb and Fe) significantly increased their ground-water concentrations from about seven weeks before the earthquake

(Fig. 3). A similar element clustering and increasing trend marked by significant CPs have been statistically demonstrated by PCA and CP analysis, respectively (Figs. 6 and 7). It is noteworthy that no major chemical elements or stable oxygen–hydrogen isotope ratios of water (i.e. $\delta^{18}O$ and δ^2H) significantly changed their groundwater concentration before this earthquake (Skelton et al., 2019). This evidence is a significant clue that trace elements may be hydrogeochemically sensitive to pre-seismic crustal deformation, particularly for intermediate magnitude earthquakes, such as the one occurred on 19 February 2018 in northern Iceland (M_w 5.2). Further evidence is necessary in the future to support or refute this idea because, in the case of the 2013 M_w 5.4 earthquake, pre-seismic hydrogeochemical anomalies in major element concentrations were recorded (Skelton et al., 2014; Andrén et al., 2016; Skelton et al., 2019), whereas any anomaly in the same samples regarding trace elements was found (Fig. 3). The deviation from the equilibrium between labradorite and analcime was invoked by Andrén et al. (2016) to explain Na and Si variations during the 2012–2013 seismic events. This process was triggered by a new input of Holocene groundwater (Skelton et al., 2014, 2019), which probably had lower trace element content than the two other members involved in the mix (pre-Holocene meteoric water and an ^{18}O-enriched component due to interaction with fresh basalt; Skelton et al., 2014). Therefore, the variations in the stable isotope ratios documented before the 2012 earthquake (Skelton et al., 2014) and the generalised and smoothed decrease in trace element concentration (Fig. 3), but marked by Al, Mo and Ga CPs during July 2011 (Fig. 7), are probably related to these hydrological/permeability changes. Indeed, it should be noted that the depleted ^{18}O-water component that was affected by water–rock interaction showed a significant input from April 2011 to May 2012 (Fig. 3b in Skelton et al., 2014). The geochemical relationship between Al and Ga, also highlighted by similar trends in Fig. 7, and the fact that Mo is not concentrated in a modern-day groundwater component has already been underlined.

On the contrary, significant pre-eruptive anomalies in the trace elements were recorded during 2014 (Figs. 6 and 7) without significant anomalies concerning major elements (Skelton et al., 2014, 2019). The complex role and sensitivity of potential hydrogeochemical precursors, the role of influencing factors, such as type, distance and magnitude of the causative geological events (e.g. earthquakes, volcanic eruptions) and the subsurface geological setting (site-specificity) indicate that we are only at the beginning of understanding this process.

Our interpretation of the recorded hydrogeochemical changes as potential seismic or volcanic precursors is questioned by the observation that, in 2016–2017, some hydrogeochemical variations occurred when no significant seismic and volcanic activities were recorded. In particular, two elemental triplets (Li, Ga, Mo and B, Al, V) exhibited a substantial increase in groundwater concentration during this time (Fig. 3). PCA demonstrated that the grouping of trace elements with K that occurred from late 2014 to late 2017/early 2018 could be related to the thermal phase that marked the transition between the post-eruptive phase of the Bárðarbunga and the seismic event that occurred during 2018 (Fig. 6). Furthermore, in the same periods, the concentration of some major chemical elements in the HA01 water showed anomalous changes (Skelton et al., 2019), possibly caused by the rupture of a hydrological barrier due to fluid overpressure and/or slow deformation.

4.8. Potential precursor interpretation

From the aforementioned results, we speculate that the following hydrogeochemical changes in trace element concentrations could contribute to the reliable forecasting of future geological events. In particular, we interpret that:

(1) the hydrogeochemical changes in B, Al, Mo and Li, V, Ga concentrations recorded before and immediately after the onset of the 2014 Bárðarbunga eruption are potential remote volcanic precursors and inceptive post-cursors of this event, respectively.

(2) the hydrogeochemical changes in Li, B, Ga, Mo, Sr, Rb and Fe concentrations that occurred before the 2018 M_w 5.2 earthquake are potential earthquake precursors, indicating that trace elements may be hydrogeochemically sensitive to pre-seismic crustal deformation, particularly for earthquakes of an intermediately strong magnitude.

Our interpretations have to be further confirmed and validated by future hydrogeochemical monitoring, which must always include the analyses of major elements and isotopes of groundwater to obtain a complete overview.

5. Conclusions

Long-term hydrogeochemical monitoring of trace elements is a promising method for identifying potential precursors to significant geological events, such as $M_w \geq 5$ earthquakes and remote volcanic eruptions. This method should be integrated by further hydrogeochemical monitoring, such as concentrations of major elements and isotopes in groundwater. The role of each element (major, trace and isotope) as a potential precursor can be different and should be clearly identified and understood as a function of many influencing factors, such as site-specificity (i.e. subsurface geology) and type, distance and magnitude of geological events (e.g. earthquakes or volcanic eruptions).

The obtained results confirm that B is highly mobile during water–rock interaction in a basaltic-hosted geothermal system. Therefore, this trace element shows a relevant volcanic hydro-sensitivity as it is a good indicator of rock leaching.

PCA can help identify the specific role of elements in different events, highlighting that approximately 115 events can be better explained by major constituents (e.g. 2012 and 2013 $M_w > 5$ earthquakes) and other trace elements (e.g. 2014 Bárðarbunga eruption; 2018 M_w 5.2 earthquake). CP detection of a specific cluster of elements identified by PCA helps to statistically validate the trend variability in the time series. The trace elements showed different behaviours between volcanic and tectonic earthquakes and between the $M_w > 5$ tectonic earthquakes occurring in 2012–2013 and 2018. In particular, the contributions of modern-day groundwater affected by water–rock interaction that occurred one year before the 2012 earthquake seem to be coeval with the CPs detected in the concentration trends of Al, Mo and Ga.

The combined use of PCA and CP helps to eliminate the human influence in evaluating chemical concentration changes in groundwater samples collected in a time series. In particular, in long-term borehole monitoring, such as for HA01, the data reduction capability of PCA was useful to understand what trace elements (components) and samples (loadings) deserved particular attention. After that, the time series analysis by CP detection on those specific trace elements was helpful to confirm whether the trends had significant changes during a seismic or volcanic event. Both statistical tools help to reduce background and other redundant data variability typical of trace elements monitoring.

Pre- and post-eruptive hydrogeochemical changes in the groundwater from the HA01 borehole, which is located farther than 140 km from the Bárðarbunga volcano, should not be surprising. All seismically active faults have envelopes of critically high-pressure pore fluids. Indeed, an increase in stress accumulation was detected at the HFF system before the Bárðarbunga volcanic seismic crisis (Hong et al., 2020). Consequently, although both stations monitoring shear-wave splitting and the HA01 borehole in northern Iceland are well over 100 km from Bárðarbunga, they seem to be sensitive to stress changes that when recording stress accumulation and chemical variations before the Bárðarbunga eruption.

Certainly, the diffusion of long-term hydrogeochemical monitoring sites and networks over seismic and volcanic territories will allow scientists to make significant progress in the science of geological risk precursors (Franchini et al., 2020).

Supplementary data to this article can be found online at https://doi.org/10.1016/j.scitotenv.2021.148635.

References

Aiuppa, A., Allard, P., D'Alessandro, W., Michel, A., Parello, F., Treuil, M., Valenza, M., 2000. Mobility and fluxes of major, minor and trace metals during basalt weathering and groundwater transport at Mt. Etna volcano (Sicily). Geochim. Cosmochim. Acta 64, 1827–1841. https://doi.org/10.1016/S0016-7037(00)00345-8.

Aiuppa, A., Moretti, R., Federico, C., Giudice, G., Gurrieri, S., Liuzzo, M., Papale, P., Shinohara, H., Valenza, M., 2007. Forecasting Etna eruptions by real-time observation of volcanic gas composition. Geology 35, 1115–1118. https://doi.org/10.1130/G24149A.1.

Andrén, M., Stockmann, G., Skelton, A., Sturkell, E., Mörth, C.M., Guðrúnardóttir, H.R., Keller, N.S., Odling, N., Dahrén, B., Broman, C., Balic-Zunic, T., Hjartarson, H., Siegmund, H., Freund, F., 2016. Coupling between mineral reactions, chemical changes in groundwater, and earthquakes in Iceland. J. Geophys. Res. Solid Earth 121, 2315–2337. https://doi.org/10.1002/2015JB012614.

Armienta, M.A., De la Cruz-Reyna, S., 1995. Some hydro-geochemical fluctuations observed in Mexico related to volcanic activity. Appl. Geochem. 10 (2), 215–227. https://doi.org/10.1016/0883-2927(94)00044-7.

Armienta, M.A., De la Cruz-Reyna, S., Gómez, A., Ramos, E., Ceniceros, N., Cruz, O., Aguayo, A., Martínez, J., 2008. Hydrogeochemical indicators of the Popocatépetl volcano activity. J. Volcanol. Geotherm. Res. 170, 35–50. https://doi.org/10.1016/j.jvolgeores.2007.09.006.

Árnadottir, T., Geirsson, H., Jiang, W., 2008. Crustal deformation in Iceland: plate spreading and earthquake deformation. Jökull. 58, 59–74.

Árnason, K., 2020. New conceptual model for the magma-hydrothermal-tectonic system of Krafla, NE Iceland. Geosciences 10 (1), 34. https://doi.org/10.3390/geosciences10010034.

Arnórsson, S., 1969. A Geochemical Study of Selected Elements in Thermal Waters of Iceland. Ph.D. Thesis. Faculty of Science of the University of London, Royal School of Mines, Imperial College.

Arnórsson, S., Andrésdóttir, A., 1995. Processes controlling the distribution of boron and chlorine in natural waters in Iceland. Geochim. Cosmochim. Acta 59, 4125–4146. https://doi.org/10.1016/0016-7037(95)00278-8.

Arnórsson, S., Óskarsson, N., 2007. Molybdenum and tungsten in volcanic rocks and in surface and < 100 C ground waters in Iceland. Geochim. Cosmochim. Acta 71, 284–304. https://doi.org/10.1016/j.gca.2006.09.030.

Awaleh, M.O., Boschetti, T., Adaneh, A.E., Daoud, M.A., Ahmed, M.M., Dabar, O.A., Soubaneh, Y.D., Kawalieh, K.D., Kadieh, I.H., 2020. Hydrochemistry and multi-isotope study of the waters from Hanlé-Gaggadé grabens (Republic of Djibouti, East African Rift System): a low-enthalpy geothermal resource from a transboundary aquifer. Geothermics 86, 101805. https://doi.org/10.1016/j.geothermics.2020.101805.

Barberio, M.D., Barbieri, M., Billi, A., Doglioni, C., Petitta, M., 2017. Hydrogeochemical changes before and during the 2016 Amatrice-Norcia seismic sequence (central Italy). Sci. Rep. 7, 11735. https://doi.org/10.1038/s41598-017-11990-8.

Barberio, M.D., Gori, F., Barbieri, M., Billi, A., Caracausi, A., De Luca, G., Franchini, S., Petitta, M., Doglioni, C., 2020. New observations in Central Italy of groundwater responses to the worldwide seismicity. Sci. Rep. 10, 17850. https://doi.org/10.1038/s41598-020-74991-0.

Barbieri, M., 2019. Isotopes in hydrology and hydrogeology. Water (Switzerland) 11 (2), 291. https://doi.org/10.3390/w11020291.

Barbieri, M., Boschetti, T., Barberio, M.D., Billi, A., Franchini, S., Iacumin, P., Selmo, E., Petitta, M., 2020. Tracing deep fluid source contribution to groundwater in an active seismic area (central Italy): a combined geothermometric and isotopic (δ13C) perspective. J. Hydrol. 582, 124495. https://doi.org/10.1016/j.jhydrol.2019.124495.

Berger, G., Schott, J., Guy, C., 1988. Behavior of Li, Rb and Cs during basalt glass and olivine dissolution and chlorite, smectite and zeolite precipitation from seawater: experimental investigations and modelization between 50 and 300 C. Chem. Geol. 71, 297–312. https://doi.org/10.1016/0009-2541(88)90056-3.

Blomgren, V.J., Crossey, L.J., Karlstrom, K.E., Fischer, T.P., Darrah, T.H., 2019. Hot spring hydrochemistry of the Rio Grande rift in northern New Mexico reveals a distal geochemical connection between Valles Caldera and Ojo Caliente. J. Volcanol. Geotherm. Res. 387, 106663. https://doi.org/10.1016/j.jvolgeores.2019.106663.

Boschetti, T., Cortecci, G., Bolognesi, L., 2003. Chemical and isotopic compositions of the shallow groundwater system of Vulcano Island, Aeolian Archipelago, Italy: an update. GeoActa 2, 1–34.

Boschetti, T., Barbieri, M., Barberio, M.D., Billi, A., Franchini, S., Petitta, M., 2019. CO2 Inflow and elements desorption prior to a seismic sequence, Amatrice-Norcia 2016, Italy. Geochem. Geophys. Geosyst. 20 (5), 2303–2317. https://doi.org/10.1029/2018GC008117.

Bryant, F.D., Yarnold, P.R., 1995. Principal components analysis and exploratory and confirmatory factor analysis. In: Grimm, L.G., Yarnold, P.R. (Eds.), Reading and Understanding Multivariate Analysis. American Psychological Association Books.

Buttitta, D., Caracausi, A., Chiaraluce, L., Favara, R., Morticelli, M.G., Sulli, A., 2020. Continental degassing of helium in an active tectonic setting (northern Italy): the role of seismicity. Sci. Rep. 10, 1–13. https://doi.org/10.1038/s41598-019-55678-7.

Caracausi, A., Italiano, F., Paonita, A., Rizzo, A., Nuccio, P.M., 2003. Evidence of deep magma degassing and ascent by geochemistry of peripheral gas emissions at Mount Etna (Italy): assessment of the magmatic reservoir pressure. J. Geophys. Res. Solid Earth 108 (B10). https://doi.org/10.1029/2002JB002095.

Chaudhuri, H., Barman, C., Iyengar, A.S., Ghose, D., Sen, P., Sinha, B., 2013. Network of seismo-geochemical monitoring observatories for earthquake prediction research in India. Acta Geophys. 61, 1000–1025. https://doi.org/10.2478/s11600-013-0134-0.

Chen, C.H., Wang, C.H., Wen, S., Yeh, T.K., Lin, C.H., Liu, J.Y., Yen, H.Y., Lin, C, Rau, R.J., Lin, T.W., 2013. Anomalous frequency characteristics of groundwater level before major earthquakes in Taiwan. Hydrol. Earth Syst. Sci. 1, 1693. https://doi.org/10.5194/hess-17-1693-2013 2013.

Chen, C.H., Tang, C.C., Cheng, K.C., Wang, C.H., Wen, S., Lin, C.H., Wen, Y.Y., Meng, G., Yeh, T.K., Jan, J.C., Yen, H.Y., Liu, J.Y., 2015. Groundwater–strain coupling before the 1999 Mw 7.6 Taiwan Chi-Chi earthquake. J. Hydrol. 524, 378–384. https://doi.org/10.1016/j.jhydrol.2015.03.006.

Chiarabba, C., De Gori, P., Segou, M., Cattaneo, M., 2020. Seismic velocity precursors to the 2016 Mw 6.5 Norcia (Italy) earthquake. Geology. 48 (9), 924–928. https://doi.org/10.1130/G47048.1.

Chiodini, G., Cardellini, C., Di Luccio, F., Selva, J., Frondini, F., Caliro, S., Rosiello, A., Beddini, G., Ventura, G., 2020. Correlation between tectonic CO2 Earth degassing and seismicity is revealed by a 10-year record in the Apennines, Italy. Sci. Adv. 6. https://doi.org/10.1126/sciadv.abc2938 eabc2938.

Claesson, L., Skelton, A., Graham, C., Dietl, C., Mörth, M., Torssander, P., Kockum, I., 2004. Hydrogeochemical changes before and after a major earthquake. Geology 32, 641–644. https://doi.org/10.1130/G20542.1.

Claesson, L., Skelton, A., Graham, C., Mörth, C.M., 2007. The timescale and mechanisms of fault sealing and water-rock interaction after an earthquake. Geofluids 7 (4), 427–440. https://doi.org/10.1111/j.1468-8123.2007.00197.x.

Coppola, M., Correale, A., Barberio, M.D., Billi, A., Cavallo, A., Fondriest, M., Nazzari, M., Paonita, A., Romano, C., Stagno, V., Viti, C., Vona, A., 2021. Meso-to nano-scale evidence of fluid-assisted co-seismic slip along the normal Mt. Morrone Fault, Italy: implications for earthquake hydrogeochemical precursors. Earth Planet. Sci. Lett. https://doi.org/10.1016/j.epsl.2021.117010 in press.

Cucci, L, 2019. Insights into the geometry and faulting style of the causative faults of the M 6.7 1805 and M 6.7 1930 earthquakes in the Southern Apennines (Italy) from coseismic hydrological changes. Tectonophysics 751, 192–211. https://doi.org/10.1016/j.tecto.2018.12.021.

De Argollo, R.M., Schilling, J.G., 1978. Ge/Si and Ga/Al variations along the Reykjanes ridge and Iceland. Nature 276, 24–28. https://doi.org/10.1038/276024a0.

De Luca, G., Di Carlo, G., Tallini, M., 2018. A record of changes in the Gran Sasso groundwater before, during and after the 2016 Amatrice earthquake, central Italy. Sci. Rep. 8, 15982. https://doi.org/10.1038/s41598-018-34444-1.

De Moor, J.M., Aiuppa, A., Pacheco, J., Avard, G., Kern, C., Liuzzo, M., ... Fischer, T.P., 2016. Short-period volcanic gas precursors to phreatic eruptions: insights from Poás Volcano, Costa Rica. Earth Planet. Sci. Lett. 442, 218–227. https://doi.org/10.1016/j.epsl.2016.02.056.

Einarsson, P., 1991. Earthquakes and present-day tectonism in Iceland. Tectonophysics 189 (1-4), 261–279. https://doi.org/10.1016/0040-1951(91)90501-I.

Einarsson, P., Björnsson, S., 1979. Earthquakes in Iceland. Jökull 29, 37–43.

Einarsson, P., Theodórsson, P., Hjartardóttir, Á.R., Guðjónsson, G.I., 2008. Radon changes associated with the earthquake sequence in June 2000 in the South Iceland seismic zone. Terrestrial Fluids, Earthquakes and Volcanoes: The Hiroshi Wakita Volume III. Birkhäuser, Basel, pp. 63–74 https://doi.org/10.1007/978-3-7643-8738-9_5.

Elmi, S.A., 2009. Gallium and germanium distribution in geothermal water. Geothermal Training Programme, Reports. 2009, pp. 1–13.

Filzmoser, P., Todorov, V., 2013. Robust tools for the imperfect world. Inf. Sci. 245, 4–20. https://doi.org/10.1016/j.ins.2012.10.017.

Fournier, R.O., 1989. Lectures on Geochemical Interpretation of Hydrothermal Waters. UNU Geothermal Training Programme, Report 10. Reykjavik, Iceland, p. 73.

Fournier, R.O., Potter II, R.W., 1979. Magnesium correction to the Na-K-Ca chemical geothermometer. Geochim. Cosmochim. Acta 43, 1543–1550. https://doi.org/10.1016/0016-7037(79)90147-9.

Fournier, R.O., Truesdell, A.H., 1973. An empirical Na-K-Ca geothermometer for natural waters. Geochim. Cosmochim. Acta 37 (5), 1255–1275. https://doi.org/10.1016/0016-7037(73)90060-4.

Franchini, S., Agostini, S., Barberio, M.D., Barbieri, M., Billi, A., Boschetti, T., Pennisi, M., Petitta, M., 2020. HydroQuakes, central Apennines, Italy: towards a hydrogeochemical monitoring network for seismic precursors and the hydro-seismo-sensitivity of boron. J. Hydrol. 125754. https://doi.org/10.1016/j.jhydrol.2020.125754.

Gale, A., Dalton, C.A., Langmuir, C.H., Su, Y., Schilling, J.G., 2013. The mean composition of ocean ridge basalts. Geochem. Geophys. Geosyst. 14, 489–518. https://doi.org/10.1029/2012GC004334.

Galeczka, I., Eiriksdottir, E.S., Pálsson, F., Oelkers, E., Lutz, S., Benning, L.G., ... Ólafsdóttir, R., 2017. Pollution from the 2014–15 Bárðarbunga eruption monitored by snow cores from the Vatnajökull glacier, Iceland. J. Volcanol. Geotherm. Res. 347, 371–396. https://doi.org/10.1016/j.jvolgeores.2017.10.006.

Galeczka, I., Sigurdsson, G., Eiriksdottir, E.S., Oelkers, E.H., Gislason, S.R., 2016. The chemical composition of rivers and snow affected by the 2014/2015 Bárðarbunga eruption, Iceland. J. Volcanol. Geotherm. Res. 316, 101–119. https://doi.org/10.1016/j.jvolgeores.2016.02.017.

Garson, G.D., 2018. Factor Analysis. Statistical Associates, Blue Book Series 146 pp.

Giggenbach, W.F., 1991. Chemical techniques in geothermal exploration. In: D'Amore, F. (Ed.), Applications of Geochemistry in Geothermal Reservoir Development. UNITAR/UNDP publication, Rome, pp. 119–142.

Gislason, S.R., Arnorsson, S., Armannsson, H., 1996. Chemical weathering of basalt in Southwest Iceland; effects of runoff, age of rocks and vegetative/glacial cover. Am. J. Sci. 296, 837–907.

Gudmundsson, A., 2007. Infrastructure and evolution of ocean-ridge discontinuities in Iceland. J. Geodyn. 43, 6–29. https://doi.org/10.1016/j.jog.2006.09.002.

Gudmundsson, A., Brynjolfsson, S., Jonsson, M.T., 1993. Structural analysis of a transform fault-rift zone junction in North Iceland. Tectonophysics 220, 205–221. https://doi.org/10.1016/0040-1951(93)90232-9.

Gudmundsson, M.T., Jónsdóttir, K., Hooper, A., Holohan, E.P., Halldórsson, S.A., Ófeigsson, B.G., Cesca, S., Vogfjörd, K.S., Sigmundsson, F., Högnadóttir, T., Einarsson, P., Sigmarsson, O., Jarosch, A.H., Jónasson, K., Magnússon, E., Hreinsdóttir, S., Bagnardi, M., Parks, M.M., Hjörleifsdóttir, V., Pálsson, F., Walter, T.R., Schöpfer, M.P.J., Heimann, S., Reynolds, H.I., Dumont, S., Bali, E., Gudfinnsson, G.H., Dahm, T., Roberts, M.J., Hensch, M., Belart, J.M.C., Spaans, K., Jakobsson, S., Gudmundsson, G.B., Fridriksdóttir, H.M., Drouin, V., Dürig, T., Aðalgeirsdóttir, G., Riishuus, M.S., Pedersen, G.B.M., van Boeckel, T., Oddsson, B., Pfeffer, M.A., Barsotti, S., Bergsson, B., Donovan, A., Burton, M.R., Aiuppa, A., 2016. Gradual caldera collapse at Bárdarbunga volcano, Iceland, regulated by lateral magma outflow. Science 353. https://doi.org/10.1126/science.aaf8988.

Hatcher, L., O'Rourke, N., 2013. A Step-by-step Approach to Using the SAS® System for Factor Analysis and Structural Equation Modeling - Second Edition. SAS Institute Inc., Cary, North Carolina, USA.

He, A., Singh, R.P., 2019. Coseismic groundwater temperature response associated with the Wenchuan earthquake. Pure Appl. Geophys. 177 (1), 109–120. https://doi.org/10.1007/s00024-019-02097-4.

Hong, Q., Crampin, S., Gao, Y., 2020. Changes in shear-wave splitting at the 2014 Bárðarbunga seismic crisis and dyke intrusion in Iceland compared with earthquakes and other eruptions. Phys. Earth Planet. Inter. 300, 106446. https://doi.org/10.1016/j.pepi.2020.106446.

Hosono, T., Masaki, Y., 2020. Post-seismic hydrochemical changes in regional groundwater flow systems in response to the 2016 Mw 7.0 Kumamoto earthquake. J. Hydrol. 580, 124340. https://doi.org/10.1016/j.jhydrol.2019.124340.

Hosono, T., Yamada, C., Manga, M., Wang, C.Y., Tanimizu, M., 2020. Stable isotopes show that earthquakes enhance permeability and release water from mountains. Nat. Commun. 11, 1–9. https://doi.org/10.1038/s41467-020-16604-y.

Hubert, M., Reynkens, T., Schmitt, E., Verdonck, T., 2016. Sparse PCA for high-dimensional data with outliers. Technometrics 58 (4), 424–434. https://doi.org/10.1080/00401706.2015.1093962.

Hutcheson, G., Sofroniou, N., 1999. The Multivariate Social Scientist: Introductory Statistics Using Generalized Linear Models. Sage Publications, Thousand Oaks, CA.

IBM, 2019. IBM SPSS Statistics Base 26. Copyright IBM Corp. 1989. 2019. https://www.ibm.com/support/pages/ibm-spss-statistics-26-documentation.

Igarashi, G., Saeki, S., Takahata, N., Sumikawa, K., Tasaka, S., Sasaki, Y., Takahashi, M., Sano, Y., 1995. Ground-water radon anomaly before the Kobe earthquake in Japan. Science 269, 60–61. https://doi.org/10.1126/science.269.5220.60.

Ilgen, A.G., Kukkadapu, R.K., Leung, K., Washington, R.E., 2019. "Switching on" iron in clay minerals. Environ. Sci. Nano 6, 1704–1715. https://doi.org/10.1039/C9EN00228F.

IMO, 2016. Icelandic Meteorological Office. www.vedur.is. (Accessed 22 December 2020).

Ingebritsen, S.E., Manga, M., 2014. Earthquakes: hydrochemical precursors. Nat. Geosci. 7, 697–698. https://doi.org/10.1038/ngeo2261.

Jóhannesson, H., 2014. Geological Map of Iceland 1:600 000. Bedrock Geology. 2nd edition. Icelandic Institute of Natural History, Reykjavik.

Joinpoint Regression Program, 2020. Version 4.8.0.1 - April 2020; Statistical Methodology and Applications Branch, Surveillance Research Program. National Cancer Institute https://surveillance.cancer.gov/joinpoint/Joinpoint_Help_4.8.0.1.pdf. (Accessed 22 December 2020).

Jónsson, S., Matrau, R., Viltres, R., Ófeigsson, B., 2019. An update of GPS measurements in north Iceland. In: Jónsson, S., et al. (Eds.), Proceedings to the Northquake 2019 Workshop. Húsavík Academic Centre , pp. 107–110. https://hac.is/wp-content/uploads/Northquake2019.pdf.

Jung, H.W., Yun, S.T., Kim, K.H., Oh, S.S., Kang, K.G., 2014. Role of an impermeable layer in controlling groundwater chemistry in a basaltic aquifer beneath an agricultural field, Jeju Island, South Korea. Appl. Geochem. 45, 82–93. https://doi.org/10.1016/j.apgeochem.2014.03.008.

Kaasalainen, H., Stefánsson, A., 2012. The chemistry of trace elements in surface geothermal waters and steam, Iceland. Chem. Geol. 330, 60–85. https://doi.org/10.1016/j.chemgeo.2012.08.019.

Kaasalainen, H., Stefánsson, A., Giroud, N., Arnórsson, S., 2015. The geochemistry of trace elements in geothermal fluids, Iceland. Appl. Geochem. 62, 207–223. https://doi.org/10.1016/j.apgeochem.2015.02.003.

Kawabata, K., Sato, T., Takahashi, H.A., Tsunomori, F., Hosono, T., Takahashi, M., Kitamura, Y., 2020. Changes in groundwater radon concentrations caused by the 2016 Kumamoto earthquake. J. Hydrol. 584, 124712. https://doi.org/10.1016/j.jhydrol.2020.124712.

Kim, H.J., Feuer, E.J., Midhune, D.N., 2000. Permutation tests for joinpoint regression with applications to cancer rates. Stat. Med. 19, 335–351. https://doi.org/10.1002/(SICI)1097-0258(20000215)19:3<335::AID-SIM336>3.0.CO;2-Z.

Kim, J., Kim, H.J., 2016. Consistent model selection in segmented line regression. J. Statist. Plann. Inference 170, 106–116.

Kim, J., Lee, J., Petitta, M., Kim, H., Kaown, D., Park, I.W., ... Lee, K.K., 2019. Groundwater system responses to the 2016 ML 5.8 Gyeongju earthquake, South Korea. J. Hydrol. 576, 150–163. https://doi.org/10.1016/j.jhydrol.2019.06.044.

King, C.Y., Zhang, W., Zhang, Z., 2006. Earthquake-induced groundwater and gas changes. Pure Appl. Geophys. 163, 633–645. https://doi.org/10.1007/s00024-006-0049-7.

Koh, D.C., Chae, G.T., Ryu, J.S., Lee, S.G., Ko, K.S., 2016. Occurrence and mobility of major and trace elements in groundwater from pristine volcanic aquifers in Jeju Island, Korea. Appl. Geochem. 65, 87–102. https://doi.org/10.1016/j.apgeochem.2015.11.004.

Kokfelt, T.F., Hoernle, K.A.J., Hauff, F., Fiebig, J., Werner, R., Garbe-Schönberg, D., 2006. Combined trace element and Pb-Nd–Sr-O isotope evidence for recycled oceanic crust (upper and lower) in the Iceland mantle plume. J. Petrol. 47, 1705–1749. https://doi.org/10.1093/petrology/egl025.

Kristmannsdóttir, H., 2008. Jarðhitaauðlindir: Tækifæri til atvinnuköpunar og byggðaeflingar á Norðausturlandi með heilsutengdri ferðaþjónustu. https://www.ferdamalastofa.is/static/files/upload/files/200892516292jardhitaaudlindir_hrefna.pdf.

Kristmannsdóttir, H., 2011. Grunnvatnsrannsóknir í Norðurþingi 2010. Report LV-2011/074, Landsvirkjun. http://gogn.lv.is/files/2011/2011-074.pdf.

Kristmannsdóttir, H., Klemensson, V., 2007. Grunnvatnsrannsóknir á Norðausturlandi - Skilgreining á grunnástandi og tillögur um framtíðareftirlit með hugsanlegum breytingum á grunnvatnsstraumn í kjölfar vinnslu á háhitasvæðum. Report LV-2007/086, Landsvirkjun. https://www.landsvirkjun.is/Media/Grunnvatnsrannsoknir_a_Nordausturlandi_2007.pdf.

Kristmannsdóttir, H., Guðrúnardóttir, H.R., Akureyri, H., 2009. Grunnvatnsrannsóknir í Norðurþingi 2008. Report LV-2009/147, Landsvirkjun. https://www.landsvirkjun.is/Media/Grunnvatnsrannsoknir_i_Nordurthingi_2008.pdf.

Kristmannsdóttir, H., Arnórsson, S., Sveinbjörnsdóttir, A.E., Ármannsson, H., 2010. Chemical variety of water in Icelandic heating systems. Proceedings of the World Geothermal Congress 2010. 1477, pp. 1–9.

Li, S., Sigmundsson, F., Drouin, V., Parks, M.M., Ofeigsson, B.G., Jónsdóttir, K., ... Hreinsdóttir, S., 2021. Ground deformation after a caldera collapse: contributions of magma inflow and viscoelastic response to the 2015–2018 deformation field around Bárðarbunga, Iceland. J. Geophys. Res. Solid Earth 126 (3). https://doi.org/10.1029/2020JB020157.

Ma, L., Qian, J., Zhao, W., Curtis, Z., Zhang, R., 2016. Hydrogeochemical analysis of multiple aquifers in a coal mine based on nonlinear PCA and GIS. Environ. Earth Sci. 75, 716. https://doi.org/10.1007/s12665-016-5532-6.

Manga, M., Wang, C.Y., 2015. 4.12. Earthquake hydrology. Treatise on Geophysics. 328, p. 305. https://doi.org/10.1016/B978-0-444-53802-4.00082-8.

Manga, M., Brodsky, E.E., Boone, M., 2003. Response of streamflow to multiple earthquakes. Geophys. Res. Lett. 30 (5). https://doi.org/10.1029/2002GL016618.

Marcovecchio, J.E., Botté, S.E., Domini, C.E., Freije, R.H., 2014. Heavy metals, major metals, trace elements. In: Nollet, L.M.L., De Gelder, L.S.P. (Eds.), Handbook of Water Analysis, Chapter 15. Taylor & Francis Group, Boca Raton, Florida, pp. 385–434 https://doi.org/10.1201/b15314-19.

Marini, L., 2013. Reaction path modeling: theoretical aspects and applications. In: Censi, P., Darrah, T.H., Yigal, Erel Y. (Eds.), Medical Geochemistry - Geological Materials and Health, Chapter 4. Springer, Dordrecht, pp. 47–66 https://doi.org/10.1007/978-94-007-4372-4_4.

Martinelli, G., Facca, G., Genzano, N., Gherardi, F., Lisi, M., Pierotti, L., Tramutoli, V., 2020. Earthquake-related signals in central Italy detected by hydrogeochemical and satellite techniques. Front. Earth Sci. 8, 584716. https://doi.org/10.3389/feart.2020.584716.

Marzocchi, W., Bebbington, M.S., 2012. Probabilistic eruption forecasting at short and long time scales. Bull. Volcanol. 74, 1777–1805. https://doi.org/10.1007/s00445-012-0633-x.

McNutt, S.R., Roman, D.C., 2015. Volcanic seismicity. The Encyclopedia of Volcanoes. Academic Press, pp. 1011–1034 https://doi.org/10.1016/B978-0-12-385938-9.00059-6.

Montgomery, D.R., Manga, M., 2003. Streamflow and water well responses to earthquakes. Science 300, 2047–2049. https://doi.org/10.1126/science.1082980.

Nakagawa, K., Yu, Z.Q., Berndtsson, R., Hosono, T., 2020. Temporal characteristics of groundwater chemistry affected by the 2016 Kumamoto earthquake using self-organizing maps. J. Hydrol. 582, 124519. https://doi.org/10.1016/j.jhydrol.2019.124519.

Nicholson, K., 1993. Geothermal Fluids: Chemistry and Exploration Techniques. Springer Science & Business Media.

Nigro, A., Sappa, G., Barbieri, M., 2017. Application of boron and tritium isotopes for tracing landfill contamination in groundwater. J. Geochem. Explor. 172, 101–108. https://doi.org/10.1016/j.gexplo.2016.10.011.

Oelkers, E.H., Bénézeth, P., Pokrovski, G.S., 2009. Thermodynamic databases for water-rock interaction. Rev. Mineral. Geochem. 70, 1–46. https://doi.org/10.2138/rmg.2009.70.1.

Onda, S., Sano, Y., Takahata, N., Kagoshima, T., Miyajima, T., Shibata, T., Pinti, D.L., Lan, T., Kim, N.K., Kusakabe, M., Nishio, Y., 2018. Groundwater oxygen isotope anomaly before the M6. 6 Tottori earthquake in Southwest Japan. Sci. Rep., 1–7 https://doi.org/10.1038/s41598-018-23303-8.

OriginLab, 2019. Principal Component Analysis. Origin Help, Section 17.7.1. https://www.originlab.com/doc/Origin-Help/PrincipleComp-Analysis. (Accessed 20 July 2020).

Patanè, D., De Gori, P., Chiarabba, C., Bonaccorso, A., 2003. Magma ascent and the pressurization of Mount Etna's volcanic system. Science 299, 2061–2063. https://doi.org/10.1126/science.1080653.

Petitta, M., Mastrorillo, L., Preziosi, E., Banzato, F., Barberio, M.D., Billi, A., Cambi, C., De Luca, G., Di Carlo, G., Di Curzio, D., Di Salvo, C., Nanni, T., Palpacelli, S., Rusi, S., Saroli, M., Tallini, M., Tazioli, A., Valigi, D., Vivalda, P., Doglioni, C., 2018. Water-table and discharge changes associated with the 2016–2017 seismic sequence in central Italy: hydrogeological data and a conceptual model for fractured carbonate aquifers. Hydrogeol. J. 26, 1009–1026. https://doi.org/10.1007/s10040-017-1717-7.

Reimann, C., De Caritat, P., 1998. Chemical Elements in the Environment: Factsheets for the Geochemist and Environmental Scientist. Springer Science & Business Media.

Reynolds, H.I., Gudmundsson, M.T., Högnadóttir, T., Axelsson, G., 2019. Changes in geothermal activity at Bárdarbunga, Iceland, following the 2014–2015 caldera collapse, investigated using geothermal system modeling. J. Geophys. Res. Solid Earth 124, 8187–8204. https://doi.org/10.1029/2018JB017290.

Ricolfi, L., Barbieri, M., Muteto, P.V., Nigro, A., Sappa, G., Vitale, S., 2020. Potential toxic elements in groundwater and their health risk assessment in drinking water of Limpopo National Park, Gaza Province, Southern Mozambique. Environ. Geochem. Health, 1–13 https://doi.org/10.1007/s10653-019-00507-z.

Rögnvaldsson, S.T., Gudmundsson, A., Slunga, R., 1998. Seismotectonic analysis of the Tjörnes Fracture Zone, an active transform fault in north Iceland. J. Geophys. Res. Solid Earth 103, 30117–30129. https://doi.org/10.1029/98JB02789.

Ruch, J., Wang, T., Xu, W., Hench, M., Jónsson, S., 2016. Oblique rift opening revealed by recurring magma injection in central Iceland. Nat. Commun. 7, 12352. https://doi.org/10.1038/ncomms12352.

Sano, Y., Takahata, N., Kagoshima, T., Shibata, T., Onoue, T., Zhao, D., 2016. Groundwater helium anomaly reflects strain change during the 2016 Kumamoto earthquake in Southwest Japan. Sci. Rep. 6, 37939. https://doi.org/10.1038/srep37939.

Sano, Y., Onda, S., Kagoshima, T., Miyajima, T., Takahata, N., Shibata, T., Nakagawa, C., Onoue, T., Kim, N.K., Lee, H., Kusakabe, M., Pinti, D.L., 2020. Groundwater oxygen anomaly related to the 2016 Kumamoto earthquake in Southwest Japan. Proc. Jpn. Acad. Ser. B 96, 322–334. https://doi.org/10.2183/pjab.96.024.

Sato, T., Takahashi, H.A., Kawabata, K., Takahashi, M., Inamura, A., Handa, H., 2020. Changes in the nitrate concentration of spring water after the 2016 Kumamoto earthquake. J. Hydrol. 580, 124310. https://doi.org/10.1016/j.jhydrol.2019.124310.

Schoeller, H., 1962. Les Eaux souterraines: hydrologie, dynamique et chimique, recherche, exploitation et évaluation des ressources. 642. Masson et Cie, Paris.

Scholz, C.H., Sykes, L.R., Aggarwal, Y.P., 1973. Earthquake prediction: a physical basis. Science 181, 803–810.

Seyfried Jr., W.E., Bischoff, J.L., 1979. Low temperature basalt alteration by sea water: an experimental study at 70 C and 150 C. Geochim. Cosmochim. Acta 43, 1937–1947. https://doi.org/10.1016/0016-7037(79)90006-1.

Seyfried Jr., W.E., 1987. Experimental and theoretical constraints on hydrothermal alteration processes at mid-ocean ridges. Annu. Rev. Earth Planet. Sci. 15, 317–335. https://doi.org/10.1146/annurev.ea.15.050187.001533.

Shi, Z., Wang, G., 2014. Hydrological response to multiple large distant earthquakes in the Mile well, China. J. Geophys. Res. Earth Surf. 119, 2448–2459. https://doi.org/10.1002/2014JF003184.

Shi, Z., Zhang, H., Wang, G., 2020. Groundwater trace elements change induced by M5. 0 earthquake in Yunnan. J. Hydrol. 581, 124424. https://doi.org/10.1016/j.jhydrol.2019.124424.

Shorttle, O., Maclennan, J., Piotrowski, A.M., 2013. Geochemical provincialism in the Iceland plume. Geochim. Cosmochim. Acta 122, 363–397. https://doi.org/10.1016/j.gca.2013.08.032.

Sigmundsson, F., Hooper, A., Hreinsdóttir, S., Vogfjörd, K.S., Ófeigsson, B.G., Heimisson, E.R., Dumont, S., Parks, M., Spaans, K., Gudmundsson, G.B., Drouin, V., Árnadóttir, T., Jónsdóttir, K., Gudmundsson, M.T., Högnadóttir, T., Fridriksdóttir, H.M., Hensch, M., Einarsson, P., Magnússon, E., Samsonov, S., Brandsdóttir, B., White, R.S., Ágústsdóttir, T., Greenfield, T., Green, R.G., Hjartardóttir, Á.R., Pedersen, R., Bennett, R.A., Geirsson, H., La Femina, P.C., Björnsson, H., Pálsson, F., Sturkell, E., Bean, C.J., Möllhoff, M., Braiden, A.K., Eibl, E.P.S., 2015. Segmented lateral dyke growth in a rifting event at Bárðarbunga volcanic system, Iceland. Nature 517, 191–195. https://doi.org/10.1038/nature14111.

Skalska, H., 2017. Software for Changepoints Detection. Mathematical Methods in Economics 2017, Conference Proceedings, September 13th - 15th, 2017. University of Hradec Králové, Czech Republic.

Skelton, A., Andrén, M., Kristmannsdóttir, H., Stockmann, G., Mörth, C.M., Sveinbjörnsdóttir, Á., Jónsson, S., Sturkell, E., Guðrúnardóttir, H.R., Hjartarson, H., Siegmund, H., Kockum, I., 2014. Changes in groundwater chemistry before two consecutive earthquakes in Iceland. Nat. Geosci. 7, 752. https://doi.org/10.1038/ngeo2250.

Skelton, A., Claesson, L., Wästeby, N., Andrén, M., Stockmann, G., Sturkell, E., Mörth, C.M., Stefansson, A., Tollefsen, E., Siegmund, H., Keller, N., Kjartansdóttir, R., Hjartarson, H., Kockum, I., 2019. Hydrochemical changes before and after earthquakes based on long-term measurements of multiple parameters at two sites in Northern Iceland—a review. J. Geophys. Res. Solid Earth 124, 2702–2720. https://doi.org/10.1029/2018JB016757.

Sparks, R.S.J., 2003. Forecasting volcanic eruptions. Earth Planet. Sci. Lett. 210, 1–15. https://doi.org/10.1016/S0012-821X(03)00124-9.

Stefansson, R., Gudmundsson, G.B., Halldorsson, P., 2008. Tjörnes fracture zone. New and old seismic evidences for the link between the North Iceland rift zone and the Mid-Atlantic ridge. Tectonophysics 44, 117–126. https://doi.org/10.1016/j.tecto.2006.09.019.

Thordarson, T., Larsen, G., 2007. Volcanism in Iceland in historical time: volcano types, eruption styles and eruptive history. J. Geodyn. 43, 118–152. https://doi.org/10.1016/j.jog.2006.09.005.

Tibaldi, A., Corti, N., Bonali, F.L., Mariotto, F.P., Russo, E., 2020. Along-rift propagation of Pleistocene-Holocene faults from a central volcano. J. Struct. Geol. 141, 104201. https://doi.org/10.1016/j.jsg.2020.104201.

Trick, J.K., Stuart, M., Reeder, S., 2008. Contaminated groundwater sampling and quality control of water analyses. Environmental Geochemistry. Chapter 3 - Environmental Geochemistry (Second Edition). Site Characterization, Data Analysis and Case Histories. . Elsevier, pp. 29–45 https://doi.org/10.1016/B978-0-4.

Van Vliet-Lanoë, B., Bergerat, F., Allemand, P., Innocentd, C., Guillou, H., Cavailhes, T., Guðmundsson, Á., Chazot, G., Schneider, J.L., Grandjean, P., Liorzou, C., Passot, S., 2020. Tectonism and volcanism enhanced by deglaciation events in southern Iceland. Quat. Res. 94, 94–120. https://doi.org/10.1017/qua.2019.68.

Verma, M.P., Santoyo, E., 1997. New improved equations for Na/K, Na/Li and SiO2 geothermometers by outlier detection and rejection. J. Volcanol. Geotherm. Res. 79, 9–24. https://doi.org/10.1016/S0377-0273(97)00024-3.

Vigier, N., Burton, K.W., Gislason, S.R., Rogers, N.W., Duchene, S., Thomas, L., Hodge, E., Schaefer, B., 2006. The relationship between riverine U-series disequilibria and erosion rates in a basaltic terrain. Earth Planet. Sci. Lett. 249, 258–273. https://doi.org/10.1016/j.epsl.2006.07.001.

Wakita, H., 1975. Water wells as possible indicators of tectonic strain. Science 189, 553–555. https://doi.org/10.1126/science.189.4202.553.

Wakita, H., Nakamura, Y., Notsu, K., Noguchi, M., Asada, T., 1980. Radon anomaly: a possible precursor of the 1978 Izu-Oshima-kinkai earthquake. Science 207, 882–883. https://doi.org/10.1126/science.207.4433.882.

Wang, C.-Y., Manga, M., 2021. Water and Earthquakes. Springer Nature Switzerland AG, Cham, Switzerland https://doi.org/10.1007/978-3-030-64308-9.

Wästeby, N., Skelton, A., Tollefsen, E., Andrén, M., Stockmann, G., Claesson, L., Sturkell, E., Mörth, M., 2014. Hydrochemical monitoring, petrological observation, and geochemical modeling of fault healing after an earthquake. J. Geophys. Res. Solid Earth 119, 5727–5740. https://doi.org/10.1002/2013JB010715.

Willis, J.P., 1979. Some aspects of the geochemistry of gallium in silicate rocks and stoney meteorites. Ph.D. Thesis, 2nd ed University of Cape Town, unpublished.

Zhou, Z., Wang, J., Su, R., Guo, Y., Zhao, J., Zhang, M., Ji, R., Li, Y., Li, J., 2020. Hydrogeochemical and isotopic characteristics of groundwater in Xinchang preselected site and their implications. Environ. Sci. Pollut. Res. 27, 34734–34745. https://doi.org/10.1007/s11356-019-07208-1.

ORIGINAL PAPER

Climate change and its effect on groundwater quality

Maurizio Barbieri [ID] · **Marino Domenico Barberio · Francesca Banzato ·
Andrea Billi · Tiziano Boschetti · Stefania Franchini · Francesca Gori ·
Marco Petitta**

Abstract Knowing water quality at larger scales and
related ground and surface water interactions
impacted by land use and climate is essential to our
future protection and restoration investments. Popu-
lation growth has driven humankind into the Anthro-
pocene where continuous water quality degradation is
a global phenomenon as shown by extensive recalci-
trant chemical contamination, increased eutrophica-
tion, hazardous algal blooms, and faecal
contamination connected with microbial hazards
antibiotic resistance. In this framework, climate
change and related extreme events indeed exacerbate
the negative trend in water quality. Notwithstanding
the increasing concern in climate change and water
security, research linking climate change and

groundwater quality remain early. Additional research
is required to improve our knowledge of climate and
groundwater interactions and integrated groundwater
management. Long-term monitoring of groundwater,
surface water, vegetation, and land-use patterns must
be supported and fortified to quantify baseline prop-
erties. Concerning the ways climate change affects
water quality, limited literature data are available.
This study investigates the link between climate
change and groundwater quality aquifers by examin-
ing case studies of regional carbonate aquifers located
in Central Italy. This study also highlights the need for
strategic groundwater management policy and plan-
ning to decrease groundwater quality due to aquifer
resource shortages and climate change factors. In this
scenario, the role of the Society of Environmental
Geochemistry is to work together within and across
geochemical environments linked with the health of
plants, animals, and humans to respond to multiple
challenges and opportunities made by global warming.

M. Barbieri (✉) · M. D. Barberio ·
F. Banzato · S. Franchini · F. Gori · M. Petitta
Earth Sciences Department, Sapienza University of Rome,
Rome, Italy
e-mail: maurizio.barbieri@uniroma1.it

A. Billi
Institute for Environmental Geology and Geoengineering,
National Research Council Rome, Rome, Italy

T. Boschetti
Department of Chemistry, Life Sciences and
Environmental Sustainability, University of Parma,
Parma, Italy

Introduction

A survey of global climate changes since 1700 has
recognised that over the centuries, twenty climatic
events covering continental-scale temperature dips,

Springer

211

hydroclimatic anomalies, stratospheric perturbations and global atmospheric composition changes have occurred, hitting millions of people in many ways (Bronnimann, 2015; Easterbrook, 2016).

The global surface temperature has grown by 0.74 °C during the past 100 years (1906 ∼ 2005), according to the International Panel for Climate Change (IPCC) report (Bronnimann, 2015). Hence, global warming is currently an indisputable fact. The ordinary rate of warming over the last 50 years (0.13 ± 0.03 °C per decade) is nearly double the increase observed during the previous 100 years (Trenberth et al., 2007). A large number of climate changes have been observed on both global and local scales, including long-term changes in the surface temperature, precipitation, wind patterns, radiation, and other extreme weather events, such as droughts, floods, and heatwaves (Joehnk et al., 2008; Jones et al., 2010; Trenberth et al., 2007).

By 2020, models forecast that global surface temperature will be more than 0.5 °C warmer than the 1986–2005 average (NOAA, 2020).

It is often said "water is life", but it would be better to say "water quality is health". Water quantity and quality (in terms of access and management) are related to the global health-preserving sustainable network, including vegetation, animals, and humans. Knowing water quality at larger scales and related ground and surface water interactions impacted by land use and climate is essential to our future protection and restoration investments (UNESCO, UN-Water, 2020). In the last 60 years, we have seen significant acceleration of population growth (in people and animals), land-use change, fertilizer load, and water withdrawals. This increase has driven us into the Anthropocene, where continuous water quality degradation is a global phenomenon as shown by extensive recalcitrant chemical contamination, increased eutrophication, hazardous algal blooms, and faecal contamination connected with microbial hazards antibiotic resistance. In this framework, climate change and related extreme events indeed contribute to exacerbating the negative trend in water quality.

In addition, climate change is a factor that influences more than just water quantity. Notwithstanding progress in water resource evaluation and protection, research on the impact of climate change on water quality occurred only recently. Integrated into the global change concept, land use evolution, deforestation, urban growth, and area waterproofing may also increase water quality degradation (Barbieri et al., 2019; Xia et al., 2015).

Extreme weather events, including typhoons, storms, and temperature jumps mainly result in water events such as floods and droughts, which may further affect water quantity (Forbes et al., 2011; Green et al., 2011; Lasagna et al., 2020; Rodell et al., 2009; Tate et al., 2004).

For the ways climate change affects water quality, restricted literature data are available. Papers studied changes in water quality induced by climate change, and the ways climate changes affect water quality and thus put forward corresponding countermeasures are reported in Table 1.

Groundwater, the vast water reserve below Earth's surface (Taylor et al., 2013), is a vital resource for humans and ecosystems. More than one-third of the water used arises from underground (Famiglietti, 2014). Globally, about two billion people use groundwater for drinking purposes (Cui et al., 2020; Huan et al., 2018). However, global groundwater resources can be threatened by anthropogenic activities and the lesser-known consequences of climate change (Green et al., 2007). Dissolved trace elements in groundwater are mainly derived from chemical weathering and anthropogenic input (Ayari et al., 2021; Devic et al., 2014; Huang et al., 2014; Li et al., 2019).

Indeed, not much is known about the response of groundwater to climate change and how this process is affecting the present availability and the future sustainability of groundwater resources (Andrei et al., 2021; Green et al., 2007).

Evaluating the impact, as mentioned earlier, is imperative because groundwater is resilient to drought and performs a crucial role in regions where climate change is limiting renewable surface water resources (Fiorillo et al., 2015).

Climate change will intensify anthropogenic pressures by interfering with the frequency and regime of the aquifer recharge due to the change in land use, soil characteristics and rainfall (Ricolfi et al., 2020).

Furthermore, the potential decrease in aquifer recharge rates induced by climate change could affect aquifers' recharge/discharge balance. In this context, it is helpful to deepen the knowledge of the water balance on a regional scale to better manage the

Table 1 Papers reports changes in water quality under climate change

Studies	References
Impact of climatic variability on the availability and features of natural mineral water springs used for bottled water	Bastiancich et al. ([2021](#))
Impacts of droughts on water quality	Caruso ([2002](#)), Evans et al. ([2005](#)), Ducharne et al. ([2007](#)), Monteith et al. ([2007](#)), Hejzlar et al. ([2003](#)), Van Vliet et al. (2008), Lasagna et al. ([2020](#))
Changes in water quality caused by climate change and the ways climate changes affect water quality and thus put forward corresponding countermeasures	Barbieri et al. ([2019](#)), Xia et al. ([2015](#)), Chen et al. ([2020](#)), Fu et al. ([2020](#)), Lu et al. ([2020](#)), Fei et al. ([2020](#))
Impact of climate change on human health (influence of heavy metals on soil, which helps predict the risk of their presence in foods)	Liu et al. (2020)
The effects of climate change on Chinese Medicinal Yam (CMY)	Fan et al. (2020)

groundwater resource both from a qualitative and a quantitative point of view.

In this framework, groundwater is rarely adequately included within the Integrated Water Resource Management (Baba et. al., 2011).

Carbonate rocks are present on all continents, and karst regions are our planet's most diverse hydrogeological environments (Goldscheider et al., 2020).

The largest total surface area is found on Asia's largest continent, where carbonate rocks are present, corresponding to 18.6% of Asia's land surface (Goldscheider et al., 2020). However, the highest percentage of karst is current in Europe (mainly in the Mediterranean region), with a total area of 21.8% (Goldscheider et al., 2020).

China and Russia have the most extensive and nearly identical absolute karst surface areas in terms of surface area and population (Goldscheider et al., 2020).

In addition to climate change, population growth is a significant challenge for water resources management in karst regions. Therefore, the relations between karst and population highlights that about 17% of the global population lives in karst areas (Goldscheider et al., 2020).

In some areas, like in the Mediterranean region, the climate change impact seems to be severe, hindering our ability to manage available water resources (Howard, 2011). In fact, few studies have examined the potential impacts of climate change on groundwater resources in a region where meteorological

conditions and sea and lake levels are expected to change at unprecedented rates in modern times. The climate of the Mediterranean Sea is, indeed, highly sensitive to atmospheric changes, particularly the North Atlantic Oscillation (NAO). The NAO and global climate change pose a serious threat to water resources (Howard, 2011; Palutikof & Holt, 2004).

The medium temperatures in the Mediterranean region have already risen by 1.4 °C since the pre-industrial era, indicating a warming of 0.4 °C higher than the global average. It has outcomes on various levels, such as rising sea levels (6 mm in 20 years) and increasingly extreme meteorological phenomena and drought (Cramer et al., 2018). Moreover, a notable decrease in precipitation, especially in the warm season, was observed in the southern Mediterranean areas (Brunetti et al., 2006; Giorgi et al., 2008).

To verify the hypothesis of significant changes in groundwater chemistry in the Mediterranean region due to climate variability, we select a fractured regional aquifer in Central Italy affected by significant anthropic impacts with a hydrogeological basin reaching high elevation.

This paper performed a preliminary step showing the changes in dissolved ions over time (2004–2020) in three main springs on the eastern side of the Sibillini aquifer in Central Italy.

The time series of springs and meteorological parameters from 2004 to 2020 are studied to evaluate annual behaviour. Moreover, trend and cross-

correlation analyses are used to assess whether climatic variability impacts spring water quality and discharge.

The chemical associations and time trends observed in this small dataset are only provided as an example of how initial observations can be used to build the hypothesis to be tested in the future.

Thus, this study represents the first regional-scale investigation in the Central Italy of the groundwater feature variation in mountain aquifers due to climate variability. Moreover, researching possible trends in quality and quantity could provide helpful information for the owners and stakeholders and the whole community.

For all these reasons, the study of the role of climate change on the recharge of aquifers is relevant for ensuring the proper management of water resources (Fiorillo et al., 2015). In addition, a detailed evaluation of the possible effects of climate change on groundwater quality and related health effects is vital. Undoubtedly, various studies have reported that water pollution has developed in the last decades. Consequently, water-related diseases impact the health of many citizens, mainly in developing countries, and climate change may impact water chemistry and sea-level rise so that salinization may be affected, which influences the depletion of freshwater and river environments. The related health effects varying from a significant cause of cardiovascular diseases, hypertension, methemoglobinemia in infants, skeletal and dental fluorosis, laxative effects for sulfate at high levels (Ahmed et al., 2000).

Nevertheless, the scenario analysis only gives us the scales of the impacts and the relationships between climate change, society and human health still need to be investigated. To respond to multiple challenges and opportunities made by global warming, the Society of Environmental Geochemistry and Health (SEGH) needs to stress a more systematic recognition of the domestic facts of societal impacts of climate change. In addition, research on the mechanism and points of climate change still needs to be strengthened; additional attention is required to research and develop climate change adaptation technology.

The role of the SEGH is to work together within and across geochemical environments linked with the health of plants, animals, and humans.

Hydrogeological selection of monitoring sites

To verify the hypothesis of significant changes in groundwater chemistry due to climate variability, the selection of relevant sites is a preliminary fundamental step. The aquifers and the related springs directly affected by changes in recharge have been selected on the basis of the following conditions:

- Groundwater resources affected by significant anthropic impacts, in terms of withdrawals and of potential pollution, are not indicated for our research. In fact, natural conditions of water table and spring discharge can easily evidence shortage due to external climate inputs. At the same time, groundwater quality characteristics can be investigated where their changes are not due to human pollution inputs. For the same reasons, coastal aquifers, where ion content would be affected by marine intrusion, are not useful for our scope. Consequently, groundwater resources in protected and/or pristine areas have to be selected.
- Secondly, aquifers that respond quickly to climate inputs can highlight, in a limited time (months to few years), variations in the dissolved ion content due to their direct dependence on recharges. For this reason, fractured aquifers, specially fractured, and karstified carbonate aquifers would be selected for monitoring water quality changes.
- Where the groundwater is characterised by fast flow and, generally, by fracture network flow, responses to recharge reduction would be easy to identify. At the same time, the calcium-bicarbonate nature of the rock is reflected in groundwater ion content, offering the possibility to look into a limited number of qualitative parameters.
- Finally, hydrogeological basins reaching high elevation, where snow covers may be present for some months each year, offer the additional possibility to verify how the recharge process is affected by snow cover reduction, which is a primary consequence of temperature increases. The reduction of snow cover is the undoubtedly one of the first effects of climate changes recorded all around the world.

Taking these characteristics into account, we selected the large carbonate fractured (and locally karstified) aquifers of Central Apennines for a preliminary evaluation of the impact of climate change on

groundwater quality. These aquifers are significantly fed by snow cover and snowmelt, which consistently occurs during spring, and are frequently located in mountain protected areas and National Parks. A specific example can be seen in case described below regarding the Sibillini Mts. Aquifer (Fig. 1a). Aquifers and springs considered in this study are partially collected for drinking purposes from CIIP SpA (Consorzio Idrico Integrato Piceno). The aqueduct serves approximately 400.000 citizens in an area of about 1900 km^2 in Central Italy.

The Meso-Cenozoic sequence constituting the regional aquifer (Boni et al., 2010; Pierantoni et al., 2013) was affected by a compressive tectonic phase from Upper Miocene to Lower Pliocene and, afterwards, by extensional tectonics starting from the Early Pliocene (Boni et al., 2010; Brozzetti et al., 2019; Porreca et al., 2018). The hydrogeological setting (Mastrorillo et al., 2010; Mastrorillo et al., 2020) includes three main aquifers corresponding to the carbonate formations, namely the Basal Aquifer, the Maiolica and the Scaglia aquifers.

Capodacqua (S1), Pescara (S2), and Foce (S3) are the main springs on the eastern side of the Sibillini aquifer, located close to the overthrust front (Fig. 1a).

All three springs have calcium-bicarbonate equilibrium with a low mineralization. Only spring S3, that directly emerges from the Basal Aquifer within a wide hydrogeological basin, shows a slight enrichment in sulphates (Nanni et al., 2020). The water flow of springs S1 and S2 occurred in the epiphreatic portion of the aquifer, characterized by fissure and karst, and showed rapid travel time. Recent tracer tests prove that the two springs are draining fissured areas associated with normal faults having Apennine direction (Brozzetti et al., 2019; Nanni et al., 2020). As shown by literature data, the stability of the chemical-physical parameters during the hydrological year indicates that the feeding aquifer is large and has high volumes of stored groundwater. Furthermore, the low electrical conductivity and temperature can be associated with the thermometric values of the aquifer recharge waters, which are largely due to the snow melting (Nanni et al., 2020).

Material and methods

The chemical-physical parameters and major ions (from 2004 to 2020), trace elements concentration (from 2019 to 2020), and discharge values (from 2010, 2004 and 2014 to 2020 for S1, S2, and S3, respectively) of selected the springs were provided by CIIP spa (https://www.ciip.it/). The rainfall and snow data from 2004 to 2020 are available on the Civil Protection Department website (http://app.protezionecivile. marche.it) and refer to the "Monte Prata" rain gauging station (see location in Fig. 1a).

Major cation (Ca, Mg, Na, K) and anions (Cl, SO$_4$, NO$_3$, F) were analyzed by ion chromatography. The selected trace elements Sr and Ba were analyzed by inductively coupled plasma mass spectrometry (ICP-MS method 3125; Baird 2017). The QA/QC of the analytical methods was checked according to Baird 2017 (method 3125). For the pluviometric data, the QA/QC was according to the World Meteorological Organization.

Total dissolved solids (TDS) and hardness (mg/l as CaCO$_3$) were calculated from electrical conductivity and Ca + Mg concentration, respectively, according to Baird et al. (2017). Geochemical parameters (saturation indexes, total carbon) were calculated by PHREEQCI, version 3 (Parkhurst & Appelo, 2013). All chemical data are listed in Table S1 in the electronic supplementary material (ESM).

Results and discussion

The evolutionary trends of climatic characteristics and their impacts on chemical characteristics were studied through the comparison of historical time series of rainfall, snow data, discharge, and chemical content of selected springs (Fig. 1b). In addition, the chemical ratio of some major ions (e.g. Ca/Na and Mg/Na molar ratio) was reported to constrain the potential involved in the hydrodynamic process. The analysis of the trace elements has been carried out to understand better the possible consequences of a further decrease in recharge rates and potential implications for climate change studies.

Figure 1b shows the chemical time series of Ca, Mg, Cl, and SO$_4$ concentrations with respect to rainfall, snow, and discharge from 2004 to 2020. Bearing in mind the fact that the period under

consideration is long, the concentrations of ions do not show relevant variations through the 16 years of monitoring.

Rainfall variability causes changes in groundwater recharge that can influence groundwater quality by different processes. The statistical analysis on calcium concentration series at spring S3 has allowed us to detect a harmonic trend similar to that of rainfall amount (Fig. S1 in the electronic supplementary material, ESM).

However, it is noteworthy that some ions show particular trends and spikes. Indeed, in the SO_4 concentrations, a progressive increase of about five mg/l from 2007 to 2020 for S1 and S2 is evident. However, spring S3 shows an increase in SO_4 content from 2007 to 2016 and an abrupt decrease. This is probably due to the 2016–2017 Amatrice–Norcia seismic sequence caused by a change in the hydrodynamic flow (Mastrorillo et al., 2019). These increases (from 2007 to 2016–2020), characterized by a good coefficient of correlation, R, reflect decrease trends identified in the snowfall, which is the primary recharge factor of the springs (Fig. 1b). Furthermore, the available discharge values show similar snowfall values and SO_4 concentration trends, especially for spring S2, where a more extensive historical series is available (2004–2020). The discharge values of S1 are consistent with snowfall data, showing two different decreasing trends also reflected in the SO_4 concentrations. However, the S3 spring discharge values (2014–2020) are steady from 2014 to 2017 and decrease later, coupled with a sharp decrease in SO_4 concentration.

Combining major ion concentrations in the mixing diagrams (e.g. Gaillardet et al., 1999), it is possible to observe some characteristic trends (Fig. 1c). The S1 and S2 springs have well-defined, detailed trends with different slopes, remaining in the same range of Ca/Na (Molar) values but differing in C/Na and Mg/Na values (Fig. 1c). The peak value of this latter ratio

corresponds to that of Mt Sibillini (ARPAM, 2001; Chiodini et al., 2013) (Fig. 1c). Conversely, the shift towards the lowest values of both Mg/Na and Ca/Na ratios seems in agreement with the importance of the streambed springs (reworked data from ARPAM, 2001). Therefore, while the higher values of the ratios are reached during drought periods, the lower values of the ratios correspond with rainy periods since these values are similar to those of runoff waters. Such an effect was also confirmed during 1998–1999 when the S2 spring showed a switch from lowest to highest values of the above-described ratios (reworked data from Cambi et al., 2003) as a response to significantly different rainfall amounts in these years.

In addition, the analysis of trace elements concentrations performed in 2019–2020 highlights the relationship between some ion concentrations (Sr and Ba) and the hydrogeological recharge/discharge cycle (Fig. S2 in the electronic supplementary material, ESM).

The concentration of barium (Ba) in groundwater derives from barite ($BaSO_4$) solubility. Barite is unstable in reducing environments due to the reduction of sulphate. Therefore, the principal controlling factor of barium in groundwater is the SO_4 concentrations. Barite precipitation from the aqueous solution improves the Sr/Ba ratio in the residual solution (Hanor, 2000). In the study area, the predominant sources of strontium are Triassic formations (e.g. dolomite and evaporite formation). The relationship between strontium and barium in groundwater is controlled by the dissolution of sulphate salts containing strontium and barite precipitation. This explains why strontium in groundwater can usually be connected to fluids rich in SO_4 and Ca and characterized by high Sr/Ba ratios (Hanor, 2000). Thus, the Sr/Ba ratio variation could be symptomatic of changes in deep SO_4-rich fluid contribution derived from the deepest portion of the aquifer.

Indeed, in Northern Apennines, cold to hot Na-Cl and Ca-SO_4 waters interacting with evaporites of the Burano Formation (Late Triassic) showed a mean Sr/Ba weight ratio of 336 ± 210 (N = 45; Boschetti et al., 2005; Boschetti et al., 2017; Capecchiacci et al., 2015; unpublished data). The lower value outliers (Sr/Ba < 100) are mainly related to waters mixed with Ca-HCO_3 and freshwaters interacting with Mesozoic limestones (Sr/Ba < 10).

In the proposed case study, the increases of the Sr/Ba ratio (Fig. S2 in the electronic supplementary material, ESM) are potentially related to the recharge periods that induce changes in the pressure field of the aquifer. Therefore, we argue that a more extended time series of trace elements would highlight the temporal increase of the Sr/Ba ratio in line with the SO4 trend caused by a progressive deepening of flow paths.

Hence, climate changes could cause variation in the hydrodynamic condition, and consequently, groundwater chemical content. These changes in groundwater chemistry can refer to major ions and some metals and metalloids affecting water quality, with the main consequence being the hardness of the water. The main natural sources of water hardness are polyvalent metallic ions dissolved by sedimentary rocks, infiltrations, and runoffs from soils. Ca and Mg, which are the two principal ions, are essential minerals and beneficial to human health in several respects. Inadequate intake of both nutrients can cause adverse health consequences (WHO, 2010).

Hard water, particularly significantly hard water, could provide an essential supplementary contribution to total Ca and Mg intake (Galan et al., 2002). The health impacts of hard water are mainly due to the salts dissolved, resulting primarily in Ca and Mg. Generally, people are protected from excess intakes of Ca by the intestinal absorption mechanism (Galan et al., 2002). However, calcium can interact with Fe, Zn, and Mg within the intestine, decreasing the absorption of these minerals (Galan et al., 2002). Nevertheless, the primary cause of hypermagnesemia is renal insufficiency, associated with a significantly decreased ability to excrete Mg (Sengupta, 2013). In addition, the increased intake of Mg salts may cause a change in bowel habits such as diarrhoea (Galan et al., 2002). Therefore, drinking water or a diet in which Mg and SO4 are about 250 mg/l each can have a laxative effect. (Galan et al., 2002).

To sum up, as shown for the studied area, a decrease in snowfall and consequently in recharge can induce significant hydrogeochemical change in fractured carbonate aquifers. In particular, we recognised an increasing trend in SO_4 concentration in the selected basal springs and a connection to a decrease in snowfall in the recharge areas. Furthermore, the trace element analysis allows attribution of the SO_4 increase to the deepening of the groundwater flow path. Lower recharge values induce a limitation in the renewable rate of the aquifer resources, feeding the springs with a more significant contribution by deeper flow paths, which increases the ion concentrations. In addition, rainstorms can also cause changes in the steady regime of basal springs, modifying the geochemical content towards values characteristic of streambed springs, which are located at a lower elevation. In this scenario, variations in recharge dynamics induced by climate changes can practically alter groundwater quality and therefore represent a potential risk for human health.

Conclusions

Groundwater is a fundamental source for the survival of humanity, and consequently, it is necessary to learn the proper management of this resource.

This case study confirmed that groundwater, compared to surface water, is more resilient to climate change. Nevertheless, climate change can affect groundwater quality by reducing aquifer recharge and increasing anthropogenic pressures. In addition, the effects of climate change on groundwater are enhanced by human activity, such as changes in land use or increased demand for drinking water or agricultural use.

Furthermore, the aquifer's recharge is closely linked to the distribution of global rainfall and, consequently, is directly influenced by climatic variability, including extreme events.

A variation in groundwater chemistry in studied springs has been recorded in rainier years, especially in calcium and sulphates and in the characteristic Ca and Mg, Na and Cl, and SO_4 and Cl ratios. This change can affect the quality of groundwater, modifying the water–rock interaction times and, therefore, the mobility of some elements and water properties such as hardness, which has a relevant implication for human health.

Some epidemiological investigations have displayed the relationship between risk for cardiovascular disease, growth retardation, reproductive failure, and other health problems and the hardness of drinking water or its magnesium and calcium content.

Chemical associations and time-series trends observed in this study are only provided as an example of how initial observations can be used to build a hypothesis. Indeed, a hydrogeochemical analysis must

conduct on a regional scale and with more extended time series.

Over time, the hydrogeological balance linked with hydrogeochemical analyses highlights the connections between the quality/quantity of groundwater and climate changes. However, although the effect of climate change on groundwater availability is evident, the one on groundwater quality is still poorly understood and needs additional efforts to be correctly evaluated. Therefore, it is necessary to monitor and quantify the hydrogeological cycle to verify how groundwater quality can change climate change. Due to these specific characteristics, both climate change and groundwater quality must be considered to be of increasing interest because of their relevance to the world's water supply.

One of the keys focuses of future engagement of the SEGH should be to explore the internal and external connections between environmental geochemistry and climate systems.

In the context of climate change, this new water quality challenge draws the SEGH members working to:

- Promote and develop effective technology and policy responses to mitigate and adapt to climate change impacts on water quality.
- Share answers, best practices and lessons learnt on climate change impacts in water quality to support the education and social awareness and subsequently in improving human health mainly in developing countries.

Declarations

References

Ahmed, T., Zounemat-Kermani, M., & Scholz, M. (2020). Climate change, water quality and water-related challenges: a review with focus on Pakistan. *International Journal of Environmental Research and Public Health, 17*, 8518. https://doi.org/10.3390/ijerph17228518

Andrei, F., Barbieri, M., Muteto, P.V., Ricolfi, L., Sappa, G., Vitale, S. (2021). Water resources management under climate change pressure in Limpopo National Park Buffer Zone (Book Chapter). *Advances in science, technology and innovation*, pp. 129–132

ARPAM (2001). Libro bianco sulle acque potabili. Agenzia Regionale per la Protezione Ambientale (ARPAM). http://www.arpa.marche.it/images/pdf/libro_bianco/ascoli_piceno/Libro-bianco-Ascoli.pdf

Ayari, J., Barbieri, M., Agnan, Y., Sellami, A., Braham, A., Dhaha, F., & Charef, A. (2021). Trace element contamination in the mine-affected stream sediments of Oued Rarai in north-western Tunisia: A river basin scale assessment. *Environmental Geochemistry and Health, 21*, 1–16. https://doi.org/10.1007/s10653-021-00887-1

Baba, A., Tayfur, G., Gunduz, O., Howard, K. W. F., Friedel, M. J., & Chambel, A. (2011). *Climate change and its effects on water resources issues of national and global security*. Springer. https://doi.org/10.1007/978-94-007-1143-3

Baird R.B., Eaton A.D., Rice, E.W., (2017). *Standard methods for examination of water and wastewater*, 23rd edn. American Public Health Association (APHA), American Water Works Association (AWWA), Water Environment Federation (WEF), Washington DC

Barbieri, M., Ricolfi, L., Vitale, S., Muteto, P. V., Nigro, A., & Sappa, G. (2019). Assessment of groundwater quality in the buffer zone of Limpopo National Park, Gaza Province, Southern Mozambique. *Environmental Science and Pollution Research, 26*(1), 62–77. https://doi.org/10.1007/s11356-018-3474-0

Bastiancich, L., Lasagna, M., Mancini, S., et al. (2021). Temperature and discharge variations in natural mineral water springs due to climate variability: A case study in the Piedmont Alps (NW Italy). *Environmental Geochemistry and Health*. https://doi.org/10.1007/s10653-021-00864-8

Boni, C. F., Baldoni, T., Banzato, F., Cascone, D., & Petitta, M. (2010). Hydrogeological study for identification, characterization and management of groundwater resources in the Sibillini Mountains national park (Central Italy). *Italian Journal of Engineering Geology and Environment, 2*, 21–39. https://doi.org/10.4408/IJEGE.2010-02.O-02

Boschetti, T., Venturelli, G., Toscani, L., Barbieri, M., & Mucchino, C. (2005). The Bagni di Lucca thermal waters (Tuscany, Italy): An example of Ca-SO4 waters with high Na/Cl and low Ca/SO4 ratios. *Journal of Hydrology, 307*(1–4), 270–293. https://doi.org/10.1016/j.jhydrol.2004.10.015

Boschetti, T., Toscani, L., Barbieri, M., Mucchino, C., & Marino, T. (2017). Low enthalpy Na-chloride waters from the Lunigiana and Garfagnana grabens, Northern Apennines, Italy: Tracing fluid connections and basement interactions via chemical and isotopic compositions. *Journal of Volcanology and Geothermal Research, 348*, 12–25. https://doi.org/10.1016/j.jvolgeores.2017.10.008

Brozzetti, F., Boncio, P., Cirillo, D., Ferrarini, F., de Nardis, R., Testa, A., Liberi, F., & Lavecchia, G. (2019). High-resolution field mapping and analysis of the August–October 2016 coseismic surface faulting (central Italy earthquakes): Slip distribution, parameterization, and comparison with global earthquakes. *Tectonics, 38*, 417–439. https://doi.org/10.1029/2018TC005305

Bronnimann, S. (2015) Climatic changes since 1700. *Advances in global change research*. Springer, Cham

Brunetti, M., Maugeri, M., Monti, F., & Nanni, T. (2006). Temperature and precipitation variability in Italy in the last two centuries from homogenized instrumental time series. *International Journal of Climatology: A Journal of the Royal Meteorological Society*, 26(3), 345–381. https://doi.org/10.1002/joc.1251

Cambi, C., Dragoni, W., & Valigi, D. (2003). Water management in low permeability catchments and in times of climatic change: The case of the Nestore River (Western Central Italy). *Physics and Chemistry of the Earth, Parts a/b/c, 28*(4–5), 201–208. https://doi.org/10.1016/S1474-7065(03)00029-9

Capecchiacci, F., Tassi, F., Vaselli, O., Bicocchi, G., Cabassi, J., Giannini, L., & Chioccciora, G. (2015). A combined geochemical and isotopic study of the fluids discharged from the Montecatini thermal system (NW Tuscany, Italy). *Applied Geochemistry, 59*, 33–46. https://doi.org/10.1016/j.apgeochem.2015.03.010

Caruso, B. (2002). Temporal and spatial patterns of extreme low flows and effects on stream ecosystems in Otago, New Zealand. *Journal of Hydrology, 257*(1–4), 115–133. https://doi.org/10.1016/S0022-1694(01)00546-7

Chen, J., Li, J., Zhang, X., et al. (2020). Ultra-sonication for controlling the formation of disinfection by-products in the ClO2 pre-oxidation of water containing high concentrations of algae. *Environmental Geochemistry and Health, 42*, 849–861. https://doi.org/10.1007/s10653-019-00312-8

Chiodini, G., Cardellini, C., Caliro, S., Chiarabba, C., & Frondini, F. (2013). Advective heat transport associated with regional Earth degassing in central Apennine (Italy). *Earth and Planetary Science Letters, 373*, 65–74. https://doi.org/10.1016/j.epsl.2013.04.009

Cramer, W., Guiot, J., Fader, M., Garrabou, J., Gattuso, J.-P., Iglesias, A., Lange, M. A., Lionello, P., Llasat, M. C., Paz, S., Penuelas, J., Snoussi, M., Toreti, A., Tsimplis, M. N., & Xoplaki, E. (2018). Climate change and interconnected risks to sustainable development in the Mediterranean. *Nature Climate Change*, 8, 972–980.

Cui, X., Huang, C., Wu, J., Liu, X., & Hong, Y. (2020). Temporal and spatial variations of net anthropogenic nitrogen inputs (NANI) in the Pearl River Basin of China from 1986 to 2015. *PloS one, 15*(2), e0228683

Devic, G., Djordjevic, D., & Sakan, S. (2014). Natural and anthropogenic factors affecting the groundwater quality in Serbia. *Science of the Total Environment, 468*, 933–942. https://doi.org/10.1016/j.scitotenv.2013.09.011

Ducharne, A., Baubion, C., Beaudoin, N., Benoitc, M., Billena, G., Brissond, N., Garniera, J., Kiekene, H., Lebonvalletd, S., Ledouxb, E., Maryf, B., Mignoletc, C., Pouxe, X., Saubouaf, E., Schottc, C., Therya, S., & Viennotb, P. (2007). Long term prospective of the Seine River system: Confronting climatic and direct anthropogenic changes. *Science of the Total Environment, 375*(1–3), 292–311. https://doi.org/10.1016/j.scitotenv.2006.12.011

Easterbrook, D.J. (2016) *Evidence-based climate science: Data opposing CO₂ emissions as the primary source of global warming. Elsevier*

Evans, C., Monteith, T. D., & Cooper, M. D. (2005). Long-term increases in surface water dissolved organic carbon: Observations, possible causes and environmental impacts. *Environmental Pollution, 137*(1), 55–71. https://doi.org/10.1016/j.envpol.2004.12.031

Famiglietti, J. S. (2014). The global groundwater crisis. *Nature Climate Change, 4*(11), 945–948.

Fei, J., Ma, J., Yang, J., et al. (2020). Effect of simulated acid rain on stability of arsenic calcium residue in residue field. *Environmental Geochemistry and Health, 42*, 769–780. https://doi.org/10.1007/s10653-019-00273-y

Fiorillo, F., Petitta, M., Preziosi, E., et al. (2015). Long-term trend and fluctuations of karst spring discharge in a Mediterranean area (central-southern Italy). *Environmental Earth Sciences, 74*, 153–172. https://doi.org/10.1007/s12665-014-3946-6

Forbes, K. A., Kienzle, W. S., Coburn, A. C., Byrne, M. J., & Rasmussen, J. (2011). Simulating the hydrological response to predicted climate change on a watershed in southern Alberta. *Canada, Climatic Change, 105*(3–4), 1–22. https://doi.org/10.1007/s10584-010-9890-x

Fu, C., Li, J., Lv, X., et al. (2020). Operation performance and microbial community of sulfur-based autotrophic denitrification sludge with different sulfur sources. *Environmental Geochemistry and Health, 42*, 1009–1020. https://doi.org/10.1007/s10653-019-00482-5

Gaillardet, J., Dupré, B., Louvat, P., & Allegre, C. J. (1999). Global silicate weathering and CO₂ consumption rates deduced from the chemistry of large rivers. *Chemical Geology, 159*(1–4), 3–30. https://doi.org/10.1016/S0009-2541(99)00031-5

Galan, P., Arnaud, M. J., Czernichow, S., Delabroise, A. M., Preziosi, P., Bertrais, S., Franchisseur, C., Maurel, M., Favier, A., & Hercberg, S. (2002). Contribution of mineral waters to dietary calcium and magnesium intake in a French adult population. *Journal of the American Dietetic*

Association, 102(11), 1658–1662. https://doi.org/10.1016/S0002-8223(02)90353-6

Giorgi, F., & Lionello, P. (2008). Climate change projections for the Mediterranean region. *Global and Planetary Change, 63*, 90–104.

Goldscheider, N., Chen, Z., Auler, A. S., et al. (2020). Global distribution of carbonate rocks and karst water resources. *Hydrogeology Journal, 28*, 1661–1677. https://doi.org/10.1007/s10040-020-02139-5

Green, T. R., Taniguchi, M., & Kooi, H. (2007). Potential impacts of climate change and human activity on subsurface water resources. *Vadose Zone Journal, 6*(3), 531–532.

Green, T. R., Makoto Taniguchi, M., Kooi, H., Gurdak, J. J., Allen, M. D., Hiscock, K. M., Treidel, H., & Aureli, A. (2011). Beneath the surface of global change: Impacts of climate change on groundwater. *Journal of Hydrology, 405*, 532–560. https://doi.org/10.1016/j.jhydrol.2011.05.002

Hanor, S. (2000). Barite-celestine geochemistry and environments of formation. *Reviews in Mineralogy and Geochemistry., 40*(1), 193–275. https://doi.org/10.2138/rmg.2000.40.4

Hejzlar, J., Dubrovsky, M., Buchtele, J., & Ružička, M. (2003). The apparent and potential effects of climate change on the inferred concentration of dissolved organic matter in a temperate stream (the Malše River, South Bohemia). *Science of the Total Environment, 310*, 143–152.

Howard, K. W. (2011). Implications of climate change on water security in the Mediterranean region. In Climate change and its effects on water resources (pp. 9–16). Springer, Dordrecht

Huan, H., Zhang, B. T., Kong, H., Li, M., Wang, W., Xi, B., & Wang, G. (2018). Comprehensive assessment of groundwater pollution risk based on HVF model: A case study in Jilin City of northeast China. *Science of the Total Environment, 628*, 1518–1530.

Huang, J., Huang, Y., & Zhang, Z. (2014). Coupled effects of natural and anthropogenic controls on seasonal and spatial variations of river water quality during baseflow in a coastal watershed of Southeast China. *PLoS ONE, 9*(3), e91528. https://doi.org/10.1371/journal.pone.0091528

Joehnk, K. D., Huisman, J., Sharples, J., Sommeijer, B., Visser, M. P., & Stroom, M. J. (2008). Summer heatwaves promote blooms of harmful cyanobacteria. *Global Change Biology, 14*(3), 495–512. https://doi.org/10.1111/j.1365-2486.2007.01510.x

Jones, A., Haywood, J., Boucher, O., Kravitz, B., Robock, A. (2010). Geoengineering by stratospheric SO$_2$ injection: Results from the met Office HadGEM2 climate model and comparison with the Goddard Institute for Space Studies ModelE. *Atmospheric Chemistry and Physics, 10*, 5999–6006.

Lasagna, M., Ducci, D., Sellerino, M., Mancini, S., & De Luca, D. A. (2020). Meteorological variability and groundwater quality: Examples in different hydrogeological settings. *Water, 12*(5), 1297. https://doi.org/10.3390/w12051297

Li, Y., Li, J., Zhang, L., Huang, Z., Liu, Y., Wu, N., & Niu, Z. (2019). Perfluoroalkyl acids in drinking water of China in 2017: Distribution characteristics, influencing factors and potential risks. *Environment International, 123*, 87–89.

Lu, S., Fenghua, X., Zhang, X., et al. (2020). Health evaluation on migration and distribution of heavy metal Cd after reclaimed water drip irrigation. *Environmental Geochemistry and Health, 42*, 841–848. https://doi.org/10.1007/s10653-019-00311-9

Mastrorillo, L., Baldoni, T., Banzato, F., Boscherini, A., Cascone, D., Checcucci, R., Petitta, M., Boni, C. (2009). Quantitative Hydrogeological analysis of the carbonate domain of the Umbrua Region (Central Italy). *Italian Journal of Engineering Geology and Environment*, pp. 137–155

Mastrorillo, L., Saroli, M., Viaroli, S., Banzato, F., Valigi, D., Petitta, M. (2020). Sustained post-seismic effects on groundwater flow in fractured carbonate aquifers in Central Italy. Hydrological Processes hyp.13662. Doi: https://doi.org/10.1002/hyp.13662

Monteith, D. T., Stoddard, L. J., Evans, D. C., Wit, A. H., Forsius, M., Høgåsen, T., Wilander, A., Lisa Skjelkvåle, B., Jeffries, S. D., Vuorenmaa, J., Keller, B., Kopácek, J., & Vesely, J. (2007). Dissolved organic carbon trends resulting from changes in atmospheric deposition chemistry. *Nature, 450*(7169), 537–540. https://doi.org/10.1038/nature06316

Nanni, T., Vivalda, P. M., Palpacelli, S., Marcellini, M., & Tazioli, A. (2020). Groundwater circulation and earthquake-related changes in hydrogeological karst environments: A case study of the Sibillini Mountains (central Italy) involving artificial tracers. *Hydrogeology Journal, 28*(7), 2409–2428.

NOA (2020). National Center for Environmental Information, State of the Climate: Global Climate Report for Annual 2020. https://www.ncdc.noaa.gov/sotc/global/202013

Palutikof, J. P., Holt, T. (2004). Climate change and the occurrence of extremes: some implications for the Mediterranean basin. In: Marquina, A. (ed.) *Environmental challenges in the Mediterranean 2000–2050*. Kluwer Academic Dordrecht/Boston/London, pp. 61–73

Parkhurst, D. L., Appelo, C. A. J. (2013). Description of input and examples for PHREEQC version 3—A computer program for spe-ciation, batch-reaction, one-dimensional transp ort, and inverse geochemical calculationsRep., U.S. geological survey, techniquesand methods, book 6, chap. A43. http://pubs.usgs.gov/tm/06/a43/

Pierantoni, P. P., Deiana, G., & Galdenzi, S. (2013). Stratigraphic and structural features of the Sibillini Mountains (Umbria-Marche Apennines, Italy). *Italian Journal of Geosciences, 132*, 497–520. https://doi.org/10.3301/IJG.2013.08

Porreca, M., Minelli, G., Ercoli, M., Brobia, A., Mancinelli, P., Cruciani, F., Giorgetti, C., Carboni, F., Mirabella, F., Cavinato, G., Cannata, A., Pauselli, C., Barchi, M.R. (2018). Seismic Reflection Profiles and Subsurface Geology of the Area Interested by the 2016–2017. Earthquake Sequence (Central Italy). Tectonics 37, 1116–1137.

Ricolfi, L., Barbieri, M., Muteto, P. V., Nigro, A., Sappa, G., Vitale, S. (2020). Potential toxic elements in groundwater and their health risk assessment in drinking water of Limpopo National Park, Gaza Province, Southern Mozambique. *Environmental geochemistry and health*, pp. 1–13

Rodell, M., Velicogna, I., & Famiglietti, J. S. (2009). Satellite based estimates of groundwater depletion in India. *Nature, 460*(7258), 999–1002. https://doi.org/10.1038/nature08238

Sengupta, P. (2013). Potential health impacts of hard water. *International Journal of Preventive Medicine, 4*(8), 866–875.

Tate, E., Sutcliffe, J., Conway, D., & Farquharson, F. (2004). Water balance of Lake Victoria: Update to 2000 and climate change modelling to 2100/Bilan hydrologique du Lac Victoria: Mise à jour jusqu'en 2000 et modélisation des impacts du changement climatique jusqu'en 2100. *Hydrological Sciences Journal, 49*(4), 563–574. https://doi.org/10.1623/hysj.49.4.563.54422

Taylor, R., Scanlon, B., Döll, P., et al. (2013). Ground water and climate change. *Nature Climate Change, 3*, 322–329. https://doi.org/10.1038/nclimate1744

Trenberth, K.E., Jones, P.D., Ambenje, P., Bojariu, R., Easterling, D., Klein Tank, A., Parker, D., Rahimzadeh, F., Renwick, J.A., Rusticucci, M., Soden, B., Zhai, P. (2007) Observations: surface and atmospheric climate change. In: Solomon, S., Qin, D., Manning, M., Chen, Z., Marquis, M., Averyt, K. B., Tignor, M., Miller, H. L. (eds) *Climate change 2007: the physical science basis, Contribution of Working Group I to the fourth assessment report of the Intergovernmental Panel on climate change*. Cambridge University Press, Cambridge

UNESCO, UN-Water,. (2020). *UNESCO, UN-Water, 2020: United Nations World Water Development Report 2020: Water and Climate Change*. UNESCO.

Van Vliet, M., & Zwolsman, J. (2008). Impact of summer droughts on the water quality of the Meuse river. *Journal of Hydrology, 353*(1–2), 1–17. https://doi.org/10.1016/j.jhydrol.2008.01.001

World Health Organization. (2010). *Hardness in drinking-water: background document for development of WHO guidelines for drinking-water quality (No. WHO/HSE/WSH)*. World Health Organization.

Xia, X. H., Wu, Q., Mou, X. L., & Lai, Y. J. (2015). Potential impacts of climate change on the water quality of different water bodies. *J. Environ. Inform, 25*(2), 85–98.

Publisher's Note Springer Nature remains neutral with regard to jurisdictional claims in published maps and institutional affiliations.

Annex 1a

Matese Area

Spring	Date	T °C	pH	CE µS/cm
Grassano	08/01/2020	11.6	6.92	879
Grassano	17/02/2020	11.6	6.95	869
Grassano	18/06/2020	11.9	7.11	912
Grassano	23/07/2020	11.9	7.04	900
Grassano	04/09/2020	11.9	7.06	940
Grassano	05/11/2020	11.7	7.17	939
Grassano	24/02/2021	11.5	7.14	909
Grassano	16/04/2021	11.6	7.13	904
Grassano	12/05/2021	11.7	7.12	914
Grassano	18/06/2021	11.8	7.08	907
Grassano	20/07/2021	11.8	7.07	950
Grassano	31/08/2021	11.7	7.02	938
Grassano	28/10/2021	11.7	7.10	889
Grassano	31/01/2022	11.4	7.06	938
Grassano	16/03/2022	11.6	7.12	937
Telese Terme	08/01/2020	18.4	6.15	2250
Telese Terme	17/02/2020	16.8	6.17	2030
Telese Terme	18/06/2020	18.0	6.26	2380
Telese Terme	23/07/2020	18.8	6.14	2650
Telese Terme	04/09/2020	19.2	6.11	2820
Telese Terme	05/11/2020	19.4	6.05	2740
Telese Terme	24/02/2021	15.2	6.33	1680
Telese Terme	16/04/2021	14.4	6.30	1709
Telese Terme	12/05/2021	14.3	6.35	1731
Telese Terme	18/06/2021	14.7	6.27	1836
Telese Terme	20/07/2021	14.3	6.19	1873
Telese Terme	31/08/2021	15.9	6.20	2290
Telese Terme	28/10/2021	18.5	6.12	2670
Telese Terme	31/01/2022	15.3	6.21	1960
Telese Terme	16/03/2022	15	6.20	1979
Rio Freddo	08/01/2020	7.9	8.11	259
Rio Freddo	17/02/2020	7.8	8.06	266
Biferno	18/06/2020	8.6	7.85	307
Rio Freddo	23/07/2020	8.5	7.93	270
Rio Freddo	04/09/2020	8.5	8.02	304
Rio Freddo	05/11/2020	8.3	8.01	276
Rio Freddo	24/02/2021	8.3	8.06	268
Rio Freddo	16/04/2021	8.1	8.09	263
Biferno	12/05/2021	8.4	8.00	289
Biferno	18/06/2021	8.4	7.85	291
Biferno	20/07/2021	8.5	7.91	318

Biferno	31/08/2021	8.4	7.64	319
Biferno	28/10/2021	8.5	7.85	307
Biferno	31/01/2022	8.5	7.82	309
Biferno	16/03/2022	8.4	7.79	316
Capovolturno	08/01/2020	9.0	7.67	481
Capovolturno	17/02/2020	10.5	7.70	524
Capovolturno	18/06/2020	12.8	7.86	491
Capovolturno	23/07/2020	13.8	7.57	469
Capovolturno	04/09/2020	12.7	7.84	469
Capovolturno	05/11/2020	10.7	7.83	469
Capovolturno	12/05/2021	11.9	7.50	512
Capovolturno	18/06/2021	12.7	7.73	506
Capovolturno	20/07/2021	12.6	7.46	528
Capovolturno	31/08/2021	12.8	7.55	501
Capovolturno	28/10/2021	10.8	7.80	446
Capovolturno	31/01/2022	10.01	7.79	524
Capovolturno	16/03/2022	11	7.74	538

Spring	Date	Ca mg/L	Mg mg/L	Na mg/L	K mg/L	Cl mg/L	SO4 mg/L	HCO3 mg/L	F mg/L	NO3 mg/L
Grassano	08/01/2020	195.20	28.90	20.00	2.75	21.80	8.33	745.90	0.20	2.39
Grassano	17/02/2020	165.77	19.12	18.81	1.34	22.28	8.19	609.30	0.15	2.51
Grassano	18/06/2020	164.72	26.79	16.06	2.99	23.10	7.58	604.10	0.11	2.39
Grassano	23/07/2020	165.65	27.33	16.03	2.64	31.46	9.11	610.20	0.10	3.34
Grassano	04/09/2020	177.82	27.94	16.57	2.62	29.72	10.16	604.10	0.27	3.40
Grassano	06/11/2020	193.19	25.52	18.27	1.98	23.39	7.86	625.46	0.23	2.73
Grassano	24/02/2021	198.56	27.41	18.10	2.48	29.52	9.66	640.20	0.14	3.39
Grassano	16/04/2021	145.00	23.50	18.18	1.63	27.08	9.28	605.17	0.22	2.54
Grassano	12/05/2021	146.14	25.16	18.23	1.82	19.97	7.08	610.20	0.16	1.99
Grassano	18/06/2021	164.97	25.33	17.66	2.08	24.90	8.73	616.30	0.19	2.58
Grassano	20/07/2021	189.04	27.94	16.48	2.40	34.12	11.67	625.46	0.239	3.80
Grassano	31/08/2021	183.70	25.77	16.87	2.28	25.58	9.81	625.46	0.15	2.71
Grassano	28/10/2021	131.92	25.44	16.13	2.34	28.07	9.73	521.72	0.14	2.96
Grassano	31/01/2022	178.14	23.30	14.08	1.90	21.02	7.72	604.10	0.11	2.44
Grassano	16/03/2022	179.61	22.80	15.58	2.16	26.11	8.82	628.51	0.13	2.89
Telese Terme	08/01/2020	536.87	70.57	124.77	14.64	147.72	42.53	1650.00	0.45	
Telese Terme	17/02/2020	416.99	40.57	92.71	10.86	101.55	44.37	1530.00	0.50	
Telese Terme	18/06/2020	445.71	61.91	95.54	12.97	192.05	52.74	1510.25	0.46	
Telese Terme	23/07/2020	508.96	76.23	145.62	15.95	205.92	49.87	1723.82	0.24	
Telese Terme	04/09/2020	529.76	74.18	129.38	15.20	191.61	45.76	1751.27	0.76	1.24
Telese Terme	06/11/2020	567.37	69.31	139.16	15.45	180.96	47.54	1790.94	1.28	
Telese Terme	24/02/2021	424.00	41.81	62.08	7.42	89.69	40.25	1464.48	0.49	1.78
Telese Terme	16/04/2021	297.52	40.99	57.98	5.97	87.25	27.41	1128.87	0.62	0.89
Telese Terme	12/05/2021	335.70	43.94	60.66	6.49	77.65	22.03	1159.38	0.60	0.44
Telese Terme	18/06/2021	392.96	52.47	66.95	6.59	90.07	25.90	1372.95	0.50	
Telese Terme	20/07/2021	400.39	50.72	59.06	8.08	121.69	35.21	1253.96	0.58	2.39
Telese Terme	31/08/2021	456.40	53.53	89.41	9.99	139.61	43.68	1513.30	0.55	1.09
Telese Terme	28/10/2021	438.28	66.29	125.05	13.36	234.09	58.10	1391.26	0.42	
Telese Terme	31/01/2022	355.76	35.01	65.22	6.83	74.17	26.96	1226.50	0.39	0.54
Telese Terme	16/03/2022	406.26	39.33	64.36	6.82	92.66	26.53	1287.52	0.42	1.19
Rio Freddo	08/01/2020	54.48	6.57	2.70	1.80	4.52	10.20	170.00	0.09	1.58
Rio Freddo	17/02/2020	50.14	3.68	2.37	0.21	3.16	1.85	169.30	0.11	1.69
Rio Freddo	18/06/2020	50.39	8.80	1.95	0.54	3.29	2.38	204.42	0.23	1.85
Rio Freddo	23/07/2020	45.01	6.08	2.06	0.69	4.29	2.55	170.86	0.10	2.48
Rio Freddo	04/09/2020	49.73	6.38	1.97	0.46	4.02	2.60	173.91	0.18	2.17
Rio Freddo	06/11/2020	54.37	5.27	2.27	0.50	3.19	2.07	176.96	0.13	2.08
Rio Freddo	24/02/2021	62.39	7.94	2.35	0.75	4.25	2.56	201.37	0.12	1.92
Rio Freddo	16/04/2021	40.96	6.40	2.14	0.31	3.14	2.22	167.81	0.09	1.03
Rio Freddo	12/05/2021	55.13	6.93	2.24	0.20	3.50	2.56	189.16	0.14	2.06
Rio Freddo	18/06/2021	49.06	7.30	2.16	0.53	2.28	1.77	192.21	0.11	1.40
Rio Freddo	20/07/2021	58.29	9.17	2.15	0.56	4.19	3.49	207.47	0.19	2.16
Rio Freddo	31/08/2021	56.04	8.56	2.26	0.50	2.95	2.40	198.32	0.11	1.62
Rio Freddo	28/10/2021	53.75	7.73	2.13	1.04	3.97	2.91	210.52	0.07	1.42
Rio Freddo	31/01/2022	60.34	7.32	1.87	0.51	2.51	1.88	216.62	0.10	1.20
Rio Freddo	16/03/2022	56.28	7.23	1.91	0.49	3.37	2.32	204.42	0.09	1.77
Capovolturno	08/01/2020	106.25	14.30	3.22	0.73	2.61	10.98	350.00	0.15	1.05

Capovolturno	17/02/2020	103.86	9.99	2.42	0.16	2.80	13.90	335.20	0.19	1.06
Capovolturno	18/06/2020	91.09	14.06	2.08	0.57	3.67	12.97	317.30	0.18	1.33
Capovolturno	23/07/2020	93.20	15.08	2.39	1.14	3.84	12.41	314.25	0.19	1.14
Capovolturno	04/09/2020	89.44	14.13	2.02	0.49	3.18	11.57	299.00	0.19	1.33
Capovolturno	06/11/2020	94.15	12.71	2.29	0.59	2.19	8.10	317.30	0.07	1.04
Capovolturno	12/05/2021	102.95	13.99	2.03	0.36	3.06	13.80	338.66	0.17	1.19
Capovolturno	18/06/2021	90.71	12.93	2.32	0.75	2.80	12.67	341.71	0.10	1.13
Capovolturno	20/07/2021	110.88	15.49	2.12	0.60	3.67	16.66	430.19	0.17	1.56
Capovolturno	31/08/2021	98.83	14.01	2.21	0.49	2.53	11.11	329.51	0.09	0.99
Capovolturno	28/10/2021	92.25	12.54	2.04	0.71	2.75	9.13	314.25	0.07	1.02
Capovolturno	31/01/2022	95.44	12.21	1.76	0.54	2.73	10.65	308.15	0.06	0.94
Capovolturno	16/03/2022	110.25	12.54	1.80	0.47	3.09	13.09	375.27	0.10	1.12

Spring	Date	δD ‰ V-SMOW	δ¹⁸O ‰ V-SMOW
Grassano	08/01/2020	-46.8	-7.94
Grassano	17/02/2020	-46.5	-7.96
Grassano	18/06/2020	-48.1	-8.06
Grassano	22/07/2020	-47.8	-8.1
Grassano	06/11/2020	-46.1	-7.8
Grassano	24/02/2021	-46.2	-7.8
Grassano	16/04/2021	-46.80	-7.83
Grassano	18/06/2021	-46.76	-7.83
Grassano	20/07/2021	-46.75	-7.81
Grassano	31/08/2021	-46.89	-7.86
Grassano	28/10/2021	-45.32	-7.81
Telese Terme	08/01/2020	-48.1	-7.84
Telese Terme	17/02/2020	-47.9	-7.84
Telese Terme	18/06/2020	-48.1	-7.80
Telese Terme	22/07/2020	-48.6	-7.85
Telese Terme	04/09/2020	-48.8	-7.86
Telese Terme	24/02/2021	-46.1	-7.69
Telese Terme	16/04/2021	-46.20	-7.67
Telese Terme	18/06/2021	-46.63	-7.63
Telese Terme	20/07/2021	-46.85	-7.71
Telese Terme	31/08/2021	-46.82	-7.62
Telese Terme	28/10/2021	-46.15	-7.57
Rio Freddo	08/01/2020	-55.09	-8.81
Rio Freddo	17/02/2020	-54.72	-8.80
Rio Freddo	18/06/2020	-55.48	-8.89
Rio Freddo	23/07/2020	-55.83	-8.84
Rio Freddo	04/09/2020	-54.53	-8.82
Rio Freddo	24/02/2021	-51.97	-8.59
Rio Freddo	16/04/2021	-52.00	-8.58
Rio Freddo	18/06/2021	-52.74	-8.66
Rio Freddo	20/07/2021	-52.76	-8.69
Rio Freddo	31/08/2021	-53.02	-8.75
Rio Freddo	28/10/2021	-51.64	-8.76
Capovolturno	08/01/2020	-60.7	-9.22
Capovolturno	17/02/2020	-60.9	-9.34
Capovolturno	18/06/2020	-61.9	-9.42
Capovolturno	23/07/2020	-61.4	-9.42
Capovolturno	04/09/2020	-61.8	-9.45
Capovolturno	06/11/2020	-57.6	-9.20
Capovolturno	18/06/2021	-58.15	-9.18
Capovolturno	20/07/2021	-57.95	-9.22
Capovolturno	31/08/2021	-57.98	-9.22
Capovolturno	28/10/2021	-57.02	-9.35

Spring	Date	Li ppb	B ppb	V ppb	As ppb	Rb ppb	Sr ppb	Cs ppb	Ba ppb
Grassano	08/01/2020	54.02	393.4	1.462	0.51	5.78	165.2	1.627	
Grassano	17/02/2020	51.48	347.8	1.714	0.53	5.637	162.1	1.556	
Grassano	18/06/2020	63.92	346.9	1.23	0.221	5.392	151.7	1.494	
Grassano	23/07/2020	68.02	348.4	1.821	0.388	5.845	200.4	1.614	14.52
Grassano	04/09/2020	67.45	340.5	2.173	0.265	5.707	259.2	1.593	14.27
Grassano	06/11/2020	62.19	414.9	1.63	0.471	4.409	290	1.122	17.44
Grassano	24/02/2021	64.67	479.7	1.655	0.612	4.33	284	1.109	17.1
Grassano	16/04/2021	45.79	268	1.651	0.472	2.951	192.9	0.78	12.19
Grassano	12/05/2021	48.36	298.4	1.586	0.477	3.002	195.2	0.793	12.24
Grassano	18/06/2021	59.59	375.5	1.583	0.543	4.512	256.7	1.156	13.56
Grassano	20/07/2021	61.99	398.1	1.599	0.636	4.421	260.7	1.152	13.56
Grassano	31/08/2021	54.11	499.6	1.782	0.477	5.063	279.7	1.377	15.64
Grassano	28/10/2021	37.49	239.9	1.421	0.36	3.466	185.9	0.979	10.99
Grassano	31/01/2022	39.59	252.9	1.363	0.391	3.621	190.9	0.988	11.09
Grassano	16/03/2022	54.84	364.3	1.849	0.495	4.797	263.5	1.357	15.13
Telese Terme	08/01/2020	295.3	1224	0.64	0.079	30.16	407.8	15.55	
Telese Terme	17/02/2020	391.3	1065	0.59	0.02	23.64	352.4	11.61	
Telese Terme	18/06/2020	355.8	1342	0.524	0.147	31.22	424.9	15.34	
Telese Terme	23/07/2020	491.4	2240	0.63	0.319	38.87	636.9	19.36	47.65
Telese Terme	04/09/2020	730.5	3306	4.025	0.126	37.81	919.5	19.33	46.06
Telese Terme	06/11/2020	801.7	4901	1.044	<0.002	27.85	1303	13.03	51.71
Telese Terme	24/02/2021	380.1	2190	1.729	0.38	11.78	644.9	4.869	22.07
Telese Terme	16/04/2021	226.5	1180	0.689	0.153	7.88	360.5	4.021	17.73
Telese Terme	12/05/2021	230.5	1261	0.517	0.08	6.337	361.6	2.767	15.47
Telese Terme	18/06/2021	350.2	2098	0.201	0.045	13.12	669	5.574	21.95
Telese Terme	20/07/2021	343.1	2067	0.326	0.069	12.38	642.1	5.071	22.88
Telese Terme	31/08/2021	537.2	3474	0.829	0.054	22.25	1021	10.27	41.02
Telese Terme	28/10/2021	541.4	3051	0.674	0.21	23.25	940.9	11.98	40.43
Telese Terme	31/01/2022	251.3	1393	0.499	0.047	11.01	504.3	5.148	18.62
Telese Terme	16/03/2022	336.9	1992	0.724	0.018	15.6	705.1	7.079	26.98
Rio Freddo	08/01/2020	0.241	1.111	0.425	0.177	1.529	54.45	0.01	
Rio Freddo	17/02/2020	0.267	27.3	0.411	0.118	1.264	54.25	0.008	
Rio Freddo	18/06/2020	0.661	0.371	0.3	0.092	1.136	84.16	0.011	
Rio Freddo	23/07/2020	0.278	1.489	0.497	0.137	1.495	58.22	0.009	
Rio Freddo	04/09/2020	0.276	4.627	0.494	0.168	1.139	56.47	0.007	
Rio Freddo	05/11/2020	0.298	<0.002	0.4	0.106	0.961	74.84	0.007	6.42
Rio Freddo	24/02/2021	0.313	<0.002	0.483	0.141	1.035	93.11	0.005	8.699
Rio Freddo	16/04/2021	0.836	24.94	0.477	0.217	0.754	104.5	0.011	6.83
Rio Freddo	12/05/2021	0.487	5.215	0.43	0.194	0.649	68.9	0.008	4.928
Rio Freddo	18/06/2021	0.588	<0,002	0.004	0.26	0.894	83.98	0.01	5.122
Rio Freddo	20/07/2021	0.51	<0,002	<0,002	0.239	0.887	85.91	0.008	5.211
Rio Freddo	31/08/2021	0.607	5.986	0.541	0.249	1.285	101.4	0.011	6.624

Rio Freddo	28/10/2021	0.504	<0,002	0.431	0.216	0.838	82.97	0.01	5.043
Rio Freddo	31/01/2022	0.466	<0,002	0.427	0.167	0.79	75.44	0.009	4.731
Rio Freddo	16/03/2022	0.612	1.421	0.586	0.265	1.072	99.98	0.009	6.46
Capovolturno	08/01/2020	1.229	18.68	0.526	0.844	0.976	109.3	0.041	
Capovolturno	17/02/2020	1.616	24.31	0.786	1.139	1.19	123.9	0.164	
Capovolturno	18/06/2020	1.511	10.71	0.383	0.719	0.912	107.5	0.035	
Capovolturno	23/07/2020	1.486	11.15	0.513	0.844	1.102	111.5	0.028	
Capovolturno	04/09/2020	1.474	19.5	0.734	0.998	0.977	105.6	0.029	
Capovolturno	06/11/2020	1.309	5.061	0.467	0.869	1.092	133.5	0.02	16.84
Capovolturno	12/05/2021	1.213	11.77	0.501	1.114	0.588	99.37	0.018	12.24
Capovolturno	18/06/2021	1.316	4.724	0.003	1.236	0.801	125	0.021	12.95
Capovolturno	20/07/2021	1.33	4.943	0.022	1.242	0.743	122.1	0.022	12.93
Capovolturno	31/08/2021	1.291	16.5	0.552	0.932	0.889	133.9	0.026	15
Capovolturno	28/10/2021	0.943	3.957	0.477	0.871	0.706	95.66	0.03	11.39
Capovolturno	31/01/2022	1.131	6.479	0.521	0.97	0.704	105.2	0.04	12.2
Capovolturno	16/03/2022	1.487	14.28	0.574	1.339	0.914	145.5	0.03	16.22

Annex 1b

Grassano	T (°C)	pH	CE (µS/cm)
Minimum	11.4	6.92	869
Maximum	11.9	7.17	950
Mean	11.7	7.07	915
Standard deviation	0.1	0.1	24.7
Coefficient of variation	0.0	0.0	0.0

Telese	T (°C)	pH	CE (µS/cm)
Minimum	14.3	6.05	1680
Maximum	19.4	6.35	2820
Mean	16.5	6.20	2173.2
Standard deviation	2.0	0.1	399.8
Coefficient of variation	0.1	0.0	0.2

Rio Freddo	T (°C)	pH	CE (µS/cm)
Minimum	7.8	7.64	259
Maximum	8.6	8.11	319
Mean	8.3	7.93	290.8
Standard deviation	0.2	0.1	22.0
Coefficient of variation	0.0	0.0	0.1

Capovolturno	T (°C)	pH	CE (µS/cm)
Minimum	9.0	7.46	446
Maximum	13.8	7.86	538
Mean	11.6	7.69	496.8
Standard deviation	1.4	0.1	28.4
Coefficient of variation	0.1	0.0	0.1

Grassano	Ca	Mg	Na	K	Cl	SO4	HCO3	F	NO3
Minimum	131.9	19.1	14.1	1.3	20.0	7.1	521.7	0.1	2.0
Maximum	198.6	28.9	20.0	3.0	34.1	11.7	745.9	0.3	3.8
Mean	172.0	25.5	17.1	2.2	25.9	8.9	618.4	0.2	2.8
Standard deviation	19.7	2.5	1.5	0.4	4.1	1.2	44.2	0.1	0.5
Coefficient of variation	0.1	0.1	0.1	0.2	0.2	0.1	0.1	0.3	0.2

Telese	Ca	Mg	Na	K	Cl	SO4	HCO3	F	NO3
Minimum	297.5	35.0	58.0	6.0	74.2	22.0	1128.9	0.2	0.4
Maximum	567.4	76.2	145.6	16.0	234.1	58.1	1790.9	1.3	2.4
Mean	434.2	54.5	91.9	10.4	135.1	39.3	1450.3	0.6	1.2
Standard deviation	76.6	14.2	32.6	3.8	53.5	11.2	215.1	0.2	0.6
Coefficient of variation	0.2	0.3	0.4	0.4	0.4	0.3	0.1	0.4	0.5

Rio Freddo	Ca	Mg	Na	K	Cl	SO4	HCO3	F	NO3
Minimum	41.0	3.7	1.9	0.2	2.3	1.8	167.8	0.1	1.0
Maximum	62.4	9.2	2.7	1.8	4.5	10.2	216.6	0.2	2.5
Mean	53.1	7.0	2.2	0.6	3.5	2.9	190.2	0.1	1.8
Standard deviation	5.7	1.4	0.2	0.4	0.7	2.1	17.3	0.0	0.4
Coefficient of variation	0.1	0.2	0.1	0.6	0.2	0.7	0.1	0.4	0.2

Capovolturno	Ca	Mg	Na	K	Cl	SO4	HCO3	F	NO3
Minimum	89.4	10.0	1.8	0.2	2.2	8.1	299.0	0.1	0.9
Maximum	110.9	15.5	3.2	1.1	3.8	16.7	430.2	0.2	1.6
Mean	98.4	13.4	2.2	0.6	3.0	12.1	336.2	0.1	1.1
Standard deviation	7.6	1.4	0.4	0.2	0.5	2.2	34.7	0.1	0.2
Coefficient of variation	0.1	0.1	0.2	0.4	0.2	0.2	0.1	0.4	0.1

Grassano	Li	B	V	As	Rb	Sr	Cs	Ba
Minimum	37.49	239.90	1.23	0.22	2.95	151.70	0.78	10.99
Maximum	68.02	499.60	2.17	0.64	5.85	290.00	1.63	17.44
Mean	55.57	357.89	1.63	0.46	4.60	222.54	1.25	13.98
Standard deviation	9.64	74.92	0.23	0.12	0.99	49.03	0.29	2.13
Coefficient of variation	0.17	0.21	0.14	0.25	0.22	0.22	0.23	0.15

Telese	Li	B	V	As	Rb	Sr	Cs	Ba
Minimum	226.50	1065.00	0.20	0.02	6.34	352.40	2.77	15.47
Maximum	801.70	4901.00	4.03	0.38	38.87	1303.00	19.36	51.71
Mean	417.55	2185.60	0.91	0.12	20.88	659.59	10.07	31.05
Standard deviation	172.62	1085.17	0.93	0.11	10.65	281.54	5.61	13.27
Coefficient of variation	0.41	0.50	1.02	0.88	0.51	0.43	0.56	0.43

Rio Freddo	Li	B	V	As	Rb	Sr	Cs	Ba
Minimum	0.24	0.37	0.00	0.09	0.65	54.25	0.01	4.73
Maximum	0.84	27.30	0.59	0.27	1.53	104.50	0.01	8.70
Mean	0.46	8.05	0.42	0.18	1.05	78.57	0.01	6.01
Standard deviation	0.18	10.45	0.14	0.06	0.26	17.30	0.00	1.24
Coefficient of variation	0.39	1.30	0.33	0.31	0.25	0.22	0.19	0.21

Capovolturno	Li	B	V	As	Rb	Sr	Cs	Ba
Minimum	0.94	3.96	0.00	0.72	0.59	95.66	0.02	11.39
Maximum	1.62	24.31	0.79	1.34	1.19	145.50	0.16	16.84
Mean	1.33	11.70	0.47	1.01	0.89	116.77	0.04	13.72
Standard deviation	0.18	6.62	0.23	0.19	0.18	15.06	0.04	2.03
Coefficient of variation	0.14	0.57	0.49	0.19	0.20	0.13	0.99	0.15

Annex 2

Contursi Area

Spring	T °C	pH	EC µS/cm	Eh mV	TDS mg/L	Ca mg/L	Mg mg/L	Na mg/L	K mg/L	Cl mg/L	SO4 mg/L	HCO3 mg/L	F mg/L
S1	7.8	7.8	354	272.4	224.9	78.7	7.2	4.0	1.0	5.7	3.2	250.2	0.07
S2	7.9	7.7	300	252.7	191.6	55.2	10.2	3.2	1.0	5.1	2.4	228.8	0.05
S3	9.7	8.4	298	206.5	180.6	48.1	12.2	3.9	1.0	5.7	3.0	213.6	0.05
S4	10.5	7.4	518	298.7	306.6	92.5	14.8	5.9	1.4	7.9	5.7	357.0	0.12
S5	10.1	7.8	352	301.8	222.3	74.1	8.6	4.9	1.0	6.6	3.5	247.1	0.08
S6	12.1	7.5	398	178.3	259.9	97.0	1.9	7.6	1.3	9.5	5.3	274.6	0.07
S7	12.8	7.2	664	299.01	400.9	121.2	17.5	12.9	2.3	18.5	11.9	433.2	0.22
S8	14.3	7.5	613	166.3	380.5	132.6	5.5	13.5	0.9	19.4	14.9	387.5	0.16
S9	14.1	6.5	1090	85.8	722.4	243.4	22.8	21.5	3.9	28.7	16.1	771.9	0.25
S10	17.3	6.1	1981	-197.3	1436.3	454.3	47.8	88.1	9.8	102.1	40.0	1388.2	0.40
S11	14.7	6.5	1435	228.9	986.8	329.9	31.0	41.4	5.8	52.5	25.9	1000.7	0.24
S12	18.5	6.0	1924	-147.8	1403.4	407.5	49.6	112.3	12.2	136.8	52.0	1266.2	0.27
S13	14.4	6.6	1298	213.6	872.0	295.4	25.7	30.3	4.9	40.3	20.8	909.2	0.24
S14	13.8	6.8	1054	198	719.2	239.6	25.4	21.9	4.1	28.9	16.4	765.8	0.25
S15	26.4	6.3	2570	-224.5	1813.1	427.9	40.4	206.0	31.4	252.1	162.7	1385.2	1.12
S16	26.4	6.3	2560	-219.2	1964.4	440.4	43.1	210.0	31.0	320.6	202.3	1434.0	1.51
S17	24.8	6.2	2770	-197.5	2112.3	455.4	44.5	223.9	30.3	397.0	238.1	1446.2	1.15
S18	36.8	6.2	4460	-273.2	2628.0	248.7	94.3	438.5	67.8	795.4	266.3	1434.0	0.61
S19	37.5	6.3	4640	-258.5	3324.1	608.9	78.4	444.5	56.2	769.4	254.6	2224.2	1.49
S20	34.3	6.2	5240	-273.9	4020.6	639.1	85.5	617.4	73.7	1027.1	479.5	2196.7	1.84
S21	46.7	6.4	6380	-285	4345.1	288.4	132.9	995.8	115.7	1694.0	321.9	1592.6	1.39
S22	47	6.4	6470	-263	4951.8	598.2	127.3	1063.0	113.4	1485.9	389.3	2349.3	1.69

Spring	Li	B	Rb	Sr	Cs	Ba	δ2H ‰ V-SMOW	δ18O ‰ V-SMOW	3H TU	δ18O ‰ V-SMOW	δ34S ‰ V-CDT
	µg/L	µg/L	µg/L	µg/L	µg/L	µg/L					
S1	3.1	<0.002	3.9	33.8	1.6	8.2					
S2	<0.002	<0.002	2.0	29.9	0.04	5.2	-50.4	-8.5	1.4		
S3	0.2	<0.002	1.3	33.7	0.02	5.9					
S4	4.3	<0.002	1.8	114.9	0.04	13.2	-47.2	-8.0	1.0		
S5	<0.002	<0.002	1.8	32.9	0.03	5.6					
S6	<0.002	<0.002	2.5	81.4	0.01	9.6					
S7	24.3	132.5	2.6	191.7	0.7	13.8	-46.4	-7.8	2.2		
S8	3.5	21.8	0.5	721.8	0.04	30					
S9	94.4	688.7	5.6	359.1	2.6	13.9	-44.6	-7.5	2.2	6.8	9.7
S10	576.9	3545	18.6	902.0	10.4	22.2	-43.9	-7.4	1.7	8.4	18.0
S11	302.7	1818	13.6	566.1	11.9	21.3					
S12	779.9	4925	20.7	984	10.1	29.1					
S13	263.3	1871	9.4	516.4	4.9	15.8					
S14	108.7	1067	6.4	380.5	2.7	15.0					
S15	1602	9107	50.8	2331.0	57.7	53.4					
S16	1574	9176	52.7	2425.0	60.6	55.4	-38.4	-6.3	2.3	7.3	9.9
S17	1730	10620	103.3	2524.0	80.9	46.6	-39.0	-6.4	1.3	5.3	10.7
S18	3434	20470	203.1	4867.0	149.3	67.0	-42.1	-6.4	1.1	8.2	16.8
S19	3846	23230	219.1	5247.0	162.1	71.8					
S20	4737	28360	288.5	6810.0	214.5	78.2					
S21	6588	40650	409.5	9130.0	313.6	102.9	-48.1	-6.3	1.4	6.7	21.9
S22	6342	38640	387.5	8936.0	293.2	102.5					

Annex 3

Maro spring (Andalusia, Spain)

Spring	Date	Ca mg/L	Mg mg/L	Na mg/L	K mg/L	Cl mg/L	SO4 mg/L	HCO3 mg/L	F mg/L	NO3 mg/L
Maro	09/12/2021	155.5	39.1	19.3	2.3	38.0	296.1	219.3	11.1	1.0
Maro	17/01/2022	132.5	30.6	14.8	1.9	32.6	226.8	219.8	7.8	0.8
Maro	21/02/2022	132.5	31.2	15.3	2.1	34.3	238.8	216.9	8.1	0.9
Maro	21/03/2022	129.8	30.9	15.3	2.2	34.7	248.5	218.0	7.7	0.8
Maro	21/04/2022	120.7	27.1	13.7	1.9	31.8	229.7	215.7	6.8	0.8
Maro	26/05/2022	124.6	27.9	13.5	2.0	32.8	240.0	214.2	8.6	0.8
Maro	17/06/2022	127.5	28.7	14.6	2.0	33.4	246.8	214.1	8.2	0.8
Maro	15/07/2022	129.9	29.5	14.9	2.0	34.4	255.4	217.0	8.7	0.8

	Ca	Mg	Na	K	Cl	SO4	HCO3	F	NO3
Minimum	120.67	27.08	13.52	1.90	31.77	226.83	214.13	6.84	0.76
Maximum	155.45	39.15	19.28	2.28	38.02	296.13	219.80	11.06	0.96
Mean	131.61	30.64	15.17	2.04	33.99	247.78	216.88	8.36	0.83
Standard deviation	10.44	3.74	1.79	0.13	1.92	21.73	2.14	1.24	0.06
Coefficient of variation	0.08	0.12	0.12	0.06	0.06	0.09	0.01	0.15	0.08

	CE (µS/cm)	pH
Minimum	847.00	7.80
Maximum	940.00	8.20
Mean	898.14	8.08
Standard deviation	36.02	0.15
Coefficient of variation	0.04	0.02

Acknowledgements